Forschungszentrum Karlsruhe

in der Helmholtz-Gemeinschaft

Wissenschaftliche Berichte

FZKA 6820
EUR 20652 EN

Nuclear Fusion Programme
Annual Report of the
Association Forschungszentrum Karlsruhe/
EURATOM
October 2001 - September 2002

compiled by W. Bahm
Programm Kernfusion

Forschungszentrum Karlsruhe GmbH, Karlsruhe
2003

Introduction

Nuclear fusion represents a most promising option for a resource independent, sustainable, inherently safe and clean source for future global energy supply. Fusion research therefore has to fully explore this option as to provide a complete basis of proven information whether energy production by fusion is technically feasible, ecologically tolerable and finally, economically meaningful.

The FZK fusion research programme is fully integrated in the European Fusion Programme which follows a road map towards commercial fusion energy (Fig. 1). Three major elements of research and development are required in order to generate the know-how for the construction of a fusion power station DEMO/PROTO:

- A base physics programme targeted to improve capabilities to simulate plasma confinement concepts while making use of existing experimental facilities.
- A major facilities programme including ITER as the most important next step, IFMIF for the qualification of materials for DEMO and a component test facility.
- A base technology programme comprising plasma support technologies such as superconducting magnets, fuelling systems, high heat flux components, remote maintenance, reactor relevant steady state plasma heating systems etc., and fusion power technologies such as breeding blankets, helium cooled divertor and tritium extraction systems.

The activities of all the European fusion laboratories (known as EURATOM Associations) and industry are combined into one organisational structure via the European Fusion Development Agreement (EFDA). EFDA has a leader and two associate leaders (one for JET and one for fusion technology). It is guided by a steering committee, consisting of the heads of association laboratories, which has to approve the major strategy and annual work programmes as well as large contracts with industry or associations.

Within this framework FZK is developing key technologies in the areas of superconducting magnets, microwave heating systems (Electron-Cyclotron-Resonance-Heating, ECRH), the deuterium-tritium fuel cycle, He-cooled breeding blankets, a He-cooled divertor and structural materials as well as refractory metals for high heat flux applications including a major participation in the international IFMIF project. Furthermore investigations on plasma wall interactions and core and divertor modelling are carried out.

The results from experimental activities such as the tests of superconducting model coils in the test facility TOSKA, the quasi-stationary gyrotron operation and the operation of fuel cycle subsystems and components with deuterium-tritium have already been utilised for the design work for ITER. In addition large progress has been made in the development of breeding blankets and in the structural materials development as well as initial progress in the development of a He-cooled divertor for DEMO. All of this work has already been utilised in the European reactor studies.

Once the decision to build ITER is made, substantially stronger efforts need to be dedicated towards engineering design demands, which will also become increasingly true for the DEMO-related work. In order to efficiently manage these tasks a project-oriented approach is required involving a quality assured and quality controlled exploitation of R&D results. The detailed design and construction of ITER components and subsystems needs to be supported by experiments such as prototype testing, validation of scale up factors and additional R&D. This process shall result in the development of complete licensable components and systems. In a later phase support has to be provided to industrial partners who shall produce, assemble and finally install the components or systems into ITER, taking quality control and licensing aspects into account. However, the responsibility for the performance and the overall management of the procurement, installation and commissioning shall remain with the designers.

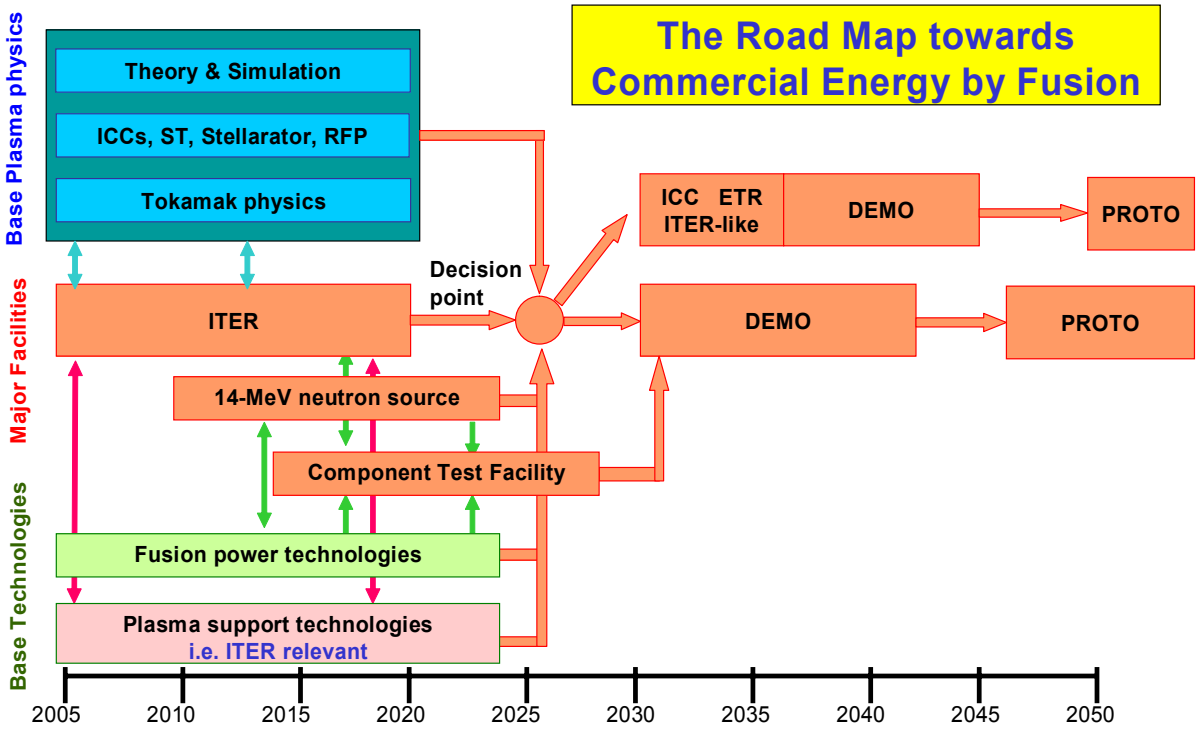

In order to meet this challenge, a project-oriented organisation structure has been introduced in the FZK fusion programme by establishing task forces in the areas Blanket/Divertor, Microwave Heating, Fuel Cycle and IFMIF (14 MeV neutron source). A task force which is responsible for a large component or subsystem to be delivered to ITER can be seen as a design and development division with a division head and several groups, each of them having a group leader. A team of design engineers supported by CAD constitutes the nucleus of each group in the task force. Besides the above-mentioned task forces, our expertise in the areas superconducting magnet development and materials research will be also applied for ITER construction and for the DEMO-relevant work.

About 200 professionals and technicians are involved in the fusion programme of the Association FZK-EURATOM with additional support of the technical departments.

Progress from October 2001 to September 2002 is reported. More information is available from the programme management and from the responsible scientists. The website www.fzk.de/fusion offers further access to the fusion activities of FZK.

Contents Page

Introduction

Page

Page

Page

Page

Heating and Current Drive

TPDC/IRRCER
Ceramics for Heating and Current Drive, and Diagnostics Systems: Irradiation Effects

1. Introduction

In electron cyclotron wave systems for heating and current drive (ECH-CD) and for plasma diagnostics, special window structures have to fulfil vacuum operation and tritium retention requirements with ideally broadband transmission and low power absorption. Actual window materials, which are CVD diamond for high power transmission and fused silica for broadband transmission, imply a potential use over a wider spectral range reaching from DC/RF applications to optical systems. Specially radiation hard 'fused quartz' silica grades, and above all the grade KU1, are studied in the framework of the ITER technology programme. Recently the grade KS-4V, which was originally developed for optical fibers, has raised interest for window applications.

Material performance analysis requires a data base of mechanical strength as well as of dielectric/optical properties including studies dedicated to the onset of radiation-induced material degradation. The R&D activity focused on effect of the structural damage caused by fast neutrons.

2. Status of the previous task period

First neutron irradiation studies which were performed for KU1 up to the 10^{-4} dpa level showed that the radiation effects were insignificant with the respect of the mechanical [1] and dielectric [2] properties at millimeter wave frequencies. This promising material behaviour should be verified for a wider spectrum of grades (i.e. KS-4V) and to higher damage levels up to 10^{-3} dpa.

Also for CVD diamond, the physical data base was well established by previous work in this task. This is especially true for dielectric loss at EC wave frequencies as well as for thermal conductivity [3]. Accordingly a torus window demonstrator prepared from a disk which was pre-irradiated to 10^{21} n/m^2 (E>0.1 MeV) was successfully tested under high power operation (see Task TPHE/ECRWIN). For diagnostic applications, the onset of radiation-induced degradation in infrared transmission and mechanical strength remained as an open issue.

3. Results from the present R&D work

Both radiation hard 'fused quartz' silica grades have a very low content of metallic impurities (< 5 ppm). A characteristic difference lies in the concentration of OH which is significant in KU1 (800-900 ppm) and extremely low in KS-4V (< 0.2 ppm). For reference, the commercially wide-spread quartz glass 'Infrasil 301' from Heraeus (Hanau, D) was included into the irradiation programme which is also produced with low OH content (< 10 ppm) but with a nominally higher metallic impurity content mainly due to the presence of 10-20 ppm Al.

Dielectric measurements were performed at 90-100 GHz which is characteristic for window materials in electron cyclotron emission (ECE) diagnostics. It is found that permittivity is larger in KU1 than in the other grades by 0.02. Specimens irradiated to 10^{21} n/m^2 did not differ in permittivity from their unirradiated control specimens. However, for the irradiation to 10^{22} n/m^2 an increase in permittivity is observed for all grades which amounts to 0.01 (KU1), 0.015 (Infrasil 301) and 0.035 (KS-4V). This small effect ranging at the 0.5-1% level is well described by an enhanced density of the dipoles extrapolated from a densification of the glass observed at this fluence level. In the dielectric loss tangent, there is a well-distinguished difference between the KU1 and the KS-4V grade. Loss in KS-4V is practically identical with that in Infrasil 301 ($3\cdot10^{-4}$). This indicates that the higher losses in KU1 ($10\cdot10^{-4}$) are related with its much higher OH-content. At the 10^{-3} dpa level, the first evidence of additional radiation-induced loss in KS-4V and Infrasil 301 is given by a 10% increase. In KU1, this small part is apparently still masked by the OH contribution [4].

For mechanical strength, one important parameter is set by the surface quality. It was shown by the previous studies on Infrasil 301 disks (11 mm dia.) that surface roughness is a major strength limiting factor even in the presence of structural damage at the 10^{-4} dpa level [1]. For the present reference tests, the specimen diameter was larger (17 mm dia.) to correspond to the geometries of the radiation hard quartz glasses. The results for the same fluence level obtained with the larger disks correspond very well to the previous results for the specimens tested with optically polished face (280 MPa as compared to 264MPa). The median strength measured for the fluence 10^{22}n/m^2 even exceeded the outstanding values found before for the control specimens (380 MPa as compared to 318MPa). Again the Weibull parameter m ranged around 7.

Also in the present studies, for each test condition only 2-4 KU1 and KS-4V specimens were available. Thus Weibull parameters could not be assessed. As a further consequence, mainly machined faces were tested which had a well-defined surface quality (Ra ≈ 0.5 µm). A comparable strength as for Infrasil 301 (machined surface quality showing median strength: 148 MPa) was observed. Some KS-4V specimens were tested separately with fine-polish faces (Ra ≈ 0.1 µm) for which the mean value of bending strength fell between data for the optical and the machined surface quality (cf. Table 1). Throughout all test conditions, the absence of any effective strength reduction even at the highest fluence level was clearly demonstrated. Also for CVD diamond, the previously assigned median strength level of 400 MPa (growth side under tensile stress) [1] was even found to be a safe lower bound for the specimens irradiated to 10^{22} n/m^2.

Tab. 1: Mean values of the bending strength measured by ball-on-ring tests on 17 mm disks of KU1 and KS-4V glass.

Neutron fluence (E>0.1MeV)	KU1 machined surface	KS-4V machined surface	KS-4V fine polish
Unirradiated	137(±35)MPa	122(±5)MPa	195(±12)MPa
10^{21} n/m^2	110(±16)MPa	143(±6)MPa	220(±50)MPa
10^{22} n/m^2	158(±27)MPa	160(±25)MPa	245(±75)MPa

Infrared transmission was measured in the NIR (1100-1700 nm), here the ideal transparency in the unirradiated state was reduced by factor of 2 in a neutron irradiated disk at 10^{21} n/m^2, and came down by one order of magnitude after a fluence of 10^{22} n/m^2 (cf. Fig. 1). Furthermore in cooperation with the FhG-IAF (Freiburg, D), it was determined calorimetrically for another optically polished disk (ER4-62-12, t=1.0 mm) irradiated to 10^{21}n/m^2, that the absorption coefficient at 10.6 □m increased from 0.1 cm-1 to 2.0 cm-1, which implies a reduction in transmittance by 20%.

4. Conclusions and outlook

The irradiation studies performed show a certain superiority of the KS-4V material with respect to microwave absorption which is apparently related with it is low OH content. The first onset of radiation-induced changes is found at 10^{-3} dpa. Yet, these

changes are small enough to be tolerated for the operation of a broadband window. Further mechanical strength is certainly not degraded up to fluences of 10^{22} n/m^2. As a major strength limiting factor, the surface quality of the glass outrules structural damage within the inspected level of up to 10^{-3} dpa. The observations underline a relative constancy of strength data for machined surfaces in the range of Ra=0.5-1 µm. When transferring the determined mechanical strength data to actual window structures, it is important to keep in mind that the actually chosen ball-on-ring test geometries study a rather small area. For large windows the critically loaded area has to be determined and the strength values scaled accordingly [1,4]. For this purpose, a safety factor of 2.5 should generally yields a conservative approach. For CVD diamond, it is confirmed that mechanical strength sets no critical bound to the fluences limit of the window structure. However, for infrared diagnostics the fluence of 10^{21} n/m^2 sets for certain an upper limit as the excellent transparency properties of CVD diamond are significantly degraded.

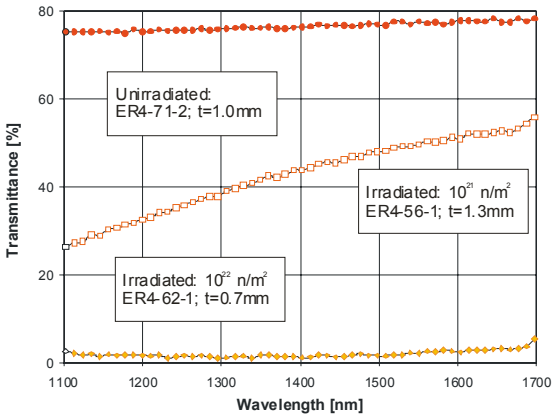

Fig. 1: Infrared transmission data through optically polished CVD diamond (expected transmittance for non-absorbing diamond: 72%).

With these studies, the data base for mechanical and dielectric properties of EC window materials has reached a consolidated base with respect to the definition of tolerable fluence levels. Questions are left open with respect to annealing effects in the degradation of the thermal conductivity which can be clarified by additional measurements of the brazed torus demonstrator. This issue like the aspect of hydrogen isotope permeation through window structure will be addressed in future in framework of the ERCH window development.

Staff:

M. Blumhofer
I. Danilov
R. Heidinger
A. Meier
M. Rohde
P. Severloh

Literature:

[1] R. Heidinger, Mechanical strength of neutron irradiated window materials, Proc. ICFRM-10, Baden-Baden (D), October 2001, Journal of Nuclear Materials, in press.

[2] R. Vila, J. Molla, R. Heidinger, A. Moroño, and E.R. Hodgson, Electrical and dielectric properties of irradiated KU1 quartz glass from DC to 145 GHz, Proc. ICFRM-10, Baden-Baden (D), October 2001, Journal of Nuclear Materials, in press.

[3] R. Heidinger, M. Rohde, R. Spörl, Neutron irradiation studies on window materials for EC wave systems, Fusion Engineering and Design, 56 – 57 (2001), 471-476

[4] R. Heidinger, Dielectric and mechanical properties of neutron irradiated KU1 and KS-4V glass, Proc. SOFT 22, Helsinki (D), September 2002

Contributions to ECRH Diamond Window Development

Introduction

Diamond disks manufactured by microwave plasma assisted chemical vapor deposition (MPACVD) have all properties to satisfy the requirements of torus windows - reliable vacuum and tritium barrier, microwave transmission characteristic. Due to low mm-wave losses (tan $\delta \leq$ 4x10-5), outstanding thermal conductivity ($\approx$ 1800 W/mK), good ultimate bending strength (400 MPa) and radiation tolerance up to a neutron fluence of 1020 n/m2 (10-5 dpa), water-edge-cooled MPACVD-diamond windows promise to provide a practical technical solution for the transmission of CW millimeter waves at power levels in excess of 1 MW.

JW1-EP ECRH FZK Window Unit for JET

As part of the JET-EP program a new design of a double-disk window unit has been performed for waveguide transmission with a diameter of 63.5 mm. In order to fulfill the JET safety rules for tritium operation a double-disk window had to be taken [1-5]. The new design of the double-disk window unit, which is based on a new brazing technology developed in collaboration with Thales Electron Devices (TED), Velizy, France, offers several important advantages compared to the window unit originally suggested for ITER. In particular the risk of Tritium contamination of the coolant is practically eliminated. Thus no special monitoring of Tritium in the coolant remains necessary. Because of the simpler mechanical design the reliability of the window unit is expected to increase. The microwave transmission characteristic allows the use of the window unit as well for 113.3 GHz and for 170 GHz.

The thickness of the single CVD-diamond disks has been specified and the geometry of the window unit has been determined. Further on, the thermal properties of the brazing contact between the CVD disk and a copper tube have been measured. As a result it has been found that no measurable increase of the thermal resistance inside the Ag/Cu-braze.

Beginning of 2002 the ECRH part of the JET EP programme has been stopped. Consequently the work on the microwave window has been concentrated on ITER and ASDEX-Upgrade. Two equally thick CVD-diamond disks (diameter: D=106 mm, thickness: t=1.808 mm) have been purchased and characterized. They are well suited for a double-disk window unit.

TW1-TPHE/ECRWIN ITER ECRF Window Development

A 1 MW, 170 GHz, CW CVD-diamond gyrotron window has been tested in collaboration with the RF-Home Team at 0.54 MW mm-wave power and 50 s pulse duration [6]. The common experiments are being continued with the aim to reach 1 MW power transmission at 100 s pulse length.

Overpressure tests on a 1 MW, 170 GHz, CW CVD-diamond torus winow unit with irradiated diamond disk (1021 neutrons/m2) (Fig. 1) were successfully performed in collaboration with JAERI, Japan. At an overpressure of 0.4 MPa (the specified value for ITER is 0.2 MPa) the displacement of the disk center was measured to be 48-50 µm in excellent agreement with FE calculations. The radial distribution of the displacement is azimuthally symmetrical. Endurance and instant overpressure tests were also carried out. The condition for the former was 0.4 MPa for 10 min (30 times for each side) and for the latter 0.7 MPa in 1 s.

Substantial progress has been achieved in collaboration with TED towards introducing a non-degrading brazing technology for CVD-diamond disks. Employing an Ag/Cu-braze (brazing temperature 800-850°) the bakeout temperature of gyrotrons can be up to 550°C and there is no corrosion of the braze. Yet a comprehensive follow-up of the window integration steps is still mandatory to keep evidence for potential increases above the ultralow bulk absorption levels and to identify efficient strategies for remedies.

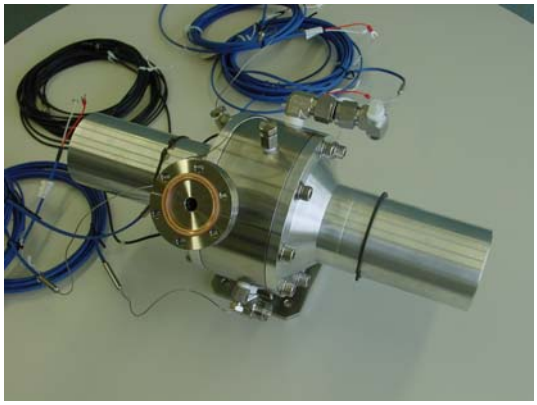

Fig. 1: View of the diamond window housing.

It has been demonstrated that light emission phenomena, as observed in high power operation, have without any doubt their origin at the vacuum face of the gyrotron window. They are created by (amorphous or nanostructured) carbon-based surface contaminants. They are concomitant phenomena and not a pre-failure alarm of high power gyrotron operation [7].

Staff:

A. Arnold (Uni Karlsruhe)
H.J. Burbach (IMF 1)
G. Dammertz
R. Heidinger (IMF 1)
S. Illy
A. Meier (IMF 1)
B. Piosczyk
M. Rohde (IMF 1)
R. Schneider
P. Severloh (IMF 1)
M. Thumm
X. Yang

Literature:

[1] X. Yang, E. Borie, G. Dammertz, R. Heidinger, B. Piosczyk, M. Thumm, D. Wagner, " Analysis of transmission characteristics for single and double-disk windows", Proc. 27th International Conference on Infrared and Millimeter Waves, September, 22-26, 2002, San Diego, USA, 2002, pp. 157-158.

[2] A.G.A. Verhoeven, W.A. Bongers, B.S.Q. Elzendoorn, M. Graswinckel, P. Hellingman, W. Kooijman, O.G. Kruijt, G.A.H. Maagdenberg, D.M.S. Ronden, J. Stakenborg, A.B. Sterk, J. Tichler, S. Alberti, M. Henderson, J.A. Hoekzema, J.W. Oosterbeek, A. Fernandez, K. Likin, A. Bruschi, S. Cirant, S. Novak, B. Piosczyk, M. Thumm, A. Kaye, C. Fleming, H. Zohm, J. Paméla, " Design of an ECRH system on JET", Proc. 27th International Conference on Infrared and Millimeter Waves, San Diego, USA, 2002, pp. 183-184 and 22nd Symposium on Fusion Technology September, 9-13, 2002, Helsinki, Finland and 12th Joint Workshop on

Electron Cylotron Emission and Electron Cyclotron Resonance Heating, May, 13-16, 2002, Aix-en-Provence, Frankreich.

[3] X. Yang, B. Piosczyk, R. Heidinger, M. Thumm, "A Double-disk Window Unit for the JET EP ECRH System", 22nd Symposium on Fusion Technology September, 9-13, 2002, Helsinki, Finland.

[4] A.G.A. Verhoeven, W.A. Bongers, B.S.Q. Elzendoorn, M. Graswinckel, P. Hellingman, W. Kooijman, O.G. Kruijt, G.A.H. Maagdenberg, D.M.S. Ronden, J. Stakenborg, A.B. Sterk, J. Tichler, S. Alberti, M. Henderson, J.A. Hoekzema, J.W. Oosterbeek, A. Fernandez, K. Likin, A. Bruschi, S. Cirant, S. Novak, B. Piosczyk, M. Thumm, A. Kaye, C. Fleming, H. Zohm, J. Paméla, " The design of the JET ECRH system and design considerations for ITER", 5th International Workshop on Strong Microwaves in Plasmas, August, 1-9, 2002, Nizhny Novgorod, Russia.

[5] M.A. Henderson, S. Alberti, J. Bird, B. Elzendoorn, T.P. Goodman, G. MacMillan, B. Piosczyk, L. Porte, A.G.A. Verhoeven, "Design of the evacuated waveguide transmission lines for JET-EP", 12th Joint Workshop on Electron Cylotron Emission and Electron Cyclotron Resonance Heating, May, 13-16, 2002, Aix-en-Provence, Frankreich.

[6] Heidinger, R., G. Dammertz, L. Steinbock, M. Thumm, "Characteristics of the light emission from CVD diamond windows", 12th Joint Workshop on Electron Cyclotron Emission and Electron Cyclotron Resonance Heating (ECE 2002), Aix-en-Provence, France, May 13-16, 2002.

[7] Borschegovsky, A.A., V.I. Ill'in, J.V. Roschin, I.N. Roy, N.V. Shapatkovskij, M.V. Agapova, V.N. Ill'in, V.E. Mjasnikov, V.O. Nichiporenko, L.G. Popov, S.V. Usachev, D.V. Hmara, G.G. Denisov, A.G. Litvak, V. I. Malygin, V.E. Zapevalov, M. Thumm, G. Dammertz, S. Illy, "Results of 170 GHz gyrotron tests", 12th Joint Workshop on Electron Cyclotron Emission and Electron Cyclotron Resonance Heating (ECE 2002), Aix-en-Provence, France, May 13-16, 2002.

TW2-TPHE/ECRDEV
ITER ECRF 170 GHz Gyrotron Development

Millimeter waves in the frequency range between 90 and 170 GHz can be used with great advantage for heating and controlling of instabilities in magnetically confined plasmas of thermonuclear fusion devices. Recently gyrotrons with an output power near 1 MW at a frequency of 140 GHz have been operated up to a pulse length of 180 s [1]. Thus 1 MW, CW gyrotrons are practically becoming state of the art.

For fusion experiments of the next generation such as the International Thermonuclear Experimental Reactor (ITER), a microwave power around 24 MW, CW at 170 GHz is required. To reduce the costs of the installations of the electron cyclotron wave (ECW) system and to make the launcher inside the torus more compact an increase of the output power per unit to about 2 MW is desired. Coaxial cavity gyrotrons have the potential to fulfill this requirement as has been demonstrated in short pulse (~1 ms) operation. Information necessary for a technical design and industrial manufacturing of a 2 MW, CW, 170 GHz coaxial cavity gyrotron has been obtained. In recent experiments on a 165 GHz, coaxial cavity gyrotron the data basis necessary for a technical design and for industrial manufacturing of such a tube has been completed. In particular the following investigations have been performed:

- measurement of the amount of microwave stray radiation inside the tube with improved accuracy
- influence of misalignment of the coaxial insert in the cavity on the gyrotron performance
- extension of the microwave pulse length
- measurement of the single-mode operating range and of the hysteresis effect due to variation of the beam voltage.

Short summary of the results [2-10]:

RF stray radiation:

The accuracy of measuring the amount of the microwave radiation P_{stray} captured inside the tube has been improved. In agreement with the previously reported results, the level of P_{stray} has been found to be (9 ± 1)% of the RF output power P_{out}. In order to decrease this value, modifications of the quasi-optical mode converter system are under consideration.

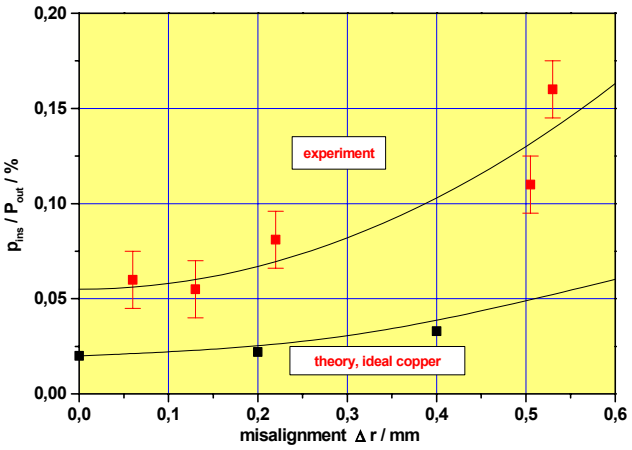

Fig. 1: The losses at the coaxial insert relative to the RF output power in dependence of the radial displacement of the coaxial insert.

Coaxial insert - influence of alignment:

The influence of misalignment of the coaxial insert on the operation of the gyrotron has been investigated. Inside the cavity the insert has been displaced with respect to the electron beam up to about $\Delta r \leq 0.55$ mm. The radial alignment of the outer cavity wall with respect to the electron beam was measured to be within 0.12 mm and has not been changed during this measurements. The experimental results are shown in Fig. 1 together with results of numerical simulations. The simulations have been performed for ideal copper at room temperature. A misalignment causes an increase of the microwave losses and in addition it results in a reduction of the range of single-mode operation due to enhanced mode competition. This effect was very pronounced at displacements above 0.5 mm. However, already at a misalignment of $\Delta r = 0.22$ mm an influence has been observed. Consequently, an alignment accuracy of the insert as good as $\Delta r \leq 0.15$ mm is required.

Extension of the pulse length:

An extension of the pulse length has been performed around the nominal parameters (beam current I_b = 50 A, cathode voltage U_c = 90 kV). After conditioning the tube for a few days microwave pulses with a length up to about 17 ms have been obtained. The limitation was due to a sudden rise of the current I_{ins} to the coaxial insert. There are strong indications that the sudden rise of I_{ins} is related to a built up of a discharge of Penning type. In an extensive numerical analysis of the whole gun, two regions have been found in which electrons can be trapped and thus perform oscillations, a small region between the cathode and the anode and a large region located between the coaxial insert and the cathode. Especially electrons from this large trapping region may diffuse along the potential surfaces into the accelerating gap and are then accelerated along the magnetic flux surface towards the coaxial insert contributing to I_{ins}.

Simulations show that the occurrence of regions with trapping character can be avoided by a proper shaping of the contours of the electrodes. The existence of regions where electrons can be trapped may degrade significantly the high voltage performance of a tube and have to be avoided by a proper design taking into account the real magnetic and electric field distribution.

Hysteresis effect:

Detailed measurements of cavity mode operation hysteresis have been performed for a constant magnetic field. The oscillating range for single-mode operation of the nominal $TE_{31,17}$ mode has been measured for different beam currents as for the rising and falling cathode voltage U_c. The hysteresis effect causes a dependence of the range of single-mode operation on the direction of the voltage variation.

Staff:

J. Anderer (Uni Karlsruhe)
A. Arnold (Uni Karlsruhe)
H. Baumgärtner
E. Borie
H. Budig
G. Dammertz
O. Drumm (Uni Karlsruhe)
S. Illy
M.V. Kartikeyan (AvH Fellow)
K. Koppenburg
H.-R. Kunkel
M. Kuntze
B. Piosczyk
J. Szczesny
M. Thumm
R. Vincon

Literature:

[1] G.Dammertz et al., "Progress of the 1 MW, 140 GHz, CW Gyrotron for W7-X", Proc. 27th Int. Conf. on Infrared and Millimeter Waves, San Diego, USA, 2002, pp. 3-4.

[2] B. Piosczyk, A. Arnold, G. Dammertz, O. Dumbrajs, M. Kuntze, and M. Thumm, "Coaxial Cavity Gyrotron - recent experimental results", IEEE Trans. Plasma Sci.June 2002.

[3] B. Piosczyk, A. Arnold, H. Budig, G. Dammertz, O. Drumm, M. Kuntze and M. Thumm, " ITER ECRF Advanced Source Development - Coaxial Cavity Gyrotron - Final Report - Wissenschaftliche Berichte, FZKA 6701, Februar 2002.

[4] O. Dumbrajs, T. Idehara, Y. Iwata, S. Mitsudo, I. Ogawa, B. Piosczyk, "Hysteresis in Gyrotrons", Proc. 27th Int. Conf. on Infrared and Millimeter Waves, San Diego, USA, 2002, pp. 331-332.

[5] B. Piosczyk, A. Arnold, H. Budig, G. Dammertz, O. Dumbrajs, O. Drumm, M.V. Kartikeyan, M. Kuntze, M. Thumm and X. Yang, " Experimental results and technical requirements for a 2 MW, CW, 170 GHz coaxial cavity gyrotron", Proc. 27th Int. Conf. on Infrared and Millimeter Waves, San Diego, USA, 2002, pp. 7-8.

[6] B. Piosczyk, A. Arnold, H. Budig, G. Dammertz, O. Dumbrajs, O. Drumm, M.V. Kartikeyan, M. Kuntze, M. Thumm and X. Yang, "Towards A 2 MW, CW, 170 GHz Coaxial Cavity Gyrotron for ITER", 22nd Symposium on Fusion Technology, September, 9-13, 2002, Helsinki, Finland

[7] B. Piosczyk, A. Arnold, H. Budig, G. Dammertz, O. Dumbrajs, O. Drumm, M.V. Kartikeyan, M. Kuntze, M. Thumm and X. Yang, "A 2 MW, CW Coaxial Cavity Gyrotron - experimental and technical conditions", 5th Int. Workshop on Strong Microwaves in Plasmas, August, 1-9, 2002, Nizhny Novgorod, Russia.

[8] D.V. Kas'yanenko, O.I. Louksha, B. Piosczyk, G.G. Sominski, M. Thumm, "Low-frequency parasitic oscillatons in the 74.2 GHz moderate-power pulsed gyrotron", 5th International Workshop on Strong Microwaves in Plasmas, August, 1-9, 2002, Nizhny Novgorod, Russia.

[9] B. Piosczyk, A. Arnold, H. Budig, G. Dammertz, O. Drumm, O. Dumbrajs, M. Kuntze, and M. Thumm,"A Coaxial Cavity Gyrotron- experimental results and technical conditions", 12th Joint Workshop on Electron Cylotron Emission and Electron Cyclotron Resonance Heating, May, 13-16, 2002, Aix-en-Provence, Frankreich

[10] B. Piosczyk et al., "A 2 MW, CW, 170 GHz Gyrotron for ITER", 19th IAEA Fusion Energy Conference, October, 14 -19, 2002, Lyon, France.

Plasma Facing Components and Plasma Modelling

T 436/01
Construction and Testing of Divertor Liner Components

Hot Liner

1. Introduction

Plasma sustained coatings play a growing role in science and technology, but particularly for soft and hard hydrocarbon coatings the underlying physical processes are not well understood. In the machines used in fusion research the formation of various films is a side-effect but do have a strong impact on the question whether or not graphite (CFC) can be used as wall material.

As long as carbon materials are the main candidates for manufacturing the divertor targets, sputtering and chemical erosion are to be expected as a result of plasma-wall interaction. It is well known that co-deposition of carbon with hydrogen isotopes on the cooler parts of the divertor surfaces is a basic mechanism for trapping of hydrogen isotopes. The gas mixtures containing hydrogen isotopes, atomic carbon, and some hydrocarbon radicals or molecules will pass the liner. The interaction between these gases and the liner surface is not only decisive with respect to deposition on the liner but also determines the properties of the released hydrocarbons. The liner is thus expected to mitigate the co-deposition problems in the pumping duct where the formation of soft, polymer-like films with high hydrogen contents (D,T/C ≈ 1) is likely.

In the framework of this project a realistic set-up (called “hot liner”) was tested for such conditions when the hydrocarbons are generated in a hydrogen plasma by chemical erosion at a graphite target. Furthermore, some additional experiments were performed where CH_4 was injected into a hydrogen discharge.

2. Starting Point and Progress

2.1 Target and target box

A target holder combined with a vacuum lock and a manipulator fitted with a 80 mm diameter graphite target, which, being exposed to the plasma, is an effective source of hydrocarbons. The nominal angle between the target surface and the magnetic field lines is 45 degree. The maximum target temperature was about 1000 K; it was controlled constant within 5 K. For all experiments we found U_{float} = 43 ± 0.5 V.

In later experiments the graphite target was enclosed in a floating molybdenum box provided with two orifices: one opening allowing the plasma beam to enter, the second allowing the formed hydrocarbons to reach the hot liner entrance. It should be noted that the floating potential of the target was not changed by the presence of the Mo-box. The reason for implementing this box was to enhance the hydrocarbon fluxes in the direction of the hot liner. In fact, no coatings were found at the inner walls of the box in post-experiment inspections.

2.2 Hot liner and duct equipment

Opposite to the target the hot liner and the pumping duct were installed. The set-up consists of an about 1 m long stainless steel pumping duct, consisting of two separate channels, combined with the hot liner head. The hot liner is supplemented by an additional turbo pump and a throttle-valve to allow a variation of the pumping speed. The side walls of the duct can be heated by six capton heaters (T_{max} = 450 K). By means of the heaters it is possible to impose a temperature profile along the duct. The duct is furthermore equipped with a number of silicon wafers, enabling an ex-situ measurement of the thickness of the coatings. Within the hot liner duct the pressure was in the same range after three hours of pumping but – caused by daily venting – the concentration of water vapour was in general one order of magnitude higher.

The arrangement of liner and pumping duct is shown in Fig. 1. For the pumping duct two different hot liner heads were manufactured (see Figs. 2 and 3). These heads act as a contact surface for the hydrocarbons arriving from the target chamber. For the head of type A, only a very low throughput could be realised. Here the heated Mo-cylinders are arranged in such a way that all hydrocarbons will have to perform at least one collision with the hot surface before entering the liner tube, i.e. there is no direct line of sight between plasma and liner duct. Each of the Mo-cylinders can be heated separately up to 1300 K.

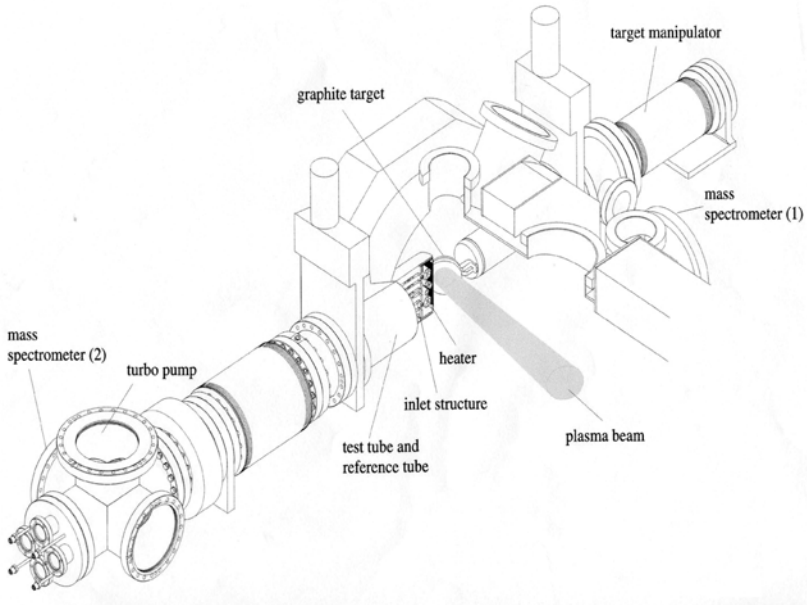

Fig. 1: Complete hot-liner arrangement in PSI-2.

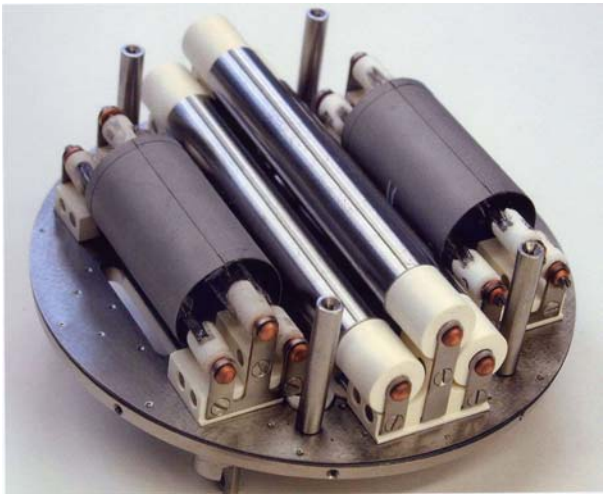

Fig. 2: View of type A hot liner: Five Mo-cylinders are in front of the entrance slits. The cylinders are heated up to 1300 K.

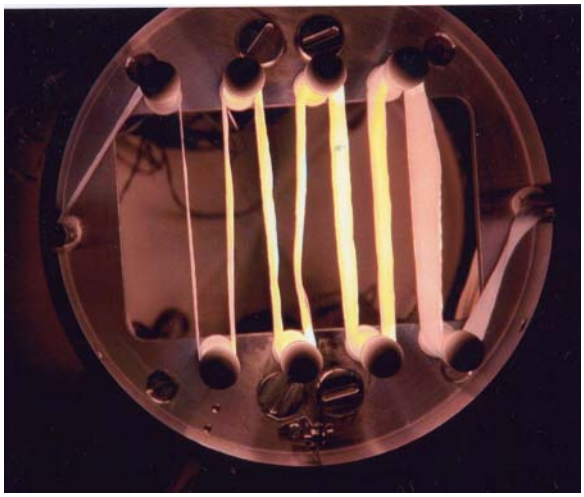

Fig. 3: Hot liner type B: A meander made from tantalum is placed at the entrance of the pumping duct.

In contrast, the head of type B, shown in Fig. 3, is optimised for a maximum gas throughput into the duct. The area of the heated band is about 220 cm^2. To achieve the desired surface temperature of 1300 K a heating current of 25 A is needed.

There are a number of parameters taking influence on the plasma in the target chamber. Among the most important ones are the neutral gas pressure in the target chamber and in the anode-cathode region and the discharge current . The end of the duct was additionally equipped with a liquid nitrogen cooled trap. Within this trap optical in-situ measurements of the layer thickness could be performed. At the end of the two identical duct halves a water cooled collector combined with an Si-wafer was installed.

Especially for the hot liner experiment the following additional diagnostics were installed:

- An OMA system was used to enable simultaneous detection of the CH-band intensity and the H_γ Balmer -line. These data give information about the stability of the hydrogen discharge (H_γ-intensity) and the concentration of methane (CH-band).

- For calibration of the diagnostics and other reasons it was required to inject known amounts of CH_4 into the target chamber. A calibrated mass flow controller was used in this context.

- During the experiments two differentially pumped quadrupol mass spectrometers (QMS) were in use. One was flanged to the target chamber, the other to the end of the hot liner duct. Starting from atomic mass 2 up to 44 (actually m/e is measured) the various hydrocarbons and other species of interest could be recorded automatically.

- In all experiments the thickness of the produced a-CH coatings was measured by two different methods:1) An ex-situ analysis of the spectral distribution of the reflected light in the visible range. 2) Based on the same principle an in-situ measurement could be established using a halogen lamp and a second OMA-system.

In both cases the refractive index of the coating must be known. For this purpose the thickness of some samples were first determined by means of an atomic force microscope and thereafter analysed by the cited optical methods. A typical number of 1.7 for the refractive index of soft hydrocarbon coatings was found this way.

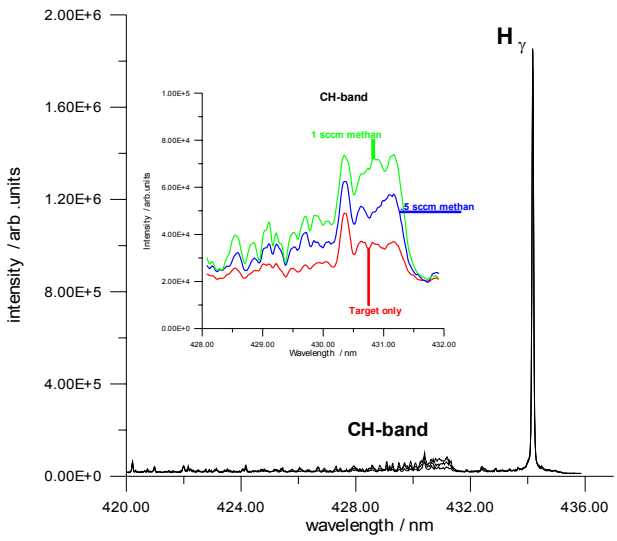

Fig. 4: Hα-line and CH-band intensities without and with injection of methane: target only (red), additional injection of 0.5 sccm (blue), additional injection of 1 sccm (green).

3. Experimental Results and discussions

3.1 Characterisation of the plasma in the target chamber

The plasma parameters were determined using the scanning Langmuir-probe. A typical value for the ion flux density is $2x10^{21}$ D^+/m^2s. For the determination of the erosion yield the CH-band emission and the CH_4-signal from the mass spectrometer were used, both being calibrated by injection of methane. An erosion yield between 3 and 5 % was found.

In Fig. 4 the CH-band and the Hα-line intensities are shown. It is obvious that the CH-intensity is very small compared to the Hα-line. Furthermore, up to injection of some sccm of methane into

the target chamber the intensity of the Balmer-line is not influenced (the typical flow of H_2 into the anode-cathode region is 100 sccm). This verifies the assumption that under such conditions the hydrocarbons as impurities have no impact on the plasma parameters. Injection of 0.5 sccm CH_4 is seen in Fig. 4 to nearly double the CH-band intensity. Hence, the methane concentration in the target chamber caused by erosion of the target is equivalent to a methane flux of about 0.5 sccm.

3.2 Equilibrium between erosion and deposition

In Fig. 5 the growth rate of the hydrocarbon layers is plotted as a function of surface temperature for two collector positions. As is to be seen from the figure this rate can be positive (deposition dominated) or negative (erosion dominated). In case of zero growth rate there is a balance between erosion and deposition. This equilibrium is found for temperatures of about 100° C, i.e. $T_0 \approx 370$ K, almost independent on collector position. In tendency this result is in agreement with the observations made by Jacobs et al. [1] but they found significantly higher transition compositions in the two experiments. In addition to surface temperature and flux density of the hydrocarbons we found indications that there is a third parameter of crucial importance: the flux density of atomic hydrogen. These chemically active particles are assumed to be essentially involved in the erosion process (either enhancing or enabling it). In earlier PSI-2 experiments [2, 3] it was found that the density of atomic hydrogen is approximately 10 % of the molecular density. Due to charge exchange processes a considerable fraction of the H-atoms acquires a rather high temperature of 2...4 eV. These information allow us to estimate a thermal flux density of about $2x10^{21}$ H-atoms/m^2s. Moreover, it was demonstrated in [4] that the contribution of these atomic fluxes to chemical erosion of graphite is by no means negligible.

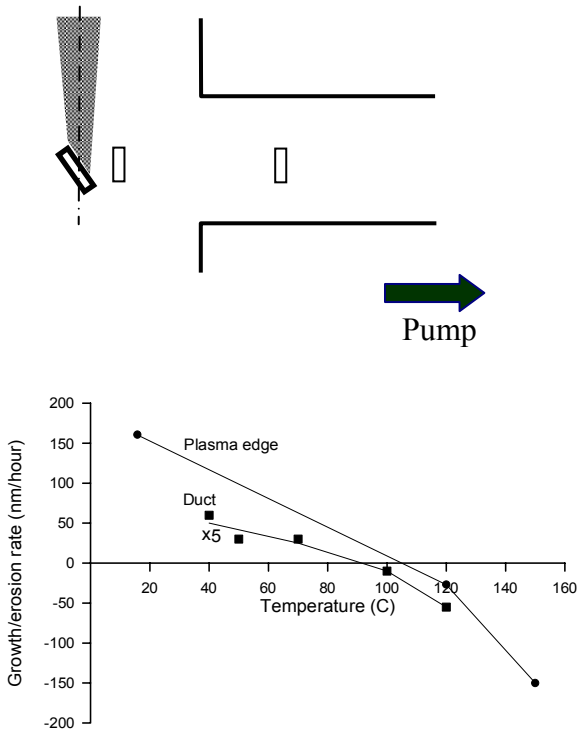

Fig. 5: Growth rate vs. Surface temperature. In the upper part the position of the two temperature for the two different distance to the target.

3.3 Film deposition and erosion in a duct equipped with a hot Ta-liner

Some experiments on film deposition inside the pumping duct were performed with a tantalum liner head at the duct entrance. In these experiments the QMS were used to measure the gas composition in the duct and in the target chamber. Several experiments were conducted at a discharge current of 160 A in which both, the temperature of the Ta-liner, and duct temperature were changed. Unfortunately the heat flux from the liner proved to be rather high making an accurate control of the duct temperature around 370 K impossible. Some caution is therefore required when interpreting the results. The trend, however, is clear: The hot Ta-liner enhances the film formation in the duct. Below only three experiments are described in details. The geometry of the experiment and the results are shown in Fig. 6. Two profiles in the bottom of the graph show the erosion rate along the duct with and without the graphite target. Again, the view of the balance between carbon sticking and film erosion is corroborated (see Fig. 5 for comparison). Very low erosion rates, even at a temperature of 440 K, indicate that the temperature is close to the transition value, probably due to the fact that recombination of atomic hydrogen by wall collisions is very effective. The thickness of the films deposited along the duct length in one of the experiments with a very hot Ta-liner is depicted on the upper half of the graph. The run started by heating the Ta-liner at 1000 - 1100 K. The head of the duct was heated from 300 to 370 K within 10 minutes. At this time the plasma was switched off. After a short break the plasma was again switched on and the duct temperature reached 440 K within the next 20 minutes. In the following 60 minutes the Ta temperature was reduced from 1100 to 700 K to keep the duct head temperature at around 440 K.

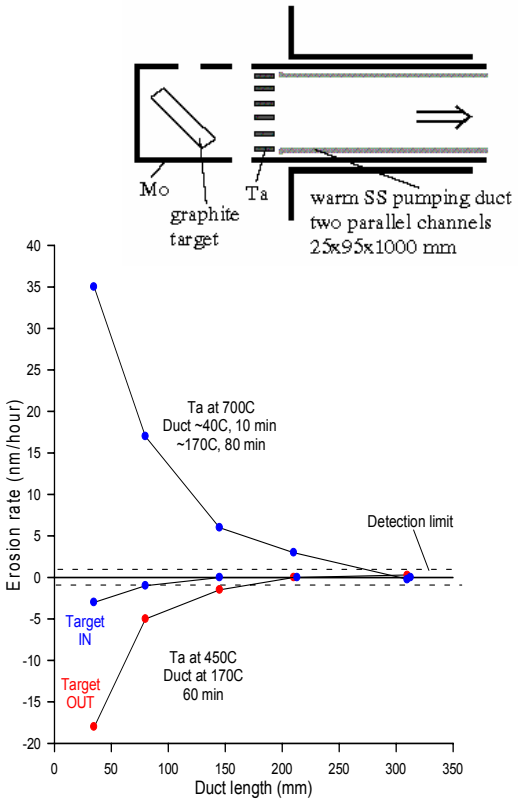

Fig. 6: Experiments on deposition and erosion in the duct with the heated Ta-liner. In the upper half of the graph the thickness (in nm, not the erosion rate) of the films as deposited during the corresponding runs is plotted.

We expected a net erosion rather than a net deposition due to the fact that the time the duct stayed at high temperature was significantly longer than the first 10 minutes of the exposure.

The result was rather surprising: the rather long exposure of the duct at 440 K did not remove the films that had been deposited in the preceding step. Three possible explanations are conceivable: 1) The hot Ta-liner produces additional reactive hydrocarbon species via pyrolysis. 2) The reflection coefficient of the reactive particles coming from the target is increased at the hot tantalum surface. 3) The recombination of atomic hydrogen is increased significantly at this surface. The latter however is not very likely because the temperature of the Ta-liner was first decreased during the run and thereafter kept around 700 K for about 60 min – conditions when erosion was observed in the first two runs (see bottom profiles). Another factor that might have to be taken into account for such non-isothermal exposure is the so called “dynamical erosion”. The erosion yield of the growing film may be higher than the static erosion of films deposited at lower temperature.

A special experiment was performed to assess the importance of pyrolysis. The graphite target was removed from the plasma beam. All other conditions were kept unchanged as far as possible. Methane was injected at a flow rate to produce nearly the same CH_4 partial pressure (measured with a QMS installed at the duct end) as in the runs with the graphite target in place. The Ta-liner temperature was increased within a few seconds from 600 to 800 and from 600 to 1100 K. In fact, the mass spectrometer showed a decrease of all hydrocarbon masses. The reduction was the larger the higher the Ta-temperature. Such a behaviour would be expected if the hydrocarbons pumped through the duct are disintegrated by pyrolysis at the liner. Without plasma, however, no remarkable changes in the hydrocarbon masses were detected. This is not in contradiction with the earlier results because for methane the pyrolysis rate is essential only at very high temperatures above 1200 K [5]. We thus conclude that plasma assisted pyrolysis of the hydrocarbons on the hot Ta-surface is of importance in our experiments.

4. Summary and consequences for ITER design

A set-up for testing of a hot liner and a pumping duct was built using the stationary hydrogen discharge of PSI-2. A large graphite target immersed into the plasma was the source of the hydrocarbons. The hydrocarbons and their behaviour under various conditions were diagnosed using QMS, optical spectroscopy, a cooled panel, and collector probes.

At all positions in the target chamber and for the first 20 cm (or beyond) of the pumping duct the film growth is determined by a balance between deposition of carbon containing species and erosion by atomic hydrogen. This balance depends on the collector temperature as a consequence of the temperature dependence of erosion. For PSI-2 conditions the critical temperature, where the transition from deposition to erosion takes place, is about 370 K.

A hot liner (a tantalum belt at about 1000 K) at the entrance of the pumping duct increases the growth rate of a-C:H films in the duct by pyrolysis of different hydrocarbons leading to species with high sticking probability.

Staff:

W. Bohmeyer
G. Fussmann
A. Markin*
D. Naujoks
H.-D. Reiner

*Guest scientist, Institute of Physical Chemistry of the Russian Academy of Sciences, Moscow

Literature:

[1] von Keudell, A., and W. Jacob: Growth and Erosion of Hydrocarbon Films Investigated by in situ Ellipsometry. J.Appl. Phys.**79** (2) (1996) 1092-1098.

[2] Steiger, A., K. Grützmacher, Ch. Seiser, M.I. de la Rosa and U.Johannsen: Measurement of Hydrogen Isotope Density by Two-Photon Induced Lyman-Fluorescence as a Proof for Tokamak Diagnostics. Spectral Line Shapes **10**, State College Pennsylvania 1998.

[3] Meyer, H.: Analyse der Plasmarotation in einer linearen Magnetfeldkonfiguration. Diss. Humboldt-Universität, Berlin 1998.

[4] Kornejew, P., W. Bohmeyer, H.-D. Reiner: Measurement of Chemical Erosion in the Plasmagenerator PSI-1. Physica Scripta **T81** (1998) 40-42.

[5] Schwarz-Selinger, T., V. Dose, W. Jacob, A. von Keudell: J. Vac. Sci. Technol. **A19** (1) (2001) 101.

T 438/01
Development and Testing of Time Resolved Erosion Detecting Technique: Speckle-Diagnostics

The project aims at the development of a non-contact optical surface measurement device based on the speckle effect, for long range and in situ diagnostics of arc traces, deformation, erosion, surface roughness and surface contour in the divertor region of experimental fusion devices.

Recent research of this project was mainly focused on phase – measurement by speckle interferometry. One disadvantage of interferometric measurements in general is a very high susceptibility to any movements and vibrations which normally have to be suppressed under laboratory conditions. Thus a new setup was developed (see Fig. 1), which is capable of recording all data necessary for contouring simultaneously by using a system of two cameras at synchronous operation. Therefore a multiline Ar-Ion Laser is used as a coherent light source. A proof of principle with first results was already presented last year.

1. Improvement of phase measurement

The performance of the measuring device was increased both by the application of better narrow band image quality interference filters and by a new, software-based and high accurate adjustment of the two cameras. The mechanical adjustment is supported by maps of calculated translation vectors showing the user the necessary changes of camera positions. Further misalignment is corrected automatically. Fig. 2 shows a measurement example obtained at a distance of 1 m with the improved measuring device.

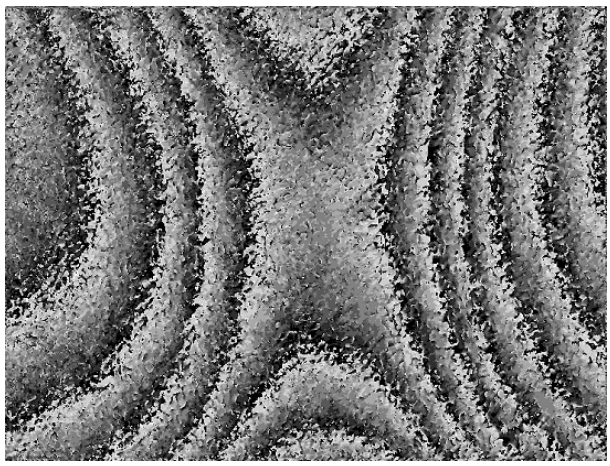

Fig. 2: Phase image of a saddle-shaped aluminium probe; synthetic wavelength λ_{synth} = 23,95 µm; measurement area: 8 mm x 6 mm.

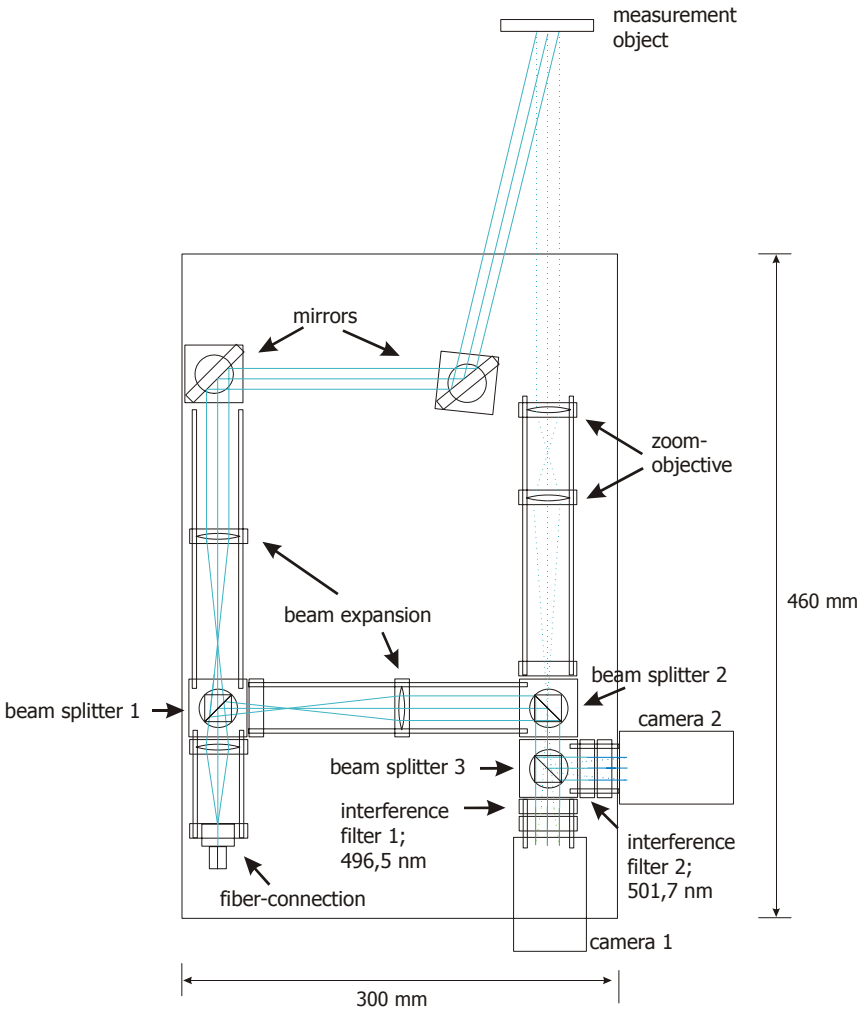

Fig. 1: Principle of the two-camera system.

One drawback of this kind of contour measurement in general is the limitation of the measurement sensitivity by the surface roughness. The synthetic wavelength λ_{synth} that determines the fringe spacing in the phase image has to be at least four times longer than the difference of height of two adjacent, resolvable points observed on the surface. In this setup the two closest Ar lines at 496,5 nm and 501,7 nm are used which provide a maximum synthetic wavelength of 23,95 µm. Thus it is possible to measure the contour of surfaces with a roughness up to 6 µm. By distinguishing at least 10 different grey levels of each fringe a resolution of surface height of about 2,4 µm is achieved. Since the gradient of surface height is also coded in the phase map, the distinction of surface erosion and material deposition is possible.

The detection of very slight erosions and microstructure changes requires even more sensitive measurement techniques. Therefore the measuring instrument was upgraded for the option of an additional, more sensitive measurements based on speckle photography.

2. Speckle image correlation

The speckle photography is a measurement technique where the scattered light reflected from a coherent irradiated measurement surface is digitally recorded. In contrast to speckle interferometry the speckle pattern is not superposed by a reference beam in speckle photography. Although speckle photographs are not suited for phase determination, they contain a lot of information of the surface microstructure. Thus for example it is possible to detect changes of the microstructure by calculating the similarity of sequentially recorded images. The similarity of images can be determined by a calculation of the two dimensional cross correlation coefficient $C_{I1,I2}$ according to equation (1), where e.g. $I_{1,n,m}$ denotes the intensity of a pixel at the position of the coordinates n, m of the first image.

$$C_{I1,I2} = \frac{\sum_{n=1}^{N}\sum_{m=1}^{M}\left(I_{1,n,m}-\bar{I}_1\right)\left(I_{2,n,m}-\bar{I}_2\right)}{\sqrt{\sum_{n=1}^{N}\sum_{m=1}^{M}\left(I_{1,n,m}-\bar{I}_1\right)^2 \cdot \sum_{n=1}^{N}\sum_{m=1}^{M}\left(I_{2,n,m}-\bar{I}_2\right)^2}} \quad (1)$$

The relation between the coefficient $C_{I1,I2}$ and surface change is given by equation (2). Here λ denotes the irradiation wavelength, Θ the angle between the observation direction and the surface normal resp. between the irradiation direction and the surface normal and $\sigma_{\Delta h}$ represents the variance of surface height changes.

$$C_{I1,I2} = \exp - [k^2 \cdot (1+\cos\Theta)^2 \cdot {\sigma_{\Delta h}}^2]; \quad k = \frac{2\pi}{\lambda}; \quad (2)$$

Since erosion leads to changes of surface heights, the variance of these changes can be determined by the purposed technique. In Fig. 3 this function is plotted for an angle Θ = 0° and different wavelengths from 400 nm to 600 nm.

As can be seen from Fig. 3 this function is very sensitive to any surface changes. Even when the variance of changes of surface heights reaches a value of 20 nm, the cross correlation coefficient is decreasing down to about 80 %.

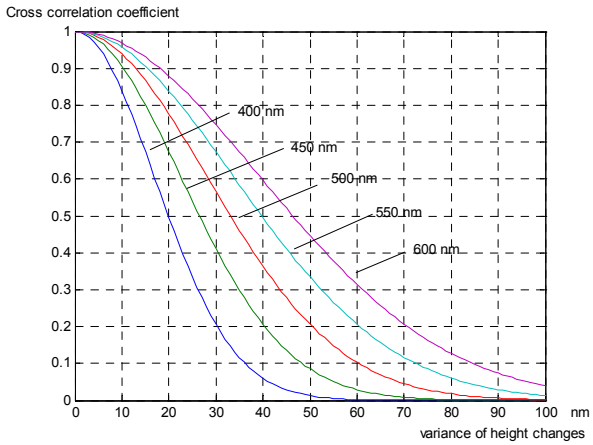

Fig. 3: Function of cross correlation coefficient versus variance of surface height changes $\sigma_{\Delta h}$; wavelengths 400 nm, 450 nm, 500 nm, 550 nm, 600 nm.

For obtaining information about surface microstructure changes with spatial resolution the images are divided into several sub-images. Then the cross correlation coefficient $C_{I1,I2}$ of each pair of sub-images is calculated and illustrated as a grey level in a correlation map. Thus each pixel of the correlation map is related to a corresponding area on the surface. The computing time depends both on the size of the images themselves and on the selected size of the sub-images. On a common personal computer with a 800 MHz CPU the calculation of a correlation map of two speckle photographs (732 x 579 pixels, 8 bit) at a size of sub-images of 10 x 10 pixels requires about 6 seconds.

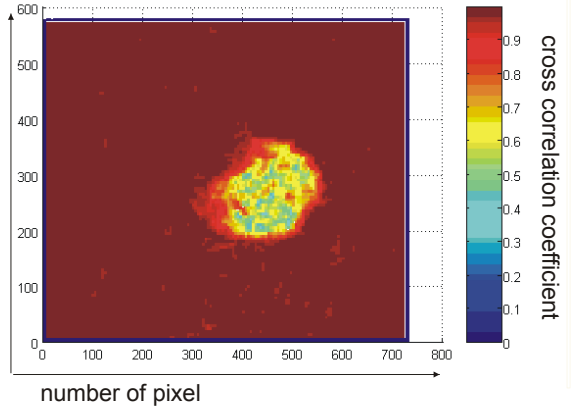

Fig. 4: Correlation map of speckle photographs recorded after the 11th laser pulse; area: 12 mm x 10 mm; size of sub regions: 10 x 10 pixe.

An example of a correlation map is illustrated in Fig. 4. This figure represents a correlation map calculated by means of speckle photographs that were recorded before and after applying a total number of 11 pulses of a Nd:YAG laser with about 150 mJ per pulse at 1064 nm at an aluminium surface. Because of the enormous sensitivity of the speckle images to any changes, the correlation coefficient is decreasing very fast to a minimum. Any further changes have no additional effect on this decrease. Thus it is necessary to compare each surface state with the next one. Fig. 5 shows the results of an experiment in which 20 laser pulses with an energy of 150 mJ

were applied to an aluminium surface. The eroded area was imaged completely. The x – axis represents the number of pulses while the y – axis denotes the correlation coefficient. Each pulse is the starting point of a new correlation curve. This technique is useful for locating and evaluating minute changes in the microstructure until changes of the surface height reach values which are in the range of the sensitivity of the contour measurement.

Further improvements are expected from the application of better high resolution cameras. Additionally a hardware based calculation of phase images and correlation maps is under development and will immensely reduce the required computing time.

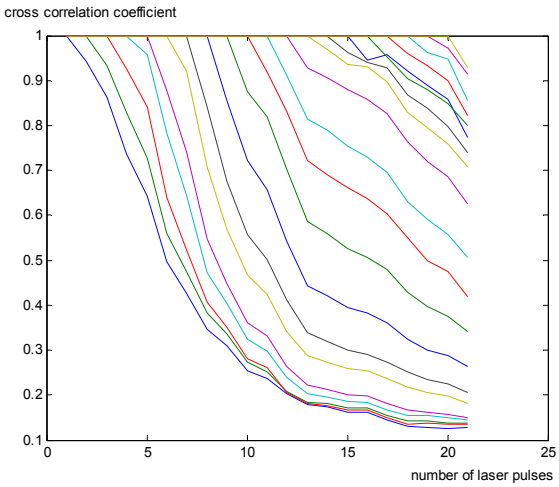

Fig. 5: Decreasing correlation of speckle images recorded before and after laser pulse erosion.

Staff:

A.W. Koch
A. Meixner

Literature:

[1] Meixner, A.; Evanschitzky, P.: *New Setup for Speckle Metrology on Slightly Moving Objects*. In: International Photonics in Measurement. Tagung in Aachen, 11./12. Juni 2002. Hrsg.: VDI Kompetenzfeld Optische Technologien. Düsseldorf: VDI Verlag, 2002. (VDI-Berichte; 1694). ISBN 3-18-091694-X. S. 245ff.

T 438/03
Electrical Breakdown and Arcing in ITER

In the framework of ITER task 438 electrical breakdown and arcing in deuterium has been investigated in model experiments to obtain data on the voltage strength of ITER components in dependence on the material and the orientation of the magnetic field. The magnetic flux density B amounted to 0.1-0.4 T. It was oriented parallel as well as perpendicular to the electric field E (EIIB and E⊥B, respectively). The experiments revealed novel phenomena for the different configurations EIIB, E⊥B and B=0. From the viewpoint of avoiding discharges, the configuration EIIB is the worst case. Therefore, in what follows only this case is reported.

At application of the voltage a glow discharge is ignited followed by a transition to an arc. The latter is characterised by the appearance of electrode spots. Spots at the cathode are typical for the existence of an arc. Figure 1 shows a time integrated picture of the glow-to-arc transition. The glow plasma is confined to a cylinder around the electrodes. A cathode spot can be seen that emits its own plasma, again confined to a small column. Figure 2 gives a time resolved sequence with exposure time 200 ns without break between the seven frames. Here the cathode spot develops during 200 ns (from frame 1 to frame 2).

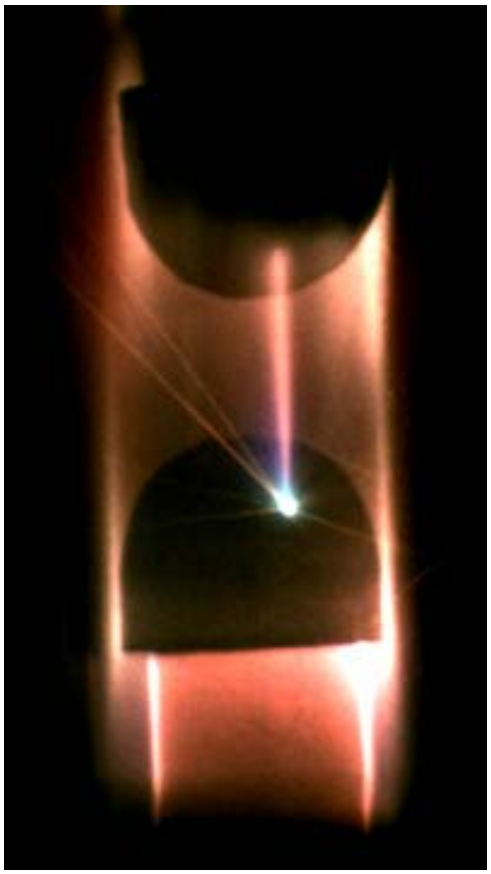

Fig. 1: Overview photograph of glow-to-arc transition between graphite electrodes. Electrode distance 7 mm, 1 mbar deuterium, EIIB. Cathode is bottom.

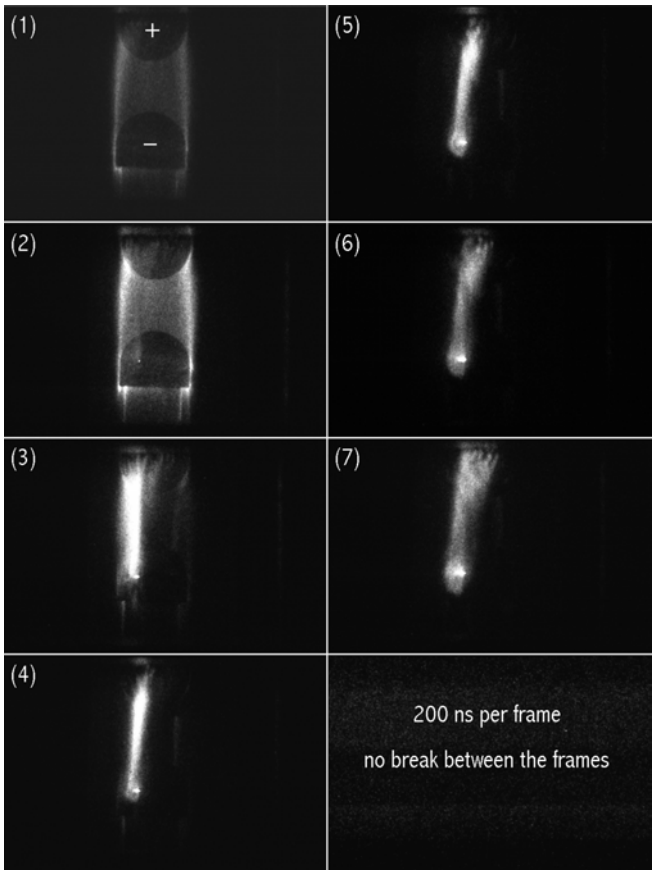

Fig. 2: Time resolved pictures of the glow-to-arc transition according to figure 1.

The voltage necessary for the development of such cathode spots increases with decreasing deuterium pressure. Also, it strongly depends on electrode material and surface conditions. To obtain stable voltage distributions, the electrodes must be conditioned by the discharges themselves. Admixture of 1 % to the deuterium gas oxygen reduced the breakdown voltage. On the contrary, heating the cathode enhances the voltage. This is shown in figure 3 for a cathode of molybdenum. Here the voltage strongly increases at about 1000 K, indicating the effect of desorption of adsorbates with high binding energy (oxides).

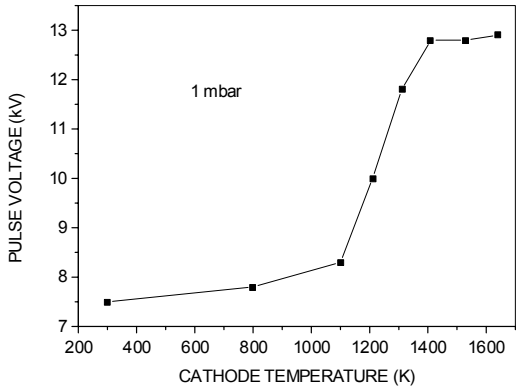

Fig. 3: Voltage for 50 % breakdown probability for a molybdenum cathode as a function of cathode temperature.

The voltage values for 1 mbar deuterium are summarised in table 1. They correspond to 50 % breakdown probability after conditioning. Here EK 98 means amorphous graphite, CFC is carbon fiber material, CFC+Si means silicon doped CFC. In parenthesis the cathode temperature is given. The table illustrates the influence of oxygen and of temperature as mentioned above.

Table 1: Summary of voltage data

Material	1 mbar D_2	1 mbar D_2 + 1% O_2
EK 98 (300 K)	2.3 kV	2.2 kV
CFC (300 K)	2.9 kV	2.4 kV
CFC+Si (300 K)	3.7 kV	3.7 kV
Mo (300 K)	7.5 kV	5.9 kV
W (300 K)	13.5 kV	5.2 kV
Mo, W, 1400 K	>15 kV	-

The results of the present work can be summarised as follows:

(i) A number of novel effects have been detected that deserve further attention. They include the role of anodic plasmas and vapours for the ignition of cathode spots, the deviation from Paschen's law and the occurrence of stationary striations in the crossed field configuration; and finally the influence of oxygen admixture and cathode temperature on the glow-to-arc transition.

(ii) At pressures <0.1 mbar the breakdown voltage for conditioned surfaces is >2 kV in the worst case, EIIB. Thus, transient arcing will not pose a serious problem for ITER.

(iii) Safe operation will require conditioning procedures prior to electric load. Contamination by oxygen can have drastic consequences in reducing the voltage strength, especially for refractory materials. The effect underlines the role of the surface state for arc ignition.

(iv) At critical locations and E⊥B, enhancement of the distances will have positive effects, while this does not help for EIIB, at least for distances <20 mm.

(v) The voltage hold-off capability can be influenced by the choice of material. Refractory metals are superior to carbon materials, and among the latter Si-doped CFC is the best.

(vi) Arcing is accompanied by considerable trapping of deuterium.

Staff:

B. Jüttner
J. Rossignol
W. Schneider

C. H. Wu from Max-Planck-Institute for Plasma Physics, Garching, contributed by valuable advice and discussions.

TW2-TVP/DISMOD
Disruption Erosion Modelling

1. Introduction

1.1 Brittle destruction erosion of CFC armour

Carbon fibre composites, CFC NB31 and NS31, developed for the divertor armour of the ITER tokamak have a rather complex structure of fibre framework and carbon matrix allowing CFC to match the thermal conductivity requirements for the tokamak stationary regimes. But for ITER off-normal events, (disruptions, VDE and ELMs) their behaviour has still not beend studied in detail. Recent experiments on the European Electron Beam Facility FE200 simulating the slow transient loads of 20 MW/m^2 have shown unusual high erosion rates of NB31 due to thermostress in the temperature range of 3000-4000K. An additional evidence of large internal thermostress in CFC is derived from the experiments with cyclic pulsed surface heat loads in the plasma gun facility MK-200 UG [1]. Fig. 1 shows the brittle destruction erosion pattern after this experiment. To simulate the behaviour of NB31 calculations are carried out using the Pegasus code [2] that has been generalized to describe three-dimensional effects of brittle destruction and heat transport in the carbon composites.

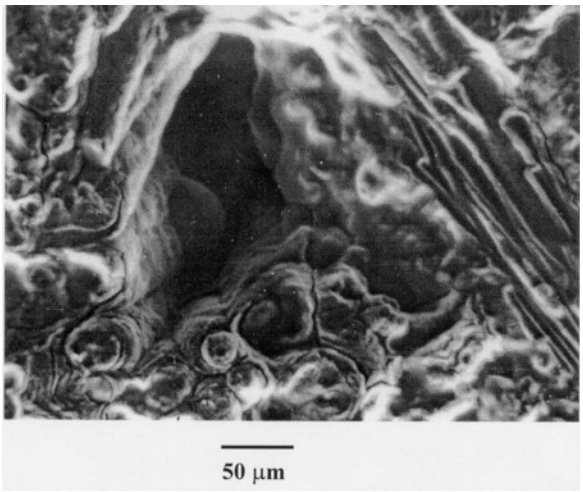

Fig. 1: Erosion pattern of NB31 CFC after cyclic heating in MK-200 UG facility.

1.2 Application of the RMHD code FOREV-2 for quantification of maximum tolerable ELM energy

During type I ELMs a significant part of the confined hot plasma is lost from the core to the scrape-off layer (SOL) enveloping the core region. Following the magnetic field lines, the hot plasma finally is guided to the divertor. ITER typical thermal loading of the divertor armour plate results in surface evaporation and thus in formation of an impurity plasma shield of eroded armour material. Close to the divertor targets, the impurities at such heat loads are plasmas with densities in the range 10^{17}-10^{18} cm^{-3} with temperatures below 1 eV. The impurity plasma expands along magnetic field lines and, after passing the x-point, fills the SOL. Due to the transport across magnetic field in the SOL the impurity penetrates in the core region. The impurity cloud is becoming potentially dangerous when it is able to dissipate energy of the edge plasma by re-radiation. From the results of planar calculation [3] it follows that an adequate modelling of formation and dynamics of plasma shield needs to take into account real toroidal geometry of the magnetic field close to the x-point and in the SOL for simulation of the impurity transport. For this purpose FOREV-2 code is developed for calculations in magnetic flux coordinates, simulating tokamak magnetic field topology.

1.3 Melt layer erosion of metals

During the off-normal events in tokamaks the energy flux at the armour material reaches values sufficient for melting of metals and a thin melt layer appears at the target surface. Experimental results from e-beam and plasma gun facilities and from tokamaks demonstrate the existence of a rather pronounced radial motion in the melt layer from the centre of the melted pool to the periphery. As a result a considerable part of the melt layer is swept away, mountains of ejected melted material are formed at the crater edge and droplet splashing occurs.

A quasi one-dimensional fluid dynamics model was developed [4] for numerical simulations of divertor melt erosion during disruptions and first wall erosion during VDE in ITER [1]. Large damage due to melt splashing has been demonstrated.

2. Mechanism of local overheating erosion

Mechanism of local overheating erosion has been found in simulations using Pegasus-3D code. The enhanced erosion of CFC materials is caused by local overheating due to preferential cracking on the fibre surface and thermal isolation of the fibres from matrix. Concentration of the cracks on the fibre surface is shown in Fig. 2.

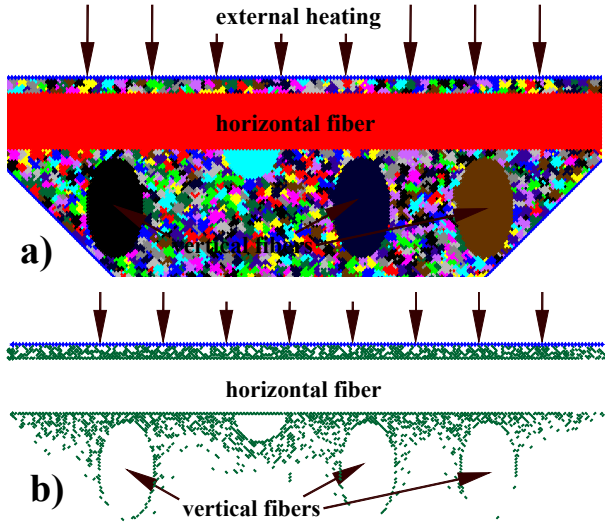

Fig. 2: Concentration of the cracks on the surface of fibres in numerical simulation of CFC heating. Shown are a) CFC structure in planar cross section of the sample, b) the cracks in the section.

Calculated erosion pattern from Fig. 3b shows maximal carbon matrix destruction close to site of perpendicular cross of the fibres – similar patterns were obtained in experiment, see Fig. 1. Principal results of the simulation reasonably correlate with available experimental results despite of the fact that the simulation has been done for rather approximate values of the thermomechanical parameters.

3. Implementation of magnetic flux coordinates in the FOREV-2 code

FOREV-2 code routinely calculates the 2D plasma and magnetic field dynamics and allows a detailed radiation transport

calculation for continuum and line radiation [5]. For an adequate modelling of the energy transfer between the hydrogen edge plasma and the impurity cloud as well as the re-radiation from the impurity cloud the code has been generalized upon the toroidal geometry of the magnetic field with the x-point and two divertor legs. Basic equations of the radiation magneto-hydrodynamics code FOREV-2 are rewritten from reference coordinate system (r,z) to the curvilinear orthogonal coordinate system (x,y) with y-coordinate following the magnetic field lines.

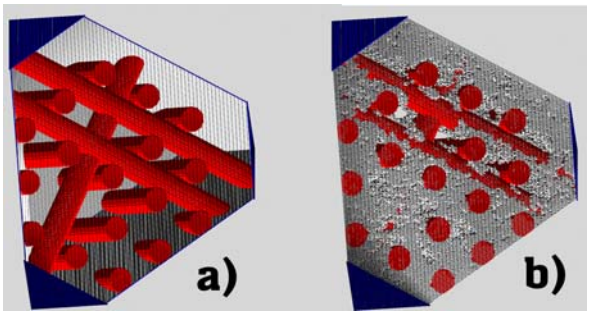

Fig. 3: Results of numerical simulation of the CFC brittle destruction under surface heating. a) fibre structure of the CFC, carbon matrix is removed b) erosion pattern.

The coordinate frame is being constructed automatically at the start of the calculations and then is used for the time evolution of the impurity cloud. Verification of the FOREV-2 with the magnetic flux coordinates and multifluid option is still under way. Preliminary results for pollution plasma density in the SOL are shown in Fig. 4.

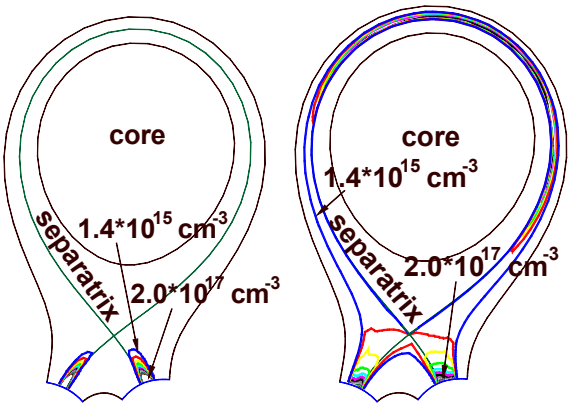

Fig. 4: Pollution plasma density contours showing transport of the pollution material from divertor armour to SOL after ELM. Preliminary calculations with magnetic flux coordinates.

4. Melt layer erosion during single ELM

The physical processes taken into account in the model are heat transport, melting, evaporation from the surface re-solidification, and viscous melt motion. Numerical results on crater depth and melt layer thickness are in rather good agreement with experimental results for tungsten and beryllium from the e-beam facilities JEBIS (JAERI) and JUDITH (FZJ). This allows application of the model for numerical simulations of metallic armour erosion during off-normal events in ITER.

For simulation of the armour erosion it was assumed that typical ELM conditions are: peak energy density deposition W=1-3 MJ/m^2 and time duration τ=0.1-0.5 ms. The armour heat loads and pressure profiles were calculated with FOREV-2, see Fig. 5.

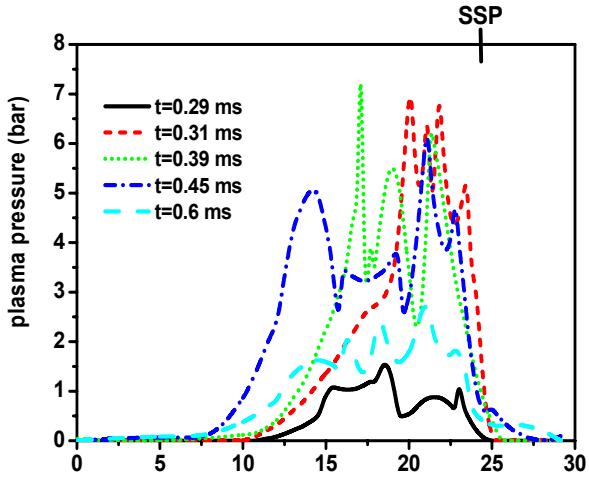

Fig. 5: Plasma pressure at the armour as calculated with FOREV-2 for ELM with W=3 MJ/m^2.

For the typical ELM with peak power density above 4 GW/m^2 maximum static melt layer thickness is about 60 microns and maximal size of roughness due to melt motion is about 5 microns as shown in Fig. 6.

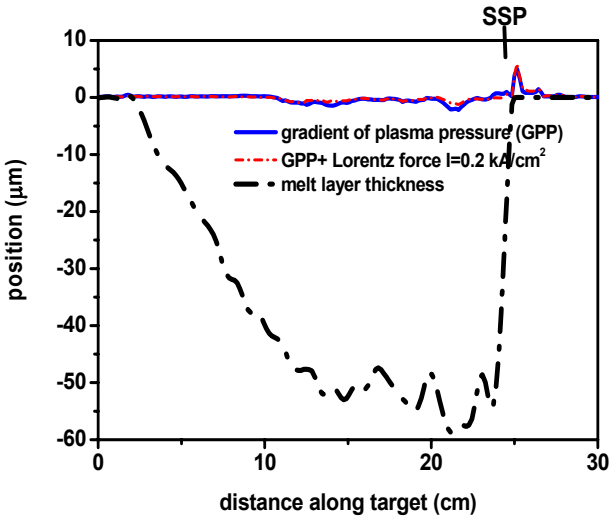

Fig. 6: Crater depth for tungsten armour during ELM with W=3 MJ/m^2.

Conclusion

New erosion mechanism is discovered in simulation of CFC brittle destruction. A thermostress, arising due to the large difference of fibre and matrix coefficients of thermal expansion, is essential for the mechanism. New experiments in collaboration with FZJ and simulations in FZK are necessary to draw a final conclusion on applicability of CFC for divertor armour. The Pegasus code will be used for investigation of the local overheating erosion, aiming on further improvements of CFC technological advantages.

For realistic calculations of the tolerable ELM energy the current version of the FOREV-2 has been modified for the magnetic flux

coordinates. First results obtained using magnetic flux coordinates show reasonable behaviour of pollution cloud transport along the divertor legs and inside the SOL. Realistic estimation of the tolerable ELM energy still needs an appropriate simulation of the impurity cloud heating by the hot hydrogen plasma and a realistic model for the transport of the pollutant and of the hot hydrogen plasma across magnetic field in the SOL.

ELMs with peak power density $Q<2$ GW/m^2 are acceptable because of no melting. ELMs with $Q<4$ GW/m^2 cause weak melt motion due to Lorentz force only because evaporation of the melted material is practically absent up to 0.5 ms. For ELMs with $Q>4$ GW/m^2 the pressure gradient of the plasma shield and Lorentz force cause appreciable melt motion.

Assuming summation of erosion for multiple ELMs the total erosion during a 400 s discharge can achieve several hundreds micrometers which is not acceptable. In successive off-normal events, the position of the separatrix strike point (SSP) at the divertor plate can be different. Both the motion of SPP during each event and the averaged position at different events may stochastically change. Accordingly, the distribution of the heat flux and the momentum of the impacting plasma stream transferred to the wall will vary both in time and across the divertor cassettes, which can significantly influence the erosion of the metallic armour compared to the previous analyses for the single events. The investigation of the consequences of the multiple off-normal events will be carried out.

Staff:

B. Bazylev (guest scientist)
I. Landman
S. Pestchanyi (guest scientist),
V. Safronov (guest scientist)
H. Wuerz

Literature:

[1] H. Wuerz, B. Bazylev, I. Landman, S. Pestchanyi, V. Safronov, “Macroscopic erosion of divertor and first wall armour in future tokamaks”, Journal of Nuclear Materials (2002) accepted for publication.

[2] S. Pestchanyi and H. Wuerz, “Brittle destruction of carbon based materials under off-normal ITER-FEAT conditions”, Physica scripta. T91, 84-89, 2001

[3] S.E. Pestchanyi, H. Wuerz, I.S. Landman, “Impurity production and edge plasma pollution during ITER-FEAT ELMs”, Plasma Phys. Control. Fusion 44 (2002) 845-853.

[4] B.N. Bazylev, H. Wuerz “Melt layer erosion of metallic armour targets during off-normal events in tokamaks”, Journal of Nuclear Materials (2002) accepted for publication.

[5] H Wuerz, S. Pestchanyi, I. Landman, B. Bazylev, V. Tolkach, F. Kappler, “A 2-D numerical simulation of ITER-FEAT disruptive hot plasma wall interaction and model validation against disruption simulation experiments”, Fusion science and technology 40, (2001), 191-246.

TW1-TVP/TUMO1
Molecular Dynamics Simulations of Oxygen Impact on D Sputtering Threshold

1. Introduction

One important problem for future tokamak reactors with tungsten divertor armor is chemical erosion. Corrosive impurities of SOL hydrogen isotope plasma, for instance oxygen, coming to the divertor surface, form volatile molecular complexes W_xO_y thus removing W atoms and causing erosion.

This work on chemical erosion started at the end of 2001. To avoid a difficult quantum chemistry problem, the analysis is based on molecular dynamics (MD) simulations with artificial interatomic potentials. To carry out the calculations, the code CADAC ('Classical Atomic Dynamics Analysis Code') was developed, and the first results will be published [1]. The collected interatomic potentials, a new calculation method, and the MD results are described in Sections 2 – 4.

The surface chemistry is also influenced by H atoms coming to the wall as plasma ions and implanted in the tungsten lattice (H is deuterium and tritium). Interstitial H atoms retained in the implantation layer create volatile complexes H_xO_y, which reduces the formation of W_xO_y and mitigates the corrosion effect. The possibility of a reduction of chemical erosion due to the retained H atoms is demonstrated and the results on the retention effect are reported [2]. The retention problem coupled with the surface processes is described in Section 5.

2. Interatomic potentials

For light projectile ions, first principle potentials are derived only for interaction energies much larger than 10^2 eV. For energies of a few eV some empirical potential functions are available for the involved interactions, but they have been suggested only for two-atomic systems. Hence, for the many-body interactions at the surface neither available potential would be a good choice. In such situation the classical MD simulation can rely on some reasonable combinations from the two opposite limits.

The fine quality of the potentials in their appropriate energy ranges becomes irrelevant in the intermediate situation where the simplicity of the approximations seems to be preferable. Therefore the Bohr potential V_B and the Morse potential V_M are chosen to be applied. For tungsten-oxygen (W–D), oxygen-deuterium (O–D), and deuterium-deuterium (D–D) interactions it was realized that the Bohr and Morse potentials are replacing each other rather consistently: at 10 eV V_B dominates and at –2 eV V_M dominates. For this situation the linear combination $V = V_B + V_M$ represents the interatomic potential V sufficiently. For W-W, W-O, and O-O interactions also $V = V_B + V_M$ is used, albeit at energies below 10^2 eV the Bohr potentials contribute negligibly. Fig. 1 shows the interatomic potentials $V_{ij}(r)$ (i,j = W, O, D) as the functions of the interatomic distance r.

3. MD simulation method and Code CADAC

The Newton equations in CADAC are approximated with a simple finite-difference scheme. Given appropriate initial conditions, the time evolution of the atomic system is calculated step by step, with exact momentum conservation and small energy non-conservation errors, which is important being the only essential feature of the background quantum system which the Newtonian model can tackle.

The time step Δt depends on the atomic masses m and kinetic energies E. The interatomic field imposes a limitation Δr_{max} on atomic displacements, which results in the limitation $\Delta t < (m/E)^{1/2}\Delta r_{max}$. This means that the positions of a few incident deuterium or oxygen atoms must be updated much more frequently than that of many tungsten lattice atoms. With ordinary algorithms, all atoms would be computed with a same smallest Δt and thus the lattice atoms would waste processor ti[illegible]

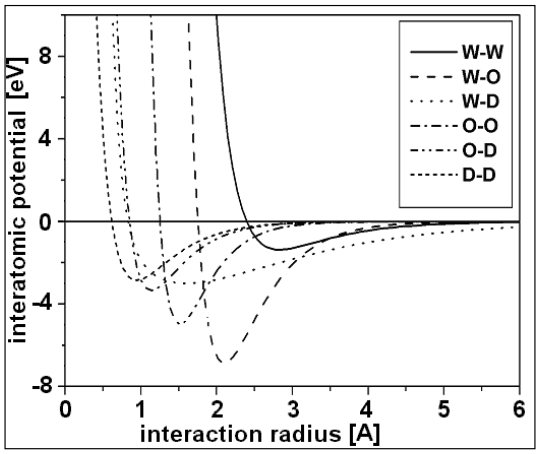

Fig. 1: The interatomic potentials used in the calculations for the assemblies of tungsten, oxygen, and deuterium atoms.

Therefore, for the first time for this problem, individual time steps Δt for each atom were introduced in CADAC, which increases the calculation speed drastically. The atomic assembly is divided into several indexed groups, the 'time step clusters', with equal individual Δt in each group. The atoms of the 0^{th} cluster have some maximum step Δt_{max} and the smaller steps of the j-th clusters are given by $\Delta t_j = \Delta t_{max}/2^j$ (j = 0..J). In the course of the calculation, the atoms automatically change the clusters when necessary for required accuracy. Δt_{max} and the required number of clusters J are variable, which additionally improves energy conservation and performance.

4. First results of MD simulation

The calculations are done simultaneously at two opposite sides of a 19 Angstrom cubical piece of simulated tungsten bcc-lattice shown in Fig. 2. Along the other four sides, the periodical boundary conditions are imposed.

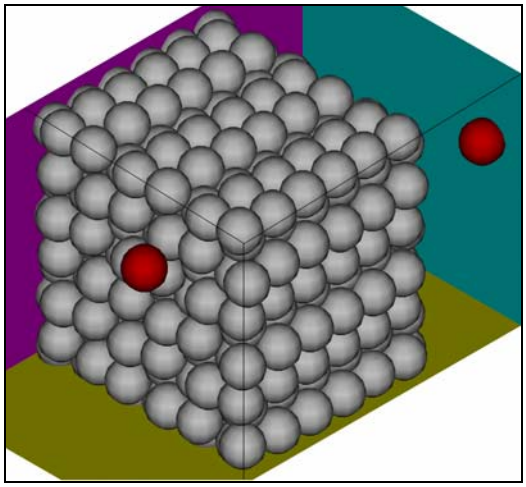

Fig. 2: A typical CADAC lattice configuration and the projectiles are shown, with 1024 W atoms and 2 oxygen atoms.

The effective sputtering yield Y_{eff} is shown in Fig. 3. At small impurity concentrations the obtained tungsten erosion fluxes are much smaller than that of the quasi-thermo-equilibrium (QTE) theory, which is attributed to the enhanced oxygen sputtering and the destruction of the molecular complexes by the hot scrape-off layer (SOL) plasma.

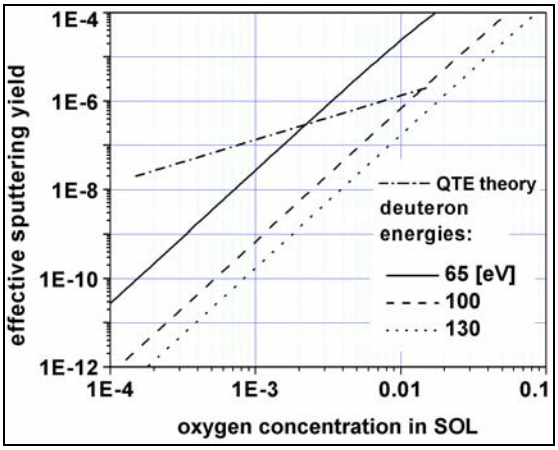

Fig. 3: Dependence of the WO_3 sublimation tungsten erosion on the oxygen concentration for SOL plasma density $N_D = 10^{20}$ m^{-3}. The oxygen impurity temperature is equal to 20 eV.

5. Hydrogen retention effect

Hot H-atoms penetrating into the implantation layer where they undergo collisions with W-atoms start to diffuse with some chance to escape back. In the course of diffusion, they slow down due to the friction with the lattice and finally stop. In this fast process, the interstitial diffusion is negligibly slow compared to that of the hot ones. However, gradual accumulation of the interstitial atoms increases their flux and finally the interstitial diffusion will establish the retention density.

On the surface only simplest molecular complexes are considered. If an O-atom is trapped at a site occupied by one or two O-atoms, the complex WO_2 or WO_3 is created, thus lessening the binding of the involved tungsten atom to the lattice. The appearing WO_3-complexes are assumed to sublimate immediately. Only the surface reactions of H-atoms with WO-complexes are implied as follows. If a cold H atom comes to the site occupied by an O-atom, it can be trapped there. If a second cold H-atom comes to this site, an H_2O molecule can form and then immediately evaporate. This evaporation provides one possible mechanism of reduction of the surface oxidation that may be significant.

The chemical erosion yield Y_{chem} is obtained. This result is compared with the sputtering erosion for given plasma and wall temperatures T and T_W. The comparison is based on sputtering yields Y_{sput} at lowest impact energies E achieved in available experiments. Fig. 4 shows the yields Y_{chem} and $Y_{sput}(T, T_w)$.

Conclusions and outlook

The process of chemical erosion by oxygen coming as deuterium plasma impurity to a hot tungsten surface was investigated under the conditions of a low physical sputtering. For this purpose the MD simulation code CADAC was developed. It was shown that the chemical erosion yield can be made small compared to the QTE theory, provided that the deuterium impact energies are rather high. First estimations show that both the retention effect and the bombardment significantly reduce the chemical erosion down to the levels of sputtering by tritium and oxygen. Retained hydrogen isotopes can significantly reduce the tungsten chemical erosion yield, providing a natural mechanism of the surface cleaning from corrosive impurities.

In further investigations, more advanced interatomic potentials should be applied, and additional processes should be analyzed. For instance, the oxygen sticking may result in not easily removable complexes and thus in corrosion. CADAC is a useful tool for further investigations in this area. Better models are needed for the chemical erosion, for instance, an elaborated description of hydrogen reactions with oxygen at the tungsten surface.

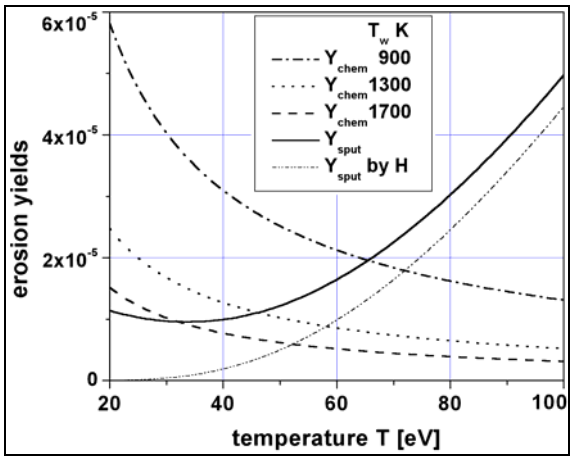

Fig. 4: Chemical and sputtering yields in comparison are shown. The non-monotonic behaviour of Y_{sput} at small T is due to a linear dependence of Y_{sput} by oxygen on $1/\sqrt{T}$.

Staff:

I. Landman
H. Wuerz

Literature:

[1] I.S. Landman and H. Wuerz, "Molecular dynamics simulations of the effect of deuterium on tungsten erosion by oxygen", 15th Plasma Surface Interaction Conf. (PSI-15), May 2002, Gifu, Japan, to be published in Journ. Nucl. Mat.

[2] I.S. Landman and H. Wuerz, "Hydrogen retention effect on tungsten divertor armor erosion by oxygen", 22nd Symposium on Fusion Technology (SOFT-22), September 2002, Helsinki, Finland, to be published.

Divertor and Core Plasma Modelling for ITER

1. Introduction

ITER performance modelling is increasingly important to establish the expected performance of ITER and to define the operating scenarios to obtain this performance. This requires an integrated plasma model which describes in a coherent way the entire plasma from the centre via the pedestal and the scrape-off layer to the divertor plate. Based on previous work in this area in the ITER framework, ([1-8]) a quadripartite collaboration has been established in June 2002 between FZ Karlsruhe, ITER International team, Hydro-Québec, Varennes, Québec, Canada, and INRS-EMT, Varennes, Québec, Canada to develop such a model on the basis of comparison with existing experiments, apply it to ITER, and continue further development and improvement.

The integrated ICPS model presently consists of two parts: the core, from the centre of the plasma to the separatrix and including the pedestal, is modelled with the 1-1/2 D code ASTRA, and the scrapeoff layer and divertor plasma is modelled with the coupled fluid-Monte Carlo code B2-EIRENE. A variant of the model uses a simpler two-point model for the scrape-off and divertor plasma. Whereas this variant can be expected to reproduce trends, quantitative predictive modelling of ITER, particularly of the time evolution of the fusion gain Q, requires a degree of accuracy available only from the complete 2D simulation with plasmas and neutrals. Given the different time scales and models for the core (hundreds of seconds, close to 1D) and edge (tens milliseconds, 2D), it is presently impractical to couple the codes directly. Instead, the solutions for the edge are parameterised in terms of the variables resulting from core simulations, and the output quantities from the 2D simulations are used as boundary conditions for the 1-1/2D core plasma code. The natural choice for the edge input parameters, is the input power to the SOL P_{SOL}, the pumping speed S_{DT}, the DT particle throughput Γ_{DT}, the fraction of the throughput supplied by core fuelling $\eta_c = \Gamma_{core}/\Gamma_{DT}$, the ratio of power input in the electron and ion channels $\xi_{ei} = P_e/P_i$, and the helium ion flux across the separatrix which is determined by the fusion power and the helium atom influx into the core. These edge input parameters are calculated using the relevant output quantities of the core calculation. The edge plasma output quantities, which serve as the boundary conditions for the core plasma, are the averages along the separatrix surface of the electron and ion temperatures T_{e_sep} and T_{i_sep}, of electron, He, and C densities, n_{sep}, n_{He_sep} and n_{C_sep}, of DT and He neutral outfluxes from the divertor $\Gamma_{DT\_n\_sep}$ and $\Gamma_{He\_n\_sep}$, and of the mean energy of these neutrals E_{DT_sep} and E_{He_sep}. Besides this, the peak power loading of the target q_{pk} is used to constrain the operational window of the core plasma.

First results from applying this model were reported at the 2002 IAEA Fusion Energy Conference ([9], [11]) and an extended version is being submitted for publication ([10], [12]).

2. Divertor Plasma Modelling

Recent studies of ITER divertor operation [4-7] have shown that there is an operational window for which the ITER divertor is expected to provide both acceptable target loading and the required efficiency of helium ash removal. At the same time, these studies showed that the upstream plasma density saturates with an increase of the fuelling rate [3, 4], thus limiting the operational window to rather low plasma density at the separatrix, $n_s \sim (3 \text{ to } 4)\cdot 10^{19} m^{-3}$, which is consistent with experimental indications that good plasma confinement in the H-mode requires low separatrix density. To produce sufficient fusion power and Q, the average plasma density in ITER must be $8\text{-}10\cdot 10^{19} m^{-3}$ with a flat density profile in the centre. Consequently, a significant density gradient must be sustained in the "pedestal" region just inside the separatrix, and thus considerable particle fluxes must traverse this region [1, 6]. Since the neutral particle influx across the separatrix also saturates at a comparatively low level [6,7], it is necessary to employ an additional fuelling scheme such as pellet injection which fuels inside the separatrix.

A large number of simulations have been performed for the standard ITER geometry. In these scans, the power crossing the scrape-off layer and the pumping speed were varied (Fig. 1a). The saturation in upstream density (average density at the separatrix) is clearly seen, e.g. the curve for 100 MW and a pumping speed of 20 m^3/s. Further variations, i.e. core fuelling rather than gas puffing, and variations of the ratio of power carried by the electrons to that carried by the ions, are shown in Fig. 2a) as a function of divertor neutral pressure. (The divertor neutral pressure is determined at the entrance to the private flux region, i.e. is simply the throughput divided by the pumping speed).

These results can be unified [7,10,11] as shown in Fig. 1b) and Fig. 2b) by a two-regime power-law scaling in terms of the quantity $(\Gamma_{\#}/S_{\#})P_{\#}^{-0.87}f_f^{-2}$, which is simply the divertor pressure (throughput over pumping speed) divided by an almost linear function of the SOL power and corrected by a factor close to 1 which depends on the type of fuelling. (The scaling has been established only for ITER, for the standard divertor geometry, and for inherent carbon impurity resulting from carbon divertor plates). Each of these quantities is normalised (the subscript "#"); the numerical values are given in Tables 1and 2.

The plasma is in the unsaturated regime when $(\Gamma_{\#}/S_{\#})P_{\#}^{-0.87}f_f^{-2}<1$. Above this value, saturation occurs, associated with a progressive detachment of the divertor plasma in the inner divertor [7,11,12] which becomes fully detached for $(\Gamma_{\#}/S_{\#})P_{\#}^{-0.87}f_f^{-2}>1.2$. To avoid the reduced confinement found experimentally when one of the divertors becomes completely detached, we require that for normal operation the plasma be partially attached, i.e. in the unsaturated regime for which $(\Gamma_{\#}/S_{\#})P_{\#}^{-0.87}f_f^{-2}<1$.

A good fit is also obtained for the other quantities whose separatrix-averaged values are to be passed to the core modelling code. In the presence of He-DT collisions, the helium density (Fig. 3a) and neutral flux decrease strongly as the DT throughput (and neutral pressure) increases, and therefore helium recycling does not contribute strongly to the central helium concentration for ITER. The separatrix temperatures vary little with operating conditions. Fig. 3b shows that the DT neutral flux across the separatrix for ITER conditions is small (8 to 15 $Pa\text{-}m^3/s$) and varies little (Fig. 3b), so that significant core fuelling (80 - 100 $Pa\text{-}m^3/s$,) must be provided to fuel the density pedestal and generate the required core density. ([1] and next section). Fits for other quantities, such as the helium neutral flux and the separatrix temperatures, are found in [11, 12].

The peak power loads at the divertor plate are shown in Fig. 4. The peak power load increases strongly with power, but, at given power, depends practically only on the neutral pressure in the divertor. The latter dependence, although plausible, is non-trivial - the peak power load is made up of electron and ion heat conduction, convection, recombination at the plate, and radiation, and all of these components are significant and have different profiles along the plate.

The exponents in the power law scaling of the critical point are summarised in Table I, and those for the parameter scaling in the unsaturated regime are given in Table II. The fuelling factor $f_f = 1 + 0.18\eta_c$ is introduced because the simulations show that fuelling of the SOL by ions from the core (resulting from e.g.

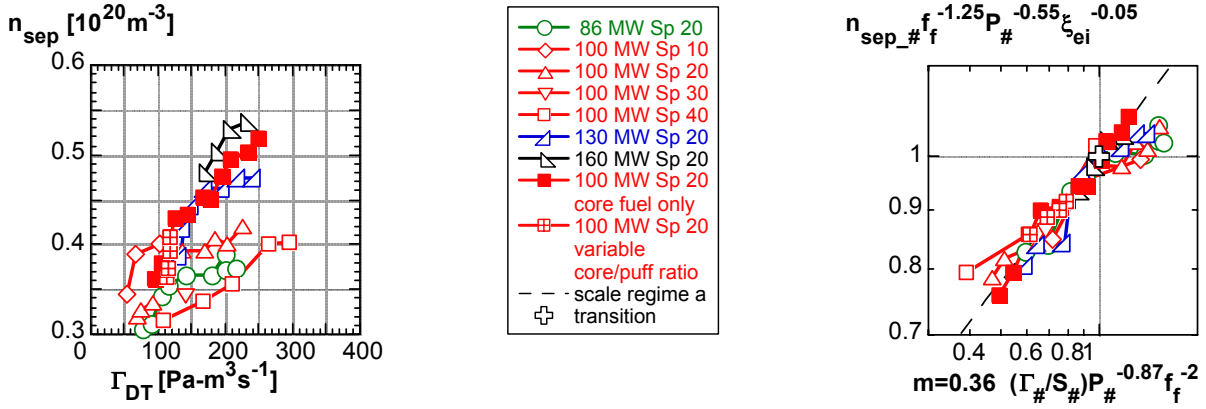

Fig. 1: (a) Separatrix-average density n_{sep} vs. DT throughput for different powers crossing the scrape-off layer and different pumping speeds S_p for fuelling by gas puffing. For one power and pumping speed, scenarios with variable ratios of gas puffing to core fuelling and with core fuelling only are also shown.
(b) Fit to the separatrix-average densities n_{sep} which is used as the boundary condition for the core model. The subscript "#" means normalisation to the constants of Tables 1 and 2.

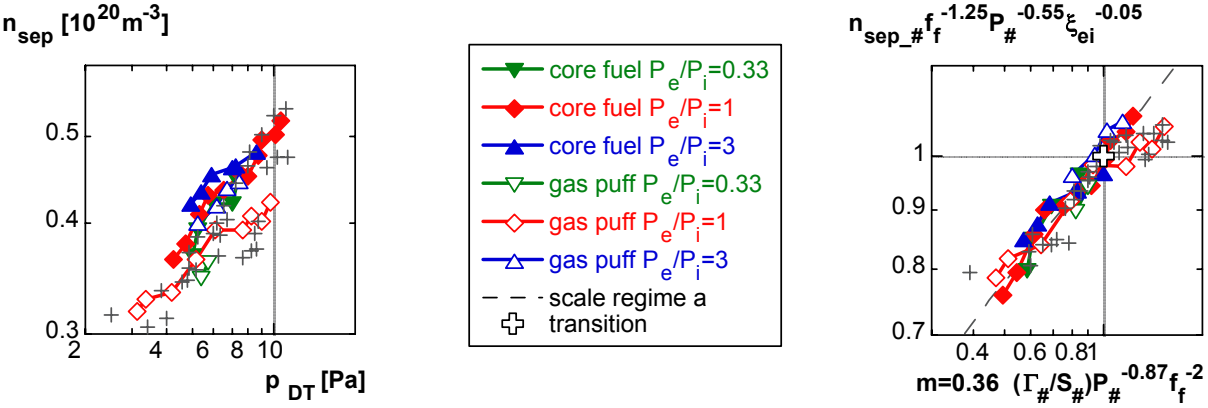

Fig. 2: (a) Separatrix-average density nsep vs. DT neutral pressure in the divertor for different fuelling scenarios and different values of the electron-to-ion power input ratio. Additional data from Fig.1 are shown with crosses.
(b) Fit to the separatrix-average densities nsep which is used as the boundary condition for the core model. The subscript "#" means normalisation to the constants of Tables 1 and 2.

pellet fuelling) is 18% more efficient than fuelling by gas-puffed neutrals from the edge. The helium particle source as given corresponds to the input power when Q=10 and the core radiation fraction f_{rad} is 0.3; for other values it must be multiplied by the factor $f_{He} = 0.21(5Q/(Q+5))/(1-f_{rad})$. For example, at the critical point, $q_{pk\ \#} = ff^{1.7}\ P_{\#}^{1.26}$ where $q_{pk\ \#}$ is q_{pk} in units of 7.55 MW/m^2 and $P_{\#}$ is P_{SOL} in units of 100 MW.

Note the strong dependence of the peak power and the helium density on the power to the SOL, as power to the 2 and 2.44 respectively, and the strong decrease with divertor neutral pressure, as pressure to the -0.85 and -2 respectively. Together with the shift of the critical point to higher pressures and densities as given in Table I, these variations led to the conclusion [7-8] that high power operation in ITER would remain uncritical as far as helium is concerned but would lead to higher peak power loads than the nominal operation.

Further detailed studies of the SOL/divertor plasma described in [12].

3. Core Plasma Modelling

The Integrated Core Pedestal Sol Model (ICPS Model) implemented in the 1.5D Astra code contains transport formulations for the plasma core as well as for the self-consistently determined pedestal region near the separatrix ([1,2] and references therein). In the core, both the ion and the electron energy transport channels are described by critical temperature models, with a stiffness of 1 for electrons and 5 for ions, i.e. the temperature profiles are appreciably stiffer for ions than for electrons (the value of 3.5 for ions given in [2] should have been 5).

The model for non-classical transport can be summarized as follows (for the equations see [2]). In the core, the dominant ion energy transport is neo-classical plus ITG, the latter based on a modified IFSPPL model (e.g. shorter gradient lengths adjusted to a JET discharge). Electron energy transport is similar to the RLW model (the RLW critical gradient is modified to depend on shear and adjusted to JET). An Alfven drift term dominant at the plasma edge disappears once a certain edge β is achieved and thus can trigger the H-mode transition. The particle transport for helium and DT is formulated as the Ware pinch and a diffusion coefficient given by $D = 0.1\ (2\chi_e+\chi_i)$. Fuelling is accomplished by the inward neutral flux at the separatrix, to which is added pellet fuelling (approximated by fuelling inside the separatrix with a fall-off length of about 50 cm). The total helium source is determined by the fusion reactions, to which is added the inward neutral helium flux across the separatrix.

The non-classical transport is taken to be stabilized by radial electric field shear and magnetic shear. The effect of type I or type II ELM's is implemented as a time-averaged ELM model, which limits the pressure gradient to the ballooning limit by increasing transport equally for both electrons and ions when this limit is reached.

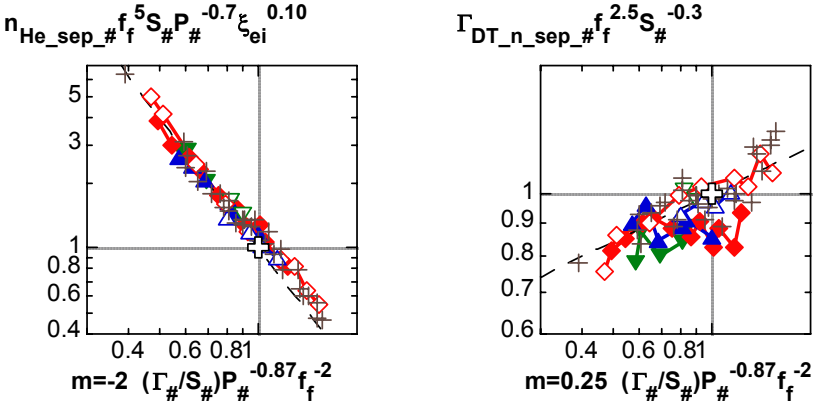

Fig. 3: Fit to separatris-averaged a) Helium density
b) DT neutral flux . Legend as in Fig. 2. The subscript "#" means normalisation to the constants of Tables 1 and 2.

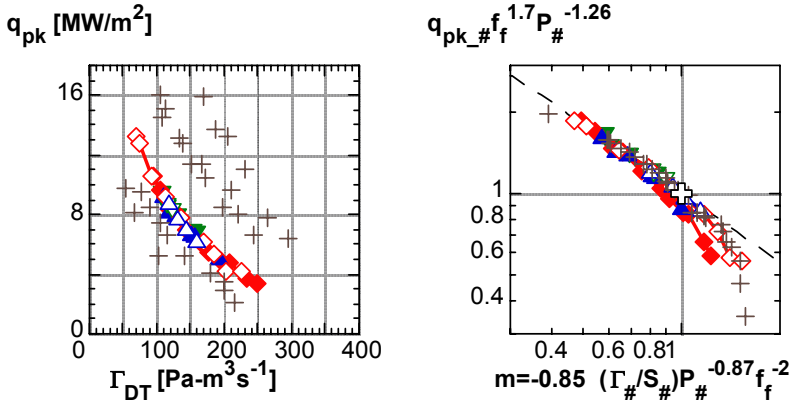

Fig. 4: a) Peak power load at the divertor plate vs DT throughput
b) Fit to peak power load to the divertor plate . Legend as in Fig. 2. The subscript "#" means normalisation to the constants of Tables 1 and 2.

Table 1: Exponents in the parameter scaling at the critical point

	scale	q_{pk}	n_{sep}	$\Gamma_{DT\_n\_sep}$	n_{He_sep}	$\Gamma_{He\_n\_sep}$	T_{e_sep}	T_{i_sep}	Γ_{DT}
scale		7.55 MW/m^2	3.89·10^{19} m^{-3}	16.4 Pa·m^3/s	3.06·10^{17} m^{-3}	0.512 Pa·m^3/s	162 eV	270 eV	124 Pa·m^3/s
f_{He}	1	-	-	-	+1	+1	-	-	-
f_f	1	–1.7	+1.25	–2.5	–5	–5.42	–0.4	–0.9	+2
S_{DT}	20 m^3/s	-	-	+0.3	–1	–1	–0.02	–0.04	+1
P_{SOL}	100 MW	+1.26	+0.55	-	+0.7	0.52	+0.32	+0.36	+0.87
ξ_{ei}	1	-	+0.05	-	–0.1	-	+0.049	–0.115	-

Table 2: Exponents in the parameter scaling in terms of divertor pressure Γ_{DT}/S_{DT} for the non-saturated regime (throughput below critical).

	scale	q_{pk}	n_{sep}	$\Gamma_{DT\_n\_sep}$	n_{He_sep}	$\Gamma_{He\_n\_sep}$	T_{e_sep}	T_{i_sep}
scale		7.55 MW/m^2	3.89·10^{19} m^{-3}	16.4 Pa·m^3/s	3.06·10^{17} m^{-3}	0.512 Pa·m^3/s	162 eV	270 eV
f_{He}	1	-	-	-	+1	+1	-	-
f_f	1	-	+0.53	–3	–1	–1	–0.06	–0.32
S_{DT}	20 m^3/s	-	-	+0.3	–1	–1	–0.02	–0.04
P_{SOL}	100 MW	+2	+0.24	–0.22	+2.44	+2.44	+0.47	+0.61
ξ_{ei}	1	-	+0.05	-	–0.1	-	+0.05	–0.116
Γ_{DT}/S_{DT}	6.2 Pa	–0.85	+0.36	+0.25	–2	–2.21	–0.17	–0.29

The Astra code calculates the time evolution of the radial profiles (1D) of the discharge with self-consistent 2D equilibrium for the magnetic surfaces. Thus, when the density and power are ramped up from the initial low β conditions, the equilibrium, i.e. the current distribution and the associated magnetic shear, relaxes from the initial conditions to the stationary state on the resistive time scale (100's of seconds in ITER with appreciable fusion power). As the expressions for anomalous transport depend strongly on magnetic shear, the pedestal and core confinement also relax on this time scale, leading to a slower relaxation of plasma parameters than at constant transport. An example of this relaxation is shown in Fig. 5. (More detail is given in [9-10], as is an application to JET). Transiently, the fusion performance in ITER is enhanced over the stationary value (fig. 5) by a factor depending on the rampup scenario (Q_{max}~120 here), relaxes in ~200s to $Q = 14.3$, and attains a stationary value of $Q = 13$. In the following sections, all results apply to close to fully relaxed conditions.

As explained in the introduction, core operation consistent with divertor conditions is obtained by applying the scaling relations of the previous section as boundary conditions at the separatrix. Control parameters for the core simulation are then Γ_{core} ("pellet" fuelling, set to give the desired core density), the gas puff flux into the vessel Γ_{puff}, S_{DT}, and the additional heating power P_{aux}. Furthermore, DT gas puffing is used to control the peak power on the divertor plates. Γ_{puff} is thus set such that q_{pk} from the scaling does not exceed the desired value. Only the scaling of the unsaturated regime (see previous section) is employed; in the figures, points within this regime are plotted with solid symbols and continuous lines.

The core operational space has been explored for a peak power load of 10 MW/m^2 on the divertor plate, by varying central density and pumping speed (fig. 6, 7, 8). For the scans, we have chosen to hold P_{SOL} approximately constant by varying P_{aux} as the density is varied, because this is a key quantity for the SOL and divertor plasma.

Fig. 6 shows the behaviour of alpha power and of core fuelling, at S_{DT} = 10 m^3/s. Above an average density of 10^{20} m^{-3}, P_α > 80 MW for all values of P_{SOL}, rising as the density is increased to ~120 MW at 1.45×10^{20} m^{-3}. These quantities vary little as the pumping speed is varied (e.g. P_α varies less than +/- 5 MW for S_{DT} = 5 – 20 m^3/s).

The major determinant of the alpha power is therefore the core density, which is largely determined by the core fuelling rate For operation at or above P_α ~ 80 MW, a core fuelling source of 40 – 80 Pa-m^3/s is required.

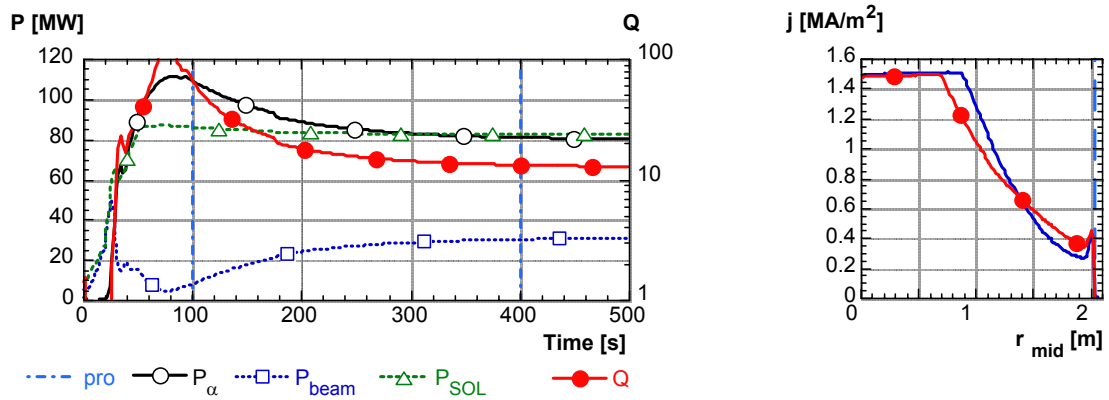

Fig. 5: Relaxation to stationary conditions with S_{DT}=10 m^3/s, P_{SOL}~80 MW, $q_{pk} \leq$ 10 MW m^{-2}, $\langle n \rangle$=1.×10^{20} m^{-3}. Left alpha power, heating power, and Q as a function of time, right current profiles early (100s,blue, no symbols) and late (400s, red with symbols).

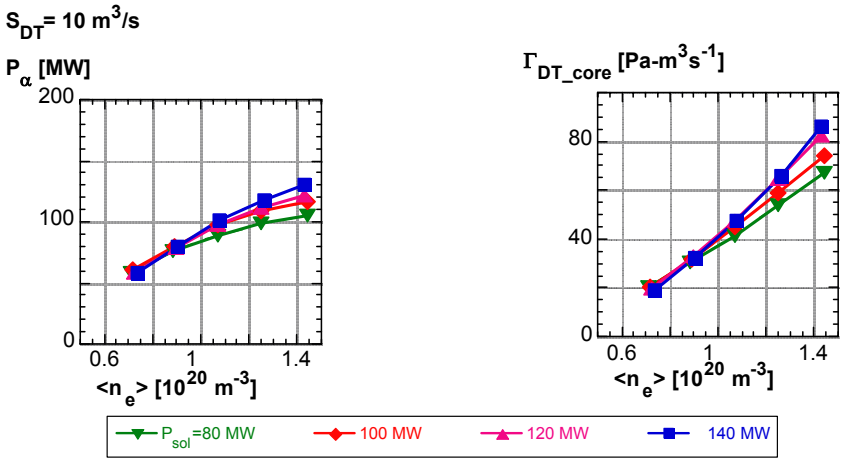

Fig. 6: P_α and $\Gamma_{DT\text{-}core}$ at S_{DT}=10m^3/s

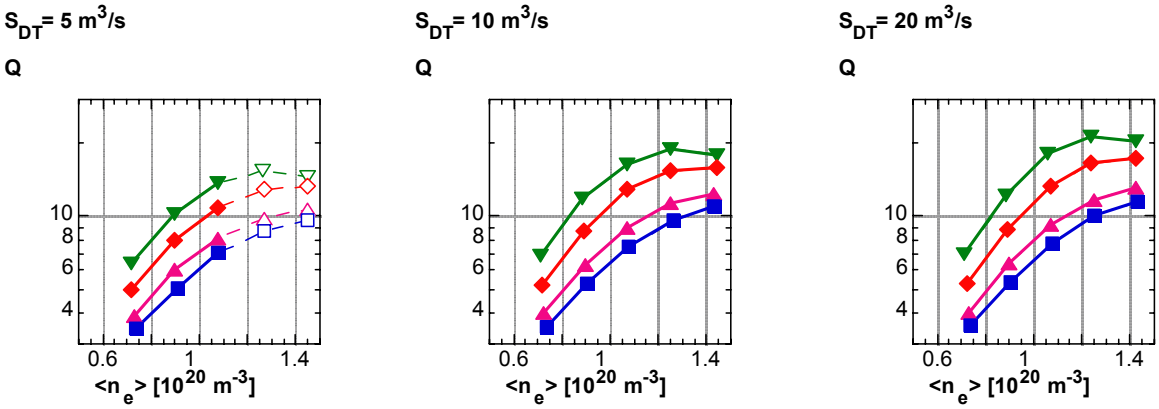

Fig. 7: .Illustration of core operational space. Variation of Q with density at variable P_{SOL} for S_{DT} = 5,10, and 20 m^3/s resp.Legend as on fig. 6.

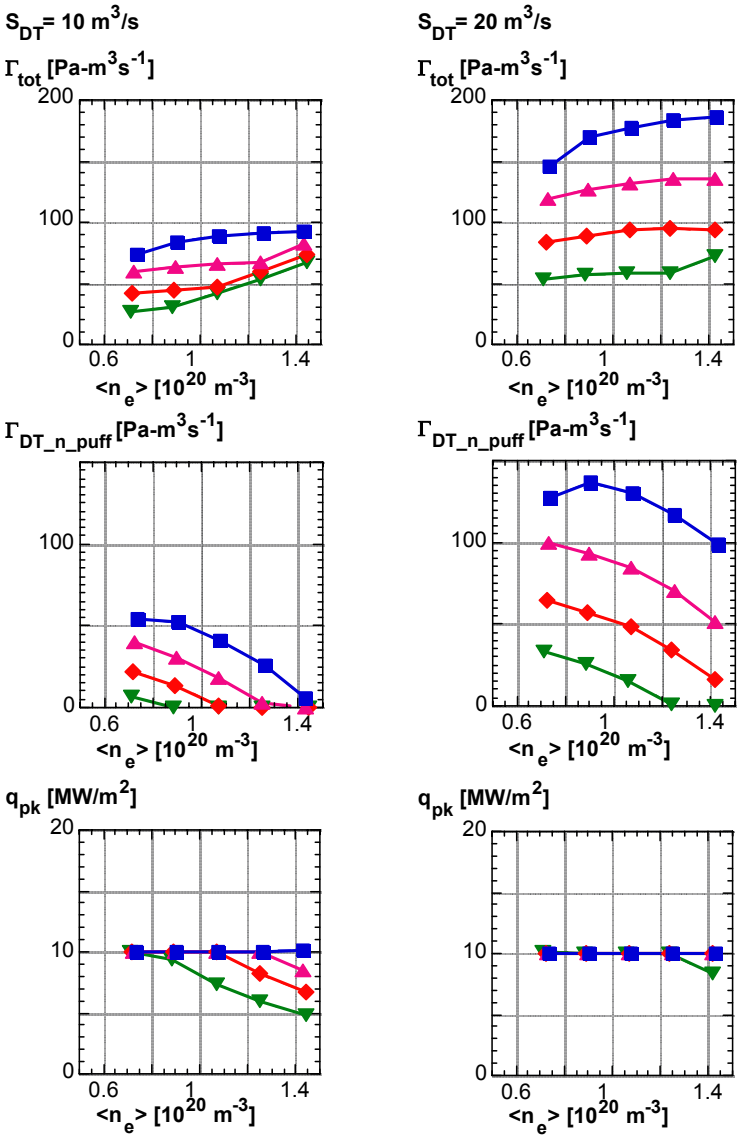

Fig. 8: Throughput Γ_{tot}, Γ_{puff}, q_{pk} at S_{DT}=10, and 20 m^3/s. Legend as in fig. 6.

The fusion performance for these variations is shown on fig. 7. Because of the stiffness of the core transport, the fusion power is relatively insensitive to heating power, and depends mainly on core density (e.g. also [14]). Q therefore tends to increase with density (fig. 7); it saturates at high density for the lower power because then the effective reacting volume contracts because of the lower operating temperature. The fusion performance increases with decreasing P_{SOL} because then the profile stiffness causes the additional heating power to decrease faster than fusion power.

The behaviour of throughput and gas puff is shown on fig. 8 for S_{DT} = 10 and 20 m^3/s (at 5 m^3/s, the gas puff is small). On the one hand, an increase of P_{SOL} (moving from one curve to another on the same graph) requires a strong increase of the gas puff when the peak divertor power load is close to the limiting value. On the other hand, at constant P_{SOL} and constant pumping speed (i.e. on the same curve), toward higher densities the required core fuelling increases, increasing the throughput and thus dropping the peak heat load (according to the scalings of Table II) to the point where gas puffing is no longer required at the highest densities. An increase of pumping speed tends to reduce the divertor pressure and therefore to increase peak power load. A strong increase of the gas puff rate is then required to maintain the peak power load at the limiting value. For Q=10 operation, a minimum throughput of ~40 Pa-m^3/s is required.

4. Conclusions

An integrated plasma performance model for ITER based on input from ongoing experiments has been generated. The extensive modelling effort of the SOL/divertor B2-EIRENE code has led to an efficient power law parametrisation of the plasma and neutral parameters at the separatrix, the interface between the edge and core plasma. These constraints of divertor operation have been applied as boundary conditions to ITER core plasma simulations. Only such an integrated approach leads to a set of resultant core parameters which are consistent with the divertor parameters and vary consistently with these. At the nominal average core density for ITER ($1.0\times10^{20}m^{-3}$) with the core transport model described above, stationary operation with a fusion power multiplier Q between ~12 and ~16 (with P_{fusion} between 390 and 440 MW respectively and P_{SOL} ~83 MW) is obtained for divertor pumping speeds between 5 and 20 m^3/s and peak divertor plate power loads up to 10 MW/m^2. Core fuelling rates of 40 – 80 Pa-m^3/s, depending on the parameters, are required to attain these values. Q values above 20 are accessible at $n_{Greenwald}$ and above, which is not unreasonable considering the predominant core fuelling. A reasonable operating range exists for all parameters. Higher pumping speeds, higher allowable peak power load, and higher density are generally favourable for maximizing Q. In the relevant regime, the fusion power is mainly determined by the direct core fuelling rate, and the peak power load on the divertor plate can be controlled almost independently by gas puffing. The relaxation to stationary conditions is very slow, and transient values of fusion multiplier close to ignition are obtained, appreciably higher than the fully relaxed values of 12-16 quoted above.

Further work is in progress. Further 2D SOL/divertor simulations are being undertaken to extend the scaling to cases having carbon re-erosion at the walls and/or additional impurity seeding, to optimise the divertor geometry and extend the scaling to variations of the geometry, to investigate steady state operation, and to provide scaling of impurities other than helium at the separatrix. Further 1D core simulations will be carried out to investigate transport models based more on first principles and to integrate also the intrinsic and seeded impurity behaviour into this treatment. Improved stability treatments in the pedestal, time-dependent ELM simulations, and more detailed scenario calculations including current rampup are also planned.

Staff:

G. Janeschitz
A. S. Kukushkin (ITER International Team)
I. Landman
H. D. Pacher (INRS-EMT, Varennes, Québec, Canada)
G. W. Pacher (Hydro-Québec, Varennes, Québec, Canada)
S. Pestchanyi

with the collaboration of
G. Pereverzev (IPP Garching)
Yu. Igitkhanov (IPP Garching)

Literature:

[1] G.W. Pacher, H.D. Pacher, G. Janeschitz, G. Pereverzev, O. Zolotukhin, Yu. Igitkhanov, M. Sugihara, "H-mode operation in ITER: determination of trajectories in edge operational space", Proc. 28th EPS Conf.on Contr.Fusion and Plasma Physics, Madeira 2001, ECA Vol. 25A (2001) 625

[2] G. Janeschitz, G.W. Pacher, O. Zolotukhin, G. Pereverzev, H.D. Pacher, Yu. Igitkhanov, G Strohmeyer, M. Sugihara "A 1-D Predictive Model for Energy and Particle Transport in H-mode", IAEA Technical Committee Meeting on H-mode Physics, Japan, 2001, Plasma Phys. Control. Fusion 44,No 5A (2002) A459-A471

[3] A.S. Kukushkin, G. Janeschitz, A. Loarte, H.D. Pacher, D. Coster, D. Reiter, R. Schneider, Critical issues in divertor optimisation for ITER-FEAT, Journal of Nuclear Materials 290-293 (0) (2001) pp. 887-891 .

[4] A. S. Kukushkin, G. Janeschitz, A. Loarte, H. D. Pacher, D. Coster, G. Matthews, D. Reiter, R. Schneider, V. Zhogolev, "Basic Divertor Operation in ITER-FEAT", Nucl. Fusion 42 (2002) 187

[5] A. S. Kukushkin, H. D. Pacher, G. Janeschitz, A. Loarte, D. Coster, D. Reiter, "Operational Space of a Shaped Divertor in ITER", Proc. 28th EPS Conf.on Contr.Fusion and Plasma Physics, Madeira, (2001)

[6] A. S. Kukushkin, H. D. Pacher, "Divertor Modelling and Extrapolation to Reactor Conditions", Proc. IAEA Technical Committee meeting on divertor concepts, Cadarache, France, Sept. 11-14, 2001, Plasma Physics and Contr. Fusion 44 (2002) 931–943

[7] H. D. Pacher, A. S. Kukushkin, G. W. Pacher, G. Janeschitz, "Scaling of ITER divertor parameters - interpolation from 2D modelling and extrapolation", Proc. 15th International Conference on Plasma Surface Interactions in Controlled Fusion Devices, May 27-31, 2002, ,Gifu,Japan, to be publ. in J. Nucl. Mat. (2002)

[8] A. S. Kukushkin, H. D. Pacher, G. Federici, G. Janeschitz, A. Loarte, G. W. Pacher, "Divertor Issues on ITER and Extrapolation to Reactors", Proc. 1st International Workshop on Innovative Concepts for Plasma-Interactive Components in Fusion Devices, May 23rd -25th, 2002, Osaka, Japan, to be publ. in Fusion Engineering and Design (2002)

[9] G.W. Pacher, H.D. Pacher, A.S. Kukushkin, G. Janeschitz, G. Pereverzev, "Application of a 1-D Predictive Model for

Energy and Particle Transport to the Determination of ITER Plasma-SOL Interface parameters", Proc. 19th IAEA Fusion Energy Conf., Lyon, France, Oct. 2002, paper FT/P2-11 (2002)

[10] G.W. Pacher, H.D. Pacher, A.S. Kukushkin, G. Janeschitz, G. Pereverzev, "Core Plasma Operation Consistent with SOL Parameters in ITER", submitted to Nucl. Fusion (2002)

[11] A. S. Kukushkin, H. D. Pacher, G. W. Pacher, G. Janeschitz, D. Coster, A. Loarte, D. Reiter, "ITER Divertor Plasma Modelling with Consistent Core-Edge Parameters", Proc. 19th IAEA Fusion Energy Conf., Lyon, France, Oct. 2002, paper CT/P-07 (2002)

[12] A. S. Kukushkin, H. D. Pacher, G. W. Pacher, G. Janeschitz, D. Coster, A. Loarte, D. Reiter, ITER Divertor Plasma Modelling with Consistent Core-Edge Parameters", submitted to Nucl. Fusion (2002)

[13] M. KOTSCHENREUTHER, W. DORLAND, et al., Phys. Plasmas 2(6) (1995) 2381.

[14] G. Pereverzev, G. Janeschitz, A. S. Kukushkin, G. W. Pacher, H. D. Pacher, A. R. Polevoi, O. V. Zolotukhin, " Comparative simulation of H-mode ITER plasmas with first-principle-based transport models, Proc. 29th EPS Conf.on Contr.Fusion and Plasma Physics, Montreux, (2002)

Coil System

EFDA 01/598
Design, Development and Constructing of High Temperature Superconductor Current Leads for 70 kA

Introduction

Forschungszentrum Karlsruhe and the Centre de Recherches en Physique des Plasmas CRPP are working together in a joint development program to construct and test a 70 kA current lead using High Temperature Superconductors HTS for the Toroidal Field Coil system of ITER.

This program follows on the development program of an HTS current lead in the 20 kA range, which was successfully completed in 2000.

The current lead will be of the binary type, i.e. an HTS part in the temperature range from 4.5 K to 70 K and a conventional copper part in the range from 70 K to room temperature (RT). A two-cooling circuit concept will be used, i.e., the HTS part will be conduction cooled from the 4.5 K level and the copper part will be actively cooled with 60 K helium. This concept was also successfully applied in the former program.

The current lead will be operated in horizontal position as it is foreseen in the ITER design. Due to this the lead would also be qualified for an envisaged development program for a complete feeder line for ITER.

Due to the stringent budget, the HTS current lead will be manufactured at the Forschungszentrum Karlsruhe. The HTS part will be manufactured in industry whereas the heat exchanger should be built in house. The dimensions have to meet the boundary conditions and the interfaces to the TOSKA facility taking into account the necessity of a horizontal installation in TOSKA.

The HTS current lead will be tested in the TOSKA facility of the Forschungszentrum Karlsruhe, which has the cryogenic and high current equipment. There is some equipment from the TFMC program available, which gives a good basis for the test, i.e. 80 kA conventional current lead, which was already successfully operated in the test of the TFMC, superconducting short circuit bus bar.

Construction of the HTS Current Lead

As a first step, a comparative study on HTS current leads fabricated and tested by different institutes and industry was done. The study included the prototype work performed at CERN for the 13 kA HTS current leads of the Large Hadron Collider (LHC) and the development work done so far at NIFS, Japan, for phase II of the Large Helical Device (LHD) experiment. The extrapolation of the present designs to 70 kA was done using Bi-2223 tape material as a favored material.

Parallel to the study, the design of the 70 kA HTS current lead as a prototype current lead for the TF coil system of ITER was started taking into account the boundary conditions of ITER and of the test facility. Special emphasis is given to the contact regions between the HTS module and both the conventional copper heat exchanger and the clamp contact to the superconducting bus bar. For this, design optimisation and mock-up tests are necessary. The manufacturing of the HTS module will be performed in industry. The manufacturing and assembling of the whole lead will be performed at FZK.

A call for tender was sent to industry for a design and the manufacturing of the 70 kA HTS module. After a detailed technical discussion, one of the industrial offers was accepted and the order placed.

Figure 1 shows a CAD view of the current lead including the clamp contact and the room temperature end. The region where the HTS module is located is empty because the module is in the design phase in industry.

Modification work for the TOSKA facility

It is planned to test the 70 kA HTS current lead in the TOSKA facility. This will be subject of the separate task, which is currently in the evaluation and decision phase at EFDA.

For the test purpose, some equipment from the TFMC program can be used, i.e. 80 kA conventional current lead as return terminal, superconducting short circuit bus bar (BB3). One of the existing 80 kA current leads including its cryostat extension and water cooled connection to the bus bars will be replaced by the HTS current lead. Due to the horizontal installation, an extension of one of the water cooled aluminum bus bars is necessary. A first modification plan for the TOSKA facility has been started, which includes the design of the water cooled aluminum bus bars and connection of the radiation shield cooling of the He transfer line to TOSKA. The latter one is required for providing the coolant of the heat exchanger of the HTS current lead.

Outlook

The contract for fabrication of the HTS module in industry is placed. The module will be delivered six months afterwards. Parallel to this the components needed for the conventional parts

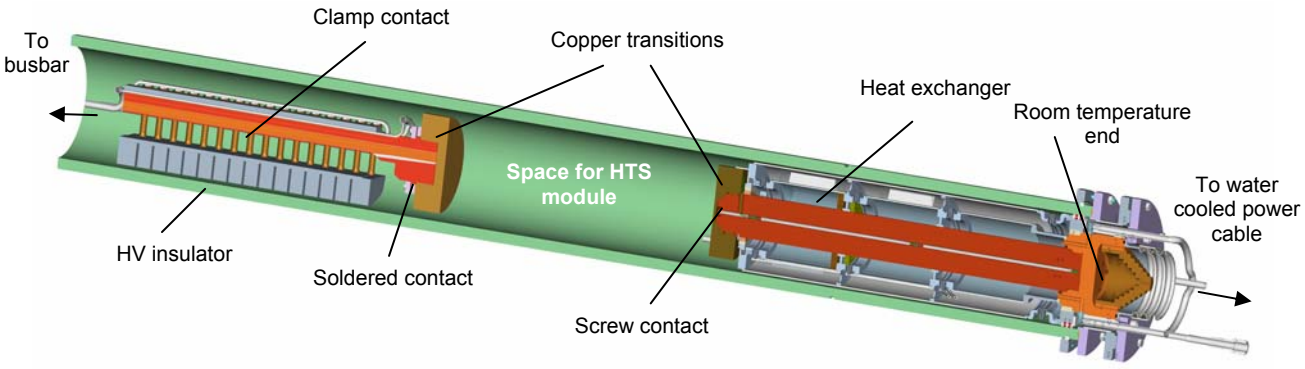

Fig. 1: CAD view of the 70 kA HTS current lead

of the current lead as well as the cryostat extensions will be fabricated. Afterwards the whole lead will be assembled.

After the task is signed and the TFMC is removed from TOSKA, the facility will be prepared for the test of the HTS current lead.

Staff:

A. Akhmetov
M. Darweschsad
W. Fietz
G. Friesinger (until Febr. 2002)
R. Heller
A. Kienzler
A. Lingor
I. Meyer
V. Schulmeister
S. Zimmer

EFDA 01/605
TFMC testing with the EURATOM LCT coil

The TOSKA facility at Forschungszentrum Karlsruhe was upgraded for testing of the ITER TF model coil. The facility has been taken into operation in two steps:

- Test of the LCT coil at 1.8 K (1996/1997)
- Test of the stellarator prototype coil W 7-X (1999)

The first step qualified the LCT coil for the use as background coil for the TFMC test configuration. The basic facility with its electrical and cryogenic supply system as well as data acquisition and control was taken into operation. The test of the W 7-X coil counted besides the test of the coil as an intermediate step for gaining operation experience and improving the facility components. The specific facility configuration needed for the TFMC test was complete December 2000. The assembling of two 80 kA current leads with the cryostat extensions was ready in March 2001.

The test of the TFMC is being performed in two phases as it has been concluded by the TFMC Coordination Group and the EURATOM Association Forschungszentrum Karlsruhe Steering Committee:

- Test Phase I of the TFMC without LCT coil (June – October 2001).
- Test Phase II of the TFMC in the background of the LCT coil (2002)

The intention of the testing in two phases is to achieve results of the TFMC as soon as possible in less sophisticated configuration with a lower risk of occurring faults.

For the performance of the TFMC test, an organization scheme was approved for decision making and handling the daily work of testing. The management of the test is handled by the Coordination Group which is supported by the Operation and the Test Group. Members of the groups are delegates from the ITER IT and the Home Teams.

The acceptance tests and the preparation of the test program of the TFMC have been accompanied by the special skills of the European superconducting laboratories. The areas of EURATOM Association Forschungszentrum Karlsruhe are:

- Instrumentation (Task M44 concluded)
- Conductor measurements (NET Contract No.: NET/97-458 concluded)
- Mechanical material and component testing (EU Task No: M45 concluded)
- High voltage component delivery and testing (NET Contract No.:NET/96-438 concluded)
- Finite element analysis (EU Task M12 concluded, continued in running Task EFDA / 1 - 605)
- Electromagnetic and thermohydraulic analysis (Task M44 and 3 D quench analysis with code system MAGS concluded, IRS, EU Task SEA 5)
- Transient voltage behavior of the TFMC (Task M 44 concluded, continued in running Task EFDA / 1 - 605)
- Leak testing acceptance tests during fabrication (Task M44 concluded).

The acceptance tests of the TFMC at European industry site (Alstom SA) were completed in December 2001. The TFMC arrived at the TOSKA site in January 11, 2001.

After performance of the TFMC acceptance test at TOSKA site the test configuration for testing without LCT coil was assembled and installed in the TOSKA vacuum vessel. The test ran very successful from June to October 2001. After that the TFMC was removed from the TOSKA vacuum vessel and assembled with the EURATOM LCT coil and installed again in the TOSKA facility. The test configuration achieved beginning September 2002 the operation temperature. The test program is running now.

1. Installation of the TFMC with the EURATOM LCT coil in the TOSKA facility for test phase II

For the test phase II, the TFMC was assembled with the LCT coil. The 117 t heavy test configuration was lifted in the TOSKA vacuum vessel by means of the two cranes (50 t and 80 t) and a lifting gear (Fig. 1). The configuration was connected to the electrical and cryogenic supply system. The 80 kA and 20 kA current leads were assembled to the TFMC and the EURATOM LCT coil. That included the piping of the two coils, its structure and the two pairs of current leads. About 500 single weld seams had to be leak tested. The low voltage instrumentation cables of the sensors of both coils had to be soldered to the feedthrough sockets. The high voltages cables of both coils were routed to the provided flanges in their feedthrough boxes. Continuity and insulation tests assured the proper function of all sensors including the signal conditioning electronics and the data acquisition. The installation was concluded by an overall vacuum leak test and a high voltage insulation test for each coil. An overall leak rate at room temperature of 10-7 mbarl/s was achieved. The high voltage tests at 10 kV DC voltage for the TFMC and 3.2 kV DC voltage for the LCT were successfully performed.

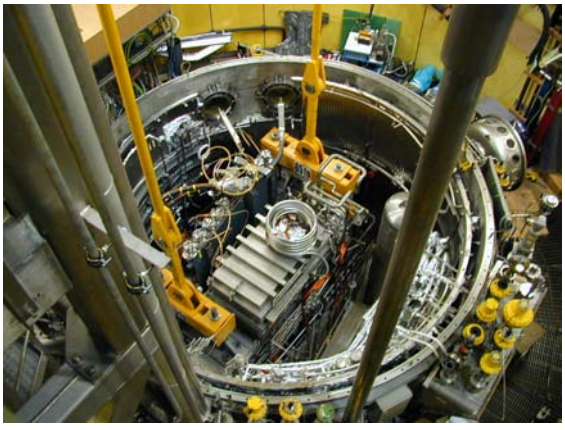

Fig. 1: The TFMC (left) with the EURATOM LCT coil (right) after lifting in the TOSKA vacuum vessel

For the performance of the test phase II a detailed test procedure including a time schedule was elaborated and discussed with EFDA /CSU and the other European superconductor laboratories.

The cool down was started August 20, 2002. After two weeks cool down the test configuration achieved beginning September its operation temperature at 4.5 K (Fig. 2). After another week for

the stabilisation of the cryogenic system the high voltage tests were performed according to the test procedure.

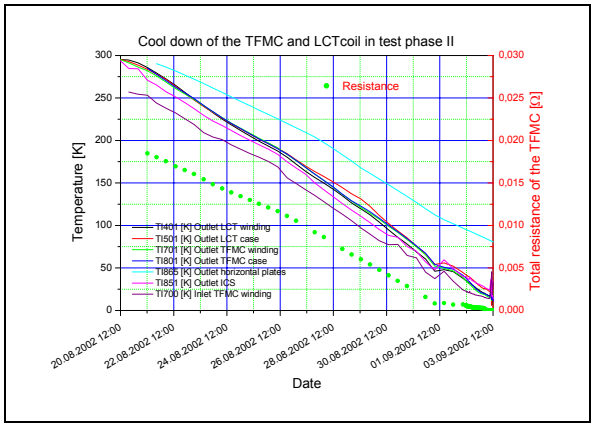

Fig. 2: The cool down of the test configuration for test phase II, TFMC with LCT coil

The next steps of the test procedure are the single coils tests of the TFMC and the EURATOM LCT coil. After that both coils will be tested together (max. currents: TFMC 70 kA and EURATOM LCT coil 16 kA) and the operation limits of the TFMC conductor will be determined by measuring the current sharing temperature. The mechanical stresses in both coils and its structure will be measured and compared with the predictions. For getting higher Lorentz forces at the conductor, a load case with 80 kA in the TFMC and 12 KA in the EURATOM LCT coil was investigated by a FEM analysis. The stress levels are compatible with the design.

The goal is to conclude the test phase by end of 2002.

2. Evaluation test results of the test phase I

The measurements for determination of the electromagnetic, thermohydraulic, mechanical and dielectric properties were evaluated. The evaluation were performed in collaboration with EFDA / CSU Garching and the European superconductor laboratories on the basis of preparing experimental work and code development [1].

2.1 Electromagnetic properties

Determination of the operation limits: The operation limits of a superconducting magnet are characterised by its load line, which gives the relation between the current and the highest magnetic field region in the magnet as well as the operation temperature (Fig. 3). The crossing of the load line with the field of the temperature line gives the operation point where the conductor of the magnet starts the transition to the normal state. For the measurement of this so called current sharing temperature T_{CS}, the inlets of the two pancakes of double pancake DP1 are equipped with heaters, temperature sensors and flow meters. Since T_{CS} at the high field point cannot be directly measured, a code called Multi Conductor Mithrandir (M&M) has been developed to optimise the heating procedure without the occurrence of thermo-acoustic oscillations and determination of T_{CS} from the inlet temperature [2]. The result was a multi-step heating strategy by increasing carefully the heating power in small steps to get a homogeneous heating power and temperature profile in the conductor, [3], [4]. The heating was continued till a resistive voltage occurred, which finally led to a propagating quench initiating a safety discharge. The heating was performed at three current levels (56.6 kA two times, 69.3 kA one times, 80 kA five times). The results are summarised in Fig. 4 and compared with the predicted values, which are in fair agreement. The TFMC conductor achieved the expected performance. A refined analysis shows however that, for ITER design of stainless steel large cable-in-conduit conductors, the fully bonded model is more adapted than the relaxed bonded model used for ITER design and that the field gradient across the conductor has to be taken into account [5].

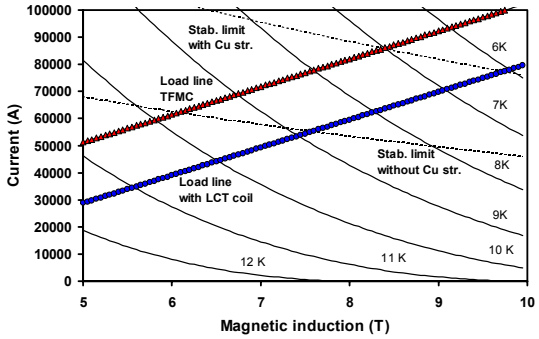

Fig. 3: The TFMC load lines for the high field point for the two test configurations: Phase I without LCT coil; Phase II with LCT coil#

An attempt was also performed with a linear heater power ramp for 80 kA, which was more difficult to be interpreted [2], [6].

Joint resistances: All joints achieved the specified resistance between 1 – 2 nΩ at maximum current. The joint resistances were determined by an electrical voltage drop measurement and by calorimetric measurements [7]. For the demountable joints, the Ag or Au coating of the copper contact surfaces brought an improvement of a factor 10 compared to that obtained in former times without coating.

Coil losses: The coil losses are composed of steady state losses and AC losses. The steady state losses at a given current are produced by the resistance of the pancakes joints and by the plate losses induced by the current ripple. AC losses are produced during current transients and are composed classically of hysteresis and coupling losses in the cable and of eddy currents in the plates, which are specific to this coil.

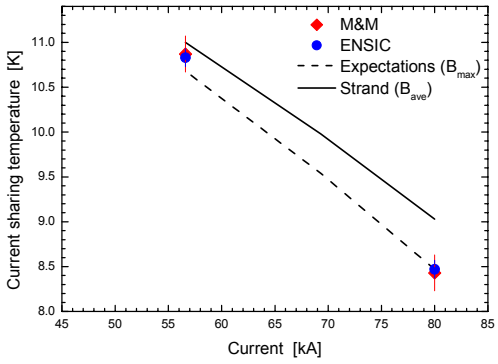

Fig. 4: Measured and predicted current sharing temperatures

These losses were discriminated using so-called trapezoidal current runs of the TFMC. In these runs the current is increased at given rate, kept constant at a plateau of 40 kA up to extinction of the thermal transient and decreased with the same current rate. The current rate was varied from 100 A/s to 400 A/s. The

results were in agreement with the model. As expected, the plates losses were dominant [8]. In addition cycling of the TFMC current was done without plateau in different conditions and the results confirmed the analysis from the trapezoidal runs. For a ramp rate of 200 A/s, respectively 400 A/s, the winding losses were about 220 W and 550 W, which were within 15 % in agreement with calculated ones.

2.2 Thermohydraulic properties

Pressure drop: For the thermohydraulic analysis, the TFMC conductor has to be considered as a dual cooling channel system, which reflects the parallel helium flow in the central channel and in the sub-cables of the conductor (Fig. 5). Therefore experimental work was performed in advance on a conductor piece of few meters in length for the determination of the friction factor [9], [10]. A comparison between the measured and calculated pressure drop at 4.5 K for the heated pancakes DP1.1 and DP1.2 are presented in Fig. 6. The agreement is satisfying.

Fig. 5: The conductor cross section of the TFMC with the central hole and the bundle region (light strands: Cu; dark strands: Nb_3Sn

Safety discharge: The most stringent thermohydraulic load case during magnet operation is the safety discharge where a part of the magnetic energy is dissipated by eddy current losses and stored in the enthalpy of the coil material by increase of the temperature up to about 23 K. A fraction is immediately transferred to the hydraulic system and generates a pressure increase, which has to be released automatically by the cryogenic control system. All safety discharges were mastered without helium release to the atmosphere. The cooling circulation has to be started carefully to cool down the test configuration. Two to three hours were needed before starting again operation with current. The energy balance of a safety discharge is presented in Fig. 7. The biggest part of the magnetic energy (92 %) is dissipated in the resistor of the discharge circuit. An attempt was made to analyse temperature, pressure, normal zone propagation and mass flow rate traces with the code GANDALF/FLOWER and MAGS [2]. The measurements met the predictions within 30 %, which reflected the limits of the applied models and partly unknown boundary conditions.

2.3 Mechanical properties

In preparation of the TFMC single coil test the configuration was investigated by a finite element (FEM) analysis [11]. The most critical item for a superconducting magnet is the force transmission between the winding pack and the supporting structure of the coil case. In a parameter study the effect of the sliding between winding and coil case was investigated using friction coefficients between zero and excessive values. The latter ones lead to slightly lower stresses in the winding and higher stresses in the case. An assessment of the force transmission between winding and case is the measurement of the overall deformation of the coil case in the horizontal and vertical plane (Fig. 8). The periphery of the outer joints was identified as a critical area by the FEM analysis, too and therefore was also equipped with displacement transducers. The agreement between predicted and measured values of the overall deformations is good [12]. The equivalent stresses measured by strain gauge rosettes are in fair agreement with the FEM analysis. Stronger deviations were observed for uniaxial strain gauges. This is probably caused by local pretensions in the material due to the manufacturing of the coil case. The mechanical sensor values, which could be obtained only at accessible outer parts of the coil case surface, have validated the FEM model. From this it can be concluded that the mechanics is predicted reasonably inside the casing not accessible for the measurements.

2.4 Electrical insulation properties

The electrical insulation system is the most important component, which determines the lifetime of the magnet. Specially the high stored magnetic energy acting as constant current source with nearly unlimited voltage respectively power has a high damaging potential in case of serious fault of the insulation system. Therefore a careful insulation diagnostic and understanding of the electrodynamics of the insulation system is indispensable. The ITER TF coil insulation system is very well accessible for insulation diagnostics by DC, AC and pulse voltage.

The TFMC insulation system was tested during fabrication steps mainly using non-destructive DC and pulse voltage tests. In TOSKA the tests were extended to AC voltage with partial discharge measurements, too. All three insulation systems of the TFMC (conductor – radial plate, radial plate – radial plate, winding pack – coil case, Fig. 9) were tested [13].

An electrical network model was elaborated to optimise the fixing of the radial plate potential and to minimise over voltages by internal oscillations excited by switching transients during safety discharge by counteracting current switches [14]. The calculated and measured first resonance frequency is for the TFMC above 200 kHz (Fig. 10). Since the relevant frequency portions of the usual switching transients are much lower than 200 kHz no excitation of critical voltage oscillations of the ITER TFMC winding occurs. This is with several μs as rise time far outside the usual switching transients.

Investigations of the ITER EDA TF full size coil design by a network model show a much lower first resonance frequency of about 4 kHz [15], which is in the range of the frequency spectrum of switching transients.

The insulation resistance of all three insulation systems was several tens of GΩ after 1 minute and 100 GΩ after 15 minutes. Under ambient conditions no degradation of the insulation resistance was found over the whole test time. The AC test on ground insulation showed a constant reactive current in the expected range, which corresponds to a ground capacitance of 132 nF. Partial discharge activity (PDA) of the ground insulation was 0.75 nC. The finger prints (accumulation of apparent charge as function of AC voltage phase angle) indicate voids in the ground insulation. PDA of radial plates and conductor insulation were covered by the noise level.

Unexpected DC breakdowns were observed in the range of the Paschen minimum up to about 400 mbars vacuum vessel pressure. The DC breakdowns vanished at operation temperature and a vacuum vessel pressure of 10^{-6} mbar. During pulse voltage test breakdowns were found for a pulse voltage level > 4 kV for the positive terminal (negative terminal grounded). Reversing the connection to the impulse generator (negative terminal at high voltage, positive terminal grounded) no breakdowns were observed. After warming up to room temperature lightening effects allowed the localisation at the supply pipe feedthrough holes through the coil case side wall near the inner bore and the backside of the coil where the superconducting bus bars were located. Since the safety discharge voltage is < 1 kV sufficient safety margin has been available for the high current operation.

No discharge traces were localised by visual inspections. This means a high resistance breakdown mechanism, which could be combined with sliding discharge mechanism for pulse voltage. Therefore it was decided to go ahead with this fault into the test phase II (test of the TFMC with LCT coil) with careful monitoring of the insulation system during testing.

2.5 The TOSKA facility

Through the whole test phase I the TOSKA facility worked very reliably [16]. Some outstanding results for the different systems are presented in the following:

Cryogenic supply system: The system was operated during the current sharing temperature experiments outside the rated cooling capacity of the refrigeration system by the use of stored liquid helium and feeding helium carefully back by sharing of helium gas to the refrigerator and to the room temperature recovery system. The very low total heat load of about 63 W was achieved by the excellent vacuum (about 10^{-6} mbar) and additional super-insulation mats around the test configuration. The remaining leak rate was at 200 K about 10^{-7} mbarl/s and at 4.5 K about $2 \cdot 10^{-7}$ mbarl/s.

Two newly developed 80 kA current leads were operated successfully including a water cooled flexible bus bar system acting as connection between the rigid Al bus bars and the current leads.

Electrical supply system: Two power supplies were operated successfully in parallel to get a current of 80 kA. In the safety discharge circuit commercially available DC breakers were used. They were capable for 13 safety discharges > 50 kA in one maintenance period and a peak switching power of about 72 MW.

Protection, control, data acquisition: The quench detection system worked very reliably. All quenches were detected and safety discharges were triggered. No unintentional safety discharge was released by the quench detectors. A sensitivity of +/-10 μV was achieved for accuracy of the joint resistance measurements. All data are directly accessible and available around the world by download from the WWW.

12 scientists from the European superconducting laboratories and EFDA as well as 3 scientists from Japan and USA participated in the test.

2.6 Conclusions

From the results of the first test phase the following conclusions can be drawn:

- The engineering design principles and manufacturing procedures are sound and suitable for the ITER TF coils.
- The conductor operation limits were successfully determined by measuring the current sharing temperature T_{CS}. The measured T_{CS} values were in agreement with the predicted ones. The results were reproducible within the given accuracy over the testing time. The scaling law to higher field levels is being under discussion and needs further investigation.
- The AC losses of the winding are in fair agreement with the predictions.
- All joints were in the range between 1-2 nΩ. The reproducibility of industrial fabricated joints was successfully demonstrated.
- The dual cooling channel principle can be described by the codes GANDALF / FLOWER in the range of about 30 % accuracy. For the optimisation of the stepwise heating for the current sharing measurements the developed code Multi conductor MITHRANDIR (M&M) was applied. The input parameters for the codes were gained by measurements on 5 m conductor pieces.
- The global ANSYS FEM model of the TFMC in the single coil test leads to a description of the overall deformations, which have been in good agreement with measurements.
- The insulation system of the TFMC was investigated by DC, AC and pulse voltage. The most stringent DC insulation test was performed in the Paschen minimum, in which weak points were indicated. These weak points could be reproduced also by the pulse voltage test at voltage levels > 4.7 kV and 10^{-6} mbar vacuum vessel pressure. The faulty insulation areas could be localised. They shall be repaired after the test phase II. The voltage margin for the performance of the safety discharge with a voltage level of about 900 V is sufficient in order to go ahead with the test program in phase II.
- The TOSKA facility was operated very reliably during the whole test phase I with an availability of 98 %. Therefore the TOSKA facility is qualified and well equipped for testing components in the ITER construction phase.

3. Outlook

The low current tests for the check outs of the interlocks of the cryogenic and electrical system for both coils in single and joint operation were completed. The high current test will start in the last week of September.

The operation experience gained up to now looks promising to complete the test by the end of 2002.

Staff:

A. Augenstein
S. Darweschsad
I. Donner
G. Dittrich
P. Duelli
W. Eppler
W. Fietz
S. Fink
G. Friesinger (till Febr. 2002)
A. Grünhagen
R. Heger
R. Heller
W. Herz
R. Kaufmann
A. Kienzler
O. Langhans
W. Lehmann
V. Leibbrand
V. Marchese
I. Meyer
J. Müller
G. Nöther
U. Padligur
S. Raff
P. Rohr
M. Röhrling (since Mai 2002)
P. Schanz
V. Schulmeister
E. Specht
H.-J. Spiegel
M. Süßer
A. Ulbricht (for 2, 3)
D. Weigert
F. Wüchner
G. Zahn (for 1)
V. Zwecker

Literature:

[1] A. Ulbricht and the L2 project team, Test results of the ITER toroidal field model coil experiment in the TOSKA facility of the Forschungszentrum Karlsruhe, Proc. 22nd SOFT, Helsinki, Finland, Sept. 9-13, 2002

[2] P. Libeyre, J. L Duchateau, R. Heller, S. Raff, S. Fink, P. Hertout, C. Marinucci, A. Martinez, R. Meyder, S. Nicolett, L. Savoldi, G. Zahn, R. Zanino, ITER Toroidal Field Model Coil (TFMC), Test and analysis summary report, Chapter 1: Specific analysis results needed for testing, CEA Cadarache, AIM/NTT-2001.005, April 12, 01

[3] L. Savoldi, R. Zanino, V. Marchese, N. Martovetstki, M.Süßer, A. Ulbricht, F. Wüchner, G. Zahn, First measurement of the current sharing temperature at 80 kA in the ITER toroidal field model coil (TFMC), Proc. MT-17, Geneve, Sept. 24-28. 2001, IEEE Trans. on Applied Supercond. 2002 in print

[4] R. Zanino, L. Savoldi-Richard, Measurement of current sharing temperature and performance evaluation of the ITER toroidal flied model coil, submitted to Cryogenics 2002

[5] D. Cyazinski, J.L. Duchateau, R. Heller, V. Marchese, L. Savoldi, R. Zanino, Evaluation of the current sharing temperature of the ITER toroidal field model coil, Proc. ASC 2002,

[6] C. Marinucci, L. Bottura and P. Bruzzone, Analysis of the measurement of the current sharing temperature in the ITER TF Model Coil, Proc. 22nd SOFT, Helsinki, Finland, Sept. 19-13, 2002

[7] D. Ciazynski, M. Ricci, J.L. Duchateau, V. Marchese, A. Ulbricht, F. Wuechner, G. Zahn, H. Fillunger, R. Maix, Resistances in electrical joints in the TF model coil of ITER: comparison of first test results with sample results, Proc. MT-17, Geneve, Switzerland, Sept. 24-28, 2001, IEEE Transaction on Appl. Supercond. 2002, in print

[8] J. L. Duchateau, P. Hertout, S. Nicollet, M. Ricci, A. Ulbricht, G. Zahn, AC losses in the ITER TF Model coil: a comparison between model and experimental results, Proc. ICEC-19, Grenoble, France, July 22-26, 2002

[9] S. Nicollet, J. L. Duchateau, H. Fillunger, A. Martinez, Calculations of pressure drop and mass flow distributions in the TFMC of the ITER project, Cryogenics 40, (2000), pp. 569-575

[10] R. Zanino, P. Santagati, L. Savoldi, A. Martinez, S. Nicolett, Friction factor correlation with application to the central cooling channel of cable-in-conduit superconductors for fusion mahgnets, IEEE Trans. App. Supercond. 10, 2000, pp. 1066-1069

[11] S. Raff, P. Schanz, H. Fillunger, B. Glasl, Structural analysis and verification of the ITER TF model coil test conditions, Proc. 21st SOFT, Madrid, Spain, 11 –15 Sept. 2000, pp. 247-251

[12] S .Raff, P. Schanz, F. Wüchner, H. Fillunger, P. Libeyre, Mechanical behaviour of the ITER Toroidal Field Model Coil (TFMC) in the single coil test, Proc. 22nd SOFT, Helsinki, Finland, Sept. 19-13, 2002

[13] S. Fink, A. Ulbricht, High Voltage Tests of the ITER Toroidal Field Model Coil Insulation System, Proc. MT-17, CERN, Geneva, Switzerland, Sept. 24-28, 2001

[14] A. M. Miri, C. Meinecke, N. Riegel, A. Ulbricht, S. Fink, Influence of the radial plates on the transient oscillations in the ITER TF model coil using a finite element approach,

[15] C. Sihler, A. Ulbricht, A. M. Miri, Transient voltage effects on ITER TF coils, Final Report, Interner Bericht F.130.0016.012/B, , Dec. 1996 and Addendum to Final Report, Interner Bericht F.130.0016.012/E, June 1997, Forschungszentrum Karlsruhe / ITP

[16] G. Zahn, R. Heller, Forced flow cooling of large superconducting magnets for fusion application, Proc. ICEC-19, Grenoble, France, July 22-26, 2002

TW1-TMC/CODES
Design and Interpretation Codes. Subtask: Installation of Hall Probes on ITER Toroidal Field Model Coil

Non-uniform current distributions affect both the steady state and the transient performance of superconducting magnets. A good understanding of the phenomena leading to non-uniform current distributions in sub-cables (Fig. 1) and the validation of computer codes able to interpret experimental results and to predict the behaviour of complete superconducting systems is therefore essential for a reliable design of those magnets and for an optimisation of their design parameters. The attempts to obtain the re-construction of the profile of the current density are normally based on sets of magnetic field probes, for instance based on the Hall effect, suitably located as near as possible to the conductors (Fig. 2). From the field measurements, the determination of the current distribution is then formulated as a linear inverse problem, which can be solved by minimising the errors between measured and calculated fields at the probes' locations [1, 2].

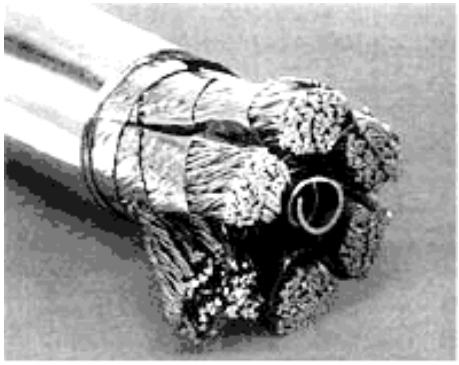

Fig. 1: TFMC superconductive cable.

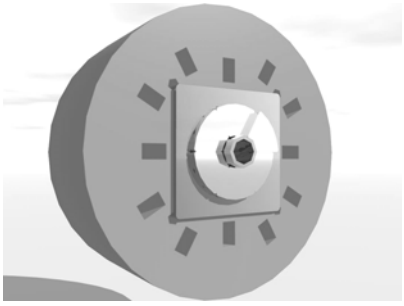

Fig. 2: H-probe allocation in a meas. head

The experimental conditions relevant for the scope of this task are met during the Phase II test campaign of the Toroidal Field Model Coil (TFMC) on-going at the TOSKA facility of the Forschungszentrum Karlsruhe[1]. The work, co-ordinated by EFDA-CSU, is conducted in co-operation with IEE Bratislava, supplier of the measuring heads, and the consortium ENEA-Create, responsible for the data acquisition system and the interpretation codes.

The aim of the subtask is the participation in the design and assembly of a magnetic field measurement system for the evaluation of the current distribution of an ITER type NbTi cable, used for busbar type 1, and to provide technical support for the system set up (fixing of the measuring heads, cabling and wiring, calibration and data archiving on an FZK server) and for the experimental campaign.

Two measuring heads, each provided with twelve Hall probes, have been installed on the TFMC negative type 1 busbar at a distance of a quarter of pitch from each other and at an average distance of about 600 mm from the busbar type 1 and busbar type 2 joint (Fig. 3). The head on the left (H4) is provided with six "tangential" probes and six "radial" ones, the head on the right (H2) is provided with ten tangential and two radial probes. The wiring from the measuring heads to the vacuum feed-through has been performed with Kapton insulated quads (two twisted pairs with screen). The wiring from the vacuum feed-through to the data acquisition system cabinet, located about 25 meters away, has been performed with Teflon insulated quads.

The current sources, housed inside the data acquisition system cabinet, have a current range up to 100 mA with stability better than $\pm$15 ppm over 6 hours. Up to six Hall probes have been connected in series in order to reduce the number of current sources. The amplitude of the sensing current is selected in such a way that voltage signal from the Hall probes, in absolute value, does not exceed100 mV at the maximum field. The data acquisition system hardware includes the NI signal conditioning board SCXI 1102B for the Hall probes (32 differential inputs, gain 100 and 200 Hz anti-aliasing filter), the SCXI 1120 (8 differential isolation amplifier channels + 4Hz low pass filter) for LCT and TFMC currents, the SCXI multiplexer and the PCI 6032E (16 bit ADC board, maximum sampling speed 333 kS/s). The data acquisition system software has been developed with LabVIEW. The maximum absolute error of the chain signal conditioning unit, multiplexer and ADC at full scale ($\pm$100 mV) is of the same order of magnitude of the quantization error.

The precision of the measurements is affected by geometrical errors such as the positioning errors of the probes and the uncertainties of the actual position of the conductor axis inside the insulated steel jacket. An attempt has been made to identify positioning inaccuracies by feeding the TFMC in resistive state (e.g. at 77 K) and, therefore, with a current distribution essentially uniform (see Fig. 4, 5 and 6). The difference between the actual measured fields and the expected ones, which are expected for uniform current distribution in "nominal" geometry, should give a quantitative indication of the probes and conductor axis misalignment.

Since the transport current in resistive state can only be relatively low, particular care has been taken in calibrating each individual Hall probe at ambient temperature, at 77 K and at cryogenic temperature. The compensation of the external fields is achieved calculating the magnetic field produced by the external currents (i.e., coils and + busbar). The experimental campaign will be concentrated in October and November 2002 in the three configurations foreseen: LCT alone, TFMC alone and combined operation. A report on current balance in the six petals in the last two configurations is expected for the end of 2002.

Staff:

V. Marchese
F. Wuechner

Literature:

[1] F Bellina, T Bonicelli, M Breschi, M Ciotti, A Della Corte, A Formisano, Yu Ilyin, V Marchese, R Martone, A Nijhuis, M Polak, A Portone, Superconductive Cables Current Distribution Analysis, 22nd SOFT Conference, Helsinki, 9-12 September, 2002.

[1] Subtask EFDA/01-605, TFMC testing with the EURATOM LCT coil.

[2] A. Formisano, R. Martone, Current reconstruction from magnetic measurement in superconducting cables, IGTE Symposium 2002, Graz, Austria, September 2002.

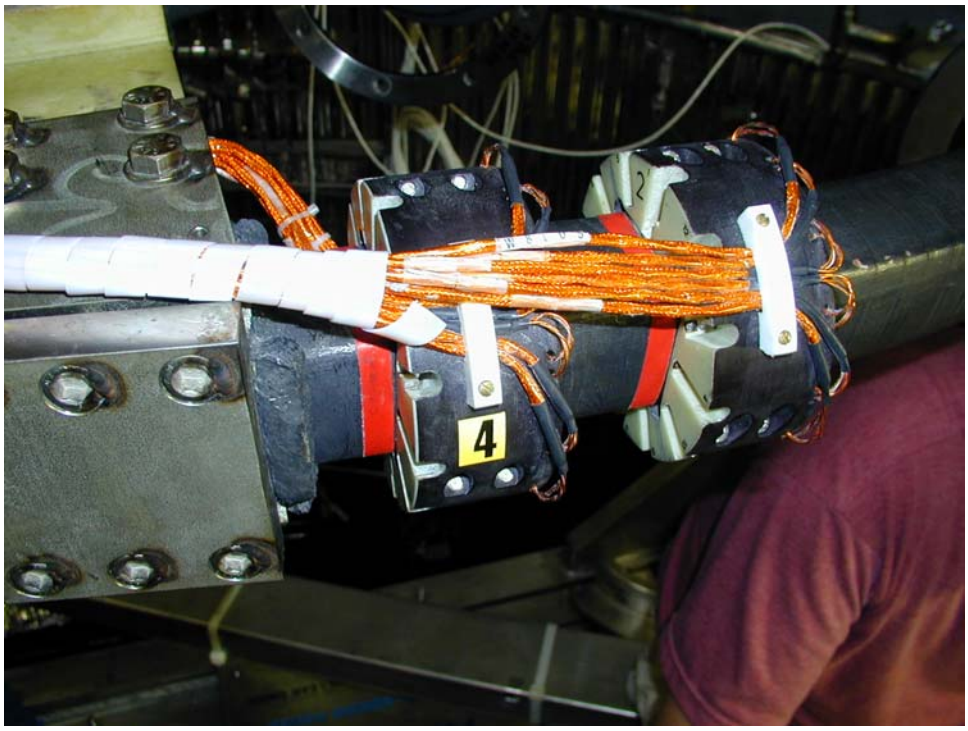

Fig. 3: Physical location of the two Hall probe measuring heads.

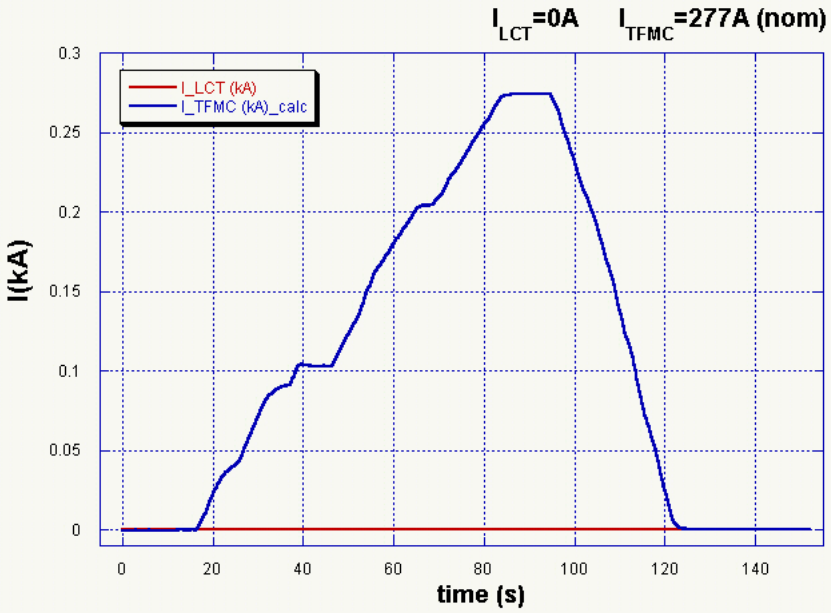

Fig. 4: Injected current in a resistive case.

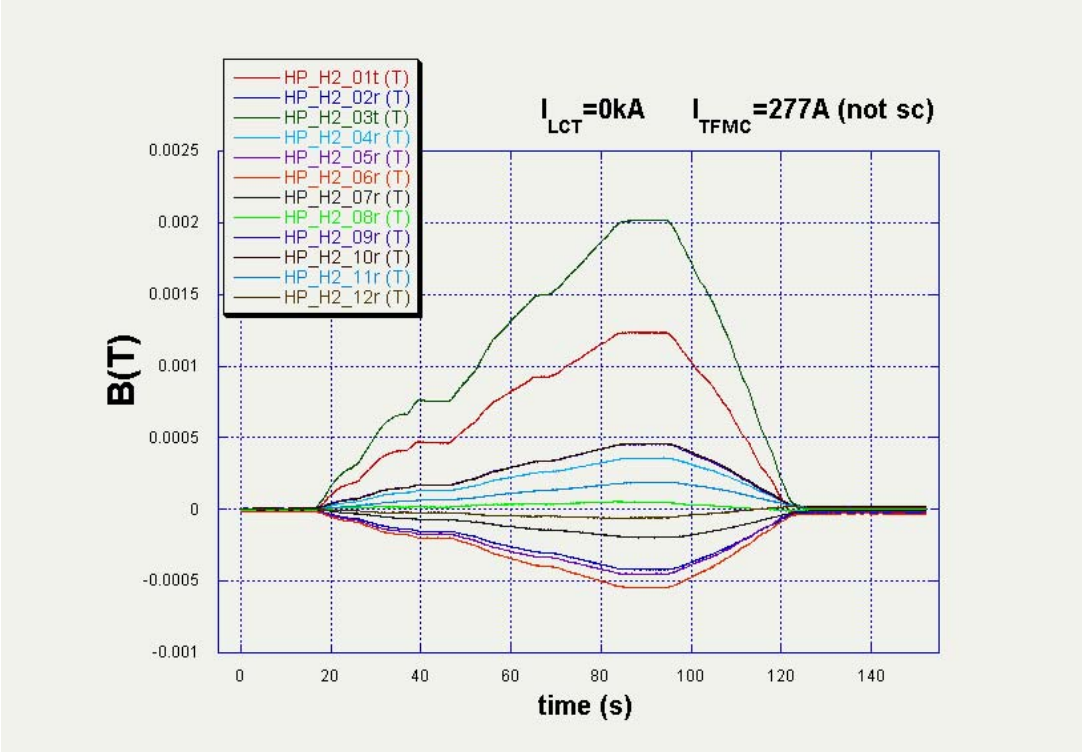

Fig. 5: Magnetic field measurements obtained from Head H2 in resistive case.

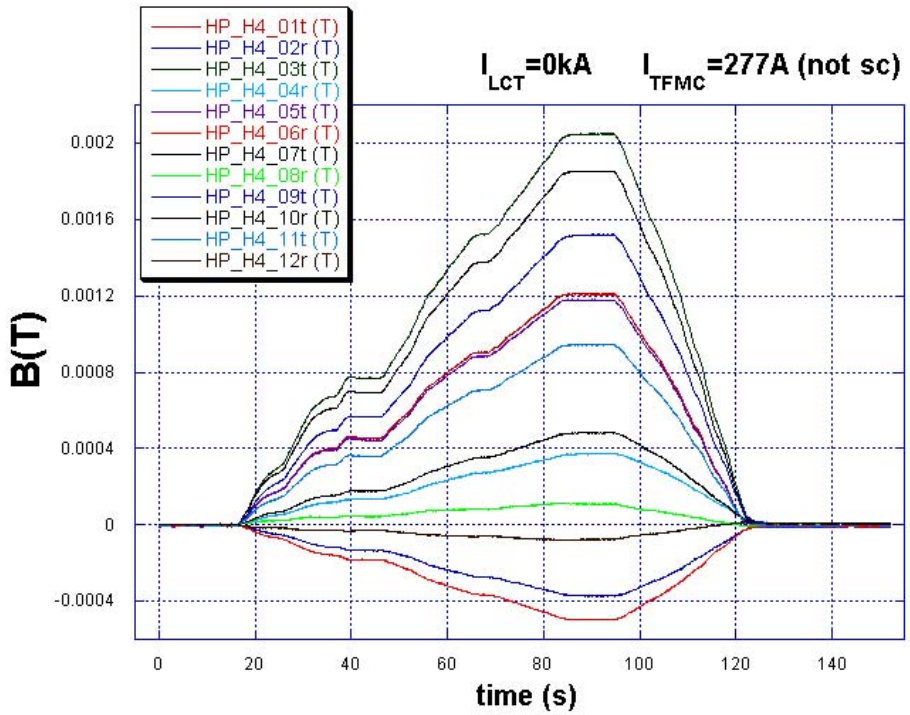

Fig. 6: Magnetic field measurements obtained from Head H4 in resistive case.

TW2-TMSM-CRTEST 5.1b
Cryogenic Testing of Materials and Welds for Magnet Structures

Within the present framework, investigations have been performed with respect to cryogenic mechanical properties of central solenoid (CS) jacket materials. The target of these investigation series was to reevaluate the potential of Type 316LN materials for the application as extruded jacket structure (square cross section of 51 x 51 mm with a central bore of 38 mm Ø). One of the major disadvantages of the Type 316LN compared to the presently used Incoloy 908 material (selected and successfully tested in CS model coil) is the inferior cryogenic fatigue crack growth rate (FCGR) resistance. A replacement of the material Incoloy 908 by a Cr-Ni-N stainless steel can be therefore achieved if the cryogenic FCGR properties of the material in extruded and aged (heat treatment for 200 h at 923 K) condition meet the ITER cryogenic cyclic requirements. To determine the application potential of type 316LN materials two different materials have been industrially produced. These materials designated under the company brand names were, Cefival and Siderval in comparison to the former already tested candidate jacket material Valinox. The provided ~400 mm long jacket samples from these materials have had an orbital butt weld located in the middle of the extruded jacket. These present investigations comprised cryogenic FCGR tests with standard 4 mm thick compact tension specimens, machined from the jacket structure. Beside the cyclic tests also standard cryogenic tensile tests were carried out to check the static loading performance of these new materials. All these tests were performed in as received and as well as in aged condition between 7 K and 4 K. In addition, a full size 300 mm long jacket material having a weld zone in the middle was tested in cyclic four point load mode in the newly installed 630 kN cryogenic test facility.

Beside these structural material tests related to the CS coil conductor jacket, also case materials of mock-ups designated as model 3 were tested to characterize the properties.

For PF insert the candidate structural aluminum alloy 7075-T6 is foreseen for the tie rods. This material is also investigated with respect to tensile and fracture behavior at 7 K.

Furthermore, thermo-physical properties such as thermal contraction between 290 K and 7 K were determined for a series of structural materials, which are intended to be used in the design of ITER coils. In addition to the thermal contraction measurements the thermal diffusivity is also estimated for the alloy 7075-T6.

Results with tensile and FCGR measurements of jacket materials

Table 1 gives the chemical composition of the three different jacket materials and the chemistry of the model 3 mock-up case materials with two Japanese structural materials in addition. As shown, the material Cefival does not differ much from the former Valinox material, whereas the Siderval is a modified Type 316LN new material with higher manganese content. The measured tensile properties as given in Table 2 show that the material Cefival in aged and unaged condition fulfills the static loading requirements without any major embrittlement during the long aging period. However, the material Siderval as given in Table 3 shows an embrittlement due to the low elongation at fracture. Scanning electron microscopic investigations confirmed a grain boundary chromium carbide precipitation after aging. The material Siderval has the potential to replace the Incoloy 908 regarding the FCGR findings as given in Figure 1. However, a further micro alloying (presumable with niobium or boron) is necessary to prevent the grain boundary precipitation.

Results with fatigue life investigations of full size jacket structure

To confirm the validity of the results obtained with small size fatigue life specimens, a full size test has been performed using the 300 mm long jacket section with a weld joint in the mid position. For this action the newly installed servo hydraulic test facility (Schenck 630 kN) equipped with a liquid helium bath cryostat of 400 mm Ø bore was used. The designed 4 K rig allowed to test (at 2 Hz) by pull-pull the jacket section in four point bending mode, thus introducing cyclic surface stresses in the range of 900 MPa at ΔP ~ 360 kN. Figure 2D shows the assembled experimental setup beneath the lower bottom plate of the 4 K rig. Prior to these tests the weld residual stresses were estimated from the bending stress required to distort the removed samples from the mid position of the jacket sample. The sample bars were removed by electro discharge machining (EDM) as shown in Figure 2A. All four removed samples (130 mm long and 20 mm wide) were bent due to the release of the residual stresses. The calculations showed that for aged jacket samples the residual stresses at the surface were approximately +430 MPa. An independent residual stress measurement obtained using neutron diffraction tests confirmed this value within 5 %. In addition, for the full size fatigue life test, the jacket weld surface was prepared by machining of two small artificial flaws (semicircular ~ 0.2 mm deep) using the EDM technique to obtain cryogenic cyclic information for worse case. The full size jacket section (unaged condition) fatigue life test performed under four point cyclic bending mode resulted in a survival of the structure at 4 K after 62 000 cycles for 900 MPa (load range of 360 kN). Besides, small size fatigue life tests carried out with aged and unaged flat and circular specimens for Valinox and aged Incoloy 908 jacket materials (Figures B and C) resulted in a scatter band without any clear indication about a significant difference for both materials using different type specimens. Therefore all these measured data were merged together and a common regression line was computed, which gives:

$$\text{Stress} = -57.815 \cdot \ln(\text{cycle number}) + 1770.1 \text{ [MPa]}$$

Considering this equation and the fact of residual surface stresses of +430 MPa, which should be actually added to the applied cyclic stress (900 MPa) the obtained result with full size

Table 1: Chemical composition of investigated structural materials.

Material	C	Si	Mn	P	S	Cr	Ni	Mo	N
Valinox jacket	0.012	0.24	1.64	-	-	17.20	12.00	2.43	0.180
Cefival jacket	0.020	0.400	1.79	0.013	0.0005	17.04	13.28	2.57	0.170
Siderval jacket	0.024	0.690	5.90	0.018	0.001	17.90	13.80	3.20	0.200
Model 3, forged	0.024	0.690	5.90	0.018	0.001	17.60	13.80	3.20	0.200
JK2, 250 mm, JAERI	0.050	0.36	21.3	0.005	0.001	12.90	9.20	1.00	0.240
JJ1, 250 mm, JAERI	0.030	0.54	10.1	0.022	0.002	12.00	11.7	4.90	0.240

Table 2: Tensile properties of jacket material Cefival in aged and unaged condition at 4 K.

Data file & condition	Specimen Ø Temperature K	Young's Modulus GPa	Yield Strength MPa	Ultimate tensile strength MPa	Total Elongation %
Cefun-1 unaged	4 mm Ø 4.2	193	1173	1571	33
Cefun-2 unaged	4 mm Ø 4.2	192	1181	1588	39
Cefag-1 aged	4 mm Ø 4.2	204	1202	1678	37
Cefag-2 aged	4 mm Ø 4.2	203	1187	1670	46

Table 3: Tensile properties of jacket material Siderval in aged and unaged condition at 7 K and at 4 K.

Data file& condition	Specimen Ø Temperature K	Young's Modulus GPa	Yield Strength MPa	Ultimate tensile strength MPa	Total Elongation %
Sidun-1 unaged	4 mm Ø 4.2	167	1244	1560	30
Sidun-2 unaged	4 mm Ø 4.2	170	1309	1608	29
Sidag-1 aged	4 mm Ø 7	172	1296	1490	9
Sidag-2 aged	4 mm Ø 7	173	1303	1559	16
Sidag7-1 aged	6 mm Ø 4.2	181	1310	1502	11.5
Sidag7-2 aged	6 mm Ø 4.2	181	1288	1514	17.5
Sidag7-3 aged	6 mm Ø 4.2	182	1291	1536	17.5
Sidag7-4 aged	6 mm Ø 4.2	181	1290	1524	16.5
Sidag7-5 aged	6 mm Ø 4.2	177	1252	1469	12
Sidag7-6 aged	6 mm Ø 4.2	182	1270	1503	15.5
Sidag7-7 aged	6 mm Ø 4.2	182	1306	1498	15
Sidag7-8 aged	6 mm Ø 4.2	179	1280	1442	8.5

Table 4: Tensile properties of investigated aluminum alloy 7075 at 295 K and at 7 K

Data file & code	Temperature K	Orientation	Young's Modulus GPa	Yield Strength MPa	Ultimate Tensile strength MPa	Uniform longation %	Total elongation %
AW7075-1	7	long	82	566	766	12.0	14.3
AW7075-2	7	transverse	82	534	727	7.3	7.3
AW7075-3	7	transverse	82	530	731	8.5	8.5
AW7075-4	7	long	81	556	753	12.0	14.0
AW7075-5	295	long	76	458	531	6.0	7.2
AW7075-6	295	long	76	447	519	6.0	7.4
AW7075-7	295	transverse*	72	419	498	6.0	7.0
AW7075-8	295	transverse*	75	420	502	6.5	8.3

* Fracture of specimens occurred at RT and in transverse orientation. The fracture is in 45 ° shear mode.

jacket shows that the loaded member at 4 K has a high safety against cyclic loads even in case of remarkable surface defects.

Results with tensile and FCGR measurements of Model 3 material

Tensile results with model 3 inner leg structure of the coil case (L- sections) forging showed that the required yield strength of 1000 MPa at 4 K could be so far achieved in the bottom and mid section of the heavy sample. However, in top section of the forging several specimens ranged below the required 1000 MPa minimum value. An additional small forged block of the size 300 x 300 x 300 mm from a similar material batch showed yield strength values at 4 K in all three orientations well above 1000 MPa.

Results with tensile and fracture toughness tests of Al-alloy 7075 – T6

The extruded 80 mm diameter Al-alloy 7075 - T6 (chemical composition: 0.26% Si, 0.30 % Fe, 1.49 % Cu, 0.16 % Mn, 2.59 % Mg, 0.20 % Cr, and 5.48 % Zn) tensile test results are given in Table 4 for 295 K and 7 K. Fracture toughness at 7 K were determined using the small specimens by J-test method (ASTM

E 813-89 standard). Fracture toughness of the material at 7 K depends on orientation significantly. At 7 K a crack plane parallel to extrusion direction results in a value of K_{IC} ~ 27.0 MPa√m, whereas the perpendicular orientation results into 47.5 MPa√m. The crack plane has a clear tendency to divert parallel to the extrusion direction.

Results with thermal properties of structural alloys

For thermal contraction measurements a technique has been developed using a 50 mm gauge length double extensometer system clamped onto the 60 mm long and 5 mm thick bar type specimen. The warm up curve was evaluated between 7 K and 290 K by taking account of the reference curve determined prior to these tests. The reference material is the extreme low thermal expansion glass ceramic material. The thermal contraction of all investigated structural materials was determined successfully. The determined contraction curves of Japanese structural materials JK2 and JJ1 (see Table 1) were cross checked by the Metrological Institute at Tsukuba, Japan. A nearly ideal matching between our values and the Japanese values confirm the exact working of the measurement setup. For Al 7075 an ~ 8 % smaller thermal contraction was determined compared to pure aluminum metal.

Furthermore, using a small 20 mm long cylindrical sample with two temperature transducers at each side, the thermal diffusivity of the Al 7075 could be estimated at 295 K and at ~100 K. The introduced heat transient at the front side by a heat pulse was tracked with 100 Hz sampling rate at the rear end of the cylinder. Using the unsteady second order partial differential temperature diffusion equation the thermal diffusivity could be estimated. The determined values were ~0.67 cm^2/s for 295 K and ~0.6 cm^2/s for 100 K.

Staff:

A. Nyilas
H. Kiesel

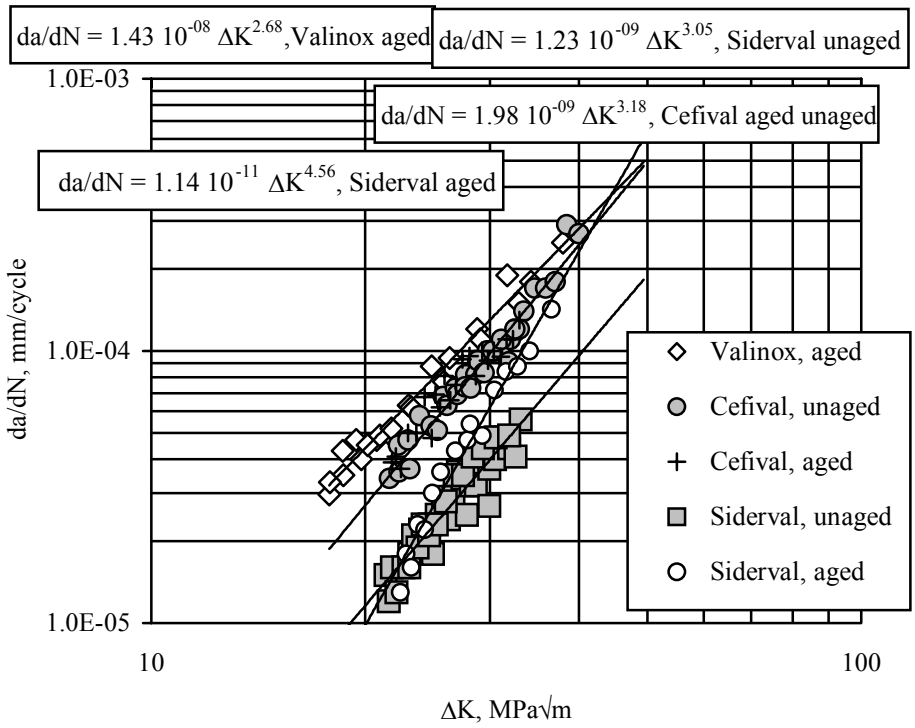

Fig. 1: Determined FCGR behavior of the aged and unaged new jacket materials at 7 K in comparison to the former Valinox materials.

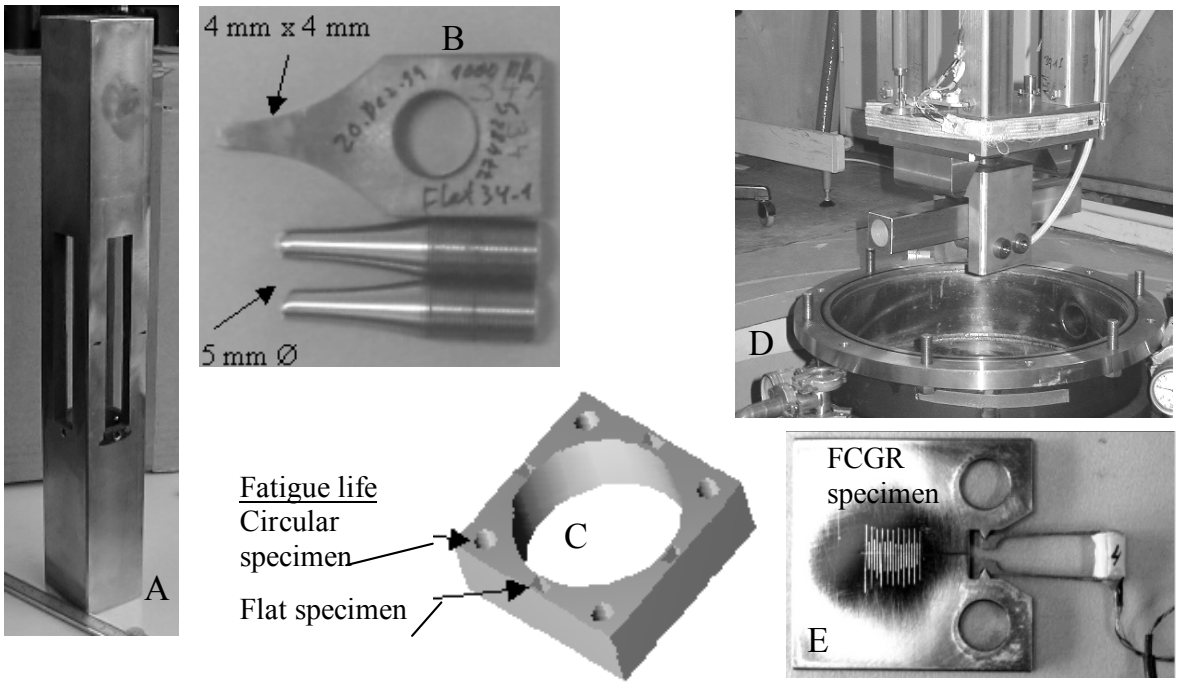

Fig. 2: Machined samples from the jacket section for residual stress estimation (A). Fatigue life specimens (B) machined from the jacket section (C). Four point bending load assembly during inserting into the cryostat (D) of the 4 K 630 kN test facility. Standard FCGR compact tension specimen with attached extensometer (E).

Fuel Cycle

01-641
European ITER Site Studies

In April 2002 the Spanish Ministry of Science and Technology selected the site of Vandellós in Catalonia near Tarragona as a possible host site for ITER and submitted a formal proposal to the commission. Consequently the European ITER Site Study (EISS), until that time solely considering the compliance of the French Cadarache site with the ITER requirements and assumptions, have been eventually extended to take also the Vandellós site into account.

The continuation of the work organized initially through a European ITER Site Study Group (EISSG) was called EISS II, and to effectively manage the activities of the associations a project board for EISS II was established. Four members of the project board - one of them from the Tritium Laboratory Karlsruhe (TLK) - have been appointed to constitute the European delegation for the Joint Assessment of Specific Sites (JASS) ad-hoc group, which had its first meeting in Clarington, Canada from the 12th to 15th September 2002 for a technical and socio-economical assessment of this proposed ITER Site. During the meeting a respective 'Findings Report' has been prepared on the basis of detailed input documents, based in turn on in depth studies, and on visits of the surroundings of the proposed site and meetings with representatives of the local authorities. The JASS process will be continued with meetings in Rokkasho, Japan, in Cadarache, European Union and in Vandellos, European Union.

To directly support the safety considerations and the licensing process for the European ITER sites in Cadarache and in Vandellos TLK has provided input information and reports for different tasks ranging from general tritium handling practices, licensing experience, human factors and radiological doses to waste categorization and treatment. One of the major contributions was on the various aspects of tritium tracking and control technologies for ITER.

No details or requirements on the tracking or accountancy of tritium are given in the ITER Design Requirements Guidelines which reflects the insufficient importance attributed to this topic. In any facility processing radioactive materials accountancy, tracking and control of the radioactive nuclides are fundamental. This is especially true for tritium since it permeates through many materials, exchanges with hydrogen and deuterium in most materials, and is easily distributed in the environment as HT and HTO. At peak performance, only about 1% of the deuterium and tritium fed into the ITER reactor will be consumed in a single experimental pulse. The remaining deuterium and tritium will be transferred to the Tritium Plant, purified and prepared for re-use. The practical viability of fusion plants producing electricity relies on the ability to recycle tritium at maximum efficiency, since tritium is a very rare (and expensive) substance, and ITER has established release guidelines for tritium and for other radioactive substances.

Up to now tritium has only been handled in two fusion devices: JET in Culham, UK and TFTR in Princeton, USA. In both machines processing and handling of tritium was carried out in a quite reasonable way, however tracking and accountancy in the various parts of the fuel cycle appeared to be more difficult than expected. This was partly due to the fact that the largest effort was put into the design, commissioning and effective operation of the tritium processing plant and not so much into accountancy aspects. Especially with respect to JET the processing and the recycling of tritium were carried out as planned; no incidences or tritium releases occurred during the whole Deuterium-Tritium Experiment (DTE) phase. Whereas the total tritium amount on the JET site was always well known, the tritium distribution within the various systems of JET could not be accurately established. The main cause of this was the unexpectedly large trapping of tritium in co-deposited layers and in plasma facing graphite tiles of the vacuum vessel and the inability to determine this amount on a shot by shot basis.

For the ITER tritium fuel cycle, a unique combination of systems which can not be simply compared with the systems of the tritium cycle at JET or TFTR, until now the main emphasis has been focused on processing and handling aspects to fulfill the requirements of the plasma physicists. However, the total amount of tritium injected into the ITER machine will be of the order of 1400 kg from the fifth to tenth years of ITER operation. The tritium throughput of ITER is more than four orders of magnitude higher than the one of JET. Therefore tritium tracking, control and accountancy for ITER will be far more important than it used to be at JET.

Staff:

C. Caldwell-Nichols
L. Doerr
M. Glugla
R. Laesser

GB 8-TR 1
Tokamak Exhaust Processing

The use of tritium in future nuclear fusion reactors calls for a careful design of all tritium exposed parts of the reactor, particularly for the entire fuel cycle to minimize the inventory and to accomplish safe handling of tritium. Not only in view of the control of effluents and releases, but also for economic incentives as much tritium as possible needs to be recovered for reuse from all off-gases and waste streams within the Tritium Plant of ITER.

The design basis scenario for the Tokamak Exhaust Processing (TEP) system of the ITER Tritium Plant during the plasma burn phase is such that about 1 kgh^{-1} of tritium needs to be recovered from the vacuum vessel off-gas. Besides the TEP product stream carrying the un-spent D-T fuel for transfer to the Isotope Separation System a waste gas stream of extremely low tritium content shall be produced, so that less than 0.1 mg of tritium (1 Ci) per day is lost into the ITER Normal Vent Detritiation System (N-VDS). Since (at least within the Final Design Report for ITER 1998) the operation time of TEP is estimated to be about 10 h per day, the tritium flow rate in the waste gas stream from Tokamak Exhaust Processing has to be $< 0.01\ mgh^{-1}$. Hence the required decontamination factor for TEP in terms of tritium flow rates is 10^8.

Such a high decontamination factor can only be achieved by multistage processes. The CAPER process developed at the Tritium Laboratory Karlsruhe (TLK) employs a palladium silver permeator as a first step ('Impurity Separation') to remove the bulk amount of un-burnt D-T fuel from the impurities. The second step ('Impurity Processing') is carried out in a closed loop involving heterogeneously catalyzed reactions combined with permeation of hydrogen isotopes through a palladium silver permeator. The third step ('Final Clean-up') is based on counter current isotopic swamping in a combined permeator / catalyst reactor called 'PERMCAT'

Fig. 1 is a picture of the CAPER facility at TLK showing the glove box (C) of the third process step with a volume of 6 m^3 on the front left. Parts of the glove box (A) on the right side (12 m^3) housing the first and second process step cannot be seen on the picture because of electrical cubicles and the PLC cubicle. A third glove box (B) with a volume of about 4 m^3 for a large pump is hiding behind. Thirteen primary (tritium bearing) pipes are secondary contained by a large diameter tube going from the upper right side of glove box (C) to the upper left side of glove box (A).

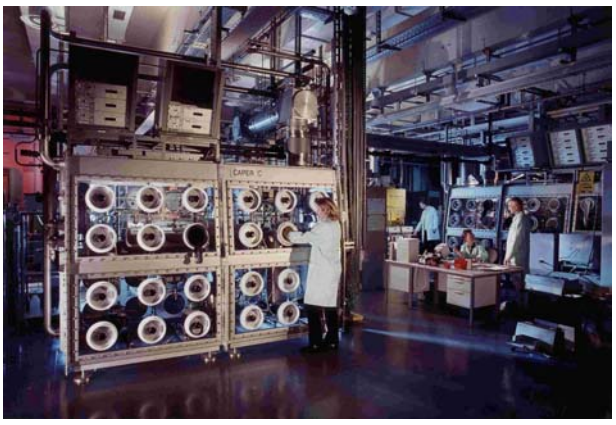

Fig. 1: Picture of the CAPER facility at TLK.

CAPER is a versatile experimental facility designed for the investigation and demonstration of the detritiation of all gases expected to be processed by the TEP system of ITER in an integral manner. Its modular set-up allows different routing of gases, and a large number of control loops along with comprehensive instrumentation installed permit a proper characterization of the chemical processes and components. The latter is particularly important to scale the process to ITER throughputs.

CAPER is also an essential and central system within the closed tritium cycle of the TLK. All primary gaseous wastes arising from other experiments at TLK, or e.g. from operation of the CAPER gas chromatograph are detritiated. The operation of the facility can therefore be considered as representative for the TEP system within the Tritium Plant of ITER.

Fig. 2 is an example of the performance of the palladium silver permeator for impurity separation (first process step) if operated under near ITER conditions. The pressure of the feed gas (about 6% of dry helium added to a hydrogen isotope mixture containing about 35% tritium, 53% deuterium and 12% protium) was kept constant at pressures above ambient, in this case at 0.14 MPa. The elevated permeate pressures have been chosen for optimization studies of the total pumping speed for all the permeators of TEP. The decontamination factors achieved in the first step under conditions as expected for ITER are typically around one hundred.

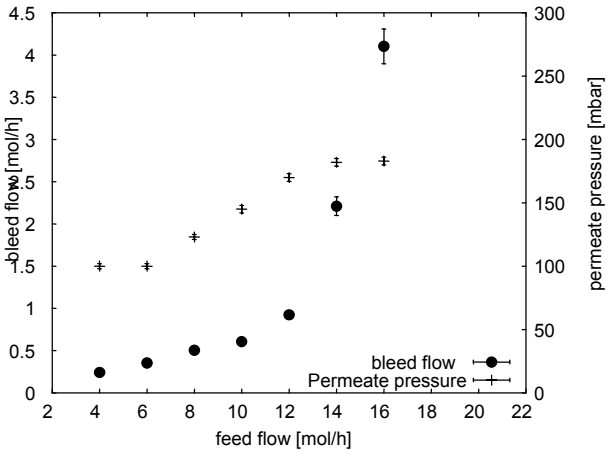

Fig. 2: Performance of the first process step of TEP.

As for the first stage of the TEP system of ITER quite a variety of gas compositions are expected to be processed in the Impurity Processing section (second process stage). Besides off-gases from the vacuum vessel gases from other sources such as from evacuation of jacket volumes of heated components (in which permeated tritium is accumulated) or gases from the ITER Analytical System will be accumulated in the TEP Impurity Buffer Vessel. While molecular hydrogen isotopes, e.g. from the carry over of the TEP Impurity Separation, will be directly recovered by the permeator in the Impurity Processing section, chemical bonded hydrogen isotopes need to be liberated to allow permeation and removal through palladium silver membranes. Heterogeneously catalyzed reactions such as hydrocarbon cracking or water gas shift reaction are well suited for that purpose. However, the water gas shift reaction, and in particular hydrocarbon cracking reactions, are typical equilibrium reactions which do not proceed to complete conversion. If these reactions are combined with the removal of molecular hydrogen with the help of a permeator, the equilibrium is permanently shifted until the processed gas

essentially does not contain hydrogen in molecular or other chemical forms.

The performance of the second process step in batch mode is illustrated in Fig. 3. In this experiment a mixture of tritiated methane, carbon oxides, helium, hydrogen isotopes and tritiated water was processed. The evolution of the activity in a loop is shown on the left axis, the methane concentration as measured by online gas chromatography (GC) sampling on the right axis. With both the catalyst bed and the permeator valved into the loop at t = 627 min the activity drops down, and methane is decomposed. Typical decontamination factors of the second process step are a few thousand.

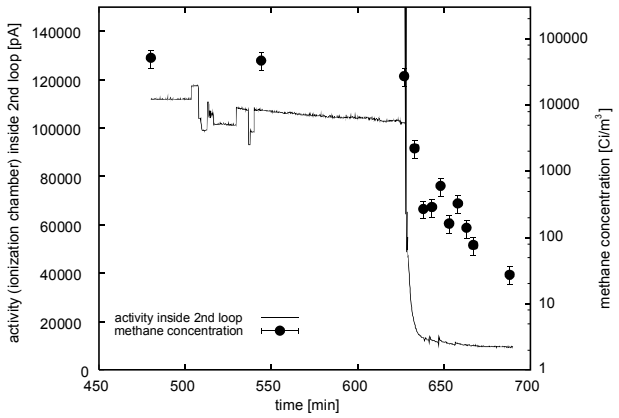

Fig. 3: Performance of the second process step of TEP.

For the final clean-up of tritiated gases by counter current isotopic swamping the PERMCAT component was developed, which directly combines a permeator and a catalyst. The PERMCAT reactor was designed for decontamination of gases containing up to about 1% of tritium in different chemical forms such as water, hydrocarbons or molecular hydrogen isotopes.

In Fig. 4 results from PERMCAT operation are illustrated as a typical example. Once the tritiated impurity feed flow into the Permcat was started the expected increase of the hydrogen purge outlet activity was observed. No increase in the impurity outlet tritium concentration was detectable with the corresponding ionization chamber, even after almost five hours of operation, when the tritium concentration in the hydrogen purge stream was already constant for more than two hours. Since the overall inlet tritium concentration in this experiment was about 42 kCim^{-3} and the impurity outlet tritium concentration 0.16 Cim^{-3}, as measured by oxidation of a gas sample and liquid scintillation counting, the decontamination factor of the technical PERMCAT in this case was $2.6*10^5$. Such high decontamination factors have been measured before with single tube PERMCATs at TLK and in collaboration with AECL at the Chalk River Laboratories. Also mathematical modeling has revealed the capability of the unit to achieve decontamination factors above 10^5. To measure impurity tritium concentrations at a level of 0.2 Cim^{-3} the sampling system and the oxidation facility need to be carefully kept at low tritium contamination levels, otherwise the contamination of the sampling system rather than the performance of the PERMCAT is measured.

As for ITER the CAPER process can not be considered as an isolated system, but only as a subsystem within a closed tritium cycle. The pure tritium for the experiments with the three stage clean-up process is provided by the Tritium Storage System of the TLK through the Tritium Transfer System. Gases detritiated by CAPER are discharged to stack through the Central Tritium Retention System of the TLK. Hydrogen isotope mixtures with tritium concentrations too low for ITER relevant experiments or the tritium containing hydrogen from operation of the PERMCAT are transferred back to the Isotope Separation System of the TLK. After recovery of pure tritium it is returned to CAPER for new experiments (or stored in the Tritium Storage System). The TLK has obviously quite a lot of similarities with the inner fuel cycle of ITER.

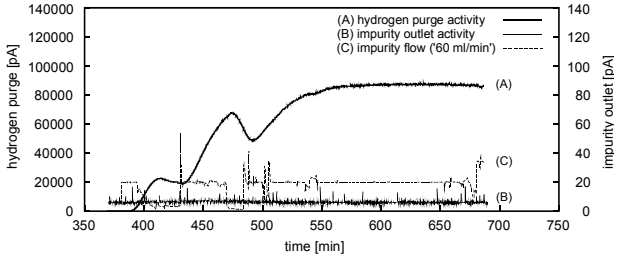

Fig. 4: Example of experimental results with a multi tube PERMCAT.

Particularly during the experiments with the PERMCAT the CAPER facility was operated round the clock. Therefore also other systems within the TLK have been operated to a level allowing the continuous and integrated operation of the CAPER facility for an extended period of time.

Besides for planned experiments the CAPER facility is also used to process waste gases from other sources within the TLK. These gases are not in each case well defined, however dumped into the impurity buffer vessels of CAPER. So far all these gas mixtures have been successfully processed and the tritium recovered at high purity for direct transfer to the Isotope Separation System of the TLK.

The integral operation of the three stages of the CAPER facility has clearly demonstrated an overall decontamination factor of at least 10^8, as required by ITER. The measured PERMCAT impurity outlet concentration of about 0.2 Cim^{-3} is equivalent to $2*10^{-5}$ gm^{-3}, while an ITER decontamination factor of 10^8 corresponds to 10^{-4} gm^{-3}.

Staff:

B. Bornschein
M. Glugla
K. Guenther
R. Laesser
T.L. Le
K.H. Simon

GB8-TR 2
Development of Tritium Instrumentation

In every chemical process the accurate characterization of the materials under treatment is of key importance. This is particularly true for radioactive substances and consequently the Tritium Plant of ITER has its own Analytical System. While gas chromatography was chosen as the main analytical tool for ITER complementary methods need to be further developed, not only to complete characterization of all the Tritium Plant processes during construction supporting R&D.

A versatile analytical method within tritium technology is Laser Raman Spectroscopy (LRS) which has been intensively employed at the Tritium Laboratory Karlsruhe (TLK) in the past to measure all six hydrogen isotopomers (including the two tritium containing species and pure tritium), and twelve (out of fifteen) isotopically labeled methanes (seven of them tritiated) have been characterized with this method. In order to improve the sensitivity of the technique a second generation set-up was designed and constructed, taking advantage of the substantial developments in laser technology and detectors in recent years, as well as considering improvements in the area of dispersive systems. The experimental set-up is illustrated in Fig. 1.

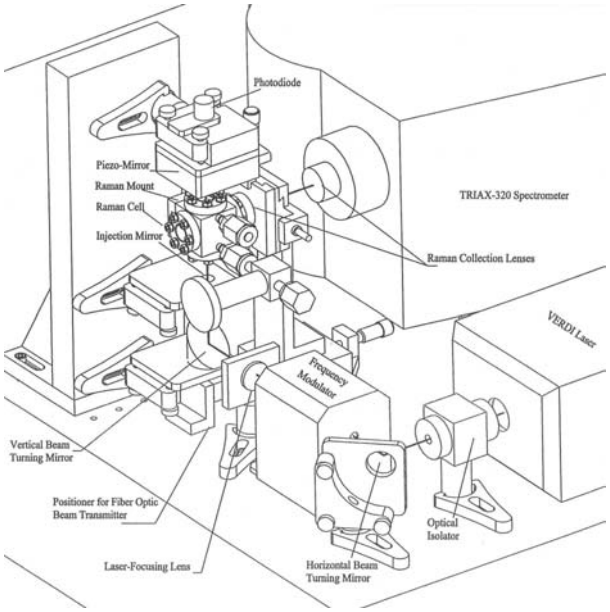

Fig. 1: Raman spectrometry using an Actively Stabilized External Resonator (ASER).

The sensitivity of single-pass LRS is limited for principal reasons. In this case the enhancement of Raman signals is based on the implementation of an Actively Stabilized External Resonator (ASER), consisting of components for conventional single-pass Raman spectrometry such as excitation laser, Raman gas cell, spectrometer/CCD, and focusing optics, plus custom-designed ASER components comprising optical isolator, frequency modulator, injection and retro-reflection mirrors, and control electronics. To achieve the most compact design, the Pound-Drever-stabilized ASER is a linear cavity rather than the more common ring cavity.

This second generation Laser Raman spectrometer is installed in a glove box at TLK. However, the measurements carried out so far have not included tritium or tritiated compounds since the secondary containment is not yet closed. In order to test the detectability of a trace component in a gas mixture the CO_2 concentration in air was determined from the Raman spectra illustrated in Fig. 2.

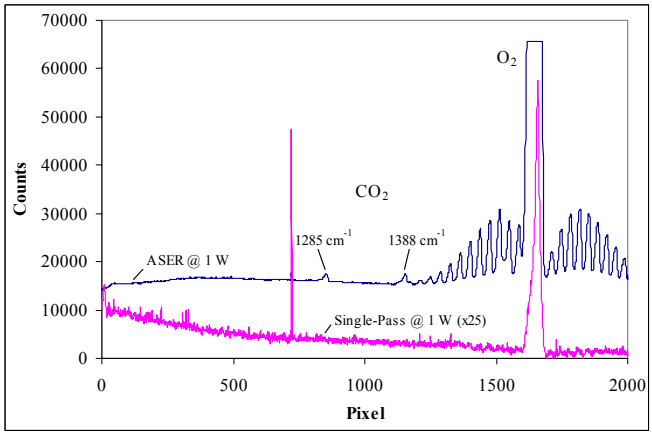

Fig. 2: Laser Raman spectra of ambient air demonstrating CO_2 detectability of about 4.5 ppm with the ASER. (The Single-Pass spectrum has been multiplied by 25 for comparison purposes.).

The Raman spectrum of CO_2 consists primarily of two narrow Fermi-resonance Q-branches at 1285 cm^{-1} and 1388 cm^{-1}, with slightly higher strength in the latter, which falls between two weak O-branch Raman lines O(27) and O(29) of oxygen molecules. Based upon the recent determination of local CO_2 concentration to be 358 parts-per-million (ppm), the detectability of CO_2 was found to be about 4.5 ppm for ASER operation. The corresponding single-pass CO_2 detectability at the same laser power level past the laser-focusing lens, based upon a comparison to the observed oxygen lines, was 675 ppm, yielding in this case a detectability improvement of 150-fold using the ASER.

Staff:

C. Caldwell-Nichols
M. Glugla

TW0-T 457/01
Development of Tritium Instrumentation

Several novel devices for tritium instrumentation have been developed at the ETHEL plant at JRC Ispra. JRC Ispra no longer undertake any fusion related work and TLK are due to continue with the development and characterisation of these instruments, primarily novel tritium monitors.

TLK is in negotiations with JRC Ispra for the transfer of these devices and other equipment to TLK. Many contractual and technical matters are agreed, however JRC Ispra is at present investigating the correct contractual procedures needed to release the equipment to TLK. When these matters are resolved the equipment will be moved to TLK and the experimental program can start.

Staff:

C. Caldwell-Nichols

TW1-TTF/TR 11
Gas Processing during In-situ Tritium Recovery from PFCs

Tritium experiments at the JET and at the TFTR tokamak have shown that substantial amounts of hydrogen isotopes are trapped in the vacuum vessel as co-deposits with carbon on Plasma Facing Components (PFCs), which in cold areas of the divertor even lead to the formation of flakes. The recovery of tritium from these non-stoichiometric carbon rich hydrocarbons has been proven to be rather difficult and potential processes involve high temperature treatment, sometimes in an oxidizing atmosphere. However, no reference process has been chosen yet and therefore within this task it is assumed that tritium will need to be eventually recovered from highly tritiated water.

Since ITER does not have a dedicated system for the treatment of gaseous wastes, all the tritium has to be recovered by the Tokamak Exhaust Processing (TEP) system. Consequently the TEP system has many more duties than the name of this particular part of the ITER Tritium Plant may suggest. The three step CAPER process developed at the Tritium Laboratory Karlsruhe (TLK) has been chosen for the retrieval of tritium from all tritiated waste gases of ITER (see report on GB8 TR1) which comprises a so-called PERMCAT (direct combination of a palladium / silver membrane with a catalyst bed) as a third step. The high decontamination factors of 10^4 to 10^5 measured with various gas mixtures in single tube and multi tube PERMCATs appear to be also promising for the recovery of tritium from highly tritiated water. The principle of the PERMCAT is shown in Fig. 1.

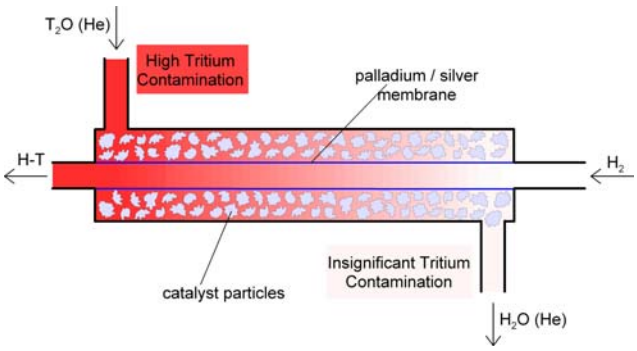

Fig. 1: Principle of the Permcat for the processing of highly tritiated water.

Helium as a carrier together with tritiated water vapor at partial pressures of up to 25 kPa is fed into the catalyst filled annulus of the coaxial arrangement. The inner tube is made out of palladium / silver exclusively permeable for hydrogen isotopes. In a counter current mode protium is introduced, permeates into the annulus and decontaminates the tritiated water by isotopic exchange. The liberated tritium is molecular and can therefore permeate into the inner tube. As a result an exponential tritium concentration profile along the axis is achieved under steady state flow conditions, the gas outlet of the unit remains essentially uncontaminated and the tritium is finally separated from the protium purge stream in the isotope separation system. The catalyst in the PERMCAT reactor is employed to support isotope exchange reactions between tritiated water and protium, the latter being supplied for swamping through the palladium /silver membrane tube.

Experiments with a single tube PERMCAT have been started to assess the potential of the component to be operated under high water vapor pressures. The tests with regular water and deuterium have shown that under certain conditions the water becomes completely deuteriated. The PERMCAT and in particular the permeation membrane is not (or at least not significantly) deteriorated due to the high water vapor partial pressures, and counter current isotopic exchange was observed. A recovery of tritium from highly tritiated water with the PERMCAT is considered to be of advantage, since it completely avoids the addition of CO for water gas shift reactions and the meanwhile known radiochemical side reactions between CO and tritium.

Staff:

B. Bornschein
M. Glugla
D. Niyongabo
S. Welte

TW1-TTF/TR 12
Development of Tritium Analytical Devices

Introduction

The exhaust gases of future fusion devices such as ITER can contain Q_2, He, Ar, Ne, N_2 up to 100%; CO and CO_2 up to 50%; CQ_4 up to 20%; higher hydrocarbons (C_2Q_6 to C_4Q_{10}) each up to 5% and Q_2O up to 20%. After processing of these gases with special catalysts and permeators, the composition of the gases changes drastically. The bleed gases of the permeators can contain CO, CO_2, CQ_4, N_2, H_2O, He, Ar and Ne at concentrations up to 100% with very small hydrogen concentrations, whereas the permeate gases will contain almost only hydrogen isotopes with small amounts of the tritium decay product ^{3}He.

Various analytical tools such as laser Raman spectroscopy, mass spectrometry and gas chromatography are nowadays available to detect the gas species mentioned above. The ones employed in the Tritium Laboratory Karlsruhe (TLK) have been recently described [1, 2]. A comparison [3] of the three techniques showed that gas chromatography is the simplest, the most used, by far the cheapest, requires minimal space, can be placed fully inside a glove box, does not need high or ultra high vacuum pumps, does not use any type of window material and is easy to operate and maintain. As a consequence, the analytical tools proposed for the ITER Analytical System (ANS) are two conventional gas chromatographs (GCs) and three micro-GCs [4].

The main disadvantages of conventional gas chromatography for the analysis of hydrogen isotopes are the long retention times of more than 30 minutes which means that on-line monitoring or on-line control of processes is not possible. Recent developments in the field of micro gas chromatography resulted in promising chromatograms for hydrogen isotope mixtures with shorter retention times. As a consequence, micro gas chromatography for hydrogen isotope analysis was further developed at the TLK to confirm the proposed design for ITER, to gain experience and to use micro gas chromatography in daily tasks of the TLK.

In the following chromatograms obtained for various hydrogen isotope mixtures with packed and capillary columns are discussed. In addition, the main advantages and draw backs of micro gas chromatography in comparison to the conventional technique with packed columns will be presented. Further details are given in [5].

Experimental set-up

In the past conventional micro gas chromatographs could not be used for the analysis of hydrogen isotope mixtures because hydrogen isotope separation requires an analytical column cooled to temperatures far below zero degree Celsius. Until now, mainly gas species have been analysed where the separation between the different gases of interest could be achieved with capillary columns heated in the devices supplied by the micro gas chromatograph producers. In this way the quantitative detection of the gas species listed above and expected in the exhaust of fusion machines can be performed using micro gas chromatography with the only exception of the detection of the hydrogen isotopes.

For the analysis of hydrogen isotope mixtures the conventional micro gas chromatograph needs to be modified. An external analytical column instead of the internal one is to be connected with the micro gas chromatograph and is to be cooled to temperatures far below 0°C. A convenient technique is insertion of the analytical column into liquid nitrogen to achieve a constant temperature of 77 K. Fig. 1 presents a side view of the special micro gas chromatograph which was used for the separation and detection of the hydrogen isotopes. Easily recognisable is the external column which is normally inserted in a liquid nitrogen filled dewar (not shown in Fig. 1).

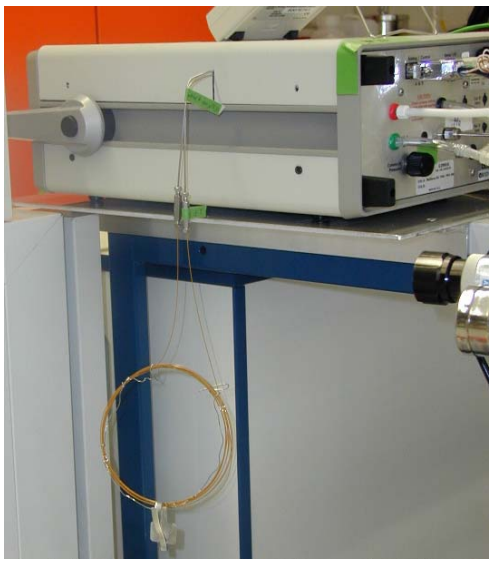

Fig. 1: The micro gas chromatograph used for hydrogen isotope analysis with the external analytical column.

Two different gas chromatographs (GCs) were used in this study: the micro gas chromatograph GC1 as shown in Fig. 1 (modified such that an external analytical column (Al_2O_3+$MnCl_2$: 4 m x 0.053 cm) could be connected) and a conventional, but special gas chromatograph called GC2 [2] which uses packed columns. With the Thermal Conductivity Detectors (TCD and micro-TCD) in use all gas species with thermal conductivities different from the carrier gases (Ne for GC1, He for GC2) can be observed.

Six gas mixtures GM1 to GM6 were used. GM1 consisted of 89% He with a mixture of 47.4% D_2 in H_2 and GM2, GM5 and GM6 consisted of 92%, 88% and 99% of He with the equilibrated 50%H/50%D mixture GM4, respectively. The certified mixtures GM3 contains 48.95% H_2, 2.31% HD, 48.74% D_2.

Experimental results

Analysis of hydrogen isotope mixtures

Fig. 2 shows the TCD-chromatograms of the mixtures GM1 and GM2. All gas species are clearly observed and well separated. The separation between the HD and D_2 peaks is good enough to allow in case of tritiated mixtures a clear baseline determination of the HT peak.

For comparison Fig. 3 shows the TCD-chromatogram of the hydrogen mixture GM3 measured with GC2. A few percent of H_2 are added just in front of the TCD to the carrier gas He to avoid the unusual protium peak form which is caused by the anomaly in the thermal conductivity of H_2-He gas mixtures.

The most remarkable difference in the chromatograms of Figs. 2 and 3 are the very different retention times of the three main hydrogen species. With the packed column the D_2 peak reaches the base line after approximately 28 minutes, with the capillary column after 200 seconds, more than 8 times faster.

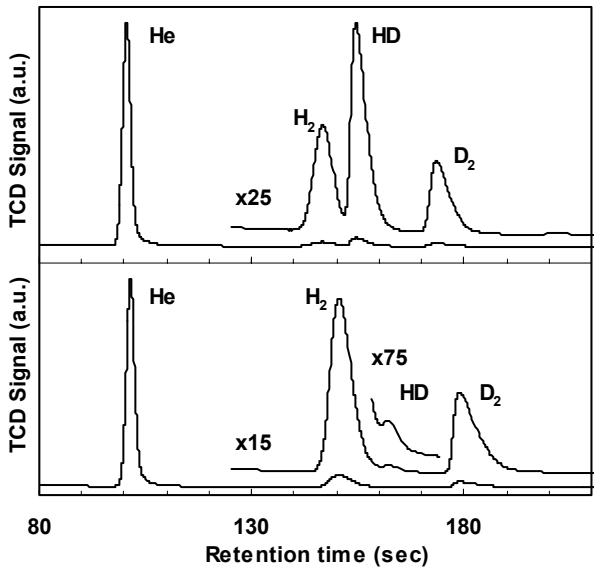

Fig. 2: TCD chromatograms of the gas mixtures GM1 (bottom) and GM2 (top) measured with GC1

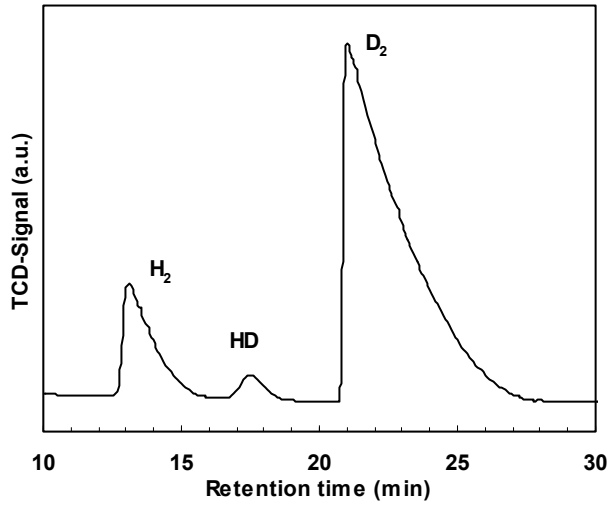

Fig. 3: TCD chromatogram of the gas mixture GM3 measured with GC2.

Separation efficiency for different injected gas amounts

Fig. 4 presents three TCD chromatograms measured with GC1 for GM4, GM5 and GM6. The hydrogen peaks in the top chromatogram overlap strongly and no baseline separation between the HD and the D_2 peak exists. In the middle and bottom chromatograms the injected hydrogen amounts were reduced to 12% and 1% by the simple addition of helium. Clear baseline separation between HD and D_2 is observed in both chromatograms which demonstrates that in the top chromatogram the analytical column was overloaded by the amount of hydrogen injected. According to the supplier of the micro GC, the injection volume is 1 microlitre. Approximately 10^2 cm^3Pa of GM5 were injected for the top chromatogram. This is already too much for the capillary column. Good separation is achieved with sample sizes below 20 cm^3Pa.

In the top chromatogram of Fig. 4 the hydrogen peaks appear earlier than in the other two spectra. Due to overloading, active places of the column are already occupied by hydrogen species during the separation process. As a result the hydrogen molecules pass faster through the column and the asymmetry of the peaks increases.

Further observations

The Al_2O_3+$MnCl_2$ capillary column seems to be quite robust, to date no failure has occurred, although the capillary column was moved daily, cooled to 77 K and occasionally put into a special oven for regeneration.

The analytical column requires regenerations from time to time probably due to very small impurity levels in the carrier gas. Regeneration of the analytical column must be performed in a special oven located in the dewar as the ITER ANS must be operated fully remotely.

A further advantage of micro gas chromatography is the small amount of sample required for analysis.

The present study of micro gas chromatography was performed with inactive gases. For use with tritium various tools (e.g. pump, valve actuation equipment, connecting tubes, etc.) of the micro GC are to be replaced by tritium compatible components.

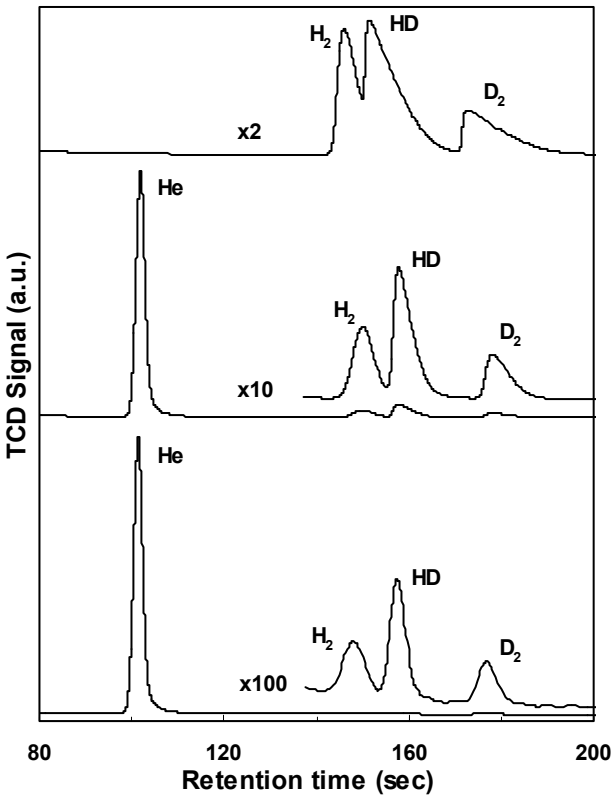

Fig. 4: TCD chromatograms for the gas mixtures GM4 (top), GM5 (middle) and GM6 (bottom) measured with GC1.

Conclusions

With micro gas chromatography the hydrogen isotope mixtures to be processed in the Tritium Plant of future fusion reactors can be determined qualitatively and quantitatively. An external analytical column is required for the analysis of hydrogen isotope mixtures. Regeneration of the column must be performed from time to time to remove impurities trapped at 77 K. To avoid manual intervention the heating device for regeneration must be installed in the dewar.

The main advantages of micro gas chromatography are the strong reduction in retention times, the small sample size required for analysis which reduces the necessary effort for detritiation, the high separation efficiency and the small amount of space required for installation of a micro GC. Disadvantages are that commercial micro GCs have to be modified to accept an external column and that components must be replaced which do not fulfil the stringent tritium standards.

In summary: micro gas chromatography can be considered as a well demonstrated analytical technique for the determination of inactive hydrogen isotope mixtures. Its use in tritium processing facilities can be recommended if the necessary enhancements of the non-tritium compatible components are made.

Staff:

S. Grünhagen
R. Lässer

Literature:

[1] R. Lässer, C. Caldwell-Nichols, L. Dörr, M. Glugla, S. Grünhagen, K. Günther and R.-D. Penzhorn: Analytics of tritium-containing gaseous species at the Tritium Laboratory Karlsruhe, Fus. Eng Des. 58-59, 411-415 (2001).

[2] R. Lässer, M. Glugla, S. Grünhagen, K. Günther, R.-D. Penzhorn and J. Wendel: Use of gas chromatography in the Tritium Laboratory Karlsruhe, Fusion Science and Technology 41, 515-519 (2002).

[3] Design Description Document (DDD): Tritium Plant and Detritiation Systems WBS 32H ANALYTICAL SYSTEM; prepared by R. Lässer, ITER N 32 DDD 33 01-07-02 R 0.1

[4] R. Lässer, M. Glugla, T. Hayashi, P. Schuster and H. Yoshida: The analytical system of the ITER Tritium Fuel Processing Plant, Fusion Science and Technology 41, 520-524 (2002).

[5] R. Lässer, S. Grünhagen and Y Kawamura: Use of Micro Gas Chromatrography in the Fuel Cycle of Fusion Reactors, to be published in the Proceed. 22th SOFT, Helsinki, 2002.

TW1-TTF/TEP 13A
Self-Assay, Fast Delivery Tritium Storage Bed

Introduction

The safest way to store tritium is in the form of metal tritides. The main advantages of this storage technique are:

- Quite a few metals (e.g. ZrCo, U, Nb, Ti, etc.) have a high affinity to hydrogen and tritium and are able to absorb large amounts tritium. These metals act in a similar way as a pump, but selectively in the case of hydrogen. The pumping action is achieved without any moving mechanical parts, it is only necessary to remove the heat generated during the absorption process. If only hydrogen gas is present, the ultimate pressure achievable above the getter is determined by the hydrogen equilibrium pressure, which is a function of temperature and hydrogen concentration in the metal hydride. These equilibrium pressures can be very low, far lower than the lowest pressures achievable with oil lubricated mechanical pumps.

- The interaction of tritium with the wall surfaces and the driving force for tritium permeation through the surrounding primary containments are negligible due to the very low tritium equilibrium pressures at room temperature above appropriate metals. This is important because hydrogen can penetrate fairly easily metals, especially at higher temperatures. Furthermore, due to the low pressures, beta induced reactions in the gas phase and on the surfaces are far less likely than at higher pressures. In this way with the tritium absorbed in the metal, it is far easier to keep the tritium purity preserved than with the tritium in the gas phase where it could interact with other species adsorbed or absorbed in the walls (e.g. carbon dissolved in stainless steel) and generate hydrocarbons.

- The hydrogen or tritium can be released from metal tritides at relatively modest temperatures reversibly. With an appropriately chosen metal tritide, large amounts of tritium can be supplied at the same pressure. The metal storage bed functions as a hydrogen compressor, again in the absence of moving parts which makes repair and maintenance far less likely. In contrast, if the tritium were stored in a reservoir the supply pressure of that storage tank would continuously decrease. To achieve high hydrogen or tritium supply rates the power required for desorption must be supplied to the metal powder.

- Due to the tritium decay tritium gas mixtures always contain certain levels of helium-3. The use of metal tritide beds offers a simple application for the separation of helium from tritium because during absorption only the hydrogen isotopes are absorbed whereas helium stays in the gas phase and can be removed.

- Many hydrogen absorbing materials disintegrate during the uptake of hydrogen into powder creating large surfaces allowing high absorption rates. On the other hand, the spread of powder to other equipment needs to be avoided. This can be done by the use of special filters. Furthermore, the heat conductivity in powder is far less than in the bulk, a point which needs to be considered in the design of fast delivery tritium beds.

Storage beds for the ITER Tritium Plant

Due to the advantages mentioned above tritium is nowadays stored in the form of metal tritides in most tritium laboratories. For the ITER Tritium Plant a large number (up to 19) of hydrogen storage beds is foreseen. The high number is partly due to the low hydrogen supply rate achieved per storage bed until now and the ITER requirement of a total high hydrogen supply rate during a plasma shot of up to 200 Pam^3s^{-1}. As a consequence the decision was made to develop a prototype tritium storage bed with high delivery rate and in-bed accountancy.

The main requirements of the new storage bed for ITER are:

- High standard of safety,
- Use of only tritium compatible materials,
- High hydrogen/tritium supply rates of up to 200 Pam^3s^{-1},
- In-bed accountancy allowing the determination via the decay heat of the absorbed tritium.

Design of a tritium storage bed

A high standard of passive safety is achieved by designing the bed for the maximum pressures and temperatures considering software and hardware interlocks.

The tritium compatibility of the tritium storage bed is achieved by the use of only tritium compatible materials and the design of a primary containment which is fully surrounded by a secondary containment to collect tritium permeated through the first heated wall.

7.7 kW of heating power are necessary for the maximum required hydrogen desorption rates and are produced by the use of internal and external thermocoax heaters.

Cu fins are installed in the primary containment to conduct the power generated in the thermocoax heaters to the metal powder located between the Cu fins in the primary containment.

Vacuum brazing techniques are used to achieve optimum thermal conductivity transitions between all parts within the primary containment of the storage bed.

The heat generated by the tritium decay inside the primary containment is removed by a gas flow passing through a U-shaped tube which is again vacuum brazed to all Cu fins. The temperature increase of the gas flow circulated through the storage bed is determined. From this the tritium amount stored in the material can be calculated using the relationship that 1 g of tritium produces the power of 0.324 W.

The heat generated during absorption is removed by a counter current gas flow through the coaxial central stainless steel tube vacuum brazed into the internal heater assembly.

Manufacture of a tritium storage bed

The following steps in the manufacture of the storage beds were performed:

- Manufacture of all single items,
- Assembly of various parts,
- Vacuum brazing of various subassemblies,
- Welding of various items,
- Part of the pressure tests,
- Part of the He leak tests.

In the following the manufacture of the storage bed shall be discussed using four pictures shot during the production process.

Fig. 1 presents the two internal heaters wound into two bifilar grooves of the Cu cylinder. The two cold ends of the thermocoax heaters return via long parallel bores to the same end of the Cu block. Thermocouples for determination and control of the temperatures will be placed into the three empty bores in the Cu cylinder.

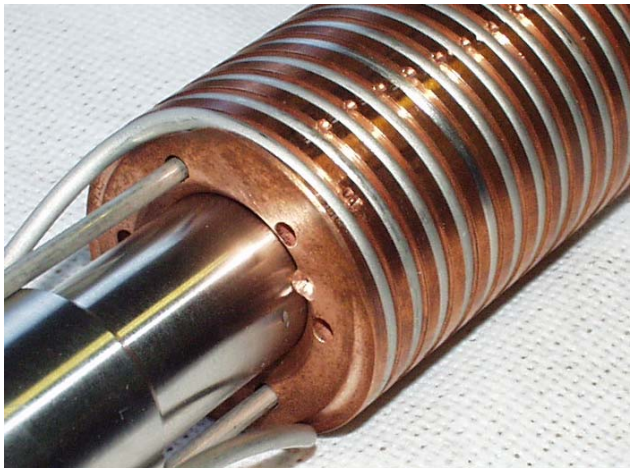

Fig. 1: The two inner thermocoax heaters wound into the grooves of the Cu cylinder.

Fig. 2 shows a top view on the interior of the upper section of the primary containment. Clearly visible are the Cu fins (stacked on top of each other), the inner and outer stainless steel walls of the primary containment, the two 6 mm outer diameter stainless steel tubes of the U shaped calorimetric loop to measure the decay heat, the grooves machined into the outer surface of the outer wall to accept the external thermocoax heaters, and the three different sizes of four brazing rings. The Cu cylinder shown in Fig. 1 will be placed - after application of the vacuum brazing paste into its grooves - into the central hole shown in Fig. 2.

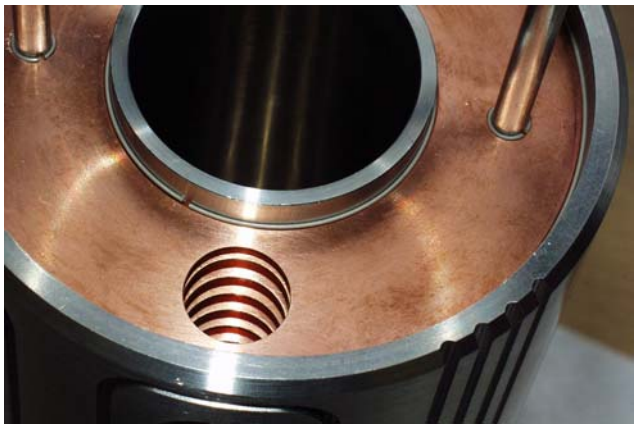

Fig. 2: Upper most Cu fins between internal and external walls with brazing rings.

Fig. 3 presents the top view of the primary containment of the getter bed after the brazing process with the thermocoax heaters installed and the brazing material molten, but with the top cover and the filters not in place.

Fig. 3: Upper most fins and thermocoax heaters after the brazing process.

The whole primary containment of the storage bed with its process and electrical connections through the DN 160 CF flange and the secondary containment are shown in Fig. 4.

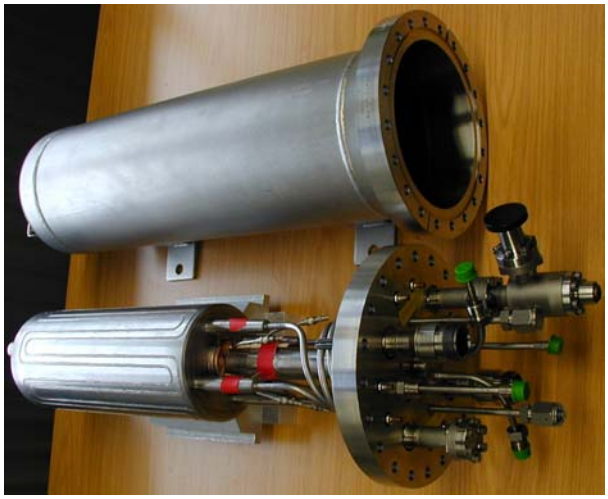

Fig. 4: View of primary and secondary containments of the tritium storage bed.

The following work needs to be performed before any testing of the storage bed can be started at the Tritium Laboratory Karlsruhe (TLK):

- Installation of electrical connections between the feedthroughs in the flange and the thermocoax heaters,
- Filling of the ZrCo powder into the compartments between the Cu-fins,
- Final pressure tests,
- Final leak tests.

Staff:

W. Jung
R. Lässer

TW1-TTF/TR 16
Tritium Recovery from Ceramic Breeder Test Blanket Module

Components and system design concepts for the recovery of tritium from the purge gas stream of a ceramic breeder blanket test module for ITER have to be developed. The tritium extraction loop of the Helium Cooled Pebble Bed Test Blanket Module HCPB-TBM includes as main components a liquid-nitrogen cooled cold trap for the retention of tritiated water produced in the breeder and a liquid-nitrogen cooled molecular-sieve adsorber bed to extract various isotopic species of hydrogen (H_2, T_2, HT) as well as N_2 and O_2.

In a pre-test loop a cold trap containing a series of cooled copper plates as surface for water condensation has been investigated in parametric studies. The results achieved with the cold trap during the test runs with helium flows between 100 l h^{-1} and 2000 l h^{-1} and humidity concentrations in the gas of 10 ppm_v (the estimated concentration of the purge gas leaving the HCPB) and above show that this design is able to dry the gas flow to less than 0.1 ppm_v under the conditions mentioned above. The most important operating parameters in the trap are the temperature profile gradient along the cooling plates (Figure 1) and the gas velocity. The recommended velocity for this freezing process is 10 cm s^{-1} for the gas passing over the cooled surfaces; this allows optimum freezing conditions and avoids very small frozen particles (aerosols) being entrained by the gas flow. The dimensions of the cold trap used at the TLK are such that the average velocity is approx. 10 cm s^{-1} with a He flow of 1000 l h^{-1} and approx. 20 cm s^{-1} with a He flow of 2000 l h^{-1}. The satisfactory results obtained even at the higher level show that velocity is not a very sensitive parameter. However the cold trap should be operated in this range. Figure 2 shows the He flow as a function of the freezing surface needed for good drying. The numbers attached to the measured points indicate the inlet and outlet humidities, respectively.

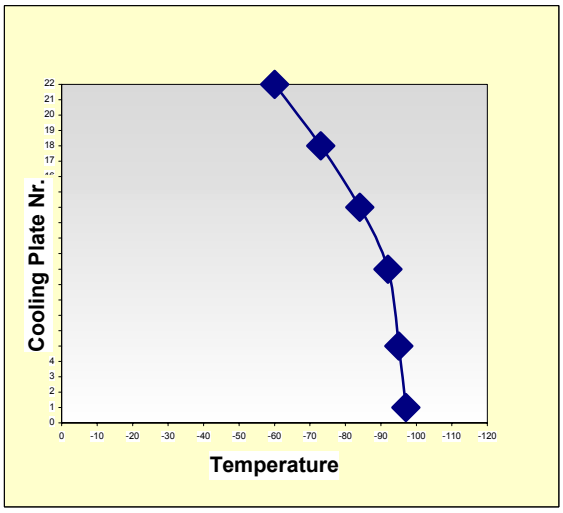

Fig. 1: Temperature profile in the cold trap freezing zone.

The flow rate of the purge gas of the HCPB-Test Blanket Module in the Tritium Extraction system of ITER is 12 std.m^3 h^{-1}, six times the maximum possible flow rate of the test cold trap. A scaled-up cold trap thus must have six times the freezing surface of the test trap, i.e. approximately 0.33 m^2. Simply increasing of the diameters of the copper plates to reach the 1.98 m^2 (six times 0.33 m^2) and keeping the gas velocity at the required value leads to a diameter of the trap which is not compatible with the dimensions of the glove boxes in the ITER tritium plant. Equally, such big plates are difficult to be cooled symmetrically. Hence the logical solution to split the process gas flow and operate with the corresponding number of cold traps in parallel. Four parallel cold traps with a plate diameter of 600 mm and 20 mm gap between the 22 plates per trap will meet this condition (Figure 3). The gas precooler cooled by the cold process gas return flow from the cold traps is always necessary to cool the gas to the inlet temperature of the traps. The parallel traps will be integrated in a common vacuum vessel for thermal insulation together with the precooler (Figure 3). The vertical arrangement of the four traps in the vacuum vessel leads to the outside dimensions of approx. 700 mm diameter (800 mm flange) and approx. 4000 mm length of the vessel. This is compatible with the dimensions of the gloveboxes (height: 6 m; length: 4m; width: 1.2m) to house the tritium systems in the ITER tritium plant including the TES [1].

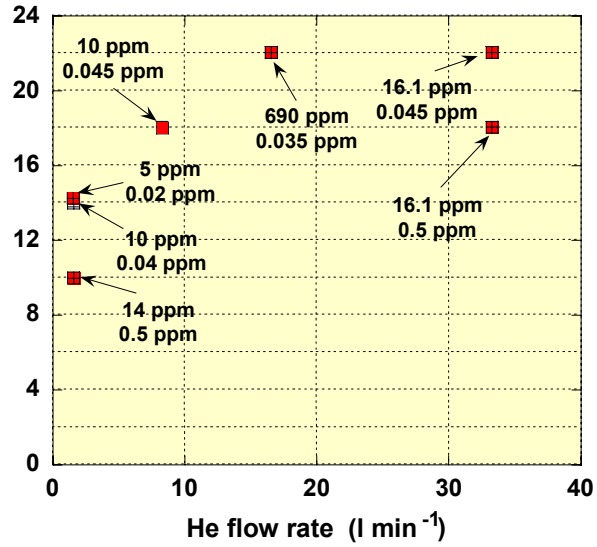

Fig. 2: Flow rate vs. freezing surface.

The molecular sieve adsorber, designed in 2001, is under construction in the workshops of the FZK. The test rig in which it shall be investigated is also under preparation to receive it.

An existing glove box system in the TLK will be modified to house the PILATUS facility which is foreseen to demonstrate the tritium extraction as well as the coolant purification of the HCPB-TBM in a closed loop under tritium.

Staff:

N. Bekris
C. Caldwell-Nichols
E. Hutter
G. Macarawietz

Literature

E. Hutter, N. Bekris, C. Caldwell-Nichols, Cold trap and cryogenic molecular sieve adsorber: Components for tritium extraction from the purge gas of the HCPB-breeder blanket for ITER, 22th SOFT, Helsinki, September 9-13.2002.

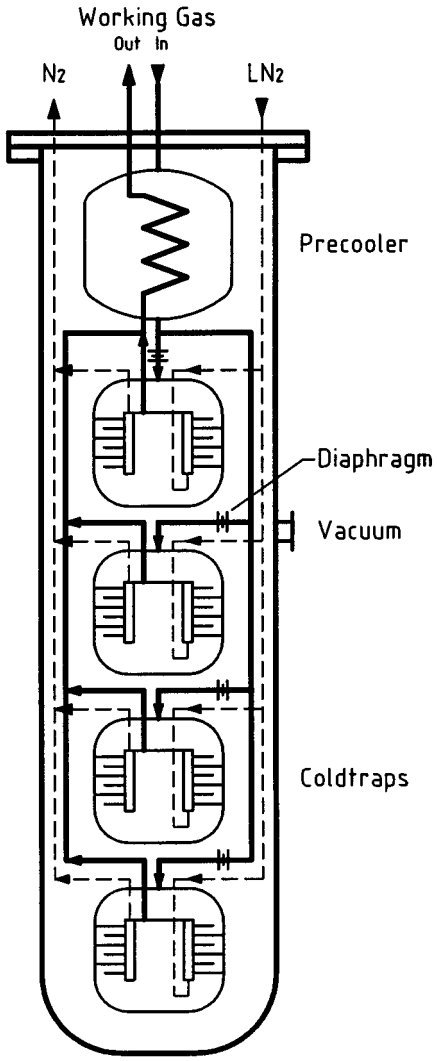

Fig. 3: Cold trap design for ITER.

TW2-TTF/TR 24
Determination ex-situ of Tritium Content in Plasma Facing Components

Carbon Fibre Composite (CFC) is currently the candidate material for the vertical target tiles in the ITER divertor because of its superior thermomechanical properties. However, its affinity for hydrogen isotopes and their co-deposition with eroded carbon may severely limit ITER plasma operations. Recently tritium depth profiles in divertor tiles retrieved from the Joint European Torus (JET) have been obtained by the coring/full combustion technique. The results revealed that a surprisingly large fraction (up to 61%) of the retained tritium had diffused deep into the bulk of the tile, most probably between the woven sheets of the CFC.

Since the tiles must eventually be disposed off in a repository it is necessary to reduce the total tritium inventory in the tiles down to the corresponding Low Level Waste (LLW) category (12MBq kg^{-1} in UK). In this context, the development of detritiation techniques for graphite and CFC tiles removed from the first wall of fusion machines is of paramount importance. The experimental techniques investigated until now are limited by the conditions and techniques permissible inside the torus having the main objective of reducing the total in-vessel tritium inventory. Nevertheless, for tiles removed from the reactor more severe treatment techniques are acceptable. To accomplish this it is necessary to develop simple, reliable, and effective detritiation technologies allowing the conditioning of a large number of graphite and CFC tiles. Working in that direction, numerous detritiation techniques have been tested or evaluated at the Tritium Laboratory in Karlsruhe (TLK) as the bake of tiles.

To assess the detritiation method used at PPPL, 4 TFTR carbon tiles (2 CFC and 2 graphite) were send to the TLK. To evaluate the technique, in each couple of tiles, one was thermally treated in air at 500°C for one hour, while the other was not. The coring/full combustion technique was then used at the TLK to measure the tritium amount remaining in TFTR tiles after the detritiation process. The CFC tiles used in TFTR have a multi-directional fibres weave called 4D woven structure. Several tritium depth profiles of a 4D CFC tile were compared with the corresponding tritium profiles obtained for the non treated tile. In Fig. 1 a comparison between tritium depth profiles for the TFTR tile KC18 (4D CFC) and two divertor tiles from JET (2D CFC) is shown. All cylinders have almost the same surface activity i.e. $1 \cdot 10^{17}$ T/cm^2. A remarkable point is that the bulk activity of all cylinders sharply decreases after the first sample (1mm below the plasma exposed surface) and seems to reach, in the case of the TFTR tile, an almost constant value at about $2 \cdot 10^{14}$ T cm^{-3}. Moreover, in comparison to the bulk values observed for the 2D CFC tiles of JET, the TFTR value is more than one order of magnitude lower. Comparing tritium profiles for both type of CFC tiles (2D and 4D) it appears that for a similar tritium surface activity the tritium inventory on a 4D CFC is much lower. On the other hand, a diffusion profile (as observed for the JET divertor tiles) is not present for the TFTR.

Detritiation of small disk carbon specimens tested at the TLK have shown that tritium release from co-deposited layers is very rapid when temperatures rise above 350°C. In a new series of experiments, complete CFC and graphite tiles retrieved from TFTR were heated under air at temperatures up to 500°C, not only to improve the detritiation factor but also to assess the technique in full scale. The tiles were heated up to 500°C at PPPL (Princeton Plasma Physics Laboratory) under air atmosphere for one hour. Then they were sent to TLK where several cylinders were drilled out and their tritium content measured using the coring/full combustion technique. The results for the 4D CFC tile KC11 are illustrated in Fig. 2. It is remarkable to see that after the bake-out the surface activity of the tiles strongly decreases by up to 3 orders of magnitude. However, the total tritium contained in the bulk of the tiles is reduced by a factor two.

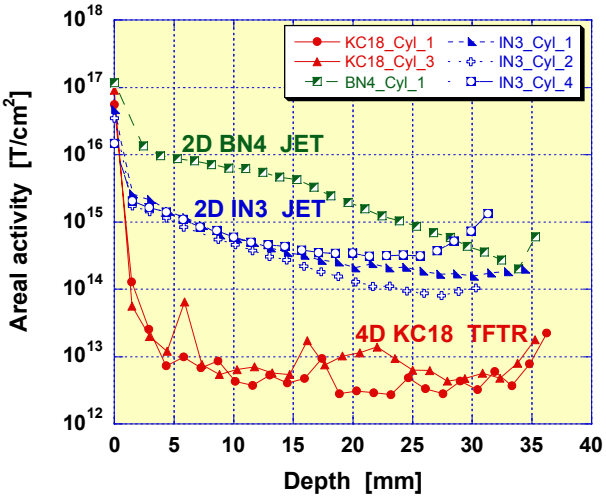

Fig. 1: Tritium depth profile comparison for TFTR KC18 (4D CFC) tile and two JET tiles (2D CFC).

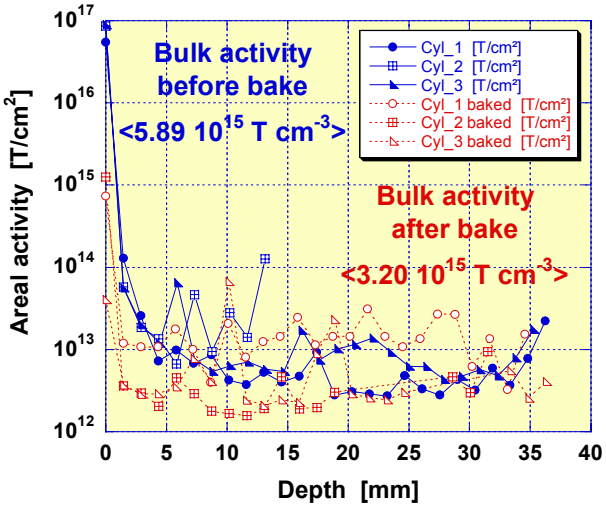

Fig. 2: Comparison of depth tritium profiles for the baked 4D KC11 and the unbaked 4D KC18 TFTR tiles

Tritium depth profiles in divertor tiles retrieved from TFTR and JET have been obtained by the coring/full combustion technique. For approximately identical surface activity, the tritium distribution into the bulk is quite variable in level and profile. The results revealed that a surprisingly large fraction (up to 61%) of the retained tritium had diffused deep into the bulk of the 2D CFC tiles from JET in comparison to only few percent found in the 4D CFC tile from TFTR. Additionally, the coring/full combustion technique has shown that only the surface tritium (few ten μm) is efficiently released by air baking while the bulk tritium is almost not affected. Baking the tile under air even at 500°C does not detritiate the bulk.

In conclusion, if the multi-directional CFC allows a very low tritium level in the bulk of the tiles the development of a detritiation technique to treat the tile's surface in-situ may be sufficient to significantly reduce the tritium inventory in fusion machines.

Staff:

N. Bekris

TW1-TTF/VP 11
Torus Exhaust Cryopump Development and Testing

1. Introduction

The point design of the ITER high-vacuum system is based on cryosorption pumps located inside the vacuum vessel in the divertor ducts. The cryopump design evolved from an earlier concept and some redirection was needed especially to obtain a more compact design in terms of valve integration and housing. However, the model pump which is currently being tested extensively in the TIMO test facility [1] at Forschungszentrum Karlsruhe is still believed to be a good representation of the ITER pump. The model pump provides a coated pumping surface of 4 m² which is a factor of three smaller than what has been proposed for the ITER torus cryopumps [2]. It necessitates several cryopumps in staggered operation to provide for quasi-continuous pumping. With the cryopumps being accumulation pumps, each will have to be regenerated after a certain period of time for regeneration of the sorption material, as required for reasons of explosion safety.

Within the first test campaign with a limited cooling power, but operation conditions typical of the ITER pumping phase, the principal interrelation of valve position, limited gas throughput, and resulting pumping speed for different gases and gas mixtures could be determined [3, 4].

In the meantime, the test facility has been upgraded such that more cooling power is available and ITER-relevant total cycle times are replicated. The aims for the second test campaign at TIMO were to perform additional pumping tests at a full ITER relevant gas load as well as to study the possibility of operating the cryopanels at elevated temperatures and with the leak detection tests, the feasibility of using the cryopumps for the detection of small leaks should be checked.

2. Modifications of TIMO

The aim of the TIMO upgrade was to increase the available cooling power for cool-down operation as well as to prepare a larger liquid helium storage for the foreseen “long-term cycling tests" and "poisoning tests" with model pump. These requirements could be fulfilled by the installation of a new control cryostat, a new water bath in the return line, and new transfer lines.

2.1 New control cryostat

The new control cryostat delivered by the company L’Air Liquide consists essentially of a 3500 l liquid helium tank. Its piping system includes the cold valves and a helium pump. With help of this helium pump delivered by the company Barber Nichols, a maximum helium mass flow of 250 g/s at 5 K can be used for the cooling of the cryosorption panels installed in the ITER model pump.

2.2 New water bath

A new water bath also had to be installed in the return line to the LINDE refrigerators according to the increased helium mass flows. With this new heat exchanger in the return line back to the LINDE plant the increased helium gas flows could now also heated up to a temperature level higher than 280 K.

In accordance with the higher helium mass flows, all transfer lines between the new facility parts, i.e. the new control cryostat as well as the new water bath and the valve box, had to be changed.

2.3 New aspects for the operation with the model pump

The operation of the model pump was not only improved by the new parts of TIMO described, but also by establishing a connection to the second refrigerator plant available at the Institute for Technical Physics (ITP). With this new connection, either the 300 W refrigerator or the larger 2 kW LINDE plant can be used. During operation with the new LINDE, a maximum Joule Thomson flow of 60 g/s at 4.2 K is utilizable for the cooling of the model pump instead of the previously available 30 g/s. As a further improvement by this new connection to the 2 kW LINDE plant [5] the model pump can now be cooled down for pump tests to an arbitrary temperature level between 4.2 K and 100K.

Fig. 1 shows the 2 kW LINDE plant operation for the model pump tests within a temperature range of 15 K and 76 K.

3. Tests performed with the ITER model pump

The main objective of the new test series was to execute parametric pump tests, capacity tests, and leak detection tests and, thus, complete the already available data-base of the ITER model pump. From the capacity and leak detection tests using different gases at various temperature level, further information was obtained about the operational range of the pump.

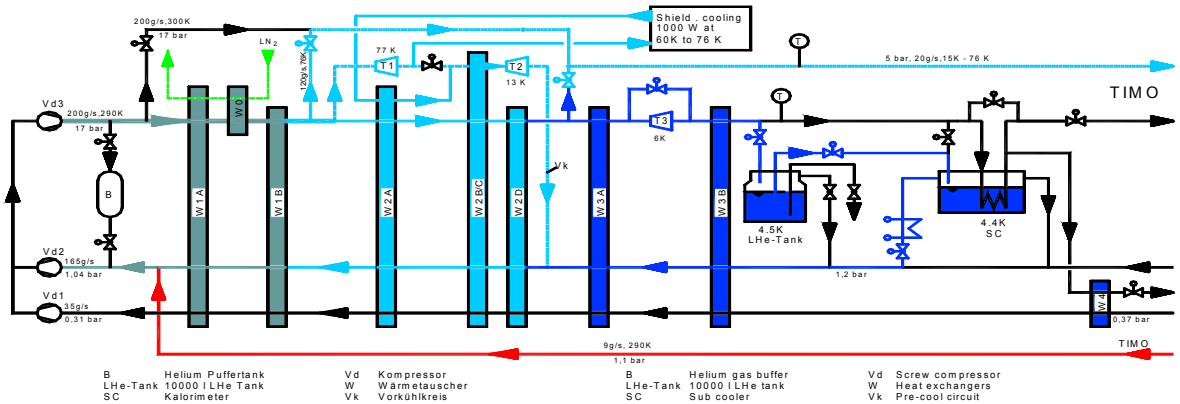

Fig. 1: Flow scheme of the 2 kW refrigerator.

3.1 Pump tests with different gases and gas mixtures

Following the test campaign with the ITER model pump in the year 2000, additional parametric pumping tests were performed with the pure gases of helium, protium and deuterium as well as with the ITER-typical exhaust gas mixtures D_2-base/He(10%) and H_2-base/He(7%), including variable helium shares and 3% impurities (CO, CH_4 , CO_2 ,O_2) [6]. Apart from varying positions of the pump inlet valve and the dosage steps at 100, 300, 500, 800, 1000, 3000, 5000 sccm, each over a metering time of 3 min, the max. ITER-relevant throughput of 10000 sccm over 4 min was now included into the test procedure. The duration available to reach the equilibrium pressure was fixed at 5 min between the dosage steps which were performed consecutively. With the additional metering step of 10000 sccm the total gas load of the model pump was increased from 32500 mbar·l to 72500 mbar·l.

Comparison of the helium pumping speed data revealed that the results are reproducible very well also after a break of two years. The pumping speed values measured exhibit comparable dependencies on the opening of the inlet valve as well as on the very high gas loads for all gases examined. The check with the ITER-relevant throughputs demonstrated that the designed values for the pumping speed were well achieved with all tested gases.

3.2 Capacity tests

As one of the most important activities during the actual test campaign, capacity tests were carried out at elevated temperature using helium and a D_2-base / He (10%) gas mixture. The matrix of the capacity tests included a variation of the temperature level (8 K, 10 K, 14 K), of the throughputs (10000 sccm, 2000 sccm) and of the position of the pump inlet valve (35%, 50%, 100%) open.

Metering conditions in the helium tests were specified to comprise a dosage/metering time combination of 10000 sccm over 40 min and 2000 sccm over 200 min. Due to the results achieved during the tests with helium, additional tests were carried out at the temperature level of 6 K. All achieved pumping speed results of the helium capacity tests are summarized in Fig. 2.

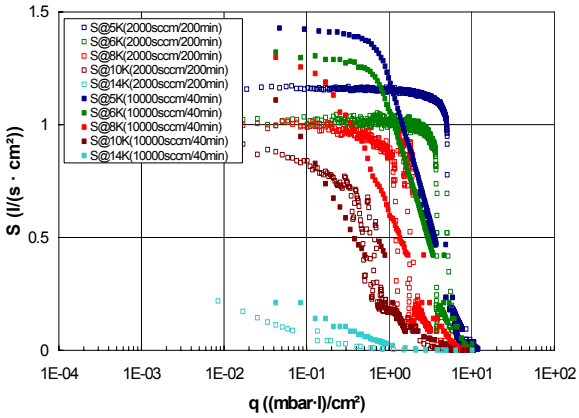

Fig. 2: Results of helium capacity tests at elevated temperatures.

It could be shown, generally speaking, that the available capacities and the accompanying pumping speed values fulfil the requirements up to a temperature of 10 K. The actual ITER requirements, when related to the pumping surface, correspond to a capacity of 0.57 (mbar·l)/cm² and a specific pumping speed of ~0.7 l/(s·cm²). It can be noticed that the pumping speed values for helium during tests with flows of 2000 sccm, corresponding to 50 % of the ITER maximum value for the He-shot operation, show an unstable behaviour at temperatures of 6 K to 10 K and for capacities between 0.5 (mbar·l)/cm² and 1.75 (mbar·l)/cm². Stable pumping speed conditions over the complete test duration were measured for the 5 K tests only.

When using the D_2-base / He (10%) gas mixture, the max. gas load was limited to 91200 mbar·l due to safety regulations. Therefore, the metering conditions for these tests were 10000 sccm over 9 min and 2000 sccm over 25 min. The results of these measurements represented in Fig. 3 show that also for the D_2-base / He (10%) gas mixture, the required values can be almost reached on all examined temperature levels examined.

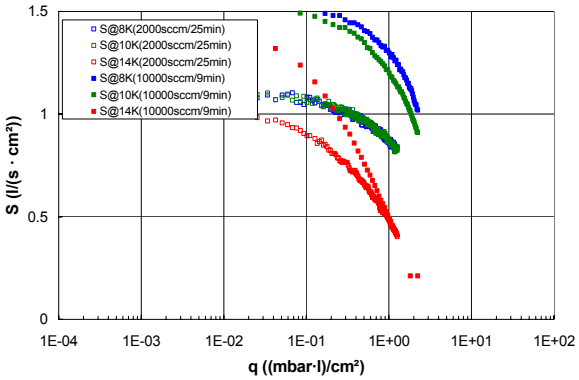

Fig. 3: Results of D_2-base/He (10%) capacity tests at elevated temperatures.

3.3 Leak detection tests

To check the possibility of using the cryopumps as a supporting tool [7] for the detection of small leaks, it was decided to perform tests with the ITER model pump at temperature levels of 20 K and 40 K. The metering conditions in terms of dosage and metering times were varied between 300 sccm over 15 min and 1000 sccm over 5 min. The tests were performed with helium, deuterium and D_2-base mixtures at fully opened inlet valve of the model pump.

With the help of the determined data, both the obtained pumping speed values as well as the available capacities could be examined as a function of the temperature. Fig. 4 shows the pumping speed results measured for helium and deuterium vs. the cryosorption panel temperature.

The helium pumping speed decreases by more than three orders of magnitude from 56 m³/s (@5 K) to a value of 0.04 m³/s (@40 K) with increasing temperatures. For deuterium the results reveal a very weak dependence of the pumping behaviour with pumping speed values between 72 m³/s (@5 K) and 27 m³/s (@40 K). Depending on the temperature, the ratio of the pumping speeds S(D2) / S(He) increases from 1.3 (@5 K) to 675 (@40 K).

This result is a quantitative experimental proof of earlier estimations based on natural warm-up tests [7]. Thus, there is no doubt that the cryopumps, when operating at 40 K, can provide a He in D_2 resolution of more than 10^3. So, in combination with a high resolution mass spectrometer, a

dynamic range of eight orders of magnitude as required for the ITER leak detection systems, should be feasible.

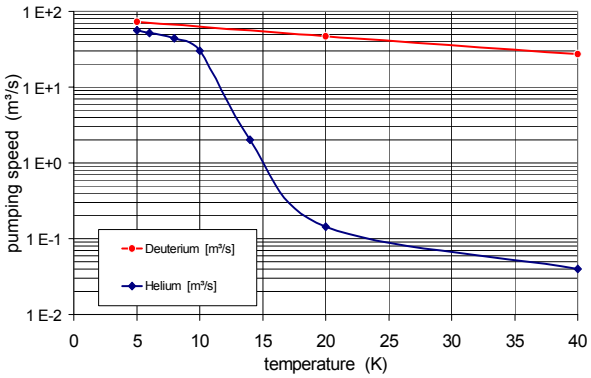

Fig. 4: Pumping speed of D_2 and He within temperature range 5 – 40 K.

4. COOLSORP

The COOLSORP facility was operated continuously throughout the last two years. Experiments were made to measure the sorption isotherms of different gases on the activated carbon SC 2 (ITER reference material). In the last report period (2001) the isotherms of N_2, He and H_2 from two samples were measured. In the new stage of experiments, the adsorption of nitrogen, helium, deuterium and hydrogen was studied on a third sample (also SC 2) at different temperatures (4—77K).

The new adsorption isotherms obtained show a clear dependence on temperature and are similar to IUPAC type I (microporous material). For example, Fig. 5 shows the adsorption isotherms of deuterium at 23, 27, 40 and 77 K. The isotherms for 23 and 27 K relate to the subcritical temperature range, whereas the isotherms for 40 and 77 K were measured at supercritical conditions. The curves show a very similar shape compared to those for hydrogen H_2.

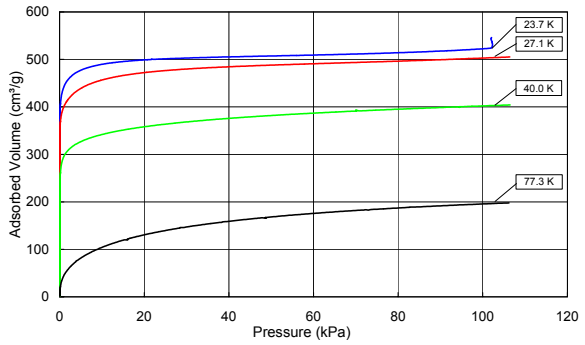

Fig. 5: Adsorption isotherms for deuterium at various temperatures.

Evaluations by various methods were made to determine the total surfaces and pore surfaces and volumes, respectively [8]. The results vary as a function of the gas and the method selected. Interpolation of the measured results by the Langmuir method (except for helium) and the Dubinin-Radushkevich equation was found to be easily applicable. Further studies must be conducted to see whether extensions of both methods (e.g. according to Tóth, Dubinin-Astakhov or Rudzinski) can result in improvements. However, the stored measurement data are considered to be sufficient for qualification of any new carbon material, which may be proposed in the future to replace the SC 2 material.

Application of the BET equation produced unsatisfactory results, as was to be expected for an almost exclusively microporous activated carbon. However, as the BET method according to DIN 66131 constitutes a standard, variations of the BET equation will be examined in the future for better interpolation of the measured results. Density Functional Theory (DFT) was used to derive the differential pore distribution information from the measured isotherm, see Fig. 6 for nitrogen at 77 K. However, due to the limited number of available kernel files, this approach can currently only be applied to nitrogen at 77 K data.

Other measurements are planned as well. Higher hydrocarbons are to be studied in detail as a new sorptive. Measurements performed on a different activated carbon with a larger total surface are to improve comparability with measurements by other authors.

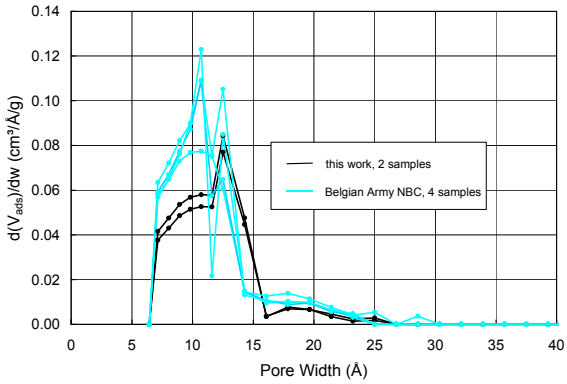

Fig. 6: Differential pore distribution for nitrogen at 77 K.

5. Microwave regeneration

Within the ITER reference scenario, the heating step for regeneration of the cryopump panels, is performed by changing the temperature of the coolant (supercritical helium) from 4.5 K to about 100 K. However, the cryogen consumption for the subsequent fast cool-down is especially high, as the total installed panel stainless steel mass is involved in the temperature change. The use of microwave heating would have the advantage to limit the heating effect to the charcoal part on the panel surface, and, by that, reduce the heating power needs down to 10%.

Complementary to the high power heating experiments with the 140 GHz Thales gyrotron, performed at the Institute for Pulsed Power and Microwave Technology at FZK, which demonstrated the principle feasibility of this technique, low power experiments at the same frequency were also performed at various angles of incidence and polarisation, at University of Stuttgart. For example, at an incidence angle of 45°, the absorption was measured to be about 64% (perpendicular case) and 84% (parallel case), respectively. In order to be able to derive the influential properties, a simulation tool was developed, involving electrodynamic and heat flux calculations [9]. Fig. 7 illustrates a typical result, showing the interrelation of the absorption coefficient and variable (carbon+glue) layer thicknesses, which is in good agreement with the measurements. The oscillatory function is due to the positive and negative interference of the reflection at the two boundaries gas-carbon and carbon-steel.

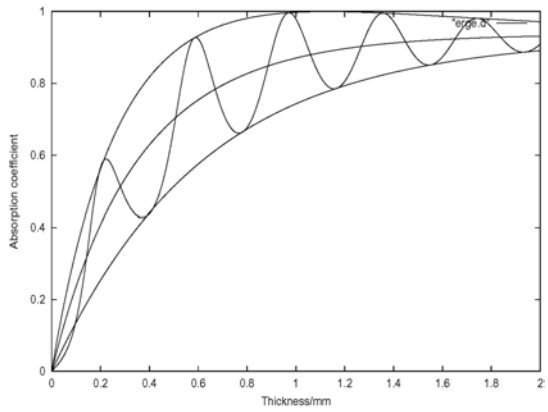

Fig. 7: Calculated absorption vs. layer thickness.

Currently, a proposal is developed, how to integrate a microwave heating system into the ITER torus cryopumps, involving antenna, window and mirror conceptual design. In parallel, low temperature measurements of the active carbon electric properties are under preparation.

Staff:

A. Antipenkov
G. Dammertz
Chr. Day
A. Edinger
J. Grimm
H. Haas
V. Hauer
T. Höhn
H. Jensen
A. Mack
R. Simon
R. Töpfer
R. Wacker
J. Weinhold
D. Zimmerlin

Literature:

[1] H. Haas, Chr. Day, A. Mack, S. Methe, J.C. Boissin, P. Schummer, D. Murdoch, Test facility TIMO for testing the ITER model cryopump, Proc. 17th IAEA Fusion Energy Conference, Yokohama, Japan, October 1998, Vol. 3, pp. 1077-1080.

[2] A. Mack, A. Antipenkov, J.C. Boissin, Chr. Day, S. Gross, H. Haas, V. Hauer, D.K. Murdoch, Th. Waldenmaier, Design of the ITER torus cryopump, ISFNT-6, San Diego, US, April 2002.

[3] A. Mack, Chr. Day, H. Haas, D.K. Murdoch, J.C. Boissin, P. Schummer, First operation experience with ITER-FEAT model pump, Fusion Engineering and Design 58-59 (2001) 365-369.

[4] Chr. Day, H. Haas, A. Mack, Development of the cryovacuum pump system for ITER-FEAT, Proc. Ann. Meeting on Nuclear Technol., Dresden, Germany, May 2001, pp. 603-606.

[5] K. Spath et al., Performance tests of a 2 kW He refrigerator for SC magnets tests down to 3.3 K, Advances in Cryogenic Engineering, Vol. 39 (1994), 563-570.

[6] H. Haas, Chr. Day, A. Mack, D.K. Murdoch, Performance tests of the ITER model pump, 22nd SOFT, Helsinki, FIN, Sept. 2002.

[7] Chr. Day, H. Haas, A. Mack, D.K. Murdoch, New operational aspects of the ITER-FEAT primary vacuum pump system, Fusion Engineering and Design 58-59 (2001) 301-306.

[8] Chr. Day, V. Hauer, The use of hydrogen and helium as probe molecules for pore characterisation of charcoal cryosorbents, 6th International Symposium on Characterisation of Porous Solids COPS-VI, Alicante, Spain, May 2002.

[9] A. Möbius, A. Mack, Chr. Day, G. Dammertz, R. Wacker, Regeneration of cryosorbing exhaust gas panels by means of gyrotron radiation, 27th IEEE Int. Conf. On Infrared and Millimeter Waves, San Diego, US, Sept. 2002.

TW1-TTF / VP 12
Performance of Evaluation of Roots Blower with Ferrofluidic Seal

Introduction

Cryogenic and mechanical pumps of various types will play an important role in the future tritium fuel cycle of fusion reactors. They are required to evacuate the plasma vacuum vessel and connected auxiliary systems after ventilation and plasma shots, to transfer the gases from the cryogenic pumps during/after regeneration to the tritium plant and to circulate the gases inside the tritium plant to achieve the detritiation of impurities, the enrichment of the tritium for re-injection into the plasma and the tritium accountancy. Industry offers a large variety of different pumps, but most of them do not fulfil the stringent tritium requirements with respect to the required He leak rate ($<10^{-9}$ Pam^3s^{-1}) and the compatibility of the employed materials with tritium.

Roots pumps for ITER

Roots pumps are planned in the pumping trains for evacuation of the vacuum vessel and for transfer of the regenerated gases to the tritium plant because they offer very high pumping speeds and a very compact design. The main disadvantages of commercial Roots pumps are the relatively high leak rates due to the use of elastomer O-ring seals and the tritium contamination of the oil required for lubrication of the precision gears and bearings. Conversely the pumped gases are contaminated by oil streaming along the rotating shafts caused by pressure differences between the pumping and the oil filed volumes.

Test of ferrofluidic seal

Whereas the required overall He-leak rate to the environment can be achieved by replacement of the elastomer seals with metal seals, it was hoped that the gas streams between the oil filled volumes and the pumping volume can be considerably reduced by the use of ferrofluidic seals. A test rig was built to test ferrofluidic seals under various conditions.

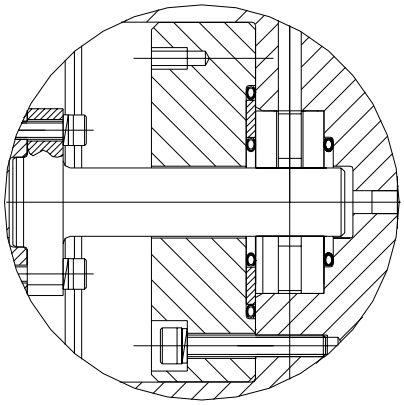

Fig. 1: Cross section through the main parts of the test rig showing the rotating stem in the middle of a ferrofluidic seal.

The main part of the test rig, the ferrofluidic seal with the rotating shaft in the middle, is presented in Fig. 1. The ferrofluidic seal itself is sealed by three metal seals against the surrounding metallic body of the test rig.

The results of the various leak tests were very convincing. Very small He leak rates slowly increasing with time were observed. The longest continuous duration test of 1 month resulted into a He leak rate of less than 6 10^{-10} Pam^3s^{-1} with a He pressure difference of 25 kPa applied across the seal and the shaft rotating with a speed of 1500 rpm. Furthermore, the test rig was re-used again after a pause of more than half a year. The ferrofluidic seal showed exactly the same leak tightness. Due to these encouraging results the decision was made to design and build a Roots pump with a pumping speed of 250 m^3h^{-1}.

Design and construction of a tritium compatible Roots pump with a pumping speed of 250 m^3h^{-1}

The design requirements for the tritium compatible Roots pump were the following:

- Manufacture of a Roots pump with a pumping speed of 250 m^3h^{-1};
- Use of tritium compatible materials as far as possible;
- Overall He leak rate of the pump to the environment: $<10^{-9}$ Pam^3s^{-1};
- Use of four ferrofluidic seals on the shafts of the two rotors to separate the pumping volume from the oil filled volumes;
- Consideration of maintenance in the design.

To achieve the low overall leak rate to the environment metal seals are used as well as magnetic coupling system between the motor and the main driving shaft. All construction materials to be used are metallic or ceramic. The only materials not fully tritium compatible are the oil required for lubrication and the ferrofluidic liquid. The four ferrofluidic seals on the shafts will reduce the gas streams between the oil filled volumes and the pumping volumes and minimise the potential contamination of the oil by tritium and of the pumped gases by oil. Maintenance is considered by the onion like construction of the pump which allows disassembly of the outer most parts of the pump and access to the oil filled volumes, the precision gears, the bearings, the inner part of the magnetic coupling, etc., without any breach of the tritium contaminated pumping volume as long as the ferrofluidic seals perform as expected.

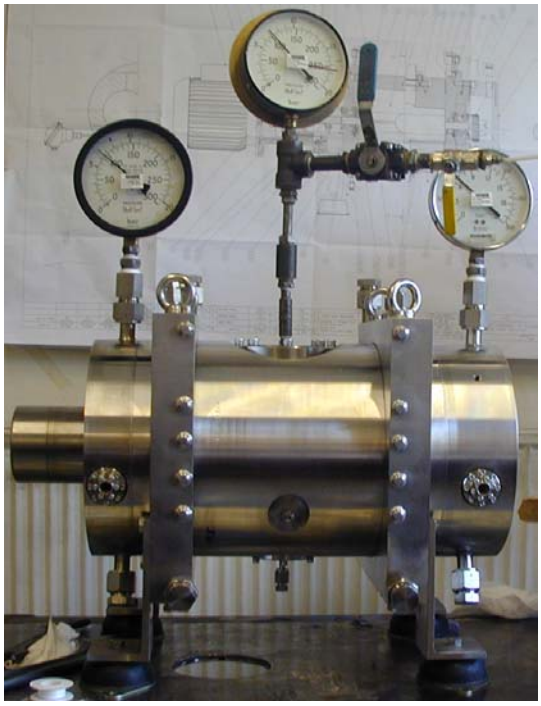

Fig. 2: Assembly of the Roots pump during the pressure test.

Fig. 2 shows the main parts of the Roots pump during the pressure test (the motor and the magnetic coupling will be installed on the smaller cylinder on the left hand side). Three pressure gauges were connected to the main three compartments of the pump because the small amounts of ferrofluidic liquid painted on the shafts functioned already as a seal between the volumes. Furthermore, easily recognisable are the two viewing windows on the left and right side to check the oil levels, the DN 63 CF inlet and DN 40 CF outlet flanges at the top and bottom in the middle of the pump, the two Cajon connectors at the top on the left and right side for filling oil into the oil reservoirs, the two Cajon connectors at the bottom on the left and right side to drain the oil and the connection for a thermocouple in the middle to measure the temperature of the Roots pump near the exit.

Various pressure tests and initial He leak tests have already been performed with the Roots pump, but before its shipment to the Forschungszentrum it has still to pass some further performance checks and the final leak tests.

Investigation of the pump market

The study of the necessary modification of a catalogue pump design towards its tritium compatibility has been started. The commercially available oil-free pumps market has been investigated and requests were sent to 17 companies which have Roots blowers in their program. 11 companies have either not replied or expressed no willingness to cooperate. Three companies have expressed their willingness to cooperate, but the pump performance from their program does not suit ITER requirements:

K.Busch GmbH: Two parallel Roots blower PANDA WV0250-2000C (2140 m^3/h) and Screw pump COBRA AC2500 (2700 m^3/h)

Ulvac GmbH: stand DYM-18RAN-12RAN-18CLN, 6 units are needed

Vacuummash (Kazan, Tatarstan-RF): Pump system DVN-1500+DVN-500+DVN-150

Work is ongoing with three companies, Leybold, Aerzener and Pfeiffer. The ITER pumping system based on Edwards Roots blowers has been revised and three different pumping set compositions were considered, see Fig. 3.

Leybold Vacuum can offer a system consisting of the Roots blower RUVAC WS 2001 FC with a frequency converter, allowing for up to 4000 m^3/h capacity, backed by the screw pump ScrewLine SP630. This screw pump is promising for tritium use because its housing is an aluminium casting and it has a cantilevered bearing scheme for the rotor which has the shaft seals on the high pressure side only.

Aerzener Machinenfabrik: 1st stage: GMb 15.11 HV, 2nd stage: GMa 13.8 HV, backing pump: 2×VN300K reciprocating pumps of the Toyo program (Fig. 4). The first and the second stage blowers are equipped with frequency converters, allowing adjustment of the rotation speed in accordance with the different process gases and the inlet pressures. The manufacturer of a pump can give recommendations to companies developing the pumping systems.

Pfeiffer Vacuum: 1st stage 2×WKP4000, 2nd stage WKP2000, 3rd stage 2 or 4×VN300K reciprocating pumps of the Toyo program (Fig. 5). The company has made tests on helium and calculated the performance curve for an ITER-relevant pumping scheme.

Revision of the roughing requirements

In the on-going evolution of the ITER project (it tends to reduce the numbers of cryopumps, reduce fuelling rate, more compact piping lay-out) the requirements for the roughing pumps can change. In order to be able to follow the progress in ITER within this task as well, a revision of ITER roughing requirements has been performed.

During the cryopump regeneration the gas held in its volume remains cold because the baffle will be hold at 85-100K. Based on the curve received from Pfeiffer Vacuum, the pumping performance of the ITER roughing system was checked with the following assumption: the gas in the cryopump volume during regeneration remains cold, but it has an ambient temperature at the entrance to the roughing system. Thus the initial pressure will be less and the evacuation time will be longer than if the gas in the full volume is warm, see the curve in Fig. 6.

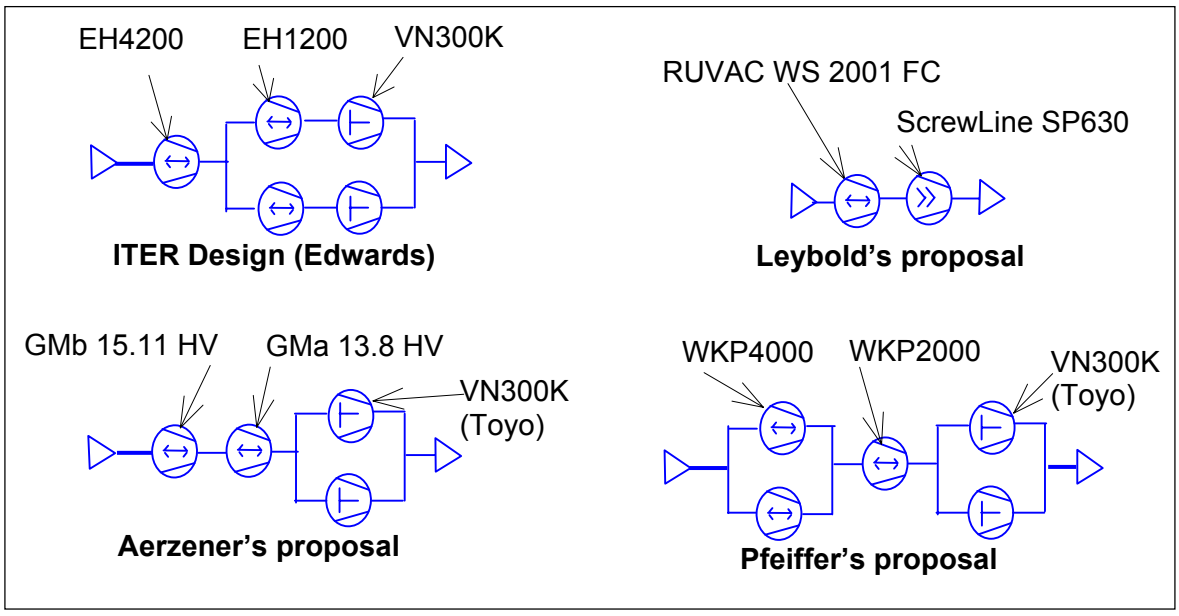

Fig. 3: Roughing pump set schemes considered by different companies.

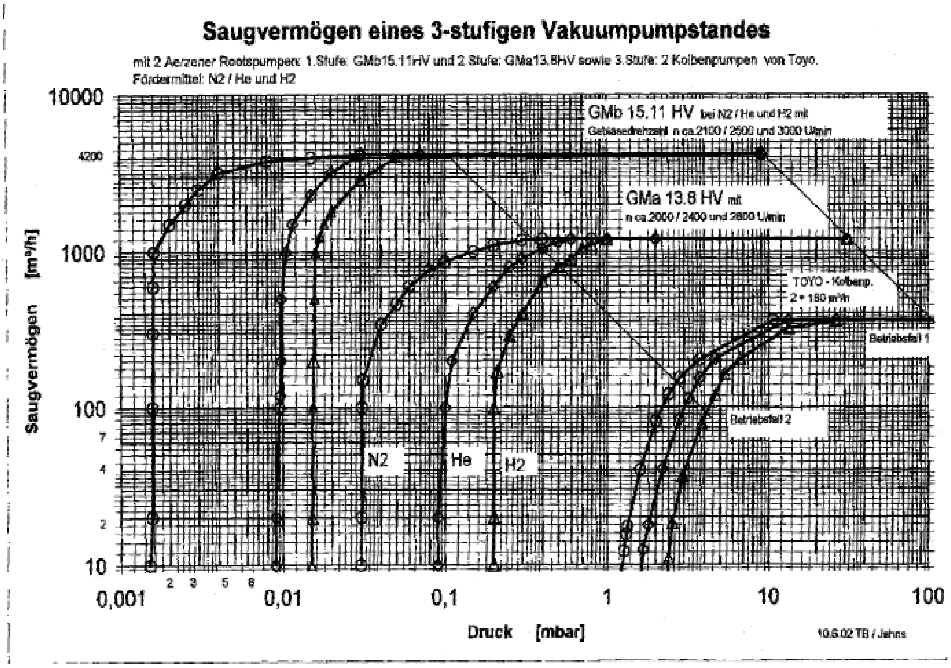

Fig. 4: Pumping curves from Aerzener for hydrogen, helium and nitrogen.

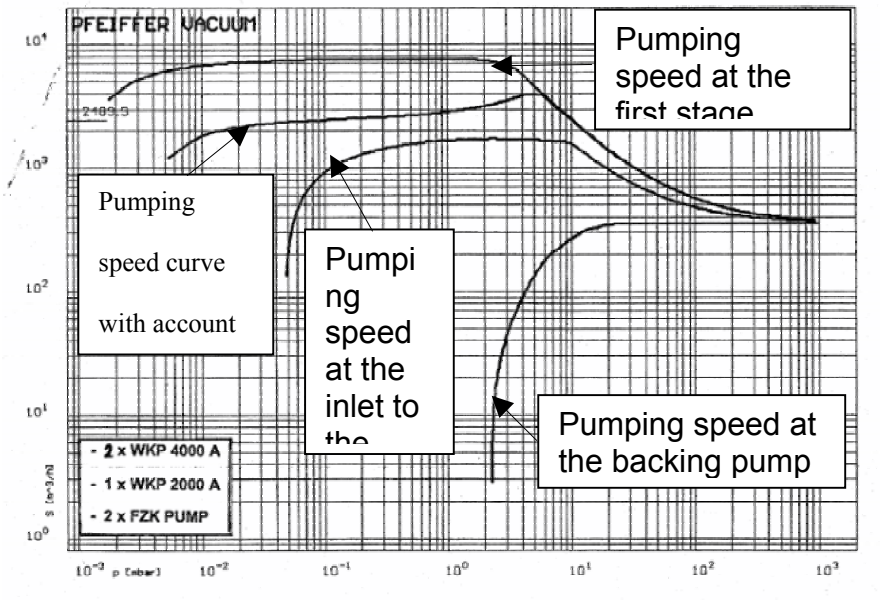

Fig. 5: Pumping curve for Pfeiffer pumping system.

Tritium compatible seal design

Using the drawings of Roots blowers received from Aerzener Maschinenfabrik and Pfeiffer Vacuum, work has been started towards the integration of ferrofluidic seals into the design. The partner company involved in this activity is FerroTec GmbH.

Future activity within the rest of 2002- middle 2004

Technical specification and concept of the mechanical pump design. Study to determine modification for its tritium compatibility: shaft seal (Ferrofluidic), flange seal (Helicoflex®), housing material and technology. Study to determine all operating requirements and modes of the ITER forevacuum system. Process design, system configuration

and performance. Layout of complete pump unit. Mechanical, electrical and control design.

Staff:

B. Antipenkov
W. Jung
R. Lässer
A. Mack
R. Simon

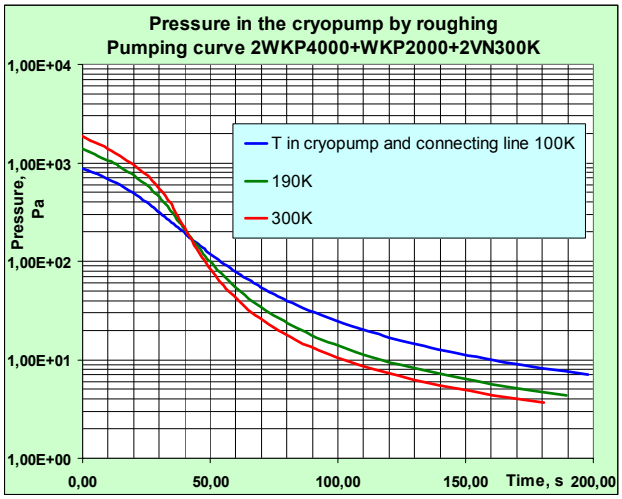

Fig. 6: Pump down curves for the Pfeiffer system and the torus cryopump, which holds the gas at low temperatures.

TW1-TTF/D465-3 (EFDA 01-606)
Torus Cryopump and NBI Injector Cryopanel Design

Introduction

The success in the ITER plasma performance depends on the reliability and efficiency of the main cryopump. The cryopump design evolved over the ITER history and in its last modification was not comprehensively analysed. The design of the NBI cryopanels has been recently modified in comparison with its initial design of 1994 and needs better analyses as well.

The purposes of this study in the frame of task D465-3 are to review and analyse the revised design proposed during year 2001 for both cryopumps, for the NBI - particularly in the vacuum and cryogenic aspects, to propose revised torus pump concepts on the basis of Monte Carlo optimisation, to assess the vacuum and thermal performances of the design and to compare it with the pumping requirements, to formulate recommendations to improve the design.

Torus Cryopump

The new design proposed for the torus cryopump in ITER-FDR 2001 was analysed and compared with the 1995-1998 design.

The main characteristics estimated for the ND750 new pump concept are the following:

Pumping performances:

$S(D_2)$ molecular, of the inlet port ≅ 75 m^3/s
$S(D_2)$ at 0,1 Pa, of the inlet port ≅ 90 m^3/s
S(pure He) molecular , of the inlet port ≅ 69 m^3/s
S(pure He) at 0,1 Pa, of the inlet port ≅ 83 m^3/s
Helium capacity per pump > 8000 $Pa \cdot m^3$ He at 273 K
$q(H_2)$ max allowable, limited by H_2 safety = 15 000 $Pa \cdot m^3$ at 273K

Refrigeration requirements:

- **80 K refrigeration:**

Cooling down 300K ⇒ 80K: ΔH = 47 MJ + 100 litres cryogen

Steady state refrigeration during:	Stand-by:	1.8 kW
	Discharge :	2.9 kW
	Partial regeneration:	5.6 kW

- **4.5 K refrigeration:**

Cooling down 300K ⇒ 4.5K: ΔH = 15.7 MJ + 1.2 MJ + 43 litres cryogen

Steady state refrigeration during:	Stand-by:	145 W
	Discharge:	265 W

According to the results of the analysis it is reasonable to make the following improvements in the pump design:

1. Replacement of the second louver baffle by a plain 80 K shield, actively cooled,

2. Reduction of the photon transmission of the inner baffle, with regard to the warm valve elements which are looking to the baffle,

3. Confinement of the intermediate shields with respect to the pumped gases inlet stream, in order to reduce the risks of gas condensation, pressure instabilities and particles contamination of these shields,

4. Optimisation of the additional shielding system. Replacement by a vacuum insulated double wall casing could be evaluated,

5. Optimisation of the geometry and dimensions of the inner baffle and 4.5K panels array,

6. Thermal shielding of the pump plug and cryogenic piping.

Taking into account the above recommendations, two modified conceptual designs are proposed fig.1 and fig 2, with the aim to improve both pumping and thermal performances as well as the manufacturing process of the pump. These proposals have to be evaluated and optimised by Monte Carlo calculations.

Both designs offer the same panel pumping area of 5 m², which should comply with the ITER FEAT helium pumping requirement, on the basis of the sorbent He capacity of 1500 $Pa \cdot m^3/m^2$ sorbent determined from the model pump tests.

The alternative B, although less easy to manufacture than A, should offer a better pumping speed at full valve opening and a better uniformity of gas deposition onto the panels compared to alternative A.

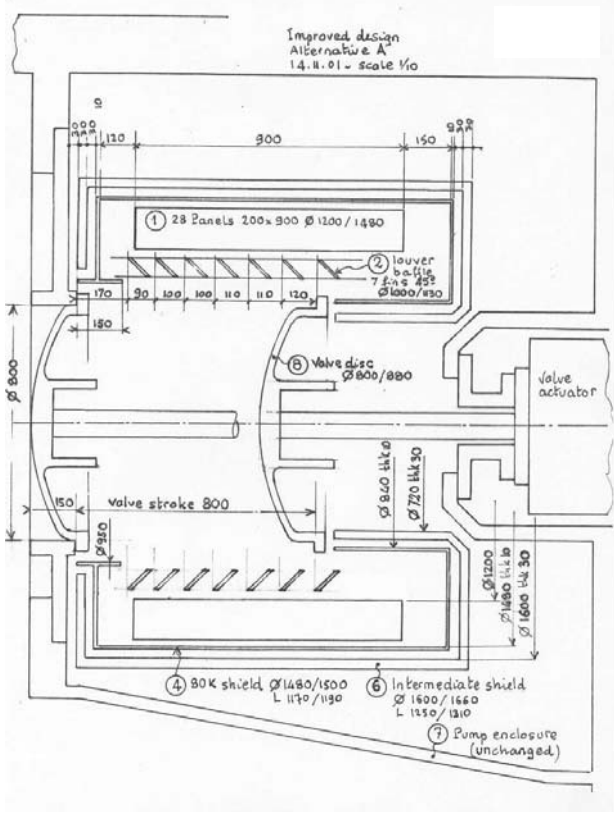

Fig. 1: Torus cryopump improvement.
Alternative A

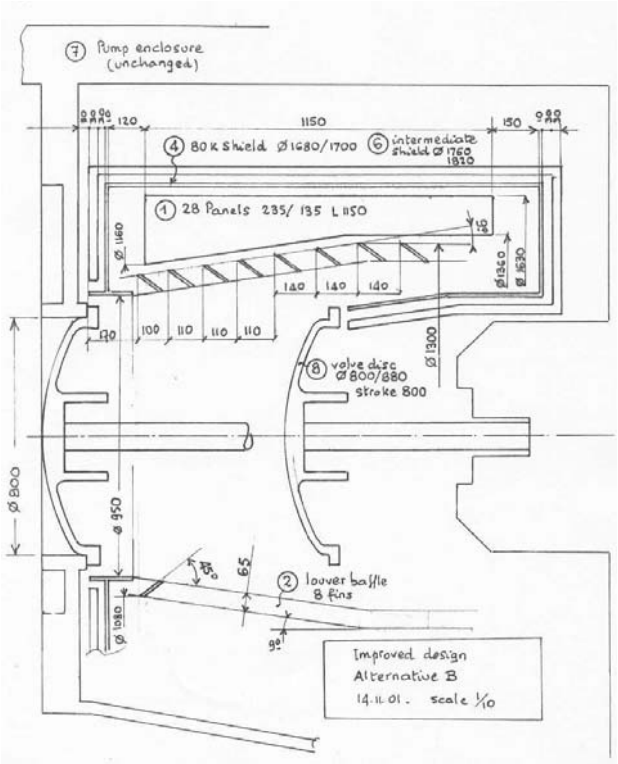

Fig. 2: Torus cryopump improvement.
Alternative B

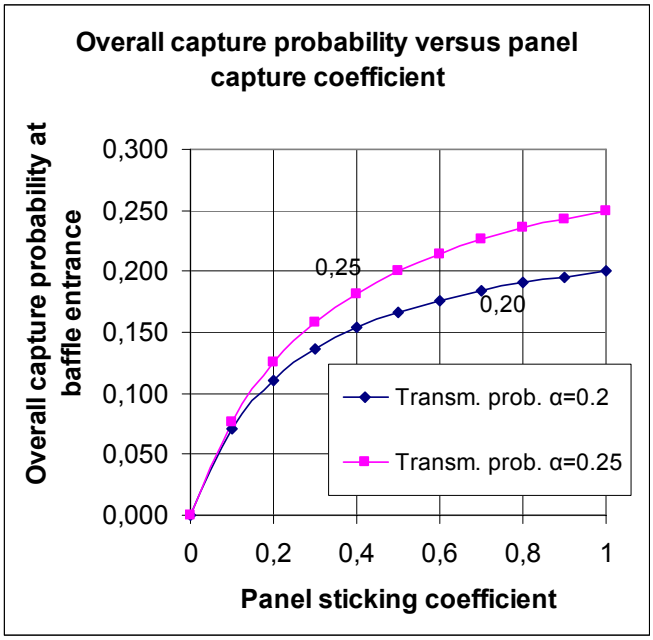

Fig. 3: NBI cryopump capture probability

Heating and Diagnostic Neutral Beam Injector (NBI) Cryopanels

The design proposed for the HNB and DNB cryopumps have been reviewed on the basis of the documentation of ITER Final Design Report 2001 for two options: two cylindrical plain panels per sub-module, and a louver array of 168 longitudinal flat panels. The conclusions mainly apply to the design of the Heating NB cryopump, the Diagnostic NB cryopump has a similar design but is one third shorter and some results can be correspondingly scaled.

The plain panels option offers simplicity and better reliability, the louver array option allows to apply different properties to the sides of a panel and to use the back sides sorbent for H_2 cryosorption and the front sides for condensation cryopumping of other gases such as N_2, etc., then the panel front side can be polished and therefore the radiation heat transfer from the black baffle to the panels will be reduced by a factor close to 10. The louver array is recommended as a preferable option.

The refrigeration in the ITER design is achieved by forced flows of 80 K gas helium (GHe) for shields/baffles. For the pumping panels the same quilted design as for the torus cryopump panels is used. The pumping of H_2 and D_2 gases can be performed by using the cryosorption process on activated charcoal particles which are bonded on the surface of the panels. This procedure allows to pump H_2 and D_2 at temperatures between 15 and 20K.

The main characteristics of the HNBI cryopanel design have been estimated for the panel array option and 15 K SHe cooling. The results are presented in Table 1 and the calculated curve of the cryopump capture probability is shown in Figure 3.

It is recommended to increase the chevron baffle area by approx 13 % and to adapt the design of the diaphragm attached to RID entrance, to have 27 % of the chevron baffle surface available in chamber 1 (source & neutraliser) and 73 % of the chevron baffle surface available in chamber 2 (RID & calorimeter).

Refrigeration requirements :

80 K refrigeration:
Steady state refrigeration during:
Stand-by without gas load: 10 kW
H_2 pumping (36 Pa·m^3/s): 12 kW

15 K refrigeration :
Steady state refrigeration during:
Stand-by without gas load: 38 W
H_2 pumping (36 Pa·m^3/s): 160 W

H_2 safety:

In case of an air ingress accident, the H_2 pumping capacity of the pump could permit to exceed the explosion safety limit of 1.7% in the 156 m^3 of HNB vacuum vessel. In order not to exceed the 1.7% safety limit, the H_2 inventory has to be limited to :

q(H_2) max allowable for safety = 268000 Pa·m^3 H_2 at 273K

which corresponds to 7400 s pumping of the 36 Pa·m^3/s specified H_2 gas flow.

Action shall be implemented to forbid operation beyond that limit.

Location	Parameter	Requirement	Design	Design / requ.
Chamber 1 (source)	H_2 gas flow Q_1	33 Pa·m^3/s	33 Pa·m^3/s	
	Pressure P_1	3,0E-02 Pa		
	Pumping speed S_1	1100 m^3/s	1785 m^3/s	**1,6**
	Fraction of total	27 %	50 %	1,9
	H_2 quantity (18 pulses x 450 s) q_1	117,7 mole	186,9 mole	1,6
Chamber 2 (RID)	H_2 gas flow Q_2	3 Pa·m^3/s	3 Pa·m^3/s	
	Pressure P_2	1,0E-03 Pa		
	Pumping speed S_2	3000 m^3/s	1785 m^3/s	**0,6**
	Fraction of total	73 %	50 %	0,7
	H_2 quantity (18 pulses x 450 s) q_2	10,7 mole	129,4 mole	12,1
Total for HNB	H_2 gas flow Q_1+Q_2	36 Pa·m^3/s	36 Pa·m^3/s	
	Pumping speed S_1+S_2	4100 m^3/s	3570 m^3/s	**0.87**
	H_2 quantity (18 pulses x 450 s) q_1+q_2	128.4 mole	316.3 mole	2.5

Table 1: Comparison of HNB pumping requirements and cryopump design performances during H_2 operation

Staff:

A. B. Antipenkov
Chr. Day
V. Hauer
H. Haas
A. Mack

Literature:

[1] A. Mack et. al., Design of the ITER Torus Cryopump, Proceedings of the 6th International Symposium on Fusion Nuclear Technology, April 7-12, 2002 – San Diego, USA

TW0-T 450/01
Leak Localisation in ITER Water Circuits

TTFD / VP 23
Localisation on In-vessel Water Leaks

The object of this work is to investigate a proposed method of locating leaks in the ITER water cooling circuits. This works follows on from the initial investigations by JRC Ispra where they proposed using specific tracer materials and then looking for these tracers in the exhaust gases from the torus. The method uses a gas chromatograph / mass spectrometer (GC/MS) combination to detect the very small amounts of tracer that would be in the exhaust gases of the torus in the event of a leak.

JRC Ispra proposed a system which would be in continuous operation, however this would have many disadvantages. It has now been agreed that such a tracer method would only be initiated in the event of a leak and after ITER has been shutdown. This overcomes many of the problems associated with a continuous system. A water leak into the torus will be very obvious by other indications, the problem is to locate the water circuit that is leaking.

The outline plan is to use the TIMO facility at the ITP of FZK to simulate the ITER pumping system and connect a GC/MS system to examine the exhaust gases after full regeneration. Small quantities of water with tracers will be introduced into the high vacuum side of the TIMO facility and the tracer will be looked for in the exhaust. The main features to be investigated are the temperatures to which the cryo panels will have to be raised in order to release water and the tracers.

A standard GC/MS with a thermal desorber system has been purchased and is being commissioned at TLK and various potential tracers will be examined for suitability. The combination of the thermal desorber and the gas chromatograph separate out the trace compounds in a gas and feed the compounds, separated by time of elution, into a mass spectrometer. A typical gas chromatogram of an air sample is shown below.

The mass spectrogram for the eluant at time 6.72 minutes is below, which is most probably cyclotrisiloxane according to the spectrum library. For leak detection, specific compounds with known mass spectra will be searched for which should also have a characteristic time for elution.

The MS/GC will be moved to the TIMO facility next year at the relevant stage in the TIMO test schedule. There is an outstanding problem in making the addition of the GC/MS compatible with the safety requirements of TIMO, particularly with respect to hydrogen detonations. The modification of a standard detonation barrier is being investigated to make it compatible with the vacuum requirements of TIMO and the GC/MS.

The method to identify individual cooling water circuits that may be leaking into the ITER vacuum vessel by detecting specific tracer materials placed in the water circuits will not identify where the leak is inside the vessel. Localisation of the leak inside the vessel is highly desirable in order to minimise the number of components that have to be replaced to be sure that the leak has been eliminated. An extension of the technique used for the external identification of leaking circuits. The proposed method will use a probe to scan the internal surfaces of the ITER vacuum vessel. Samples of gas will be extracted and analysed for indication of a water leak. A remotely controlled arm is required to move the probe inside the vacuum vessel and a device is proposed to be developed for this and other task, the In-Vessel Penetrator (IVP). The IVP is planned to have several sections with which it can reach every part of the vacuum vessel. It is therefore likely to be of the order 10 meters long.

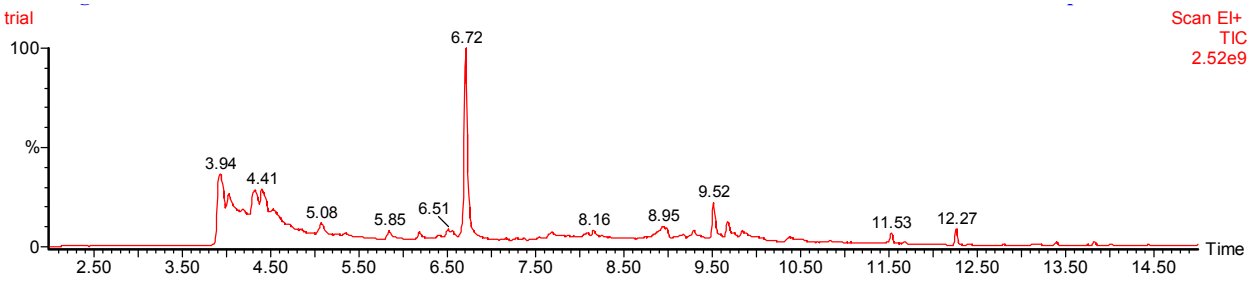

Fig. 1: Gas chromatogram of a laboratory air sample

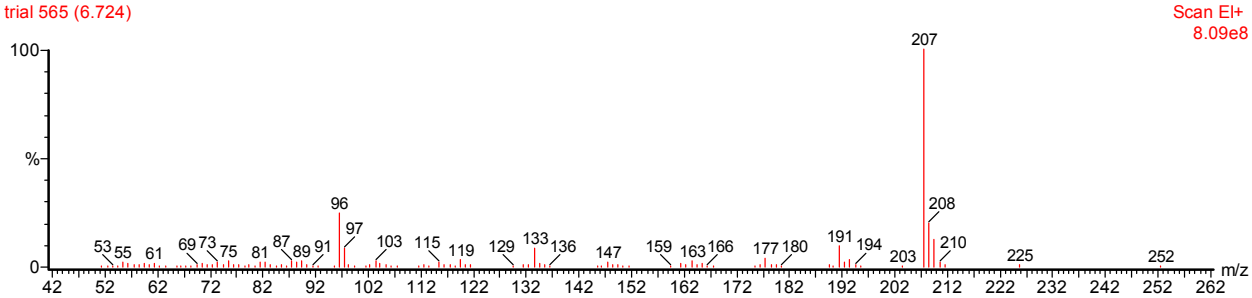

Fig. 2: Mass spectrogram of the peak at 6.72 min

It is of crucial importance to the technique for the pressure and composition of the gases inside the vacuum vessel to be determined before further work is undertaken. The choices for the gas conditions are either nitrogen at atmospheric pressure or high vacuum. A major factor of the choice is if an IVP can be developed that can operate at high vacuum, this has not been decided yet. For leak localisation this is important as it affects the mass of gas that can be extracted up through a very long narrow bore tube and hence the sensitivity of the detection. All detection instrumentation will have to be outside of the ITER vessel, primarily as the IVP will not be able to carry the detection equipment but also due to the high radiation conditions.

A meeting is planned with the ITER design team to resolve the issue of the IVP, vacuum conditions and possibly the whole strategy for leak localisation. The experimental work will await the decision of ITER.

Staff:

C. Caldwell Nichols
S. Grünhagen
C. Day

JET Exploitation

JW0-FT-1.1
Characterisation of JET Flakes

Among the possible mechanisms taking place in tokamak experiments which are responsible for in-vessel sequestration of tritium re-deposition of eroded carbon with incorporation of tritium into the deposited films appears to be the more important.

Hydrogen reaction with the eroded carbon produces a large spectrum of products mainly methane (50 - 75%) and some other less important hydrocarbons such as C2Hx (C2H2, C2H4, C2H6, etc.) (20 - 35%) and C3Hy (C3H6, C3H8, etc.) (5 - 15%), via C+, CH+x and H+ ions impinging on the divertor and producing C2Hx, radicals via a polymer-like C:H intermediate.

Thick carbon deposits containing high levels of hydrogen isotopes have been observed in JET as well as in TFTR after exposure of first wall materials to discharges. Examination of a complete set of poloidal tiles revealed the highest deposition was on the plasma shaded lower edge of inner tiles 3 and 4 of the Mark IIA divertor. Inner base tile 4 was characterised by strong deposition and also flakes falling or hanging from the side shadowed from the plasma.

It appeared that the deposited material has a thickness of several tens of microns (up to 90 µm) and accumulates on lower horizontal surfaces. Spalled-off deposits constitute what has been identified as dust and flakes. Dust and flakes naturally have accumulated in this region during the course of several years of operation.

Co-deposits, flakes and dust are also of much concern because of the associated progressive increase of tenaciously held in-vessel tritium inventory. Furthermore, detailed knowledge of the distribution of tritium and other hydrogen isotopes within the vessel constitute an important database for modelling carbon transport phenomena from regions of high flux of incident particles to regions of low flux. It also represents fundamental information needed for the selection of suitable plasma facing materials and the development of concepts to mitigate the negative effects of co-deposition.

Data concerning some physical properties of flakes retrieved from JET after the PTE (Preliminary Tritium Experiment) and the DTE1 (First Deuterium Tritium Experiment) campaign are presented hereafter.

Particle size

In-vessel dust and flakes from the divertor region are in principle discernible by their respective sizes. Most flakes from the PTE campaign of JET were found to have dimensions of the order of 0.5 mm with a thickness of about 20 µm (occasionally flakes having lengths up to 20 mm were also collected). SEM showed that the flakes collected after PTE have a distinct layered structure, each layer being several µm thick.

The thickness of highly tritiated DTE1 flakes varied within a range of 46- 60 µm and, as in the case of the PTE flakes, they showed individual sub-layers with a thickness that varied from 8 to 30 µm. Nevertheless, at times single massive pieces of 15 x 50 mm were also observed. The majority of the flakes collected with a cyclone vacuum cleaner from the JET machine after the DTE1 campaign was found to be in the range of 375 and 410 µm (Fig. 1).

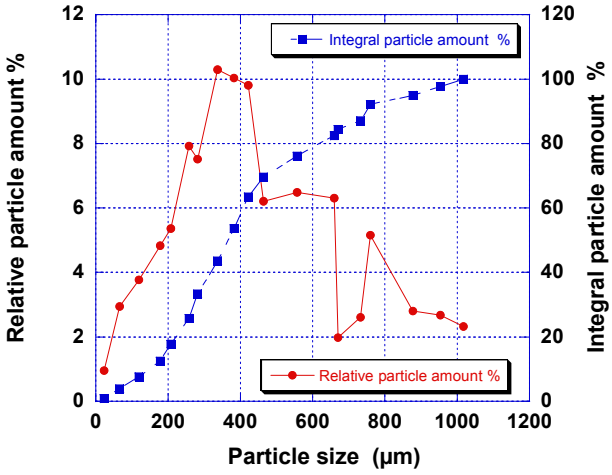

Fig. 1: Size distribution of dust retrieved from the vacuum vessel of JET after DTE1 campaign.

The density of a single JET flake collected after the DTE1 campaign was determined with a commercial helium pycnometer to be 1.6 g cm^{-3}.

BET surface

BET surface areas of 675 and 1000 m^2 g^{-1} respectively, have been reported for flakes and dust collected from the vacuum vessel of JET after the DTE1 campaign (Table 1). In contrast, for a large size fraction of flakes after PTE, a specific BET surface area of (4 ± 2) m^2 g^{-1} has been reported. The latter is in line with the measures done at the TLK on PTE JET flakes sample 3-4. Indeed, the sample had a mass of 155.9 mg, an average tritium activity of 1MBq g^{-1} and a BET surface of 7.2 m^2 g^{-1}.

Elemental composition

Flakes and dust from JET were found to consist mainly of carbon (> 70%), oxygen (2 - 15%, for dust up to 34%), iron (0.1 - 2%), chromium (2%), nickel (0.1 - 3%), aluminium (0.3 – 5 % beryllium (traces up to 8%) and hydrogen isotopes. Ion beam analyses showed the deuterium content in JET flakes to be rather high, i.e. D/C ~ 0.75.

Table 1: Physical properties of JET flakes.

Property	PTE flakes	DTE1 flakes
Particle size [µm]	(< 40) x (< 2000) (most about 20 x 500 [µm])	375 to 410
flakes: thickness x width		46 to 60 x (< 50 000)
Density [g cm-3]	-	1.6
BET surface area [m2 g-1]	4 ± 2 7.2	675??
Tritium content [GBq g-1]	0.009 to 0.015	1200

Table 1 summarises the physical properties of the flakes. Finally, the tritium content of flakes collected after the DTE1 was evaluated by calorimetry to be 1.2 TBq g^{-1} of flakes, i.e. about 3.3 mg tritium per gram of flakes.

Staff:

N. Bekris
U. Berndt
L. Doerr
P. Haeffner
W. Hellriegel
D. Niyongabo
B. Schweigel

JW0-FT-2.1
Water Detritiation

A water detritiation system with a throughput of 20 000 kg/year needs to be developed and installed at JET. The system will be based on the CECE process comprising an electrolyser for the conversion of water to hydrogen, a cryogenic distillation column for tritium enrichment and either a liquid phase catalytic exchange (LPCE) or vapour phase catalytic exchange (VPCE) column for the tritium recovery from the gas phase.

The objectives of this tasks are:

Selection and testing of the most suitable catalyst

Provision of a database of LPCE for comparison with VPCE through dedicated experiments

Design, building and operation of an experimental facility in semitechnical scale at the TLK.

The separation performances for different catalysts (from Russia, Belgium, Romania and Japan) expressed as HETP and mass transfer coefficients have been determined [1]. The most promising catalyst/packing mixture was that developed by TLK-ICIT Romania. Considering the specific operational conditions required by JET and ITER for LPCE columns, the performances of the catalyst developed by TLK can be improved. Hence at TLK tests are on-going to evaluate the separation performances for different in-house made catalysts and various types of structured packing.

A new experimental CECE facility was designed (Figure 1) and built (Figure 2). It consists of 2 electrolysers with 1 Nm^3/h each and a glass column with 55 mm diameter.

The column is foreseen with several extracting points that will allow to measure the gas composition along the column. The deuterium and tritium content in the aqueous flows are determined by infrared (FT-IR) spectroscopy and liquid scintillation counting (LSC), respectively, whereas deuterium in the gas phase is measured by an Omegatron mass spectrometer. Gaseous samples of hydrogen-deuterium-tritium mixtures from column streams are converted to water to determine the tritium content with LSC.

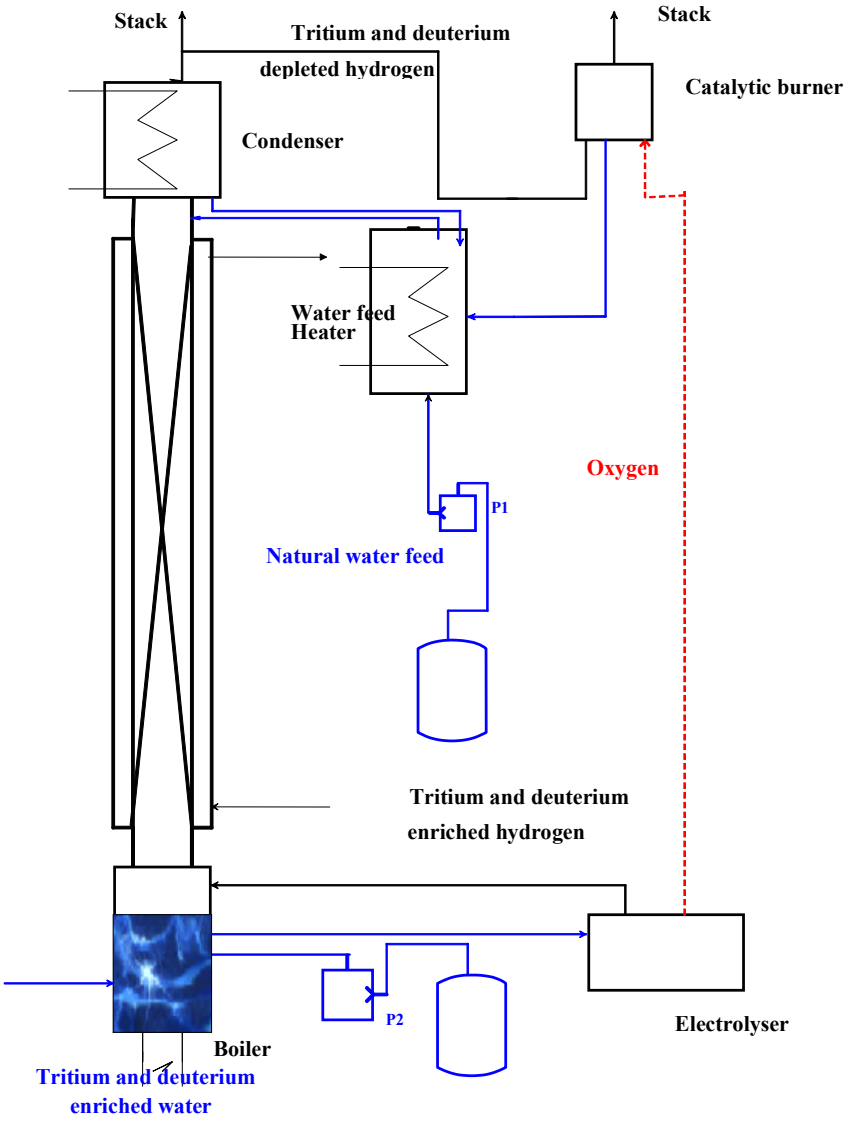

Fig. 1: CECE Facility for Water Detriation

Fig. 2: View of the Experimental Facility for Water Detriation at TLK

Catalyst-Packing Mixture Performances at Simultaneous Tritium and Deterium Transfer

For simultaneous tritium and deuterium transfer, two possible processes have been investigated in the experiments performed at TLK:

I. Tritium transfer from tritiated water to gaseous hydrogen. The LPCE column was fed in at the top with tritiated water and at the bottom the LPCE column was fed in with hydrogen.

II. Isotopic transfer between tritiated water and deuteriated hydrogen gas, when tritium is transferred from liquid to gas and deuterium is transferred in the opposite direction from gas to liquid. For this case the LPCE column was fed in at the top with tritiated water and deuteriated hydrogen was fed in at the bottom of the column.

The separation performances of four catalyst-packing combinations from different manufacturers (SCK-CEN Belgium, Mendeleev University Russia, Institute of Cryogenics and Isotopic Technologies (ICIT) Romania-TLK) have been investigated at a column temperature of 70°C, gas flow rate equivalent to a linear velocity of 0.1 m/s and the molar gas to liquid flow rate ratio was 2.

In Figure 3 the typical evolution for all catalysts under tests with respect to the HDO concentration and tritium activity at the bottom of the LPCE column is presented. For case I the tritium activity in the feeding water was in the range 30-36 $Bq \cdot cm^{-3}$ and for case II the deuterium content in the hydrogen feed was approximately 4 % at.

The corresponding values for HETP and mass transfer coefficients are presented in Table 1.

Preliminary Tests of the Enrichment Factor in the Electrolyser

Two solid polymer type electrolysers are used in the experimental facility at TLK. The main advantage of this kind of electrolysers is that the liquid hold-up is 1/10 of an alkaline electrolyser. In addition no stripper for KaOH need to be considered when such electrolysers are used. To obtain tritium compatible electrolysers, at the time being some improvements are made. The hydrogen production is 1 Nm^3/h each, at a product purity of 0.02% O_2 in H_2 and 0.1% H_2 in O_2.

Several tests with respect to the enrichment factor in the electrolysers have been carried out. Deuteriated water with a deuterium content of 2000 ppm at. and 4.5% at. was used as feeding water in the electrolyser. The enrichment factor in the electrolyser was found to be between 2.3 and 2.8 mainly depending on the current density in the electrolysis cell. The results are in agreement with other obtained on higher capacity electrolysers. During the measurements more then 120 hours of continuous operation were found to be necessary until steady state was reached.

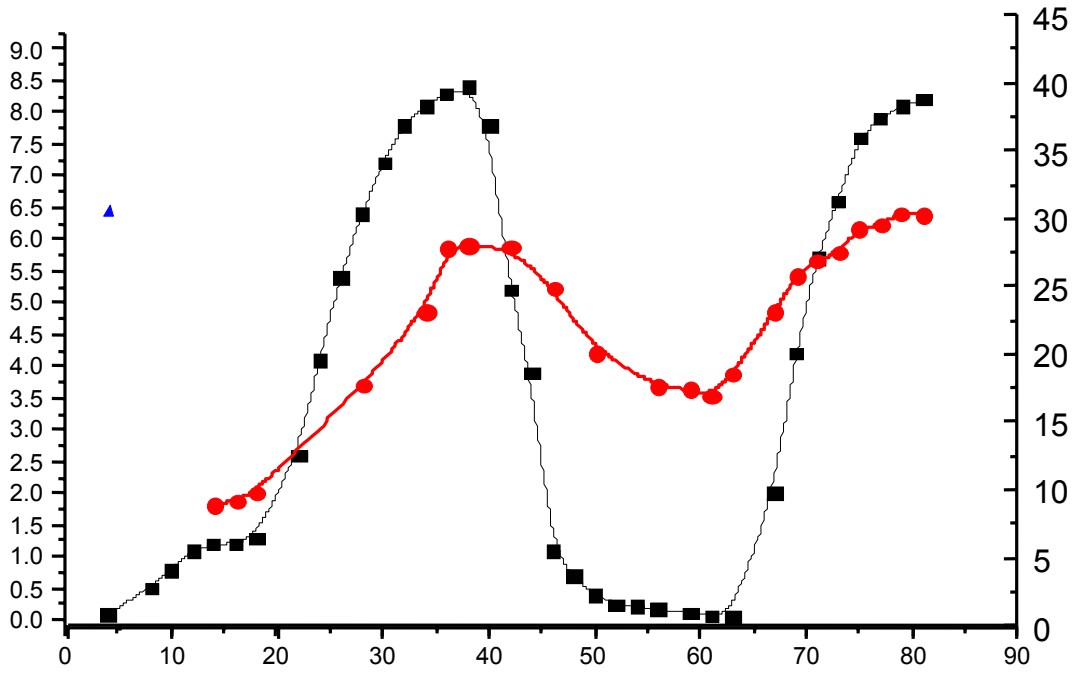

Fig. 3: Time evolution of Deuterium and Tritium concentration in Liquid phase

Table 1: Performances evaluation at simultaneous Tritium and Deuterium transfer

Exp.	Catalyst	Deuterium			Tritium		
		HETP (cm)	K_S (kmol·m^{-3}·h^{-1})	K_D (kmol·m^{-3}·h^{-1})	HETP (cm)	K_S (kmol·m^{-3}·h^{-1})	K_D (kmol·m^{-3}·h^{-1})
I	SCK-CEN Belgium	-	-	-	~135	58	89
	Mendeleev Univ.	-	-	-	~109	176	132
	TLK-ICIT	-	-	-	78	206	148
II	SCK-CEN Belgium	85	74	149	>150	37	42
	Mendeleev Univ.	35	319	296	>150	45	59
	TLK-ICIT	31	312	402	>150	52	64

According to the experimental results one can conclude that any of the catalyst/packing manufactured by SCK-Mol, ICIT-FZK and Mendeleev University allows a decontamination factor of 5000-10000, as required by JET water detritiation facility, for a column height of about 9 m.

For all the catalyst-packing mixtures investigated, at simultaneous transfer of tritium and deuterium in opposite directions, the mass transfer coefficient for tritium is lower than the value when only tritium is transferred (and correspondingly the value of HETP is higher).

The separation performances of various catalyst-packing mixtures for different tritium concentration ranges and the enrichment factor in the electrolyser are the basic knowledge necessary for designing a CECE system for tritium removal from water. Further experiments at a higher range of tritium are necessary to investigate the simultaneous tritium and deuterium transfer in a LPCE process and the tritium enrichment factor in the solid polymer electrolyser. Besides the deuterium concentration that influences tritium transport between gas phase and liquid phase, the transport relative directions of deuterium and tritium have also to be considered for the design of a LPCE column.

Staff:

C.J. Caldwell-Nichols
I. Cristescu (guest scientist)
I.-R. Cristescu (guest scientist)
U. Tamm

Literature:

[1] I. Cristescu, Ioana-R. Cristescu, U. Tamm, R.-D. Penzhorn, C.J. Caldwell-Nichols - Fusion Science and Technology, 41, pp. 1087-1091(2002)

JW0-FT-6.1
Impact of Tritium on the Performance of a Prototype Cryosorption Pumping Panel

Introduction

This task is an essential complement to the parallel assessment of the pump performance of the ITER model cryopump (Task VP11), where the tritium fractions have been replaced by deuterium. The central objective of this task, which will be performed at JET, is to study the interaction of tritium and tritiated gas mixtures with the panel, in terms of pumping performance, desorption characteristics and structural influences. The existing knowledge in this field is limited to qualitative results gained in other fusion devices and only one small scale phenomenological experiment. Together with the existing data for protium and deuterium, a sound assessment of any isotopic effect is aimed at. The understanding of the pumping mechanism of tritiated gases, which is expected from this experiment, is needed to develop advanced regeneration procedures for cryosorption panels [1]. This experiment is a benchmark test which would reveal any showstoppers to the ITER cryopumping concept arising from tritium interaction, which is the only field not having been fully covered yet.

Within this task, an existing cryogenic forevacuum module of the Active Gas Handling System (AGHS) at JET will be modified and adapted so as to house the Prototype Cryosorption Pump (PCP) [2]. The panel set-up exactly meets the ITER point design and the test results are, therefore, fully representative. The major parts of the modification are the integration of the separate PCP test vessel and the adaptation of the peripherical gas and cryogen supply systems.

PCP manufacturing status

The PCP design work has been finished in January 2002 resulting in a complete set of manufacturing drawings, issued from FZK to UKAEA. Fig. 1 illustrates the cross-section according to the final design. Thereupon, the drawing set was approved by the relevant JET departments and was examined with respect to the strict JET quality assurance requirements. After approval in early May, the procurement could be initiated.

The total manufacturing process was shared among two main partners. FZK took over the responsibility for the cryopanel arrangement itself, including all sensors (temperature and pressure), cabling and internal wiring. The manufacturing of the PCP vessel, especially the welding work, was given to the vacuum company PVA (Pfeiffer-Vakuumanlagenbau GmbH, Aßlar, Germany). In addition, a special vacuum bellow is being manufactured at BOA (Rothenburg, Switzerland) under full JET quality assurance. Before initiating any manufacturing step, detailed welding and quality plans were put forward by the companies involved. In this frame, PVA has been audited this year by UKAEA/JET to ensure correct welding procedures and documentation.

For all PCP components, suppliers have been identified; almost all components have already been delivered, including certificates of conformity. The preparation of the cryopanel arrangement has made good progress; the panels, which have been coppered and equipped with heating elements, see Fig. 2, are currently being coated with activated charcoal. Following that, the temperature sensors will be attached and the work will be continued with the final assembly of the PCP and acceptance testing at PVA, foreseen for the end of the year 2002.

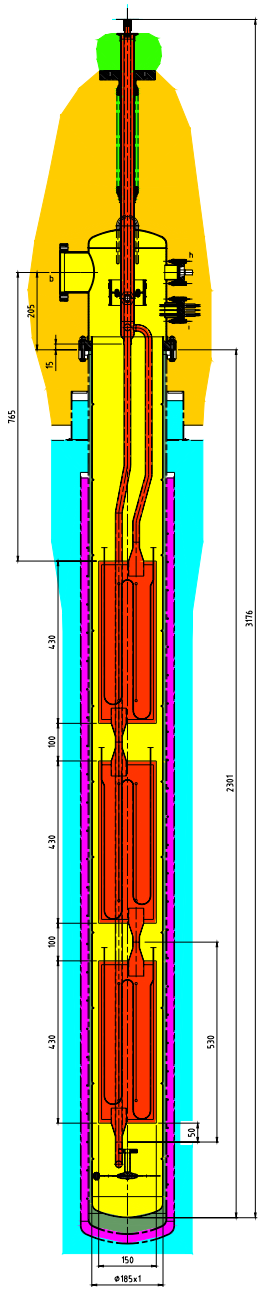

Fig. 1: Cross-section of the PCP, highlighting the several sub-volumes in different colours

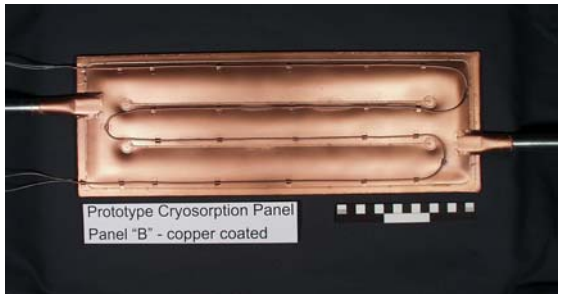

Fig. 2: One of the three PCP cryopanels, after electroplating with copper

Experimental programme

Regarding the experimental programme the former scope has been enlarged [3]. This is because it has been decided to perform a trace tritium experiment (TTE), currently scheduled for October 2003, and the PCP should be included in this experimental campaign. This is a unique chance to operate a cryopump of ITER type directly on a tokamak under tritium conditions.

A staged procedure has been agreed for the PCP experiments. In the first test stage, following the acceptance tests at AGHS, the PCP will be operated separately from the torus, and supplied with tritiated gas mixtures of defined composition via an external U-bed loop. These tests are predominantly, to cross-check the PCP performance with available data for H_2 and D_2 to delineate the isotopic effect, and to perform key-experiments for tritiated gases. Then, when the performance parameters will be established, the pumping module will be reconnected to the torus matrix line and the PCP will be operated on-line to the torus during TTE.

Preparations have been made and are still ongoing at JET for the installation of the PCP. For example, the cryogenic supply has to be shifted from reduced pressure operation of the liquid helium at 3.4 K to normal pressure boiling helium at 4.2 K. In order to facilitate defined flowrates during the external experiments a dosage valve, which was especially modified to get JET approval, is currently under extensive calibration under vacuum conditions at FZK.

Staff:

Chr. Day
J. Grimm
S. Horn
H. Jensen
A. Mack
R. Simon
R. Töpfer
D. Zimmerlin

Literature:

[1] Chr. Day, A. Mack, M. Glugla, D.K. Murdoch, Tritium inventories in the high vacuum pumps of ITER, Fusion Science and Technology 41 (2002) 3-2, 602-606.

[2] P.D. Brennan, Long term operation of the JET Facilities` Active Gas Handling System, Fusion Science and Technology 41 (2002) 3-2, 578-582.

[3] Chr. Day, D. Brennan, H.S. Jensen, A. Mack, A large scale cryopanel test arrangement for tritium pumping, 22nd SOFT, Helsinki, FIN, Sept. 2002.

JW1-FT-1.6
Tritium Profiling in JET Tiles

Plasma-wall interactions in the vacuum vessel of thermonuclear fusion machines take place predominantly on the immediate surface of all first wall materials directly or indirectly exposed to plasmas. Indeed, the first wall is continuously bombarded with hydrogen isotope ions mostly hitting the surface at flat oblique angles. The resulting net erosion and implantation, limits the lifetime of first wall components and determines the tritium wall inventory, which builds up principally via co-deposition of tritium together with eroded materials at the colder regions of the machine. It follows, that detailed information on the depth profiles of hydrogen may contribute significantly to improve the present state of knowledge of plasma-wall phenomena in the machine and deliver the basic data needed for a self-consistent modelling of plasma edge and wall effects.

Therefore, depth profiles of H, D, T, and Be in tiles used in D-D and D-T campaigns covering a wide range of contamination by tritium were determined on the plasma-exposed surface and on the surface of bulk specimens from diverse graphite and CFC tiles obtained from JET and TFTR.

The technique mainly used was Accelerator Mass Spectrometry (AMS). Tritium results by AMS were compared with full combustion measurements of samples taken from immediately adjacent positions either on or in the tile. These techniques can provide fundamental information on plasma-surface interactions and tritium uptake by first wall materials.

An AMS depth profile of carbon, beryllium and tritium in a disk obtained from the plasma-exposed side of a cylindrical specimen drilled from JET graphite tile 004/2-20 is shown in Fig. 1.

From the results plotted in Fig. 1 it can be concluded that tritium is retained on that specimen in a mixed $^{9}Be/^{12}C$ co-deposited layer with a thickness of more than 10 µm. Beyond a depth of 10 µm the concentration of ^{12}C reaches a maximum approaching a concentration of 1.13 x 10^{23} cm^{-3} which is what would be expected for a pure ^{12}C layer. The concentration profiles of ^{9}Be and tritium show the same general trends, both going through a maximum at a depth of approx. 5 to 6 µm and then dropping to smaller values.

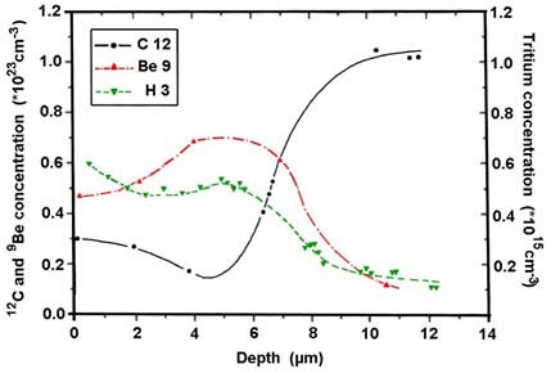

Fig. 1: Tritium carbon and beryllium depth profiles in a graphite specimen from the first wall material of JET (tile 004/2-20) coated with beryllium.

Table 1 gives a comparison between accelerator mass spectrometry and full combustion measurements for the two inner wall limiter tiles 5B17R and 5B17L. As it is illustrated tritium concentrations for both techniques are in basic agreement, at least with respect to the order of magnitude.

As it is also perceptible from the AMS spectra in Fig. 2, peak concentrations of beryllium are observed at depths in the range 3 to 7 µm on both disks. On account of the decreased Be concentrations on the immediate surface there appears to be a late carbon/hydrogen deposition layer on top of the beryllium film. This is in line with the protium, deuterium and tritium, profiles depicted in Fig. 3, where high but narrow protium, deuterium and tritium, peaks are seen at depths below approx. 2 µm. From this the conclusion can be drawn that the tile surface is probably covered by a co-deposit consisting of carbon, beryllium and hydrogen isotopes at varying compositions.

Table 1: AMS determination of hydrogen isotopes in specimens obtained from the surface of tiles 5B17R and 5B17L.

				AMS		FC	
Tile	specimen	H cm^{-2}	D cm^{-2}	T cm^{-2}	Closest neighbour, specimen	T cm^{-2}#	MBq cm^{-2}
5B17L	$7A_1$*	3.0 10^{18}	5.0 10^{17}	1.1 10^{16}**	$4A_1$	4.9 10^{16}	86
5B17R	$8A_1$	6.7 10^{18}	3.2 10^{18}	2 2 10^{16}	$1A_1$	3.1 10^{16}	56
5B17R	$9A_1$	3.7 10^{18}	2.7 10^{18}	1.1 10^{16}	$1A_1$	3.1 10^{16}	56

** According to the nomenclature used $7A_1$ stands for "coring" cylinder 7 and A_1 for the first disk seen from the plasma-exposed side of the cylinder. $7A_2$ would be the second disk from cylinder 7 etc.*

** *Determined with a Faraday cup in the range 30 to 100 pA. The carbon current used for the calibration was stable during the measurement.*

Tritium in 1 mm depth, i.e. the thickness of a disk.

Table 2 Effect of temperature on the hydrogen isotope distribution. Measures by AMS.

Tile #	Specimen	Temperature, carrier gas, time	H cm^{-2}	D cm^{-2}	T cm^{-2}	T/(T+D)
004/2-20		untreated	$2.4\ 10^{18}$	$8.3\ 10^{17}$	$2.5\ 10^{12}$	$3.0\ 10^{-6}$
004/2-20	f	300°C, moist air, 1 h		$1.5\ 10^{18}$	$2.3\ 10^{12}$	$1.5\ 10^{-6}$
004/2-20	g	400°C, moist air, 1 h		$1.0\ 10^{18}$	$1.6\ 10^{12}$	$1.6\ 10^{-6}$
004/2-20	h	460°C, moist air, 1 h		$3.0\ 10^{17}$	$7.0\ 10^{11}$	$2.3\ 10^{-6}$
004/2-20	i	500°C, moist air, 1 h		$1.1\ 10^{17}$	$5.0\ 10^{11}$	$4.6\ 10^{-6}$
5B17L	9A1*	Untreated			$1.17\ 10^{17}$	
5B17L	$7A_1$	Untreated			$8.8\ 10^{15}$	-
5B17L	$7A_1$**	Untreated	$3.0\ 10^{18}$	$5.0\ 10^{17}$	$1.1\ 10^{16}$	$2.2\ 10^{-6}$
5B17L	$8A_1$	450°C, moist air, 6 h		$1.1\ 10^{16}$	$1.6\ 10^{11}$	$1.5\ 10^{-6}$
5B17L	$11A_1$	500°C, moist air, 6 h		$4.0\ 10^{15}$	$1.0\ 10^{11}$	$2.5\ 10^{-6}$
5B17L	$13A_1$	500°C, moist air, 6 h		$4.0\ 10^{15}$	$2.2\ 10^{11}$	$5.5\ 10^{-6}$
$IN3_{s1}$	$14A_3$	untreated	$1\ 10^{17}$	$4.0\ 10^{14}$	$1.0\ 10^{10}$	$2.5\ 10^{-6}$
$1N3_{s1}$	$14A_2$	400°C, moist air, 4 h	$2\ 10^{16}$	$2.1\ 10^{14}$	$1.7\ 10^{9}$	$8.1\ 10^{-6}$

#At JET the inner wall tiles were routinely maintained at ~320°C.

*Measured by combustion

**Second measurement

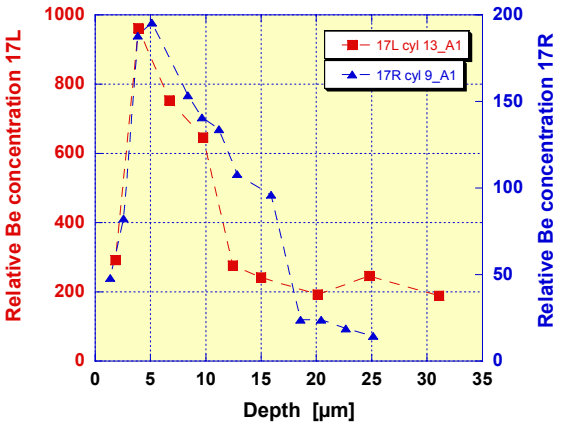

Fig. 2: Be Concentration in IWGL tiles 5B17L and 5B17R.

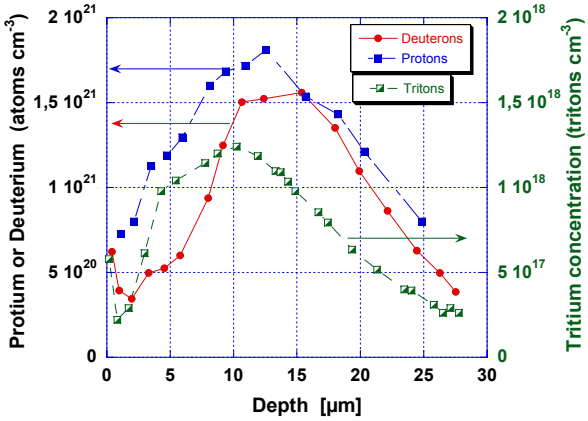

Fig. 3: Depth profiles of all hydrogen isotopes in specimen 9A1 from Inner wall guard limiter tile 5B17R.

Effect of thermal treatments on elemental surface profiles

In a limited number of runs the protium, deuterium and tritium content as well as the corresponding depth profiles on disks removed from the plasma-exposed side of i) graphite tile 004/2-20, ii) CFC tile 5B17L and iii) the bulk of CFC inner divertor tile $IN3_{s1}$ were examined before and after prolonged heat treatments either under moist air or moist helium carrier gas at several progressively increasing temperatures. As the data in Table II show and in full accordance with expectations, each increase in temperature, particularly when exceeding 400°C, is associated with a reduction in the concentration of all three hydrogen isotopes. This holds for specimens from the plasma-exposed region as well as from the bulk of CFC and graphite tiles.

When, however, the temperature is raised up to 450°C or above, a considerably more drastic reduction of the original content of deuterium and tritium is registered. The two tritium measurements performed with the untreated disk $7A_1$ provide an idea on the kind of reproducibility attainable with these measurements and the hydrogen isotope concentration measurements on disks $11A_1$ and $13A_1$, removed from tile 5B17L, provide an indication of the comparability between two adjacent cylinders after heat treatment.

Staff:

N. Bekris
U. Berndt
W. Jung
W. Hellriegel
B. Schweigel

JW2-FT-2.8
Detritiation and Deactivation of Tritium Storage Beds

TW1-TTF/TR 13
Extended Lifetime Tests of Specified Tritium Plant Components

When getter beds used for tritium storage are no longer required they have to be prepared for long term storage. This involves reducing the amount of tritium to a minimum and preparing the beds so they no longer present any fire or chemical hazard. Two sets of experiments have been carried out. The first was to determine how far a getter bed could be detritiated by repeated isotopic swamping. The second was to oxidise getter beds to chemically inert them.

Amersham-type transport beds, containing both uranium and zirconium cobalt, which have been used to store tritium have been repeatedly isotopically swamped with deuterium and the resulting remnant tritium activity measured by calorimetry. This is to determine the practical limit of detritiation by isotopic swamping. Tritium will be contained not only in the storage medium but also be embedded in the primary containment walls due to permeation. The lower limit for this size of bed appears to be about 1 Ci. Calculations show that up to 0.4 Curies per cubic centimetre could be locked in the primary containment material as a result of permeation. This represents a considerable inventory but is immobile and hence may be acceptable for disposal. In general it will not be possible to measure the tritium remaining in a storage bed after detritiation, however the results from this work will indicate the levels that can be expected on larger beds that will be used on ITER. This information is required for correct disposal.

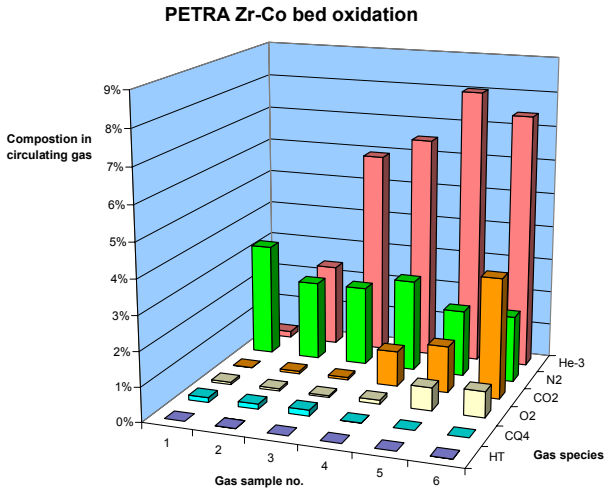

Fig. 1: Compositions of gas samples taken during progressive oxidation of the JET type ZrCo getter bed used in the PETRA facility

A ZrCo getter bed used in the PETRA facility at TLK has been oxidised to prepare it for disposal. The objectives were to reduce it to a safe state where no further chemical reactions could take place, such as with atmospheric oxygen which would create a fire hazard in a long term store, and to reduce the tritium content to as low as possible. The storage bed was isotopically swamped with deuterium to remove as much tritium as possible, then oxygen was slowly introduced and the bed progressively heated up to 450°C until no further reactions were evident. The composition of the resulting gases was analysed at various stages. The main result was that further tritium was released and also a considerable amount of helium-3. The quantity of tritium has not been established but work is in hand to do this. It is expected that any tritium has been oxidised and a molecular sieve is under construction to remove the oxidised tritium.

The figure shows the evolution of He-3 after successive heating runs at increasing temperature up to 450°C. The increase of carbon dioxide is a result of oxidation of methane and carbon in the steel container.

The amount of tritium will be measured by calorimetric measurements on the molecular sieve bed. It is clear that oxidation of ZrCo getter beds is an effective method of deactivation, noting that there was no significant reaction until the bed was raised to about 250°C. This feature is an additional safety feature of ZrCo getter beds as it means there is unlikely to be a rapid exothermic reaction in the event of an air ingress event into such a bed.

An unused uranium bed will soon be oxidised by a similar procedure to establish the reaction characteristics. Later, a U-bed which has been used with tritium will be oxidised when a suitable glove box is available. TLK will use these results as it has several U-beds which have to be disposed of.

Several components from a redundant experimental tritium rig used for laser Raman spectroscopy and Omegatron mass spectrometer studies are to be investigated for effects of extended use with tritium. These include a permeator, a small zirconium-cobalt metal getter bed and catalytic reactor. These components have been dismantled from the experimental rig and are due to be connected to the CAPER facility where they will be subject to experiments to determine their performance before dismantling for post-service examination.

The programme for the CAPER facility has not yet allowed this work to proceed yet. It is expected that an experimental plan can be agreed before the end of the year with actual experiments carried out in the first quarter next year.

Staff:

C. Caldwell-Nichols
H. Kissel
E. Kirste

JW2-FT-2.9
Tritium Removal from JET Tiles

The main goal of the present work is the development of reliable technologies for the detritiation of whole tiles and of other plasma facing components.

The present ITER design includes beryllium, tungsten and carbon as plasma facing components. Of these, the fraction of carbon fibre composite, which is located in the outer and inner vertical divertor targets, is the smallest, i.e. 6.2 %. Nevertheless, it represents a surface area of approx. 55 m^2 giving a total carbon amount of about 7 tons. Based on results from JET it is estimated that of the order of 2 g tritium will be incorporated into the carbon of ITER with each 400 s pulse.

The conditioning of graphite and CFC tiles collected from thermonuclear devices operated with tritium requires a process capable of achieving very high degrees of detritiation. This will be necessary in order to satisfy the current stringent regulations established for the conditioning and disposal of highly radioactive as well as chemically toxic waste. For UK low level waste (LLW) the maximum allowable tritium activity is presently specified to less than 12 MBq kg^{-1}. To achieve such low levels with tiles previously exposed to D-T plasmas it is estimated that decontamination factors (ratio of initial over final tritium activity) covering several orders of magnitude will have to be realised.

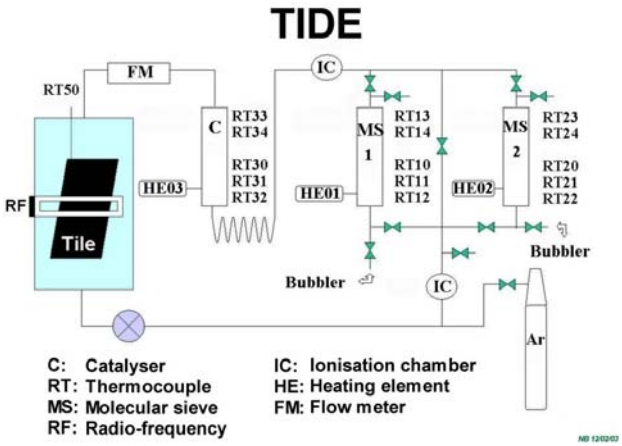

Fig. 1: Schematic representation of the TIDE facility for the detritiation of entire tritiated tiles.

The process concept TIDE (Tritium Decontamination Facility) presently under development at TLK basically contemplates very rapid heating of carbon tile surfaces by induction heating. The temperature treatment is carried out in a closed loop operation mode in the presence of a noble carrier gas to which, depending upon future experimental results, a low partial pressure of oxygen may be added. The closed loop used for the investigation of the conditioning of whole carbon tiles is shown schematically in Fig. 1. The basic aim is to achieve conditions on the tile surface that ensure full oxidation of all liberated hydrogen isotope species and tritium-containing hydrocarbons into tritiated water and carbon oxides. As a complementary measure an oxidation step has been incorporated downstream into the loop. It comprises a heated oxygen donating catalyst bed that ensures quantitative oxidation of all non-oxidised species remaining in the gas phase after the treatment of the tile. The tritiated water produced in that way is adsorbed, if possible selectively, on a molecular sieve bed installed further downstream in the loop. The adsorber bed can be regenerated periodically in a counter current flow mode to recover the retained tritium and thus restore the original process conditions. Conceivably, the performance of the proposed thermo-chemical treatment could be enhanced by a preliminary mechanical treatment of the tiles, e.g. abrasion with a brush or by other mechanical means, to remove all loosely attached highly contaminated layers from the component surface. The impact of such a treatment still needs to be assessed experimentally.

To perform tests under realistic conditions a virgin JET graphite tile having dimensions of 135 x 155 mm has been installed in TIDE. Figure 2 illustrates a typical run using that tile.

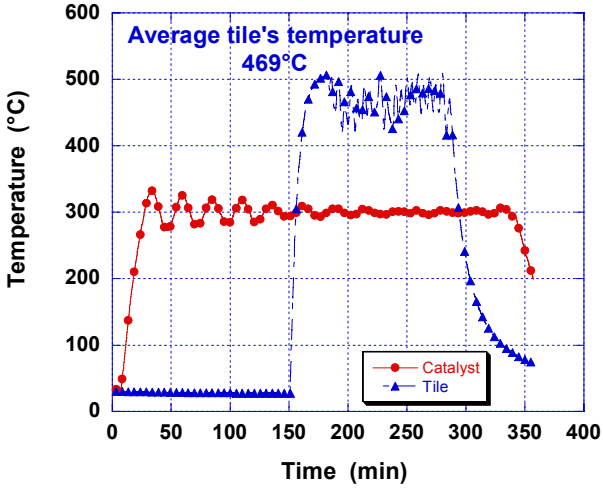

Fig. 2: Typical temperatures for a non active limiter tile and the catalyst bed, during a preliminary heating test (V=3.75 kV and I=0.7 A).

It is planned to examine the efficiency of such a thermo-chemical treatment on the tritium release from the surface of first wall component by measuring the tritium activity of the tile by calorimetry, before and after the detritiation process. The detritiation factor could also assessed by comparative measurements using the PIN diode technique before and after the treatment.

Staff:

N. Bekris
U. Besserer
H. Dittrich
W. Jung

JW2-FT-5.5
Activation and Shutdown Dose Rate Calculations for JET

For safe maintenance of the JET machine it is important to be able to predict the induced activation during D-D and D-T operation and the resulting shut down dose rates. This requires a suitable system of codes, data and interfaces which is capable of simulating both the neutron induced material activation during operation and the decay gamma radiation transport after shut-down in the proper geometry. In the frame of an ITER R&D Task the rigorous 2-step (R2S) computational system has been recently developed for the calculation of shutdown dose rate distributions in full three-dimensional geometry [1]. The system is based on the use of the MCNP [2] transport and the FISPACT [3] inventory codes linked through a suitable coupling scheme for the automated routing of decay gamma sources and neutron flux spectra. The decay gamma source distribution is sampled in a source routine linked to MCNP. This enables to conduct shut-down dose rate analyses for large and complex reactor systems such as ITER [4,5].

In the framework of the running JET Fusion Technology Task JW2-FT-5.5, the R2S system is being applied to the shutdown dose rate analysis of the JET machine. A suitable 3D MCNP of one JET octant was provided by UKAEA Culham as part of Task JW2-FT-5.5 (Fig. 1). The R2S code system was updated to be compliant with the JET octant model. To this end, the interface files for the automated routing of the neutron flux spectra and the decay gamma source distribution (MCNP $\Rightarrow$ FISPACT $\Rightarrow$ MCNP) were adapted to the specific conditions of the JET model (geometry cells, materials, volumes).

A two step approach is followed to obtain a sufficient accuracy for the calculated dose rates. In the first step the dose rates are calculated with no changes applied to the geometry model so as to identify the material cells which contribute significantly to the shutdown dose rate. In the second step these material cells are segmented in radial, poloidal and toroidal direction to provide a better spatial resolution of the neutron flux and, in effect, the decay gamma source distribution. The number of material cells increases in this way from 383 to 854. The neutron flux spectra are then calculated for all material cells in 11 separate Monte Carlo runs with weight windows optimised for the different scoring regions. These calculations are performed on the HPC Linux cluster with MCNP running in the parallel mode under PVM (Parallel Virtual Machine). FISPACT inventory calculations and MCNP transport calculations of the decay gamma radiation are

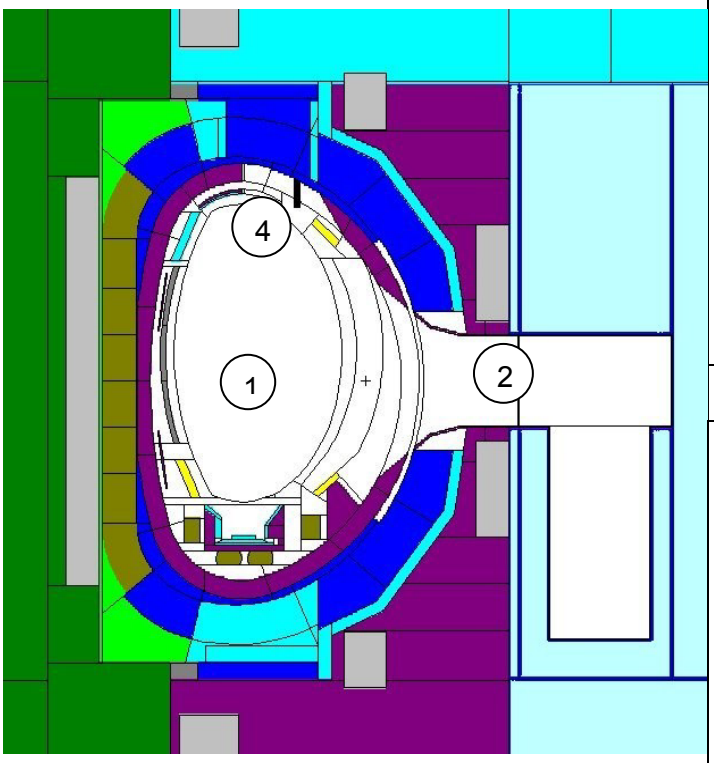

Vertical cut through octant mid plane

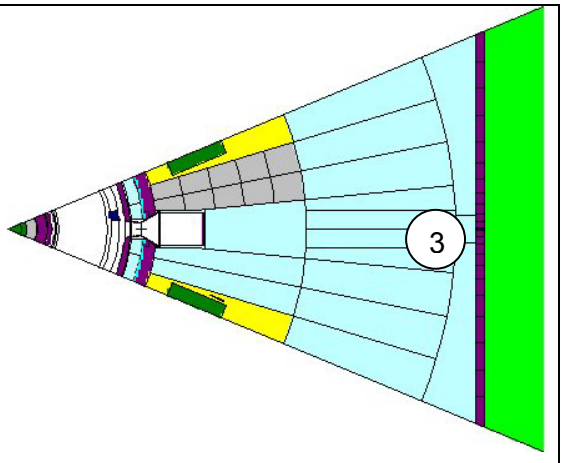

Horizontal cut at torus midplane (z=0)

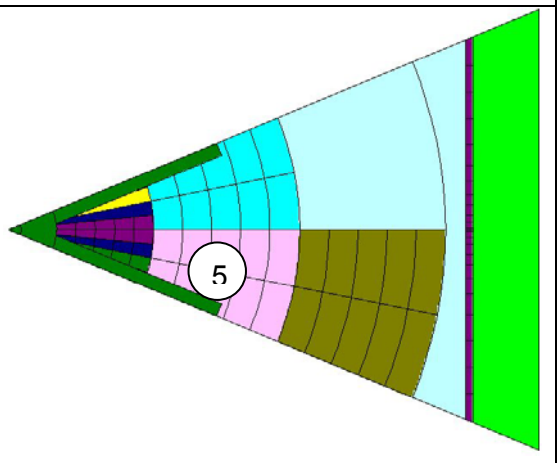

Horizontal at z=575 cm above mid-plane

finally performed for the refined models. The decay photon spectra are calculated at the specified detector locations by applying the MCNP point detector estimator. The resulting dose rates are obtained by making use of the ANSI/ANS-6.1.1-1977 photon flux-to-dose rate conversion factors. The shutdown dose rates are calculated for five detector locations interior and exterior to the machine (Fig.1) assuming a representative JET irradiation history with a total neutron production of $2.4 \cdot 10^{19}$ and decay times between 1 hour and 1 year. First results are currently underway. The final shutdown dose rates will be available with the completion of the running task JW2-FT-5.5. As part of this task, the results of the R2S dose rate calculations will be compared to those obtained with the direct one-step method to be provided by ENEA Frascati.

Staff:

Y. Chen (Institute for Plasma Physics, Hefei, China)
U. Fischer
P. Pereslavtsev (Institute for Nuclear Power Engineering, Obninsk, Russia)

Literature:

[1] Y. Chen, U. Fischer, H. Tsige-Tamirat, Rigorous MCNP Based Shutdown Dose Rate Calculations, Forschungs zentrum Karlsruhe, Internal Report, January 2001

[2] J.F. Briesmeister (ed.), MCNP - A General Monte Carlo N-Particle Transport Code, Version 4C, Los Alamos National Laboratory, Report LA-13709-M, April 2000.

[3] R. A. Forrest, J-Ch. Sublet, “FISPACT-99: User manual”, Report UKAEA FUS 407, December 1998

[4] Y. Chen, U. Fischer, ITER-FEAT Shutdown Dose Rate Analysis by Rigorous Method, Forschungszentrum Karlsruhe, Internal Report, September 2001

[5] Y. Chen, U. Fischer, Rigorous MCNP Based Shutdown Dose rate Calculations: Computational Scheme, Verification Calculations and Application to ITER, 6th International Symposium on Fusion Nuclear Technology (ISFNT-6), San Diego, California, April 7-12, 2002

HCPB Blanket Concept

TTBB-001
TBM Design, Integration and Analyses

The Design and Analysis of the HCPB Test Blanket Module (TBM) System for ITER (see Fig.1) have been completed in the year 2001. A series of documents have been delivered to the ITER Central Team for integration in the ITER final Design report. Two papers dealing with this subject have been presented to the ISFNT-6 Meeting in San Diego [1,2] and two FZKA reports are being printed [3,4] completing the documentation of these activities.

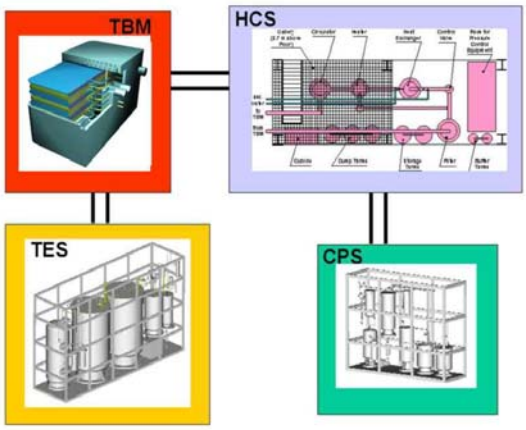

Fig. 1: TBM System for ITER: the system contains the Test Blanket Modules that will be tested in an equatorial port of ITER and the related auxiliary systems allocated in the ITER building: the Helium Coolant System (HCS), the Tritium Extraction System (TES) and the Coolant Purification System (CPS).

In the course of the year 2001 major programmatic changes occurred in the definition of the design requirements for the TBM System. In the framework of the Power Plant Conceptual Study (PPCS) in 2001, the “large module maintenance schema” (an extrapolation of the ITER maintenance schema with larger modules to increase the plant availability) has been agreed upon as basis for the development of the near term fusion power plant concepts. This decision requires substantial changes of the DEMO HCPB blanket design and consequently of the TBM design because initially the concept was based on the “segment maintenance schema” since 1994. Therefore an adaptation to the new maintenance concept was required.

The second event was a major change of the Water Cooled Lithium Lead (WCLL) concept. Due to budget reduction requirements a common decision of EFDA and the lead associations (FZK and CEA) was to keep the objective to test both the HCPB and the WCLL concepts in ITER, but with the same coolant, Helium, which is compatible with both concepts. Hence, a major cost reduction can be achieved using a similar technology for the cooling and to pursue a similar TBM structure and test programme. These decisions have been already implemented in the programme. The coolant water in the WCLL concept has been replaced by the coolant helium and the concept was renamed as HCLL.

Consequently the revision of the DEMO concept has been started in 2002, in order to cope with the modified requirements, to speed the new orientation of the programme and to have a common time schedule with our French Colleagues. A co-operation between the two Design Teams (FZK and CEA) has been started in the second half of 2002. Five common FZK/CEA design meetings (in Saclay, Karlsruhe and Garching) have already been organized. By the end of 2002 the work will converge to a base design of a module for DEMO that can be used for the both concepts, with some variations to adapt the design to the different breeders.

In following year the new DEMO Design will be completed and analyses will be performed to confirm its performance. With the new design, the overall objectives of the testing programme in ITER will be revised and a new conceptual design for the TBM System proposed.

In order to complete the design description of the TBM System [3] performed during 2000-2001, a task has been carried out in 2002 collatoration between the firm H-J. Fiek and the CAD Office in FZK aimed to define the fabrication sequences of the TBMs In the following section, the work is described.

The proposed test strategy [2] in ITER is based on four different Test Blanket Modules each devoted to a family of objectives (electromagnetics, neutronics and tritium production, thermo-mechanics and plant integration); the general external design of these modules is similar, but internals, instrumentation and operation mode will be different to cope with the specific testing objectives (Fig. 2). These modules will be sequentially tested starting from the beginning of ITER operation; the test schedule will be co-ordinated with the different plasma operation modes (H-H phase, D-D, etc.).

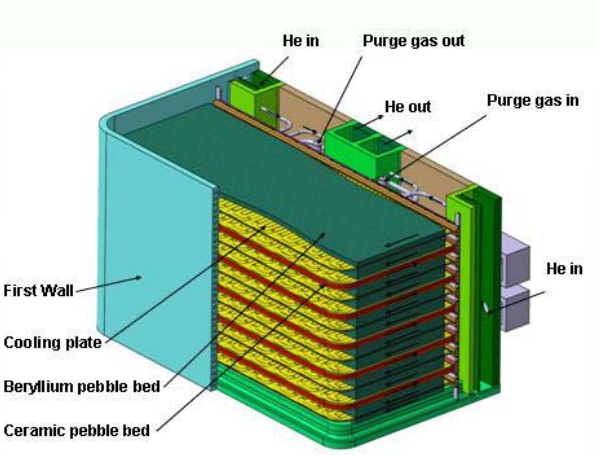

Fig. 2: Break of the 3D drawing of the HCPB TBM showing the breeding zone and the manifolds. The CAD system is CATIA (v.5).

Structural material for all TBM versions is the reduced activation ferritic martensitic (RAFM) steel EUROFER which is under development in the EU Materials Programme as reference material for the DEMO Blankets.

The fabrication paths of the four different TBM’s are similar. Fig. 3 depicts the fabrication sequence exemplarily for the example of the plant integration PI-TBM, which is representative for all TBM’s versions.

The quality achieved during the fabrication of the TBMs will strongly depend on the application of suitable quality control methods and in case of faults on the availability of repair methods. Wherever possible well known techniques are applied. The main fabrication path is mainly based on techniques which were approved by EFET, but as the material EUROFER is new, even some of these techniques will require futher R&D or at least tests to identify suitable parameters of the fabrication

processes. Cost reduction can be achieved by simultaneously carrying out similar fabrication steps.

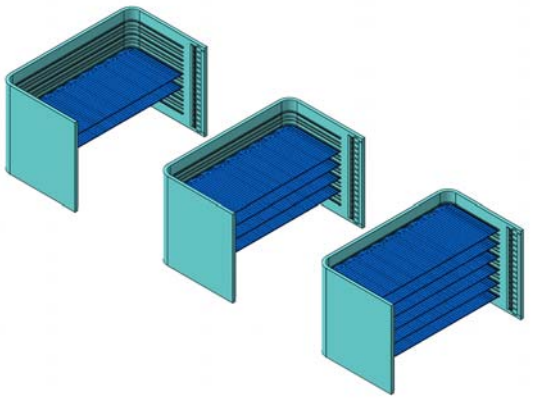

Fig. 3: Fabrication sequence for the welding of the stiffening plate into the FW shell: insertion of the plates in correct position and tack weld starting from the medium plate. A full mechanised TIG welding will follow this step. (CATIA V.5 drawings).

The respective work is ongoing; the technical report will be issued at the end of this year.

Staff:

L.V. Boccaccini
H-J. Fiek, Fa. Ingenieurbüro Fiek
S. Hermsmeyer
K. Kleefeldt, Fa. Ingenieurbüro Kleefeldt
S. Malang
R. Meyder
K. Schleisiek, Fa. Ingenieurbüro Fiek
S. Stickel

Literature:

[1] L.V. Boccaccini, N. Bekris, Y. Chen, U. Fischer, S. Gordeev, S. Hermsmeyer, E. Hutter, K. Kleefeldt, S. Malang, K. Schleisiek, I. Schmuck, H. Schnauder, H. Tsige-Tamirat, " Design Description and performance analyses of the European HCPB Test Blanket System in ITER FEAT", Proceedings of the 6th ISFNT Meeting, San Diego, April 2002, to be published.

[2] L.V. Boccaccini, U. Fischer, K. Kleefeldt, S. Malang, K. Schleisiek, "Strategy for the blanket testing in ITER", Proceedings of the 6th ISFNT Meeting, San Diego, April 2002, to be published.

[3] L.V. Boccaccini (Comp), N. Bekris, Y. Chen, U. Fischer, S. Gordeev, S. Hermsmeyer, E. Hutter, K. Kleefeldt, S. Malang, K. Schleisiek, I. Schmuck, H. Schnauder, H. Tsige-Tamirat, " Design Description Document for the European Helium Cooled Pebble Bed (HCPB) Test Blanket Modules – Status 31.12.2001", FZKA 6723, to be published.

[4] K. Kleefeldt, "Thermal–hydraulic model of the Helium-Cooled Pebble Bed Test Blanket Module for ITER FEAT", FZKA 6724, to be published.

TTBB-002
Blanket Manufacturing Techniques

TTBB-002-1
HIP Joining of Cooling Plates

The 8th HIP experiment series using two-step HIP technique for diffusion welding of structure with cooling channels

The objective of the work on hot isostatic pressing (HIP) experiments is to investigate the appropriate HIP technique, the boundary conditions and parameters in order to achieve good mechanical properties of the diffusion welding joints as well as to achieve a transition to test specimens of larger dimensions. Typical specimens for the first wall and cooling plate (size: about 100x100 mm^2) consist of two halves of plates with complex arrays of internal coolant channels on each half.

Fig. 1: Micrograph of the EB seal welded FW specimen with dry-milled surface after the 2nd HIP step.

In the past 6th and 7th experiment series [1,2,3] two-step HIP process was already successfully applied for achieving high mechanical properties. In the first HIP step, the specimens protected by pressure plates were encapsulated and diffusion welded with relatively low gas pressure at max. 12 MPa (1050 °C, about 2 h) corresponding to a surface pressure at the welding joint of about 30 MPa. After dismantling and separating, the specimens with now open cooling ducts were HIPped at a high pressure of 200 MPa (1050 °C, 4 h). With this second HIP step the still existing defect zone in the HIP joint are pressed together so that the strength and ductility of the HIP joints are improved by further diffusion process. In the following 8th series [4] specimen plates of EUROFER were exclusively used, while the welding preparation was slightly modified.

Specimens preparation

In the 8th experiment series three sets of first wall (FW) and cooling plate (CP) specimens of EUROFER were welded. The surfaces to be joined of the six pairs of specimen plates with the approximate dimensions of 100 x 100 mm^2 had been dry milled to a surface roughness of Rt ≤ 2 µm. Cleaning was performed in an ultrasonic bath with acetone. Zirconium wire bundles as getter materials were inserted into the cooling channels of two pairs of FW plates and two pairs of CP plates each. One pair of plates of each type contained no getter material. Immediately after cleaning, and after insertion of the getter material, the halves of one FW specimen and one CP specimen each were seal welded together at the edge of the joining surfaces by means of electron beam welding under a vacuum.

Specimen set No.	Material*)	joining surface preparation		
		dry-milled	Getter material	EB seal welding **)
1	E	x	x	x
2	E	x	x	-
3	E	x	-	-

*) E=EUROFER, **) at the edge of joining surface

Quartz glass mats of a fine structure were used as separators between the specimens, the pressure plates consisting of a molybdenum alloy (TZM) for protection of the internal cooling channels, and the encapsulating jacket during the first HIP step

Experimental results

The deformation of all plates was approx. 5%, which is in the desired range. Non-destructive post-welding examinations were performed to determine the yield strength (Rp0.2), the tensile strength (Rm), ultimate elongation (A), hardness, and notch-impact energy (Av) of specific specimens taken from the welding zone and from the base metal. The plates with the getter material clearly showed better results. The best results were obtained with the plates EB seal-welded at the edges. The following strength values are obtained: Rp0.2: 628 - 667 MPa; Rm: 713 - 780 MPa; and A: 12.5 - 15 %. They correspond to those of the basic material (averaged values: Rp0.2 ≈ 618 MPa, Rm ≈ 703 MPa, A ≈ 14%). The values of notch impact strength were determined from two producible samples with 4 and 7.7 J. They lie thereby in the range of 45 % to 87 % of the base material with Av ≈ 8.8 J, which is an indication of an excellent HIP result in particular for plates with internal channels and thin webs with small HIP joining surfaces.

The micrographs of the HIP welded specimens show the joining zones either very faintly or not at all. As example, the micrograph of an EB-welded first wall specimen (Table, No. 1) after the second HIP step is illustrated in Fig. 1. The joining zone can hardly be detected, which is also indicative of an excellent quality of diffusion welding.

Conclusions

This series, for the time being, completes the manufacturing tests. The results achieved constitute a sound basis on which to resume these activities at some later point in time, when it would have to be demonstrated that the same good results can be achieved also in manufacturing plates of blanket-related dimensions, e.g. 1 x 3 m for the first wall or 0.5 x 1 m for the cooling plates.

Staff:

P. Norajitra
G. Reimann

Literature:

[1] G. Reimann, Diffusionsschweißversuche in Heißisostatischen Pressen zur Herstellung von Plattenbauteilen mit inneren Kühlkanälen für Fusionsblankets - sechste Versuchsreihe -, FZK-PKF internal report, August 2000.

[2] G. Reimann, H. Kempe, P. Norajitra, R. Ruprecht, R. Vouriot: Diffusionsschweißversuche in Heißisostatischen

Pressen zur Herstellung von Plattenbauteilen mit inneren Kühlkanälen für Fusionsblankets - siebente Versuchsreihe -, FZK-PKF internal report, Mai 2001.

[3] P. Norajitra, G. Reimann, R. Ruprecht, L. Schäfer: HIP experiments on the first wall and cooling plate specimens for the EU HCPB blanket, to be published in Journal of Nuclear Materials, 2002.

[4] G. Reimann, P. Norajitra, R. Ruprecht, R. Vouriot, H. Kempe: Diffusion Welding Tests in Hot Isostatic Presses for Manufacturing Plate Components with Internal Cooling Channels for Fusion Blankets (TTBB-002-D1), - Eighth Test Series, Final Report -, FZK-Fusion internal report, March 2002.

TTBB-003
Pebble Bed Assembly Development and Testing

TTBB-003-1
Operation and Analysis of HEBLO Test Section

Introduction

The HEBLO (**H**elium **B**lanket Test **L**oop) experiment with a small-scale test object was planned according to the European HCPB blanket concept with the objective to demonstrate the feasibility of the HCPB blanket construction including the testing of diffusion welds and simulating of thermocyclic load on the first wall and the pebble beds.

The preceding steady-state and transient experiment series

After intensive preparations for the HEBLO experiment (i.e. layout, construction, fabrication and assembly of the test section as well as tests of components) the first experiment series [1] under steady-state conditions with altogether 61 measurements (each with constant temperature levels between 300 and 700 °C) was accomplished successfully. Simulation calculations for this experiment showed a good agreement with the measurements [2, 3].

Afterwards the temperature cyclic experiments with limited heating plate temperature at 700°C - to avoid an excessive strain of the heating plates - with altogether 123 temperature cycles were carried out successfully. By means of cyclic power control of the gas heaters and the pebble bed heaters a maximum temperature ramp of about 200 K within the pebble beds was reached. After an increase of the heating plate performances to an extremely high level the maximal steady-state temperatures of the first wall of 500-510°C, and the ceramic and beryllium pebble beds of 900 °C and 650°C, respectively, could be achieved corresponding to the DEMO conditions [4]. Based on this new condition additional cyclic temperature experiments with 12 temperature cycles were accomplished. A maximum temperature ramp within the ceramic and beryllium pebble beds of about 400 K and 250 K, respectively, was reached with the maximum value of pebble bed temperatures at the vicinity of the heating plates of about 900°C for ceramic and about 640°C for beryllium, respectively.

The LOFA experiments

Preparations for the 'loss of flow' accidental case (LOFA) experiments were made including installation and testing of an additional software for the automatic control of the LOFA experiments based on the shutdown scenarios assumed for ITER (Table 1). The LOFA functions were simulated by a successive shut-down of the gas heaters, the helium blower and all the heaters within the test section for simulation of the internal heat sources (beryllium and ceramic pebble bed heaters) and the plasma surface heat loads (first wall heater). For safety reasons, the gas heaters were shut-down 1 s prior to the actual start of LOFA simulated by shut-down of the He blower.

The LOFA experiments were tested first with moderate heat power of the heating plates (LOFA-1 to LOFA-5) with some adaptation and optimisation of the actual control values to the desired values. Afterwards the complete program of LOFA experiments according to the shut-down scenario (Table) for the three cases: Fast (LOFA-6), accelerated (LOFA-7), and normal (LOFA-8) was run successfully with extreme heating plate performances. The shut-down programs and the responses for the LOFA-6 to LOFA-8 are discussed in detail in [5].

Table 1: Postulated Plasma Shutdown Scenarios for Accident Analysis.

Shutdown Scenario	Delay time (s)	Ramp-down time from full power to zero (s)	
		of internal heat	of surface heat
Normal	1	100	100
Accelerated	1	20	20
Fast	1	0	20

For the LOFA-8 (normal shut-down), considered the most severe case with a shut-down ramp of 100 s for all heating plates, the measured temperatures are illustrated in Fig. 1. The maximum temperature of the first wall before and during LOFA amounts to 504/625°C (curve c). The maximum ceramic and beryllium pebble bed temperatures in the vicinity of the heating plates dropped from 908°C and 657°C at the beginning of LOFA to a value of about 635°C and 580°C, respectively, at about 10 min later. The measured temperatures within the pebble beds reach their peak at about 600°C after 1.5 min for Be and 670°C after 3 min for ceramic, respectively.

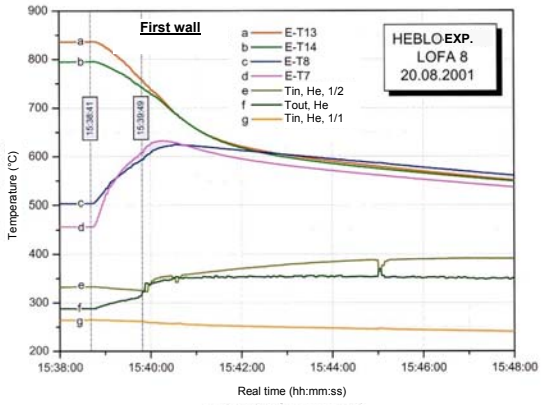

Fig. 1: Measured temperatures of the first wall (c, d), its heating plate (a, b) and the helium coolant (inlet: e/half channel, g/full channel; outlet: f) during the LOFA-8

Post-examination

After termination of the HEBLO experiments the test section including the safety tank was separated from the helium loop for the post-examination [6]. The safety tank was first disassembled at the FZK central workshop. Afterwards the HCPB test section was opened in a special glove box for beryllium handling at the company Goraieb Versuchstechnik. Fig. 2 shows the Be pebbles which had clumped over the whole width of the compartment but the clumping of the pebbles however did not remain existing after withdrawal of the pebbles. Traces of baking, however, were observed on the surface of the heating plate in lateral boundary regions. For the ceramic pebbles (Fig. 3) some small zones with baked particles at the bottom of the heating plates were also detected. Depending upon different temperatures, which these pebbles may have been exposed to, different colouring from bright to dark has been observed.

Conclusions

With the termination of the LOFA experiments, the HEBLO experiments on the HCPB “look-alike” test section have been completed. The entire series of experiments containing steady-state, temperature transient and LOFA experiments were successfully accomplished, due to intensive experiment preparations containing layout calculations, the test section and the helium loop functioned perfectly and construction, fabrication and assembly of the test section as well as the preceding tests of components. All components of withstood all thermal-mechanical loads corresponding to the DEMO layout coditions. The reproducibility of the operating conditions and the measured temperatures was always given. This indicates that the pebble beds, the heating plates and the steel structure are still intact. The results of the post-examination show, that for the ceramic and beryllium pebble beds slightly clumping of the pebbles was observed locally in the bottom zone. However, the sintered pebbles could be separated easily by using any tool and still looked spherical. No damages were detected in the whole test section.

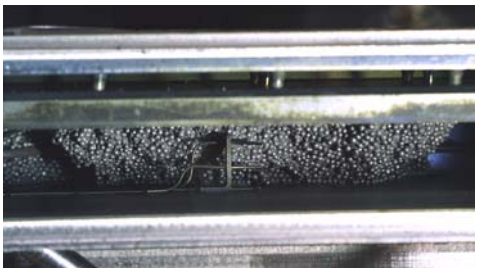

Fig. 2: Clumping and locally baked beryllium pebbles at the heating plate.

Fig. 3: Locally baked ceramic pebbles at the heating plate.

Staff:

R. Kruessmann
P. Norajitra
D. Piel
G. Reimann
R. Ruprecht

Literature:

[1] P. Norajitra, H. Lehning, D. Piel, G. Reimann, R. Ruprecht, State-of-the-art of the third HEBLO experiment based on the EU Helium-cooled pebble bed blanket concept, Proceedings of the 20th Symp. on Fusion Technology, Sept. 7-11, 1998, Marseille, France, Vol. 2, pp 1187-1190.

[2] P. Norajitra, D. Piel, G. Reimann, R. Ruprecht, The First Series of the HEBLO Experiment with the HCPB Small-scale Test Section, FZK-PKF Internal Report, 2000.

[3] P. Norajitra, D. Piel, G. Reimann, R. Ruprecht, The first HEBLO Experiments Based on the Eu HCPB Blanket Concept, Fusion Engineering and Design 58-59 (2001) 623-627.

[4] P. Norajitra, Thermohydraulics Design and Thermo-mechanics Analysis of Two European Breeder Blanket Concepts for DEMO; FZKA 5580, 1995.

[5] P. Norajitra, D. Piel, G. Reimann, R. Ruprecht: The HEBLO Transient and LOFA Experiments with the HCPB Small-scale Test Section and post-examination - TTBB-003a-D1, Final Report -, FZK-FUSION Internal Report, Juni 2002.

[6] P. Norajitra, D. Piel, G. Reimann, R. Ruprecht: Post-examination of the HEBLO Experiments with the HCPB Small-scale Test Section - TTBB-003a-D2 -, FZK-FUSION Internal Report, Juni 2002.

TTBB-005
Development of Ceramic Breeder Pebble Beds

TTBB-005-1
Characterization of Li_4SiO_4-Pebbles

Since 1990 FZK is investigating, in collaboration with Schott Glaswerk GmbH, lithium orthosilicate pebbles made by the melting and spraying method. The material is composed of lithium orthosilicate with a small amount of SiO_2 and it is fabricated in a semi-industrial scale small facility. The characteristics of the final product depends on many parameters, which are rather difficult to control. Therefore It is necessary to characterise every charge of pebbles received from the small scale facility in order to check to what extent the delivered material meets the requirements of the HCPB blanket. The produced pebbles should:

- Withstand loads caused by neutron irradiation, pressure, temperatures, temperature gradients and thermal shocks up to blanket relevant peak burnups without an unduly high amount of broken particles;
- Result in a sufficiently high tritium breeding ratio and a sufficiently low residence time at the HCPB blanket conditions;
- Allow the pebble bed thermal conductivity to be high enough to assure acceptable peak temperatures in the blanket.

Quality control

Several batches of lithium orthosilicate pebbles produced starting from Li_4SiO_4, Li_2CO_3 or LiOH and SiO_2 powders were delivered during the last two years, to be used in the on going experimental activities. The quality control of these batches was started and, in particular, the characterisation activities of seven charges produced by Li_4SiO_4 and SiO_2 powders were carried out at the Hot Cells of FZK (optical and electron microscopy, density and porosity measurements, crush loads) and at the Institute for Material Research (chemical analyses). A first visual analysis showed no particular difference in comparison with previously delivered material. The majority of the pebbles appear as 'pearl white' colored or glassy spheres. (Fig. 1).

Due to the production process individual pebbles are agglomerated or egg-shaped. The cross sections show as the dominating pattern a dendritic solidification structure containing a network of interdendritic micropores and cracks, which reach, in some cases, the external surface of the pebble (Fig. 2).

According to the specifications, the pebble's diameters should be in the range 250µm-630µm. The analyses carried out by optical microscopy showed that the number of pebbles found outside this range is quite small. Fig. 3 shows the diameter distribution obtained for one of the batches.

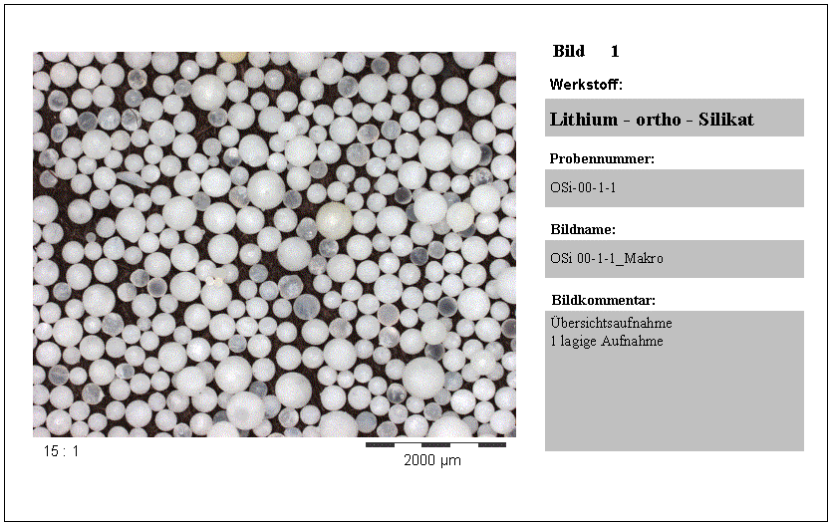

Fig. 1: Appareance and morphology of the pebbles.

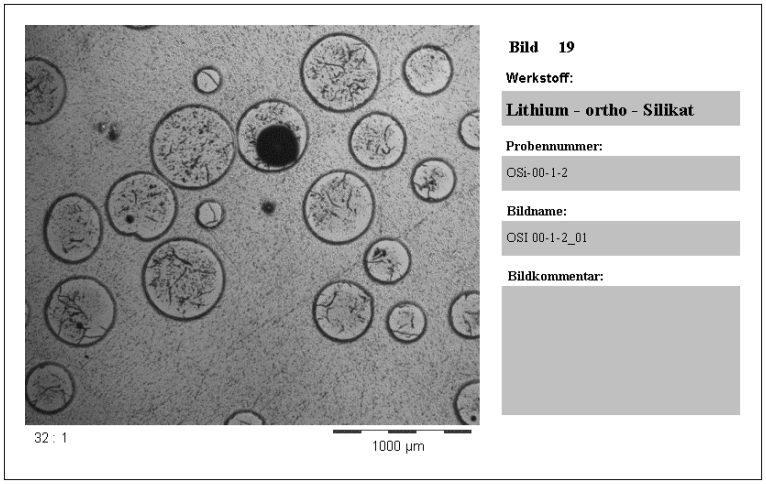

Fig. 2: Cross section of orthosilicate pebbles.

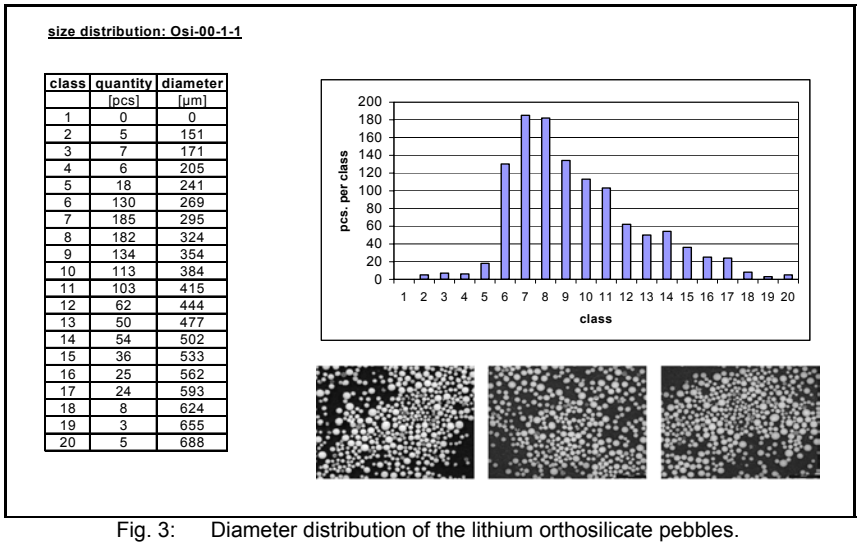

Fig. 3: Diameter distribution of the lithium orthosilicate pebbles.

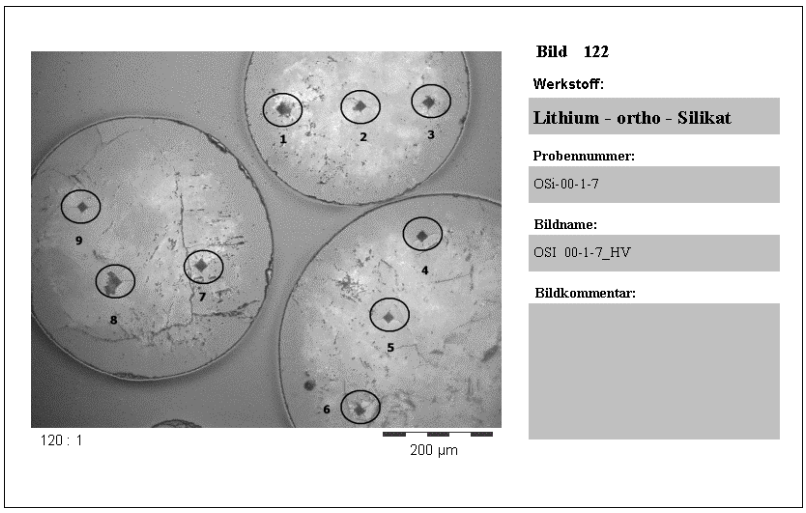

Fig. 4: Pebbles with the inprints of the micro-hardness measurements.

Scanning electron microscopy showed some pebbles characterized by an irregular coating with thick radial or reticular structures and others showing no coating and a clearly visible dendritic solidification of the surface. The different surface structures result from irregular cooling conditions during the production process and, according the mechanical tests on the pebbles, they have no effect on the pebble performances.

The micro hardness was measured as Vickers hardness. It is quite similar in all charges, and an average value of 420 MPa ± 8 MPa has been calculated (Fig. 4).

Densities between 98,5% and 99,5% of the theoretical density (2.4 g/cm^3) were measured by helium-pycnometry. This corresponds to a closed porosity between 0,5 and 1,5%. The open porosity of the pebbles is being measured by using Hg-porosimetry (results from this measurements are not yet available).

Few grams of pebbles were thermally conditioned (2 weeks at 1000 °C in air). After the conditioning no glassy (transparent) pebbles were any more present and the surface roughness increased (recrystallisation took place). These results are in agreement with previous ones.

A long term annealing experiment (96 days at 970 °C) was started in September, in which lithium orthosilicate pebbles from the Li_2CO_3 and the LiOH production routes (Schott production) and of lithium metatitanate (CEA production) are being annealed. The annealing is expected to be completed in December. Next year, the characterisation activities of the delivered batches will be continued together with the investigation of the pebbles from the long term annealing.

Staff:

C. Adelhelm
R. Bosbach
J. Erbe
E. Günther
R. Knitter
G. Piazza
R. Rolli
O. Romer

TTBB-005-7
Thermal-Mechanical Pebble Bed Tests

Present ceramic breeder blanket designs are based on ceramic breeder and beryllium pebble beds with maximum temperatures of 900°C and 650°C, respectively. Because of different thermal expansions of the pebble beds and the structural material and of irradiation effects, compressive stresses might cause considerable plastic deformations of pebbles. Thermal creep of pebble beds will partly release the build-up of stresses, might improve heat transfer due to increased contact areas between the pebbles and might compensate a stress build-up due to irradiation induced swelling. For the design of ceramic breeder blankets the knowledge of thermal creep and thermal conductivity of deformed pebble beds is, therefore, of significant importance.

The thermomechanical properties of pebble beds are generally characterised by uniaxial compression tests (UCTs). It is important that the results from these UCTs are blanket relevant, that is, representative for shallow beds (bed heights H small compared to the other dimensions).

Detailed UCTs have been performed using different cylindrical cavities (diameter D) and two types of pebbles (Li_4SiO_4 pebbles: diameters $0.25 \le d(mm) \le 0.6$; Li_2TiO_3: $0.8 \le d(mm) \le 1.2$). The dependence of the stress strain behaviour from H, D, d, and the packing factor γ was investigated; results were presented by [2,3]. In this context, filling techniques for blanket relevant pebble bed geometries were also investigated; results are given below.

Thermal creep strain of metatitanate pebble beds

Previous experiments [1,2] showed that the thermal creep behaviour differed significantly for metatitanate pebble beds, depending on sintering temperature, grain size, density and other parameters. The experiments were performed in an uniaxial test facility with a maximum pressure of 8MPa and a maximum temperature of 850°C. In order to obtain small creep rates, grain sizes should be > 5μm and the percentage of theoretical density > 90%. This requires sintering temperatures of ≥ 1100°C. However, other pebbles characteristics, such as shape, size, and surface roughness might also influence the creep behaviour.

Previous batches of CEA metatitanate pebbles consisted of pebbles with mean diameters of d ≈ 1mm. A recently produced batch, Ti-H, with smaller pebbles (d ≈ 0.85mm) showed also very satisfactory results. This might be influenced by the larger achievable packing factor which is also desired for other reasons (breeding ratio, heat transfer). At present, experiments are performed with Ti-M, consisting of pebbles with a mean diameter of ≈ 0.7mm. Creep rates of pebble beds with this material are also very small, as shown in Fig. 1. The thermal creep behaviour of this material can be also described sufficiently well by a correlation presented in [1,2].

Filling of Blanket Relevant Cavities

In order to investigate the mechanical pebble bed behaviour for blanket relevant bed geometries and filling techniques, the test section shown in Fig. 2 was used where the shallow bed was filled from one side through a small pipe.

The use of a glass plate was helpful in order to optimise the filling procedure where the vibration energy was varied and the test section was placed on different sides of the hexagonal frame to fill the corners. For such an optimised filling, the same maximum packing factors and stress-strain relations were obtained as with the standard UCT set-up. The pebble stress distribution in the bed was homogeneous as demonstrated by using pressure sensitive foils (FUJI PRESCALE FILM) on the bottom of the cavity.

If during filling a steel plate was used instead of the glass plate it was much more difficult to obtain homogeneous pebble distributions, respectively the maximum packing factors. In general, zones with smaller local stresses due to smaller pebble densities were observed, as shown in Fig. 3. The measured strains were smaller compared to homogeneously filled beds having the same packing factor. The achievement of homogeneous pebble distributions in large blanket components is, therefore, an issue which requires further investigations.

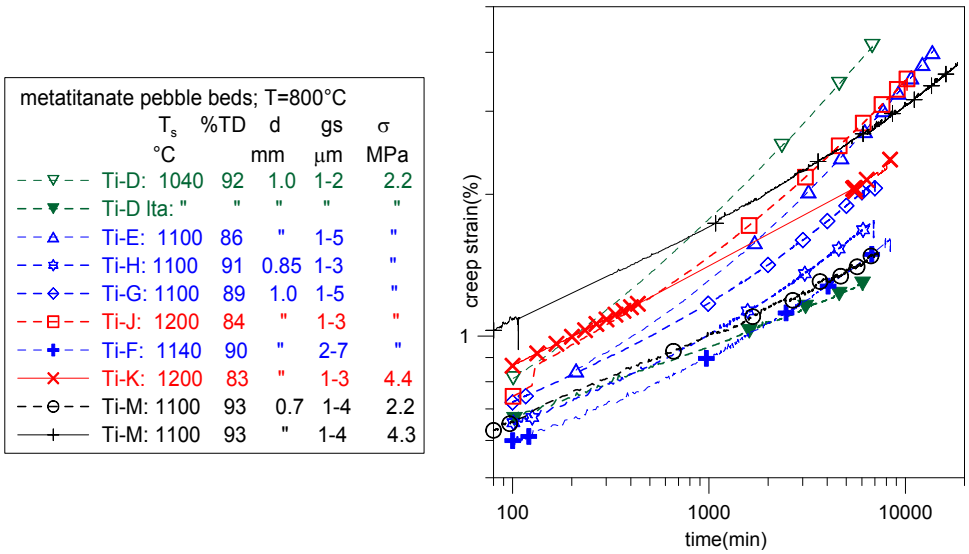

Fig. 1: Thermal Creep strains of different metatitane pebble beds.

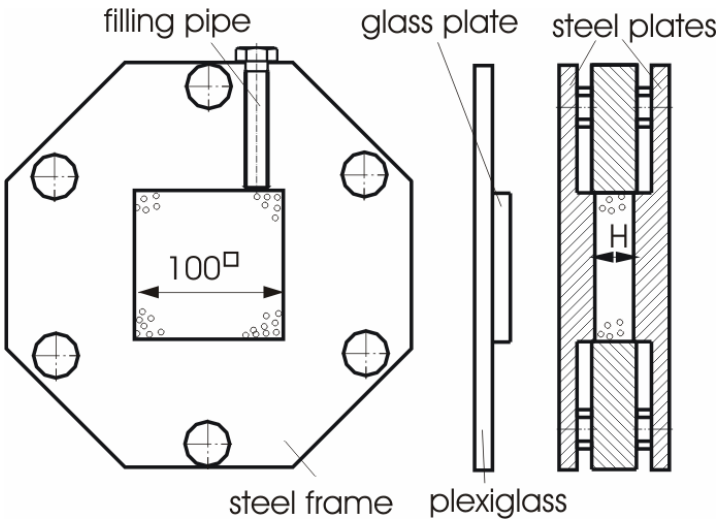

Fig. 2: Test section for blanket relevant filling experiments.

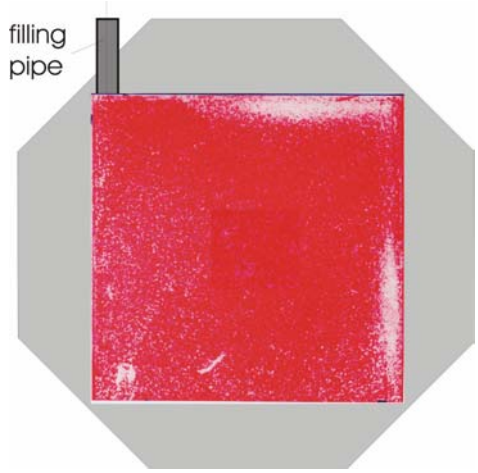

Fig. 3: Pebble stress distribution for non-optimised filling.

Staff:

D. Ericher
H. Harsch, Fa. Goraib
J. Reimann

Literature:

[1] J. Reimann; J.-D. Lulewicz; N. Roux; G. Wörner, Thermal creep of metatitanate pebble beds, CBBI-10, Karlsruhe, Germany,Oct.22-24, 2001.

[2] J. Reimann, L. Boccaccini, M. Enoeda, A. Ying, Thermomechanics of solid breeder and Be pebble bed materials, 6th Int. Symp. Fusion Nucl. Techn., San Diego, USA, April 7-12, 2002.

[3] J. Reimann, D. Ericher,G. Wörner, Influence of pebble bed dimensions and filling factor on mechanical pebble bed properties, 22nd Symp. Fusion Techn., Helsinki, Finland, 9th-13th Sept. 2002.

TTBB-005-8
Model Development

The deformation of granular material “pebble beds” in solid breeder fusion blankets is expected to release stress due to thermal expansion by volume compaction and pebble flow. Drucker-Prager soil models seem well suited for this task as they are based on the physical laws of the process. These models need to be calibrated and qualified to be applied in the prediction of pebble bed blanket behaviour under fusion typical conditions. The capability of prediction is particularly important for breeding blanket development as experimental methods using relevant boundary conditions like volumetric heating are limited and expensive.

Drucker-Prager models calibrated with data from pebble bed experiments, excluding creep, had been used to predict the mechanical behaviour, as well as the temperature distribution, of an in-pile HCPB test element to be tested in Petten. The Drucker-Prager model had been extended by a creep model calibrated with iso-thermal creep experiments at 800°C.

Bi-axial model

As part of the qualification of the existing soil model for a Lithium orthosilicate pebble bed, an ABAQUS finite element model of a bi-axial compression experiment, Figure 1, was devised and model predictions of stress, strain and displacement compared to experimental results.

The 2D plain strain model was a close linking of the brick shaped test volume, with an inclinable top edge representing the vertical piston and the movable right hand edge the lateral piston of the experiment. Contact surfaces between bed and box were modelled allowing sliding and wall friction.

In the experiment the vertical piston pushed onto the bed and shear failure was recorded for different constant forces on the horizontal piston. It was found that at some stage, and earlier for higher beds, an effect similar to the perfect plasticity of tri-axial experiments takes place where the bed flows away horizontally without further increase in the vertical load.

The simulation results confirmed that the model produces plausible results of pebble flow, bed deformation and stress/strain levels. Quantitatively, results matched well during the beginning of the pebble flow up to a horizontal strain of 4%, but could not reproduce well the unhindered flow in the later stages of the experiment. The results suggest that the shear failure physics of the pebble bed are covered by the model.

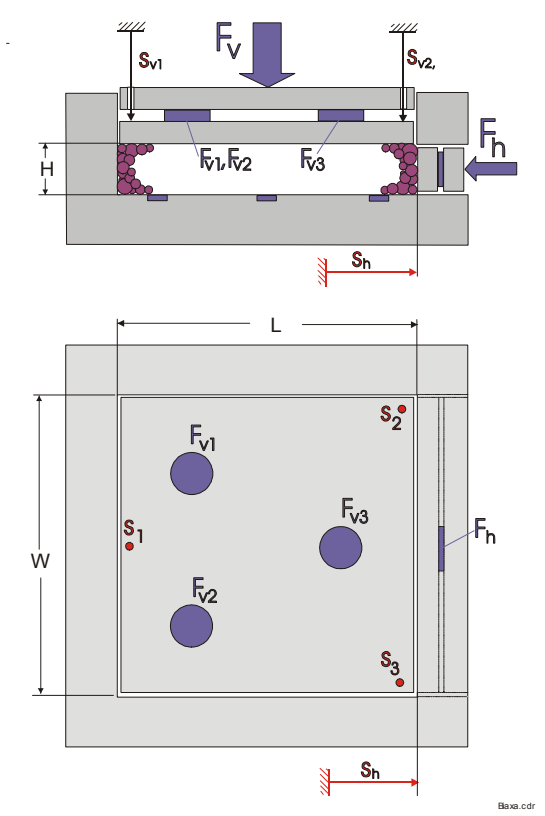

Fig. 1: Test section for bi-axial compression experiments.

Investigations of soil model numerical behaviour

Applying the calibrated pebble bed model including creep to fusion-relevant boundary conditions including volumetric heat sources, has been found to cause significant numerical problems. The planned work needed to be re-scheduled, and instead of improving and qualifying the creep model attention was focussed on understanding numerical difficulties and developing soil modelling for fusion purposes.

In a first step, a finite element model was built of the SCATOLA experiment, a box heated iso-thermally and producing stress by differential expansion of ceramic breeder bed and steel box, that was carried out by NRG Petten a couple of years ago and produced some creep data. Successively, the finite element model of this box was applied using (i) iso-thermal boundary conditions; (ii) using a volumetric heat source, applying un-coupled and coupled solver; and, (iii) employing the creep model in the presence of volumetric heating. The results show

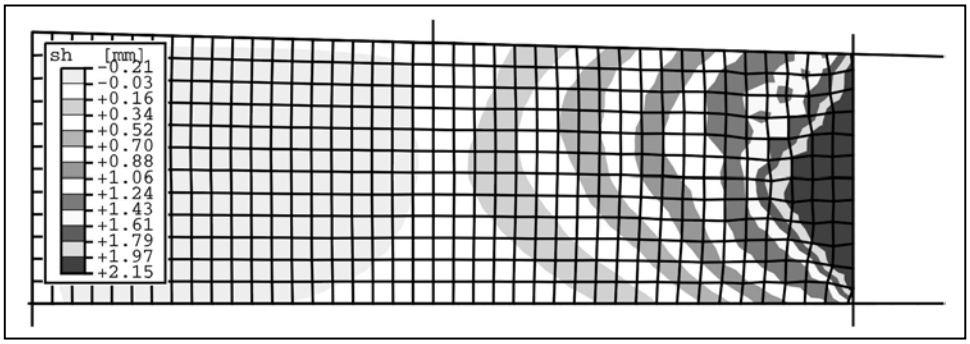

Fig. 2: Finite element model, mesh, deformations and contour plot of horizontal displacement.

for (i) that the model predictions match measurements reasonably well

for (ii) that the stability of coupled solving can be improved by a pre-compression of the pebble bed

for (iii), that convergence could not be achieved with the given creep model.

The modelling of Beryllium pebble beds in the HCPB blanket is based on the same soil model approach as the ceramic breeder material, with particular extension for deformation-dependent thermal conductivity and large neutron induced swelling. Progress in model development met the same problems as the ceramic breeder. As a consequence, resources for both materials were focussed on investigating the soil model numerical behaviour.

Conclusions and further work

The modelling work suggests that pebble bed modelling without creep is producing realistic results. Doubt has been raised on the approach used to model creep. The work of the coming year will have to focus on resolving this issue, to allow models for ceramic breeder and Beryllium to be applied to fusion-relevant conditions and improve the understanding on the mechanical behaviour under neutron irradiation. The goodness of the model under such conditions will be qualified by data from an in-pile test of a pebble bed assembly.

Staff:

S. Hermsmeyer
P. Norajitra

Literature:

S. Hermsmeyer, J. Reimann, Particle flow of ceramic breeder pebble beds in bi-axial compression experiments, Fus. Eng. Des., 61-62, pp 367-373, 2002.

P.A. Di Maio, E. Oliveri, G. Vella, Fusion pebble bed thermo-mechanical modelling, Parts A-C, Internal reports, Nuclear engineering department, 2002.

TTBB-006
Irradiation of Ceramic Breeder Pebble Beds

TTBB-006-2
Contribution to the PIE of EXOTIC-8 Pebbles

The EXOTIC-8 irradiation experiment in the HFR Petten [1] mainly aimed to investigate the tritium-release behaviour and the consequence of high burn-up on the integrity and the mechanical properties of lithium orthosilicate pebbles. Tritium release has been studied by in-pile thermal transients and post irradiation inventory measurements, optical and electron microscopy together with crush load tests are used to investigate the mechanical behaviour of the pebbles.

In 1997 EXOTIC-8 was started with two FZK capsules containing orthosilicate pebbles with a small addition of TeO_2:

Capsule E8/3 containing Li_4SiO_4 + 2wt% TeO_2 pebbles with 50% ^6Li-enrichment. In this capsule the behaviour of the material at high burnups (about 10%) should be studied;

Capsule E8/4 containing Li_4SiO_4 + 2wt% TeO_2 pebbles with natural enrichment. This capsule should give information on the behaviour of lithium orthosilicate at burnups up to 3%, and on the tritium release characteristics and tritium residence time.

After starting the irradiation, it was found that tellurium is released at high enough temperatures and the material is not suited as breeder. The specimens in the capsules were replaced with pebbles without tellurium.

The lithium orthosilicate pebbles containing tellurium from capsules E-8/3 and E-8/4 were sent back to Forschungszentrum Karlsruhe to be examined. Tab. 1 shows irradiation temperatures and Li-burn up (percentage of total lithium) of lithium orthosilicate pebbles.

	EXOTIC-8-3	EXOTIC-8-4
Temperature [°C]	500-690	483-592
Li Burn-up %	2.65-4.09	1.38

Tritium release measurements were performed in 2001 and in 2002 metallografic investigations were carried out.

Fig. 1 and fig. 2 show EXOTIC8-8-4 pebbles before and after the irradiation respectively. The pebbles before the irradiation show the golf ball structure typical of the material with tellurium oxide.

After the irradiation the pebbles changed their colour from white to grey (light to dark grey). The change of colour is already been observed in not irradiated pebbles annealed in reducing atmosphere, and might be due to the impurities present in the material (e.g. Fe, Al) whose oxides are reduced by the purge flow. The pebbles were sticking together but no sintering took place: light mechanical action could separate them and in Fig. 3 no sintering necks are visible. Fig. 4 shows the cross section of pebbles from EXOTIC 8-8-3. As far as the microstructure is concerned, the pebbles in initial conditions are already characterised by a dendritic structure with pores and cracks that is not strongly changed by the irradiation. Few broken pebbles are present.

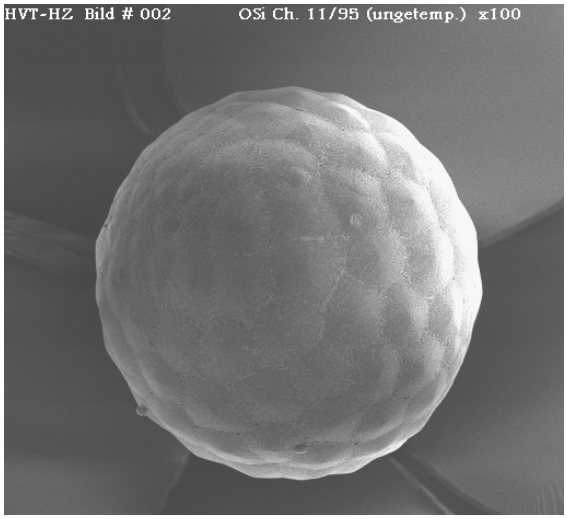

Fig. 1: Lithium orthosilicate before irradiation (EXOTIC 8-4).

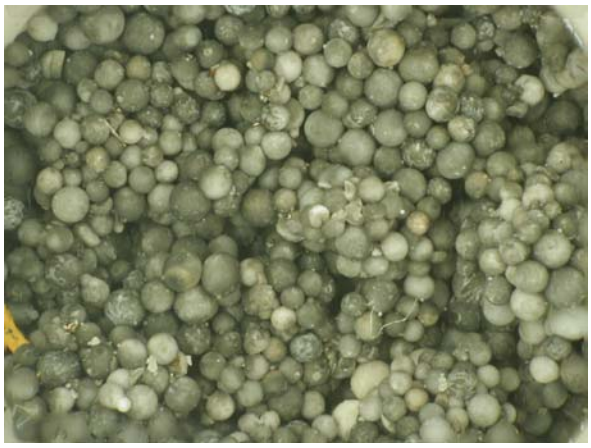

Fig. 2: EXOTIC 8-4 pebbles after irradiation.

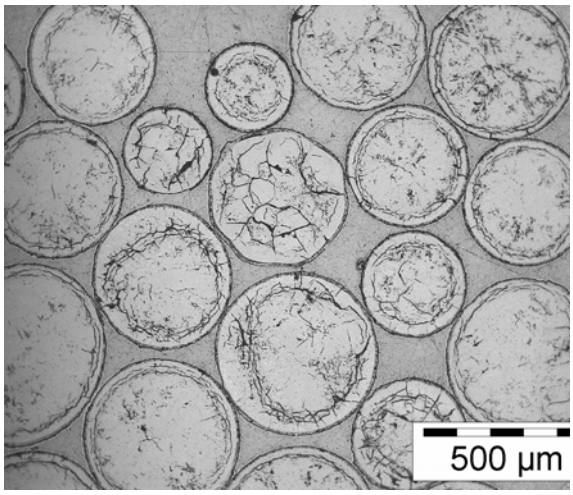

Fig. 3: EXOTIC 8-4 pebbles after irradiation.

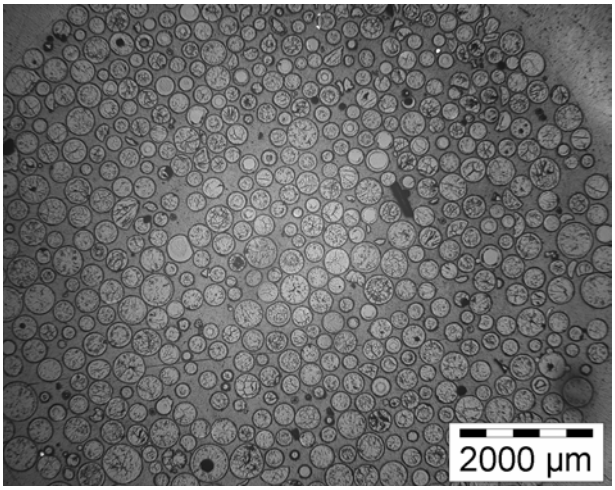

Fig. 4: EXOTIC 8-3 pebbles after irradiation.

The end of 2002 foresees the conclusion of the P.I.E. of all delivered EXOTIC-8 specimens.

Staff:

E. Damm
A. Erbe
M. Holzer
D. Knebel
S. Lautensack
P. Lauterbach
G. Mangei
G. Piazza
Fr. D. Reichmann
H. Ries
R. Rolli
O. Romer

Literature:

[1] J. G. van der Laan, K. Bakker, R. Conrad, A. Magielsen, G. Piazza et alii, “Performance of ceramic breeder pebbles to DEMO representative lithium burnups”. Proceedings of the 21st SOFT, Sept.11-15, 2000, Madrid, Spain.

TTBB-007
Development of Beryllium Pebble Beds

TTBB-007-1
Characterisation of Beryllium Pebbles

The main objective is the supply of the HCPB blanket reference beryllium pebbles to be used in experimental activities and their quality control (optical and electron microscopy, helium pycnometry and Hg-porosimetry, micro-hardness tests, mechanical behaviour of single pebbles at high temperatures). As the possibly of low tritium release from the beryllium pebbles at operating temperatures in the blanket represents a concern, in parallel to the characterisation and optimisation of the available reference NGK pebbles, also the possibility is being considered to improve the tritium release of the neutron multiplier in the blanket by acting on its microstructural characteristics. Specifically, recent parametric calculations with the ANFIBE code have shown that the tritium release properties of the metallic beryllium pebbles can be strongly improved by reducing the grain size under 10 μm, hence the development of beryllium pebbles having smaller grain size is being investigated.

Pebbles from Rotating Electrode Process

The NGK insulators Ltd. produces the reference beryllium pebbles with 1 mm diameter by rotating electrode process (REP) (Fig. 1).

Fig. 1: Beryllium pebbles produced by NGK

This method consists of arc melting the end of a long cast cylinder, which is rotating about its axis in a chamber filled with helium. Molten droplets of metal are thrown off the end of the rotating cylinder and solidify in flight. The size and quality of the REP beryllium pebbles depends essentially on the material used and on the production process parameters (e.g. electrode impurity content, electrode diameter, electrode angular velocity, cooling velocity, etc.). Usually, this method mostly produces spherical pebbles (diameters approximately in the range 0.2 mm - 2 mm) with a very small surface roughness and a beryllium oxide layer covering the pebbles with thickness estimated to be about 50-150 nm. The optical microscopy of the as-fabricated pebbles show an almost fully dense metallographic structure characterized by the presence of large grains (average grain size 100-300 μm). However, a quite large number of pebbles exhibit a big pore (up to 0.1-0.2 mm) at their centre together with a fully dense region near the external surface. This kind of pebble structure (which has been already observed in other types of pebbles subjected to fast thermal treatments) is typically generated during the cooling phase of the fabrication process. A possibility to decrease the grain size of the pebbles could be by increasing the cooling rate of the molten beryllium but, according information from NGK, as the pebbles solidify in a quite short time (~13000 °C/s cooling rate) and the temperature of molten beryllium is relatively low, it seems uncertain whether it is possible to reduce the grain sizes from hundreds μm down to few μm, only by changing the parameters of the process to reach higher cooling efficiency. An option could be to add certain additives to the beryllium electrodes, which would work as nuclei of grains. In this case, the effects of the additives on the properties of the pebbles, especially during irradiation, should be carefully investigated.

Pebbles produced by sintering of small size beryllium powder

A different way to produce pebbles with small grain size could be by sintering of small grain size (~1μm) powder. In this option two main steps have to be foreseen

1. Powder production;

2. Pebble production by sintering of the powder.

Up to now only the point 1 has been investigated. There are different methods to produce fine-grained powders and the followings seem presently the most promising:

Production of powder by wet chemical processes

There are several methods to obtain small sized metallic powders by chemical processes and many of these are also applied at industrial scale for producing continuously metallic powders with high purity. Beryllium powder can be produced by dissolving in an appropriate acid the material and, afterwards, by evaporating the obtained solution. The remaining powder should be washed (i. e. with dilute acid) and then used in the sintering process of the pebbles. The solvents used in this process should be oxygen free in order to reduce the BeO formation.

Milling

Milling of beryllium down to particles having diameters in μm-ranges could also be a possibility. In this case, better results could be obtained by milling at very low temperature (e.g. liquid N_2 cooling systems) and in a liquid to reduce the safety problem connected to the use of beryllium powders.

The activities aiming to produce the beryllium powder will continue in 2003.

Pebbles of beryllium intermetallic compounds

Since a couple of years JAERI has been investigating Be-Ti, Be-V and Be-Mo intermetallic compounds (beryllides) in view of their use for the Japanese pebble bed blanket concept. Presently, $Be_{12}Ti$ produced by NGK insulators Ltd. seems the most promising beryllide and characterisation work has been being performed in cooperation with several universities in Japan. According the available test results, $Be_{12}Ti$ shows, in comparison with metallic beryllium, faster tritium release, much smaller swelling, smaller reactivity with stainless steel, steam and water, therefore, it is becoming interesting also in view of its use in the EU-HCPB blanket. In a past meeting JAERI agreed to irradiate some $Be_{12}Ti$ samples in the European HIDOBE experiment (HIgh DOse BEryllium irradiation) starting in the second quarter of next year at the HFR Petten. The specimens should be delivered till the end of March 2003 to FZK for the pre-irradiation characterisation:

- Microstructure and composition investigations;

- Mechanical behaviour of single specimens (microhardness);

Moreover, following investigations are planned on the $Be_{12}Ti$ samples:

- Measurements of thermal conductivity;
- Experiments of tritium uptake kinetics and tritium release in $Be_{12}Ti$ (loading experiments at different temperatures);
- Compatibility tests with structural materials;

In 2006, after the irradiation, a campaign of post irradiation examinations is foreseen at FZK.

Staff:

A. A. Goraieb (Firm Goraieb Versuchstechnik)
J. Erbe
G. Piazza
E. Rabaglino
R. Rolli
O. Romer

TTBB-007-2
Improvement, Verification and Application of the ANFIBE Code

Aim and general overview

In the beryllium pebbles of the Helium Cooled Pebble Bed (HCPB) blanket, large quantities of helium and a non-negligible amount of tritium are produced under fast neutron irradiation. The code ANFIBE (ANalysis of Fusion Irradiated BEryllium) is being developed in order to predict swelling due to helium bubbles and tritium inventory in the range of operating and accidental conditions of a fusion power reactor. Due to the absence of data in this range, ANFIBE has to be extrapolated. Consequently, in comparison to codes which predict gas retention in UO_2, the development of a more sophisticated solid state physics model for the description of gas kinetics and a more careful and detailed validation procedure are required. The programme for the improvement of ANFIBE runs under the European Fusion Development Agreement on a period of five years (2000 – 2004) and is carried out in collaboration with the JRC - ITU (Karlsruhe, Germany), the NRG (Petten, the Netherlands), the SCK-CEN (Mol, Belgium) and the ESRF (Grenoble, France), as far as a part of the experimental studies are concerned. The theoretical evaluation of experimental data and related development of ANFIBE, as well as the definition of open key issues to be solved with further experimental studies, is under the responsibility of FZK. The contribution of FZK to the experimental activities is focused on the following points: (1) study of gas diffusion and release during out-of-pile temperature transients up to the melting point; (2) study of the microstructure of irradiated beryllium in connection with different gas release stages. The final aim of these studies is to improve the gas kinetics model in ANFIBE and to validate it also from the microscopic point of view, i.e. to verify if the different gas diffusion phases (atomic diffusion, precipitation into bubbles, bubble diffusion and growth, gas release pathways) are correctly described.

Progress in 2002

In 2001 a study of gas release and microstructure evolution was performed on weakly irradiated beryllium pebbles from the BERYLLIUM irradiation experiment [1, 2], with the following characteristics: 2 mm diameter, produced by Brush Wellman by Fluoride Reduction Process, coarse grains (40-200 micron size), irradiated in the High Flux Reactor in Petten for 93 days in 1994 at 780 K up to a fast fluence of 1.24 10^{25} m^{-2}, resulting in the production of 480 appm helium and 12 appm tritium (8 appm in 2001) [3]. In 2002 the study of this material was continued, in particular with the following achievements:

- assessment of ***helium and tritium diffusion coefficients*** on the basis of an inverse analysis of the gas release curves;
- validation and improvement of the ***model for gas precipitation into bubbles*** inside the grains and its migration to grain boundaries;
- experimental characterisation and theoretical modelling of ***the gas percolation stage***.

The same kind of characterisation was started on other types of irradiated beryllium, in order to assess the effect of different irradiation conditions (neutron fluence, temperature) and different material characteristics (grain size, pebble size) on the gas release modes. In addition to the pebbles from the BERYLLIUM irradiation experiment, two other materials were considered:

- Fragments of the disposed moderator of the BR2 reactor (SCK-CEN, Mol, Belgium) produced by vacuum hot pressing, with fine grains (20 micron size), irradiated for 15 years (1980 -1995) at 420 K up to the production of about 19200 appm helium and 6800 appm tritium in 1995 [4].
- Pebbles from the EXOTIC 8 experiment, 0.1-0.2 mm diameter, produced by Brush Wellman by Inert Gas Atomisation, coarse grains (40-200 micron size), irradiated in the High Flux Reactor in Petten for 200 days in the range 800 - 900 K up to a fast fluence of 5 10^{24} m^{-2} [5].

In addition, some preliminary parametric calculations of the effect of grain size on gas release from irradiated beryllium during operation in the reference fusion power plant have been performed by the version 0 of ANFIBE. On the basis of the results, some improvements of the reference beryllium pebbles have been suggested.

Out-of-pile gas release from different irradiated beryllium samples

Figure 1 shows helium and tritium release rates from the weakly irradiated 2 mm pebbles from the BERYLLIUM experiment (Fig. 1a), the weakly irradiated 0.1 mm pebbles from EXOTIC 8 (Fig. 1b, helium only) and the highly irradiated fragments from BR2 moderator (Fig. 1c). The samples are heated in a vacuum at 10 K/min to the melting point and helium and tritium release rates are measured by a mass spectrometer. In spite of the different pebble size, the samples from EXOTIC and BERYLLIUM exhibit a similar behaviour. In the range 700 – 1500 K gas release is due to migration of atoms, initially frozen in a supersaturated solution in the lattice, to free surfaces. At the same time, most of the gas atoms precipitate into bubbles. The gas trapped in bubbles (about 75 % of the inventory) is abruptly released above 1500 K, when growth and coalescence of bubbles at grain boundary lead to the formation of porosity networks connected to the free surface (percolation stage). The previous conclusions have been fully proved by the analysis of the microstructure evolution during the temperature transient [2], performed on the pebbles from BERYLLIUM. After irradiation, no gas bubbles are visible; at 1000 K a population of very small elliptical bubbles (6 nm average diameter) appears inside the grain (Fig. 3a); at 1300 K chains of large lenticular bubbles are visible on grain boundaries; at 1500 K percolation paths crossing the whole pebble have been identified (Fig. 5) [6].

The gas kinetics stages in the highly irradiated fragments from BR2 moderator are remarkably different, due to different irradiation conditions and grain size. Helium release begins already at 500 K and after a diffusion stage, an early bubble venting stage is superimposed in the range 1000 – 1200 K. Then a second stage of pure diffusion occurs and finally a second gas release peak starts at 1350 K, followed by smaller gas release bursts. It is believed that the first peak is related to sudden formation and coalescence of bubbles at grain boundaries, due to large quantities of gas already stored there at the end of the irradiation. The second peak is related to the release of gas trapped in bubbles inside the grains, precipitated during the transient, so it corresponds to the only gas release peak in the weakly irradiated pebbles. These conclusions need to be validated by a microstructure characterisation.

Analysis of the gas release curves

A theoretical analysis of the gas release curves for the pebbles from the BERYLLIUM experiment has been performed. The experimental curve is fitted by a model that, with the assumption of an initial uniform concentration of gas atoms in the lattice, takes into account both gas migration to grain boundaries and

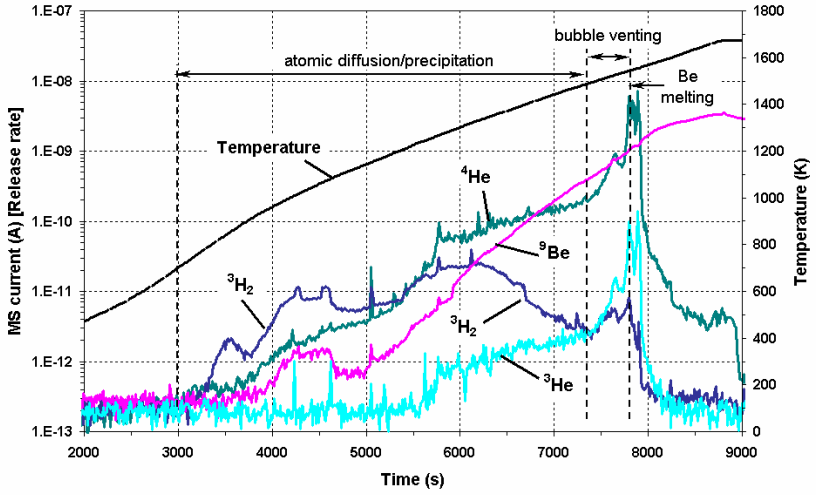

Fig. 1a

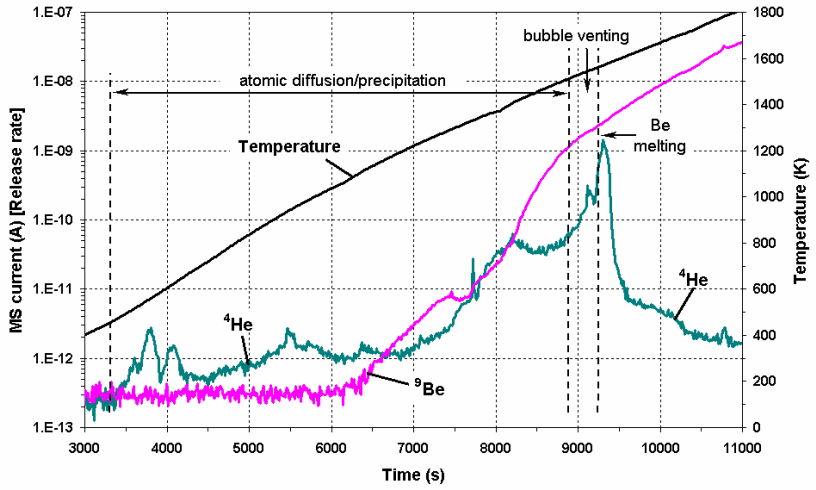

Fig. 1b

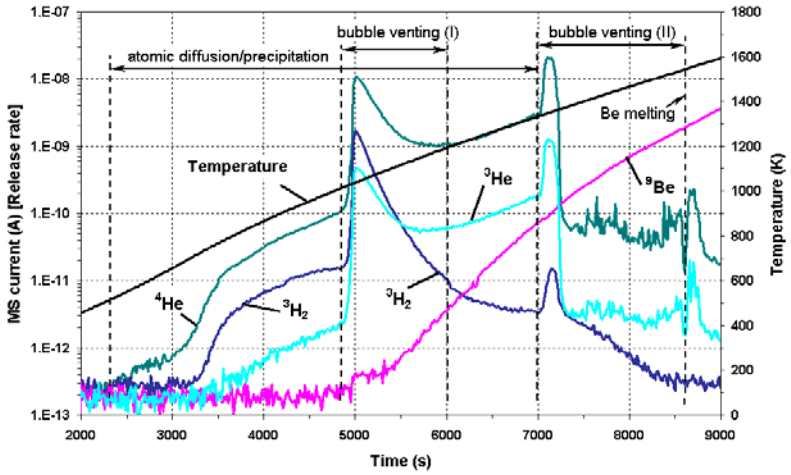

Fig. 1c

Fig. :1 Helium and tritium release in a vacuum from different irradiated beryllium samples: (a) BERYLLIUM irradiation experiment (pebbles 2 mm diameter, 40-200 micron grains, 780 K irradiation temperature, 480 appm ^{4}He) [4]; (b) EXOTIC 8 irradiation experiment (pebbles 0.1 mm diameter, 40-200 micron grains, about 190 appm ^{4}He); (c) Fragment from BR2 moderator (20 micron grains, 315 K irradiation temperature, 19200 appm ^{4}He).

precipitation into bubbles inside the grain during the temperature transient. Since the analytical model of gas atomic diffusion and precipitation is the same as in the ANFIBE code, this analysis makes it possible to assess directly some key parameters in ANFIBE, in particular:

1. the gas atomic diffusion coefficients;

2. the time constant for gas precipitation, which is related to the probability that a gas atom is trapped by a bubble inside the grain instead of reaching the grain boundaries;

3. a gas diffusion characteristic distance, which depends on the material microstructure and is a key parameter for the correct description of macroscopic gas release.

The fitting of an experimental gas release curve, performed by the code EFFUSX, is shown in figure 2. The fitting allows assessing also the quantity of gas trapped in bubbles as a function of temperature.

Modelling of the gas percolation stage

The inverse analysis of the gas release curves by the code EFFUSX did initially not take into account the presence of a bubble venting stage at the end of the transient: this limited the range of the fitting to 300 – 1500 K. The problem concerned in particular helium, because up to 1500 K only 25 % of helium inventory is released. In order to extend the fitting range to the melting temperature (1556 K) and to larger helium inventories, a simple model of bubble venting has been successfully implemented in EFFUSX. Bubble venting is described as a thermally activated creep process, with a linear dependence of the creep rate on the bubble pressure. The pre-exponential factor and the activation energy have been assessed as a result of the fitting of the experimental gas release curves. Figure 2 shows that this model not only can reproduce the experimental curve of gas release up to the melting point, but it also predicts the expected decrease of the gas inventory trapped in bubbles during the percolation stage, which is related to bubble release.

This assessment makes it possible to attempt a better validation and the improvement of the existing model of the gas percolation stage in ANFIBE.

The gas precipitation hindering factor

Gas precipitation into bubbles is described as the probability that gas atoms, as they diffuse in the lattice, are captured by bubbles inside the grain, instead of reaching the grain boundaries. The strength of the precipitation sinks, i. e. the intragranular bubbles, depends on their radius and concentration:

$$k_{sc} = \sqrt{4\pi\ r_{bubble}\ N_{bubble}}$$

The precipitation sink strength is in principle a function of temperature, since as temperature increases, bubbles grow and coalesce. An average value of the precipitation sink strength during the temperature transient in the range 300 – 1556 K is a result of the inverse analysis of the gas release curves performed by the EFFUSX code. At the same time, the precipitation sink strength can be directly assessed on the basis of the bubble population characteristics, by performing Transmission Electron Microscopy examinations of the sample microstructure. This study was performed at 1000 K (Fig. 3) and at 1340 K (Fig. 4), with the following result: though the bubble population had different characteristics, the precipitation sink strength maintained the same order of magnitude and it was in any case much higher than predicted by the EFFUSX code on the basis of the gas release curves.

In other words, gas precipitation during the temperature transient was much less intense than expected on the basis of the classical model. This bias effect had already been identified in irradiated UO_2 and has been modelled by multiplying the sink intensity strength by a precipitation hindering factor [7]. This takes account of the reduction of the effectiveness of small overpressurised bubbles as precipitation sinks, due to the presence of strong stress fields in their vicinity.

In our study the precipitation hindering factor was assessed as:

$$\chi = \frac{k^2_{sc,EFFUSX}}{k^2_{sc,microstructure}} = 10^{-4} \div 10^{-3}$$

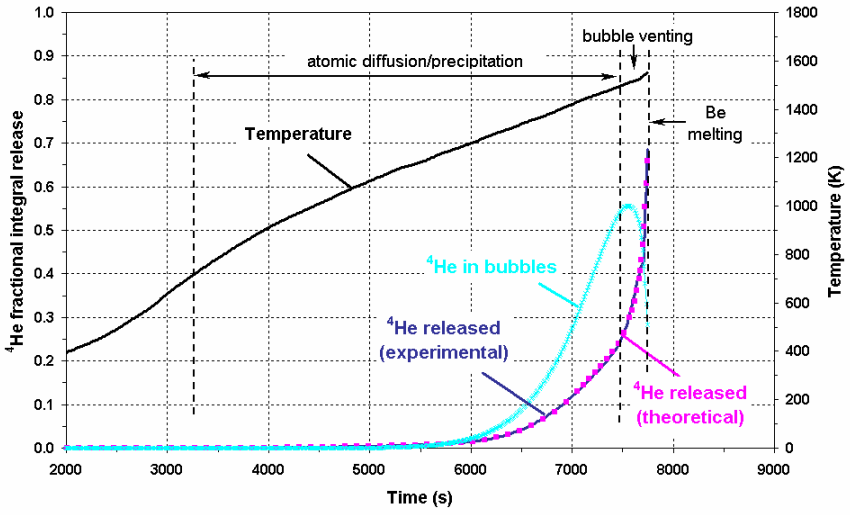

Fig. 2: Fitting by the EFFUSX code of a ^{4}He integral release curve in a vacuum for beryllium pebbles from the BERYLLIUM irradiation experiment.

A small precipitation hindering factor means that the migration of gas atoms to grain boundaries is enhanced, so a stronger gas release occurs. If the precipitation bias factor is neglected, the gas inventory trapped in bubbles is overestimated and a correspondent underestimation of the gas inventory that reaches the grain boundaries occurs.

Since the present value for the precipitation hindering factor in ANFIBE is 1, this analysis suggests that the code assessment of gas release is remarkably conservative and has to be improved.

The gas diffusion coefficients

On the basis of the fitting of the gas release curves by the EFFUSX code, taking into account the precipitation hindering factor and the bubble venting stage, the thermal diffusion coefficients have been assessed as follows:

For ^{4}He: $D \approx 10^{-4} \exp\left(\frac{-29500}{T}\right) \; m^2 s^{-1}$

For ^{3}H $D \approx 10^{-4} \exp\left(\frac{-21500}{T}\right) \; m^2 s^{-1}$

in the range 900 – 1500 K, for the irradiated beryllium bebbles from the BERYLLIUM experiment.

The gas diffusion characteristic distance for this kind of material was found to be 100 microns, value that roughly corresponds to the average grain radius.

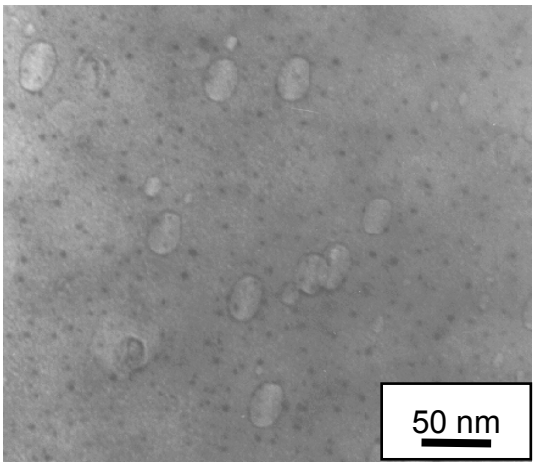

Fig. 3a

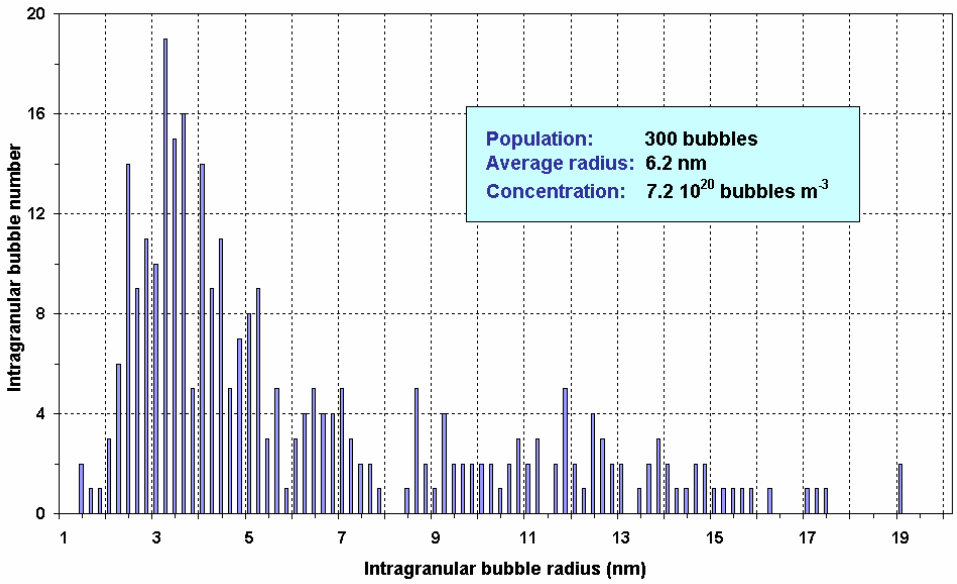

Fig. 3b

Fig. 3: Bubble population in a beryllium pebble from the BERYLLIUM irradiation experiment, heated at 10 K/min to 1000 K. (a) Transmission Electron Microscopy micrograph; (b) Bubble size statistics.

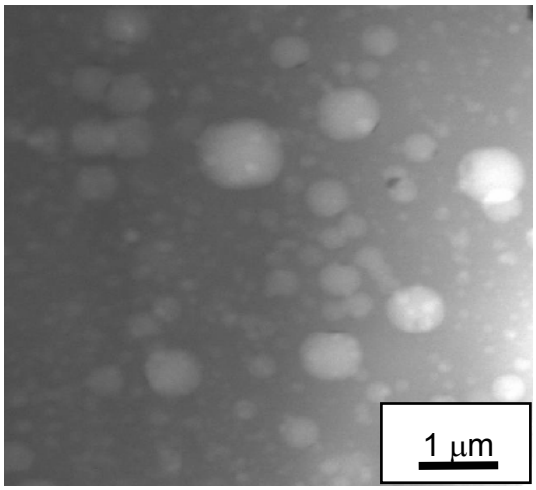

Fig. 4a

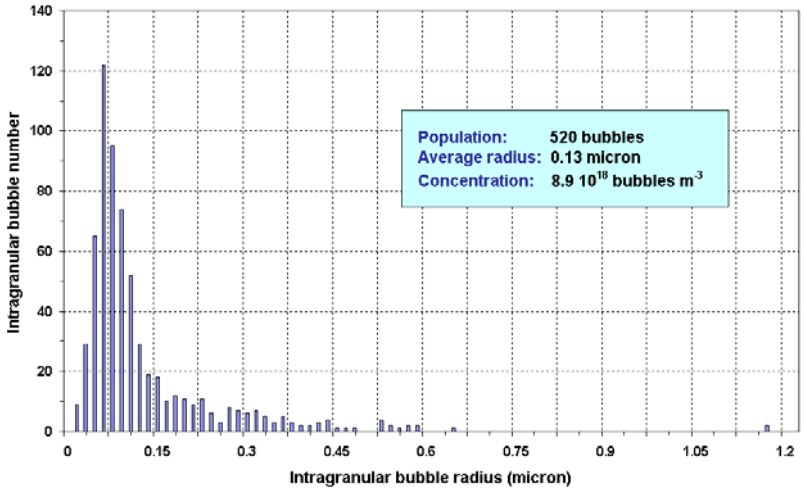

Fig. 4b

Fig. 4: Bubble population in a beryllium pebble from the BERYLLIUM irradiation experiment, heated at 10 K/min to 1300 K. (a) Scanning Transmission Electron Microscopy micrograph; (b) Bubble size statistics.

Characterisation by microtomography of the gas percolation stage

The gas trapped in bubbles is released only when, at high irradiation dose and/or high temperature, large lenticular bubbles at grain boundaries form open porosity networks. A correct understanding and modelling of the gas percolation stage is extremely important since this phenomenon is responsible of the release of most part of the gas inventory (Fig 1).

The characterisation of the microstructure of a beryllium pebble from the BERYLLIUM irradiation experiment has been performed after heating to 1500 K, when the percolation stage begins (Fig. 1a) [6]. Due to the complex 3D structure of gas percolation paths, an X-ray microtomography techinque based on synchrotron light has been applied at the European Synchrotron Radiation Facility (Grenoble, France). Figures 5a and 5b show two perpendicular cross sections of the pebble. Extended porosity networks run across the sample. The percolation paths are anisotropic, since they are probably related to the initial presence of columnar grains.

Figure 5c shows the reconstruction of the pebble surface with the open pores where internal porosity networks emerge.

Effect of grain size on gas release from beryllium under irradiation.

On the basis of the study of the gas precipitation stage described in paragraph 4, the present version of the ANFIBE code is believed to underestimate gas release from beryllium under irradiation. Some preliminary calculations on the effect of grain size on gas release in the reference Fusion Power Plant show that, in spite of a conservative assessment, almost the whole of gas inventory would be released in-pile, if the grain size decreased below 1 micron. The present reference material (NGK pebbles, 1 mm diameter) is from this point of view not completely satisfactory, because it has coarse grains (40-200 micron). A reduction of grain size would be beneficial in order to reduce in-pile gas accumulation.

Conclusions and future work

The studies performed in 2002 have allowed remarkable progress in the understanding and modelling of gas diffusion and release stages in irradiated beryllium, in particular from the microscopic point of view. In 2003 a new version of the ANFIBE code will be released, where these achievements will be implemented. At the same time, the experimental characterisation of the highly irradiated beryllium from BR2

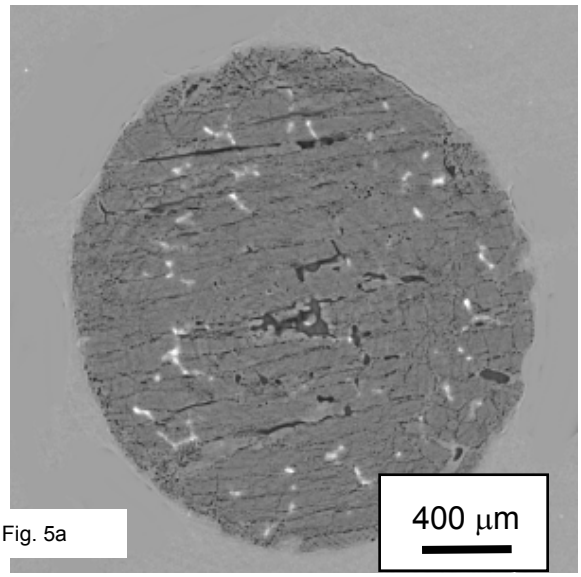

Fig. 5a

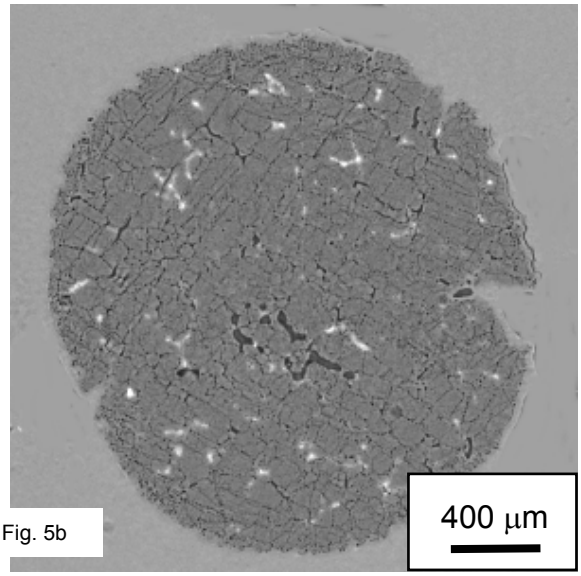

Fig. 5b

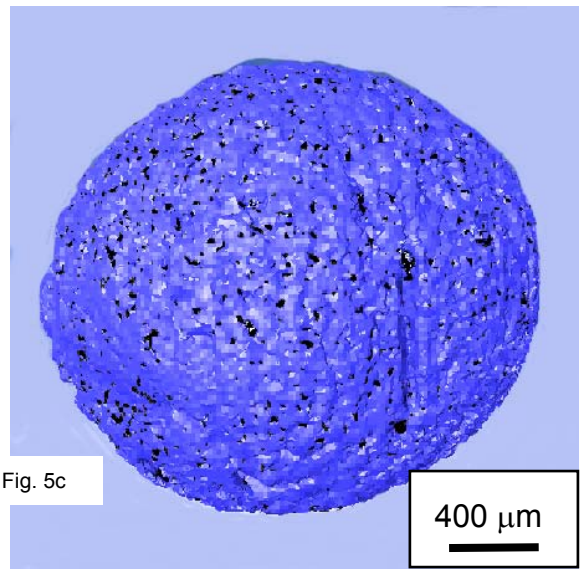

Fig. 5c

Fig. 5: Microtomography of a beryllium pebble from the BERYLLIUM irradiation experiment, heated at 10 K/min to 1500 K (a) Cross section perpendicular to the z axis. (b) Cross section perpendicular to the x axis. (c) 3D view of the reconstructed surface (blue) with the open porosities (black).

reactor will be completed. A quantitative study of the gas percolation stage in the pebbles from the BERYLLIUM experiment will be attempted by improving the experimental technique, in order to allow the validation of the gas percolation model in ANFIBE.

Staff:

E. Rabaglino (FZK)
C. Ronchi (JRC-ITU)

Contributors at the JRC-ITU:
F. Capone
J. Y. Colle
J.P. Hiernaut
M. Murray-Farthing
H. Thiele
T. Wiss

Literature:

[1] E. Rabaglino, J.-P. Hiernaut, C. Ronchi, F. Scaffidi-Argentina, Helium and tritium kinetics in irradiated beryllium pebbles, in: Proc. 10th Int. Conf. on Fusion Reactor Materials, Baden-Baden, Germany, 2001, J. Nucl. Mat. (2002), in press

[2] E. Rabaglino, C. Ferrero, J. Reimann, C. Ronchi, T. Schulenberg, Study of the microstructure of neutron irradiated beryllium for the validation of the ANFIBE code, in: Proc. 6th Int. Symposium on Fusion Nuclear Technology, San Diego, USA, 2002, Fus. Eng. Des. 61-62c (2002) 769-773

[3] R. Conrad, R. May, BERYLLIUM Final irradiation report, EC-JRC-IAM Report P/F1/96/15 (1996)

[4] V. Van Alsenoy, F. Druyts, M. Gysemans, L. Sannen. C. De Raedt, J. Fays, Beryllium waste conditioning strategies, 1: Physical, chemical and radiological properties of beryllium waste from the BR2 reactor of SCK-CEN, Report R-3598, SCK-CEN, May 2002

[5] F. Scaffidi-Argentina, Fus. Eng. Des. 58-59 (2001) 641-645

[6] E. Rabaglino, J. Baruchel, E. Boller, E. Elmoutaouakkil, C. Ferrero, C. Ronchi, T. Wiss, Study by microtomography of 3D porosity networks in irradiated beryllium, in: Proc. E–MRS 2002 Spring Meeting, Strasbourg, France, 2002, Nucl. Inst. and Methods B (2002), in press

[7] C. Ronchi, On the diffusion and precipitation of gas-in-solid, J. Nucl. Mat. 148 (1987) 316-323

TTBB-007-4
Thermal-Mechanical Pebble Bed Tests

In the helium cooled pebble bed (HCPB) blanket for fusion power reactors [1] the neutron multiplier and the breeder material are arranged in pebble beds between flat cooling plates. The maximum temperatures in the breeder and beryllium pebble beds are about 900 °C and 650 °C respectively. Because of temperature differences and different thermal expansion coefficients between pebble beds and structural materials and because of irradiation effects (swelling up to 10 vol.% during the lifetime of the blanket has been calculated), constrained strains occur, which cause elastic and plastic pebble deformations influencing the effective thermal conductivity of the beds.

The modelling of the thermal mechanical behaviour of beryllium pebble beds requires, as important input data, the thermal conductivity of the pebble bed as a function of temperature and deformation. Therefore, in the frame of the European Fusion Technology Programme, several experimental activities have being carried out at the Research Centre of Karlsruhe (FZK) to measure thermal conductivity and heat transfer coefficients to the containing walls: in the PEHTRA and Super PEHTRA [2,3] experiments the investigations were limited to small bed deformations. First results for strongly deformed pebble beds with an independent variation of temperature and deformation were presented in [4,5] using the Hot Wire method. This method has proven to be an accurate measurement technique for low conductivity materials but the accuracy for materials like beryllium was somewhat questionable. An important result was a linear relationship between conductivity and strain for the first pressure increase and a small conductivity decrease during depressurisation. In order to perform measurements with a higher accuracy and a larger parameter range, the test section HECOP (**HE**at **CO**nductivity in **P**ebble beds) was built and first experiments were performed.

Experimental apparatus

The HECOP design requirements were: independent adjustment of temperature and deformation of the beryllium beds, minimisation of uncontrolled heat losses, and reliable measurement of temperature gradients in the bed. Operating ranges were: Mechanical uniaxial pressure up to 6 MPa; average pebble beds temperature up to 600 °C.

Pebbles were used having 1 mm diameter and produced by NGK Insulators Ltd by the rotating electrode process, see Fig. 1.

The HECOP test section, Fig. 2, is positioned between the pistons of a hydraulic press, which can exert a maximum compression load of 50 kN. Both the upper and lower pistons can be heated up to 500 °C and are connected to a water-cooling system. The pebble bed loading was measured by load cells, four displacement transmitters (not shown in Fig. 2) were used to determine the mean bed strain, ε. The beryllium pebbles are contained in a cylindrical steel cavity with a diameter 100 mm and a bed height of 50 mm. A system of 7 heaters (H1...H7) is used in total. H1 and H2 generate the temperature gradient in the bed, whereas H2 is also used to calculate the thermal bed conductivity. H3, H4, and H5 are used to minimise both radial and axial heat losses of the heat flowing from H2 to H1 through the pebble bed in the axial direction. The radial heat loss from H2 is minimised by controlling the power of the annular guard heater H4 such that the temperature difference between two neighbouring thermocouples becomes zero, (see Fig. 2). The axial heat flow from H2 to the press bottom plate is controlled in a similar way using H5 and the thermocouple pair in H2 and H5. An analogous system of guard heaters (H1 and H3) and thermocouple pairs in the upper part of the HECOP test section contributes in controlling the uniformity in radial direction of the temperature in the pebble beds. In order to allow fine controlling (i.e. reducing oscillations) of the temperatures of H1 and H2, which define the temperature gradient in the bed, the maximum power of these heaters is relatively low (230 W and 150 W respectively). For the experiments in high temperature range, additional heating by the heaters H6 and H7 is required.

Fig. 1: 1 mm NGK beryllium pebbles (FZK Hot cells: optical microscopy).

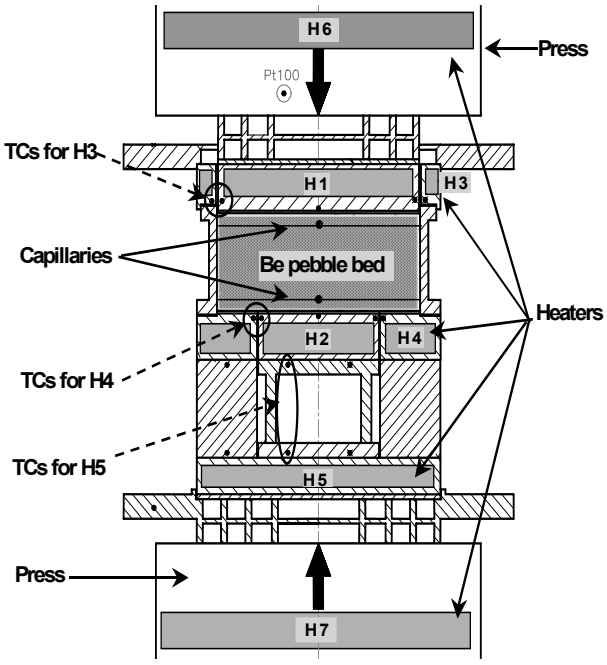

Fig. 2: Schema of the HECOP test facility (black dots schematically indicate some of the 36 thermocouples). In circles the thermocouples (TCs) are indicated, which are used to control the heaters H3, H4 and H5.

To thermally insulate HECOP from the environment, refractory ceramic fibre (Kerlane) was used. The whole test section is put in a steel lateral containment.

A total of 36 NiCr-Ni thermocouples gives information on the thermal status of the system and allows controlling it (in fig. 2,

black dots schematically indicate some of the 36 thermocouples). Within the pebble bed the temperatures are measured by two pairs of thermocouples located inside capillary tubes at two defined bed's heights (for simplicity only one dot pair is shown in fig. 2). X-ray analyses of compressed beryllium pebble beds have shown that the variation of the distance between capillaries in the bed is not significant for loads up to 6 MPa. In order to individuate any permanent deformations of the position of the capillaries, it is measured before starting each experiment.

The experiments are performed in a glove box filled with helium at constant temperature (an external water-cooling system is coupled to the box). This provides safe handling of beryllium pebbles avoiding any contact with toxic beryllium powder. During the experiments three separate safety systems are active in order to control the temperatures in the HECOP test section, inside the glove box and in the press.

As the test section weighs about 20 kg, a special arm is used to move the HECOP test section between the measurement position in the press and the filling position outside the press. During the filling, the test section is vibrated at 50 Hz to obtain dense packing.

The thermal conductivity k [W/m K] is determined by

$$k = Q_2 \bullet \Delta x / \Delta T \qquad [1]$$

with Q_2 [W/m^2] the heat flux produced by H2, Δx [m] the axial distance between the thermocouples in the bed (about 25 mm) and ΔT [K] the corresponding temperature difference. In order to measure heat losses, experiments were performed at 250 °C and 350 °C, in which an isothermal condition was reached with practically no temperature gradient in the pebble bed. In the ideal case, no heat would flow through the bed, i.e. H2 power production should be zero. In these tests, however, H2 power production was not zero, showing heat losses lower than 10 % of the power flowing through the pebble bed in experiments with a temperature gradient of 50 °C.

Results

Experiments were performed at average temperatures of 250 °C and 350 °C and with temperature gradients of about 50 °C over the bed height. Packing factors (ratio of pebble volume to total volume) of about 62% were reached.

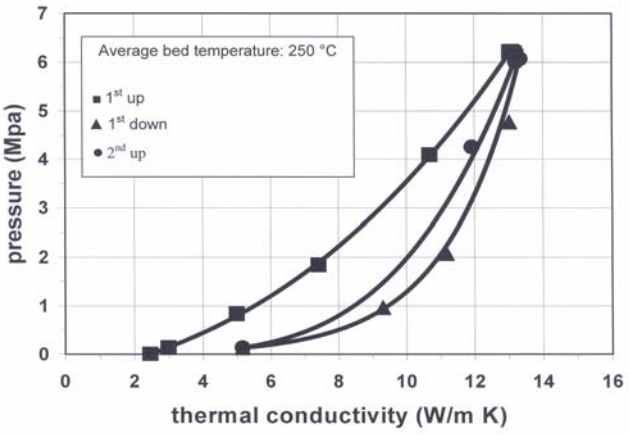

Fig. 3: Thermal conductivity of 1 mm NGK heryllium pebble bed as a function of pressure. Bed average temperature is 250°C and temperature gradient in the bed about 50°C.

Fig. 3 shows the results of measurements at 250 °C average bed temperature. At a pressure of about 5 kPa, which corresponds approximately to a non deformed bed, the thermal conductivity was 2.4 W/m K. At about 0.14 MPa there was a slight increase of the thermal conductivity. With increasing pressure, conductivity increased significantly up to a value of about 13 W/m K at 6 MPa (1st up in Fig. 3) in consequence of the pebble bed compaction and the enlargement of the contact surfaces between the pebbles. After reaching its maximum the pressure was decreased down to about 0.14 MPa (1st down in Fig. 3). During the pressure decrease the conductivity decreases first only slightly (about 15 % for a pressure decrease of 70%) For pressures less than 2 MPa the reduction of thermal conductivity is larger and at 0.14 MPa the thermal conductivity is about 5 W/m K.

This value is still significantly larger than the initial value for the non-deformed bed. In the second pressure increase (2nd up in Fig. 3) the thermal conductivity practically follows the previous decrease curve up to 13 W/m K. Similar results were obtained for experiments at 350°C.

Due to problems with the displacement measurement system in HECOP, the pebble bed deformation ε was determined from previous measurements [4]. Figures 4 and 5 show the experimental points and the curve fittings obtained at 250 and 350 °C. The results are qualitatively in quite good agreement with those obtained in the HOT WIRE experiments [4], i.e. after compaction at a certain pressure the pebbles tend to maintain the reached configuration in the beds in terms of contact points and contact surfaces. Further reduction of the mechanical pressure (below 2 MPa) determines a larger bed relaxation and, consequently, a stronger reduction of thermal conductivity.

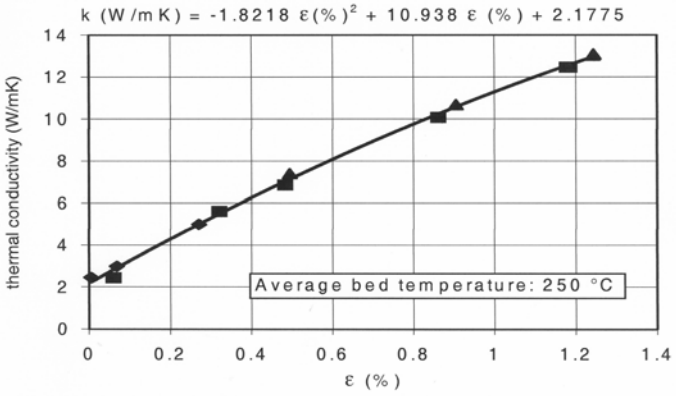

Fig. 4: Thermal conductivity of 1 mm NGK beryllium pebble bed as a function of the pebble bed deformation for the first pressure increase (experimental points and fitting curve).

Quantitatively, the thermal conductivities measured in the HECOP facility are about 20-30 % higher than those from the hot wire experiments [4] and the thermal conductivity/strain dependence slightly deviates from the linearity. This might be due to a decreasing accuracy of the HOT WIRE method with increasing bed conductivity.

Concluding summary

Measurement of thermal conductivity of single size 1 mm pebble beds in helium atmosphere have been performed in the HECOP test section. In particular, thermal conductivity as a function of mechanical compression load was obtained at two temperatures (250 °C and 350 °C) and for pressures in the range 0-6 MPa. The relationships between thermal conductivity and deformation were obtained indirectly by using pressure/deformation correlations obtained in previous uniaxial tests.

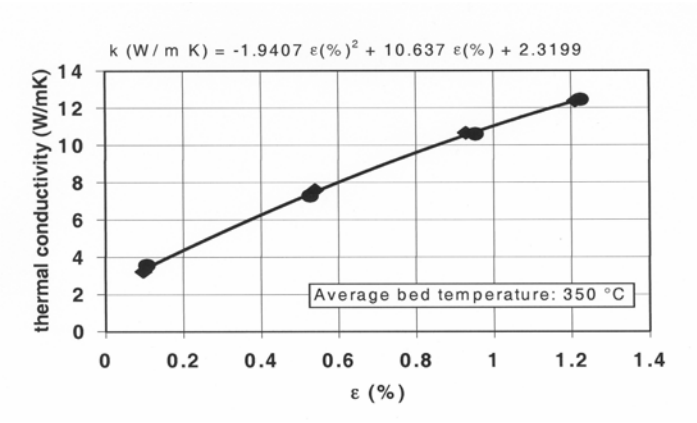

Fig. 5: Thermal conductivity of 1 mm NGK beryllium pebble bed as a function of the pebble bed deformation for the first pressure increase (experimental points and fitting curve).

The compression of the beds causes an arrangement of the pebbles (number of contact points and dimensions of the contact surfaces between pebbles) that is practically maintained for a wide pressure range when the mechanical pressure decreases (almost constant thermal conductivity is the consequence). Only at very low pressures, there is a stronger reduction of thermal conductivity as a consequence of larger bed relaxation but the conductivity remains higher compared to the initial conditions. The present results confirm the tendencies observed in previous hot wire measurements, however, the thermal conductivities measured in the HECOP facility are about 20-30 % higher. Further investigations are needed to better understand the causes of this difference.

Due to the failure of the heater H4, the HECOP test section is presently out of operation. This situation is used to modify fundamentally the total system, e.g. the deformation will be measured in a different way and the temperature operating range will be extended to about 650 °C. This will enable better to investigate thermal creep of beryllium pebble beds (these data are currently missing) and the consequences on thermal conductivity.

Staff:

Fa. Goraieb Versuchstechnik
G. Hofmann
G. Piazza
J. Reimann

Literature:

[1] S. Hermsmeyer, U. Fischer, K. Schleisiek,: Improved helium cooled pebble bed blanket, proceedings of the 21st Symposium on Fusion Technology, Madrid, September 11-15, 2000, Fusion Engineering and Design 58-59 (2001) 689-693.

[2] M. Dalle Donne, G. Piazza, A. Goraieb, G. Sordon, Measurement of the thermal conductivity and heat transfer coefficient of a binary bed of beryllium pebbles, Proceedings of the 3rd IEA-International Workshop on beryllium technology for fusion, Mito-city, Japan, October 22-24, 1997.

[3] Dalle Donne, A. Goraieb, G. Piazza, F. Scaffidi-Argentina, Experimental investigations on the thermal and mechanical behaviour of single size beryllium pebble beds, Proceedings of the 4th IEA International Workshop on Beryllium technology for Fusion, Sept. 15-17, 1999 Forschungszentrum Karlsruhe, Germany, Fusion Technology, November 2000, vol. 38, 290-298.

[4] J. Reimann, S. Hermsmeyer, G. Piazza, G. Wörner, Thermal conductivity measurements of deformed beryllium pebble beds by hot wire method, proceedings of the CBBI-9, Sept 27-29, Toki, Japan.

[5] J. Reimann, L. Boccaccini, M. Enoeda, A. Ying, Thermomechanics of solid breeder and Be pebble bed materials, proceedings of the 6th Int. Symp. Fusion Nucl. Techn., San Diego, USA, April 7-12, 2002.

[6] G. Piazza, G. Hofmann, J. Reimann, S. Malang, A. Goraieb, H. Harsch: “Thermal conductivity measurements of deformed beryllium pebble beds”. Proceedings of the 5th international Workshop on Beryllium technologies for Fusion, October 10-12, 2001, Moscow, Russia.

WCLL Blanket Concept

TTBA-003
Coating Qualification and Irradiation Tests

TTBA-003-32
Fabrication and Characterisation of Permeation Barriers made by Hot-Dipping and Testing in VIVALDI

Previous experiments with steel samples of sheet and tube geometry have shown that tritium permeation can be significantly reduced by an adapted surface coating. The developed Hot-Dip aluminising process (HD) leads in combination with adjusted heat treatments to a significantly reduced tritium permeation. In addition to the function as Tritium Permeation Barrier (TPB) the formed oxide scale increases the corrosion resistance compared to the uncoated steels in liquid Pb-alloys. However, for technical applications a further development of the process is required. The most obvious aspects are to increase reproducibility in production of coated parts without defects and to apply the process to parts more complex in geometrical structure.

The development of the HD process and the coating of steel tubes (EUROFER 97) is performed in the frame of the European Permeation Barrier Qualification program. Some first hot-dip aluminised EUROFER 97 tubes (one end closed) were prepared in 2001 for permeation testing in H_2-gas and in Pb-17Li-H_2 in the VIVALDI apparatus at ENEA-Brasimone. The data about VIVALDI apparatus, which can work up to 500 °C, and the parameters for HD coating process are given in an earlier report.

The obtained results indicate that permeation can be reduced significantly by coating with the developed Hot-Dip process and that the HD process has distinct advantages compared to other coating processes. The planed reduction in Tritium permeation by a factor of 100 was achieved. However the detected (Permeation Reduction Factor) PRF ratio vs. temperature is not constant or monotonic - a hint on scale defects or special low temperature behaviour of the scales.

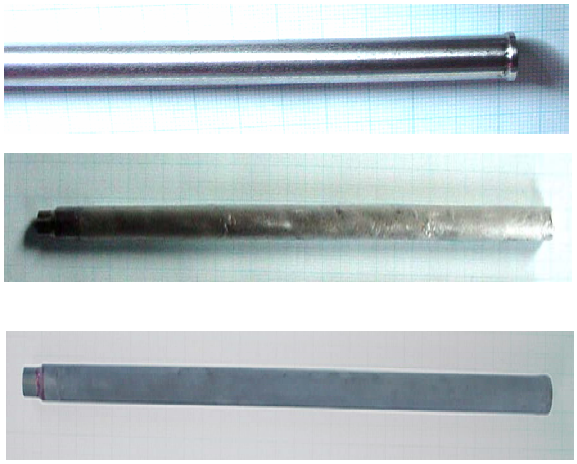

Fig. 1: Steel tubes for HD processing (from top to bottom).
Tube as delivered after surface conditioning.
Tube after aluminization by HD.
Tube after heat treatment.

Based on these challenging test results a second test series was planned for 2002. The main goals were optimization of the coating process, modification of assembling the test configuration into VIVALDI apparatus and extending test conditions to study self healing tendencies of the formed scales.

In the previous HD test series it was found that wetting of the steel by the Al melt is very important to obtain a homogeneous coating. By this reason we modified our process and performed first a surface conditioning (grinding and polishing) of the steel tubes, which were fabricated and delivered by ENEA. The complete Hot Dip process was performed in Ar/H_2 atmosphere to reduce tendency of slag formation on top of our aluminization bath and to avoid formation of unacceptable thick new oxide films on top of the steel tubes.

Fig. 1 shows steel tubes for HD processing in the states as delivered inclusive surface cleaning, aluminized and surface equalized (excess Al removed), and after heat treatment to form Al diffusion layers and Al_2O_3 skins. By the performed macroscopic inspection tests no defects were obvious. The coated test samples were delivered in mid 2002 to ENEA to mount them into the test rig.

The expected test results are required to optimize the HD process e.g. in the frame of surface conditioning, slag removal, environment (melt) conditioning. Besides these more technical aspects the new tests should lead to an better understanding of the foregoing mechanisms in the diffusion zone and the oxide skin during contact with the Pb – H_2 containing - melt and, additionally, under thermal cycling conditions. One of the main interests is the knowledge on the ability of self-healing behaviour of the scales, which should guarantee the long-term behaviour in corrosion resistance and TPB function.

Staff:

J. Konys
W. Krauss
Z. Voß
O. Wedemeyer

Literature:

[1] J. Konys, G. Müller, Corrosion and compatibility of structural materials in liquid lead alloys, Proc. Int. Symposium on Material Chemistry in Nuclear Environment MC'02, March 13-15, 2002, Tsukuba, Japan

TTBA-006
Magneto-Hydrodynamics (MHD)

TTBA-006-32
Forced Convection MHD Experiments related to the EU-WCLL Blanket

Introduction

In currently investigated liquid-metal (LM) blankets for fusion reactors the LM - a lithium-lead alloy - serves mainly as breeding material [1] and not as coolant.

A crucial issue for all liquid metal cooled blankets is the **m**agneto-**h**ydro**d**ynamic (MHD) situation in the header where the flow is distributed/collected from the individual ducts. There, high flow velocities appear which generate due to the large amount of structural material located in the header high pressure drops. An even more peculiar feature of the MHD flow in the header is that uneven flow rates in the individual feeding and draining ducts may appear, which are caused by the electric coupling of channels via the electrically conducting structural material. This effect is called **m**ulti-**c**hannel-**e**ffect (MCE).

The flow distribution from one large feeding line into the large flow channels necessary for Tritium breeding mostly coincide with dramatic cross section changes leading to undesirable MHD flow features

New fabrication technologies allow an electrical separation of the individual feeding/draining ducts and hence drastically reduce the MHD pressure drop and avoid uneven flow rates, the MCE effect. The electrical separation is performed via an electrically insulating coating being plasma-sprayed on the ducts. Afterwards the individual ducts are hipped to a full header module.

The intense magnetic field required for confining the plasma is responsible for pressure drop by Joule dissipation in regions of the blanket where the magnetic field has a transverse component to the flow direction. This dissipation could be reduced by reducing the field intensity inside the pipes or by reducing the fraction of the induced current that goes from the fluid to the wall. The first option is achieved by using ferromagnetic materials for the walls. This is the case of the actual design of the European Helium Cooled Lithium Lead Blanket (HCLL). In fact it is planned to fabricate this blanket from EUROFER steel, which has relative magnetic permeability up to μ=400. This means that before reaching the saturation magnetization of this material, which occurs around 1.5T, the magnetic field intensity inside the pipe is 400 times lower than the externally applied field. The second way to reduce the MHD losses is to insure a reliable electrical decoupling by using insulating layers between the liquid and the surrounding massive structure. The use of such insulating layers has also a safety role in stopping any penetration of the breeding product tritium, contained in the liquid metal, towards the water-cooled system.

The first part of the R+D program being treated in 2002 has been focussed on the theoretical and experimental investigation of a forced convective MHD flow in ducts of circular cross-sectional shape for three different duct flow types:

a) MHD flow channels with an electrical separation between structure material and liquid metal containing duct.

b) MHD flow in thick electrically conducting ducts.

c) MHD flow in thick-walled ferromagnetic ducts.

The second part has been dedicated to the design and the fabrication of a test section with a dramatic expansion or contraction. At these expansions/contractions extremely thin shear layers appear which are responsible for the flow distributions far downstream. The three-dimensional currents accompanying these MHD flows in expansions determine the additional three-dimensional pressure drops appearing there.

All these issues are subsequently discussed below.

Blanket relevant MHD- flows in circular ducts

One important question for the design of liquid metal blankets is availability of a long term reliable electrical insulation of the duct walls, which is capable to withstand the high neutron fluxes present in the reactor. The research to develop such electrically insulating materials is still an ongoing task although the insulation requirements for such a material with respect to MHD are far below the ones set up by the electric industry. In the absence of an electric insulation of the duct walls global electric currents induced by the fluid motion can circulate within the blanket structure. This effect known as multi-channel effect (MCE) may lead especially for self-cooled blankets to pressure drops exceeding the allowable material stresses. But also the actually discussed Helium-Cooled-Lead-Lithium (HCLL) blanket can be significantly affected by the MCE since it yields uneven flow distributions in the individual ducts.

The pressure drop caused by MHD flows in most of the relevant duct geometries may be minimized by the use of thin conducting walls or by direct insulations (coatings or ceramics). Thin conducting walls can be achieved by the use of so-called Flow-Channel Inserts (FCI), where an electrically insulating ceramic sheet is sandwiched by thin steel plates. These FCI's are fitted loosely in the ducts. The physical effect leading to the reduced MHD pressure drop is that the electric current density minimized, because the thin steel sheets represent a higher ohmic resistance than a thick wall facing the liquid metal. A second advantage are the low requirements on the FCI's with respect to their stiffness, since the pressure level in- and outside the FCI is nearly the same. Nevertheless, the usage of FCI's in long geometries requires the insertion of several FCI's. At the junctions where the FCI's overlap three-dimensional MHD flows appear due to the jump of the electrical conductivities.

MHD flow in thick- walled ducts

The MHD pressure drop in ducts with electrical separation is given by the electric wall conductivity of the liquid metal facing thin steel duct. The leading parameter there is the wall conductance ratio *c* which is defined by relation (1a):

$$c = \frac{\sigma_W \cdot t_W}{\sigma \cdot a} \quad (a); \nabla p = \frac{c}{1+c} \quad (b). \qquad (1)$$

Herein, σ_W is the specific electrical conductivity of the duct wall, t_W the wall thickness of the liquid metal facing structure, a the ducts and ∇p the dimensionless pressure gradient scaled with the electromagnetic pressure given by $a\sigma v_0 B^2$. The dimensionless pressure gradient to be expected in a two-dimensional fully developed MHD flow in a circular tube is given by relation (1b).

In case of thick walled electrically conducting ducts the pressure gradient is by orders of magnitudes larger than in case of electrical separation; but, as shown by Bühler [3,4] significantly lower than that of a Hartmann-flow, where the pressure gradient per unit length is 1. The Hartmann flow assumption has been

formerly used as a design tool in blanket designs. The pressure gradient in a fully developed MHD flow in a thick walled duct is given by equation 2.

$$\nabla p = -\frac{1}{1+\frac{\sigma}{\sigma_w}\frac{R^2+1}{R^2-1}}, \qquad (2)$$

where R is the radius of the thick-walled duct as depicted in figure 1.

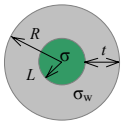

Fig.1 : Sketch for the definition of an MHD- flow in a thick walled duct.

The structural material considered for the EU-HCLL blanket (EUROFER) owns a ferromagnetic behavior ($\mu_r \approx >> 1$). and a magnetic saturation field strength of 1.64Tesla. Unfortunately, the magnetic field strength being present in a Tokamak are around 4-7 Tesla and hence far above the saturation value. As a consequence the electro-magnetic boundary conditions at the liquid metal-duct interface are different than in the case of non-ferromagnetic materials. Especially, the magnetic field produced by the electric current (, which originates form the interaction of moving liquid and plasma confining magnetic field) circulating within the liquid metal and the magnetic field lines compressed in the ferro-magnetic duct interact with each other, leading to other current pathes. This modification of the boundary condition leads to different MHD flow features than investigated in the past.

A new model was derived capable to describe the two-dimensional MHD flow in a ferromagnetic duct. If the plasma confining magnetic field is above the saturation value of material the magnetic field leading to the MHD pressure drop is reduced significantly. Nevertheless, in this case the field lines remain parallel so that the velocity distribution is the same as in a non-ferromagnetic duct. The figures 2 show the magnetic field lines and the electric current distribution in a ferromagnetic material (figure 2b) compared to a non-ferromagnetic material (figure 2a).

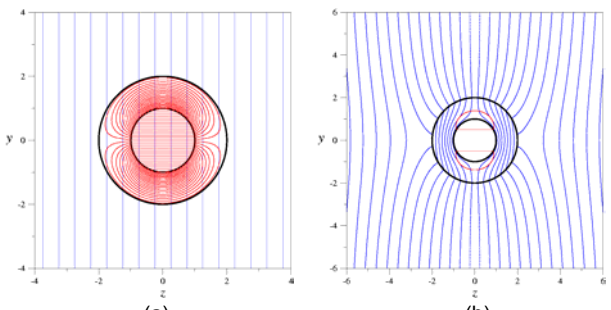

Fig. 2: Magnetic field lines and electric current distribution in a 2D MHD flow in a circular duct above the magnetic saturation field. (a) Non-ferritic wall (μ=1); (b) ferritic wall (μ=100).

If the magnetic field is below saturation range of the material (M_s) a non-linear regime evolves, which is expressed by curvilinear magnetic field lines inside the pipe. This effect is shown in figure 3. These curvilinear field lines yield velocity profiles, which differ from the well-known classical solutions.

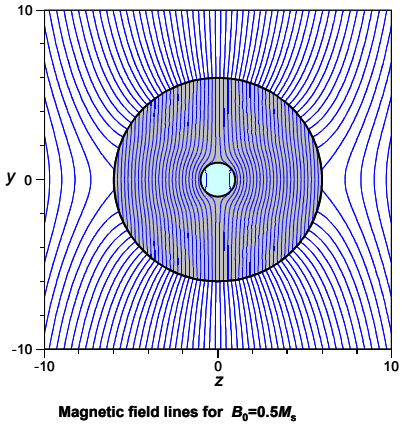

Fig. 3: Calculated magnetic field lines in a circular electrically conducting duct at half of the saturation field strength M_s

These curvilinear field lines yield velocity profiles, which differ from the well-known classical two-dimensional MHD- solutions. In figure 4 the velocity distribution of a fully developed MHD flow in a thick-walled electrically conducting duct at half of the saturation field strength is shown as a function of dimensionless distances z and y.

Here at the singularity points of the circular tube normal to the magnetic field B velocity jets evolve reaching values of 1.5 times more than the mean velocity v_0.

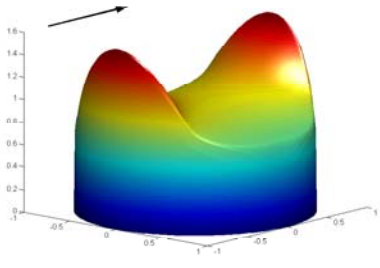

Fig. 4: Calculated velocity profile in a circular electrically conducting duct at half of the saturation field strength M_s for the experimental configuration lateron discussed.

All computational results yield the following pressure gradient results for the 2D MHD flow in a circular tube.

MHD flow in a electrically conducting thick walled duct

$$\nabla p = -\frac{\alpha^2}{1+\frac{\sigma}{\sigma_w}\frac{R^2+1}{R^2-1}} \quad \text{with } \alpha = -\frac{4}{\mu_r}\frac{R^2}{R^2-1} \; for \; \mu_r >> 1 \qquad (3)$$

MHD flow in an electrically insulating ferromagnetic duct.

$$\nabla p = -\frac{3\pi}{8Ha}\alpha \quad , \tag{4}$$

where Ha is the Hartmann number describing the ration of the electromagnetic forces versus viscous forces. Ha is given by the relation ship (5) with υ as the kinematic viscosity.

$$Ha = a\,B\sqrt{\frac{\sigma}{\rho\upsilon}}\,, \tag{5}$$

In fusion application the Hartmann number is usually of order $O(10^3\text{-}10^4)$.

Experimental results in MEKKA for MHD flow in ducts of circular shape

Three different test sections (two ferritic and one non ferritic, from left to right respectively on the figure 5) are mounted in the NaK loop of the Mekka facility.

The MHD flow in thick-walled ducts was examined in the other two test sections shown in figure 5. Here, pressure drop measurements between 5 positions along the flow direction will be performed.

The flow near the magnetic saturation (non-linear regime) is studied carefully in order to adjust the analytical and numerical models.

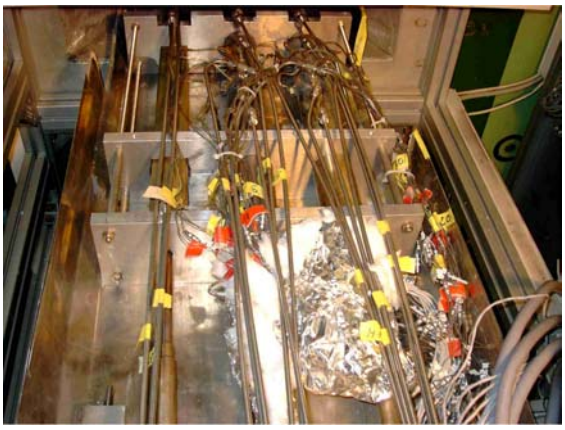

(a) (b) (c)

Fig. 5: Test sections being installed in the MEKKA-facility of the Forschungszentrum Karlsruhe. (a) Test section with electrical separation of liquid metal containing duct from rectangular shaped structure material. (b) ferromagnetic thick walled test section. (c) non-ferromagnetic stainless steel test section.

In order to compare all three test sections in terms of the pressure gradient we introduce a factor α_k which measures the effective magnetic field strength within the duct to the applied external magnetic field B_0 in the following form

$$\alpha_k = B_{eff} / B_0 \quad , \tag{6}$$

In principle the introduced coefficient α_k determines the pressure drop. α_k exhibits two asymptotes. One is for very strong magnetic fields for which the material reaches perfect saturation for $B_0/M_s >> 1$. In this regime we have $\mu_W \to 1$, $\alpha_k \to 1$ and classical solutions apply. For small magnetic fields α_k approaches very small values according to equation (3) and the pressure drop becomes very small. From these considerations we conclude, that if the magnetic field in the centre of the pipe is known by either measurements or calculations one can estimate the pressure drop with reasonable accuracy by standard relations. The experimentally found coefficient α_k, derived from the pressure drop measurements is compared to that predicted by the asymptotic analysis. For engineering applications the agreement is reasonable for all three cases.

In figure 6 the measured pressure gradient in terms of α_k is shown as a function of the ratio B_0/M_s.

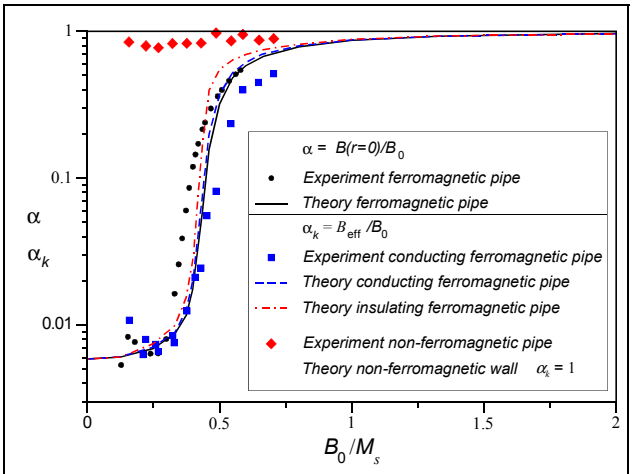

Fig. 6: Magnitude of the effective magnetic field α_k and α (representing a measure for pressure drop) inside the pipe depending B_0/M_s.

For most applications α_k is close to the field measured on the duct axis, scaled by the external field B_0. The value of α_k depends on the externally applied field especially in a region $0.4M_s<B_0<2M_s$. For stronger magnetic fields α_k approaches unity as $B_0>>M_s$. If the magnetic field is weaker, α_k approaches the value α_k obtained by the analytic solution for the linear problem and the pressure drop becomes very small and of the order of the hydrodynamic one.

A more detailed description of the numerical treatment of such MHD problems and a report on the experimental results may be taken from Bühler et al. [5]

MHD flow in expansions/contractions

In most of the fusion blanket geometries unsteady flow geometry changes with respect to the magnetic field appear. At these singularities free extremely thin shear layers often called Ludford layers appear carrying O(1) flow rates. These Ludford layers determine the flow distribution for several characteristic length a downstream. The tree-dimensional electric currents accompanied by the flow singularities lead to undesired additional pressure drops. Mostly these singularities are due to the restricted space in the blanket header unavoidable.

In order to study the quality and thickness of these Ludford layers in dependence of the magnetic field strength and the flow velocity a test module has been designed in which a sudden expansion/contraction of the order of 1:4 is realized in one direction, namely that of the magnetic field B_0. The test module will be fabricated of stainless steel plates of the thickness 3mm. The larger part of the module has the dimensions 100mmx 100mm, the smaller part 100mmx 25mm. Within the test rig simultaneously 2 velocity sensors consisting of 4 sensors can be

traversed. In addition to the velocity measurements pressure gradients as well as electric potentials on the ducts surface will be evaluated by means of pressure taps and potential probes.

The test module is licensed by the authorities and currently fabricated, it will be inserted in the NaK-loop of the MEKKA facility up to the end 2002. The traversing module is also fabricated. The design of the test module is depicted in the figures 7-9.

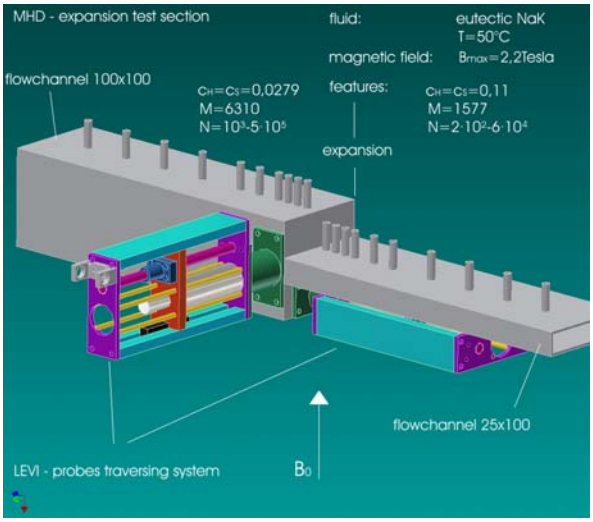

Fig. 7: MHD expansion/contraction test module designed and currently fabricated.

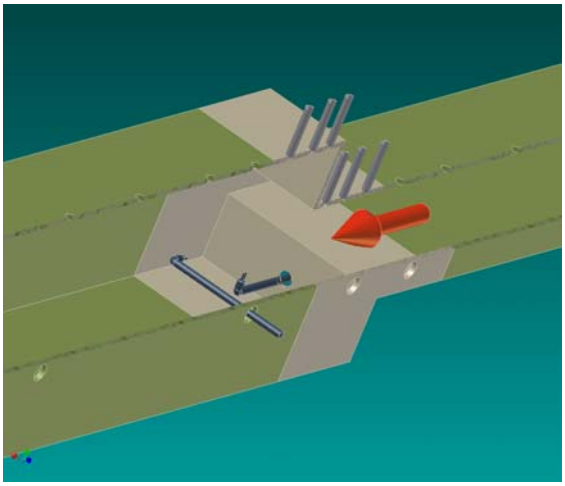

Fig. 8: Traversing capabilities of the LEVI-probes in the MHD expansion/contraction test module.

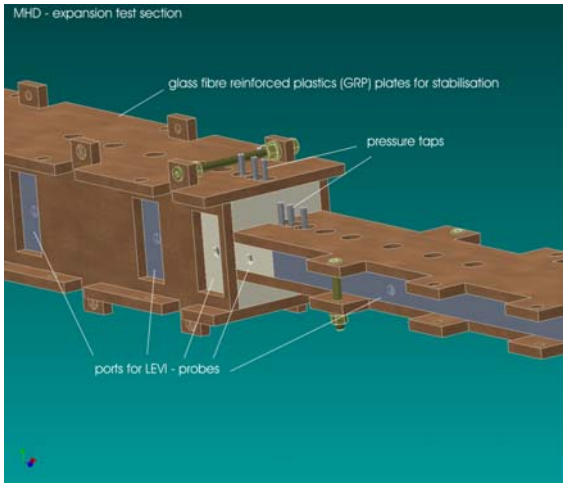

Fig. 9: Support structure and measurement ports in the MHD expansion/contraction test module.

Literature:

[1] Giancarli, L. et al. (1992), Water-cooled lithium-lead blanket design studies for DEMO reactor, Fusion Technology 21, 2081

[2] Fütterer, M.; Giancarli, L. (1996) Design Description Document for the European Water-Cooled Pb-17Li Blanket. DMT 96/349 SERMA/LCA/1911.

[3] Bühler, L. (1998) MHD-flows in thick-walled ducts, FZKA-6066.

[4] Bühler, L. (1998) Magnetohydrodynamic flows in thick walled ducts. Proceddings of 20th Symposium on Fusion Techn., Marseille, Sept. 7th-11th 1998.

[5] Bühler, L., Messadek, K., Stieglitz, R. (2002) MHD flow in thick walled pipes of ferro-magnetic and non-ferromagnetic material. Proc. 5th Int. Pamir Confererence. Vol. (1), p. 93-100.

Staff:

R. Stieglitz
E. Arbogast
L. Bühler
K. Messadek
F. Pfeffer
J. Reimann

Structural Materials Development

TTMS-001
Irradiation Programme

TTMS-001/05
HFR Irradiation Programme

The HFR Phase IIB programme is abbreviated SPICE (Sample Holder for Irradiation of Miniaturised Steel Specimens Simultaneously at Different Temperatures). It complements the former HFR irradiation programmes MANITU, SIENA, HFR Phase IA, and IB (cf. TTMS-001/14).

The objectives are to evaluate the mechanical properties of material samples after irradiation at doses of 15 dpa and different irradiation temperatures. The material used is the reduced activation alloy EUROFER 97 in different variations: different heat treatments, a HIP powder steel, and various boron contents to investigate the effect of He embrittlement. Heat treatments of the irradiated alloys are given in Tab. 1.

Table 1: Heat treatments of the irradiated alloys.

Alloy	Heat treatment
EUROFER 97, as delivered	980 °C + 760 °C
EUROFER 97	1040 °C + 760 °C
EOROF. ODS HIP powder steel	-
EUROFER 97, variations in B and 10B contents	1040 °C + 760 °C
F82H mod., reference steel	950 °C + 750 °C
GA3X, reference steel	1000 °C + 700 °C

The "quasi-saturation" of irradiation-induced embrittlement between 10 and 15 dpa, found for conventional steels in former programs (SIENA), will be investigated for the EUROFER alloys. The low irradiation temperature ranges of the High Flux Reactor will give a look at embrittlement effects increasing progressively with decreasing temperature in all bcc-alloys irradiated up to now.

Three different sample holders, each of them placed in a central core position of the High Flux Reactor at Petten, are being irradiated at 5 different temperature levels of 250/300/350/400/450°C. Post-irradiation examinations (PIE) will be carried out in the Fusion Materials Laboratory of FZK. Activation detectors in the sample holders and active thermocouple control of the liquid sodium cooling are additionally applied to ensure the high-quality level of HFR irradiations even at higher doses (Fig. 1). The design provides space for 130 charpy, 91 tensile, and (for the first time simultaneously) 160 fatigue specimens. As result, a full data set of the irradiation effects on Charpy impact, tensile, and fatigue behaviour will be obtained. During the irradiation phase, unirradiated reference samples are investigated. Regarding the EUROFER steel, an embrittlement behaviour comparable to the best alloys investigated in former irradiation programmes is expected, accompanied by good mechanical properties. The higher irradiation dose of 15-dpa will represent a step towards fusion-relevant doses.

Mechanical preparations, sample holder fabrication, and sodium filling were finished in July 2001. Neutron irradiation has started in August 2001, the target dose of 15 dpa will be reached by October 2003. At the moment, an accumulated dose of 8 dpa is reached in irradiation capsule cycle 14, cf. Fig. 2. The irradiation programme is running according to schedule, active temperature control by sodium – used for the first time - is providing very constant temperature ranges in the different levels of the sample holders. After dismantling, transportation, and decontamination, the PIE will start in mid-2004. Examination will be completed by mid-2006.

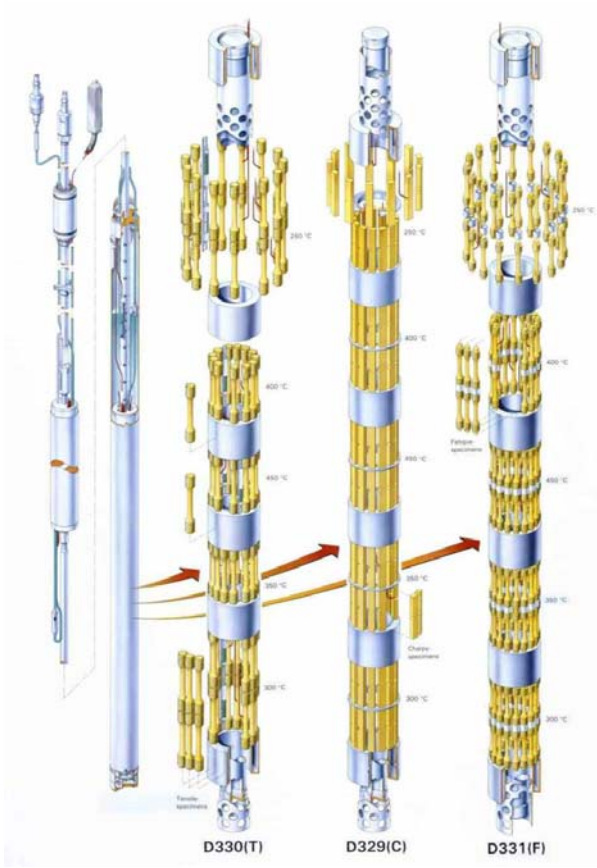

Fig. 1: Irradiation capsule with sample holders. D330: 91 tensile specimens; D329: 130 charpy specimens; D331: 160 fatigue specimens.

Staff:

J. Aktaa
B. Dafferner
H.-C. Schneider

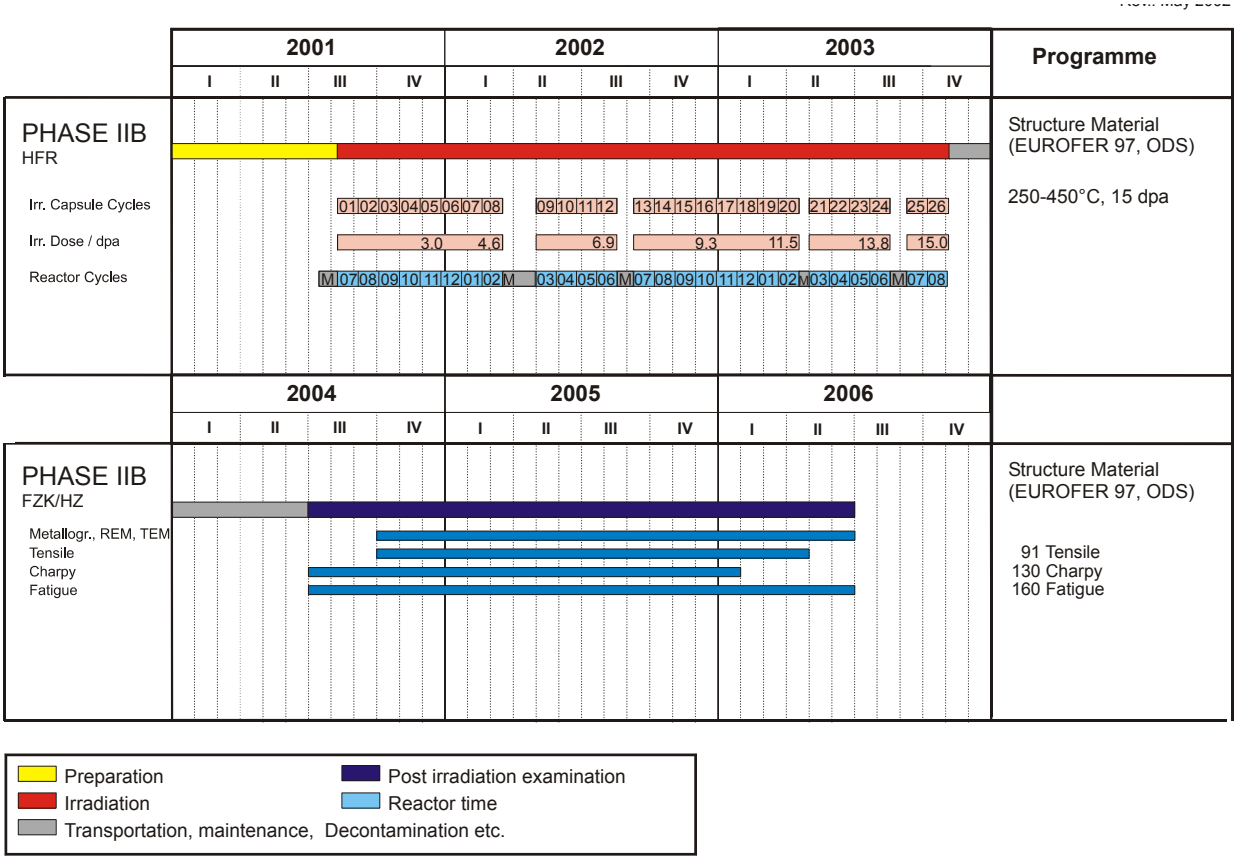

Fig. 2: SPICE Irradiation Programme - Time Schedule for Irradiations and Post Irradiations Examinations

TTMS-001/9
Fast Reactor Irradiations

1. Objectives

In an energy generating fusion reactor structural materials will be exposed to very high levels of irradiation damage of about 100 dpa. Due to the fact, that fast reactor irradiation facilities in Europe are not available anymore, a cooperation with the Russian institution: State Scientific Centre of Russian Federation Research Institute of Atomic Reactors (SSC RF RIAR) has been implemented.

2. The irradiation project ARBOR 1

In the irradiation project "ARBOR 1" (for Associated Reactor Irradiation in BOR 60) 150 mini-tensile/low cycle fatigue specimens and 150 mini-charpy (KLST) specimens of different reduced activation ferritic/martensitic (RAF/M) steels are under irradiation in a special designed irradiation rig of the BOR 60 at a temperature lower than 340°C since 22 November 2000. The irradiation started in the core position D-23, where temperature measurement is possible and is being continued in an identical position G-23 of the 5th row of BOR 60 core until 30 dpa will be reached.

The irradiation rig is instrumented with neutron monitors in the central tube and on three of ten levels of specimen positions as well as with three temperature detectors also on three of ten levels.

3. Specimens and materials

For tensile and low cycle fatigue testing a small size cylindrical specimen has been developed and for charpy testing the KLST specimen was selected. Tensile, low cycle fatigue and charpy specimens of the following materials are under irradiation: The European RAF/M heat EUROFER 97 is included in two annealing conditions. EUROF 1: EUROFER 97 (as received: 980°C 31 min/air cooled + 760°C 90 min/ air cooled), EUROF 2: EUROFER 97 (1040°C 31 min/ air cooled + 760°C 90 min/ air cooled). Whereas EUROF 1 is optimised for good fatigue resistance and EUROF 2 for good charpy ductile to brittle behavior. The Japanese RAF/M steel F82H mod. is implemented as international reference steel: F82H mod. (as received: 1040°C 38 min/ air cooled + 750°C 2h/ air cooled). The German development OPTIFER IVc (OPT IVc: 950°C 30 min/ air cooled + 750°C 2h/ air cooled, is included as reference material to be compared to data from the HFR-irradiation. The following three materials ADS 2, ADS 3 and ADS 4, based on EUROFER 97, are experimental heats to study the He influence on RAF/M-steels. ADS 2 is an EUROFER 97-steel with 82 wppm nat. B (1040°C 31 min/ air cooled + 760°C 90 min/ air cooled), ADS 3 an EUROFER 97-steel with 83 wppm B10 (1040°C 31 min/ air cooled + 760°C 90 min/ air cooled) and ADS 4 an EUROFER 97-steel with 1160 wppm B10 (1040°C 31 min/ air cooled + 760°C 90 min/ air cooled).

The real feature of this ARBOR irradiation is the implementation of specimens of mechanically alloyed EUROFER 97 with 0,5% Y_2O_3 as the recent development of higher heat resistant RAF/M-steels. The specimen denomination is EURODShip: as received: 980°C 31 min/ air cooled + 760°C 90 min/ air cooled.

The NRG, Petten, contribution covers technological questions with a British Steel batch of EUROFER 97, called BS-EUROF: as received: 1050°C 60 min/ air cooled + 760°C 120 min/ air cooled, as reference material for electron beam welded EUROFER 97, called EUROF-EB: as received: 980°C 31 min/ air cooled + 760°C 90 min/ air cooled, then EB welded with a post weld heat treatment at 730°C 120 min/ air cooled.

4. State of the art of ARBOR 1

At the end of the 4th reactor cycle (7 August 2002) a damage dose of 26.6 dpa has been reached at middle position of the rig. As final date for the 30 dpa level is foreseen October 2002. Than the rig will be unloaded and 50 % of the specimen will be tested in post irradiation experiments (PIE) in the hot cells of SSC RF RIAR beginning in 2003.

The other half of the specimens will be reloaded into the ARBOR 2 rig where they shall reach an irradiation damage of 70 dpa together with Fusion relevant specimens from the ALTAIR 1 rig of CEA, Saclay, and new specimens from FZK and CEA to reach 40 dpa. The new samples are in the manufacturing process.

5. Preparation of testing facilities for PIE

As it was agreed in an Annex of the ARBOR 1 contract, the mechanical PIE will be performed in the hot cells of SSC RF RIAR. For this reason a used but modernized LCF-testing facility and a new charpy testing facility had been ordered to be contributed to SSC RF RIAR after delivery and functional control at FZK. The LCF-testing facility will be ready end of October 2002 and the functional control of the charpy tester is foreseen at the beginning of November 2002. Than the packing and transport to Russia is planned for the end of 2002. To reach custom and tax free transport conditions it is planned to perform the PIE under an ISTC partner contract.

Staff:

C. Petersen
D. Rodrian

Literature:

C. Petersen, V. Shamardin, A. Fedoseev, G. Shimansky, V. Efimov and J.W. Rensman: "The ARBOR irradiation project", to be published in Journal of Nuclear Materials (in press).

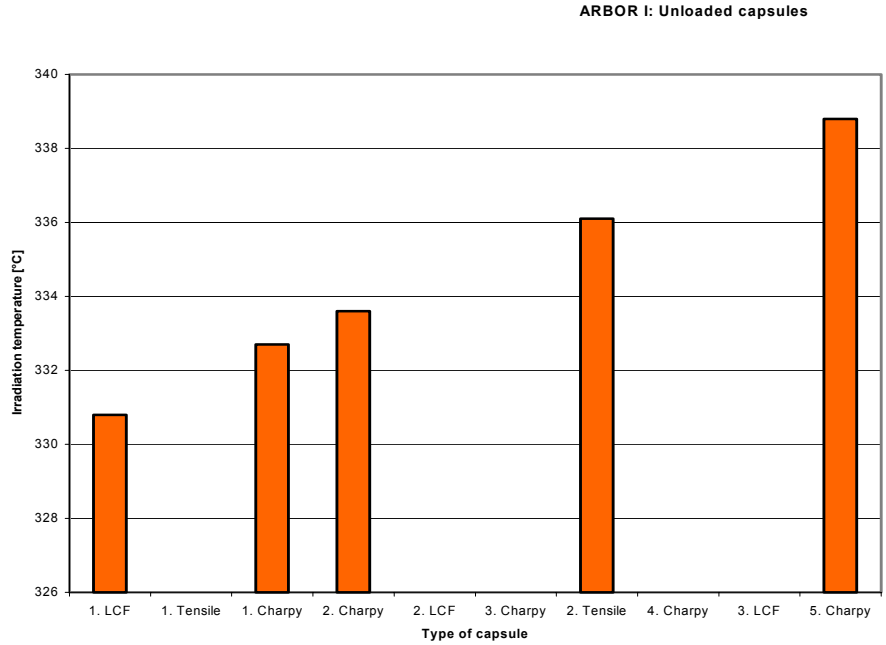

Fig. 1a

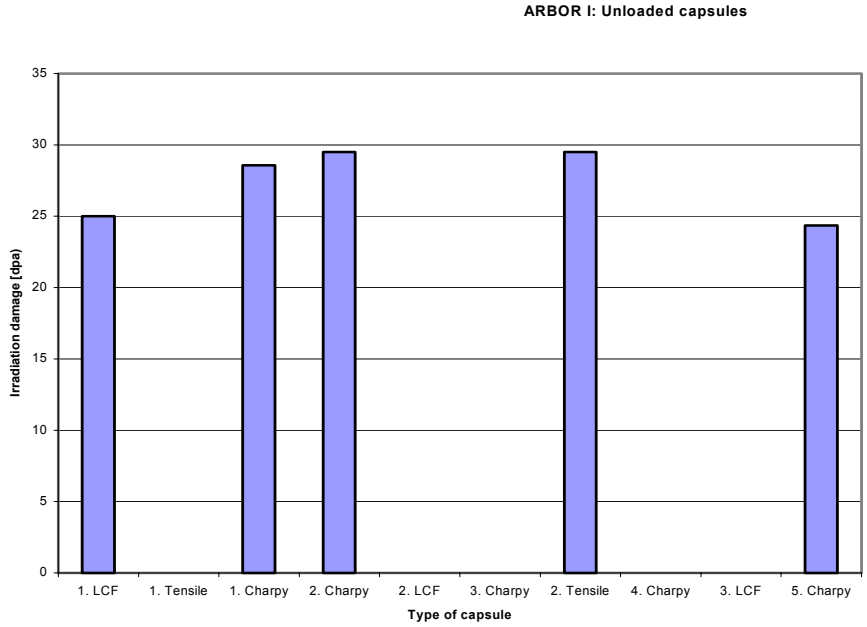

Fig. 1b

Fig. 1: ARBOR 1 rig unloading scheme, whereas each column contains 30 specimens of the indicated kind: a) Irradiation temperature profile vs. capsule type and b) irradiation damage profile vs. capsule type. (These are calculated values)

.

TTMS-001/10
Helium in RAFM steels: Comparison between TEM and SANS

In agreement with earlier investigations at FZK, the crucial impact of helium on strength, ductility reduction and embrittlement increase has been again confirmed by several recent international investigations. However, a detailed and statistically meaningful analysis of He bubble size and density distribution is hardly possible by using only transmission electron microscopy (TEM). Therefore, TEM is being combined with small angle neutron scattering (SANS) in order to get full information not only on bubbles below a diameter of about 1-2 nm that are hardly visible in TEM, but also to get sufficiently good statistics on He bubble morphology. This investigation will present results of a study, carried out using TEM and SANS, to investigate the growth of He-bubbles in 7-9%CrWVTa RAFM steels. Samples with standard heat treatments have been homogeneously implanted with 400 appm He at 250 °C, using the 104 MeV α-particle beam of the cyclotron facility at FZ-Karlsruhe. In order to obtain information on He-bubble growth as a function of the temperature, after irradiation/implantation the samples were submitted to 2h thermal annealing (at 525°C, 825°C, 975°C) in high vacuum, together with non-irradiated reference samples. For the case of as-implanted samples, the thermal reference was provided by a sample of the same material submitted to thermal annealing at 250°C for a time equivalent to the irradiation time. The SANS experiments were carried out in collaboration with ENEA Frascati using the D11 and D22 instruments at the High Flux Reactor of ILL-Grenoble.

The as-implanted F82H samples with 400 appm He show in the TEM analysis an almost homogeneous distribution of very small helium bubbles with typical diameters around 1-2 nm, practically at the TEM resolution limit. This is completely consistent with SANS investigations that revealed a pronounced maximum between 0.6-2 nm for as-implanted samples. After isochronal annealing at 525 and 825 °C, according to TEM investigations, the average bubble diameters are 2-3 nm and 3-5 nm, respectively. This is consistent with the He-bubble volume distribution functions derived from SANS.

However annealing at 975 °C, that is above the $\alpha \rightarrow \gamma$ transition temperature, shows in the TEM analysis a very broad range of large bubbles ranging from less than 3nm to 25 nm with unusual distribution function. After annealing at 975 °C SANS reveals with a very high confidence a bimodal bubble distribution with a well defined peak below 1 nm and a secondary distribution of bubbles one order of magnitude larger. This fraction of very small He bubbles peaked at a bubble diameter of about 0.4 nm is not visible in the TEM. However from the present initial analysis is seems that the high intensity of these small He bubbles or clusters might play an important role in the bubble coarsening mechanism above the $\alpha \rightarrow \gamma$ transition temperature. Whether in the fcc lattice above 880-920 °C the bubbles dissolve and form larger ones or migrate and coalesce, or coarsen by an other mechanism, needs to be further clarified. In any case, as substantial bubble growth in short time does not appear before annealing beyond the $\alpha \rightarrow \gamma$ transition temperature, any temperature excursions beyond 880-920 °C of RAFM steels containing helium should be avoided. Not only substantial swelling would occur in the fcc phase but also long range migration of helium and substantial bubble formation at grain boundaries which in turn would lead to high temperature helium embrittlement already well known in austenitic steels.

Fig. 1: TEM micrograph showing the He bubble distribution after implantation of 400 appm He at 250 °C and subsequent annealing at 525 °C/2h (top), and 975 °C/2h (bottom), respectively.

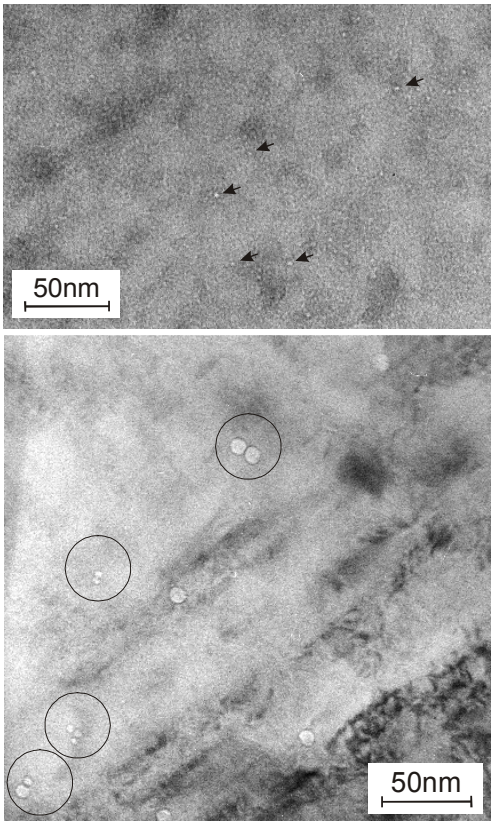

Fig. 2: He-bubble size distribution from TEM analysis; please note that bubbles below ~1 nm are not visible in TEM.

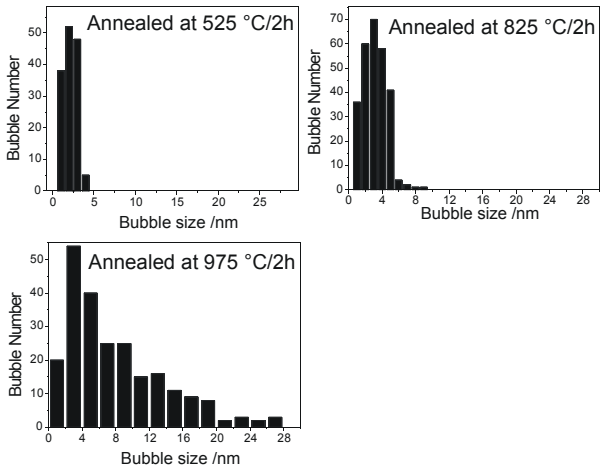

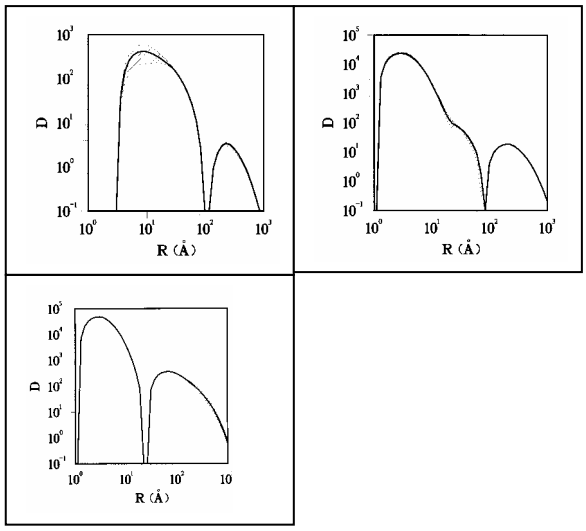

Fig. 3: He-bubble size distribution from SANS analysis after annealing at 525 °C/2h (top left), at 825 °C/2h(top right), and at 975 °C/2h (bottom left).

Conclusion:

Below the $\alpha \rightarrow \gamma$ transition temperature A_{c1e} (880-920 °C) TEM and SANS results are completely in agreement.

Above A_{c1e} a significant increase in bubble size is observed. SANS reveals a pronounced bimodal distribution.

$\rightarrow$The impact of He-bubble evolution above A_{c1e} on embrittlement (joining, temperature excursions) is made obvious with these initial results, but further investigations are needed to quantify in more detail also the relation between embrittlement, bubble stability and morphology after controlled annealing or after temperature excursions.

Staff:

G. Bürkle
P. Graf
R. Lindau
M. Klimiankou
Mrs. E. Materna-Morris
A. Möslang
D. Preininger
H. Zimmermann

Literature:

[1] R. Coppola, M. Klimiankou, E. Materna-Morris, A. Möslang, M.Valli; Helium bubble morphology in RAFM steels – correlation between SANS and TEM; IEA Modelling workshop 30 Sept-4 Oct 2002, Les Diablerets; Switzerland; to appear in Journ Nucl. Mater.

TTMS-001/14
PIE on Microstructure and Fracture Mechanics

The HFR Phase IB irradiation programme complements the former MANITU and HFR Phase IA investigations on promising reduced-activation ferritic/martensitic steels (RAFM). Post-irradiation examinations (PIE, Charpy and tensile tests) of RAFM steels are performed after irradiation in the HFR Petten up to 2.4 dpa at temperatures of 250/300/350/400/450°C (irradiation experiment HFR Phase Ib). The materials investigated are RAFM steels (OPTIFER V-VII, F82H mod., JLF1) subjected to different heat treatments and F82H mod. weldings (EB and TIG). To provide early information on generic issues of the effect of the powder HIP process on impact properties after irradiation, samples of F82H mod. HIP powder steel (trial material from the Japanese reference steel) are tested as well.

Tensile Tests

Tensile specimens were manufactured from the OPTIFER V-VII alloys, the Japanese steel F82H mod., and F82H mod HIP (ODS steel). The chemical compositions are given in Tab. 1 and the heat treatments of the alloys in Tab. 2. The tensile tests were carried out in the Fusion Materials Laboratory of Forschungszentrum Karlsruhe.

Table 2: Heat treatments of the irradiated alloys – tensile specimens.

Alloy	Heat treatment
OPTIFER V	1040 °C + 750 °C
OPTIFER VI	1040 °C + 750 °C
OPTIFER VII	1040 °C + 750 °C
F82H mod.	950 °C + 750 °C
F82H mod.HIP	As received

The unirradiated tensile specimens were tested at room temperature and 450 °C, whereas the irradiated specimens were tested at their irradiation temperature. The maximum yield strength $R_{p0.2}$ of all irradiated alloys could be determined at an irradiation temperature and test temperature of 300 °C (Fig. 1), the; corresponding tensile strength R_m is shown in Fig. 2. This behavior was also observed in former irradiation programs. In conformity with these former results, maximum hardening always occurred at around 300 °C. For F82H mod. and F82H mod. HIP, however, the yield strength $R_{p0.2}$ had the same value or was lower than the tensile strength Rm after the irradiation at 250 and 300 °C. As expected, total elongation exhibited a nearly contrary development: At the highest strength, the lowest elongation could be measured (Fig. 3).

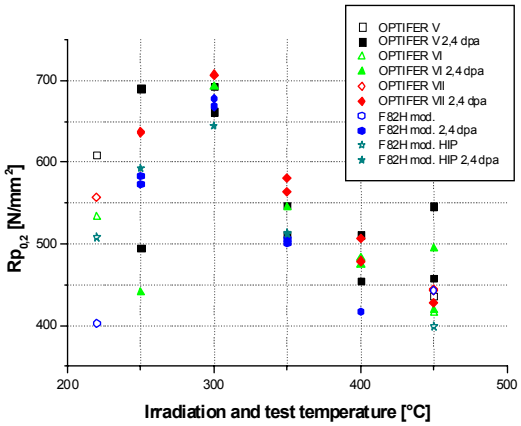

Fig. 1: Yield strength $R_{p0.2}$.

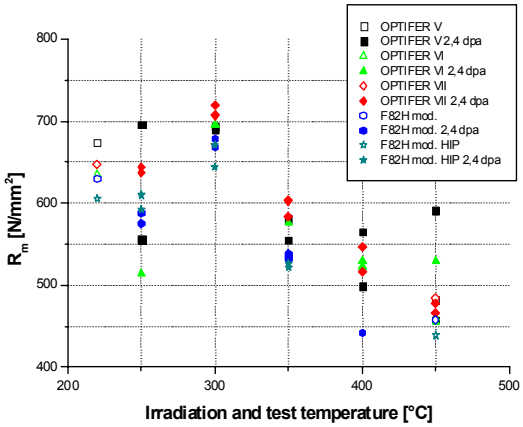

Fig. 2: Tensile strength R_m.

Table 1: Chemical composition of the irradiated alloys.

Alloy	Cr	C	Mn	V	Ta	W	Ge	P	S	B	N	O	Ce	Nb
	In wt.% →							In ppm →						
OPTIFER V	9,48	0.12	0.39	0,25	0.06	0.99	-	35	25	2	225	60	<100	
OPTIFER VI	9,35	0.13	0.61	0.28	0.08	0.005	0.4	43	30	2	250	160	<100	
OPTIFER VII	8.38	0.09	0.37	0.21	0.07	1.03	-	36	25	2	263	170	<100	
F82H mod. and F82H mod.HIP	7.68	0.09	0.16	0.16	0.02	2.17	-	20	10-20	2	60-80			1

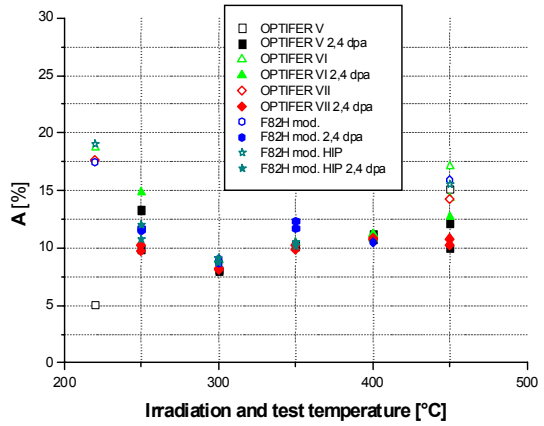

Fig. 3: Total elongation.

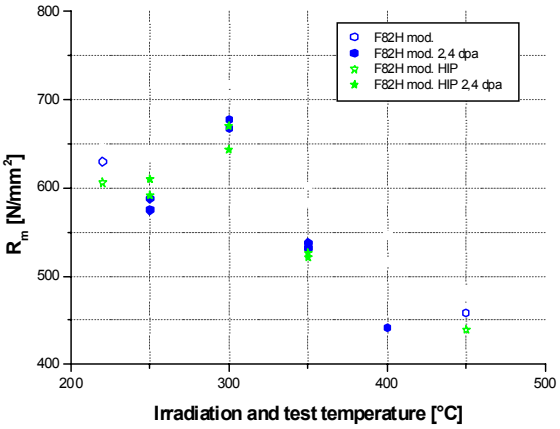

Fig. 4: Tensile strength R_m.

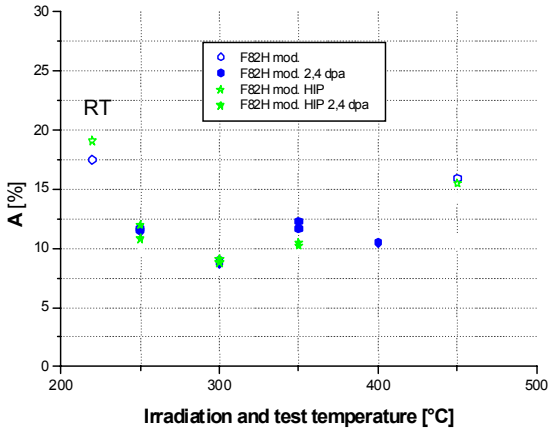

Fig. 5: Total elongation.

It is remarkable that the results of the tensile tests of F82H mod. and HIP did not reveal any clear difference in the material behavior after irradiation (Figs. 4, 5).

The next step will be further investigations of the fracture surfaces and microstructures to understand the mechanical behavior. Detailed information is required to understand the material strengthening at 300 °C. In former alloys, irradiation-induced development of He-bubbles, loops, and small precipitates could be found. The future investigation will give an explanation of the chemical change in the alloys and their irradiation-induced change in the structure of the material.

Impact Tests

KLST charpy subsize specimens (3x4x27 mm) are subjected to instrumented PIE (Charpy tests). As a result, force-deflection curves are obtained, the further evaluation of which yielded the impact energy, dynamic yield stress, ductile to brittle transition temperature (DBTT), and upper shelf energy (USE). Decontamination and testing of the HFR-IB-specimens were continued in the reported period.

The major aim of the impact test matrix is to define the influence of the alloys heat treatment, especially lower austenitization temperatures, and the effect of strongly reduced boron contents on the embrittlement behavior. Chemical composition of the investigated alloys is given in Tab. 1. The heat treatment is comparable to that of the tensile specimens with higher austenitization temperatures being applied in addition (cf. Tab. 3). The OPTIFER V alloy – providing outstandingly good results – is very similar to the EUROFER 97 which became available only after the irradiations.

Table 3 Heat treatments of the irradiated alloys – impact specimens

Alloy	Heat treatment
OPTIFER V	1040 °C + 750 °C
OPTIFER V*	950 °C + 780 °C
OPTIFER VI	1040 °C + 750 °C
OPTIFER VI*	950 °C + 780 °C
OPTIFER VII	1040 °C + 750 °C
OPTIFER VII*	950 °C + 780 °C
F82H mod.	950 °C + 780 °C

High upper shelf energy is found for all RAFMs at all temperatures (Fig. 6). Compared to earlier investigations, OPTIFER steels and F82H mod. are significantly better than the reference steels F82H and ORNL 3971. All materials show irradiation hardening which decreases with higher irradiation temperatures.

At low irradiation temperatures, worsening of the ductile-to-brittle transition temperature is significantly reduced (Fig. 7). OPTIFER-V, -VI, and -VII steels are in the range of the best RAFMs formerly investigated and even better than the F82H mod. steel.

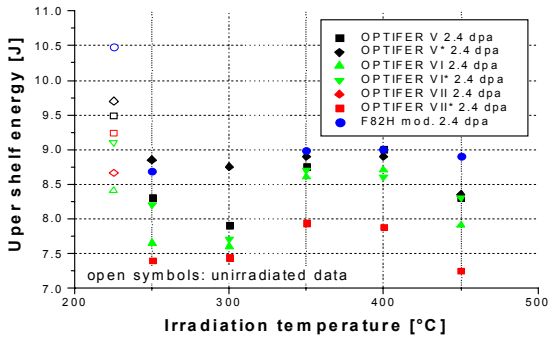

Fig. 6: Upper shelf energy.

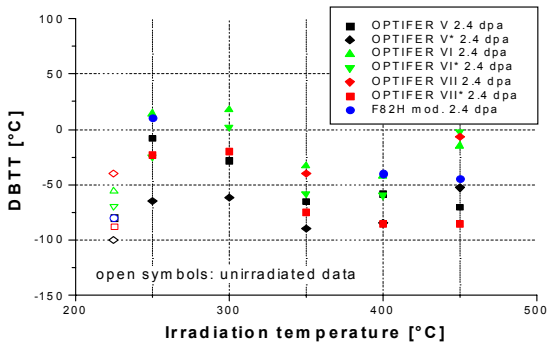

Fig. 7: Ductile-to-brittle-transition-temperature (DBTT).

The influence of the heat treatment is not affected by irradiation: Both heat treatments of the OPTIFER alloys show approximately the same shift in USE and DBTT. As can be seen in Fig. 8, the influence of the changed austenitization temperature on the DBTT is even higher than the influence of irradiation.

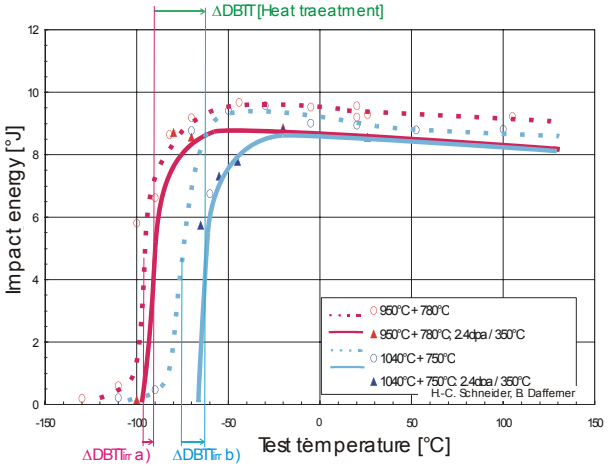

Fig. 8: Influence of heat treatment and irradiation (OPTIFER-V, 2.4 dpa, 350°C).

In comparison with the tensile results, the USE nicely corresponds to total elongation (Figs. 6 and 3) as well as the DBTT to the tensile strength (Figs. 7 and 2). The highest loss in USE and the maximum shift in DBTT as indicators of the embrittlement are found at an irradiation temperature of 300°C – as was maximum hardening for the tensile results. After the remaining impact results will have been obtained, a more detailed comparison and analysis of tensile and impact results will be accomplished.

For the ongoing investigations, results of EB and TIG weldings with F82H mod. and of diffusion weldings with MANET-II are expected together with a characterization of the F82Hmod HIP base material and the influence of the notch root.

Staff:

J. Aktaa
B. Dafferner
P. Graf
M. Holzer
M. Klimiankou
W. Kunisch
E. Materna-Morris
A. Möslang
B. Neufang
H. Ries
R. Rolli
O. Romer
H.-C. Schneider
H. Zimmermann

Literature:

E. Materna-Morris, H.-C. Schneider, B. Dafferner, R. Rolli, and O. Romer: Irradiation Influences on Mechanical Properties and Structures of Martensitic Low-Activation Alloys. 10th Int. Conf. On Fusion Reactor Materials, October 14 – 19, 2001 Baden-Baden, Germany.

H.-C. Schneider, B. Dafferner, J. Aktaa: Embrittlement Behaviour of OPTIFER Low-Activation Alloys after Neutron Irradiation. 10th Int. Conf. On Fusion Reactor Materials, October 14 – 19, 2001 Baden-Baden, Germany.

TTMS-001/16
Modelling and Analysis of Irradiation Effects on Strength, Tensile Ductility and Impact Behaviour of RAFM and ODS- RAFM Steels

The effect of particle strengthening on work-hardening, tensile ductility (uniform and fracture strain) and impact behaviour (DBTT, USE) of ferritic-martensitic ODS (9-13)CrWVTa(Ti) RAFM steels have been modelled and compared with experimental results including high nitrogen (≤0.2wt.%) martensitic 9-12Cr steels, strengthened by fine nitride precipitates [1,2]. Particularly, the influences of particle morphology parameters as the volume content f_v and mean sizes d_p of fine Y_2O_3 particles and nitrides in connection with a superimposed irradiation-induced defect hardening are considered. The obtained partly complex analytic microstructure-property relations are especially useful for microstructural optimisation and development of ductile ODS (9-13)Cr steels for unirradiated and irradiated conditions.

Besides, also the superimposed effect of displacement damage dpa and helium generation via the $^{10}B(n,\alpha)^7Li$ transmutation on strength, tensile ductility and Charpy impact behaviour have been modelled [3-6] and analysed for various boron alloyed 7-9CrW(Ge)VTa - RAFM and conventional 9-12CrMoVNb steels, irradiated at 250-475°C to 0.8-15 dpa. Based on these and literature data, the RAFM irradiation behaviour has been extrapolated to fusion relevant high doses ≤100 dpa and helium contents, where measurements are still absent. A summarising report [4] considers this irradiation behaviour generally for 7-12Cr steels in dependence of irradiation temperature, helium content and defect generation rate. For low irradiation temperatures 70-300°C, irradiation strengthening and tensile ductility as well as impact properties vary with different strengths logarithmically without any saturation tendency below ≈50 dpa. At higher irradiation temperatures 350-475°C, a distinct saturation behaviour of all considered mechanical properties is predicted as indeed observed below ≤25 dpa. The saturation values strongly depend on irradiation temperature but also on defect generation rate, He/dpa ratio and sink strengths of formed irradiation defects (He-bubbles, precipitates). In boron-doped, neutron-irradiated 7-12Cr steels, helium generates strongly localised within and around coarser $M_{23}(B,C)_6$ boroncarbides due to their strong enrichment of boron, replacing carbon atoms [3]. He-bubble/clusters formed at the boroncarbide interfaces promote their interfacial decohesion, which at least decreases the ductile fracture stress at higher He(^{10}B) contents, more pronounced around mean irradiation equal test temperatures of $T_I \cong 300$°C. By the same process, the upper shelf energy USE of Charpy test strongly decreases particularly for 9-12CrMoVNb steels showing higher irradiation strengthening and, thus, also higher ductile-to-brittle transition temperatures (DBTT) values. The irradiation-induced shifts of DBTT, $V=\Delta DBTT/DBTT_o$ and USE, $U=\Delta USE/USE_o$, normalised to their initial values correlate and mainly depend on irradiation defect strengthening and changes of ductile fracture stresses in the case of USE, but also weaker by reductions of dynamic fracture stresses at higher irradiation temperatures $T_I=T_T=350$-475°C for DBTT. The ductile fracture stress changes are more pronounced for conventional 10-12CrMoVNb compared to 7-9CrW(Ge)VTa steels and clearly related to chemical composition as Cr, N, C and B content. Fig. 1 demonstrates the different behaviour of 7-9CrWVTa and 10-12CrMoVNb steels by the shown influence of nitrogen alloying (18-600 ppm wt.) on the initial $DBTT_o$ value of unirradiated material together with their maximum irradiation-induced embrittlement shifts V_{max}, obtained at $T_I=T_T=250$°C for 2.4 dpa (HFR). While $DBTT_o$ of 10-12CrMoVNb steels increases with increasing nitrogen content and N/B ratio, for 7-9CrWVTa steels it decreases weakly or remains constant. Shifts of V_{max} otherwise decrease by heavy N-alloying. The measured dynamic yield strength of both steels groups shows qualitatively the same behaviour. It indicates, that irradiation defect strengthening causes mainly the irradiation-induced DBTT increase, particularly for lower $T_I \leq 350$°C [5]. Helium, however, contribute to an additional DBTT shift only weakly via a weak increase of thermal strengthening at low $T_I<300$°C. The irradiation-induced degradation of fracture strain and impact energy USE otherwise is caused by irradiation strengthening in connection with the pronounced He-induced decrease of the ductile fracture stress at higher He(10B)-content and TI=200-400°C.

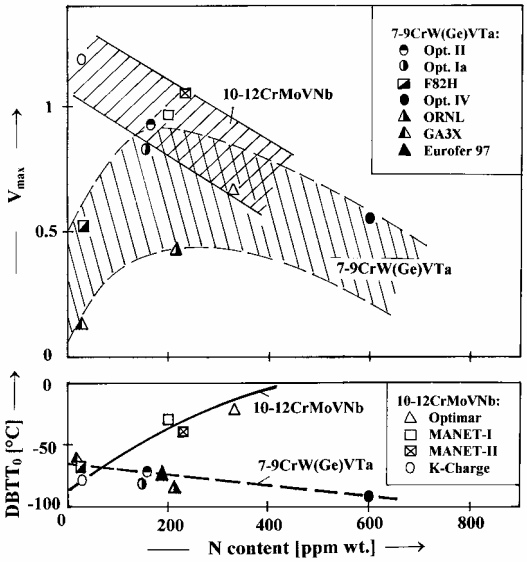

Fig. 1: Effect of nitrogen content on DBTT0 of various unirradiated 7-12Cr steels and their maximum irradiation-induced DBTT shifts Vmax for TI=250°C, 2.4 dpa (HFR).

The predictions regarding the influence of particles on strength, work-hardening, tensile ductility and impact behaviour basically describe the observations on various ODS (9-13)CrWVTa (Ti) steels containing 0.1-0.5wt.%Y_2O_3, as ODS-Eurofer 97 [1]. These particle strengthened ferritic-martensitic ODS steels analogous to high nitrogen martensitic 9-13Cr steels show particularly at high yield strengths larger uniform ductilities but lower fracture strain and impact energy USE values. Localised deformation at higher temperatures ≥300°C, induced by inhomogeneous particle distribution due to the mechanical alloying process decreases further fracture strain and also impact energy USE via reduction of the ductile fracture stress due to coarse slip band formations. With increasing particle strengthening, as Fig. 2 for ODS-Eurofer 97 shows, the normalised ultimate tensile to yield strength ratio $\eta_v=\sigma_{uts,n}/\sigma_y$ - which according to model results is unequivocal related to uniform ductility [2] - increases by particle strengthening for both unirradiated and strong irradiation hardened condition at lower $T_I \leq 300$°C. An optimum particle strengthening $\Delta\sigma_p^*$ around the maximum appears at mean values of $\Delta\sigma_p^*=530$-767 MPa, $\Delta\sigma_p^*/\sigma_o \approx 0.5$-0.6 corresponding to mean optimum particle sizes of $d_p^*=13$-22 nm for unirradiated ODS- Eurofer 97 [2]. With increasing particle volume content, the optimum uniform ductility increases together with corresponding optimum particle strengthening and particle size. By irradiation strengthening up to the expected maximum of about $\Delta\sigma_i \approx 600$ MPa [5] for lower $T_I \leq 300$°C, uniform ductility and η_v generally decrease, whereby the optimum particle strengthening distinctly shifts to higher values $\Delta\sigma_p^*=1760$-2030 MPa well behind the ductile fracture stress, corresponding to smaller optimum particle sizes $d_p^*=3.1$-

6 nm. The ductility maximum, however, distinctly levels off with increasing irradiation strengthening. It demonstrates, that for strong irradiated ODS steels a high strengthened fully martensitic structure with very small particles ≥6 nm as observed in Ti- alloyed Y_2O_3- particle strengthened ODS RAFM steels are more useful for improvement of uniform ductility. These small particles themselves might additionally reduce irradiation strengthening by absorbing atomic irradiation defects, which improves further uniform ductility.

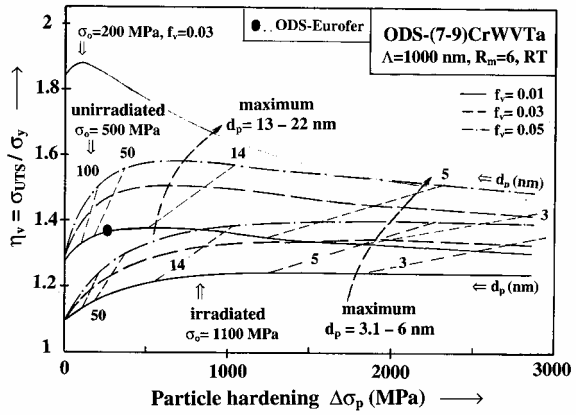

Fig. 2: Effect of particle strengthening, volume content and particle size on uniform ductility and parameter $\eta_v = \sigma_{uts,n}/\sigma_y$ increase of ODS-Eurofer 97 in unirradiated and high irradiation strengthened state - Comparison of model predictions with results.

Contrary to uniform ductility, fracture strain and also impact energy USE decrease mainly due to enhanced work-hardening by the operating Orowan process. As shown in Fig. 3 by the comparison of predictions with experimental observations for irradiation strengthened (T_I=T_T=300°C) and Y_2O_3-particle hardened ferritic and ferritic-martensitic ODS (9-13)Cr steels, the reduction in area at fracture A_f for T_T=RT, similar as the impact energy USE strongly reduce with increasing strengthening and are particularly lower in the case of strong work-hardened ODS steels. Additionally, particle strengthening reduces the strength-induced degree of A_f. At higher particle, matrix and irradiation strengthening $\sigma_{y,total}=\sigma_L$, the increase in uniform ductility becomes generally limited by the condition $\varepsilon_u \geq \varepsilon_f$, where fracture strain becomes lower than uniform strain. This upper yield strength limit σ_L increases with increasing ductile fracture stress but decreases by particle strengthening. Fig. 3 additionally shows the deduced ductile fracture stresses by fitted experimental results. Whereas at high strengths ductile fracture occurs stress-induced at constant fracture stress, it decreases to lower strengths, corresponding to larger achieved strains. Thus, at lower strengths, ductile fracture becomes primarily damage controlled by strain-induced microcrack formation with their coalescence, which reduces ductile fracture stress.

Whereas the particle strengthening-induced DBTT shifts V of ODS-steels are comparable to that observed by irradiation defect strengthening at T_I=T_T=250/300°C, the corresponding impact energy decreases U are quite stronger. In accordance to predictions, this results again mainly by the particle-induced enhancement of work-hardening, which decreases both tensile fracture strain and impact energy, more pronounced for the ODS steels with the weaker strengthened ferritic structure and higher temperatures (DBTT). Further studies are in progress for structural optimisation of ODS RAFM steels by metallurgical processes including irradiation effects.

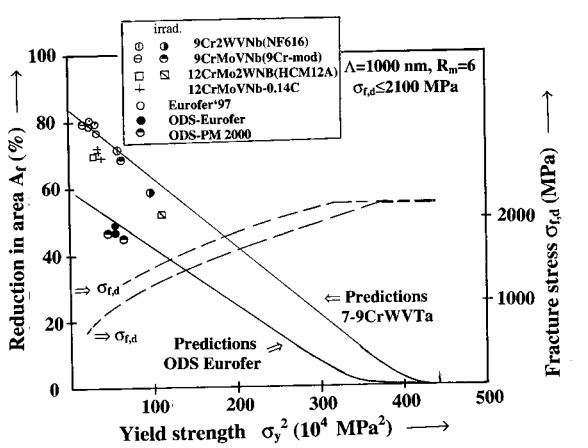

Fig. 3: Comparison of model prediction with the strength-induced degree of fracture strain A_f vs. σ_y^2, obtained for irradiation strengthened 7-12Cr (T_I=T_T=300°C, 2.4-3 dpa, HFR) and ODS (9-13)Cr steels. Indicated are also the deduced ductile fracture stresses.

Staff:

D. Preininger

Literature:

[1] D. Preininger, Modelling of the effect of precipitates on work-hardening, ductility and impact behaviour of ferritic-martensitic Cr steels, ICFRM-10, appears in the Conference Proceedings (J. Nucl. Mater.).

[2] D. Preininger, Modelling of Strength, Ductility and Impact Behaviour of ODS ferritic-martensitic 7-13 Cr steels. Materials Week`2002, 30. Sept.-2.Oct. 2002, München, abstract in http\\www.materialsweek.org.

[3] D. Preininger, Mechanism of boron alloying on mechanical behaviour of low-alloyed ferritic-martensitic Cr steels Materials Week`2002, Oct. 2001, München, Conference Proceedings, CD-ROM, March 2002.

[4] D. Preininger, Irradiation dose and helium effects upon strength, tensile ductility and impact behaviour of boron-doped martensitic 7-12Cr steels. Internal report to be published in J. Nucl. Mater.

[5] D. Preininger, Modelling of the irradiation damage and helium effects on strength, ductility and impact properties of 7-12 Cr steels. Conference Proceedings of the EUROMAT`2001, CD- ROM, January 2002.

[6] D. Preininger, Mechanism of the effect of helium on tensile ductility and impact behaviour of ferritic-martensitic 7-12Cr steels, presented on ICFRM-10, Oct. 2001, Baden-Baden, Book of abstracts p.455.

TTMS-002
Metallurgical and Mechanical Characterisation

TTMS-002/12
Low Stresses Creep Testing

In general, creep and creep rupture tests provide results which are explicitly used for designing structural components. Such typical design-relevant values are, for example, time-yield-limits and minimum creep rates. Especially with respect to the design of blanket components the according data of the low stress regime is urgently required but still not available. Therefore, the EUROFER Low Stresses Creep Testing Program at 500°C and 550°C has been initiated in October 2001. Due to the low creep rates it will have to be continued till 2006.

Overview

Figure 1(a) shows a typical creep curve (red) with the primary (I), secondary (II) and tertiary (III) creep regimes. The according creep rate curve (red) is illustrated in Fig. 1(b).

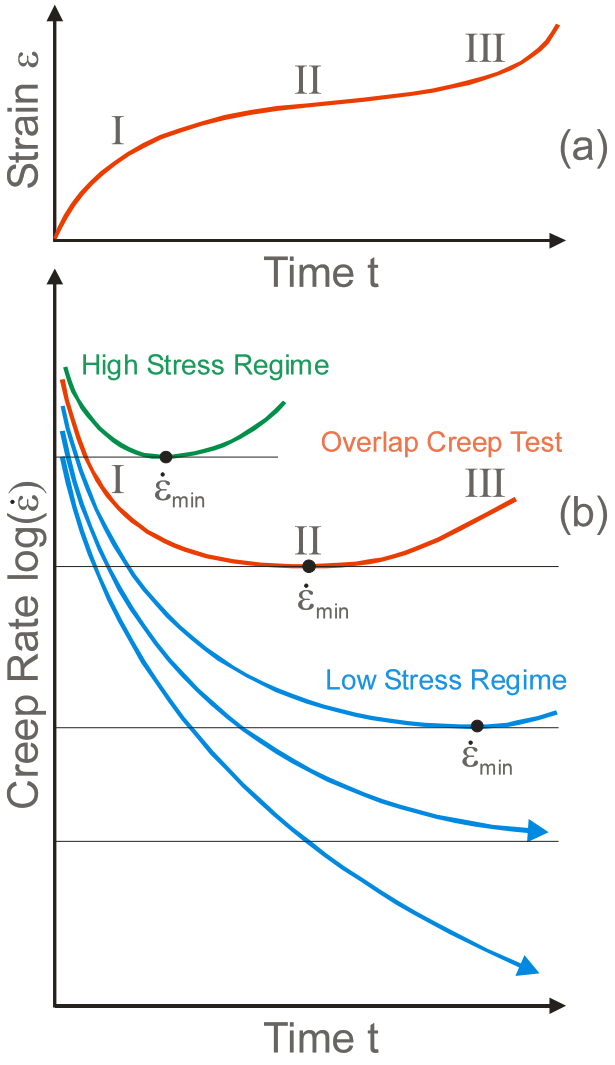

Fig. 1: Principle sketch of a typical creep curve (a) and the determination of the minimum creep rate (b).

It can be seen quite clearly that the determination of the creep rate minimum is only possible, if the test is well extended into the area of tertiary creep.

For EUROFER the high stress regime at 500-550°C (represented by the green curve in Fig. 1(b)) ranges between 180 and 300 MPa where the minimum creep rates occur at less than a few thousand hours. The low stresses selected for the current program (indicated by blue curves in Fig. 1(b)) are 100, 120, 140, 160, and 180 MPa at 500°C and 60, 70, 80, 100, 120, and 140 MPa at 550°C. Two additional tests at 500°C/230 MPa and 550°C/170 MPa will cover the overlap region and complete the test matrix. Due to the low creep rates it will be necessary to proceed the tests till 30-40 thousand hours to get all the minima.

Motivation

Plotting the stresses in a double-logarithmic scale depending on the minimum creep rates leads to straight lines for specific test temperatures (Norton's creep formula:

$\dot{\varepsilon} = k \cdot \sigma^n$).

Most often only results from the higher stress regime are available and the lower stress values are estimated by extrapolation as illustrated in Fig. 2. But in the case of the austenitic steel alloy 316L(N) a prior examination has already shown that the creep behaviour is different for lower stresses (blue line in Fig. 2).

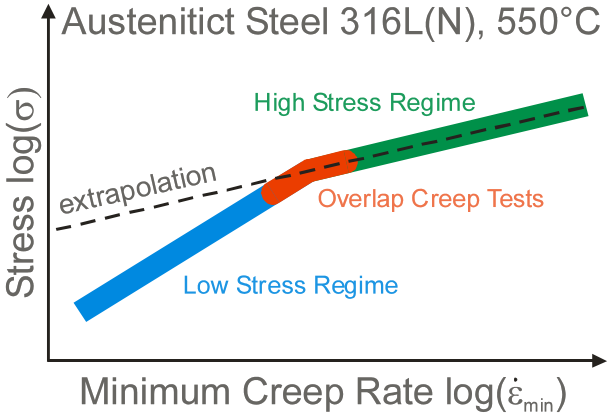

Fig. 2: The austenitic steel 316L(N) shows a distinct difference of the creep rates in the high and low stress regime. Therefore, extrapolating the higher stress data to the lower stress range leads to a significant overestimation of the design-relevant stress exponents.

As can be seen, a component design based on the indicated extrapolation from the high stress regime would definitely not meet the intended criteria, it would be too optimistic. Therefore, the outlined Low Stress Creep Testing Program has to proof whether the ferritic-martensitic EUROFER alloy shows similar results.

Progress

While the first tests have been started at October 2001 at the moment all specimens move still in the primary creep regimes with testing times between about 1000 and 8000 hours. First results for the minimum creep rates are not to be expected before 15-20 thousand hours. But some time-yield-limits in the range from 0.1 to 0.5% are already available.

Further activities

The already finished characterization work on F82H-mod has been compiled and published [1, 2]. The characterization work on EUROFER 97 has been continued [3, 4, 6] and is now almost finished. In addition, the transformation characteristics of 62 different steel grades and heats has been determined together

with the preparation of Continuous Cooling Transformation (CCT) diagrams [5].

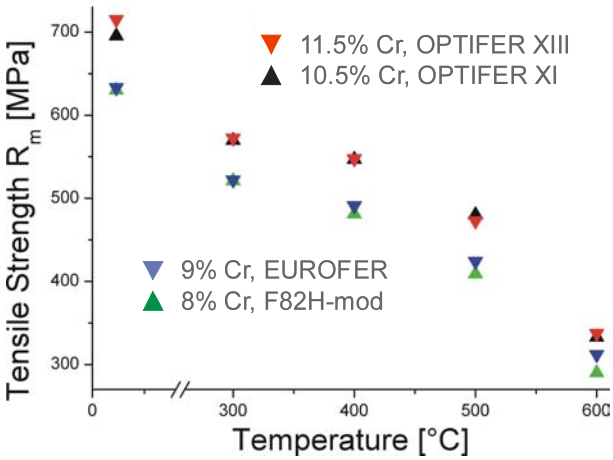

Fig. 3: Increasing the Cr-content of martensitic steel alloys improves the yield strength as can be clearly seen for the example of different LAMs. (The author would like to thank M. Klotz, IMF-II for performing the tensile tests.)

Finally, the optimization work on the OPTIFER materials development program has been continued. In particular, two special heats with a Cr-content of 10.5% and 11.5% have been produced. It is well-known that an increase of Cr leads (1) to a significant improvement of the corrosion resistance and (2) to higher yield strengths (see Fig. 3). On the other hand, increasing the Cr-content favours the occurrence of δ–Fe phases which have to be avoided due to its negative influence on the mechanical properties. First investigations have shown, however, that up to a Cr-content of 10.5% the according material structure remains stable and shows no growth of δ–Fe. Further characterization steps will include Charpy and creep rupture tests as well as detailed structural examinations.

Staff:

S. Baumgärtner
P. Graf
A. Falkenstein
S. Heger
R. Lindau
A. Möslang
E. Materna-Morris
M. Rieth (since 8/2002)
M. Schirra (till 7/2002)

Literature:

[1] S. Jitsukawa, M. Tamura, B. v. d. Schaaf, R. L. Klueh, A. Alamo, C. Petersen, M. Schirra, G. R. Odette, A. A. Tavasoli, K. Shiba, A. Kohyama, A. Kimura, “Development and the data base of a reduced activation martensitic steel F82H for fusion reactors”, 10th International Conference on Fusion Reactor Materials, 14.-19.10.2001, Baden-Baden.

[2] F. Tavasoli, J. W. Rensman, M. Schirra, K. Shiba, “Materials design data for reduced activation martensitic steel type F82H”, International Symposium on Fusion Technology (ISFNT) 6, 6. April 2002, San Diego.

[3] R. Lindau, A. Möslang, M. Schirra, “Thermal and mechanical behaviour of the reduced activation ferritic martensitic steel EUROFER”, International Symposium on Fusion Technology (ISFNT) 6, 6. April 2002, San Diego.

[4] M. Schirra, A. Falkenstein, P. Graf, S. Heger, H. Kempe, R. Lindau, H. Zimmermann, “Ergebnisse von Charakterisierungsuntersuchungen zu physikalischen und mechanischen Eigenschaften des martensitischen 9%-Cr-Stahles EUROFER’97”, FZKA 6707, April 2002.

[5] M. Schirra, H. Finkler, “Das Umwandlungsverhalten der ferritisch-martensitischen Stähle mit 8-14% Cr”, FZKA 6730, Juni 2002.

[6] M. Schirra, “EUROFER’97–Gesichtspunkte für die technologische Verwendbarkeit”, Vortrag im Arbeitskreis Metallische Werkstoffe, PKF, 12.06.2002.

TTMS-002/19
Creep Fatigue Testing on EUROFER

1. Objectives

A structural component like a Test Blanket Module (TBM) is subjected during service to alternating thermal and mechanical stresses as a consequence of the pulsed reactor operation. Since the operating temperatures of a future DEMO reactor increase due to economic considerations, the knowledge of the creep fatigue endurance of Reduced Activation Ferrite/Martensite (RAFM) steels like F82H mod. and EUROFER 97 becomes more important.

2. Isothermal LCF-experiments

The Low Cycle Fatigue (LCF) tests have been performed on solid cylindrical specimens with 77 mm length, 21 mm initial gauge length and 8.8 mm diameter in a MTS servo hydraulic testing machine operating in triangular strain controlled push-pull mode with a constant strain rate of $3x10^{-3}$ 1/s.

2.1 Isothermal LCF-behavior with and without hold times

Isothermal LCF experiments without hold times of the RAFM steel EUROFER 97 at the temperatures of 450°C and 550°C have been finished and are reported for completion. For total strain ranges larger or equal to 0.8 % it is shown in Figure 1 that the numbers of cycles to failure are not very different. For lower strain ranges the isothermal fatigue lifetime at 450°C is significantly better as compared to 550°C. For T=450°C and $\Delta\varepsilon_t$=0.4% it seems that the fatigue strength has already been reached.

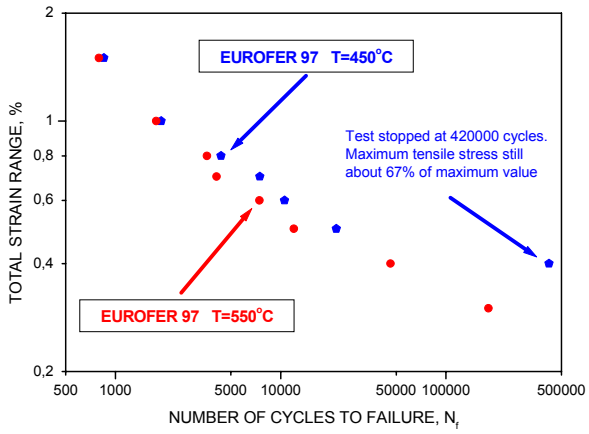

Fig. 1: Isothermal fatigue behavior of the RAFM-steel EUROFER 97 at 450 and 550°C.

Isothermal LCF experiments on EUROFER 97 with hold-times up to 600 seconds in compression and symmetrical hold-times with a 1 % strain range at 550°C show under these loading conditions a larger reduction of number of cycles to failure for compression hold-times than for tensile and symmetrical hold times. Whereas this reduction in number of cycles to failure is increasing with the increasing length of the hold time. At this higher temperature of 550°C during the hold time already thermal creep is probably the most damaging factor.

A similar behaviour has been observed in the past on other RAFM-steels.

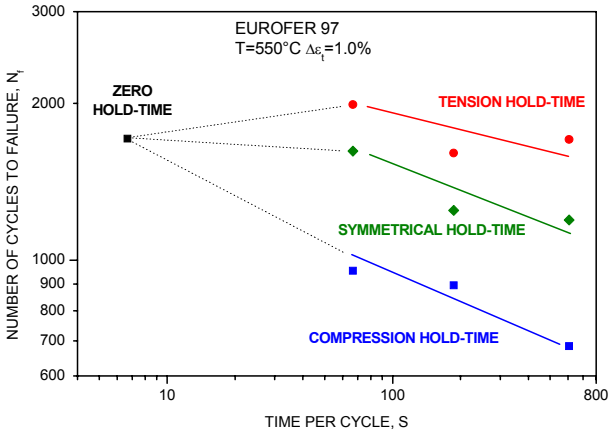

Fig. 2: Comparison of the creep fatigue behaviour of EUROFER 97 under different hold time conditions.

3. Thermal fatigue behaviour

The Thermal Fatigue (TF) test rig consists of a stiff load frame for mechanical clamping of the sample, which is directly heated by the digitally controlled ohmic heating device. Temperature rate is kept constant at 5.8 K/s for all thermal conditions and variable strain rates are applied, due to the variable temperature changes.

Cylindrical specimens of EUROFER 97 with 77 mm length and of 8.8 mm diameter in the cylindrical gauge length of the specimen with a wall thickness of 0.4 mm have been used for the TF-experiments. All tests have been performed in air.

For the hold time tests we introduced the following definition: HTH, hold time at the higher temperature T_H , HTL, hold time at the lower temperature T_L and HTHL, hold time at both temperatures. Hold times of 100 and 1000 s have been realised.

3.1 Thermal Fatigue behaviour with hold times

Results of thermal fatigue tests with hold times of 100 s and 1000 s are available for EUROFER 97 now. The actual data set covers the temperature ranges of 100 to 450 °C, 100 to 500 °C and 100 to 550 °C. For 100 s hold time the experiments under HTL - and HTH - conditions of 100 to 450 °C had been terminated before fracture occurred, because they reached the design limit of 70,000 cycles, but the HTHL tests failed at 35,000 cycles. In case of a 100 to 500 °C temperature range, the N_f - values without hold times lie around 10,000 cycles. So the hold times at the low temperature (HTL) or at the high temperature (HTH) lead to a slight decrease in cyclic life only. But at the HTHL condition a reduction in cyclic life down to 6,000 cycles (i.e. a factor of 1.6) was found for 100 s hold time with increasing $\Delta\varepsilon_{t,m}$ up to 0.4 %. At increasing hold time of 1000 s at a 100 to 500 °C temperature range even the HTL- and HTH-values are found to be less than 1000 cycles, but the HTHL-condition shortens the N_f - values down to 200 cycles at a very high $\Delta\varepsilon_{t,m}$ - value of around 0.9 % strain. This is a reduction in life of rather one and a half orders of magnitude. The similar tendency is found for the 100 to 550 °C temperature range especially for the 1000 s hold time.

With increasing hold time from 100 s to 1000 s a remarkable reduction in number of cycles to failure is observed.

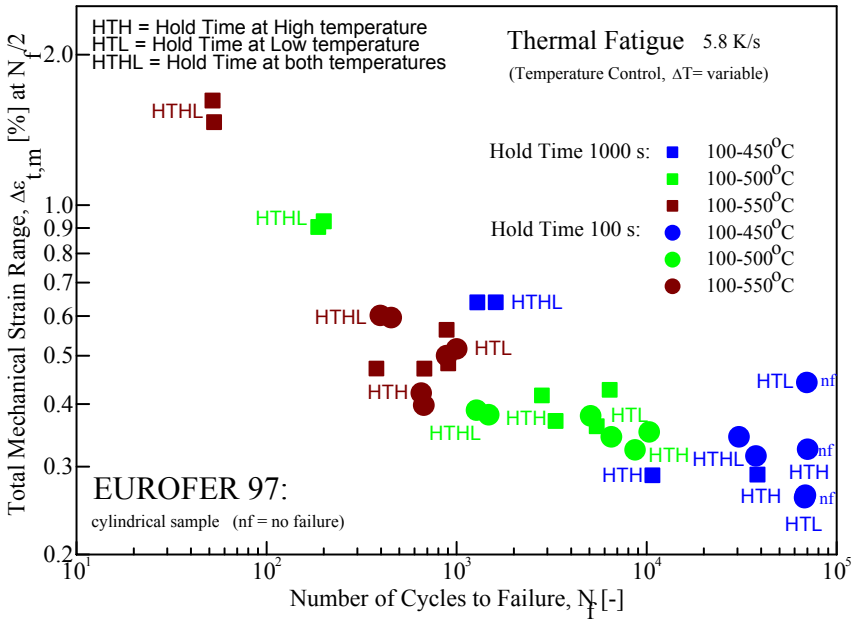

Fig. 3: Comparison of total mechanical strain range $\Delta\varepsilon_{t,m}$ of thermal fatigue behavior of EUROFER 97 with 100 s and 1000 s hold times in temperature ranges starting from 100 °C.

Staff:

J. Aktaa
M. Klotz
C. Petersen
M. Pfeifenroth
R. Schmitt

Literature:

A.F. Armas, C. Petersen, R. Schmitt, M. Avalos, I. Alvarez-Armas: „Mechanical and microstructural behavior of isothermally and thermally fatigued ferritic-martensitic stainless steels", to be published in Journal of Nuclear Materials (in press).

C. Petersen, D. Rodrian: "Thermo-mechanical fatigue behavior of reduced activation ferrite/martensite stainless steels", to be published in Journal of Nuclear Materials (in press).

Report FZKA 6634, March 2002, p 6.

TTMS-003
Compatibility with Hydrogen and Liquids

TTMS-003-14
Corrosion of RAF/M Steels in Liquid Pb-17Li

In fusion technology RAFM steels are devoted as structural materials for a future reactor system. These steels are in direct contact with the highly corrosive liquid Pb-17Li cooling and breading material and have to possess excellent long term corrosion resistance in this environment. In the last years ferritic-martensitic steels as MANET I, Optifer IVa or F82H-mod. were standing in the centre of interest. Meanwhile the improved alloy EUROFER 97 is available in well characterized form and introduced into testing for application In the water cooled liquid lead-lithium blanket concept (WCLL). Long term corrosion tests are necessary to confirm the compatibility of EUROFER 97 with the flowing Pb-17Li alloy.

In 2001 the corrosion tests of EUROFER 97 were started in the corrosion loop PICOLO to examine the compatibility of EUROFER 97 with the flowing liquid lead alloy (Pb-17Li) at 480 °C. For testing cylindrical samples were used with a diameter of 8 mm and a length of 35 mm. The planned test duration was 10000 h. Test samples were removed from the melt after test periods of about 1500, 3000, 4500, 6000, 7500 and 10000 h. The corrosion attack is qualified by post test analysis consisting of metallurgical examination, results are now available, and EDX analysis, both performed on cross sections of the tested samples.

The corrosion investigations performed with MANET I, Optifer IVa or F82H-mod. samples showed that the attack by Pb-17Li starts not immediately after exposure. A first inhomogeneous attack was registered after a certain time a so called incubation period of up to 3000 h. After this time a serious dissolution of the steel was observed. Results of these test series are described in more detail in Ref 1.

In general the behaviour of EUROFER 97 is similar to the earlier examined alloys as can be concluded from the metallographic examinations. Fig. 1 shows cross sections of EUROFER 97 after different exposure times to Pb-17Li.

Compared with the original material the pictures taken from EUROFER 97 samples, which were exposed to flowing Pb-17Li at 480 °C for about 3000 and 6000 h, no clear surface changes which can be correlated with a significant corrosion attack by liquid Pb-17Li were found. In contrast to that, a visible corrosion attack of EUROFER 97 can be seen in the micrographs taken after 7500 and 11600 h test duration. The quite rough surface (7543 h) indicates, that corrosion did not start homogeneously. During further exposure a surface flattening occurs however with tendency to formation of groove like structures.

Based on the tests performed with other RAFM alloys a depletion of Fe from the steel is expected. More detailed information will be provided by the EDX examinations on the behaviour of EUROFER 97. The performed metallographic analyses confirmed that no dense and passivating scales were formed on top of the samples. This indicates that long term corrosion is governed by dissolution and erosion processes.

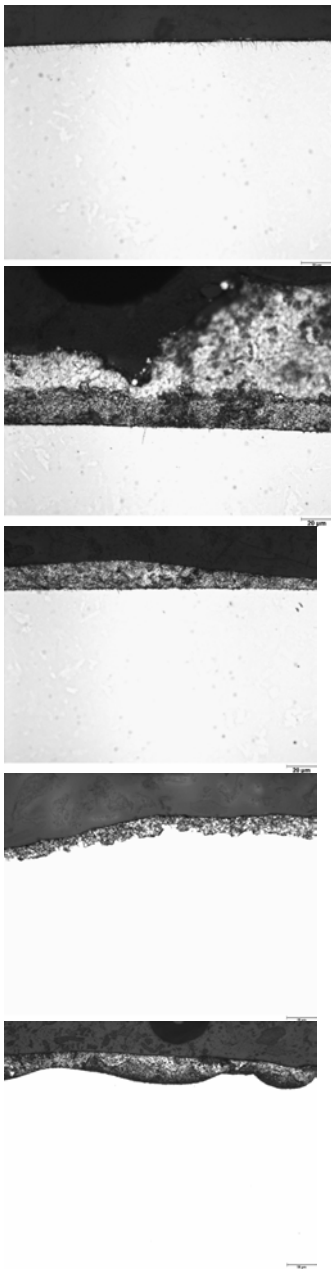

Fig. 1: Micrographs of EUROFER 97 samples in dependence of exposure time.

Staff:

J. Konys
W. Krauss
J. Novotny
Z. Voß
O. Wedemeyer

Literature:

[1] J. Konys, G. Müller, Corrosion and compatibility of structural materials in liquid lead alloys, Proc. Int. Symposium on Material Chemistry in Nuclear Environment MC'02, March 13-15, 2002, Tsukuba, Japan

TTMS-004
Qualification Fabrication Processes

TTMS-004/6
Optimisation of HIP Process

High temperature (hot) isostatic pressing (HIP) is a favoured manufacturing technique for the realisation of the complex cooling channels network in first wall structures. Since the joining mechanism is controlled by diffusion and deformation processes the temperature and pressure are important parameters in optimising the HIP process: the higher the temperature and pressure are the better is the adhesion. However, the accompanying annealing of the material at a HIP temperature higher than the heat treatment temperatures leads to microstructural changes which can not be completely relieved during the heat treatment after HIP. High pressure may lead to undesired inelastic deformation particularly in closed channels. Therefore the objective of this activity is the optimisation of a low temperature low pressure HIP process.

The approach for the optimisation of the HIP process consists not only of the performance of evaluation of different HIP experiments under variation of most important parameters, temperature, pressure, surface roughness and time, but also the use of simulation tools predicting the most promising parameters combinations. The simulations shall reduce the number of HIP experiments needed for the optimisation and are based on finite element calculations of the deformation part of the process as well as on a semi-analytical sintering model from the literature. The properties of EUROFER 97 needed for the finite element calculations were determined in tensile tests performed at temperatures in the range 900-1100 °C. Meanwhile first simulations were performed predicting for different combinations of HIP temperature, HIP pressure and roughness of joining surface the minimum time for complete adhesion. For the experimental verification HIP experiments followed by assessment tests will now be prepared.

In order to estimate the effects of high HIP temperature and pressure on the mechanical properties of the base material an experiment was performed where three pieces were cut from the same EUROFER 97 plate. One piece was annealed at 1100 °C for 4 h, one piece was annealed under 105 MPa hydrostatic pressure at 1100 °C for 4 h and one piece hold in the state as delivered. Thereafter, all three pieces were heat treated using the standard parameters (980 °C / 0.5h, 730 °C / 3h) and characterised in tensile an impact tests. As a result the annealing at 1100 °C increases the ductile-to-brittle transition temperature of about 20°C (s. Fig. 1) whereas the upper shelf energy and the tensile properties are not changed significantly. In addition, the hydrostatic pressure was found as expected to have no significant influence on both tensile and impact properties.

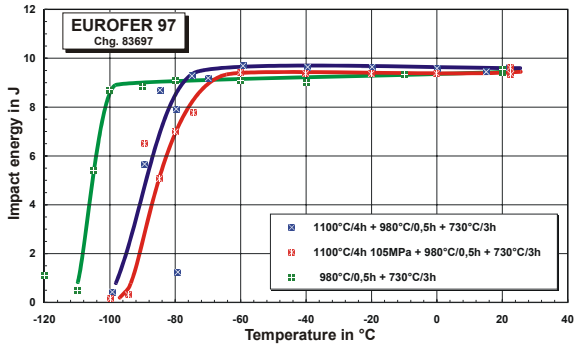

Fig. 1: Influence of high HIP temperature and pressure on the impact properties of EUROFER 97.

Staff:

J. Aktaa
H. Kempe
T. Mili

TTMS-005
Rules for Design, Fabrication and Inspection

TTMS-005/1
Development and Assessment of Design Rules

The objective of this task is the assessment and further development of a design code for ITER test blanket modules (TBM) built from RAFM steels. The design code is based on the ITER Structural Design CRITERIA (ISDC) for in vessel components. As the TBM are operated under high temperature (HT) conditions, creep and creep-fatigue are not negligible as it is for the basic ITER machine, but instead are crucial for life time assessment.

The work includes:

- Definition of additional rules, including the results of subtasks on fracture mechanics concepts and lifetime rules.
- Verification of rules on representative models.

(a) Definition of additional rules

For an extensive formulation of HT rules applicable for designers as requested in appendices B and C of ISDC, there is still more input needed from other subtasks, as on "fracture mechanic rules" and on "lifetime rules.

Some special problems have been investigated in 2002. A typical feature of RAFM steels is the low uniform elongation. In the temperature window of around 400°C to 600 °C the uniform elongation as measured from tensile tests drops below 2%, under neutron irradiation the measured uniform elongation might be close to zero. A lot of design rules for level A and C criteria (i.e. for normal operation and upset conditions) make in particular use of plastic strains if the uniform elongation exceeds 2% (and otherwise are very strict), this causes problems in design assessment for TBM.

The reason for the very low ductility measured in tensile tests are small imperfection on the tensile bars that very early cause plastic flow localisation and necking. Based on some ideas developed at the University of California at Santa Barbara, the tensile tests (which may be considered as a component test) were numerically investigated by the finite element method and stress-strain curves (which can be regarded as the basic material property) were generated. The idea is to thereafter numerically investigate simple structures which are typically for TBM application under representative loads and with the same kind of imperfection as used in the evaluation of the tensile experiments and to find some solution to "design around" the "low ductility problem". The starting point for this study were plates with cracks, holes and notches (which either are located symmetrically or with some off-set) under combined tensile and bending loads.

Currently the method is not yet fully applicable. In order to get the complete information needed for the interpretation a continuous monitoring of the necking, i.e. the reduction in area, during the test would be needed. Moreover, additionally to tensile experiments more tests are needed for verification, e.g. on three-point-bend specimens, notched bars.

(b) Verification of rules on representative models

The objective of this subtask is to define tests for verification of rules. This activity may subdivided into verification tests on samples with a simple geometry (like tubes and plates) and the definition of mock-up tests with representative geometry and loads. Experiments have been proposed for studying creep-fatigue interaction with continuous monitoring of damage evaluation which will be performed in the next framework programme. As both, the HCLL and the HCPB type of blanket, are currently undergoing larger changes in geometry, defining mock-up tests in 2002 is not appropriate.

An international collaboration on material-design interaction was started under the name VISTA (Virtual International Structural Test Assembly). In April 2002 an IEA Workshop on “Advanced Ferritic Steel -Blanket Designs, Materials and Technologies” was held in San Diego, USA. Discussions there made clear that despite significant progress in modelling material behaviour of fusion materials, a lack of an integrated "material property-structural loading performance map" is stifling design efforts. As a result, the need to develop a methodology to relate research on material properties and structural integrity modelling effort was identified. The concept of a Virtual International Structural Test Assembly was proposed. The primary goal of VISTA is to facilitate the development and implementation of advanced and fully integrated integrity and lifetime assessment methods by:

- Providing a methodology and physical basis to evaluate relations between research on material properties, failure paths and structural integrity assessment methods related to
  - various properties
  - the performance and lifetime limits of fusion structures such as blankets or divertors.
- Inserting a much higher degree of realism in so called design studies with respect to
  - geometric realization
  - multi-physical loading conditions
  - interaction of different sources of loading and damage.
- Facilitating the development and implementation of advanced and fully integrated integrity and lifetime assessment methods.

Currently the University of California Los Angeles, Argonne National Laboratory and the University of California Santa Barbara are involved the programme. The actions taken were: First, a comparative study on blanket concepts proposed for DEMO and in power plant studies will be performed, where the structural aspects are evaluated by means of 'function' and 'typical loading' of the component and sub-components (to be completed by end of 2002). The second near-term issue of VISTA will be the definition and implementation of benchmark problems. The benchmark exercises will be closely linked to future mock-up tests to be performed in the EU. For both activities, FZK has the lead.

Staff:

E. Diegele
G. Rizzi

TTMS-005/3
Local Fracture Criteria in the Ductile-to-Brittle Transition Regime

Objective

The objective of this subtask is the development and application of methods that enable the generation of design-relevant fracture mechanics material parameters on the basis of micro-mechanical failure models.

A characteristic feature of these models is the utilisation of an integrated (i.e. combined experimental and continuum mechanics) approach, which means extraction of material parameters for brittle or ductile fracture from (fracture) mechanics experiments by accompanying Finite Element stress analyses.

The main advantage of this so-called 'Local Approach' with respect to global failure criteria is the fact that a mechanism-based fracture description is combined with a numerical stress analysis. Geometrical size effects are thus already accounted for within this approach. Limitations of the local approach originate from different fracture mechanisms. Knowledge of fracture mechanisms is therefore essential, so that fractography invariably is an essential part of the evaluation of the experiments.

Local fracture criteria establish a link between metallurgy and mechanical engineering and they are currently being incorporated into design codes such as the R6 code of British Energy, where guidance on Local Approach methodology is included in the latest issue [1].

Main objective of work in 2002 is the characterization of EUROFER97 using the methods developed on F82Hmod. material and the formal description of the methods in a procedural document [6].

Experimental results, fractography

Tensile tests at –150°C are available for notched axisymmetrical specimens with notch radii of 0.5 and 2 mm, respectively. Figure 1 shows the calculated diametral contraction Δd from nonlinear Finite element stress analysis together with the experimentally obtained values of Δd at fracture.

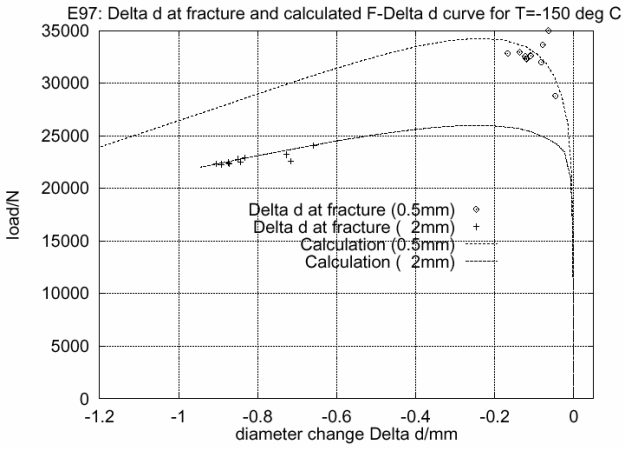

Fig. 1: Diametral contraction Δd at fracture and numerical prediction of load vs. diametral contraction relation.

For the analysis and the calculation of the force vs. diametral contraction relation of the notched tensile specimens as well as the calculation of the Weibull stress (see next paragraph), a linear hardening rule was used to interpolate the experimental results. Strains beyond the strain range that could be obtained in smooth tensile tests were extrapolated by a Hollomon-type power law of true stress vs. true plastic strain.

Fractography of the fracture surfaces is pending.

Statistical inference and modelling

The Weibull stress was calculated using the Finite Element postprocessing program WEISTRABA [3] developed at FZK. Figure 2 shows the results. Based on experience with F82Hmod., a notch radius of 0.5 mm was selected as minimum value and results were compared with notch radius of 2mm. Fig. 2 shows that the 0.5mm notched specimens show a Weibull modulus *m* of about 17, whereas for the 2mm notched specimens, *m* is quite large and attains a value of more than 90. This result shows, that the fracture behaviour of EUROFER97 is comparable to F82Hmod., where also two groups of specimen geometries with different values of *m* could be identified. The differences are so pronounced that no statistical analysis is necessary. It is expected that similar to the F82Hmod. results, presence of large plastic strains at fracture lead to a change in the fracture mechanism due to strain localization and cause a breakdown of the cleavage fracture model in a way as described in [5].

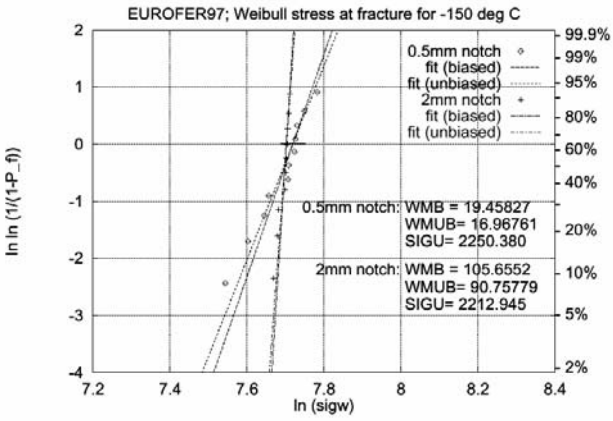

Fig. 2: Weibull stress at fracture for specimens with different notch radii tested at –150°C.

Elements of a fracture mechanics concept

A procedural description of the framework to measure and calculate cleavage fracture parameters is given in [6]. Background of cleavage fracture models is presented and the steps from design of the experiments, specimen geometries, experimental set-up are given. Statistical evaluation including numerical scheme for Weibull stress calculation and maximum likelihood estimation of Weibull stress parameters are described. The local risk of fracture is introduced as a quantity that enables quantitative comparison between findings from fractography and numerical predictions. Limitations in case of large fracture strains are addressed. In case of the F82Hmod. steel, these limitations are due to the microstructural changes at large plastic strains that lead to strain induced micro-cracking along carbide decorated martensite laths and/or former austenite grain boundaries [4,5]. In case of the EUROFER97 steel, fractography has to confirm a similar behaviour.

Staff:

E. Diegele
H. Kempe
C. Petersen
H. Riesch-Oppermann
G. Rizzi
M. Walter

Literature:

[1] British Energy Generation Ltd, Assessment of the integrity of structures containing defects R/H/R6, Rev. 4, 2001.

[2] H. Riesch-Oppermann, M. Walter, Status report on experiments and modelling of the cleavage fracture behaviour of F82Hmod. using local fracture criteria (Task TTMS-005), Report FZKA 6388, Forschungszentrum Karlsruhe, 2001.

[3] H. Riesch-Oppermann, A. Brückner-Foit, WEISTRABA - A code for the numerical analysis of Weibull stress parameters from ABAQUS finite element stress analyses – Procedural background and code description -, FZKA Report 6155, Forschungszentrum Karlsruhe, August 1998.

[4] H. Riesch-Oppermann, E. Diegele, Towards a micro-mechanical description of the fracture behaviour for RAFM steels in the ductile-to-brittle transition regime, J. Nucl. Materials (2002), (in press).

[5] M. Walter, Mechanische und fraktographische Charakterisierung des niedrigaktivierbaren Chromstahls F82H-mod. im spröd-duktilen Übergangsbereich, Dissertation, Report FZKA 6657, Forschungszentrum Karlsruhe, 2002.

[6] H. Riesch-Oppermann, Elements of a fracture mechanics concept for the cleavage fracture behaviour for RAFM steels using local fracture criteria (Task TTMS-005), Report FZKA 6668, Forschungszentrum Karlsruhe, 2002 (in preparation).

TTMS-005/4
Creep-fatigue Lifetime Prediction Rules

Structural materials of fusion reactors are subjected to complex creep-fatigue loading and high irradiation doses. Correct modelling of their deterioration is a precondition of a sufficiently reliable lifetime prediction procedure.

In the continuum mechanics approach selected for lifetime prediction of RAFM steels under creep-fatigue conditions the ISRM (Inelastic Strain Rate Modified) damage model [1] is coupled with a modified viscoplastic deformation model taking into account the complex non-saturating cyclic softening of RAFM steels. The resulting coupled model is a powerful prediction tool, which can be applied to arbitrary creep-fatigue loading provided that the material, temperature and possibly irradiation dose dependent parameters of the model have been determined [2]. Therefore a fitting procedure has been developed for the parameters identification on the base of deformation and lifetime data from standard low cycle fatigue (LCF) tests without and with hold time as well as creep tests.

The coupled deformation-damage model has been meanwhile applied to F82H mod in the reference (unirradiated) state under isothermal cyclic loading at 450, 550 and 650 °C. Fig. 1 and 2 show comparisons between model and experiment demonstrating exemplarily the capability of the model in describing fairly well the deformation behaviour. The observed lifetimes in the LCF-tests could also be fairly well calculated even for the tests with hold time, which were not considered for the identification of the damage model parameters (s. Fig. 3). However before releasing the model further verifications has to be done by applying the model to isothermal two-steps LCF-tests (low-to-high and high-to-low), to thermo-mechanical LCF-tests, to isothermal multiaxial LCF-tests as well as to a suitable benchmark component test. The verification tests are partially subject of additional experimental activities of the EFDA materials program, which have to be launched in the near future.

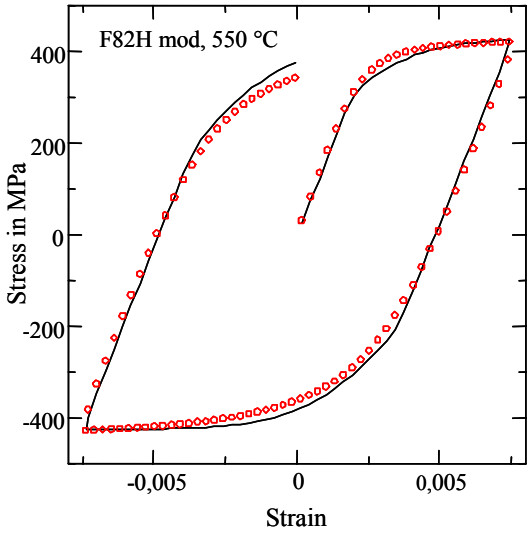

Fig. 1: Stress-strain curve of the first cycle of a LCF-test, comparison between experiment (symbols) and model (solid line).

At present the coupled deformation-damage model will be fitted to the isothermal behaviour of EUROFER 97 at 450 and 550 °C. Corresponding results are still expected within this year.

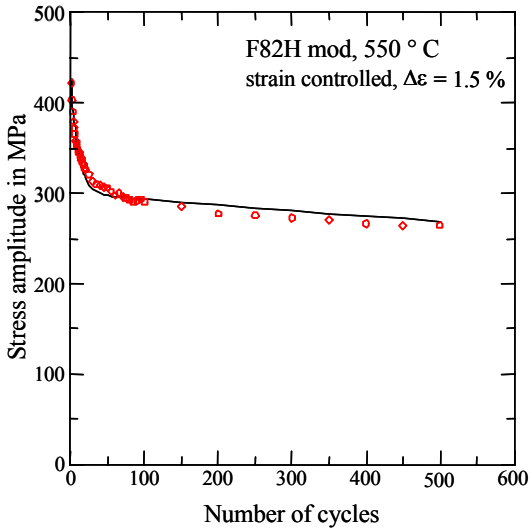

Fig. 2: Cyclic softening curve of a LCF-test, comparison between experiment (symbols) and model (solid line).

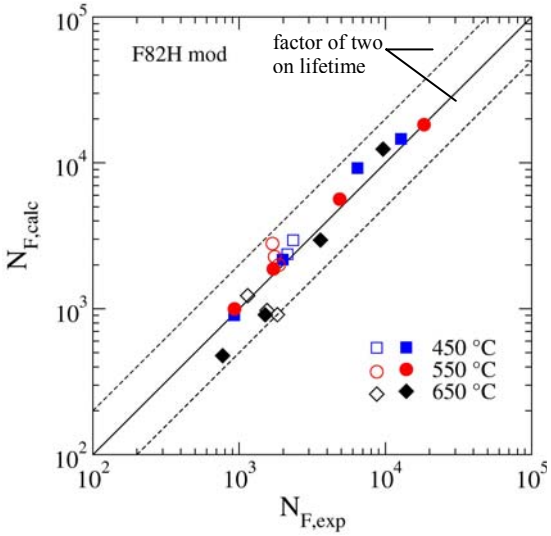

Fig. 3: Comparison between numbers of cycles to failure calculated using the coupled deformation-damage model with those observed experimentally in LCF-tests without holdtime (filled symbols) and with holdtime in tension (open symbols).

Staff:

Dr. J. Aktaa

Literature:

[1] J. Aktaa & B. Schinke, "The influence of the hardening state on time dependent damage and its consideration in a unified damage model," *Fatigue Fract. Engng Mater. Struct.* 19 (1996) 1143-1151.

[2] J. Aktaa, M. G. Horsten & R. Schmitt, "Effects of hold-time and neutron-irradiation on the low-cycle fatigue behaviour of type 316-CL and their consideration in a damage model," *Nuclear Engineering and Design* 213 (2002) 111-117.

TTMS-006
Qualification of High Performance Steels

TTMS-006/2
Metallurgical and Mechanical Characterisation of Existing ODS Alloys

In the past few years, oxide dispersion strengthened (ODS) steels produced by mechanical alloying techniques have become increasingly interesting for structural applications in nuclear fission and fusion power plants. The use of ODS alloys instead of the presently considered conventionally produced reduced activation ferritic-martensitic (RAFM) steels would allow to improve creep resistance at high temperatures and consequently increase the operating temperature of blanket structures in future fusion power reactors by 100 K to approximately 650 °C or more. The attractiveness of high strength nano-composed RAFM steels is not only due to favourable radiological properties, but also to a unique combination of small average grain sizes, high dislocation densities, and nanoclusters composed of Y-O solute atoms.

As a first step in the development of dispersion strengthened RAFM steels, two ODS alloys containing 0.5 and 0.3 wt.-% Y2O3 respectively, have been produced on the basis of a 9%CrWVTa RAFM European reference steel, called EUROFER 97. The production process of the EUROFER-ODS alloys included mechanical alloying (MA) of inert-gas-atomised steel and yttria powder, followed by hot isostatic pressing (HIP). The hipping process is regarded as the most promising production route for near net-shape structures for future fusion reactors.

Mechanical characterisation

Earlier tensile tests in the temperature range between RT and 850 °C revealed good strength and ductility. Yield strength and ultimate tensile strength of the EUROFER-ODS are raised by 50% and more, compared to the non-ODS RAFM steels like EUROFER 97 and F82H mod. This gain in strength is still persisting at elevated temperatures. The uniform elongation of the ODS material is superior to that of common RAFM steels, whereas the total elongation above 400 °C is lower, but remains always above 6%, what is not unusual for this type of alloys [1,2].

The results of impact tests on sub-size KLST specimens (Kleinstprobe acc. DIN 50115) reveal a similar impact behaviour than comparable ODS alloys, but the Ductile-to-Brittle-Transition-temperature (DBTT) is substantially higher compared to EUROFER 97 [1].

Creep tests at temperatures of 600, 650 and 700 °C were continued up to test times of 6000 hours. The creep strength of EUROFER-ODS is significantly higher compared to EUROFER 97. This corresponds to an increase of rupture time at a given stress level and temperature by a factor of 10. This is equivalent to a gain in temperature of about 80°C at a given stress level and rupture time (Fig.1) [2].

Strain controlled low cycle fatigue tests on the same type of miniaturised specimens as used for the tensile tests, show the good LCF-behaviour of EUROFER-ODS. Compared to F82H mod. and EUROFER almost no cyclic softening, a lower plastic deformation, a substantial higher stress amplitude at a given strain can be observed (Fig. 2). EUROFER-ODS shows a longer lifetime at total strain ranges below 0.7% but shorter lifetimes at higher strain ranges (Fig. 3) [2].

Microstructural characterisation

Although relevant mechanical properties, e.g. tensile strength, toughness, fatigue, and creep rupture of the alloy were screened very recently within a wide temperature range, detailed information concerning the crystalline structure of the ODS particles and its orientation with respect to the alloy matrix is still lacking. This information is important for improving RAFM-ODS alloys by means of targeted nanostructural tailoring. The knowledge about ODS particles and their interaction with the matrix would also help to prove nanoscale theory and modelling with simulation approaches that will be designed specifically to address material structures and properties in the nanoscale regime. The experience shows that lattice coherency of the particles with surrounded matrix is of importance for strengthening mechanisms.

The structure of the nanometer-sized Y_2O_3 particles analysed by HRTEM shows a strong correlation of its crystallographic orientation with the alloy lattice. The orientation correlations $[110]_{YO} \parallel [111]_{FeCr}$ and $(1\bar{1}1)_{YO} \parallel (\bar{1}01)_{FeCr}$ were found. It is believed that the strong orientation correlation appears during hipping processes around 1050°C, which is significantly lower than the melting temperature of Y_2O_3 that amounts to 2500°C.

High-resolution TEM (HRTEM) images of ODS particles are presented in Fig. 4a and Fig. 4b. The particles numbered 3, 4, and 5 have the same orientation with the [011] zone axis. The Fast Fourier Transformation (FFT) images taken from these three particles (Fig. 4c) demonstrate that these particles also have the same orientation in the image plane. Reflexes of the {222} type are marked with lines. Fig. 4b shows the particles numbered 2 and 3. It seems that the particles have a different orientation in the image plane. The FFT image presented in Fig. 4d, however, reveals that both particles are oriented along the zone axis of the <011> type and they can be attributed to one equally oriented plane of the {222} type. The reflexes of particle No. 2 are marked by the dashed lines. Indication of the coincident atomic planes with the $\mathbf{(2\bar{2}2)_{YO}}$ indexes as it was done in Fig. 4d requires to take the $\mathbf{[0\bar{1}\bar{1}]}$ direction for the zone axis of particle No. 2. Such an orientation relation between the particles can be defined as the mirror symmetry of the whole crystal using the $\mathbf{[2\bar{2}2]_{YO}}$ axis [3].

Fig. 5 shows the HRTEM image taken from a ODS particle which is surrounded by the matrix (M) lattice. This image was taken from the grain oriented with [111]M zone axis to the electron beam. The Fast Fourier Transformation of the image shows the matrix lattice as a hexagonal pattern with reflexes of the {110} type and d110=0.203 nm distance. The zone axis of the Y_2O_3 (YO) particle is oriented along the [110] zone axis and, consequently, [110]YO || [111]M. In the FFT image, the Y_2O_3 lattice is rectangular with reflexes of the {111} type. The orientation correlation of both lattices in the image plane is $(1\bar{1}\bar{1})_{YO} \| (1\bar{1}0)_{M}$. The angle between $[1\bar{1}1]_{YO}$ and $[0\bar{1}1]_{M}$ is 10.5°.

Detailed investigation of the preparation steps strongly suggests that the orientation correlation appears during the HIP process. The Y_2O_3 particles remain in the solid state during HIP processes, because the melting point of Y_2O_3 amounts to 2500°C. Although the Y_2O_3 particles remain in the solid state during the hipping process, it seems possible that they may change their crystallographic orientation by surface diffusion processes well below the melting temperature which lead to a change of the particle shape and original crystallographic orientation [3, 4].

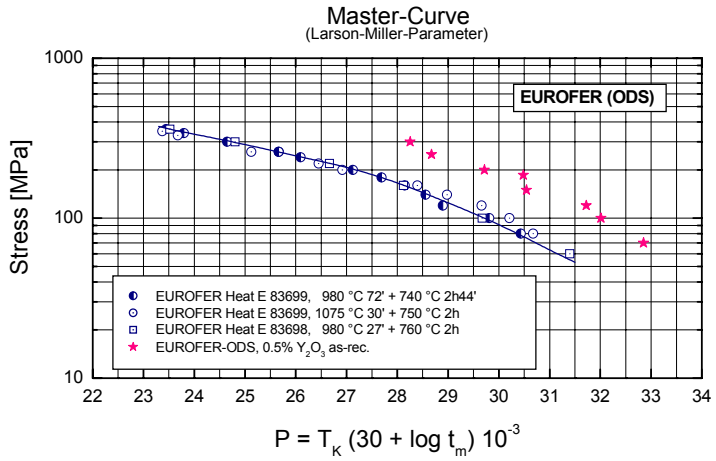

Fig. 1: Larson-Miller-Plot for EUROFER bar (○) and plate (□)material with different heat treatments compared to EUROFER-ODS (★).

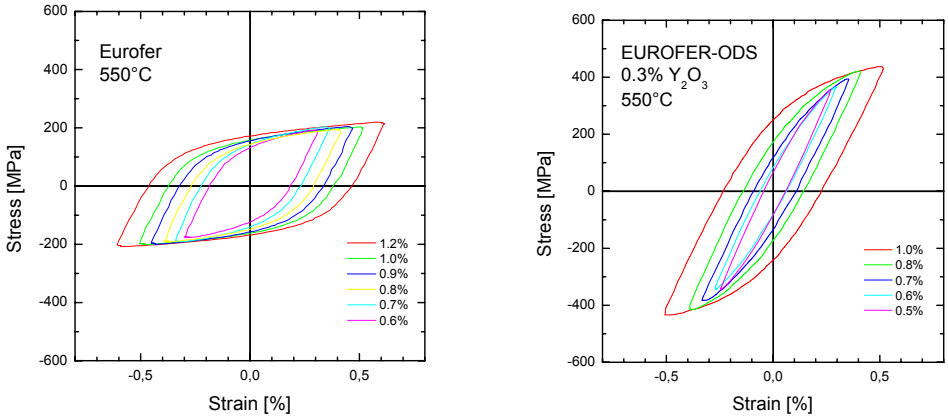

Fig. 2: Typical hysteresis loops at $N_f/2$ of EUROFER and EUROFER-ODS during strain controlled LCF tests (SSTT specimens, 2 mm diameter, 7 mm gauge length).

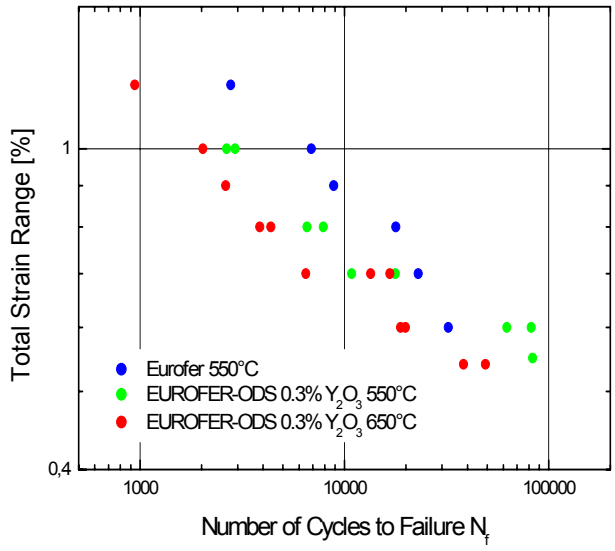

Fig. 3: Number of cycles to failure N_f of EUROFER and EUROFER-ODS.

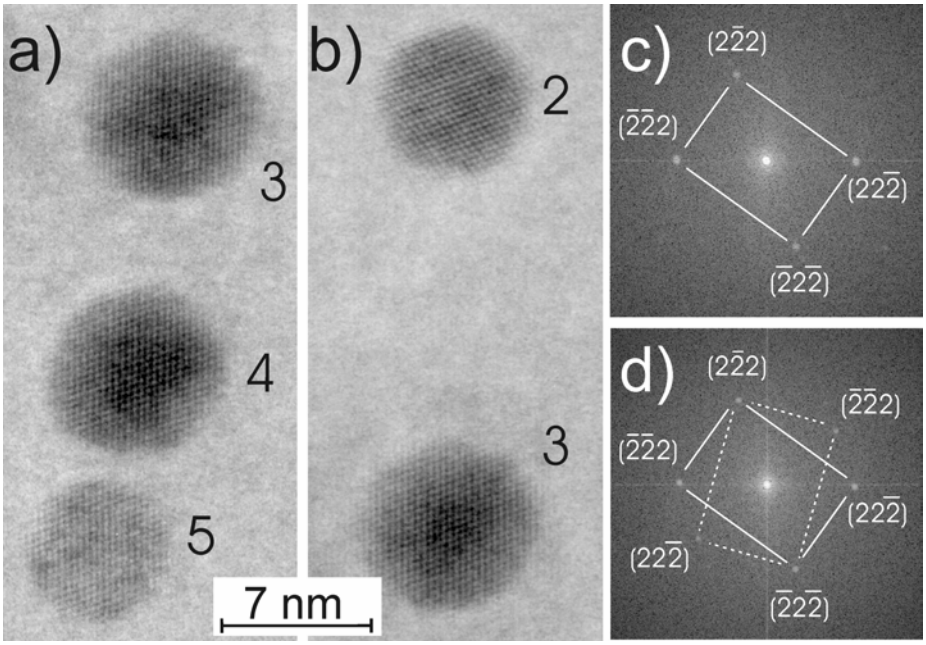

Fig. 4: a) and b) show HRTEM micrographs of Y_2O_3 particles.
Parts c) and d) give the FFT of the parts a) and b) respectively.

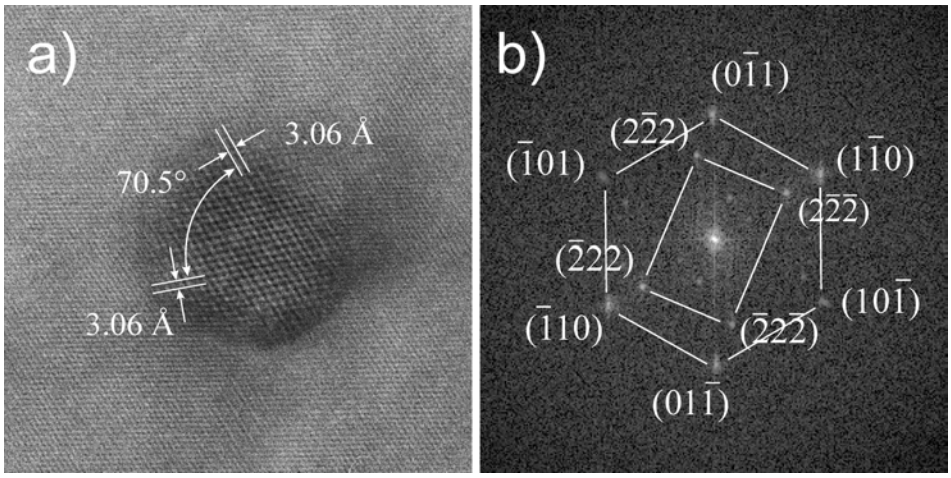

Fig. 5: HRTEM micrograph of the Y_2O_3 particle with surrounded matrix - a) with FFT of the micrograph – b).

Staff:

S. Baumgärtner
G. Bürkle
A. Falkenstein
P. Graf
M. Klimiankou
R. Lindau
A. Möslang
M. Rieth
M. Schirra
H. Zimmermann

Literature:

[1] R. Lindau, A. Möslang, M. Schirra, P. Schlossmacher, M. Klimenkov, "Mechanical and Microstructural Properties of a Hipped RAFM ODS-Steel", 10th International Conference on Fusion Reactor Materials, October 14-19, 2001, Baden-Baden, Germany.

[2] R. Lindau, A. Möslang, M. Schirra, "Mechanical Properties of Hipped RAFM ODS Steels for Fusion Application", 22nd International Symposium on Fusion Technology, September 9-13, 2002, Helsinki, Finland.

[3] Yttrium Oxide Particles in ODS Steels for Fusion Reactor Application" submitted to Journal of Crystall Growth

[4] M. Klimiankou, R. Lindau, A. Möslang, „HRTEM Study of Yttrium Oxide Particles in ODS Steels for Fusion Reactor Application" 15th International Congress on Electron Microscopy, Durban, ZA, Sept 1-6, 2002.

TTMS-006/9
ODS Powder Sieving and Distribution

About 700 kg of N-atomised EUROFER powder were screened at Studsvik giving 284 kg powder with particle sizes < 150 μm. This powder was distributed to the associations for further processing. The rest has been stock piled for future needs.

Staff:

R. Lindau

TTMS-006/13
ODS/Eurofer Joining

Assessment of Diffusion Bonding Process Feasibility

The objective of this work is to investigate the appropriate hot isostatic pressing (HIP) technique including the boundary conditions and parameters in order to achieve good mechanical properties of the diffusion welded joints of ODS EUROFER with other structure materials.

Status of work

For the first attempt on HIP joining of ODS EUROFER with EUROFER altogether six pairs of semicircular specimens from both materials with a size of each diam. 55 mm and 16.5 mm of thickness were manufactured (Fig. 1), which are suitable for later production of the standard specimens for tensile and impact tests for the HIP welding joint and the base material zone.

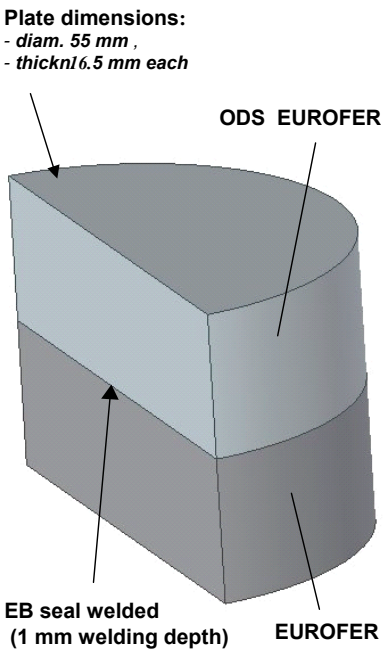

Fig. 1: Specimen layout for HIP joining of ODS EUROFER with EUROFER.

The sample preparation is accomplished using the same procedure which was successfully applied to the earlier experiments on HIP diffusion welding of EUROFER specimens [1,2]. The HIP joining surfaces are dry milled to a surface roughness of Rt ≤ 2 μm. Cleaning was performed in an ultrasonic bath with acetone. Immediately after cleaning, the specimen halves of ODS Eurofer and Eurofer each were seal welded together at the edge of the joining surfaces by means of electron beam welding under a vacuum.

Outlook

In the next step, the HIP diffusion welding will be performed in each case at a temperature of 980 °C, 1050 °C as well as 1100 °C and a pressure of 100 MPa, with a following heat treatment with and without austenitizing. Afterwards the production of the specimens for tensile and notched bar impact will take place followed by the actual strength tests.

Staff:

R. Lindau
P. Norajitra
G. Reimann

Literature:

[1] P. Norajitra, G. Reimann, R. Ruprecht, L. Schäfer: HIP experiments on the first wall and cooling plate specimens for the EU HCPB blanket, to be published in Journal of Nuclear Materials, 2002.

[2] G. Reimann, P. Norajitra, R. Ruprecht, R. Vouriot, H. Kempe: Diffusion Welding Tests in Hot Isostatic Presses for Manufacturing Plate Components with Internal Cooling Channels for Fusion Blankets (TTBB-002-D1), - Eighth Test Series, Final Report -, FZK-Fusion Report Nr. 185, March 2002.

TTMS-EP 01-622
Order of EUROFER Heats

The European programme related to fusion reactor relevant structural materials aims to develop a low activation material which can withstand high neutron loads under temperature and coolant conditions required in a Fusion reactor based on magnetic confinement plasma.

For that purpose the 8-12 Cr reduced activation ferritic/martensitic (RAFM) steel was selected as reference structural material and the present R&D aims to:

- develop, characterise and implement a RAFM steel to be used for the fabrication of the Test Blanket Modules (TBMs) to be installed in ITER,
- optimise such a RAFM steel for the utilisation in a Fusion reactor (DEMO and Power Plant).

Based on the substantial experience gained from various RAFM alloys developed in JA and EU and in order to reduce the long-term activation and improve the mechanical properties of such a steel prior and after irradiation, an industrial 3.5 tons batch of 9 CrWVTa RAFM steel, named EUROFER 97 was specified, ordered and produced.

Additional EUROFER 97 material is needed for further fabrication trials, in order in particular to build TBMs mock-ups. This new procurement has also as major objective to check the reproducibility of properties compared to batches available from the previous fabrication, to assess the achievable limits of reduction of detrimental impurities like Nb, Mo, Ni, Cu, Al, Co and others and to improve the quality of the tubing production.

Under operation the material will be exposed to temperatures up to 550°C, cyclic loading and neutron irradiation. The limitation of the undesired elements like Nb, Mo, Ni, Cu, Al, Co and others, that produce long-lived radio-active isotopes under neutron irradiation, makes this steel a so-called reduced activation steel. Components of such a steel can be handled and stored within a manageable period of time after reactor shut down. This steel will be used for components with high reliability requirements.

The scope of this task is to provide a normalised and tempered martensitic steel type 9 CrWTaV designated EUROFER 97-2, under different product forms.

Therefore a technical specification has been elaborated considering all the experiences with the procurement of the first heats of EUROFER 97.

Since reproducibility of the good properties of EUROFER 97 is one important goal of the procurement, the technical specification leans close to that of the first heats produced by Böhler in Austria.

A call for tender has been launched and finally after evaluation of the offers a producer was selected for the production of about 8 tons of different product forms that are listed in Table 1. The signature of the contract is expected before long.

Unfortunately it was not possible to find an European manufacturer for the production of rectangular tubes in an industrial production process at a reasonable price. These tubes were designated for the manufacturing of cooled First Wall segments.

Table 1: Product forms and amounts to be ordered.

Semi-finished product		Dimen-sions mm	Amount m^2	Amount m	Mass kg	Total Mass kg
Plates	Thickness	3	6		140	
		5	20		775	
		8	14		868	
		14	17		1817	
		25	12		2228	
						5828
Forging	Diameter	100		10	609	
						609
Billet for tube production	Diameter	200		3	730	730
Tubes (circular)	Outer	33.4x3.4		30	75	
	Diameter	56x3		30	116	
	x Wall-					
	Thickness					191
Tubes (rectan-gular)	Inner/outer dimensions	I18x14x O26x22		120	298	
						298
						7656

Staff:

R. Lindau

TTMA-001
Advanced Materials: SiC/SiC Ceramic Composites

TTMA-001/11 Modelling of the Damage behaviour of SiC/SiC

Lifetime Modelling

The objective of this task is the modelling of the mechanical behaviour of SiC/SiC composite. In the final run the aim is

- to simulate the stress-strain curve and the damage behaviour
- to predict the life time of blanket modules
- to define design rules for composite materials.

The first task was to evaluate models that have been used in the literature. Suitable modelling might start from different levels.

(1) Microscopic models

The description starts from the properties of the constituents (fiber, matrix, boundary). The advantage is an exact description of small samples. However, the quantitative description and evaluation of macroscopic systems is difficult even with powerful computer systems.

(2) Macroscopic models

The idea is to use a continuum mechanical model with constitutive equations including a damage variable. As a starting point the damage variable might be a scalar variable (simulating isotropic damage), but finally has to be generalised to be a tensor (describing an-isotropic damage). The advantage of this kind of models is that the mechanical analysis of blanket (sub)components is similar to design with metals. As there are already some FE-codes that include for example Lemaitre-type of damage variables, this could be seen as the fast track approach to design and analyse SiC/SiC components. The disadvantage is that knowledge from the micro-structural level cannot be directly incorporated. In the EU this approach is currently followed by CEA, France.

(3) Meso-scopic models

Simplified constitutive equations are used to describe the microscopic constituents and their interaction (e.g. laws for surface friction, energy release rate). The favourable feature is that the model combines micro- and macroscopic analyses. However, the necessary adjustments may finally lead to complex constitutive equations. This approach is followed by FZK and is described in detail in the following.

Interface bonding plays the key role in the description of damage. In case of a very strong bonding, matrix cracks are not deflected at the interface and may propagate through the interface. Then the fiber cracks with high probability and there is no bridging effect. On the other hand, in case of a weaker bonding matrix, cracks may be deviated at the interface and energy is dissipated by debonding.

(A) First, regular fiber arrangements of parallel fibers as a realisation of an *ideal reinforced material* (as depicted in Figure 1) have been considered. The mechanical behaviour is determined mainly by the elastic constants of the fiber and the matrix E_f, ν_f; E_m, ν_m, and the average fiber volume. Moreover, residual stresses due to fabrication and thermal mismatch should be included in the models. The main difference between the models available is how interface properties are treated, i.e. either by surface roughness and friction coefficients or by a critical energy release rate (here an interface-surface-crack is the fracture mechanical model behind). Two models have been considered, as representative for each of the approaches: the Marshall model and the enhanced McCartney model. Both were evaluated for a constant volume fraction and for variable radius of the matrix. The main features of the models are compared in table 1.

Table 1: Comparison of different models.

Marshall Model	Enhanced McCartney-Modell
• Shear stress at the interface determine interface debonding • Axial stresses are continuous at the transition between a adherent and a delaminated interface • No minimum load necessary to initiate debonding • Area of debonding is proportional to the load • Relative displacement between fiber and matrix is proportional to the load squared	• Energy criteria for debonding of interface • Area of debonding depends on energy release rate, load, thermal (residual) stresses and friction coefficient

The interface properties can be determined from

- pull-out-tests (pull of a single fiber)
- push-in-tests (indentation push on a single fiber)
- slice-compression-tests (weak metal plate push in fiber direction).

Properties are evaluated from the load-displacement-curve and also from measurements after unloading (REM) in case of the slice-compression-test. The last two methods are compared in table 2. For adjustment of material properties the slice compression test may be favourable.

(B) For a *real reinforced material* the size of the fibers and the relative distance between fibers is random. A Voronoi-tessellation is used to simulate a realistic arrangement of a bundle of fibers. The Voronoi-tessellation represents a cell structure constructed from a point process by introducing cell walls perpendicular to lines connecting neighbouring points. The most simple and common choice is a Poisson-Point-Process with uniformly distributed independent points. Any point generated in the process represents the middle point of a fiber. The diameter of the fibers might be also chosen randomly, see Figure 2.

To describe a more irregular arrangement of the fibers a Cluster-Point-Process can be used. If on the other hand the structure is more regular, than a so called Hardcore-Point-Process is suitable with a lower boundary for the distance between neighboring points. Finally, for finite element

application an automatic mesh generation is performed with the macro-language PCL within the pre-postprocessor MSC.-Patran.

Table 2: Comparison of different test methods.

Slice compression test	**Push-in test**
Many fibers under the same experimental conditions	Single fiber
Relative displacements determined indirectly after maximum load and from unloading	Continuous force-displacement curves
Typical interface parameters (energy release rate, coefficient of kinetic friction) directly from experimental results	Typical interface parameters (energy release rate, coefficient of kinetic friction) from force-displacement curve
Influence of geometrical variations easy to measure	High accuracy
'simple' Drawback: only two values for each fiber	Limit: single fibers are not representative

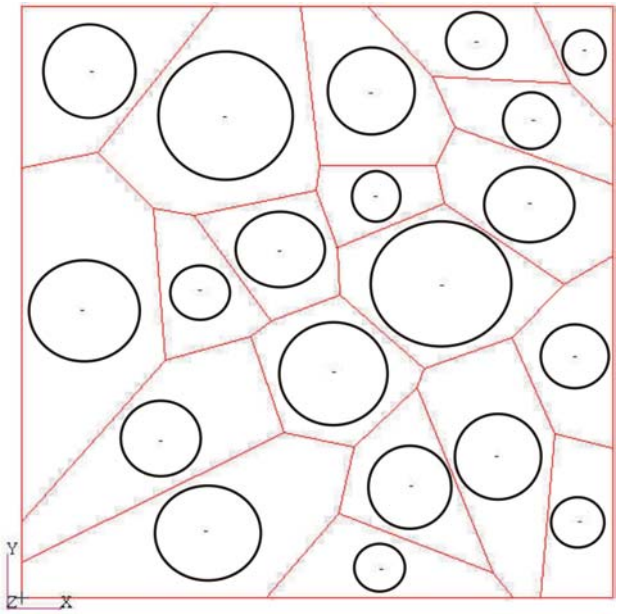

Experiments and adjustment of model parameters will be performed in 2003 with the next EU batch of SiC/SiC.

Staff:

E. Diegele
T. Fett
G. Rizzi

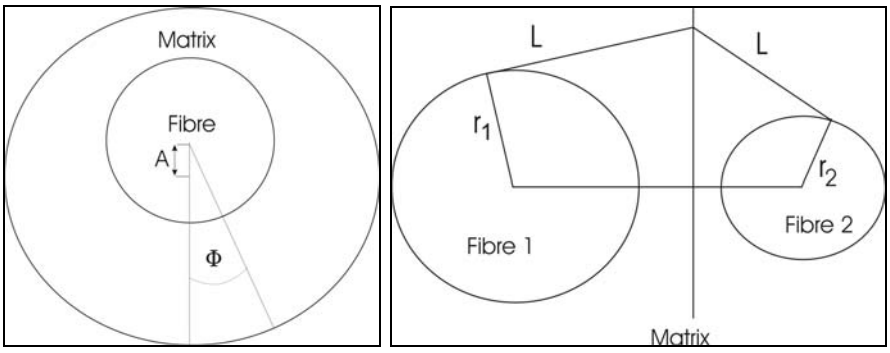

Fig. 1: Geometry as considered in regular fiber arrangements (left hand side; for axial-symmetric modelling the off-set A equals zero); and irregular fiber arrangements (right hand side).

Neutron Source

TTMI-001
IFMIF-Accelerator Facilities

I. Ion Source

I.1 Detailed layout of slit grid emittance measurement device

In order to measure the beam emittance of the Frankfurt proton/deuteron source, a new slit grid device is going to be used. The device was fabricated at the company "PET" in Darmstadt in close cooperation with us and cost about 125 k€. The measurement device was delivered and is being installed and tested on the ion source test stand for first calibration measurements.

A beam emittance measurement just behind the ion source [1] is a crucial issue. Due to the high beam current (up to 200 mA @ 55 keV) and the low beam radius, the thermal load of the slit is very high. Therefore a high power silt with an improved water cooling system was designed and implemented in the new device.

Since the beam radius and angle behind the ion source are very small, a high measurement resolution is required. The space resolution is given by the increment of the slit, whereas the increment is determined by the height of the slit. With the used slit performance, the space resolution of our device is 0.1 mm. The angle resolution is given by the grid wire distance divided by the slit - grid distance. The wire distance is fixed to 1 mm. As both feed through are integrated in different vacuum chambers, by means of the distance between the two chambers, the angle resolution can be optimized. With a slit grid distance of about 1 m an angle resolution of 1 mrad can be achieved. Table 1 summarizes the main parameters of our emittance device.

Preliminary tests of the emittance device were performed using a small ion source and two Gabor plasma lenses. The beam current was 10 mA of Ar^{1+} at an energy of 14 keV. Figure 1 presents a measured beam emittance behind the lenses. The normalized rms beam emittance was 0.06 π mm mrad.

Tab. 1: Parameter of the emittance device.

Minimal beam diameter	~ 8 mm
Maximal beam diameter	~ 30 mm
Maximal beam current	+/- 200 mA, dc and pulsed
Increment	0.05 mm, … 0.5 mm;
Slit height	0.1 – 0.2 mm
Measured displacement	+/- 30 mm
Thickness of wires	0.1 mm
Number of wires	60
Distance of wires	1 mm
Duty cycle	0.1 – 10 %
Pulse length	0.1 – 2 ms
Repetition rate	50 – 200 Hz

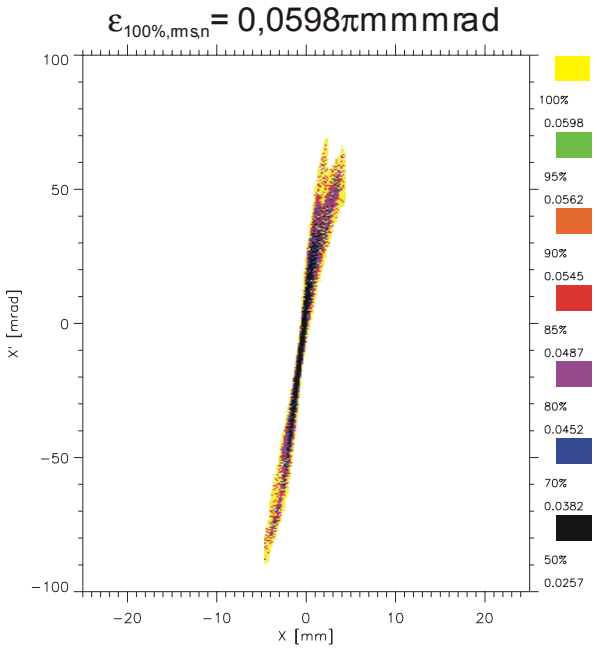

Fig. 1: First emittance measurement.

II. Investigation of 4-Rod RFQ

Investigations of the 4-Rod–RFQ structure have been made as an alternative solution to the complex 4-Vane structure. Though power dissipation is approximately the same and current densities are higher by a factor of 2-3. The fields are concentrated in the resonating stem structure, which can be cooled very efficiently. The rf-coupling of this structure is stronger so tuning sensitivity and operating stability is very high.

Work on a cw hot model is being started to test the 4-Rod RFQ structure in this parameter range. The RFQ is 4m long and designed to operate at a duty factor of 20%.

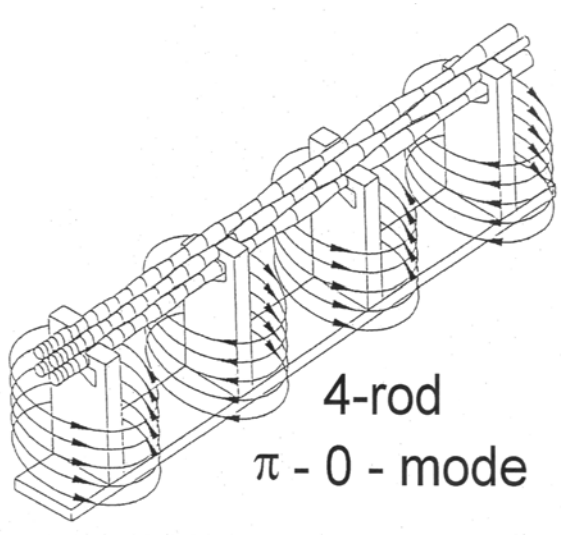

Fig 2: Scheme of the 4-Rod RFQ insert.

The alignment and tuning has been done with very good results. The 4-Rod RFQ has an input output energy of 35keV/4Mev and a resonance frequency of 200MHz. The field flatness is within 1.5%, the Q_0 = 3350. The cavity has one central rf-input coupler

and two sliding tuners for thermal compensation with a tune of Δf=0.55 MHz.

The rf-conditioning was done up to a power level of 250kW for proton beam tests. The conditioning process was successful. It was only interrupted by a melting of the rf-loop caused by a block of water flow by water problems. The RFQ has been put back into operation and is ready for beam tests.

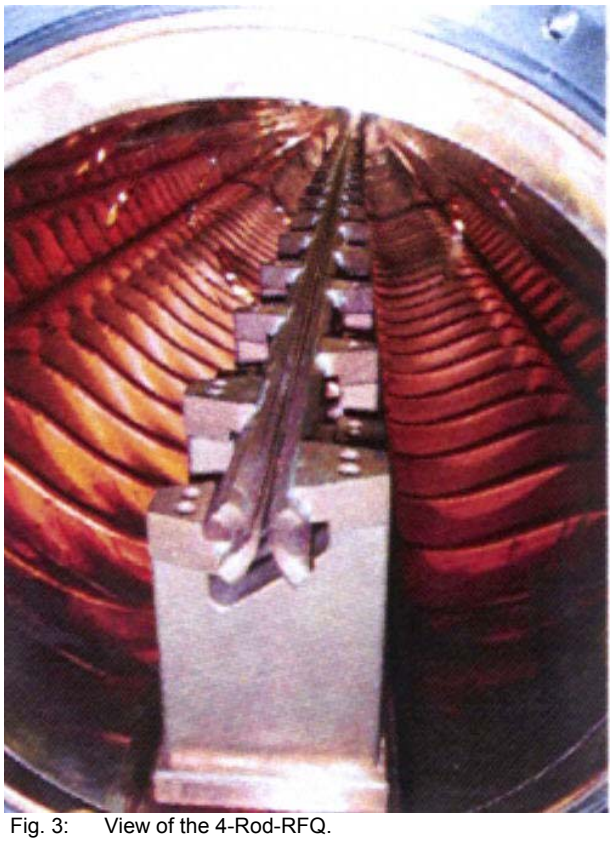

Fig. 3: View of the 4-Rod-RFQ.

III Investigation of IH- and CH-Type Structures for the IFMIF Drift Tube Linac (DTL)

III.1 IH-type DTL design

The investigation of a modular built IH-type DTL for IFMIF has been continued. Main aspects of the work have been a smooth beam behaviour, i.e. better matching between the sections and moderate rf losses in the cavities due to the required cw operation of the linac. A reconsideration of all sections led to an improved layout of the IH-linac [2]. The number of sections has been increased to 10, as shown in fig. 4. To achieve the required second end energy of 35 MeV the field amplitude in tank 9 has to be reduced to 79%, tank 10 provides no acceleration to the beam. Table 2 summarizes the most important parameters. Especially the longitudinal emittance growth could be clearly reduced to about 30 % only.

The beam dynamics calculations using the KONUS concept [3] for high linac efficiency showed 100 % transmission and a good safety margin between outer beam diameter and quadrupole aperture. To ensure the robustness of the design error studies have to be performed for the accelerator and focusing elements. In figure 5 the full transverse size of 100% of the beam is plotted along the linac for quadrupole gradient and adjustment errors. The beam stays well confined, no particle losses occurred in the calculations.

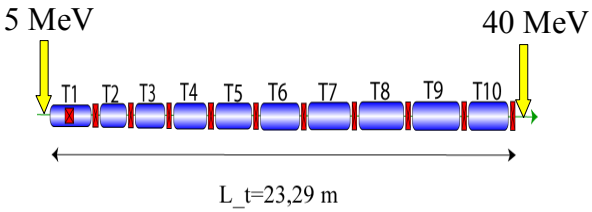

Fig. 4: Schematic layout of a modular IH-Type linac with intertank focusing.

Table 2: Structure and beam parameters of the IH-type DTL.

	IH	Units
A/q	2 (D^+)	
I design	125.0	mA
f_{rf}	175.0	MHz
N_T / N_{cell}	10 / 157	
$<L_T>$	1.97	m
$P_{Cu+Beam/T}$	0.536	MW
$P_{Cu/T}$	0.095	MW
$P_{Cu/L}$	0.0487	MW/m
W_{in} / W_{out}	5.0 / 40	MeV
$W_{tot/L}$	1.51	MeV/m
L_{tot}	23.29	m
E_oT	1.82 – 0.78	MV/m
r_o	1.5/2.0	cm
B_{quad}	1.3 - 0.94	T
ZT^2	150.00 - 58.27	MO/m
b_{Kilp}	0.43	
In/Out rms ε^n_{trans}	0.035 / 0.068	cm×mrad
In/Out rms ε^n_{long}	0.070 / 0.098	cm×mrad

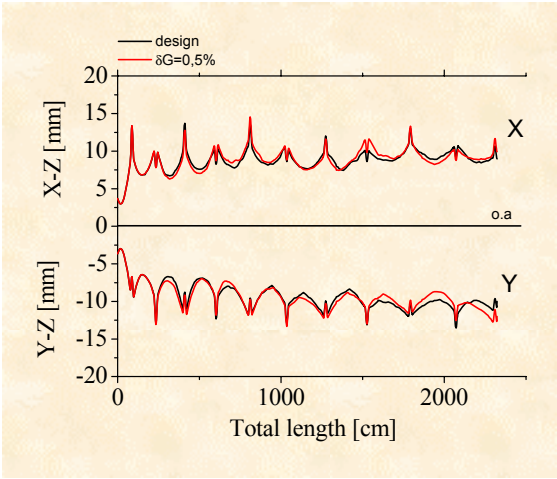

Fig. 5a: Comparison of the transverse beam behaviour for 100% of the beam without and with gradient errors of 0.5%.

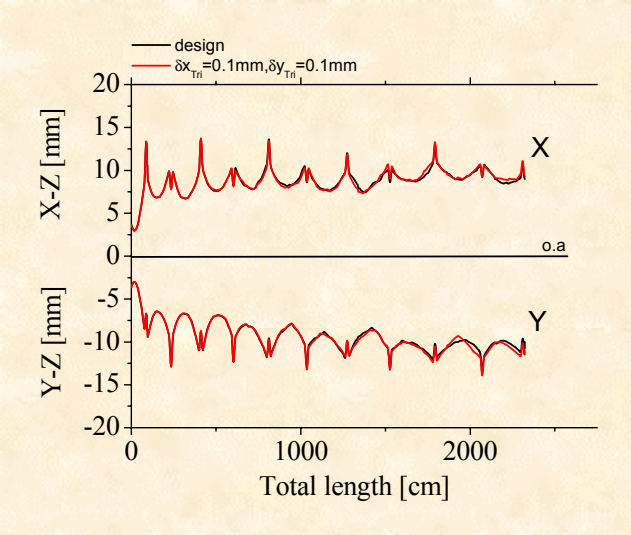

Fig. 5b: Comparison of transverse beam behaviour for 100% of the beam without and with quadrupole adjustment errors.

The rf-efficiency is clearly higher for the IH-DTL compared to the Alvarez-type DTL. In addition the intertank focusing eases handling and adjustment. Therefore the IH-Type DTL could be a suitable back-up solution for a room temperature IFMIF linac design.

III.2 Superconducting CH-type DTL design

In the IFMIF reference design a room temperature Alvarez type DTL has been proposed as a standard solution [4,5]. The required cw operation at high beam current with extremely low allowable particle losses give rise to look for a superconducting linac layout: The rf structure losses are negligible and superconducting structures allow larger sizes of drift tube apertures. A possible candidate for a superconducting multi-gap structure is the CH (Crossed bar) H-type version, operated in the H211-mode [6]. Fig. 6 gives views of the s.c. CH-cavity layout for IFMIF, as an example tank 2 of the proposed linac design for IFMIF is plotted. In fig. 7 the linac scheme is shown, consisting of one r.t IH-tank followed by 4 s.c. CH-tanks with intercavity focusing. The length is now 10.8 m only at moderate magnetic and electric peak field levels. In table 3 the main linac parameters are summarized. Table 4 gives the cavity parameters of the first superconducting cavity (tank 2) of the linac, calculated with the code Microwave Studio [6].

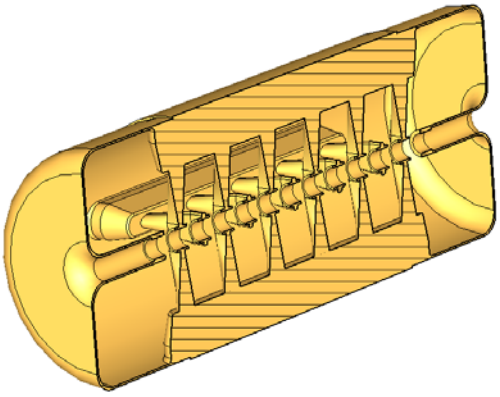

Fig. 6a: View of the 175 MHZ s.c. CH-cavity, calculated with Microwave Studio.

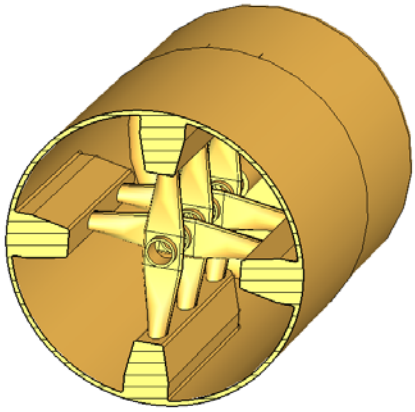

Fig. 6b: Middle cut of the 175 MHz s.c. CH-cavity for IFMIF.

Again particle dynamics calculations must be performed to ensure the capability of the s.c. CH-DTL design to handle the required high currents without losses. The calculations have been done with 10,000 particles and results show 100 % transmission and a moderate emittance growth [8,9]. The aperture radii can be opened along the linac to 4 cm giving a large safety margin. Fig. 8 illustrates the longitudinal beam behaviour, which is typical for the KONUS beam dynamics design.

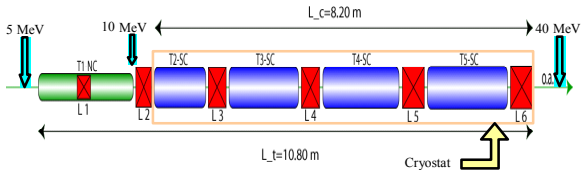

Fig. 7: Schematic layout of a 175 MHz s.c. CH-type DTL for IFMIF.

Table 3: Design parameters of the s.c. CH-DTL for IFMIF

Design current	125.0	mA
Frequency	175.0	MHz
Lattice	FDF – DFD	
Number of tanks	5 (1NC+4SC)	
P_{tot} per tank	NC:690.0 SC:740.0	kW
W_{in} / W_{out}	5.0 / 40	MeV
Cells / Length	73 / 10.8	m
E_0T: NC/SC	1.95 / 4.1	MV/m
Bore radius of DT	NC:1.5 SC:2.4 - 4.0	cm
Max quad gradient	6.40	kG/cm
Max quad field	1.28	T
Max Kilpatrick	1.00	
In- / Out RMS ε^n_{trans}	0.035 / 0.091	cm×mrad
In- / Out RMS ε^n_{long}	0.070 / 0.097	cm×mrad

Table 4: Cavity parameters of tank 2 of the s.c. CH-DTL design for IFMIF.

Cavity parameters	*Tank 2 IFMIF DTL*	*Units*
Beta:	0.1	
Frequency:	174.86	MHz
E_{acc}:	5.35	MV/m
E_{peak}:	38.7	MV/m
B_{peak}:	49.1	mT
Tank length:	1.52	m
Drift tube diameter:	5.0	cm
Tank diameter:	58.0	cm
Number of gaps:	12	
E_{peak}/E_{acc}:	7.23	
B_{peak}/E_{acc}:	9.17	mT/MV/m

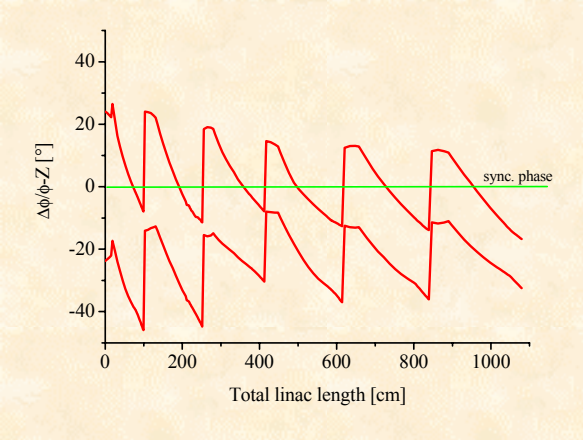

Fig. 8: Phase envelope along the linac in the KONUS design.

In the fig. 9 the transverse beam behaviour is shown for 100 % of the beam. No losses occur and the aperture to beam ratio is quite large compared to the r.t. linac layout. Finally in fig. 10 the energy-phase diagram of the beam is plotted. The beam is still well confined for the following high energy beam transport line. The particle dynamics calculations have to be continued to including error studies to guarantee the required low loss regime in order to avoid structure activation.

III.3 Model measurements

A down scaled copper model (1:2) has been built at the IAP in Frankfurt in order to determine basic rf properties (see fig. 11). The model has 18 gaps and the cell length has been kept constant with a ß of 0.17. The tank diameter is about 30 cm and the tank length about 1.2 m. The measured frequency (350 MHz) was less than 1% lower than the frequency calculated with Micro Wave Studio (352 MHz).

Measurements of the longitudinal field profile have been performed to investigate different tuning possibilities. Fig.12 shows an example of a measured field profile along the z-axis (bead pull method) [10].

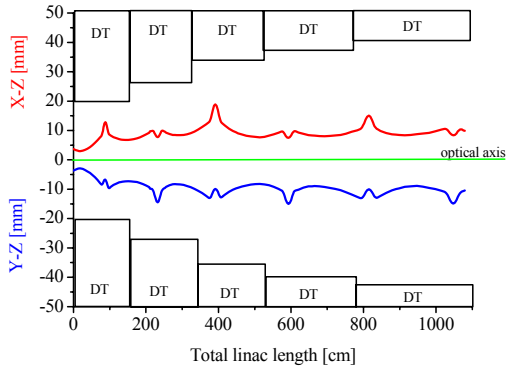

Fig. 9: Transverse beam size for 100% of the beam along the linac. For comparison the aperture radii are plotted in the different tanks.

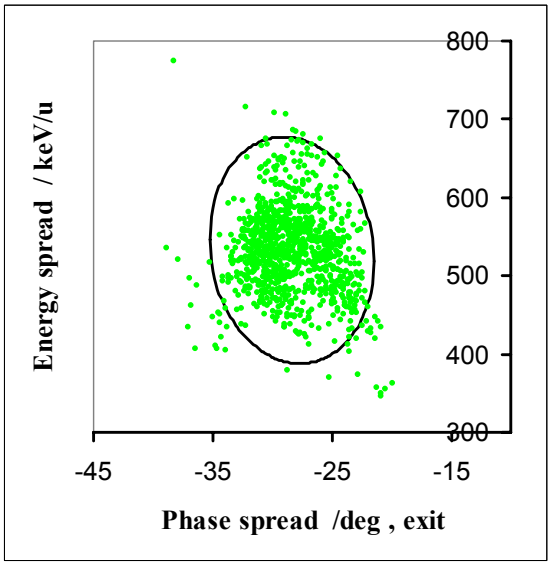

Fig. 10: Longitudinal output distribution at the linac end (40 MeV). For comparison the 95 % emittance ellipse is drawn.

Fig. 11: Photo of the copper model of the 350 MHz CH structure.

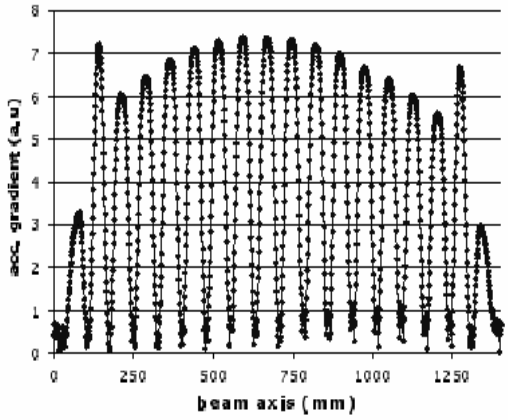

Fig. 12: Measured field profile along the z-axis.

III.4 Conclusions

Both H-type structure designs for the IFMIF DTL show the capability for high current beam operation free of particle losses. They offer a good potential for improvements within the reference layout of the IFMIF accelerator facility. Further studies concerning the technical layout and reliability are underway. In a next step a 1:2 model of tank 2 of the proposed s.c. IFMIF DTL made out of Niobium will be built and then tested in our cryolab.

IV Non destructive beam diagnostic

IV.1 Tomography of ion beams using a CCD-camera

The determination of the beam emittance using conventional destructive methods suffers from two main disadvantages. The interaction between the ion beam and the measurement device produces a high amount of secondary particles, which can influence the beam transport. Additionally the power deposited on the emittance measurement device (1kW/mm^2) can lead to extensive heat on the detector itself and can destruct the device. CCD camera measurements of the incident light emitted from interaction of beam ions with the residual gas are commonly used for determination of the beam emittance (11).

Emittance measurements methods using optical measurement devices described in the literature [12] are only applicable for rotationally symmetric ion beams. Computerized tomography allows determining any beam profiles. This can be done using the inverse Fourier transformation of sufficiency number of projections (>40) of the ion beam. For this the CCD-camera will be rotated around the ion beam (fig. 13). The accurate distribution of the beam ion density in the space phase [13] can be univocal determine from the beam profiles measured as a function of the lateral position of the camera using convenient numerical methods of data analysis [14].

Using a CCD chip with 1024 x 1024 pixels one image covers over 1000 beam profile measurements along the beam axis. (The measurements cover a drift distance of approximately 40 mm.) Therefore this method allows determining the beam profiles in a four dimensional phase space.

The tomographic measurement device yields a maximum of space resolved information about the longitudinal development of the beam profile. Due to the aspect of measurement duration this method is inapplicable for time resolved measurements.

For time resolved measurements of beam profiles in two planes two time synchronously controlled CCD cameras constructed in the same way will be installed in orthogonal arrangement.

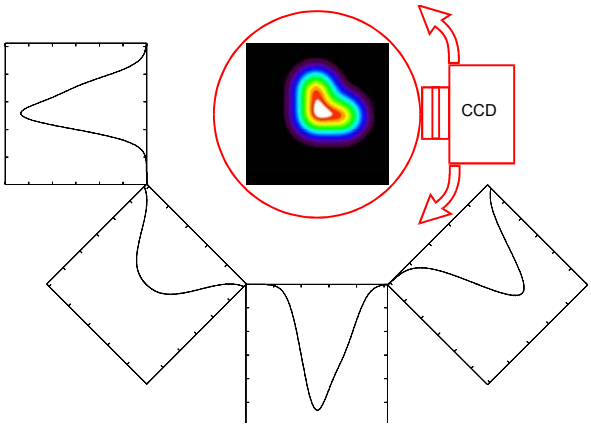

Fig. 13: Schematic drawing of the tomography set up for the determination of the density distribution of ion beams in space phase using CCD-camera images.

Staff:

H. Deitinghoff
A. Jakob
H. Klein
H. Liebermann
O. Meusel
H. Podlech
J. Pozimski
U. Ratzinger
A. Sauer
A. Schempp
R. Tiede
K. Volk

Johann Wolfgang Goethe-Universität
Institut für Angewandte Physik (IAP)
Robert-Mayer-Strasse 2-4
60486 Frankfurt am Main

Literature:

[1] R. Hollinger, P. Beller, K. Volk, M. Weber, H. Klein, *The Frankfurt 200 mA Proton Source*, Rev. Sci. Instrum., 71, Volume II, 836-838, 2000

[2] A. Sauer, R. Tiede, H. Deitinghoff, H. Klein U. Ratzinger, Investigation of a Normal Conducting 175 MHz Design for IFMIF, Proc. EPAC2002, June 2002, Paris, France, p. 951

[3] U. Ratzinger, Effiziente HF-Linearbeschleuniger für leichte und schwere Ionen, Habilitationsschrift Universität Frankfurt am Main, 1998

[4] R. Duperrier, D. Uriot, N. Pichoff, R. Ferdinand, Beams Dynamics End to End Simulations in IFMIF Linac, Proc. EPAC2002, June 2002, Paris, France, p.1335

[5] A. Sauer, H. Deitinghoff, H. Klein, Beam Dynamics Calculations for a High Current Ion Injector, Proc. LINAC200, Monterey, Ca., SLAC-R-561, p. 803

[6] R. Eichhorn, U. Ratzinger, Superconducting H-Mode Structures for Medium Energy Beams, Ibidem, p. 926

[7] CST MICROWAVE STUDIO, Computer Simulation Technology

[8] A. Sauer, R. Tiede, H. Deitinghoff, H. Klein, U. Ratzinger, Beam Dynamics Design of a Superconducting 175 MHz Design for IFMIF, Proc. EPAC2002, June 2002, Paris, France, p. 1404

[9] A. Sauer, H. Deitinghoff, H. Klein, H. Liebermann, H. Podlech, U. Ratzinger, R. Tiede, Beam Dynamics Layuot of H-Type Drift Tube Linacs for Intense Light Ion Beams Proc. LINAC2002, August 2002, Gyeongju, Korea,

[10] R. Eichhorn, C. Peschke, Superconducting CH-Cavities for Low- And Medium Beta Ion and Proton Accelerators, GSI Scientific Report, GSI-2002-1, GSI Darmstadt, (2002), p. 203

[11] K. Ebihara et al, Nucl. Instr. And Meth. 202, 403-409 (1982)

[12] Sittinger, Dissertation IAP 1995

[13] J. Radon, Berichte der Sächsischen Akademie der Wissenschaften, Leipzig, Math.-Phys. Kl. 69 (1917) 262

[14] Kak, Avinash, Principles of computerized tomographic imaging, IEEE No. PC02071

TTMI-003
IFMIF, Test Facilities

TTMI-003-1
He-cooled High Flux Test Module

1. Introduction

The reference design of the International Fusion Materials Irradiation Facility (IFMIF), described in the CDA report [1], envisages a High Flux Test Module (HFTM) with 27 rigs. The rigs house capsules which enclose the material specimens to be irradiated. The rigs have an almost squared cross section. Due to the irradiation with neutrons and gamma-radiation the specimen and the structural materials exhibit an internal volume heating. The rigs are cooled with helium flowing upward at the outside of the rig walls. The gap inside the rig and between the capsule wall act as thermal insulation. The capsule is surrounded by electric heaters. They have to keep the capsule and specimens at constant temperatures independent of nuclear heat density spatial distribution and fluctuations.

The rigs are positioned in a container. The inlet section to the container has to distribute the helium uniformly to all gaps between the rigs. According to the preceding nuclear analysis, reflector elements were arranged lateral to the container. Steel extensions of the rigs provide an axial reflector.

The re-design of the HFTM aims at “maximum space and flexibility for the specimens” which in turn means “minimum space for heater, coolant channels and structural material”.

The nuclear volume heating causes temperature gradients within the specimen and the structural material. The heat transfer from the specimen via the capsule and the rig walls to the helium coolant with variation of the heat transfer coefficient in the helium channel and increase of the helium temperature along the channel creates a complex temperature distribution. Beyond that the nuclear heat density has a spatial distribution [2]. The rig design and the lay out of the electric capsule heaters have to cope with and minimize the temperature differences within the specimen stack.

2. Spatial distribution of the nuclear heat density

Fig. 1 shows the power distribution as result of nuclear calculations [2]. The figure also depicts the geometry of the HFTM of the reference design. However an earlier described result of the nuclear calculation required an extension of the HFTM in vertical direction to about 80mm in respect of an optimal exploitation of the neutron beam. From Fig. 1 we can take the power density gradients in al three dimensions. Only at the beam entrance side at z=0 the power density varies within about 15% in x-direction till 80mm and in z-direction till about 15mm. In the y-direction the power declines by a factor of 3 within the region of interest. As this is the region with the highest power density our detailed analysis of the temperature field in the rigs and the heat removal is mainly devoted to this position in the container.

3. Rigs with chocolate plate like cross section

The design analysis started from the reference design with rigs of an almost squared cross sections. The reasons for the transition to chocolate plate like cross section are given before the new design is presented [3, 4].

3.1 Rig design with squared cross section

The temperature distribution within the specimen volume of a squared rig was calculated with the code PERMAS for the highest power density at the beam entrance position. Only with a temperature control or heat removal from all 4 rig sides the temperature variation can be kept below 10°C. This entails a cooling gap on the four sides of the rigs and for temperature control at beam shut-down situation electric heaters on all four surfaces of the capsule.

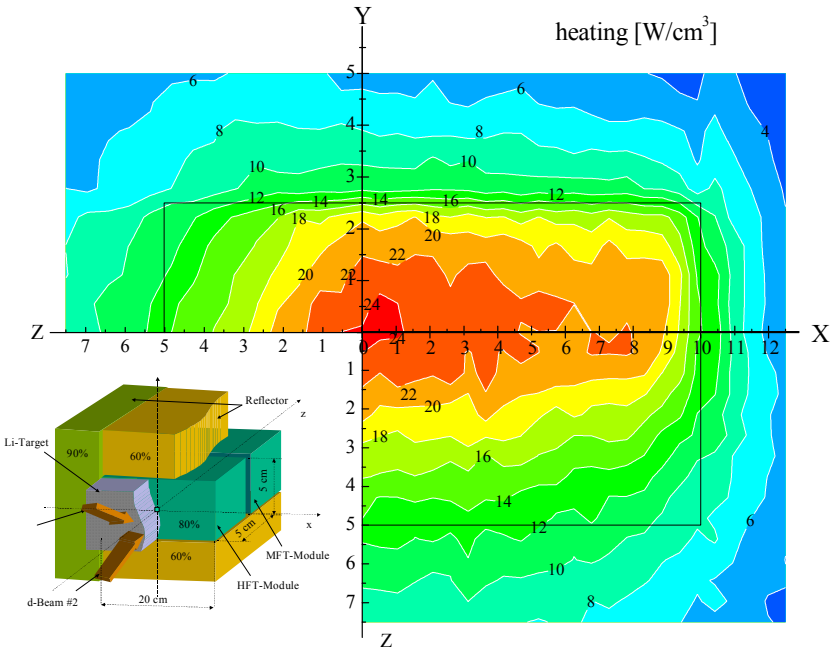

Fig. 1: Heat production in and around the HFTM with EUROFER reflector of 10 cm thickness (bottom). Black lines show geometrical boundaries of the reference test module (20×5×5 cm^3).

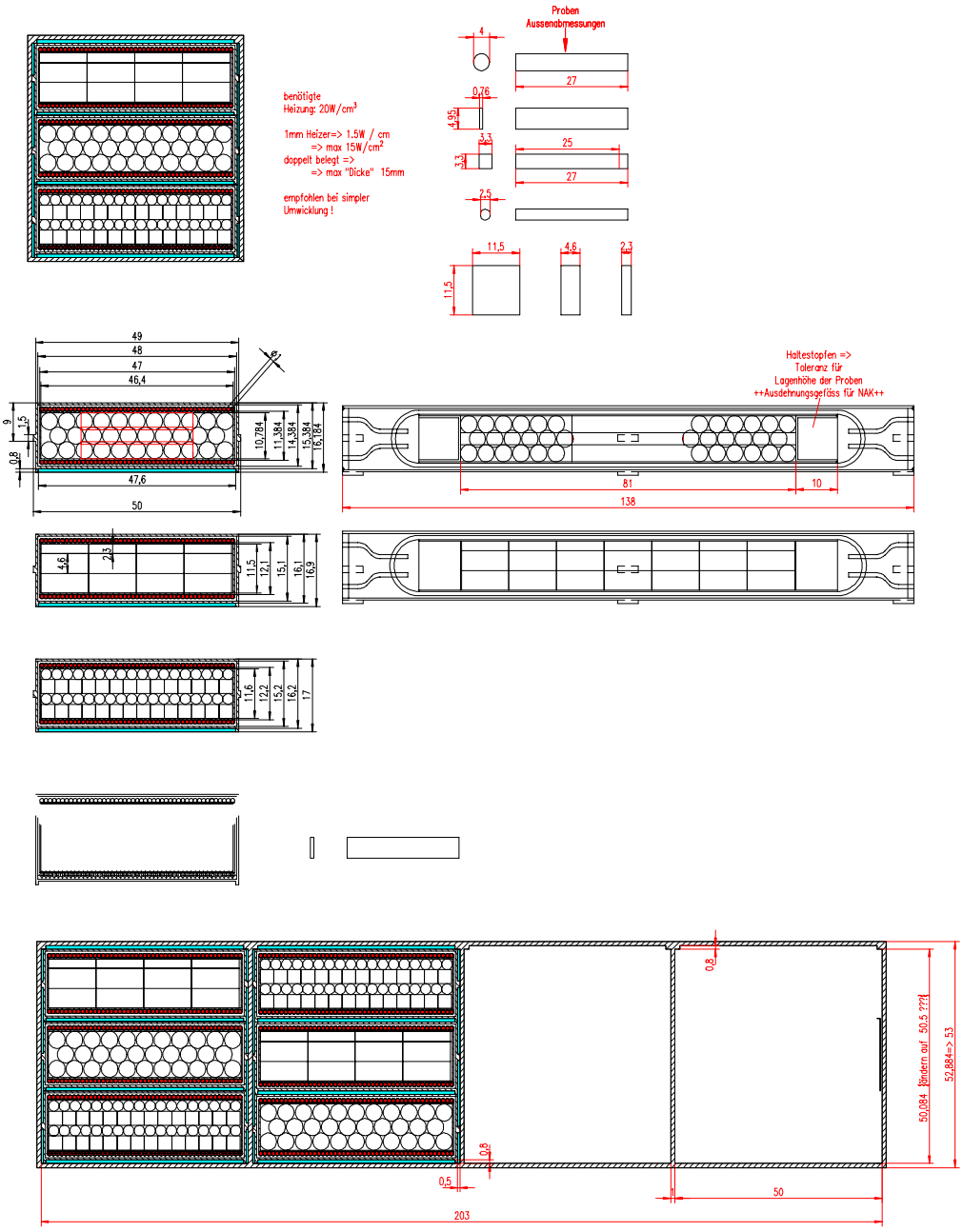

Fig. 2: Rigs with chocolate plate like cross section installed in the container which is subdivided into 4 compartments; the specimen types are depicted right on top; studies with specimen arrangements are shown on the left side; the container with compartments and rigs is presented below.

In chapter 2 the nuclear power density gradient in vertical direction was addressed. Additional heaters are necessary in order to balance the power and to prevent a vertical temperature gradient. To achieve such a power distribution with electric jacket wire heater as usually applied would require too much space.

Therefore, less space consuming flat plate heaters were suggested. Two heaters are embedded in a ceramic carrier. They can be arranged in a way that they balance the nuclear heating as well as create an apt power distribution without a nuclear contribution. A promising development on the basis of AlN-ceramic with heater tracks from TaC is investigated together with a ceramic manufacturer.

3.2 Heat transfer from specimen to specimen and to the capsule wall

Specimen inserted into the capsule will fill up the space according to their shape. This will alter the nuclear power release on the one hand, and may be mitigated by filler pieces. On the other hand the power must be transported across the boundary from specimen to specimen and finally to the capsule wall. However the heat transfer can hardly be

defined or guarantied in practice if the gap between to pieces is filled by a gas.

Supplemented by further analyses indicate that the capsules have to be filled with sodium. Nuclear calculations showed, that the small amount of sodium in the capsules had no impact on the neutron flux and the power release. The use of the eutectic alloy Na/K in order to alleviate the handling is still under discussion.

Capsules filled with a liquid metal preclude the open boxes with flat heater. Therewith, electric heaters from the jacket wire type have to be used. Nevertheless the material development for the flat ceramic heaters is continued for capsules in positions with lower power density.

3.3 Chocolate plate rigs design

Smaller width of the specimen volume, the need for wire heaters and the need for reduced space for the wire heaters lead to the decision to analyse rigs with a chocolate plate like cross section. The wish to keep individual rigs independent at different temperatures levels caused the subdivision of the container into four compartments filled with 3 rigs each. The major contour dimensions of the specimen is shown in Fig. 2 (top right). Different arrangement of the specimen within the capsules were studied (Fig. 2 left). It was found, that the better the space was used up for a maximum of specimen the less the flexibility remained for changing a specimen type or to preserve a certain position for an individual specimen.

Mainly two rig types were analysed in detail and some variants each. Fig. 2 (middle right) shows the variant with wire heaters wound vertically around the capsule. The axial inner length of the capsule respectively the specimen stack is 81mm. The length in horizontal or x-direction (see Fig. 1) is 46.4mm and the width comes to 10.74mm. The capsule is closed by weld seams at both ends. The seam is located at an extension of the capsule wall and therewith removed from the high flux area. (An expansion volume for the sodium still has to be added in this design.) Additional axial heaters may be installed into the hat like end closures of the capsules. Spacer pins with low heat conduction secure the position in the rigs. On one side of the rig leaning pads keep the distance to the container wall or the next rig. Therewith the helium channel is formed with one manufacturing tolerance only.

The electric wire heaters are embedded in grooves on the capsule. Caps with a comp like outer surface are fixed by the end closure hats. They prolong the heater positioning grooves, so that the heater wires can be wound like a coil around the capsule ends.

As noted before the electric heater on the capsules have to control the temperatures of the specimen at different temperature levels during beam operation as well as during short beam-off periods. They have to supplement the nuclear power and to cope with the nuclear power shape in axial direction. During beam-off periods the non-uniform power contribution does not take place. The design variant with the heater wound in vertical direction around the capsule was designed in order to come along with one heater only. The analysis, however, showed that a heater system with incrementally differentiated heater power in vertical direction is indispensable. The second variant of the capsule/rig design analysed, therefore, has three heaters one upon another wound horizontally around the capsule.

The triple-heater-system is subdivided in a lower, a middle and a upper heater. Simulation calculations of the temperature field in the rigs were carried on with the code STARCD. This CFD code calculates the major parameters of the helium flow like heat transfer to the helium and pressure. Several design variants were analysed. The computer model for one example is shown on the left-hand side of Fig. 3. An example of the temperature distribution in the specimen stack at nuclear heating and addition electric heater power is shown in Fig 4. With an adapted power level of the three electric heaters the temperature can be kept at 458°C within a tolerance of ±8°C over a stack height of 66mm.

4. ITHEX experiments for validating the heat transfer and pressure loss simulation calculation

The ITHEX experiment is designed for the validation of the heat transfer and pressure loss simulation calculations in the helium channels. The test section has an annular channel geometry (Fig. 5). It is heated from both sides. Electric jacket wire heaters are used as they are envisaged for the IFMIF HFTM. The channel walls are made from two concentric shells. The heaters are embedded into grooves of one shell. After installation of thermocouples and insertion in the second shell the space between the shells is filled by a braze filler. The development of the brazing procedure is now in a state that the final test section can be made. The installation of the heater was also an exercise for the milling manufacturing of the parallel grooves with a small inclination angle and the winding of the heater.

5. Proving manufacturing technologies

The crucial manufacturing technologies for the HFTM design are the milling of the grooves for the wire heater, the winding of the wires and the spark erosion of the capsule, rig and container. Fig. 6 shows the test for manufacturing technologies. The quality control revealed that those technologies can be applied for the HFTM.

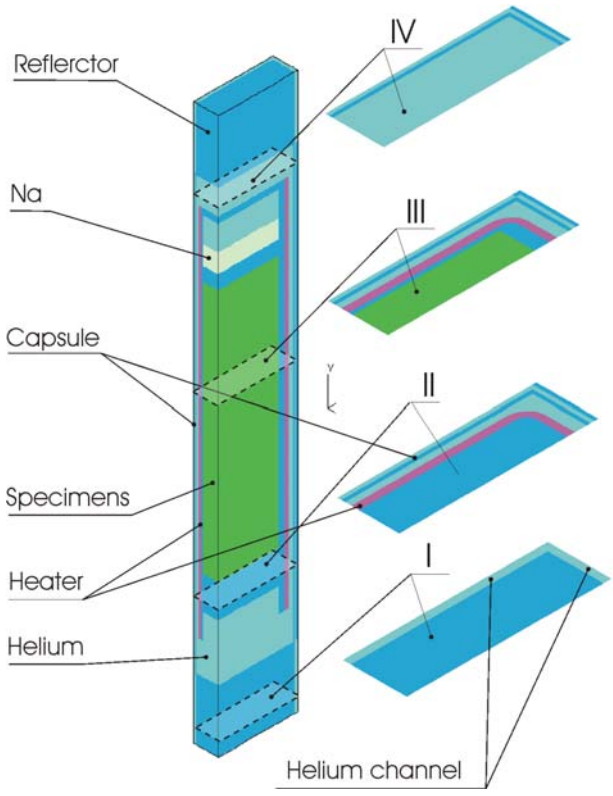

Fig. 3: Model used for the simulation calculation with STARCD.

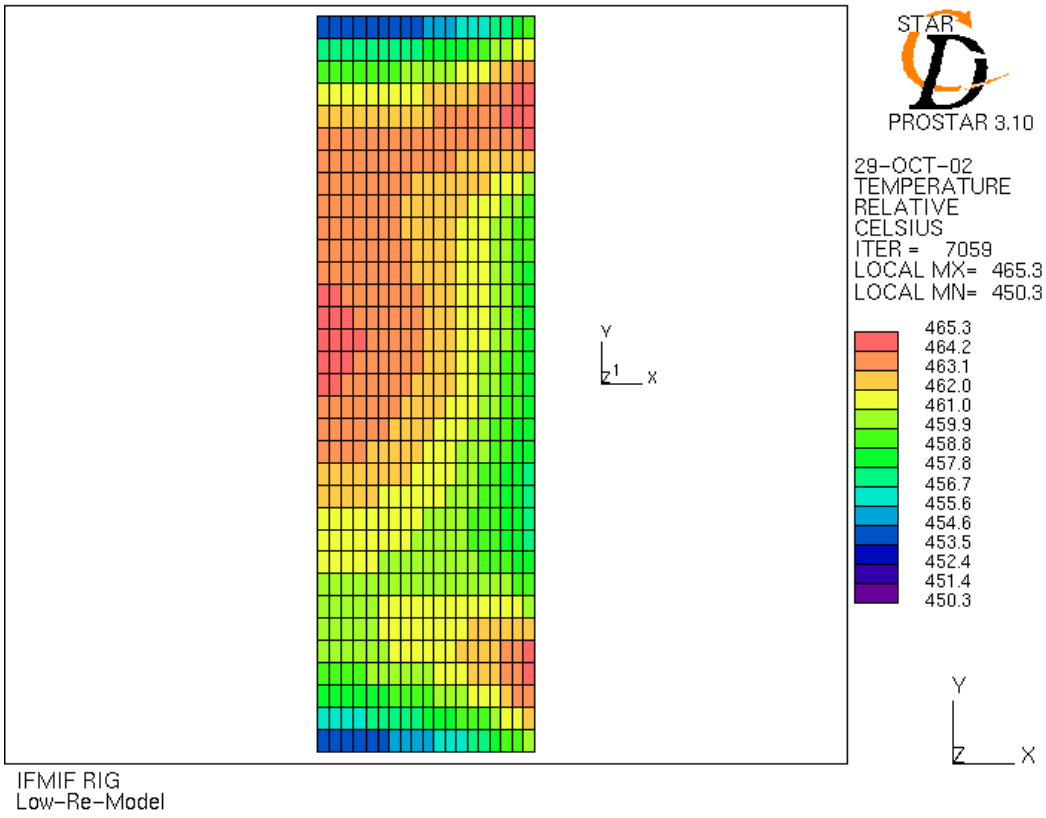

Fig. 4: Temperature distribution in the specimen stack at nuclear heating and addition electric heater power; with an adapted power distribution of the tree electric heaters the temperature can be kept within a tolerance of 15°C over a stack height of 66mm

.

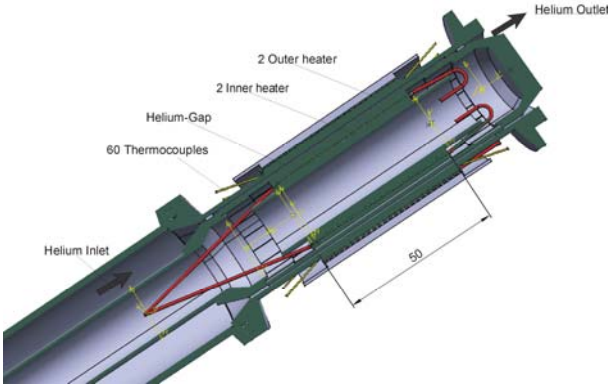

Fig. 5: ITHEX test section designed with CATIA V5.

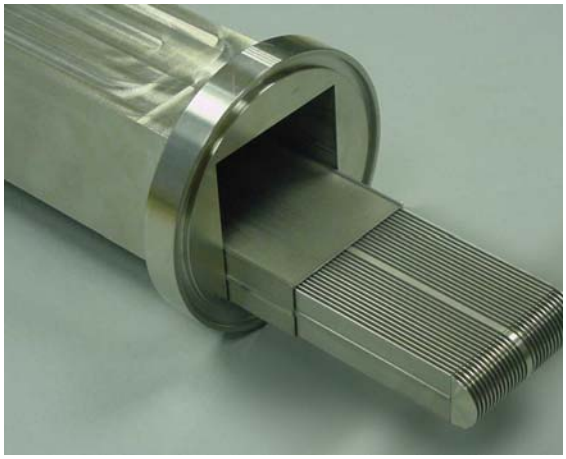

Fig. 6: Manufacturing test of capsule, rig and container; the outer surfaces and the grooves on the capsule surface (design variant with heaters wound vertically) are milled; all hollow spaces are spark eroded; the container has a flange on both sides; the wall thickness is 1mm; the components are made from solids which were annealed before milling and spark erosion.

Staff:

U. Fischer
S. Gordeev
V. Heinzel
T. Kuhn
K. Schleisiek
S. Simakov
V. Slobodtchouk
E. Stratmanns

Literature:

[1] M. Martone (Ed.), IFMIF International Fusion Materials Irradiation Facility, Conceptual Design Activity, Final Report, IFMIF CDA TEAM, ENEA Frascati, Report ENEA-RT/ERG/FUS/96-11, December 1996

[2] S. P. Simakov, U. Fischer, V. Heinzel, U. v. Möllendorf; International Fusion material Irradiation Facility (IFMIF) Neutron Source Term Simulation and Neutronics analysis of the Heigh Flux Test Module; FZKA 6743; Juli 2002

[3] V. Heinzel, U. Fischer, B. Dolensky, S. Gordeev, K. Schleisiek, S. P. Simakov, V. Slobodtchouk, E. Stratmanns; Lay-out Acticvities for the IFMIF high flux test module; ISFNT-6, San Diego, USA; April 7-12, 2002

[4] U. Fischer, S. Gordeev, V. Heinzel, S. Simakov, V. Slobodtchouk; Considerations on the Heat Transfer in the High Flux Test Module of the International Fusion Material Irradiation Facility, Jahrestagung Kerntechnik, 14. – 16. Mai 2002, Stuttgart, S. 501-504

TTMI-003-2, -10 and –11
Neutron Moderator/Reflector and Irradiation Conditions

The International Fusion Material Irradiation Facility (IFMIF) is proposed as an intense neutron source to test fusion reactor materials under relevant irradiation conditions. It should provide a proper neutron spectrum with sufficiently high damage production rates to allow also accelerated tests within an appropriate volume. The primary goal of the present study was to select on the basis of neutron transport calculations a suitable design of the IFMIF medium flux test module (MFTM) for a proper irradiation response of ceramic breeder materials. On the basis of systematic screening studies of different material combinations and test module shapes, it was shown that the IFMIF neutron spectrum could be largely adjusted to DEMO reactor conditions by combining tungsten plates serving as spectral shifter and carbon coating of the test modules acting as neutron reflector. In addition, damage code calculations confirmed that IFMIF provides over the entire energy range DEMO reactor specific primary knocked on atom (PKA) spectra, which governs the damage morphology and, hence, mechanical properties of many irradiated materials. For Li_4SiO_4 enriched with isotope ^6Li, neutron spectra, gas production and damage rates are presented and compared with those of a helium cooled pebble bed blanket of a fusion DEMO reactor. Finally, also an improved design outline is being proposed that takes largely into account the neutronics calculations and the related neutron spectral shifter and neutron reflector requirements.

Suitability of IFMIF MFTM irradiation conditions for structural materials

Previous extensive Monte Carlo simulations [1, 2] have clearly shown that the IFMIF irradiation conditions for iron-based structural materials fit quite well to those of a DEMO power reactor. In particular it was shown that a proper selection of spectral shifter material and design configuration, IFMIF meets DEMO reactor relevant H, He and dpa production rates as well as H/dpa and He/dpa ratios perfectly in structural materials. A major result of the screening study is that the integration of two 30 mm thick tungsten plates at the front and back side of the IFMIF creep-fatigue test module levels very effectively the high energy neutrons peaked around 12-16 MeV and, at the same time, notedly increase the neutron population in the range $5{\cdot}10^{-3} \div 5{\cdot}10^{-1}$ MeV [1]. Between 10^{-2} and 10^{-1} MeV the neutron flux increase is more than fourfold. This spectral shifter effect is most pronounced immediately behind the W-plates, that is, in the test module dedicated to in-situ tritium release experiments on Be and ceramic breeder materials.

These neutron transport calculations also revealed that a replacement of tungsten by e.g. iron or nickel based alloys would have only a very moderate spectral shifter effect. A substitution of tungsten by silicon carbide or graphite would increase the high energy part (>3MeV) of the neutron spectrum by about 50% and 80%, respectively, mainly due to elastic scattering but would has practically no “spectral shifter” effect.

The usual way to characterize a PKA spectrum is to use the cumulative damage production function W(T), which represents the fractional damage energy created by PKA recoils with energies below a given energy T. This function reflects the damage morphology, as low energy PKAs produce mainly isolated Frenkel pairs while high energy PKAs generate atomic collision cascades. With a proper combination of tungsten and graphite, the W(T) function inside the high flux test module follows over the entire PKA energy range that one of a DEMO reactor blanket, as Fig. 1 shows.

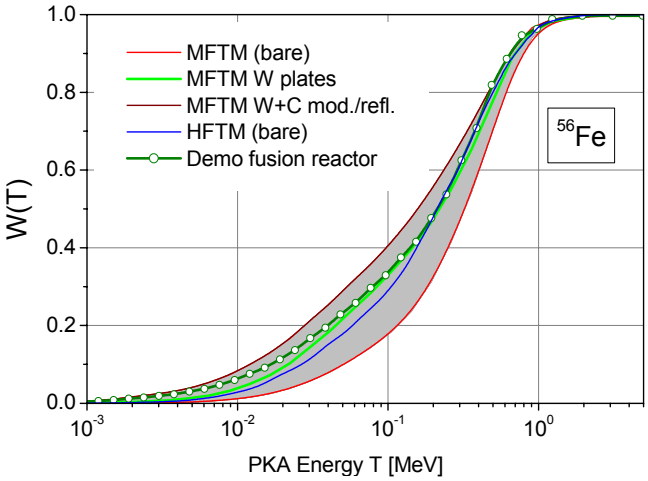

Fig. 1: Damage production function for the HCPB blanket of the fusion DEMO reactor in comparison with IFMIF HFTM and various design variants for MFTM (hatched area).

Optimization of MFTM irradiation conditions for breeder ceramics

A major requirement of breeder blanket design development is to achieve an appropriate tritium production rate throughout the blanket lifetime in order to maintain the (d, t) fusion reaction. Presently lithium-based ceramics (e.g., Li_2O, $LiAlO_2$, $LiSiO_4$, Li_2TiO_3, $LiZrO_3$) are considered as candidate materials for pebble bed blankets. The isotope ^6Li is more relevant for this purpose as the cross section of the $^6Li(n, t)^4He$ reaction is very high and increases at low energies as $\sim E^{-1/2}$. Therefore the low energy tail of the neutron spectrum at tritium release module position should have sufficient flux intensity to achieve DEMO relevant tritium production rates.

It was found in our studies that the population of epi-thermal neutrons in the former IFMIF MFTMs was not sufficient to match helium cooled pebble bed (HCPB) blanket relevant tritium production rates properly. In order to meet this additional requirement, the former MFTM reference design of the CDA phase (1995-1996) was improved by systematic neutron transport studies with the aim to soften the IFMIF neutron spectrum in the MFTMs. The related neutron spectra were calculated by means of Monte Carlo code MCNP4c [3] using several realistic geometry models of the facility.

To optimize the neutron spectra and radiation responses for breeder ceramics, the test modules were encased by neutron moderator/reflector material. Several materials were screened to obtain higher tritium production rates in the MFTM [4]. The results depend on the thickness of surrounding material. Particularly, with regard to technical realization, the best results up to now were obtained by an additional carbon jacket of 25-30 cm attached to the MFTMs and the low flux test module. Such a carbon „coating“ significantly increases the population of epi-thermal neutrons and thus greatly improves the tritium production conditions for breeding ceramics. E.g. below 10^{-2} MeV, the flux increase is more than two orders of magnitude.

Figure 2 shows typical neutron spectra of the HCPB DEMO blanket [5] and the HFR in comparison with various spectra inside IFMIF medium flux test modules. Obviously, a major result of the neutronics calculations is, that with two tungsten plates acting as “spectral shifter” and additional carbon coatings acting as “reflector”, the shape of the neutron spectrum in the medium flux test volumes follows over several orders of magnitude already pretty close that one of a DEMO-type HCPB breeding blanket.

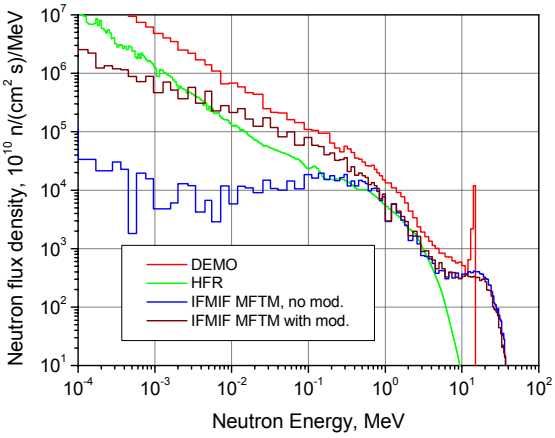

Fig. 2: Neutron spectra of the former IFMIF MFTM design (1996), and the new design with integrated W moderator and graphite reflector (2002) in comparison with the mixed spectrum reactor HFR and the HCPB blanket of a fusion DEMO reactor.

Comparison of radiation responses

The results on radiation damage, gas production rates as well as gas to dpa production ratios were obtained for several design variants. In the following we will consider only four major variants (see Table 1).

The overall intention was to increase the flux at the tritium release module (TRM) position, what is necessary to reach DEMO relevant doses for reasonable amount of time, keeping the low energy part of the spectrum high enough for sufficient tritium production. Obviously these goals are mutually exclusive. Therefore an acceptable compromise should be found.

Table 1: Description of the major design variants.

Variant	Description
1	Basic variant with W plates and carbon jacket around MFTM. Both MFTMs (CFTM and TRM) are present.
2	Same as item 1, buth with entire TRM shifted by 3 cm upstream.
3	Both W plates moved together are CFTM removed.
4	Same as previous, but with entire TRM shifted by 3 cm upstream.

The radiation responses for these design variants are summarized in Table 2. With respect to gaseous transmutation products, the implementation of moderators and reflectors improves significantly the helium and tritium production by a factor of 7.5 and 22.6, respectively in the MFTM of IFMIF, but as only a moderate effect on the less relevant proton and deuteron production (see). On the other hand, the mixed spectrum reactor HFR with its overwhelming density of low energetic neutrons has comparatively high T and He production rates coming from the ^{6}Li(n, t) ^{4}He reaction, but due to the lack of higher energetic neutrons a negligible H and D production. Compared to orthosilicate, meta-aluminate has generally smaller gas/dpa rates in all neutron sources investigated, mainly due to stoichiometric differences with respect to the lithium content.

Although the T and He production rates and, consequently, corresponding gas to dpa ratios could be significantly increased for breeder materials in the MFTM of IFMIF, the latter are about that for DEMO reactor at the MFTM creep fatigue test module (CFTM), while for the MFTM tritium release module (TRM) and HFR these ratios are somewhat too high.

The excess of low-energy neutrons in HFR spectrum stipulates for high tritium and helium production and damage rates (the most part of which is produced by tritium and helium recoils). While the time to reach a DEMO relevant dose for irradiation in HFTM is about that for DEMO reactor itself, the dose rate for MFTM is about a factor of two lower.

To increase neutron flux other design variants were considered. One option is to shift the TRM upstream as close as possible to the CFTM. The allowed shift is 3 cm. The other option would be to remove temporary the entire creep fatigue test module, move both tungsten moderator plates together and shift the tritium release module upstream by another 3 cm. The neutron flux distribution and neutron responses were calculated for these variants to get the optimal solution.

We used for the evaluation of the entire PKA spectrum the cumulative damage production function W(T) described above. For ceramic breeder materials irradiated in a HCPB DEMO reactor blanket, this damage production function W(T) continuously increases over about two orders of magnitude with increasing PKA energy, revealing a broad energy spectrum of recoils. A specific feature of breeder ceramics is the sudden increase around 2 MeV caused by an additional contribution coming from nearly mono-energetic tritium (2.6 MeV) and α-particles (2.0 MeV) emitted due to ^{6}Li(n,t)α reaction. Except of a small range (0.8-3 MeV), over the whole PKA spectrum DEMO specific recoil energy distributions can be adjusted in breeder ceramics irradiated in the present MFTM layout of IFMIF.

In contrast to lithium containing ceramics, the W(T) function in fusion structural materials continuously increases without steps. The hatched area in Figure 1 shows that the HFTM of IFMIF meets perfectly over the entire PKA energy range DEMO reactor conditions in iron based alloys, as the shape of the W(T) function can be adjusted by using an appropriate combination of W-moderator and C-reflector. On the other hand, the PKA spectrum of the HFR is too soft by about an order of magnitude.

Table 2: Radiation responses in lithium orthosilicate (30at% ^{6}Li) inside tritium release module for major design variants.

Variant	Damage, (dpa/fpy)	H, (appm/fpy)	D, (appm/fpy)	T, (appm/fpy)	He, (appm/fpy)	T/dpa, (appm/dpa)	He/dpa, (appm/dpa)
1	$8.3\cdot10^{0}$	$2.69\cdot10^{1}$	$7.74\cdot10^{1}$	$3.77\cdot10^{4}$	$3.78\cdot10^{4}$	$4.55\cdot10^{3}$	$4.57\cdot10^{3}$
2	$7.1\cdot10^{0}$	$4.11\cdot10^{1}$	$1.15\cdot10^{2}$	$2.60\cdot10^{4}$	$2.62\cdot10^{4}$	$3.67\cdot10^{3}$	$3.70\cdot10^{3}$
3	$1.57\cdot10^{1}$	$4.82\cdot10^{1}$	$1.34\cdot10^{2}$	$7.20\cdot10^{4}$	$7.22\cdot10^{4}$	$4.58\cdot10^{3}$	$4.60\cdot10^{3}$
4	$1.27\cdot10^{1}$	$7.45\cdot10^{1}$	$2.04\cdot10^{2}$	$4.55\cdot10^{4}$	$4.59\cdot10^{4}$	$3.58\cdot10^{3}$	$3.61\cdot10^{3}$

Table 3: DPA and gas production in Li_4SiO_4 (30at% ^{6}Li) irradiated in the medium (MFTM CFTM) and high flux (HFTM) test volumes of IFMIF, in a typical position of the mixed spectrum reactor HFR, and in a HCPB DEMO reactor blanket [5].]

Irradiation parameter	Demo reactor	HFR position F8	MFTM no moderator	MFTM W+C moderator	HFTM W+C moderator
Total flux, 10^{14} n/(cm^2·s)	11.94	3.83	1.54	4.84	10.09
Damage, dpa/fpy	$2.18\cdot10^{1}$	$8.04\cdot10^{1}$	$3.09\cdot10^{0}$	$8.59\cdot10^{0}$	$2.02\cdot10^{1}$
Hydrogen, appm/fpy	$3.42\cdot10^{2}$	$4.1\cdot10^{0}$	$2.21\cdot10^{2}$	$1.48\cdot10^{2}$	$6.32\cdot10^{2}$
Deuterium, appm/fpy	$1.07\cdot10^{3}$	$2.41\cdot10^{2}$	$4.99\cdot10^{2}$	$4.20\cdot10^{2}$	$1.96\cdot10^{3}$
Tritium, appm/fpy	$4.00\cdot10^{4}$	$1.11\cdot10^{6}$	$4.05\cdot10^{2}$	$9.18\cdot10^{3}$	$5.83\cdot10^{3}$
Helium, appm/fpy	$4.19\cdot10^{4}$	$1.11\cdot10^{6}$	$1.32\cdot10^{3}$	$9.89\cdot10^{3}$	$9.05\cdot10^{3}$
H per dpa	$1.57\cdot10^{1}$	$1.0\cdot10^{-1}$	$7.18\cdot10^{1}$	$1.72\cdot10^{1}$	$3.13\cdot10^{1}$
D per dpa	$4.91\cdot10^{1}$	$1.1\cdot10^{0}$	$1.62\cdot10^{2}$	$4.90\cdot10^{1}$	$9.73\cdot10^{1}$
T per dpa	$1.83\cdot10^{3}$	$5.20\cdot10^{3}$	$1.31\cdot10^{2}$	$1.07\cdot10^{3}$	$2.89\cdot10^{2}$
He per dpa	$1.92\cdot10^{3}$	$5.21\cdot10^{3}$	$4.29\cdot10^{2}$	$1.15\cdot10^{3}$	$4.48\cdot10^{2}$

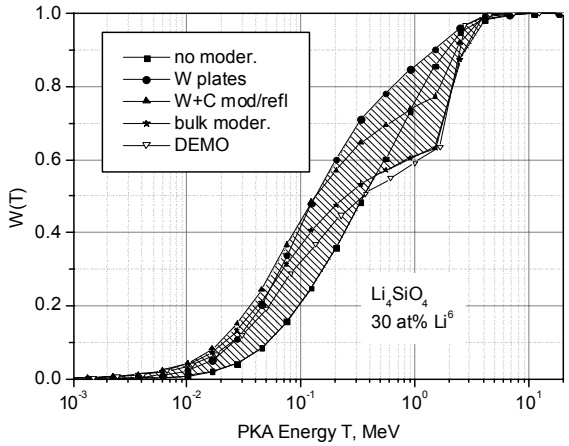

Fig. 3: Damage production function W(T) in Li_4SiO_4 for the MFTM of IFMIF (closed symbols) in comparison with HCPB DEMO blanket.

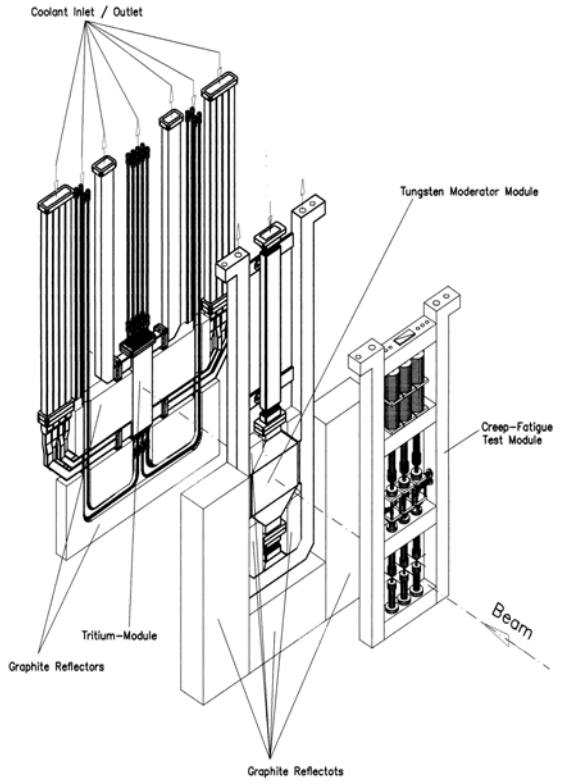

Fig. 4: Explosion view of all medium flux sub-modules

Design outline of medium flux test modules

In order to accommodate the neutron spectral shifter (or moderator) and the neutron reflectors, the original design of the MFTMs needed substantial design modifications. In the selected design, it has been tried to integrate both, the creep-fatigue and the tritium release test module into a carbon jacket and to implement a single, 60 mm thick tungsten plate between both test modules. W acts as effective neutron spectral shifter and graphite as neutron reflector. Fig. 4 shows an explosion view of all medium flux sub-test modules.

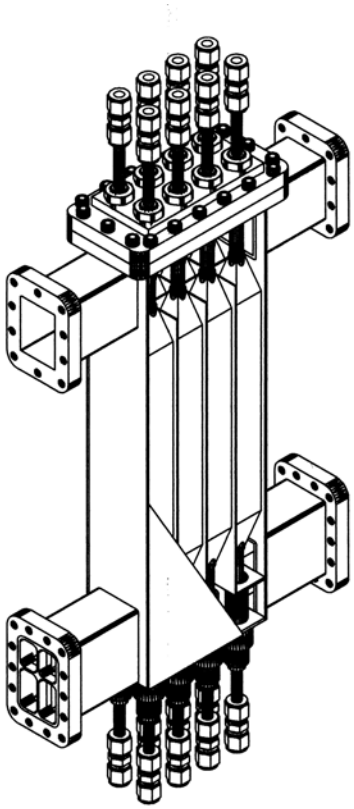

Fig. 5: Tritium module with 8 individual rigs for in situ tritium release experiments on ceramic breeders.

The design of the tritium release test module has been significantly improved by FZK already earlier and is now integrated into a graphite shielding that effectively reflects especially the lower energy neutrons, in order to significantly improve the tritium production mainly via the ^{6}Li(n,t) reaction. The design improvement has been mainly driven by above mentioned design considerations and by the requirements to effectively use the available volume of 6 L and to allow the simultaneous irradiation of both in-situ test modules. Figures 5 and 6 show that tritium release test module with helium gas coolant ducts, piping for sweep gas, instrumentation, and specimen arrangement.

The tritium release test module is divided into parallel coolant sections with an independent control of the cooling helium flow according to the temperature to be maintained for the specimens and the internal generated heat. To adjust the heat transfer rate from the test probes to the coolant gas the desired test temperature for the specimens is basically controlled by a vertical He gas flow surrounding the probes. The regulation of the heat transfer by Ohmic heating wires should allow to keep constant the desired specimen temperature during the test campaign. Similar to the high flux test module, the regulation will be flexible to set the right temperature for different specimen materials inside a coolant section, and accommodate the geometrical and physical modification during the irradiation campaign. In particular, it should be capable to cope with varying levels of heat generation due to ion beam modulation.

Conclusions

- The displacement damage of breeder ceramics is significantly affected by low energy neutrons due to the production of high energy tritium (2.6 MeV) and helium (2.0 MeV) recoils through the ^{6}Li(n,t)α reaction.
- Gas to dpa production ratios for a MFTM surrounded by a thick graphite jacket (W+C bulk) is surprisingly close to that one of a DEMO reactor, while gas and dpa production rates are by a factor of two smaller than DEMO reactor specific values.
- Variants with increased damage production rate (v3-v4) produce significantly higher gas to dpa ratio for hydrogen and deuterium than DEMO.
- In structural materials, the recoil energy distribution meets now perfectly DEMO reactor conditions in all test modules of IFMIF, while in ceramic breeder materials this distribution has become very similar to that one of a DEMO reactor HCPB blanket.
- Substantial design improvements allow in the medium flux position the simultaneous irradiation of creep-fatigue and a tritium release test modules and in addition the integration of both, a W plate acting as neutron spectral shifter and a graphite jacket acting as neutron reflector.

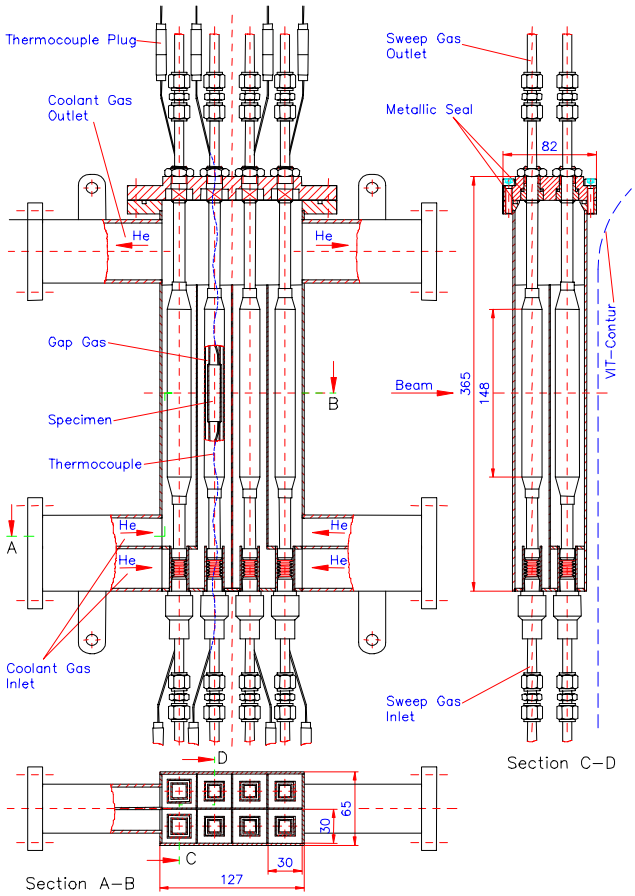

Fig. 6: Front view (left), elevation view (right) and cross section (bottom) of the tritium release test module for ceramic breeders.

Staff:

S. Baumgärtner
G. Bürkle
A. Möslang
P. Vladimirov

Literature:

[1] E. Daum, How to improve IFMIF neutron spectrum, J. Nucl. Mater. 283-287 (2000) 1001.

[2] M. Martone (Ed.), IFMIF – International Fusion Materials Irradiation Facility – Conceptual Design Activity, Final report ENEA-RT/ERG/FUS/9611, Dec. 1996.

[3] F.Briesmeister (ed.), MCNP – a general Monte Carlo N-particle transport code, version 4B, LA-12625M, March 1997; ENEA-RT/ERG/FUS/9611, Dec. 1996.

[4] Yu. Lizunov, A. Möslang, A. Ryazanov, P. Vladimirov, New Evaluation of Displacement Damage And Gas Production For Breeder Ceramics under IFMIF, Fusion and Fission Neutron Irradiation, ICFRM-10, 14-19- Oct. 2001, Baden-Baden, Germany, accepted for J. Nucl. Mater.

[5] U. Fischer, S. Herring, A. Hogenbirk, D. Leichtle, Y. Nagao, B.J. Pijlgroms, A. Ying; Comparison of nuclear irradiation parameters of fusion breeder materials in high flux fission test reactors and a fusion power demonstration reactor; J. Nucl. Mater. 280 (2000) 151.

[6] Möslang and P. Vladimirov; Neutronics calculations and Design for the Medium Flux test Module of IFMIF"; ISFNT-6, April 6-12, 2002, San Diego; proceedings

[7] Möslang, P. Vladimirov; Improvement of irradiation conditions for the medium flux volume of the intense neutron source IFMIF; Jahrestagung Kerntechnik, May 2002, Stuttgart, proceedings.

[8] Möslang et al, Recent advances at the International Fusion Materials Irradiation Facility IFMIF; 19th IAEA Fusion Energy Conference, 14-19 October 2002, Lyon, France, Proceedings.

Assessment of the Possibility of Fusion Material Irradiation at the European Spallation Source (ESS)

1. Preface

The Fusion Material Irradiation Devices Expert Group was nominated by the EFDA leader on February 2002 with the aim to examine to which extent studies on Spallation Neutron Sources (SNS) available now and in the foreseeable future in Europe or elsewhere could contribute to the solution of materials problems in nuclear fusion. In the following the results of ESS neutronics assessment made by FZK for the EFDA expert group are summarized

2. Objectives

The need to develop materials that can withstand the high-energy neutron flux environment expected for the first wall divertor and blanket regions of deuterium-tritium (D-T) fusion reactors is recognized as one of the key challenges in the fusion program aimed at producing commercial fusion power. Low activation structural alloys for the first wall divertor and blanket components, surface-protecting, tritium-breeding and neutron multiplier materials belong to the category of materials, which are intensively exposed to energetic 14 MeV neutrons. At present an appropriate materials test facility that could adequately simulate this neutron environment is not available though its need has been established on several occasions (see e.g., [1]). During the international selection process towards a feasible, reliable and near-term intense fusion neutron source, the mission of such a facility has been defined as follows:

- qualification of candidate materials up to about full lifetime of anticipated use in a fusion DEMO reactor;
- calibration and validation of data generated from fission reactors, particle accelerators and other neutron devices;
- identification of possible new phenomena which might occur due to the high-energy neutron exposure.

Altogether, there is a broad international consensus that:

- a suitable intense neutron source is inevitable for construction of a DEMO-type fusion reactor, and
- the D-Li source IFMIF (International Fusion Materials Irradiation Facility) is the best choice with the potential to fulfil the requirements within a realistic time scale.

3. The European Spallation Source (ESS)

The ESS will be driven by a proton linear accelerator (LINAC) with beam energy of 1.33 GeV and beam power of 10 MW [2]. It features two target stations, both equipped with liquid mercury target and operating with 5 MW beam power. The short pulse target station is fed with proton pulses compressed by factor of 800 to 1.4 µs duration in a double compressor ring (repetition rate 50 Hz). The long pulse target is fed directly with protons from the LINAC (proton pulse length 2.0 ms, repetition rate 16.6 Hz). A detailed description of a possible use of ESS as neutron source for fusion material testing is shortly discussed in the present report.

3.1 Position of the Irradiation Module for Fusion Material Tests

The long pulse target station was identified as the most useful one for fusion material testing (longer pulse duration, potentially higher availability). Preliminary calculations have shown that the spectrum of the irradiation particles inside the mercury target of ESS is too "hard" and leads to higher He/dpa and H/dpa rates than in the fusion case [3]. In addition the production of undesirable transmutation products in Fe such as Ca, P and S is significantly high inside the mercury target (see below). Moreover, the incorporation of an irradiation module in the target container would cause severe engineering problems and requires a re-design of the target unit. Therefore, by mutual consent, the experts of both groups (ESS and fusion) agreed on an out-of-target reference position for the fusion irradiation module.

For material irradiation a useful “high flux” volume of about 0.83 l has been identified in ESS. Larger test volume could be made available but at lower neutron flux level (1-3 dpa/fpy). As in-situ tests like creep-fatigue experiments require significant space in the direct vicinity of the irradiation volume, they are not foreseen in ESS.

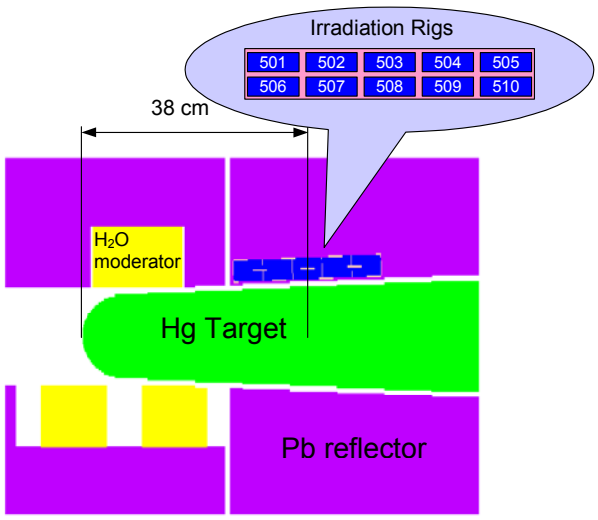

Fig. 1: Geometry model for the neutronics calculations; elevation view (cut through the target center).

The center of the fusion materials irradiation module is positioned 38 cm downstream from the front of the liquid mercury target (Figure 1 and 2). The irradiation module is made of 10 rectangular boxes (0.0833 l each) horizontally arranged in two rows. The irradiation module has the same geometry as developed for IFMIF, therefore the same miniaturized specimens and similar specimen capsules and geometry could be utilized to benefit from the optimization of the IFMIF high flux test module design. 77% Fe-23% He in weight was used as average value of the material composition and density inside the module for the neutron transport calculations. Standard ESS irradiation conditions were assumed for the neutronic calculation: proton energy 1334 MeV, current 3.75 mA, oval beam footprint on the target 6 x 20 cm^2, Gaussian distribution.

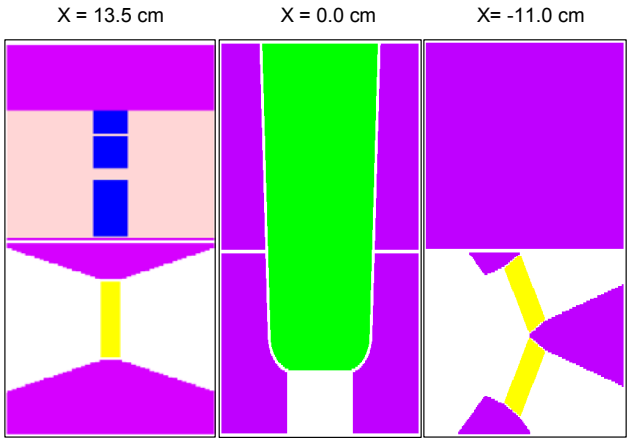

Fig. 2: Geometry model for the neutronics calculations; plan view (horizontal cut through the upper moderator and irradiation rigs (X=13.5 cm), through the mid-plane (X=0.0 cm) and through the lower moderators (X=11.0 cm)).

4. Neutronic Analysis for ESS

4.1 Neutron Energy Spectrum

The neutron energy spectrum inside the irradiation module has been calculated using the Monte Carlo transport code MCNPX [4]. The comparison of neutron spectra at the ESS irradiation module, high and medium flux modules of IFMIF as well as the spectrum at the first wall position of helium cooled pebble bed blanket for future demonstration fusion reactor (DEMO HCPB) is shown in Figure 3.

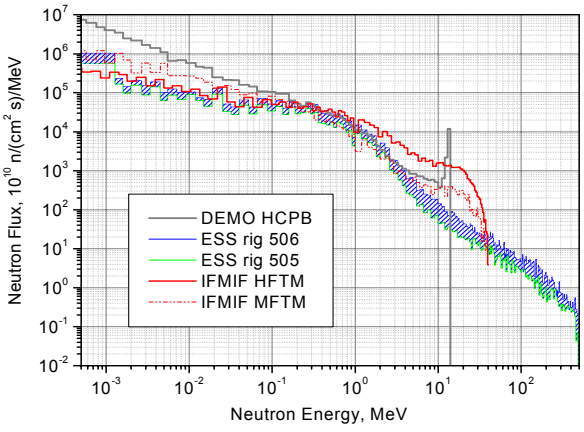

Fig. 3: Differential neutron spectra comparison for ESS irradiation rigs, IFMIF High and Medium Flux Test Modules (IFMIF HFTM and MFTM) and DEMO HCPB.

The IFMIF neutron spectrum is very similar to the DEMO First Wall (FW) one at neutron energy up to 14 MeV; in addition a neutron tail with energy up to 55 MeV is present. In ESS the neutron flux in the energy range 5-14 MeV is a factor 4-5 lower than in DEMO FW and a neutron tail with energies up to hundreds of MeV is also present.

4.2 Proton Flux Distribution

The proton flux distribution inside and around the ESS target has been calculated. At cell 508 (see Figure 1) the total proton flux is about 2.5 x 10^{12} p/cm^2 s (i.e. only 0.4% of the neutron flux which is about 6.5 x 10^{14} n/cm^2 s). However, most of the protons (~97%) have energies far above 15 MeV and thus contribute significantly to the total H and He production, which helps to match within a factor of two the H/dpa and He/dpa ratios expected for the fusion spectrum.

4.3 Damage Calculation

The results of the damage calculations (dpa/fpy) are presented in figure 4. Maximum neutron damage is observed in the cell 506 (~10 dpa/fpy), which is situated in the lower row nearest to the target front. The lowest displacement damage is in the cell 505 (~5 dpa/fpy), which is the last in downstream direction, in the upper layer. Cell 506 thus falls about a factor of 2 short from the requirement listed in table 1. This implies about two times longer irradiation campaigns to reach the same DEMO relevant irradiation dose (70-80 dpa). In IFMIF high flux test modules (HFTM) the neutron damage ranges from 55 to 20 dpa/fpy in a volume of 0.5 litres.

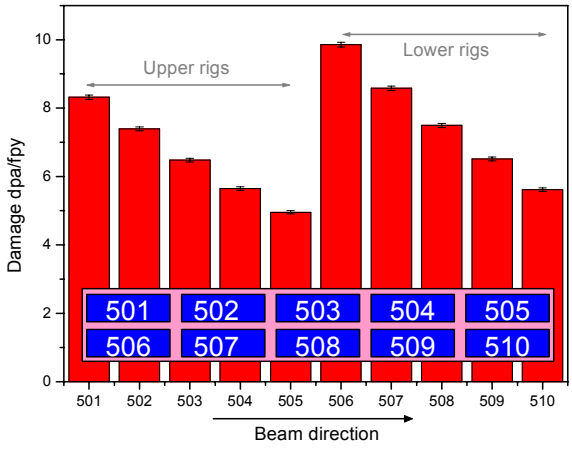

Fig. 4: Average values of the neutron induced displacement damage within the 10 specimen capsules (No. 501÷510).

The neutron flux gradient has been evaluated inside the irradiation module in ESS. Gradients are generally negligibly small with a maximum of 5% /cm near the edge of cell 506. This is well below the limit of 10% per specimen volume implied by fusion user requirements.

4.4 Gas Production

The gas production rates (He and H) in the irradiation rigs are shown in Figure 5.

The gas to dpa production ratios for the 10 specimen capsules are reported in Figure 6. It is remarkable that the ratios are very slightly dependent on module position, which reflects the fact that the shape of the neutron spectrum is very similar for all modules, while the total neutron flux and, hence, the gas production is dependent on the location.

Neutron damage (dpa), gas production rates (He and H) and gas/dpa ratios in DEMO-IFMIF and ESS are summarized in Table 1. For the IFMIF Medium Flux Test Module (MFTM) the values are averaged over the entire volume, for DEMO HCPB the maximum values (first wall outboard midplane) are given [5] and for ESS and IFMIF High Flux Test Module (HFTIM) maximum and minimum values in different irradiation rigs are reported. All the data refer to iron as a basic component of fusion structural materials.

The He/dpa ratio in Fe based alloys in ESS is between 5-6, about a factor 2 lower than expected for DEMO, while the H/dpa ratio is about 33-36 which is a factor of about 1.5 below DEMO. In IFMIF HFTM the He/dpa and H/dpa are 10-12 and 35-50 respectively and therefore practically identical to the related DEMO values. It should be noted, however, that there is at least a 10% statistical uncertainty associated to any of these calculations.

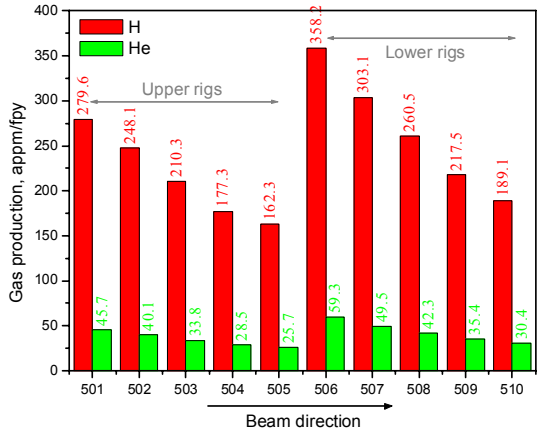

Fig. 5: Helium and hydrogen gas production rates within the 10 specimen capsules (No. 501÷510).

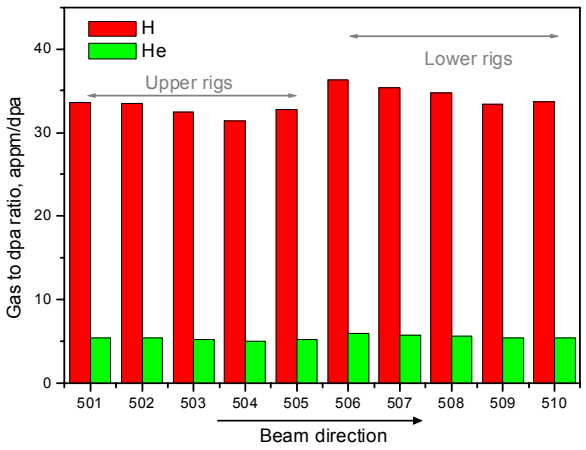

Fig. 6: Gas to dpa production ratio for the 10 irradiation capsules.

4.5 Transmutation

At present reliable data above 150 MeV are only available for the total transmutation cross sections of Fe as a function of the energy of the neutrons and protons. Considering that for energy higher than 10 MeV this cross section is nearly constant, the total number of transmutations produced by neutrons with energy higher than 14 MeV (the highest energy of neutron produced by D-T fusion reactors) has been estimated. Assuming that:

- the transmutation elements of interest in this estimation are P, S, Ca and Mn;
- the relative distribution of activation products is the same as evaluated in the benchmark calculation performed for the MEGAPIE target [6];
- the production rates of elements from Li (Z=3) to Mg (Z=12) are zero and the total transmutation rate is made up by the production of H, He and the elements from Al (Z=3) to Mn (Z=25) only;

The estimated upper limits for the concentrations of P, S. Ca and Mn produced in Fe at the highest flux region of the fusion material irradiation test module in ESS are:

Element	Rate of production, (appm/fpy)
Manganese	< 1400
Calcium	< 700
Sulphur	< 275
Phosphorus	< 75

As is immediately obvious, from the cross sections and spectra shown in Figure 3, there is significant transmutation produced also by neutrons between 1 and 14 MeV. However, the fast majority of these transmutations are hydrogen and helium isotopes.

The reference structural material for the nuclear components of a DEMO fusion reactor (first wall, blanket and divertor) is the Reduced Activation Ferritic Martensitic (RAFM) steel EUROFER. Before irradiation the measured concentrations of the considered elements in such alloy are:

Element	Concentration in EUROFER, (appm)
Mn (alloying element)	2000 ÷6000
Ca (impurity)	3 (3)*
S (impurity)	60 (20)
P (impurity)	90 (20)

* In brackets achievable values to decrease the material impurity level are indicated.

In the frame of IFMIF R&D program the transmutation and activation cross-sections for neutron irradiation up to 150 MeV neutron energy have recently been evaluated and compiled in the Intermediate Energy Activation File: IEAF – 2001 [7]. IEAF-2001 also contains the required transmutation product cross-sections for all the transmutation nuclides produced by neutron irradiation up to 150 MeV neutron energy. In IFMIF high flux test module the transmutation products in EUROFER steel have been assessed by using IEAF-2001 cross section data and neutron spectra calculated with McDeLicious code. The results are shown in Figure 7.

Table 1: Neutron damage, gas production rates and gas to dpa production ration in DEMO, IFMIF and ESS.

	DEMO FW* (3 MW/m^2)	IFMIF HFTM (0.5 l)	IFMIF MFTM (6 l)	ESS (0.83 l)
Neutron damage, (dpa/fpy)	30	20-55	8.5	5-10
H production rate, (appm/fpy)	1400	1010-2430	385	160-360
He production rate, (appm/fpy)	330	250-600	104	25-60
H per dpa, (appm)	46	35-50	42	33-36
He per dpa, (appm)	11	10-12	11	5-6

* maximum first wall loading of HCPB DEMO reactor blanket (outboard mid-plane)

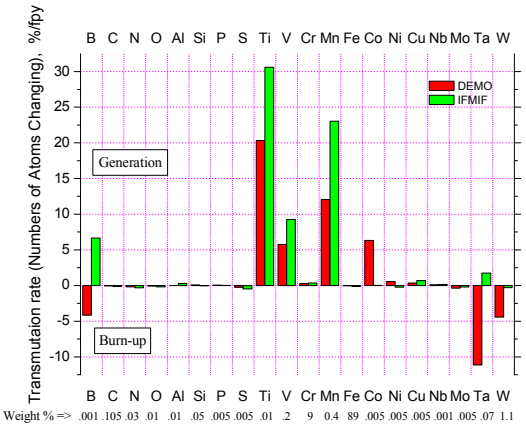

Fig. 7: Transmutation rates of Eurofer constituents when irradiated in IFMIF (high flux test module) and the first wall of a typical Demo fusion reactor.

It is noted that in IFMIF (i) the transmutation of iron does not play any significant role, (ii) there is no production of crucial elements such as Ca, P and S, and (iii) the transmutation production rate of Mn is twice the one in DEMO.

A similar assessment for ESS is foreseen to evaluate accurately transmutation products in the fusion irradiation module position.

4.6 Primary Knock-on Atom PKA

It is well known that different primary knock-on atom (PKA) spectra can produce completely different damage morphologies. A low energy PKA produces Frenkel defects, that is, isolated vacancies and interstitials; a significant fraction of these defects survive recombination. On the other hand, high-energy recoils generate atomic collision cascades in which a high fraction of produced defects is subject to in-cascade recombination. Also for a high energy PKA, the formation of sub-cascades becomes more probable, which can lead e.g. to more intense radiation hardening. Therefore, recoils of different energy produce different damage morphologies that may result in different mechanical properties of irradiated materials. On the other hand, (at very low dpa levels) data obtained from RTNS-2 (a 14 MeV D-T neutron source at Livermore) and from EBR-2 (fast breeder reactor) showed identical results if normalized to the same dpa numbers.

For the evaluation of the entire PKA spectrum, it is useful to define a function that weights each recoil by its associated damage energy. The usual way to characterize a PKA spectrum is thus to use the cumulative damage production function W(T), which represents the fractional damage energy created in all PKA recoils with energies between the threshold energy E_d and the energy T. Apart from a few exceptions like ^{6}Li based tritium breeder materials, this W(T) function increases continuously without steps in fusion structural materials. The hatched area in figure 9 shows that the relevant test volume of IFMIF meets perfectly over the entire PKA energy range DEMO reactor conditions in iron based alloys, as the shape of the W(T) function can be adjusted by using an appropriate combination of W-moderator and C-reflector. On the other hand, the PKA spectrum of the HFR is too soft by about an order of magnitude. As expected, the PKA spectrum in ESS is within a large window very similar to that one of a fast breeder reactor, that is, quite soft; while the high energy tail of ESS is only weakly visible in the W(T) representation due to its low population.

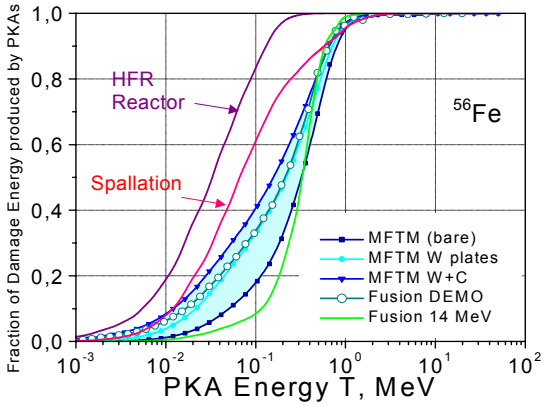

Fig. 8: Fraction of damage energy (W(T) function) versus primary knock-on atom energy for various positions in IFMIF (hatched area), for an advanced blanket (HCPB type) of a fusion DEMO reactor (open symbols), the 14 MeV fusion peak, the mixed spectrum reactor HFR, and a typical position inside the ESS test module.

4.7 Conclusion

The possibility to test in ESS fusion relevant materials at relatively high appm He/dpa ratio (conditions that are not accessible with fission reactors) could be very interesting for the fusion community if the present ESS planning can be achieved. The interest is mainly in anticipating results on one of the key issues related to irradiation damage in typical fusion neutron spectrum. Extensive modeling and analysis need to be performed to carefully interpret the meaning of the acquired data.

Despite this, IFMIF is considered absolutely necessary for the characterization of all the materials (structural, breeder, neutron multiplier, shielding etc.) needed for the DEMO fusion reactor design and licensing.

Staff:

U. Fischer
A. Möslang
P. Vladimirov

Literature:

[1] J.E. Leiss, K. Ehrlich, A.N. Goland, A. Miyahara, H. Ohno, P. Schiller (Eds.), Report on International Fusion Irradiation Facility, IFMIF Workshop, San Diego, USA, Feb. 14-17, 1989.

[2] The ESS Project Vol. III, Technical Report

[3] P. Vladimirov, A. Möslang, Unpublished results.

[4] L. S. Waters (Ed.), MCNPX^{TM} Users Manual, Version 2.1.5, TPO-E83-G-UG-X-00001, Rev. 0, Nov. 14, 1999.

[5] Fischer, Leichtle, Tsige-Tarmirat: Annual Meeting on Nucl. Technology 1999, Karlsruhe, ISSN 0720-9207, p. 553.

[6] J.C. Klein, Private Communication

[7] U. Fischer, P.P.H. Wilson, D. Leichtle, S.P. Simakov, U. von Möllendorff, A. Konobeev, Yu. Korovin, P. Pereslavtsev, I. Schmuck, Application of the IEAF-2001 Activation Data Library to Activation Analysis of the IFMIF HFTM, ICFRM-10, 14-19 October 2002, Baden-Baden.

TTMI-003-5,-6
IFMIF Neutron Source: D-Li Reaction Source Term and Neutron Data

In the framework of Task TTMI-003 of the EFDA technology work programme extensive development work is being conducted to provide the computational tools and nuclear data required to enable proper neutronic calculations for the IFMIF neutron source.

D-Li Reaction Source Term

In the IFMIF lithium target, neutrons are generated through the d-Li stripping reaction and various other nuclear Li(d,xn) reactions. The objective of Task TTMI-003, Deliverable 5, is to provide the computational tools and data required for the simulation of d-Li source neutrons in the transport calculation.

This requires developing a suitable d-Li source term model which ideally should be integrated to a standard Monte Carlo neutron transport code such as MCNP [1]. The McDeLi code [2] has been previously developed as an extension to MCNP with the capability of representing the neutron source term on the basis of a built-in semi-empirical d-Li reaction model. McDeLi can handle two beams impinging onto the lithium target taking into account different beam directions and a spatially varying intensity distribution. Deuteron slowing down in the lithium is described according to the well established empirical model of Ziegler et al. The Li(d,xn) reaction model considers as neutron producing reactions deuteron stripping and deuteron absorption followed by the formation of a compound nucleus with subsequent neutron emission. Adjustable parameters of the Li(d,xn) reaction model were obtained through numerical fits to experimental angle-energy distributions of neutron yields from thick lithium targets, bombarded by 32 and 40 MeV deuterons. Extensive testing of the McDeLi code against available experimental data over the full deuteron energy range from 5 to 50 MeV has shown that McDeLi fails to reproduce the experimental data below 30 MeV incident deuteron energy. The high energy tail above 40 MeV cannot be reproduced either since the semi-empirical reaction model does not take into account exothermic reactions.

To overcome these drawbacks, a new approach was elaborated with the objective to replace the semi-empircal Li(d,xn) reaction model of McDeLi by a complete description of the deuteron interactions with the lithium nuclei through the use of evaluated d + ^{6,7}Li cross-section data. The resulting Monte Carlo code “McDeLicious” [3] is a further enhancement to McDeLi with the new ability to sample the generation of d-Li source neutrons from tabulated d + ^{6,7}Li cross-section data. To provide the required data, a full nuclear data evaluation was performed for the reaction system d + ^{6,7}Li [4]. The evaluated data include cross-sections for all reaction channels up to 50 MeV incident deuteron energy as well as energy-angle distributions for the neutrons emitted through the various ^{6,7}Li(d,xn)-reactions. A complete data set of d + ^{6,7}Li cross-section data was prepared in standard ENDF-6 data format and processed with the ACER module of the NJOY99 code for use with McDeLicious.

Over the reporting period, the McDeLicious approach was extensively tested against experimental thick lithium target data including recent results that became available with Task TTMI-003, Deliverable 13, (P. Bem et al., NPI Rez) for 17 MeV deuterons. Calculated and measured total neutron yields are compared in Fig. 1 as a function of incident deuteron energy. A comparison of angular neutron energy spectra is shown in Fig. 2 for 17 MeV incident deuteron energy. There are included calculation results obtained with the semi-empirical d-Li reaction model of McDeLi and the ISABEL intra-nuclear cascade model of the high energy particle Monte Carlo code MCNPX 2.1.5 [5]. It is revealed that McDeLicious can predict both the neutron yield data and the angular energy spectra with considerably better accuracy than McDeLi and MCNPX. This was also observed for the angular yield spectra available at 32 and 40 MeV incident deuteron energy [6]. The accuracy of the angular yield spectra, however, needs to be further improved. With the McDeLicious approach, this can be achieved in a straightforward way through the up-dating of the d+^{6,7}Li data evaluations by using improved nuclear models and parameters and by taking into account new thin and thick lithium target measurements currently underway at NPI Rez and JAERI.

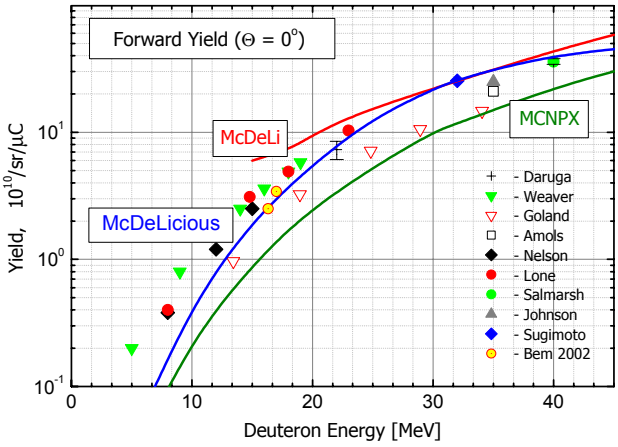

Fig. 1: Thick lithium target forward neutron yields as function of incident deuteron energy.

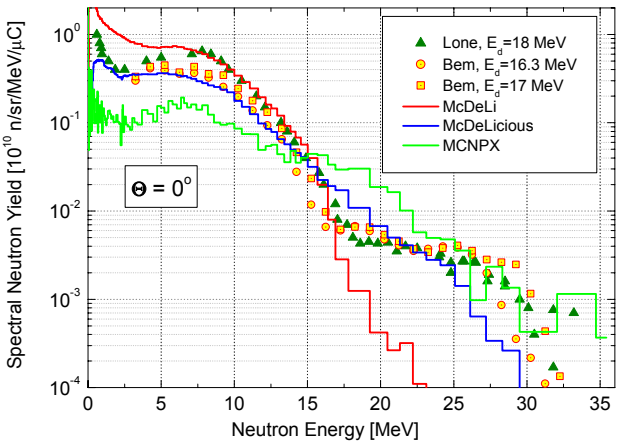

Fig. 2: Thick lithium target forward yield spectra at 17 MeV incident deuteron energy.

Neutron Cross Section Data

The objective of Task TTMI-003, Deliverable 6, is to provide the nuclear cross-section data required for neutron transport and activation calculations of IFMIF. Neutron cross-section data must be available over the whole energy range of IFMIF which extends up to ≈ 55 MeV neutron energy. In particular there is a need for neutron cross sections above 20 MeV which is the upper energy limit of the standard nuclear data libraries.

In a collaboration of Forschungszentrum Karlsruhe (FZK) and the Institute of Nuclear Power Engineering (INPE), Obninsk, Russia, general purpose neutron cross-section data files were previously prepared for selected important nuclides such as ^{1}H, ^{56}Fe, ^{23}Na, ^{39}K, ^{28}Si, ^{12}C, ^{52}Cr, ^{51}V up to 50 MeV incident neutron energy to enable Monte Carlo transport calculations. Cross-section data for other nuclides such as ^{16}O, ^{14}N, ^{27}Al, ^{28,29,30}Si, ^{31}P, ^{40}Ca, ^{50,52,53,54}Cr, $^{54,56,\ 57,58}$Fe, ^{58,60,61,62,64}Ni, ^{63,65}Cu, ^{93}Nb, ^{182,183,184,186} W became available later with the APT project from the LANL 150 MeV evaluations.

The recent evaluation effort within Task TTMI-003 was devoted to the preparation of general purpose neutron cross-section data files for the light mass nuclides ^{6,7}Li and ^{9}Be. Over the reporting period, a complete data file has been prepared for the n + ^{9}Be reaction system with double-differential cross-sections in ENDF-6 data format up to 150 MeV neutron energy. The methodology and tools developed for the description of d (n) + ^{6,7}Li reaction systems have been applied for evaluating the ^{9}Be data. The data file was processed with NJOY/ACER for use with the McDeLicious Monte Carlo code.

Validation of the data evaluations is required to ensure they provide reliable results when applied in neutronics design calculations. This can be achieved through integral experiments and their computational analyses. As part of Task TTMI-003, a benchmark experiment has been conducted on a 20 cm thick iron slab at the NPI Rez [7]. The $D_2O(^3He,xn)$ reaction at 40 MeV incident energy was employed to simulate an IFMIF-like white neutron source spectrum extending up to 35 MeV neutron energy. Spectra of neutrons from both the bare source and transmitted through the iron slab were measured with an NE-213 scintillation detector in the energy range 3.5 to 35 MeV by the pulse height technique. The experimental arrangement is shown schematically in Fig. 3. The computational analysis of the experiment was performed with the MCNP-4C and MCNPX Monte Carlo codes and iron cross-section data from the INPE/FZK and the LANL data evaluations. A detailed three-dimensional geometry model was devised to accurately represent the iron slab, the detector shield and the experimental hall. The neutron source distribution was modelled on the basis of the measured double-differential angle-energy neutron yields obtained for the bare heavy water target. Calculated and experimental neutron transmission spectra at the detector angle 20° are compared in Fig. 4. Good agreement is observed for the INPE/FZK and LANL iron data in the energy range below 15 MeV. In the higher energy domain 15 to 35 MeV the FZK/INPE evaluation satisfactorily represents the experimental results, whereas LANL-150 data overestimates them by up to 50%.

To enable activation calculations for the IFMIF D-Li neutron source, a suitable activation data library, the Intermediate Energy Activation File IEAF-2001 [8], has been recently developed by a collaboration of FZK and INPE Obninsk as part of Task TTMI-003 of the EFDA technology programme. The IEAF-2001 activation library comprises target nuclides from Z=1 (hydrogen) to 83 (bismuth) up to 150 MeV neutron incidence energy. The IEAF-2001 data library was made available on CD-ROM to the NEA data bank, Paris, and to RSICC, Oak Ridge [9]. The IEAF-2001 CD-ROM contains both the pointwise (ENDF) and the groupwise (GENDF) data files as generated with the NJOY module GROUPR in 256 energy groups. The IEAF-2001 library can be used with any activation code capable of handling an arbitrary number of reaction channels such as ALARA (Analytical and Laplacian Adaptive Radioactivity Analysis) developed at the University of Wisconsin-Madison as an advanced computational tool for simulating induced activation in nuclear facilities [10]. First IEAF-2001 application tests have been previously performed to demonstrate its applicability and suitability for IFMIF activation analyses [11].

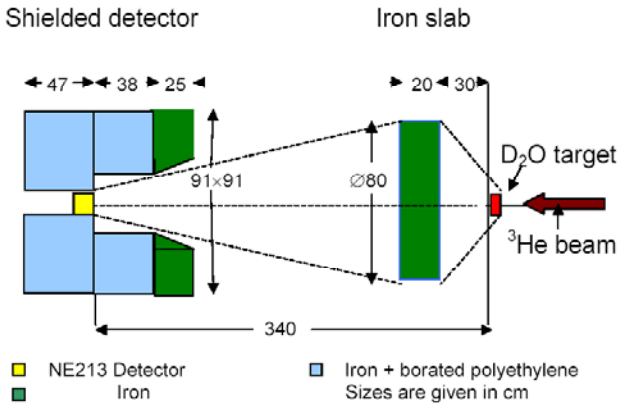

Fig. 3: Set-up of the iron transmission experiment with a ^{3}He-D_2O neutron source and shielded NE-213 detector.

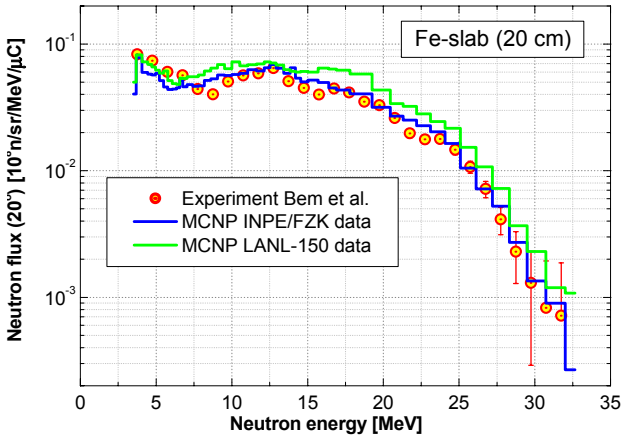

Fig. 4: Energy spectrum of neutrons transmitted trough 20 cm iron slab (^{3}He-D_2O neutron source, 20° detector angle).

Testing and validating of the IEAF-2001 data library is mandatory to ensure reliable results of the activation calculations. Over the reporting period, IEAF-2001 validation analyses were started on the basis of activation calculations with the ALARA code [12]. The validation procedure comprised several steps including various benchmark calculations and computational analyses of integral activation experiments. In the first step, ALARA activation calculations for the low activation steel Eurofer were benchmarked against FISPACT activation calculations. Since FISPACT is not capable of using IEAF-2001 cross-section data, an irradiation in the first wall neutron spectrum of a fusion Demo reactor was considered so as to enable the use of the European Activation File EAF-99 with FISPACT. The same EAF-99 data have been adopted in the IEAF-2001 library for the energy range below 20 MeV. Satisfactory agreement was found for the calculated activity inventories, the decay heat production as well as the contact dose rate (Fig. 5). Thus there is consistency between ALARA/IEAF-2001 and FISPACT/EAF-99 activation calculations for the energy range below 20 MeV.

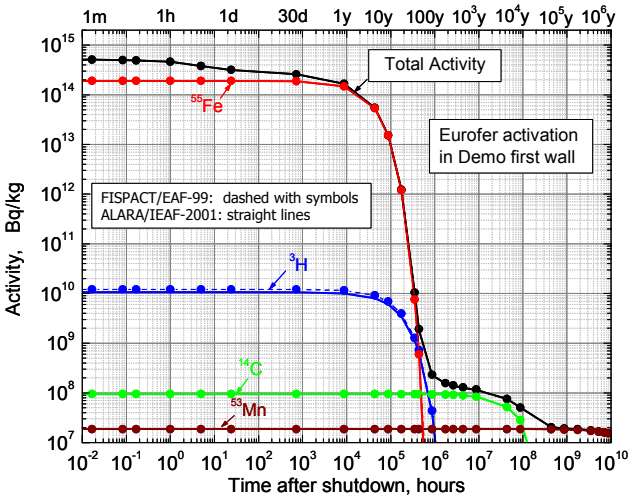

Fig. 5: Eurofer irradiation in the Demo reactor first wall: Comparison of the activity inventories calculated with ALARA/IEAF-2001 and FISPACT/EAF-99.

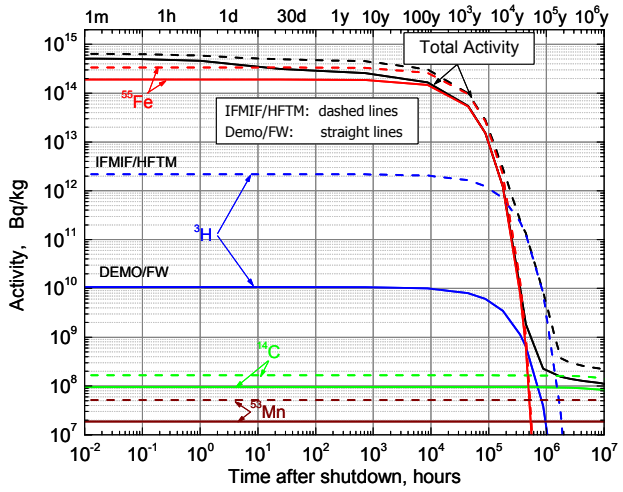

Fig.6: Eurofer irradiation in the Demo reactor first wall (FW) and the IFMIF high flux test module (HFTM): Comparison of activity inventories calculated with ALARA/IEAF-2001.

The second step was devoted to the testing of the IEAF-2001 data against integral activation measurements performed previously at FZK on samples of pure vanadium using a D-Li neutron source with a white energy spectrum extending up to 55 MeV [13]. Satisfactory agreement between the ALARA/IEAF-2001 activity results and the experiment was found for all product nuclides except ^{47}Sc and ^{51}Cr (Table 1). To resolve the ^{47}Sc discrepancy the ^{51}V(n,nα) reaction cross-section needs to be updated. As for ^{51}Cr, it was found that sequential charged particle reactions (SCPR) such as ^{51}V(n,xp) $\Rightarrow$ ^{51}V(p,n)^{51}Cr play an important role in generating ^{51}Cr from ^{51}V. The ALARA code is presently not capable of handling the SCPR mechanism and needs to be updated to this end.

Table 1: C/E (calculation/experiment) ratios for the radioactivity induced by irradiating Vanadium in a white D-Li neutron source. There are included the half-lifes $T_{1/2}$ and the dominant reaction pathways with the associated reaction thresholds E_{thr}.

Nuclide ($T_{1/2}$)	C/E	Dominant Pathways (E_{thr})
^{47}Ca (4.5 d)	0.81 ± 0.22	^{51}V(n,pα) ≈ 100% (11.7 MeV)
^{46}Sc (84 d)	0.77 ± 0.04	^{51}V(n,2nα) = 97.8% (21.3 MeV)
^{47}Sc (3.4 d)	0.17 ± 0.01	^{51}V(n,nα) ≈ 99.6% (10.5 MeV)
^{48}Sc (44 d)	1.07 ± 0.06	^{51}V(n,α) ≈ 99.7% (2.1 MeV)
^{48}V (16 d)	1.07 ± 0.24	^{51}V(n,4n) ≈ 93.3% (32.6 MeV) ^{50}V(n,3n) ≈ 6.7% (21.3 MeV)
^{51}Cr (28 d)	(0.41 ± 0.04)10^{-3}	^{54}Fe(n,α) ≈ 68.4% (0 MeV) ^{56}Fe(n,2nα) ≈ 31.6% (20.0 MeV)
^{92m}Nb (28 d)	1.32 ± 0.36	^{93}Nb(n,2n) ≈ 94.6% (8.9 MeV) ^{92}Mo(n,p) ≈ 9% (0 MeV)

The third step of the IEAF-2001 data testing was devoted to comparative analyses of the activation and transmutation of Eurofer steel irradiated in the IFMIF high flux test module (HFTM) and in a fusion Demo reactor first wall (FW). Fig. 6 shows the calculated activity inventories as function of the decay time. It is noted that the D-Li and the D-T neutron irradiation fields produce the same radioactive nuclides. The activity is dominated by ^{55}Fe during the first year after irradiation, by ^{3}H in the time interval up to one century, and by ^{14}C and ^{53}Mn afterwards. The magnitude of the nuclide activities, however, is larger for the irradiation in IFMIF, in particular for tritium by two orders of magnitude. This is the result of the harder D-Li neutron spectrum and the high energy thresholds of many activation reactions such as the dominant tritium production reaction in iron (^{56}Fe(n,t)^{54}Mn with a reaction threshold of 12.1 MeV). The elemental transmutation induced in Eurofer steel during irradiation are compared in Fig. 7. It is noted that the transmutation of the main constituents of Eurofer, including iron and chromium, is not significant. The inventory of other elements such as Ti, V and Mn, however, increases by 5-20% per irradiation year in FW/Demo and by 10-30% in HFTM/IFMIF. These elements are minor constituents of Eurofer and are produced during irradiation by (n,p) and (n,α) reactions on Cr and Fe, the main constituents of the steel. The large fraction of high energy neutrons in the IFMIF spectrum accounts for the higher transmutation rate of these elements in comparison with the D-T fusion spectrum. Similar reasons explain the different transmutation behaviour of elements such as B, Co, Ta, and W.

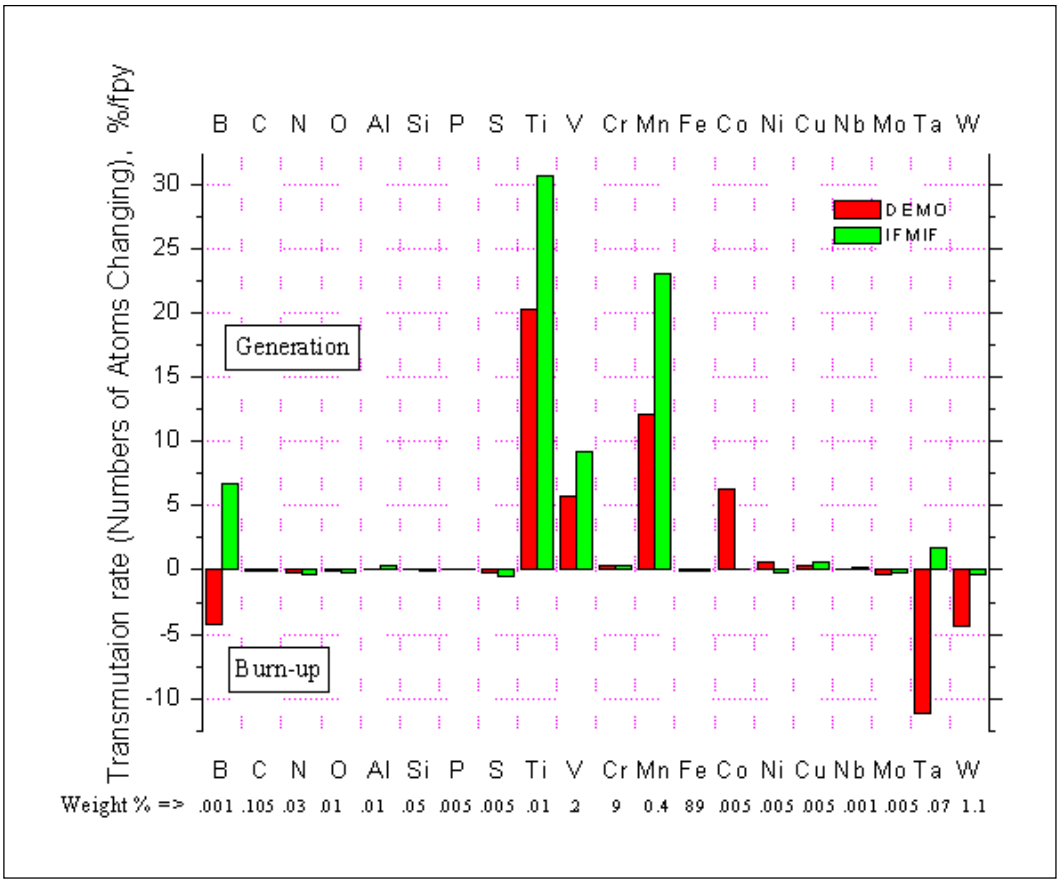

Fig. 7: Eurofer irradiation in the Demo reactor first wall (FW) and the IFMIF high flux test module (HFTM): Comparison of transmutation rates calculated with ALARA/IEAF-2001.

Staff:

U. Fischer
U. von Möllendorff
P. Pereslavtsev, INPE Obninsk
I. Schmuck
S. Simakov
P. Wilson, University of Wisconsin-Madison

Literature:

[1] J.F. Briesmeister (ed.), MCNP - A General Monte Carlo N-Particle Transport Code, Version 4C, Los Alamos National Laboratory, Report LA-13709-M, April 2000

[2] P. P. H. Wilson, Neutronics of the IFMIF Neutron Source: Development and Analysis, Forschungszentrum Karlsruhe, Wissenschaftliche Berichte FZKA 6218, January 1999.

[3] S.P. Simakov, U. Fischer, U. von Möllendorff, I. Schmuck, A.Yu. Konobeev, Yu. A. Korovin, P. Pereslavtsev, Advanced Monte Carlo procedure for the d-Li neutron source term based on evaluated cross sections files, 10th Int. Conf. on Fusion Reactor Materials (ICFRM-10), Baden-Baden, 14-19 Oct. 2001

[4] A. Yu. Konobeyev, Yu. A. Korovin, P. E. Pereslavtsev, U. Fischer and U. von Möllendorff, Developments of methods for calculation of deuteron-lithium and neutron-lithium cross sections for energies up to 50 MeV, Nuclear Science and Enginering 139 (2001) 1-23

[5] L. S. Waters (Ed), MCNPX User's Manual Version 2.1.5, available from http://mcnpx.lanl.gov.

[6] U. Fischer, S. P. Simakov, A. Konobeyev, P. Pereslavtsev, P. Wilson , Neutronics and Nuclear Data for the IFMIF Neutron Source, 6th International Symposium on Fusion Nuclear Technology (ISFNT-6), San Diego, Calif., April 7-12, 2002

[7] P. Bem, U. Fischer, S. Simakov , U. v. Möllendorff, Neutron Transport Benchmark on Iron using a White High-Energy Neutron Field, 22nd Symposium Fusion Technology (SOFT-22), Helsinki, September 9-13, 2002

[8] Yu. Korovin, A. Yu. Konobeev, P.E. Pereslavtsev, U. Fischer, U. v. Möllendorff, Intermediate Energy Activation File IEAF 2001, Int. Conf. Nuclear Data for Science and Technology (ND2001), October 7-12, 2001, Tsukuba, Japan

[9] U. Fischer, D. Leichtle, U. v. Möllendorff , I. Schmuck, A. Yu. Konobeyev, Yu. A. Korovin, P.E. Pereslavtsev, Intermediate Energy Activation File IEAF-2001, NEA data bank programme library, package NEA-1656/01 (2001), RSICC Oak Ridge, DLC-217/IEAF-2001 (2002).

[10] P. P. H. Wilson and D. L. Henderson, ALARA: Analytical and Laplacian Adaptive Radioactivity Analysis, Volume I,

Technical Manual, University of Wisconsin, Report UWFDM 1080, January 1998

[11] U. Fischer, P.P.H. Wilson, D. Leichtle, S.P. Simakov, U. von Möllendorff, A. Konobeev, Yu. Korovin, P. Pereslavtsev , I. Schmuck, Application of the IEAF-2001 Activation Data Library to Activation Analyses of the IFMIF High Flux Test Module. 10th Int. Conf. on Fusion Reactor Materials (ICFRM-10), Baden-Baden, 14-19 Oct. 2001

[12] U. Fischer, S. Simakov , U. v. Möllendorff, P. Pereslavtsev, P. Wilson, Validation of activation calculations using the Intermediate Energy Activation File IEAF-2001, 22nd Symposium Fusion Technology (SOFT-22), Helsinki, September 9-13, 2002

[13] U. von Möllendorff, F. Maekawa, H. Giese, P. Wilson, Experimental test of structural materials activation in the IFMIF neutron spectrum, Fusion Engineering and Design 51-52 (2000) 919-924.

Nuclear Data Base

TTMN-001
EFF/EAF Data File Update, Processing and Benchmark Analyses

The European Fusion File (EFF) and Activation File (EAF) projects aim at developing a qualified nuclear data base and validated computational tools for nuclear calculations of fusion reactors. The related Task TTMN-001 of the EFDA technology work programme is devoted to the evaluation, processing, application, and benchmarking of required nuclear cross section and uncertainty data as well as the development of computational tools for uncertainty calculations. The focus of the FZK contribution to Task TTMN-001 is on the qualification of new and updated EFF data evaluations through computational benchmark analyses including sensitivity/uncertainty analyses and the development of advanced computational schemes for sensitivity calculations based on the Monte Carlo technique.

Benchmark Analyses of Si and SiC

A new Si-28 EFF-3.0 data evaluation was provided by IRK Vienna in late 2001 as part of TTMN-001. The Si-28 EFF-3.0 data were processed with NJOY/ACER and cross-checked with EFF-2, FENDL-1 and –2 evaluations as well as experimental data of the neutron emission cross-section at 14 MeV incident neutron energy [1]. The EFF-3 neutron emission spectra were shown to agree largely with those of FENDL-2 (Fig. 1). First benchmark calculations were performed with the MCNP Monte Carlo code for a 14 MeV neutron transmission experiment conducted at the OKATAVIAN facility on a spherical silicon assembly. EFF-3 and FENDL-2 results again agree and do predict the experimental leakage spectra significantly better than FENDL-1 (Fig. 2).

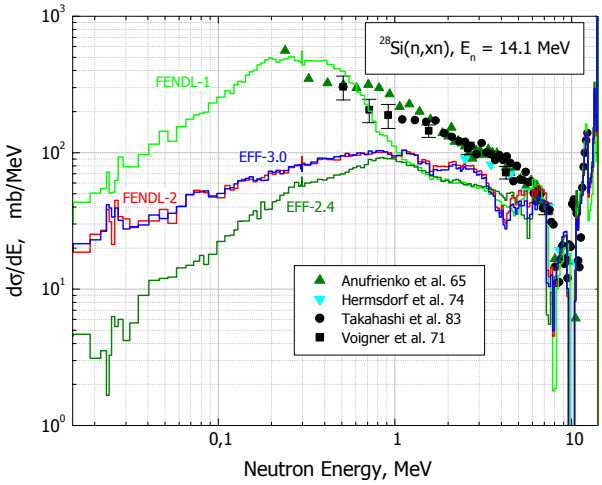

Fig. 1: Neutron emission cross section of Si-28 at 14.1 MeV incident neutron energy

More extensive investigations on Si-28 were performed as part of the computational analyses of the experiment on SiC (TTMN-002) [2]. The analyses comprised Monte Carlo calculations of the neutron and photon flux spectra at four different locations (12.7, 27.94, 43.18 and 58.42 cm) in the 71 cm thick SiC assembly, their sensitivities to the involved silicon and carbon cross-sections and, on the basis of these, assessments of the related uncertainties due to uncertainties of the underlying cross-sections [3,4]. A detailed three-dimensional model of the experimental set-up was employed in the Monte Carlo transport calculations including an accurate representation of the neutron source, the SiC assembly with integrated scintillation detector, assembly support structure and experimental hall (Fig.3). Four separate Monte Carlo calculations were run to obtain the spectra at the four different positions taking into account the fact that the NE-213 spectrometer was inserted in one of the detector holes during the measurement while the other three detector holes were filled with SiC. The basic set of calculations was performed with recent EFF-3 data for Si-28 and FENDL-2 data for all other nuclides. For comparison, calculations were run with Si-28 data from EFF-2.4 and FENDL-1. In addition, one set of calculation was performed with EFF-2.4 data for C-12 along with EFF-3 Si-28 data to see the effect of the C-12 data.

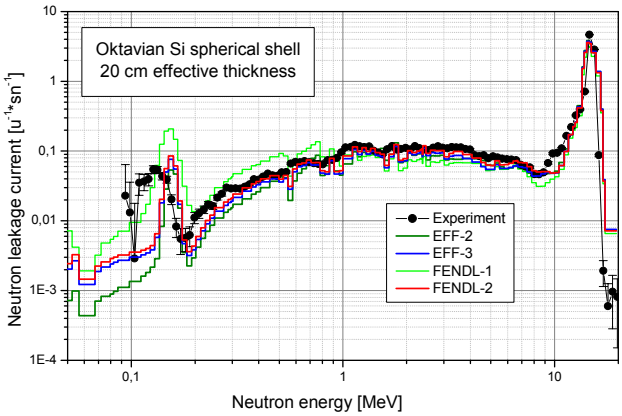

Fig. 2: Neutron leakage spectra of the Oktavian Si transmission experiment

Calculated and measured neutron flux spectra are compared in Fig. 4 for the four detector locations P1 through P4 in the SiC assembly. It is revealed that EFF-3 Si-28 data reproduce the measured neutron spectrum satisfactorily except for the first detector location. A gross underestimation is observed with FENDL-1 data. This is due to a considerably lower elastic scattering cross-section of Si-28 in FENDL-1 in the high energy range along with a strong negative sensitivity of the neutron flux to this cross-section at the deeper penetration depths.

The Monte Carlo sensitivity calculations were performed with MCSEN, a local extension to the MCNP4A code that enables the calculation of point detector sensitivities based on the differential operator method [3,4]. The sensitivity calculations showed a greater sensitivity of the neutron fluxes to the Si than to the C data. Sensitivity profiles for the neutron flux integrals were calculated in the VITAMIN-J 175 group structure to enable the calculation of data related uncertainties by making use of the EFF-3 Si-28 and EFF-2.4 C-12 co-variance data provided in the same group structure. The resulting uncertainties for the four detector positions are displayed in Table 1 along with the experimental uncertainties and C/E data for the associated neutron flux integrals.

Processing and Analyses of Beryllium Data

The Be-9 EFF-3.03 data evaluation provides a decomposition of the (n,2n) reaction into 16 partial channels. After substantial changes were applied to the NJOY modules RECONR and ACER, a complete ACE data file could be prepared for Be-9 EFF-3.03. Over the reporting period, extensive application tests have been performed by means of MCNP-calculations for the KANT transmission experiment on spherical beryllium shells and the time-of-flight (TOF) experiment on beryllium slabs of FNS/JAERI. No severe problems were encountered when using the Be-9 EFF-3.03 data in the new ACE format with MCNP4C. As compared to the angular leakage spectra of the FNS/JAERI experiment, significant improvements over the existing Be data

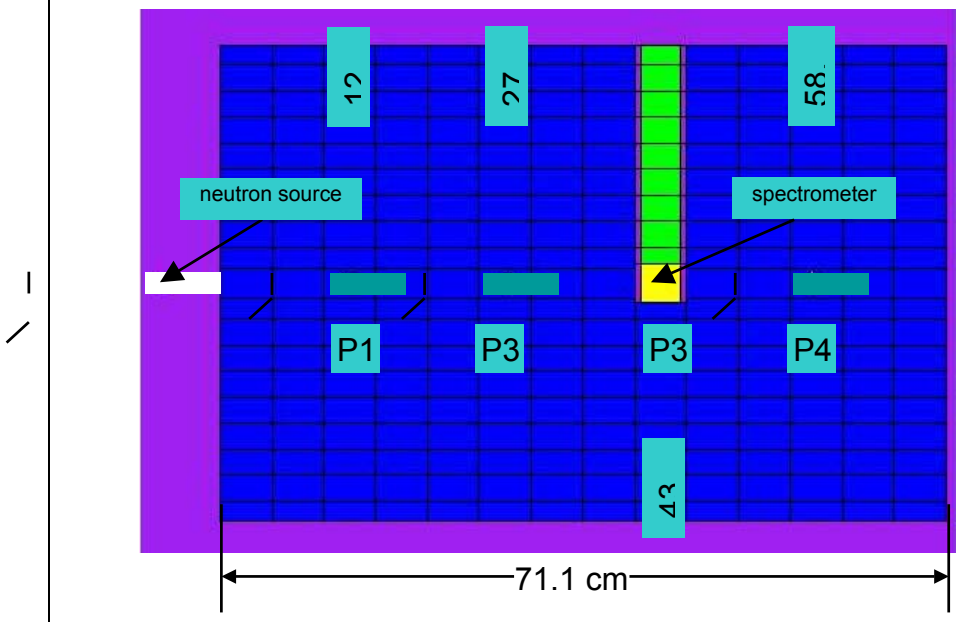

Fig. 3: MCNP model of SiC experimental assembly

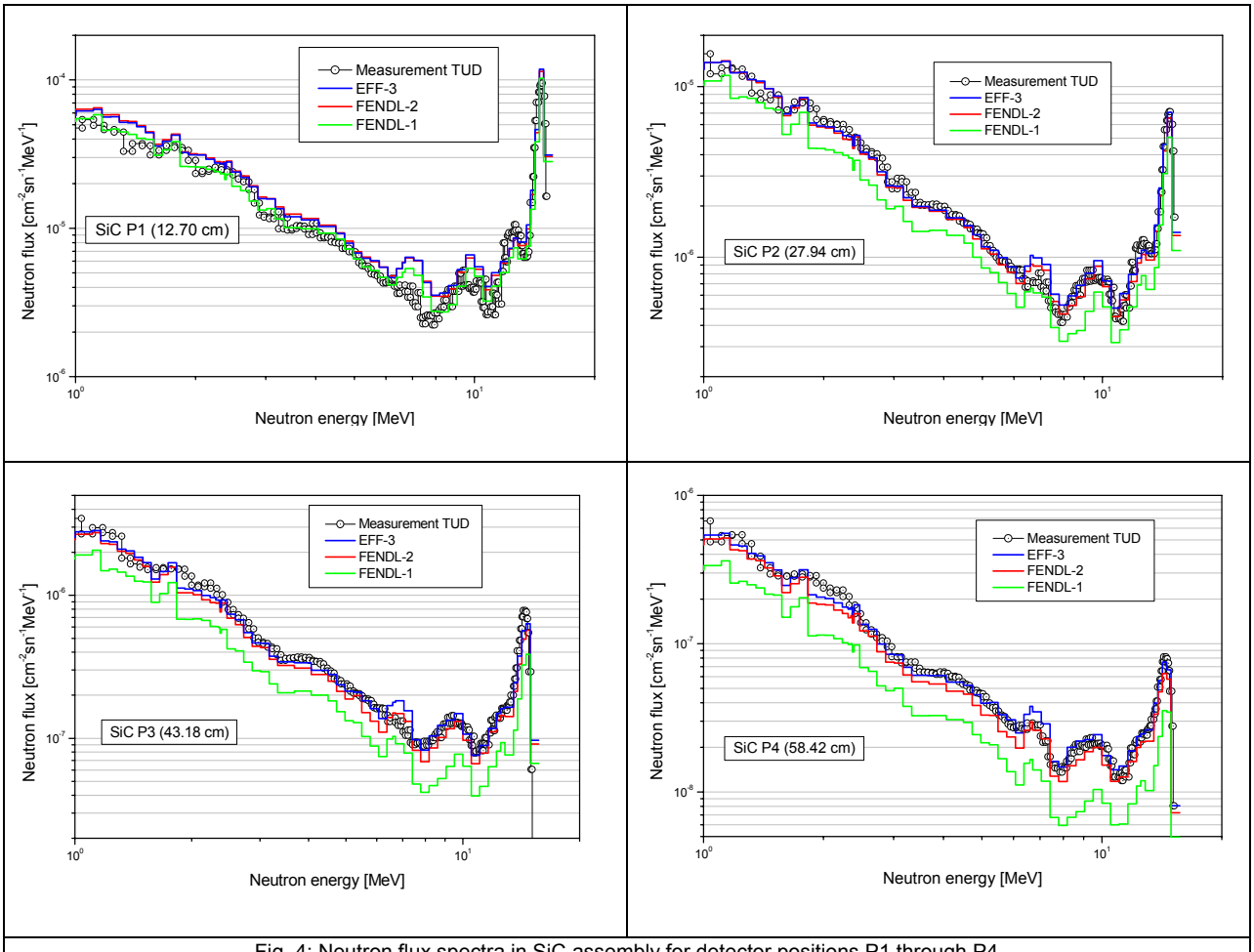

Fig. 4: Neutron flux spectra in SiC assembly for detector positions P1 through P4

Table 1: Calculated (ΔC) and experimental (ΔE) uncertainties for neutron flux integrals at the four detector locations in the SiC assembly. C/E is the ratio of the calculated and experimental neutron flux in the given energy interval.

E-low [MeV]	ΔC[%]				ΔE	C/E		ΔC[%]				ΔE	C/E	
	MC	Si	C-12	Total	[%]	C/E	Δ[%]	MC	Si	C-12	Total.	[%]	C/E	Δ[%]
Position P1 (12.70 cm)								Position P2 (27.94 cm)						
1	0.36	2.0	1.7	2.6	3.6	1.19	4	0.29	1.8	1.9	2.7	3.6	0.97	4
2.5	0.49	2.0	2.7	3.4	3.6	1.18	5	0.35	2.3	2.5	3.4	3.6	0.97	5
5	0.58	3.3	2.8	4.4	5.1	1.36	7	0.44	3.7	3.1	4.9	5.1	1.24	7
7.5	1.28	2.0	4.2	4.8	5.1	1.32	7	0.46	3.2	4.4	5.5	5.1	1.19	8
10	0.46	2.5	2.6	3.7	3.6	1.08	5	0.41	4.6	4.6	6.5	3.6	1.04	7
12.5	0.11	1.6	1.7	2.4	3.6	1.17	4	0.2	3.8	4.3	5.8	3.6	1.05	7
Total	0.27	1.0	0.9	1.4				0.2	1.2	1.0	1.5			
Position P3 (43.18 cm)								Position P4 (58.42 cm)						
1	0.36	2.2	2.3	3.2	3.7	0.94	5	0.32	2.8	2.9	4.0	3.7	1.0	5
2.5	0.46	3.2	3.0	4.3	3.7	0.99	6	0.41	3.9	3.7	5.4	3.7	1.0	7
5	0.83	4.1	3.8	5.6	5.1	1.21	8	0.33	4.7	4.6	6.6	5.1	1.3	8
7.5	0.55	4.5	5.1	6.8	5.1	1.14	8	0.39	5.7	6.2	8.5	5.1	1.2	10
10	0.85	6.4	6.9	9.4	3.3	1.02	10	0.34	8.1	9.1	12.2	3.3	1.1	13
12.5	0.36	5.7	7.0	9.0	3.3	1.04	10	0.14	7.5	9.7	12.3	3.3	1.1	13
Total	0.24	1.2	0.9	1.5				0.79	1.3	1.0	1.8			

evaluations could be obtained due to the better description of the energy-angle distributions of neutrons emitted through the different 16 reaction channels [5].

As a first step towards the Monte Carlo based uncertainty assessment for beryllium, transport and sensitivity calculations were performed for the FNS/JAERI transmission experiment on a beryllium slab using the MCSEN code with the latest EFF-3.05 data. After upgrading MCSEN to enable the handling of the EFF-3.05 data evaluation with tabulated angle-energy distributions (LAW 67 representation according to the ENDF-6 data format), sensitivity calculations could be successfully performed by taking into account all 16 partial reaction channels included in the EFF-3 Be (n,2n) evaluation [6].

Algorithm for Monte Carlo Calculation of Sensitivities to Secondary Angular Distributions

Within the running EFF-programme, development work is being conducted on computational schemes for the calculation of point detector sensitivities to secondary distributions with the objective to implement them into the MCNP Monte Carlo code. A sensitivity algorithm based on the use of the Legendre series expansion for the secondary angular distribution (SAD) has been previously developed and implemented into MCSEN, a local update to MCNP. The implemented sensitivity algorithm has been verified by means of numerical tests and MCNP comparison calculations with perturbed cross-section data.

Over the reporting period, software tools were developed to enable the calculation of point detector sensitivities to SAD perturbations in angular bin representation [7]. The software uses as input an integral description of the SAD perturbation and the sensitivities to Legendre moments as obtained with the MCSEN code. It provides the sensitivities to the SAD perturbation assuming for the integral changes either constant changes within each given angular bin or a minimal number of perturbed Legendre coefficients describing the SAD.

The MCSEN code was further upgraded to the current version 4C of the MCNP code so as to be capable of handling the most recent data formats such as tabulated angle-energy distributions used e. g. for the recent Be-9 EFF-3.03 data evaluation (LAW 67 representation according to ENDF-6 format). Another new feature was implemented into MCSEN to allow the calculation of the sensitivity to a nuclide in many cells of the geometry model. This was required for the sensitivity analysis of the SiC experiment as the assembly block had to be divided into many cells to allow the use of the weight window importance sampling technique. Testing of the new capabilities was performed as part of the benchmark analyses reported above [3,4]

Staff:

Y. Chen
U. Fischer
D. Leichtle
I. Kodeli (Josef-Stefan Institut, Ljubljana)
R. Perel (Hebrew University of Jerusalem)
S. P. Simakov
I. Schmuck

Literature:

[1] U. Fischer, S. Simakov: First Benchmark Results for the New Si-28 EFF-3 Data Evaluation, EFF-DOC-807, NEA Data Bank, Paris, November 2001.

[2] K. Seidel, M. Angelone, P. Batistoni, Y. Chen, U. Fischer, H. Freiesleben, C. Negoita, R. L. Perel, .M. Pillon and S. Unholzer, Measurement and Analysis of Neutron and Gamma-Ray Flux Spectra in SiC, 22nd Symposium Fusion Technology (SOFT-22), Helsinki, September 9-13, 2002; see also this report on task TTMN-002-2.

[3] U. Fischer, R. Perel, Y. Chen, Monte Carlo Transport, Sensitivity and Uncertainty Analysis for the TUD Benchmark Experiment on SiC, EFF-DOC-815, NEA Data Bank, Paris, April 2002.

[4] Y. Chen, U. Fischer, I. Kodeli, R.L. Perel, M. Angelone, P. Batistoni, L. Petrizzi, M. Pillon, K. Seidel, S. Unholzer, Sensitivity and Uncertainty Analyses of 14 MeV neutron Benchmark Experiment on Silicon Carbide, 22nd Symposium Fusion Technology (SOFT-22), Helsinki, September 9-13, 2002

[5] D. Leichtle, U. Fischer: Benchmarking of the 9-Be EFF3.0/NMOD=3 evaluation, EFF-DOC-788, NEA Data Bank, Paris, November 2001.

[6] R. Perel, D. Leichtle, First Results from Monte-Carlo Sensitivity Calculations using the Be EFF3.0/NMOD=5 Evaluation, EFF-DOC-817, NEA Data Bank, Paris, April 2002

[7] R. L. Perel: Algorithm for Monte Carlo Calculation of Sensitivities to Angular Segments, EFF-DOC-791, NEA Data Bank, Paris, November 2001.

TTMN-002
Benchmark Experiments to Validate EFF/EAF Data

TTMN-002-2
Measurement and Analysis of Neutron and Gamma-Ray Spectra in SiC

Silicon carbide composites are candidates for advanced structural materials in fusion reactors, mainly due to their low decay heat and activation properties. Integral experiments are required to benchmark the nuclear data, involved in design calculations, both with regard to the activation and the particle transport behaviour. As part of the European Fusion Technology Programme several activation experiments were performed (for instance Ref. [1]) and the neutron-photon transport in a thick SiC assembly irradiated with 14 MeV neutrons, was investigated by a collaboration of ENEA Frascati, FZ Karlsruhe, JSI Ljubljana and TU Dresden [2]. Inside a SiC block the spectral distributions of the fast neutron flux and of the gamma-ray flux were measured at four positions by TUD. Recently a new evaluation of the Si data was carried out for the European Fusion File EFF-3 [3] including covariance data for sensitivity and uncertainty calculations. These data and FENDL-2 [4] data for C and the other nuclides of the assembly were used by FZK for analysing the neutron and gamma-ray flux spectra.

Experiment

The experimental set-up is shown in Fig. 1. The dimensions of the SiC block were 45.7 cm x 45.7 cm x 71.1 cm of length (x-axis). The tritium target of the Frascati Neutron Generator was located at x = -5.3 cm. Flux spectra were measured in four positions (P 1,....P 4) at x = 12.70, 27.94, 43.18 and 58.42 cm. The SiC material had a density of 3.185 g/cm^3 and a elemental composition (private communication with JAERI) of 30.828 wt-% of C, 68.889 wt-% of Si, 0.190 wt-% of B, 0.079 wt-% of Al and 0.014 wt-% of Fe. The neutron and gamma-ray flux spectra were measured simultaneously, using a NE 213 liquid-scintillation spectrometer. The dimensions of the cylindrical active volume of the detector were 38 mm in both height and diameter. The scintillator was coupled to a photomultiplier by means of a 50 cm long light guide. When the detector was located at one of the positions (P 1 in Fig. 1), the other ones were filled with bricks of SiC.

The pulse-height response matrix of the detector was determined on the basis of detailed simulations of experimental distributions from mono-energetic neutron and gamma-ray sources. The DIFBAS code was employed for unfolding the measured pulse-height distributions of the present experiment in order to generate the neutron and the gamma-ray flux spectra. They were obtained as absolute fluxes, as the response matrices have been determined on an absolute scale.

The neutron flux spectra obtained at the four positions are plotted in Fig. 2, the spectral gamma-ray fluxes in Fig. 3.

Analysis

The computational analysis was performed with the Monte Carlo code MCNP-4C [5] using a full 3D geometry model of the assembly, the neutron generator and the experimental hall. The spectra were calculated as average flux in the scintillator volume by means of the track length estimator of MCNP.

The calculated *neutron flux* spectra are compared with the measured distributions in Fig. 2. The fluxes integrated over energy intervals and ratios of calculated-to-experimental values (C/E) are presented in Table 1. The uncertainties of the experimental values take into account those of the measured flux spectra, the background subtraction and the neutron source monitoring. The uncertainties of the calculated values include the statistical uncertainty of the Monte Carlo calculation (less than 1%) and those due to the cross section uncertainties of ^{28}Si and C [6].

The low-energy part of the spectra is well described; C/E deviates from unity not more than about 10% for the energy range 1.0 MeV < E < 5.0 MeV. The measured structures in the spectra are also reproduced by the calculations. In the energy range 5.0 MeV < E < 10.0 MeV, structures from inelastic scattering on single levels or on groups of levels appear in the spectra, both in the measured and the calculated ones. Some of these, especially at E around 10 MeV and 7 MeV, are overestimated by the calculations, resulting in C/E values significantly above 1.0. The high-energy part, E > 10 MeV, is satisfactorily described both in the 14 MeV peak region and below where inelastically scattered neutrons populate the spectrum.

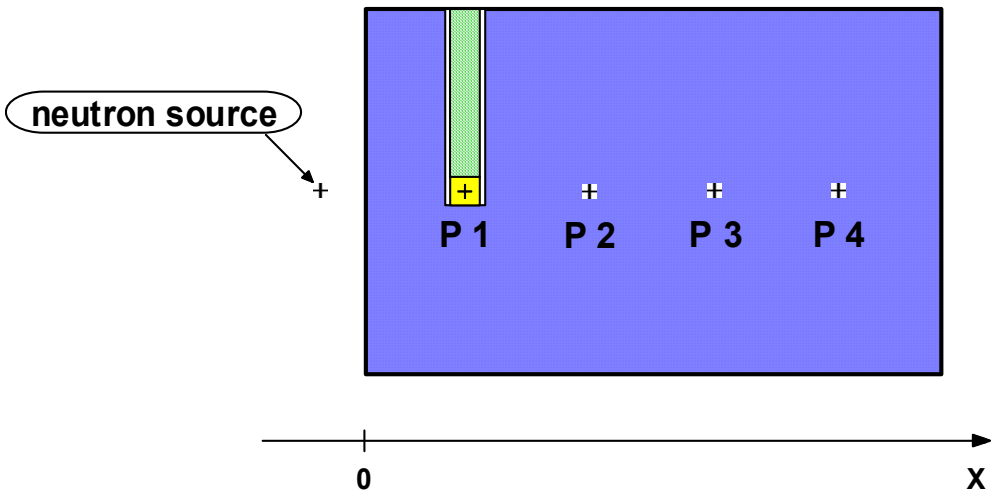

Fig. 1: Geometry of the benchmark assembly with the detector in position 1.

The calculated *gamma-ray flux* spectra are compared with the measured distributions in Fig. 3. The fluxes integrated over energy intervals and C/E values are presented in Table 2. The uncertainties of the experimental values include those of the measured spectra, the background subtraction and of the neutron source monitoring. For the calculated values only the statistical uncertainty of the Monte Carlo calculation is given.

For the flux integral with E > 0.4 MeV a general underestimation by about 20% is observed with the tendency of slightly increasing with deeper positions. Most of the strong peaks are well described (esp. at E = 1.8 MeV and 4.4 MeV from inelastic scattering of neutrons on the first levels of ^{28}Si and ^{12}C, respectively), but some are underestimated or even neglected by the calculation.

The peak at E = 0.48 MeV from thermal neutron capture by ^{10}B contributes to the underestimation at the deeper positions as shown by the C/E for E = 0.4 – 0.6 MeV in Table 2. As the B content of the material around the detector positions is not exactly known, it was varied between 0 wt-% and 0.38 wt-% in calculations for the four detector positions. As expected, its influence on the spectrum increases with deeper positions. The characteristics are shown for P 4 comparing the fluxes calculated without B and with 0.19 wt-% in Fig. 3 and in Table 2. With increasing B content the flux in E = 0.4 – 0.6 increases, but it decreases for other energy groups due to reduced capture of thermal neutrons. This balance leads to a weak dependence of the total flux for E > 0.4 MeV on the B content only, and the underestimation remains. The better C/E obtained for E > 0.4 MeV with 0 wt-% B is in contrast to the spread of the C/E for E > 0.6 MeV and E = 0.4 – 0.6 MeV, as well as to the strong capture peaks that were not observed in the measured spectra.

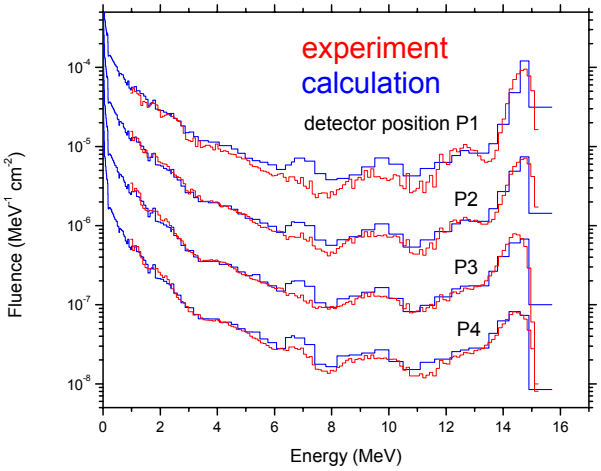

Fig. 2: Measured and calculated neutron flux spectra, normalized to one source neutron, at the four detector positions

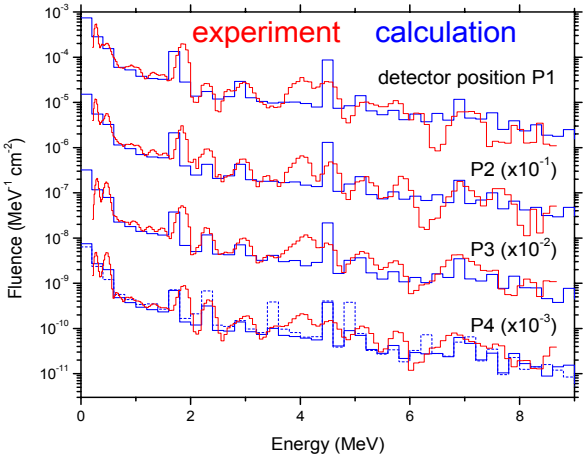

Fig. 3: Measured and calculated gamma-ray flux spectra, normalized to one source neutron, at the four detector positions. The spectrum calculated for position 4 with the assumption of 0.0 wt-% B content in the material is inserted by a dashed line

Table 1: Measured and calculated neutron fluente integrals per source neutron and C/E (calculation/experiment) ratios

Detector position, Energy range/ (MeV)	F_{exp} / (cm^{-2}·s^{-1})	F_{calc} / (cm^{-2}·s^{-1})	***C / E***
P 1 1.0 – 5.0	$(7.83 \pm 0.28)\cdot10^{-5}$	$(8.70 \pm 0.25)\cdot10^{-5}$	1.11 ± 0.05
5.0 – 10.0	$(1.96 \pm 0.10)\cdot10^{-5}$	$(2.81 \pm 0.14)\cdot10^{-5}$	1.44 ± 0.10
> 10.0	$(1.00 \pm 0.04)\cdot10^{-4}$	$(1.19 \pm 0.03)\cdot10^{-4}$	1.19 ± 0.05
P 2 1.0 – 5.0	$(1.79 \pm 0.06)\cdot10^{-5}$	$(1.72 \pm 0.05)\cdot10^{-5}$	0.96 ± 0.04
5.0 – 10.0	$(3.70 \pm 0.19)\cdot10^{-6}$	$(4.52 \pm 0.23)\cdot10^{-6}$	1.22 ± 0.09
>10.0	$(9.60 \pm 0.35)\cdot10^{-6}$	$(1.01 \pm 0.06)\cdot10^{-5}$	1.05 ± 0.07
P 3 1.0 – 5.0	$(3.51 \pm 0.13)\cdot10^{-6}$	$(3.32 \pm 0.12)\cdot10^{-6}$	0.95 ± 0.05
5.0 – 10.0	$(6.71 \pm 0.34)\cdot10^{-7}$	$(7.90 \pm 0.48)\cdot10^{-7}$	1.18 ± 0.09
>10.0	$(1.20 \pm 0.04)\cdot10^{-6}$	$(1.23 \pm 0.11)\cdot10^{-6}$	1.03 ± 0.10
P 4 1.0 – 5.0	$(6.54 \pm 0.24)\cdot10^{-7}$	$(6.47 \pm 0.29)\cdot10^{-7}$	0.99 ± 0.06
5.0 – 10.0	$(1.20 \pm 0.06)\cdot10^{-7}$	$(1.46 \pm 0.11)\cdot10^{-7}$	1.22 ± 0.11
>10.0	$(1.60 \pm 0.06)\cdot10^{-7}$	$(1.76 \pm 0.23)\cdot10^{-7}$	1.10 ± 0.14

Conclusions

The fast neutron flux in a SiC benchmark assembly of a thickness, corresponding to about 10 mean free path for 14 MeV neutrons, can be reproduced by MCNP calculations within ±20 % using EFF-3.0 data for ^{28}Si and FENDL-2.0 data for the other nuclides. The overestimation of the neutron flux for the interval E = 5 – 10 MeV may be attributed to inelastic scattering cross sections from individual levels and should be analysed more in detail.

The gamma-ray flux for E > 0.4 MeV is underestimated by up to 24% at the deepest position. To improve the C/E values, the reason for missing some gamma-ray peaks in the calculated spectra and the thermal neutron balance should be further investigated.

Staff:

H. Freiesleben
C. Negoita
K. Seidel
S. Unholzer
Y. Chen
U. Fischer
R. PErel (Hebrew University of Jerusalem)

Literature:

[1] K. Seidel, R. A. Forrest, H. Freiesleben, V. D. Kovalchuk, D. V. Markovskij, D. Richter, V. I. Tereshkin and S. Unholzer, Experimental investigation of radioactivity induced in the fusion power plant structural material SiC and in the breeder material Li_4SiO_4 by 14-MeV neutrons, Fus. Eng. Des. 58-59 (2001) 585.

[2] H. Freiesleben, C. Negoita, K. Seidel, S. Unholzer, Y. Chen, U. Fischer, R. L. Perel, M. Angelone, P. Batistoni, M. Pillon, Measurement and analysis of neutron and gamma-ray flux spectra in SiC, Report TUD-IKTP/02-02, Dresden 2002.

[3] S Tagesen and H Vonach, Evaluation of neutron cross sections for fusion relevant materials, EFF-DOC-785, NEA Data Bank, 2001.

[4] A. B. Pashchenko and H. Wienke, FENDL/E-2.0 – Evaluated nuclear data library of neutron nuclear interaction cross-sections and photon production cross-sections and photon-atom interaction cross-sections for fusion applications, IAEA-NDS-175, International Atomic Energy Agency, 1998.

[5] J. F. Briesmeister (ed.), MCNP – A general Monte Carlo n-particle transport code, version 4C, LA-13709, Los Alamos National Laboratory, 2000.

[6] Y. Chen, U. Fischer, I. Kodeli, R.L. Perel, M. Angelone, P. Batistoni, L. Petrizzi, M. Pillon, K. Seidel, S. Unholzer, Sensitivity and Uncertainty Analyses of 14 MeV neutron Benchmark Experiment on Silicon Carbide, 22nd Symposium Fusion Technology (SOFT-22), Helsinki, September 9-13, 2002; see also this report on task TTMN-001

Table 2: Measured and calculated gamma-ray fluence integrals per source neutron and C/E (calculation/experiment) ratios. Results of a calculation obtained for detector position 4 with the assumption of 0.0 wt-% B content in the material are included in italics *(P4*)*

Detector position, Energy range / (MeV)	F_{exp} / $(cm^{-2}\cdot s^{-1})$	F_{calc} / $(cm^{-2}\cdot s^{-1})$	***C / E***
P 1 > 0.4	$(2.11 \pm 0.08)\cdot 10^{-4}$	$(1.81 \pm 0.004)\cdot 10^{-4}$	0.86 ± 0.03
0.4 – 0.6	$(3.33 \pm 0.13)\cdot 10^{-5}$	$(3.10 \pm 0.01)\cdot 10^{-5}$	0.93 ± 0.04
> 0.6	$(1.78 \pm 0.07)\cdot 10^{-4}$	$(1.50 \pm 0.005)\cdot 10^{-4}$	0.84 ± 0.03
P 2 > 0.4	$(3.91 \pm 0.14)\cdot 10^{-5}$	$(3.18 \pm 0.008)\cdot 10^{-5}$	0.81 ± 0.03
0.4 – 0.6	$(8.10 \pm 0.32)\cdot 10^{-6}$	$(6.50 \pm 0.03)\cdot 10^{-6}$	0.80 ± 0.03
> 0.6	$(3.09 \pm 0.12)\cdot 10^{-5}$	$(2.53 \pm 0.008)\cdot 10^{-5}$	0.82 ± 0.03
P3 > 0.4	$(8.16 \pm 0.29)\cdot 10^{-6}$	$(6.30 \pm 0.03)\cdot 10^{-6}$	0.77 ± 0.03
0.4 – 0.6	$(2.20 \pm 0.09)\cdot 10^{-6}$	$(1.58 \pm 0.008)\cdot 10^{-6}$	0.72 ± 0.03
> 0.6	$(5.97 \pm 0.24)\cdot 10^{-6}$	$(4.72 \pm 0.024)\cdot 10^{-6}$	0.79 ± 0.03
P 4 > 0.4	$(1.81 \pm 0.07)\cdot 10^{-6}$	$(1.38 \pm 0.007)\cdot 10^{-6}$	0.76 ± 0.03
0.4 – 0.6	$(5.84 \pm 0.23)\cdot 10^{-7}$	$(3.97 \pm 0.03)\cdot 10^{-7}$	0.68 ± 0.03
> 0.6	$(1.23 \pm 0.05)\cdot 10^{-6}$	$(9.81 \pm 0.06)\cdot 10^{-7}$	0.80 ± 0.03
P 4* > 0.4	$(1.81 \pm 0.07)\cdot 10^{-6}$	$(1.54 \pm 0.01)\cdot 10^{-6}$	0.85 ± 0.03
0.4 – 0.6	$(5.84 \pm 0.23)\cdot 10^{-7}$	$(2.41 \pm 0.04)\cdot 10^{-7}$	0.41 ± 0.02
> 0.6	$(1.23 \pm 0.05)\cdot 10^{-6}$	$(1.30 \pm 0.1)\cdot 10^{-6}$	1.06 ± 0.05

TTMN-002-10
Activation Experiment in Fusion Peak Neutron Field on Tungsten

The radioactivity induced by neutrons in the materials of fusion devices represents a central topic of safety-related investigations. Radionuclides with a broad range of half-lives have to be included in the corresponding analyses. The short-term radioactivity (half-life ranging from the order of magnitude of minutes to weeks) is mainly of interest with respect to heat production and shut-down dose rates, whereas long-term radioactivity (half-life of the order of 10 – 100 years or more) determines the waste management.

The spectrum of the neutron flux in a fusion reactor consists of two parts, a DT-fusion peak at 14 MeV and a continuum ranging down to thermal energies. In the present work, the radioactivity induced by 14 MeV neutrons in W was investigated, complementary to measurements on W in a white fast-neutron field [1]. W is a candidate material for the divertor and other components of a reactor.

In a calculation with the European Activation System (EASY) [2], pure W was taken to be irradiated with 14 MeV neutrons of a flux density corresponding to the power of 1.0 MW, for a period of one year. The results obtained for the contact dose rate as a function of decay time after irradiation are shown in Fig.1.

After about 10 years the dose rate is expected to be below the recycling limit and after about 200 years below the hands-on limit. To investigate the activity of all nuclides, that dominate before the recycling limit is reached, two different irradiations were carried out. A short irradiation followed by activity measurements at decay times in the range labelled by “ts” in Fig.1 was directed to the short-term radioactivity; and after a longer irradiation with activity measurements at times “t1...t3”, the production of the other nuclides was measured.

Experiment

Three different irradiations of samples were performed at the high-intensity DT-neutron generator SNEG-13 [3] at Sergiev Posad (Table 1).

Table 1: Irradiation of samples with DT-neutrons (neutron energy: mean value and peak width at half maximum.

No.	Sample mass (g)	Neutron energy (MeV)	Irradiation time	Neutron fluence (cm-2)
1	1.816	14.93±0.27	10.0 min	$6.20 \cdot 10^{12}$
2	1.816	14.93±0.27	13.93 h	$2.32 \cdot 10^{14}$
3	1.725	14.37±0.12	13.93 h	$4.00 \cdot 10^{13}$

The applied neutron fluences were determined via activation measurement of niobium foils by the reaction 93Nb(n,2n)92mNb.

γ-ray spectra were taken from the samples several times in the range “ts” (Fig. 1, lower part) after irradiation of sample No 1, and at t1 ... t3 in the case of irradiation of the samples No 2 and 3. γ-activities identified by energy and half-life were used to determine nuclide activities, using γ-yield data from EASY.

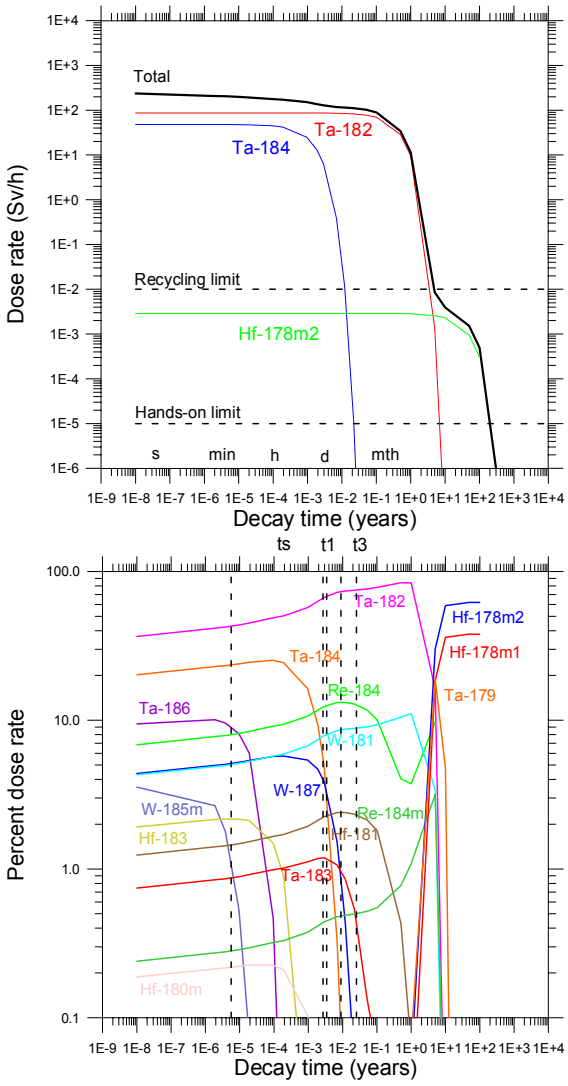

Fig. 1: Calculated contact dose rate (upper part) and contribution of the different radionuclides to the total dose rate (lower part) after irradiation of W with 14-MeV neutrons of 1.0 MW/m^2 power density for one year as a function of the decay time.

Results

The measured activities were analysed with the versions EASY-99 and EASY-2001 of the European Activation System. Results are presented in Tables 2 and 3. The uncertainty of the calculated activity includes both cross section and half-life errors as estimated by EASY. The uncertainty of the experimental values takes into account possible errors of the γ-activity measurements (statistical uncertainty of the γ-counting and efficiency calibration of the spectrometer), of the γ-yield data and of the neutron flux monitoring.

Table 2: Results from irradiation of sample No 1;
radionuclides identified, their half-life and the γ-rays used to determine the activity, the neutron reactions producing these radionuclides, the ratios of calculated-to-experimental activity (C/E), obtained with EASY-99 and EASY-2001, and the uncertainties of both the calculated (EASY-2001) and the experimental activities.

Radio-nuclide	Half-life	E_γ (keV)	Reaction Contr.(%)	C/E EASY-99	C/E EASY-2001	ΔC/C (%)	ΔE/E (%)
^{183}Hf	64 min	459 784	^{186}W(n,α) 100	1.29	1.33	18.	15.
^{184}Ta	8.7 h	253 318 414 921	^{184}W(n,p) 98.3 ^{186}W(n,t) 1.7	1.62	1.34	10.	6.5
^{186}Ta	10.5 min	738	^{186}W(n,p) 100	1.33	1.10	14.	16.
^{185m}W	1.67 min	132 174	^{186}W(n,2n) 100	0.98	0.88	61.	7.2
^{187}W	23.7 h	480 686 773	^{186}W(n,γ) 100	0.61	0.61	50.	5.9

Table 3: Results from irradiation of sample No 2.

Radio-nuclide	Half-life	E_γ (keV)	Reaction Contr.(%)	C/E EASY-99	C/E EASY-2001	ΔC/C (%)	ΔE/E (%)
^{181}Hf	42.4 d	482	^{184}W(n,α) 100.	1.77	1.66	12.	7.5
^{182}Ta	114.7 d	1121 1189	^{182}W(n,p) 86.5 ^{183}W(n,d) 6.5	1.60	1.60	52.	6.8
^{183}Ta	5.09 d	354	^{183}W(n,p) 64.0 ^{184}W(n,d) 20.7 ^{186}W(n,α)β^- 15.3	1.35	1.36	23.	7.8
^{184}Ta	8.7 h	318 414 921	^{184}W(n,p) 98.3 ^{186}W(n,t) 1.7	1.83	1.51	10.	11.
^{187}W	23.7 h	480 686 773	^{186}W(n,γ) 100	0.47	0.47	50	7.1

The results from the irradiation of sample 3 are in general agreement with those from sample 2 [4]

For the ^{187}W activity, C/E values of about 0.5 ... 0.6 were found. That may mainly be attributed to a contamination of the neutron field by DD-selftarget-neutrons [4].

The other activities investigated, typically show C/E of about 1.1 ... 1.8. These overestimations are generally in agreement with the results obtained in the white fast-neutron field [1].

The reactions by which the activities were produced are of the type (n, charged particle). Their cross sections at 14 MeV are of the order of 1 mb due to the high Coulomb barrier of W (atomic number 74), i. e. they are just above the reaction threshold. The representation of these parts in the library data should be improved. This is indicated also by the energy dependence of the C/E.

Conclusions

The activation behaviour of pure W, irradiated with fusion peak neutrons, was investigated up to the recycling limit of the material calculated for fusion reactor conditions.

The C/E obtained for the activities indicate that the total dose rate of W on fusion reactor conditions is significantly overestimated by EASY-2001 and EASY-99. The calculated total contact dose rate shown in Fig. 1, is compared in Fig. 2 with those if the partial dose rates are corrected with the C/E of the activities obtained in the present work for ^{183}Hf, ^{184}Ta, ^{186}Ta, ^{185m}W, ^{181}Hf, ^{182}Ta and ^{183}Ta.

It seems to be advisable to check the description of the cross section thresholds of (n, charged particle) reactions at their lowest values. That is also important for DT-neutrons on other targets with atomic numbers around Z = 74.

For some of the activities, improvements of EASY-2001 compared to EASY-99 were observed.

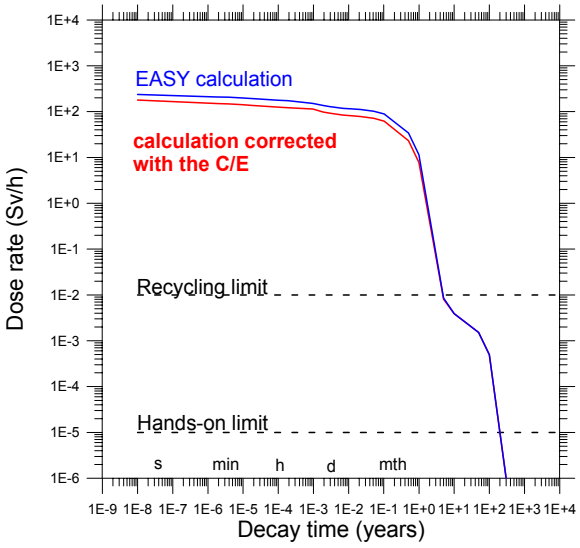

Fig. 2: Contact dose rate after irradiation of W with 14 MeV neutrons of 1.0 MW/m^2 power density for one year as a function of the decay time as calculated with EASY (blue) and compared with those (red) after multiplying the dose rates for ^{181}Hf, ^{183}Hf, ^{182}Ta, ^{183}Ta, ^{184}Ta, ^{186}Ta and ^{185m}W with the (C/E)$^{-1}$ of the present work.

Staff:

R. Eichin
H. Freiesleben
K. Seidel
S. Unholzer

Literature:

[1] U. von Möllendorff, H. Tsige-Tamirat, H. Giese, F. Maekawa, “Integral activation experiments on fusion relevant materials using a white fast-neutron field”, Report FZ Karlsruhe, FZKA 6684, February 2002.

[2] R. A. Forrest and J-Ch. Sublet, “FISPACT-99: User manual, and The European Activation File: EAF-99 cross section”, Reports Culham Science Centre, UKAEA FUS 407 and UKAEA FUS 409, December 1998.

[3] V. D. Kovalchuk, et al., “Neutron generator SNEG-13”, Report Russian Research Centre “Kurchatov Institute”, IAE-5589/8, 1992.

[4] K. Seidel, R. A. Forrest, H. Freiesleben, S. A. Goncharov, V. D. Kovalchuk, D. V. Markovskij, D. V. Maximovich, S. Unholzer, R. Weigel, “Activation experiment with Tungsten in fusion peak neutron field”, Report TUD-IKTP/02-01, TU Dresden 2002.

Safety Analysis and Environmental Impact

TW1-TSS / SEA 3
Reference Accident Sequences – Magnet Systems (2)

SEA 3.2
Magnet System Safety

Within the subtask 3.2 IRS-FZK investigates accident sequences as requested by EFDA. In the period reported here the effect of a cryogenic Helium spill into hot structures, i.e. the vacuum vessel is investigated. The concern for this accident sequence is that cryogenic Helium flows into the vacuum vessel and pressurizes the vessel beyond its design pressure of 0.2 MPa. The question is which minimum cross section of the rupture disk and the subsequent piping of about 100 m length is required to keep the vacuum vessel pressure below its design pressure during such a transient. The analysis was done with MAGS module CRYOSTAT.

The analysis shows that the pressure rises in the vacuum vessel linear up to the failure pressure for the rupture disk and reaches steady state after about 500 s. If the area of the rupture disk and the relief line behind has a circular diameter of 0.25 m or 0.05 m^2 the pressure in the vacuum vessel is below the design value of 2 bars.

Staff:

R. Meyder

Literature:

[1] R. Meyder : Report on calculation of a He spill into the vacuum vessel,May 2002.

TW1-TSS / SEA 3.5
Analysis of an ITER First-Wall Coolant Leak Scenario with Isolated Vacuum Vessel

1. Introduction

In order to assess hydrogen limits in connection with the ITER licensing process, three-dimensional distribution calculations had been performed for the ITER vacuum vessel, the pressure suppression system and the drain tank [1,2]. An ex-vessel/first-wall coolant leak without plasma shut-down had been simulated assuming a hydrogen generation phase due to the steam/beryllium reaction, a pure steam injection phase, and an air ingress phase. The steam, hydrogen and air sources for the accident sequence were taken from best-estimate MELCOR calculations [3].

In that previous analysis [1,2], after opening of the valves, steam and hydrogen, and at a later time also air, were flowing through the connecting lines from the vacuum vessel to the suppression pool and the drain tank. The time- and space-dependent gas distribution in the system was calculated using the verified 3D Computational Fluid Dynamics (CFD) code GASFLOW [4]. A new extended version of GASFLOW had been developed to model the ITER specific phenomena in adequate detail. As a result, it was found that 13,600 s after the break of the first wall, a burnable and detonable H_2-O_2-N_2 mixture had formed in the cover gas of the pressure-suppression system. The atmosphere in the vacuum vessel and in the drain tank remained inert.

As a next step, the present work was performed to assess ITER safety requirements, assuming a hypothetical worst-case situation for the vacuum vessel:

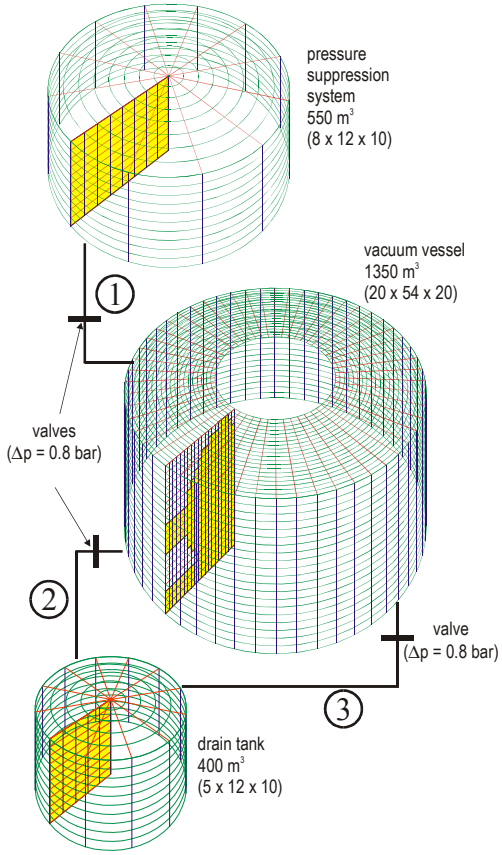

Fig.1: GASFLOW grids for the ITER model.

- The valves separating the vacuum vessel from pressure suppression pool and drain tank do not open (Fig. 1).
- All hydrogen generated by steam/beryllium reaction is kept within the vacuum vessel.
- Heat transfer to the structures/walls of the vacuum vessel is enabled, providing steam with the opportunity to condense and allow the early formation of combustible hydrogen/air mixtures.

A total of four cases has been conducted to study heat-transfer effects between the gas atmosphere and the torus walls.

2. Accident Scenario

For the analysis, the ex-vessel LOCA scenario leading to an in-vessel release of steam and air was selected, the same as applied in the previous work [1,2]. It is assumed that a break in the heat-transfer system occurs in the TCWS [*)] vault without plasma shut-down. The cooling of the affected first-wall section (one loop out of three) is drastically reduced, leading to structural failure of the first wall and an in-vessel breach within a few minutes. Steam from the cooling system is transported through the cooling pipe and the leak into the vacuum vessel, where it can contact hot beryllium and generate hydrogen. After the steam inventory in the cooling pipe has been injected into the vacuum vessel, air enters through the leak as long as the vessel is at sub-atmospheric pressure (Fig .2). In the previous analysis [1,2] a combustible hydrogen-air mixture was found on the cover gas of the suppression tank; the atmosphere in the vacuum vessel remained inert through the whole accident sequence. The recent analysis focuses on boundary conditions providing a challenging thread to the vacuum vessel, i.e. the early formation of a combustible mixture. Consequently, according to the assumed worst-case situation for this accident scenario, the valves isolating the suppression pool and the drain tank from the vacuum vessel do not open. Therefore, only the vacuum vessel is included in the calculational model.

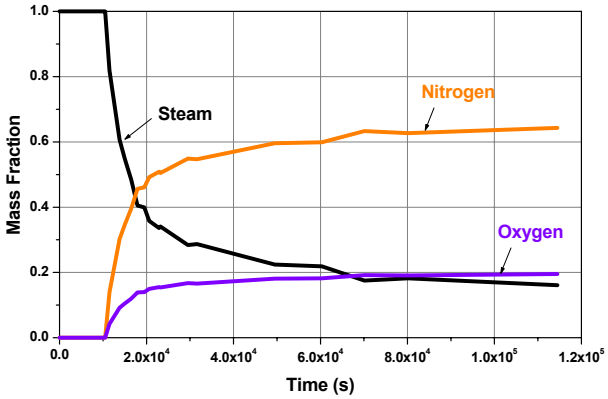

Fig. 2: Total mass flow rate of steam and air entering the ITER vacuum vessel (MELCOR result [3]).

3. Geometry, Initial and Boundary Conditions

The vacuum vessel with its volume amounting to 1350 m^3 is modeled in cylindrical coordinates using a computational grid of 20x54x20=20,600 nodes (Fig.1). The atmosphere initially consists of N_2 at a pressure of 500 Pa involving a mass of 3.5 kg. One third of the torus, corresponding to the failed cooling loop, is assumed to be at a temperature of 1,273 K. The remainder is assumed to have a temperature of 503 K [5]. The

*) Tokamak Cooling Water System

torus walls and the corresponding part of the atmosphere have the same temperature. In order to allow for steam condensation in the gas atmosphere, heat transfer to/from the torus walls is taken into account. The wall structure of the torus consisting of 3 solid material layers [6] is shown in Fig. 3:

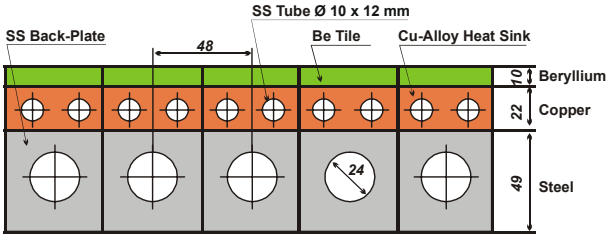

vacuum vessel [5.]

a) beryllium tiles, plasma facing surface, thickness 10 mm,

b) copper layer with heat sink, thickness 22 mm,

c) stainless steel back-plate, thickness 49 mm.

Four calculational options have been selected to approach the interaction between the gas atmosphere and the torus walls:

a) calculation without heat transfer,

b) heat transfer to the wall modeled with material properties of steel,

c) heat transfer to the composite wall using material properties of Be, Cu, and SS (stainless steel), and

d) heat transfer including radiation effects to the composite wall.

5. Discussion of Results

5.1 Pressure Histories

The calculations of the four heat-transfer options were conducted until the pressure in the vacuum vessel came close to atmospheric conditions (Fig. 4). This situation was reached between 1,000 and 1,200 s in all four cases. The average pressure curve obtained for no heat-transfer occurring in the vacuum vessel increases with the steepest rate of all cases (option a).

When heat-transfer to/from a steel or a composite wall is modeled (options b, c), the rate of pressure increase is a bit smaller, meaning that the process of pressure equilibration takes more time for both cases, and no difference is found between their individual pressure development. Including radiation (option d) leads to pressures slightly oscillating around the curve obtained for heat transfer without radiation.

The differences in the pressure histories develop due to two facts: one is the prescribed boundary condition using MELCOR data [3] to model inflow of steam mass and hydrogen generation inside the vacuum vessel, the second is heat-transfer between the gas atmosphere and the vacuum vessel walls.

5.2 Steam and Hydrogen Mass Flows

The GASFLOW calculations use fixed steam and hydrogen sources from MELCOR. In reality, the steam inflow would depend on the effective pressure difference between the interior of the vacuum vessel and its environment. However, for such a mechanistic modeling, sonic flow calculations would be necessary using a hydrodynamic pressure-loss coefficient which is not part of the task specification. Therefore, the present work was performed by applying given source terms from MELCOR calculations for a prescribed steam inflow definition. The consequence is, that for all options considered here, the steam mass contained in the vacuum vessel depends only on the time, regardless of any other physical effect such as heat-transfer to solid structures. In other words: vacuum vessel and cooling loop were treated as decoupled systems.

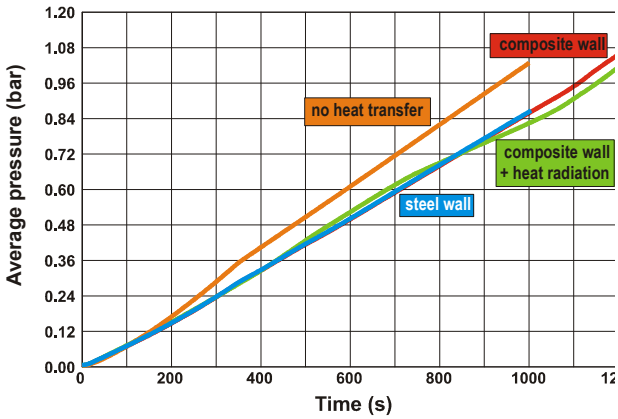

Fig 4: Calculated average pressures in the modeled ITER-FEAT vacuum vessel for the various heat transfer options.

Similarly, the amount of hydrogen generated at the beryllium surface of the vacuum vessel first-wall would depend on physical properties such as local steam and wall temperatures, and, of course, gas concentrations. Again, instead of performing complex mechanistic computations, the amount of hydrogen generation in the vacuum vessel was prescribed using data resulting from MELCOR applications [3]. And, as before, the consequence is an invariant amount of hydrogen mass, only depending on the time progress.

5.3 Average Gas Temperatures

Since the amount of gases in the vacuum vessel, due to the applied boundary conditions, is the same for all options, and only depending on the time, the above discussed pressure variation can be only a result from differing gas temperatures. Fig. 5 shows that no heat transfer (option a) leads to the highest gas temperature, which is in agreement with the resulting highest pressure (Fig.4). Starting with a sharp decrease from the initial average temperature of about 770 K to about 600 K due to isentropic thermal expansion, a peak value of more than 1,000 K is reached at 350 s, followed by a flat asymptotical decrease to roughly 935 K at 1,000 s.

In case of heat transfer to steel and composite wall models, the gas temperatures coincide as do the pressures. The decrease due to isentropic expansion is an effect much shorter in time and extending to only 700 K, not to that low level as without heat transfer - a simple effect of energy equilibration between the expanding steam flow and the hot wall structures. The average gas temperatures are at a level of 800 K. When radiation is included, the resulting gas temperatures deviate from the curve obtained for heat transfer without radiation in the same way as the related pressures.

Concerning the hydrogen risk, two statements can be derived from the present calculations:

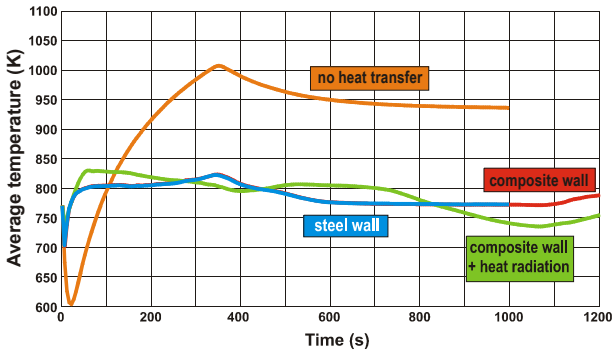

Fig 5: Calculated average temperatures in the modeled ITER-FEAT vacuum vessel for the various heat transfer options.

The pressure equilibration process being terminated after less than 1,200 s means that, according to the applied source terms based on MELCOR results, only steam mass can enter the vacuum vessel, since air inflow would start entering not before 10,500 s.

At the final vessel pressure, the calculated temperatures are much beyond the boiling point (373 K), meaning that steam condensation in the vacuum vessel would occur at no time. The presence of steam, however, would keep the gas mixture inert in case of possible air ingress, which could only be small due to the high pressure in the vessel (≈ 1 bar).

6. Summary and Conclusions

Three-dimensional distribution calculations were performed for the ITER vacuum vessel assuming an ex-vessel/first-wall coolant leak without plasma shutdown. The steam, hydrogen, and air sources for this sequence were taken from best-estimate MELCOR calculations. The time- and space-dependent gas distribution in the system was calculated using the verified three-dimensional CFD code GASFLOW.

As a hypothetical worst-case situation, it was assumed that the valves separating the vacuum vessel from the pressure suppression pool and the drain tank do not open. Consequently, all hydrogen generated in the steam/beryllium reaction was kept in the vacuum vessel. Heat transfer to the vessel structures was enabled, providing the steam with the opportunity to condense and to allow the formation of combustible hydrogen/air mixtures. A total of four cases were conducted to study the effects of heat transfer between the gas atmosphere and the torus walls:

a) calculation without heat transfer,

b) heat transfer to the wall modeled with material properties of steel,

c) heat transfer to the composite wall using material properties of Be, CU, and SS, and

d) heat transfer including radiation effects to the composite wall.

The calculations were conducted until the pressure in the vacuum vessel came close to atmospheric conditions. This situation was reached between 1,000 and 1,200 s in all four cases.

The main results of this work can be summarized as follows:

Due to elevated wall temperatures, no steam condensation takes place, meaning that the vessel pressure is continuously increasing to 1 bar. The pressure equilibration with the TCWS vault is fully accomplished prior to any anticipated air ingress according to the applied source terms. In any case, the large fraction of non-condensing steam would keep the gas mixtures inert. Hydrogen combustion could not occur during the time covered in the analysis. Later air ingress into the vacuum vessel could be envisioned, if a convection loop with the vault would be established, requiring a second break location, e.g. a failed port of the vacuum vessel. Cooling of the vessel and steam condensation late in the accident could also draw air into the torus.

Staff:

W. Baumann
W. Breitung
B. Kaup
V. Krautschick
J.R. Travis

Literature:

[1] W. Baumann, W. Breitung, B. Kaup, G. Necker, P. Royl, J.R. Travis, "Three-Dimensional Analysis of Combustible Mixture Generation in an ITER-FEAT First-Wall Coolant Leak Scenario", Report FZKA-6663 (Okt. 2001), Forschungszentrum Karlsruhe

[2] W. Baumann, W. Breitung, B. Kaup, G. Necker, P. Royl, J.R. Travis, "Three-Dimensional ITER First-Wall Coolant Leak Simulation With GASFLOW", Nucl. Fusion Programme, Annual Report of the Association Forschungszentrum Karlsruhe / EURATOM, Report FZKA 6650, EUR 20162 EN (2002), ISSN 0947-8620.

[3] MELCOR calculations, ITER-Team Japan, e-mail by H.W. Bartels (25.2.2001, 28.2.2001), and L. Topilski (20.4.2001), ITER-JCT, Garching bei München.

[4] J.R. Travis, J.W. Spore, P. Royl, K.L. Lam, T.L. Wilson, C. Müller, G.A. Necker, B.D. Nichols, R. Redlinger, "GASFLOW: A Computational Fluid Dynamics Code for Gases, Aerosols, and Combustion", Vol. I, Theory and Computational Model, Reports FZKA-5994, LA-13357-M (1998).

[5] Safety Analysis Data List-3 (SADL-3), Vers. 2.9, ITER-Server, 6.3.2001, H.W. Bartels, L. Topilski, T. Honda, ITER-JCT, Garching bei München.

[6] ITER Final Design Report, Design Description Document (2.3 Blanket), G A0 FDR 1 01-07-13 R1.0, July, 2001.

[7] Baumann, W.; Breitung, W.; Kaup, B.; Necker, G.; RoylL, P.; Travis, J.R. Three-dimensional analysis of combustible mixture generation in an ITER-FEAT first-wall coolant leak scenario, FZKA-6663 (Oktober 2001) ITER-TA: G 81 TD 05 FE (D452-EU)-Subtask3, Final Report, EFDA: TWO-SEA3.5/D4.

[8] Baumann, W.; Breitung, W.; Kaup, B.; Necker, G.; Royl, P.; Travis, J.R. A three-dimensional multi-volume analysis of combustible mixture generation during an ITER loss-of-coolant accident using the GASFLOW code. 6th Internat.Symp.on Fusion Nuclear Technology (ISFNT-6), San Diego, Calif., April 7-12, 2002

[9] Baumann, W.; Breitung, W.; Kaup, B.; Necker, G.; Royl, P.; Travis, J.R. Three-dimensional ITER accident analysis of combustible mixture generation using the GASFLOW code. Jahrestagung Kerntechnik 2002, Stuttgart, 14.-16.Mai 2002 Bonn : INFORUM GmbH, 2002 S.493-96. (Auch auf CD-ROM)

TW1-TSS / SEA 5
Validation of Computer Codes and Models

Validation of MAGS

In the frame of this task, the validation of MAGS for assessment of thermal consequences of severe accidents in superconducting magnet systems is performed under the following items:

+ Analysis of (non cryogenic) EVITA-Experiments

+ Analysis of insulation failure behavior by investigation of a coil of the Karlsruhe compact cyclotron which was damaged by an accident.

The validation of codes for simulation of condensation of steam is performed in the frame of the EVITA experiments.

In the experiments, a vessel of 0.22 m^3 volume with 1.83 m^2 inner surface is used for the condensation experiments. The steam is injected from a reservoir at 165°C and 7bar. Available experimental data are the pressure in the vessel, the temperature of the vessel volume and surface and the average mass flow rate during the injection time. The experiments are recalculated with the MAGS module CRYOSTAT.

In the experiment test2.2 an average steam flow of 1.95 g/s is given for an injection time of 400 s. The temperature of the vessel wall rises from 24°C to 51°C at 400 s in the experiment, the recalculation gives 50°C. The final pressure is 0.15 bar while 0.14 bar is the calculated value. In fact only 20 g of the total injected mass of 760 g are responsible for the gas pressure in the vessel. By this way, a few percent error in condensation rate may result in an order of magnitude error of pressure. So the pressure is a very sensitive probe for the quality of results.

The good agreement for the recalculation can only achieved by taking into account the insulation of the vessel instead of assuming adiabatic conditions as proposed by the experimentators. Due to the complicated geometry of the vessel including many flanges, the insulation properties had to be adapted once as a parameter. Keeping these insulation properties, similar agreement of results is obtained for the experiment test2.1 with a mass flow of 0.54 g/s for 570 s (exp. 0.05 bar, 32°C, cal. 0.05 bar, 32°C), and for the experiment test1.11 with a mass flow of 0.55 g/s for 400 s but now with a pre-heated wall at165°C (exp. 2.05 bar, 163°C, cal. 2.0 bar, 163°C). This provides confidence to the used model.

Figure 1 shows the stages of improvement for the experiment test2.21 with a mass flow of 1.98 g/s for 616 s. The green dataset shows a calculation under adiabatic conditions. This assumption leads to a much to high pressure, as condensation is somewhat underestimated. As mentioned above, the pressure is a very sensitive quantity.

The blue curve gives already a good quantitative agreement, here the insulation and the flanges of the vessel are taken into account with data found from the first recalculation.

For further improvement of results, the inlet tubes and valves of the EVITA-device were modeled. This allows approximating the time dependent mass flow rate during the experiment instead of assuming an average inlet mass flow rate. This is done for the red curve, where obviously the curvature of the experimental curve matches, too.

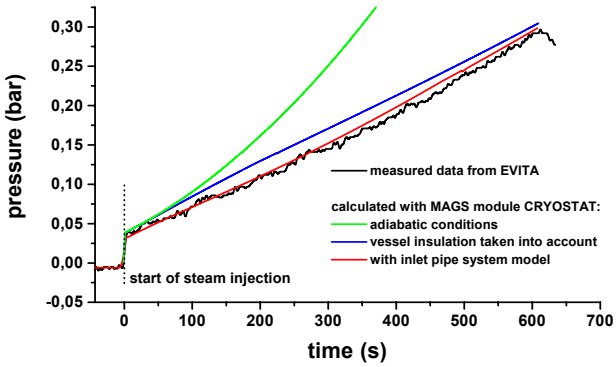

Fig. 1: Pressure during experiment test2.21. The calculated data is improved stepwise: Adiabatic conditions (green) give a poor result, taking into account the vessel insulation (blue) gives already acceptable quantitative results. A further improvement of transient behavior is achieved by modeling the transient mass flow at the inlet (red).

Recent EVITA experiments include a nitrogen cooled plate in the condensation vessel. For recalculation of these experiments, the multilayer condensation model of MAGS module CRYOSTAT used for the pre-test calculations was further improved. Next step will be the recalculation of cryogenic experiments.

For the propagation of an accident inside a coil, the failure behavior of the insulation material of the conductor and the radial plates is a crucial factor. In the last years experiments for thermal and electrical conductivity at temperatures up to 1200 K were performed to get reliable data that can be included into the MAGS material properties database. In addition to the basic material properties, knowledge of the practical results of an insulation failure accident is required to complete the picture.

The opportunity to get an insight into the behavior of insulation under thermal overload was available after an accident at the Karlsruhe compact cyclotron. There, the failure of two induction coils of a deflecting magnet was investigated. This accident was initiated after termination of an irradiation phase as the two induction coils of a deflecting magnet in the Karlsruhe compact cyclotron should be switched off on 1 May 2001 at 22:00 h. These induction coils have a copper tubular conductor, in order to be able to be cooled with water. At this time, the coils were operated in series at a current of 120 A and a voltage of 105 V. During shutdown, first the coil current is driven down to zero by the power supply unit. As soon as the current is down, the water cooling of the power supply unit and the deflecting magnets are switched off. Due to a hardware error in the power supply unit the program control of the control computer was unable to detect the malfunction of the power supply unit. As a result, the water cooling of the field coils was switched off although the full working current was still present. This error was not detected before 2 May 2001 around 18:00 h, 20 hours after the initiation of the shutdown. During this time the magnet was heated up, which caused some damage to the induction coils. However it was still possible to operate the coils and the magnet up to the delivery of the spare coils with approximately 50 % of the rated current. After delivery of the spare coils both induction coils were replaced and it was possible to examine the defective coils more exactly. The more strongly damaged coil was installed in the bottom. The insulating material, which consists of glass fabric and casting resin, embrittled strongly, however the insulating capability was preserved. In some regions resin has

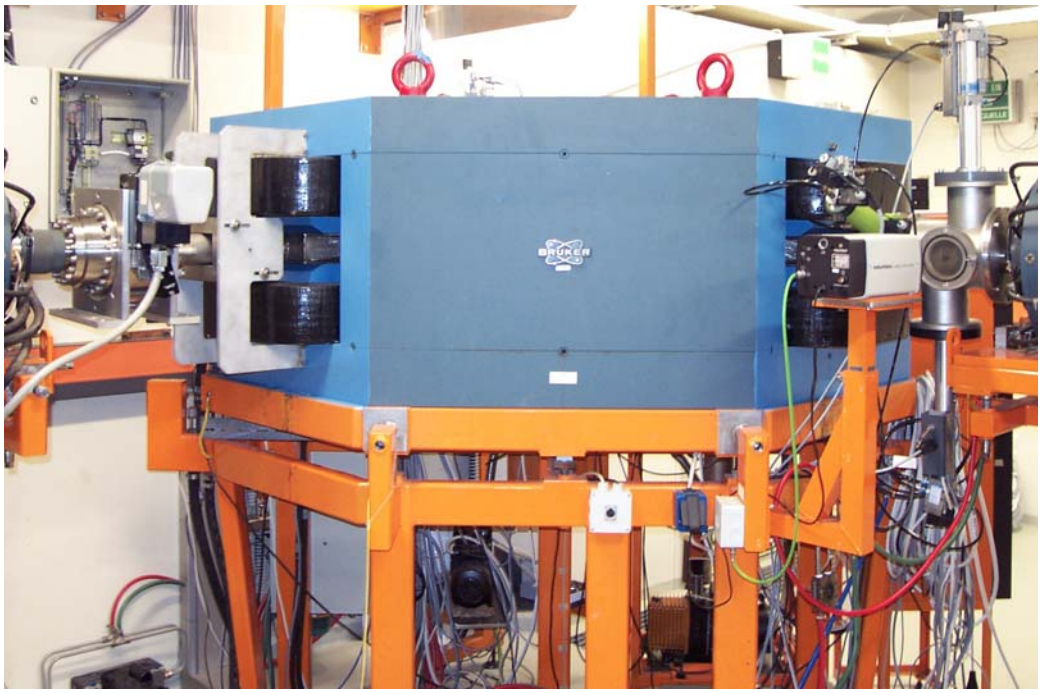

Fig. 2: Magnet of the Karlsruhe compact cyclotron with two induction coils.

Fig. 3: Damaged lower induction coil.

flowed down from the uppermost coil. Furthermore some regions showed tension cracks in the coil insulation. Some damages suggest a chipping off of some sections of the insulation by blistering.

It was tried to cut out a section from the coil by an electrical crosscut saw. After splitting some copper turns this process had to be stopped, since the section turns separated from each other. For completion, one can still infer that in the area of the strongest damage first the cover of the winding pack chipped off and then liquid casting resin flowed out from the gaps between the different sections of the copper tubular conductor.

To estimate the maximum temperatures achieved during the incident, information about the structure and the operating data of the deflecting magnet is required. Each field coil consists of 224 turns of copper tubular conductor, with the conductor having a square cross section. The external dimensions are 7.5 x 7.5 mm; the internal cooling channel dimensions are 4.5 x 4.5 mm. During manufacturing of the coil, the copper conductor is wrapped by 0.5 mm of glass cloth, which is soaked afterwards with synthetic resin. By this way, the thickness of the insulation between two conductor turns is 1 mm. The length of the copper conductor per induction coil is 912 m and the average circumference of a induction coil is 4.1 m. Each coil has 17 layers with 14 turns. During normal operation a heat output of 12.6 kW is present in both induction coils. This corresponds to a specific power per length of 6.9 W/m for the copper conductor. In case of failure of the water cooling the produced heat can be dispatched from inside the magnet to the ambient air by two different ways. On the one hand the heat can be removed over the uncovered parts of the surfaces of the induction coils

directly by air convection and on the other hand first by conduction to the iron of the deflecting magnet and then over its free surfaces by air convection. As already mentioned, the lower coil shows the larger damage, to be precise in the center of the inner side. One assumes now that there also the highest temperatures were achieved. This circumstance can be explained only by the fact that the transport of the produced heat predominantly took place in the second way mentioned above. In the other case, the higher temperatures would have been achieved in the upper coil, since there the air circulation is more strongly impeded in the area between induction coil and the iron of the deflecting magnets. At the outer surface of the magnet it is however possible to remove the produced heat by air convection from the uncovered surfaces of the induction coils.

The calculation of the maximum temperatures achieved is done according to the Dubbels Taschenbuch für den Maschinenbau. A temperature drop of 336 K turns out to be needed at the induction coil surfaces that are exposed to air for the removal of the produced heat. The two walls on the sides take over in each case 30 % of the produced heat, the upper surface 27 % and the lower surface 13 %. Within the coil for the removal of the produced heat between the center of the coils and the lateral surfaces a temperature drop of 123 K is needed. The values of the heat conductivity of the insulation vs. temperature were taken from earlier experiments. Using this data, one gets a maximum temperature of 752 K at the induction coil surfaces that are exposed to air in the region of the coil center.

The calculation of the maximum achieved temperatures inside the magnet assumes that due to the strong handicap of the air flow, about 70 % of the produced heat are transferred first to the iron of the deflecting magnet and then over its free surfaces by air convection. Two areas are to be distinguished. A part of the produced heat is removed by the half lower surface, the other section of the half wall at the inner side. An additional temperature difference by thermal conduction in the iron has to be considered. The result is that a temperature drop of 234 K at the lower surface and a temperature drop of 222 K at the side are needed for the removal of the produced heat. The appropriate temperature differences for thermal conduction in the iron are 19 K and 31 K respectively. This gives a temperature of 546 K at the bottom surface of the bottom induction coil. By each of the two surfaces, 35 % of the produced heat is dumped. The warmest point in the lower coil is assumed in the center of the 12th conductor layer counted from the bottom of the coil. The transport of the produced heat between center of the 12th conductor layer and the lower surface causes a temperature difference of 325 K. This means a maximum temperature of 871 K in the center region of the 12th conductor layer of the lower induction coil inside the magnet.

According to earlier experiments the electrical conductivity of the insulation is $1.0*10^{2}\ \Omega m$ at 871 K. In the case of a conductor length of one meter a shunt link between two conductor turns in neighboring planes is 13 Ω. The appropriate conductor resistance between the regarded points of conductor is $5.2*10^{-2}\ \Omega$. From this it results that the insulation could still fulfill their substantial function despite the abnormal operating conditions and it did not come to a destruction of the local copper structure by overheating.

For arc modeling, the improved arc model with a 2d-representation of the arc colum area developed by Prof. Titkov from his earlier models was tested. However, as pressure and other conditions at the arc spot that are relevant for the model are widely unknown, one can use also a simple, less time consuming arc model with almost the same accuracy. Due to preferences of safety considerations, the development of advanced in-coil arc models was postponed. Arc activities were shifted to the more dangerous out-of-coil (busbar) arcs where the arc propagation behavior is to be studied. For that, small scale arc experiments are in the planning phase.

Staff:

V. Pasler
G. Bönisch
G. Schmitz

Literature:

[1] G. Bönisch: Report on Post-test Calculations for non-cryogenic EVITA experiments with the MAGS-Module CRYOSTAT, April 2002.

[2] G. Bönisch: Intermediate Report on Post-test Calculations for non-cryogenic EVITA experiments with Steam Injection, Sept. 2002.

[3] G. Schmitz: Report on failure of two induction coils of a deflecting magnet in the Karlsruhe compact cyclotron, May 2002.

TW1-TSS / SEP 2
TW2-TSS / SEP 2
Doses to the Public

Objectives:

Volume IV “Normal Operation” of the ITER Generic Site Safety Report (GSSR) provides an assessment of the potential airborne and waterborne effluents and emissions from ITER. Volume VII “Analysis of Reference Events” and Volume VIII “Ultimate Safety Margins” include documentation of radioactive environmental source terms for the analysed representative accident sequences. Doses to the public due to these source terms are not given.

The objective of this task is to calculate in a consistent way these doses for realistic meteorological and siting conditions. Main computer codes to be used are UFOTRI, COSYMA and NORMTRI.

Work performed

Dose assessments for ITER-FEAT were performed with source terms defined at the beginning of 2001 /1/. That comprise deterministic calculations for releases of tritium and activation products under accidental as well as under normal operation conditions. For the latter scenarios, recorded meteorological data from the potential ITER candidate site of Cadarache were used. Within the deterministic calculations, the release height, the weather conditions and the dispersion parameter sets were varied. Other input parameters such as breathing rate and ingestion habits were the same as in previous investigations. Five different source terms, two for tritium (HT and HTO) and three for activation products (ACP, AP-tungsten and ACP-normal), were considered. Besides these calculations documented in /1/, additional assessments were carried out on request. These comprise the consideration of further materials such as steel dust, activated copper ACP and activated copper, outboard FW. A reduced set of release scenarios was applied with the new source terms and the results were documented in EXCEL spread sheets and a document sent to the EFDA team end of 2001.

Among others, the dose calculations highlighted the dominance of the cobalt isotopes for all of the three source terms. As the amount of Co-isotopes is lowest in the ACP source term, doses are lowest there. Doses from steel and copper are similar, even if the amount of Co-60 released differs. Other cobalt isotopes and Mn-56 compensate this behaviour. Doses for the outboard materials are higher than those of tungsten because the amount of Co-60 is higher in these source terms compared to that of tungsten.

Ongoing work

Following the calculations performed in the former working period, a new task was defined to refine the estimation of potential measures to the public (TW2-TSS/SEP2). Potential source terms from future fusion power plants consist of mainly activated dust (AP), activated corrosion products (ACP) and tritium in form of HTO. Main safety targets for potential accidental releases to be compared with are European intervention levels for early (evacuation, sheltering) and late (relocation, food banning) emergency actions and the regulations for European fission power plants. As the composition of realistic source terms is still open, a methodology should be developed to estimate the highest potential release which does not exceed the intervention levels. To this purpose, starting with the source terms as defined for the Power Plant Conceptual Study (PPCS) the contribution of each source term fraction to a particular dose target will be calculated. Performing this for unit releases, an equation will be derived which will allow further scaling of all three fractions that the intervention level is not exceeded. This methodology has to be developed in compliance with the European Utility Requirements. As the source terms from the PPCS study were not delivered in time, the new task is delayed, however it is anticipated that the final delivery can be achieved within the present working period.

Staff:

W. Raskob
I. Hasemann
J. Ehrhardt

Literature:

[1] Raskob, W. and Hasemann, I., Deterministic calculations for source terms from ITER-FEAT, FINAL REPORT, ITER Task G 81 TD 05 (D452) Subtask 4. Report FZKA-6625, Forschungszentrum Karlsruhe (2001)

TW1-TSS-SERF 2
Long Term Impact of Tritium Releases

Objective

The objective of this task is to perform a deeper study of the ^{3}H releases and their long term impacts, as it was initiated in the external costs study (SERF2), both for routine and accidental releases. In particular it is important to consider the potential contamination of agricultural foodstuffs.

The task of FZK consists first in reviewing the recent developments on modelling of ^{3}H behaviour in the environment (by focusing on the differences between tritium and other radionuclides). In a second step, detailed calculations of radiological impacts of ^{3}H releases for different time and space characteristics will be performed. Their impact in terms of health, and market constraints will be assessed by CEPN and discussed according to the regulations and countermeasures. These results will also be compared with existing situations.

Work performed

Calculations were assumed for accident scenarios and for routinely released tritium from future reactor sites. The computer codes NORMTRI and UFOTRI were applied for the assessments. Two different sets of input parameters were applied in the study. In a first set mainly relevant for screening purposes, the amount of 1g of HTO was used. Having identified those scenarios, which should be part of the final evaluation, the source term was set to 50 g of HTO. In this second set, only accidental scenarios were considered.

The scenarios considered changes in the release height, release duration and weather conditions under which the tritium was released in the accidental conditions. In case of routine releases, only the stack height was altered. Here recorded meteorological data from the site Cadarache was used.

The main aim of the calculations was to investigate the need for food intervention. For this purpose, the source term of 1 g of HTO was replaced by a higher value used within the SERF 2 study. Within the second set of calculations a source term of 50 g of HTO and a reduced set of release heights were investigated. All in all 2 different release heights and 5 different weather conditions were considered for accidental release conditions. No run was performed for the routine case as there is no need to investigate food banning.

Two different sets of maximum permissible levels of activity concentration in food on a fresh weight basis were considered. The first set is based on current discussions within the European Union and the second was derived from IAEA guideline 81.

Table 1: Maximum permissible levels of activity concentration in food in Bq/kg

Foodstuff, fresh weight basis	Under discussion in the EU	Derived from IAEA
Milk (Bq/l)	10000	220000
Meat (Bq/kg)	12500	280000
Leafy vegetables (Bq/kg)	12500	430000
Potatoes (Bq/kg)	12500	430000
Cereals (Bq/kg)	12500	370000

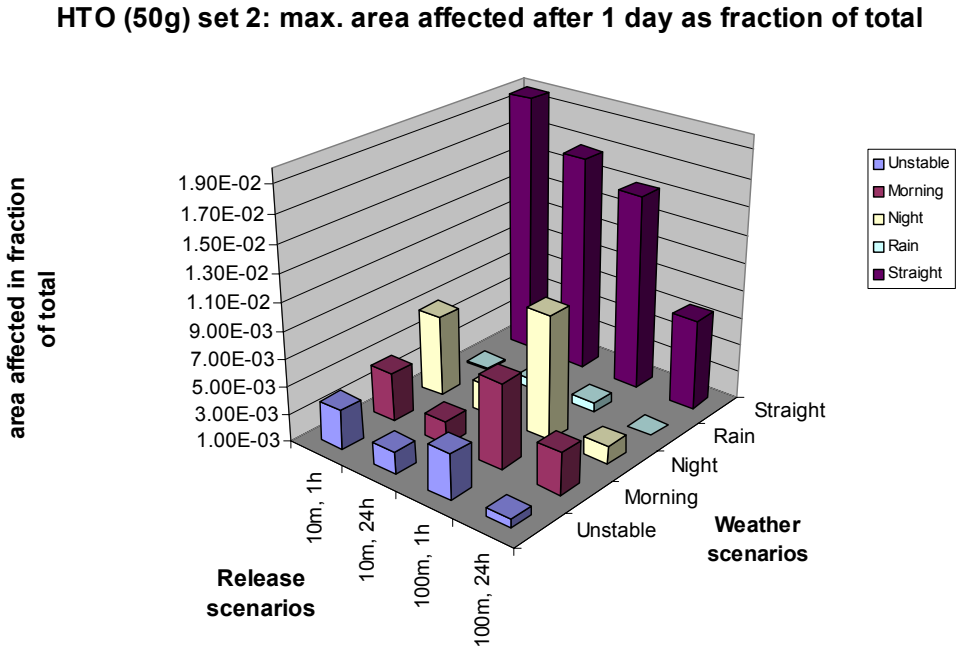

Fig. 1: Initial area affected in fraction of total exceeding the higher set of maximum permissible levels for at least 1 food (for at least 1 day) in the range between 1 and 100 km.

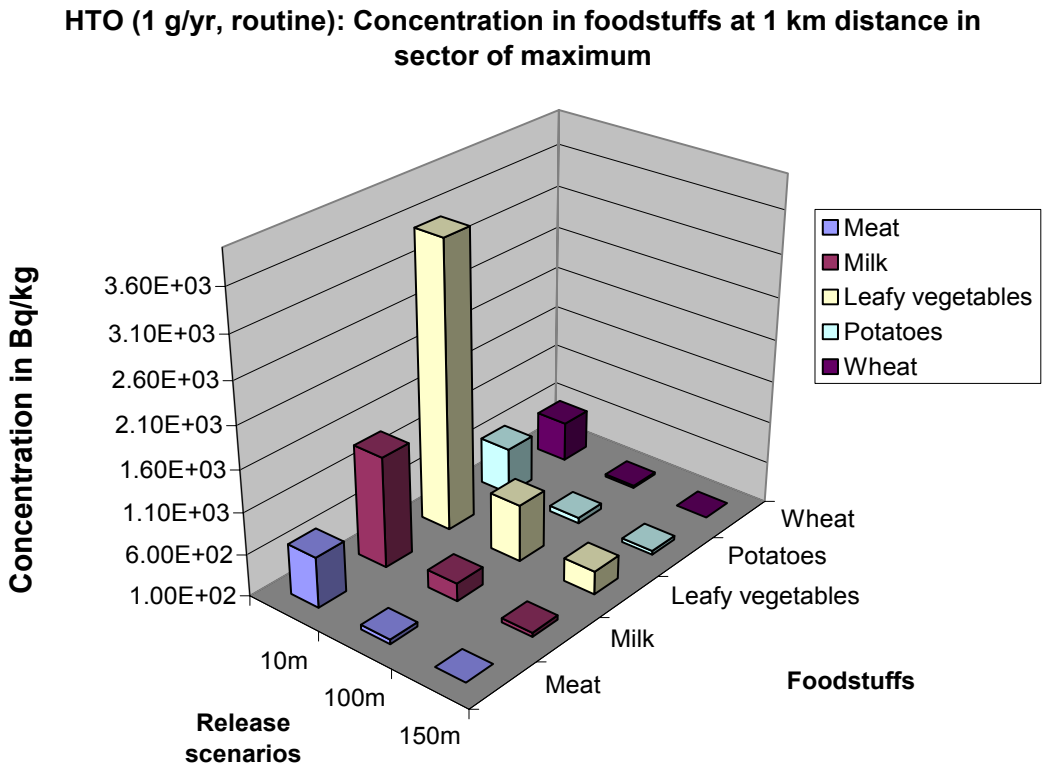

Fig. 2: Tritium concentration in Bq/kg over the vegetation period in various foods for the sector of maximum in 1 km distance from the source; release of 1 g of HTO per year.

Results achieved

The calculations with the lower set of permissible levels indicates that for up to 30000 km^2 the HTO concentration in at least one food can exceed the maximum permissible level for at least one day. Leafy vegetables was identified as that food being responsible for the large area. The area above the level becomes much smaller after one week. In case of the release scenario night and a 10 m release height, the initial 30000 km^2 drop to about 9000 km^2 and now milk is the decisive food. After one month, the area affected diminishes to about 300 km^2 with milk or cereals still above the permissible levels.

The picture changes completely when the second set with the higher permissible activity levels in food is applied. The maximum area affected amounts to about 1000 km^2 comparable to the one related to cereals in the longer term with set 1. The area affected is in no case exceeding 2 % of the total. The dominance of the straight case is an artefact of the low turbulence together with the high concentration level in food. In case of the lower concentration levels, the straight case always showed the smallest areas.

Routine releases of 1g of HTO were conducted for 3 different release heights with the meteorological conditions of the year 1991 for the potential ITER candidate site Cadarache. The highest individual dose from all exposure pathways amounts to about 15 μSv resulting from the ground level scenario. For the two elevated ones, the dose did not exceed 3 μSv at 1 km distance.

Activity concentration in food depends strongly on the type. Highest tritium concentration close to the fence at 1 km distance were obtained for leafy vegetables with values close to about 3500 Bq/kg. Even for milk, the concentration easily exceeds 1000 Bq/l. Both activity concentrations were observed for the near ground level release. A more realistic scenario with elevated releases reduces both values to about 800 Bq/kg and 300 Bq/l for leafy vegetables and milk, respectively. Activity concentrations for other foods are in the order of 100 to 200 Bq/kg, a range, which is not too unusual also for present installation. However, the release of 1g of HTO over one year is not a realistic target for ITER or a fusion reactor, but was used to have a screening value.

Staff:

W. Raskob
I. Hasemann
J. Ehrhardt

Power Plant Conceptual Study

TRP-PPCS 1
Reactor Models A-D

TRP-PPCS-1, 2, 12, 13
Neutronic Analyses for Near Term and Advanced PPCS Reactor Models

The Power Plant Conceptual Study (PPCS) is conducted with the main objective to demonstrate the safety and environmental advantages and the economic viability of fusion power, the credibility of the power plant design, and the robustness of the analyses and conclusions. In the first step of the study conducted in 2001/02, plant models with limited physics and technology extrapolations ("near term concepts") were analysed while plant variants with advanced plasma physics and technological extrapolations ("advanced concepts") were considered in the second step conducted in 2002. Two PPCS near term plants models were investigated: one with a water cooled lithium-lead (WCLL) blanket (PPCS model A, Task 1) and the other one with a helium cooled pebble bed (HCPB) blanket (PPCS model B, Task 2). Both blanket concepts use the low activation ferritic steel Eurofer as structural material. Two variants were also considered for the advanced power plant concepts: one adopting the self-cooled lithium-lead blanket with helium cooled first wall and Eurofer as structural material ("dual coolant lithium lead", DCLL; PPCS model C, task 12) and the other one employing a self-cooled lithium-lead (SCLL) blanket with SiC_f/SiC composite as structural material (PPCS model D, task 13). In the following, an overview is given of the neutronics design analyses performed at FZK both for the near term and the advanced PPCS plant models.

Near Term Models A (WCLL) and B (HCPB)

Based on the reactor parameters and neutron source distribution data provided by UKAEA Culham for the two PPCS reactor variants (Table 1), detailed three-dimensional torus sector models have been developed to enable proper design calculations with the MCNP Monte Carlo code [1]. The models include the plasma chamber, poloidally arranged blanket and shield modules, a bottom divertor port with integrated divertor, the vacuum vessel and the toroidal field coil [2].

Table 1: Main reactor parameters of the near term PPCS reactor models.

	WCLL	HCPB
Major radius [m]	9.8	8.6
Minor radius [m]	3.27	2.8
Plasma elongation	1.7	1.7
Plasma triangularity	0.25	0.27
Source peaking factor	1.7	1.7
Fusion power [MW]	5500	3300

The WCLL blanket employs a quasi stagnant pool of the liquid metal breeder Pb-17Li cooled by pressurised water at conditions similar to those of a fission pressurized water reactor [3]. The low activation ferritic steel Eurofer is used as structural material. According to the toroidal segmentation of the WCLL reactor, a MCNP torus sector model of 20° has been constructed including 3 inboard and 9 outboard blanket modules with their full toroidal extension, see Fig 1.

The HCPB blanket is based on the use of lithium ceramics (Li_4SiO_4) as breeder material, beryllium as neutron multiplier and high-pressure helium as coolant gas [4]. Breeder material and multiplier are arranged in pebble beds between flat cooling plates running in poloidal direction. The low activation ferritic steel Eurofer is used as structural material. The HCPB reactor is divided into 9 toroidal sectors of 40° each containing 1 x 4 inboard and 2 x 7 outboard blanket modules. Assuming toroidal symmetry, a MCNP torus sector model of 20° has been constructed including 4 inboard modules with half their toroidal extension and 7 outboard modules with their full toroidal extension, see Fig. 2.

The Monte Carlo neutronics calculations were performed on a HPC Linux cluster machine running MCNP4C in the parallel mode under the Parallel Virtual Machine (PVM). The neutron source distribution was described by a parametric representation in a subroutine linked to the MCNP code. Main results of the neutronic calculations are reported in the following sections, for a detailed documentation see Ref. [5]

The WCLL blanket provides a good tritium breeding potential when using Pb-17Li at a ^{6}Li enrichment of 90 at% as breeder material in the large-sized liquid metal channels. With a total radial blanket thickness of 57.9 and 91.0 cm, inboard and outboard, respectively (shielding/ manifolds not included), a global Tritium Breeding Ratio (TBR) of 1.06 is achieved at a neutron multiplication factor of 1.55. This is sufficient to compensate for potential tritium losses and account for uncertainties of the TBR-calculation. The HCPB blanket provides a high tritium breeding potential through the use of the efficient beryllium neutron multiplier. Optimisation is required for the geometrical arrangement of the beryllium and breeder pebble beds, their height and radial thickness, and the ^{6}Li enrichment of the breeder. The reference design for the PPCS reactor assumes a pebble bed height of 45 and 10 mm for Beryllium and the Li_4SiO_4 breeder ceramics, respectively, with 5 mm thick cooling plates in between. A mono-disperse pebble bed is assumed both for the breeder ceramics and the beryllium. With a total radial blanket thickness of 40.8 and 50.8 cm, inboard and outboard, respectively (shielding/manifolds not included), the global TBR amounts to 1.07 and 1.12 at a ^{6}Li enrichment of 20 and 30 at%, respectively, and a neutron multiplication factor of 1.78. Tritium is also produced in the beryllium multiplier where it accumulates to a large extent during irradiation. Assuming no release, the tritium inventory would sum up to 23.8 kg after an irradiation time of 40,000 hours [5]. The total beryllium inventory amounts to 390 tons.

The neutron wall loading distribution was calculated for the voided torus sector models by scoring the number of source neutrons crossing the first wall and normalising the related current density to the nominal fusion power. Table 2 shows the main results. It is noted that about 87 % of the fusion neutron power is loaded to the first wall of the blanket modules. The remainder flows through the divertor opening.

The nuclear power generation is shown in Table 3 as calculated for the WCLL and the HCPB reactors with a unit net electrical power of 1500 MW. In either case, ≅ 80% of the nuclear power is generated in the blanket modules including the first wall. Due to the smaller blanket thickness, the power generation in the manifold / shield region is relatively higher for the HCPB than for the WCLL reactor. The comparatively high power generation in the WCLL divertor is due to the use of a steel/water mixture which efficiently absorbs neutrons streaming into the divertor opening. It is noted that both for the WCLL and the HCPB reactor shield plugs have been employed between the blanket modules to avoid neutron streaming. As seen in Table 3, there is a considerable power generation in these plugs. The global energy multiplication, defined by the ratio of the total nuclear power generated in all

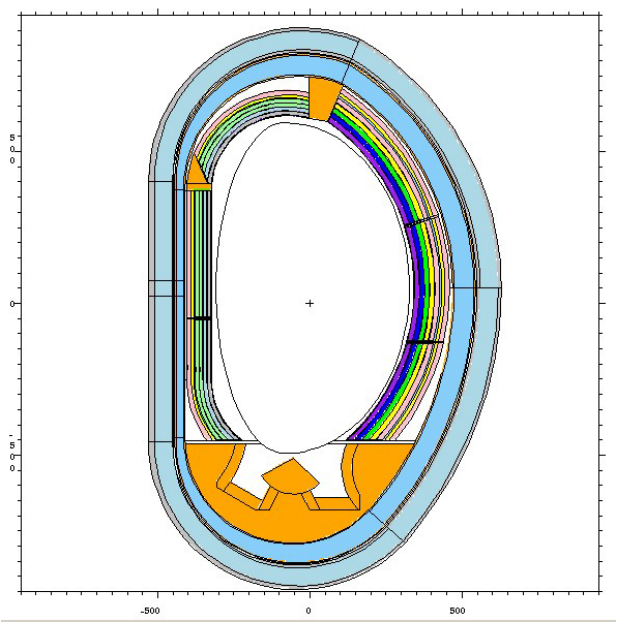

Fig. 1: MCNP torus sector model (20°) of WCLL reactor.

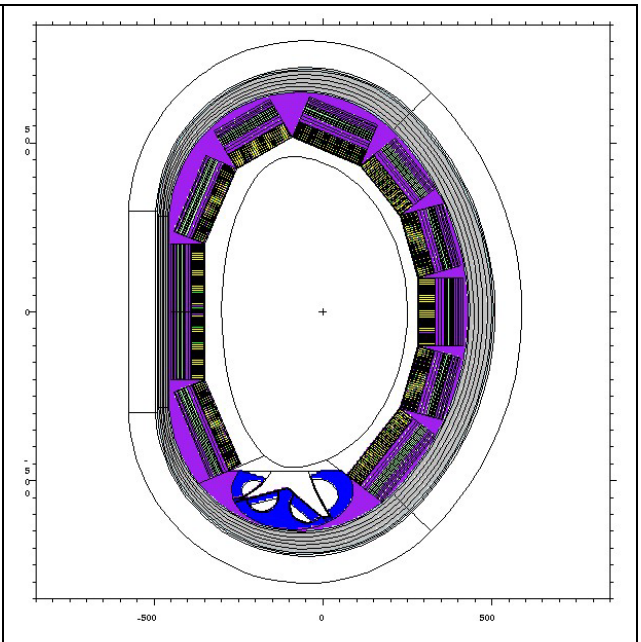

Fig. 2: MCNP torus sector model (20°) of HCPB reactor.

reactor components and the underlying fusion neutron power, is comparatively high for the HCPB reactor. This is mainly due to the high neutron multiplication because of the high Beryllium mass inventory.

Table 2: Neutron wall loading and first wall surface areas of the blanket modules of the near term PPCS reactor models.

	WCLL	HCPB
First wall surface area [m^2]	1510	1250
Fusion neutron power [MW]		
Released in plasma chamber	4400	2640
Loaded to the first wall	3810	2320
Neutron wall loading [MW/m²]		
Inboard peak value	2.39	1.78
Outboard peak value	2.96	2.24
Average value	2.52	1.85

With regard to the shielding there are two essential requirements that must be fulfilled: first, the re-weldability of life-time components made of steel (such as the vacuum vessel, and, possibly, the low temperature (LT) shield of the HCPB reactor), and, second, the sufficient protection of the super-conducting toroidal field (TF) coils. Based on existing data, the current assumption is that re-welding of stainless steel should be successful at He concentrations below 1 appm. Re-weldability after the plant lifetime of 40 full power years is achieved both for the HCPB and the WCLL blanket at a penetration depth of 85 to 90 cm [5], see Fig. 3 for the HCPB blanket. The LT shield of the HCPB blanket thus can be designed as lifetime component if weld joints are employed at its back.

Table 3: Nuclear power generation [MW] and energy multiplication factors of the near term PPCS reactor models.

	WCLL	HCPB
First wall	438	240
Blanket	3820	2762
Manifolds & shield	71	179
Shield plugs	180	114
Vacuum vessel	1.4	18
Divertor	884	323
Total	5394	3636
Global energy multiplication	1.23	1.38

The TF-coil is protected from the penetrating radiation through the blanket, the shield and the vacuum vessel. While the build of the blanket is dictated by the breeding requirements, both the shield and the vacuum vessel can be optimised for the shielding. An efficient neutron moderator (water or a hydride) is required combined with a good neutron absorber (steel, tungsten, etc.). The WCLL reference design [3] assumes a water/steel (Eurofer) shield with a thickness of 15 cm following the 9 cm thick manifold/shield region. The total thickness of the WCLL blanket/shield system amounts to 82 cm (inboard). Water must not be used in the HCPB reactor to avoid any potential reaction with the hot beryllium during a possible accident. The HCPB reference design [4] therefore employs ZrH_2 as neutron moderator in the 25 cm thick LT shield attached to the vacuum vessel. Another 17 cm thick high temperature shield made of Eurofer steel is attached to the blanket module. The total thickness of the HCPB blanket/shield system amounts to 100 cm (inboard). The ITER FDR design has been assumed for the vacuum vessel of both the WCLL and the HCPB reactor. It is made of two 5 cm thick SS-316 steel plates with a 25 cm thick shielding mixture of water (40%) and borated steel (60%) in between. The most crucial radiation loads to the TF-coil are the fast neutron fluence to the superconductor, the peak nuclear heating in the winding pack, the radiation damage to the copper insulator and the radiation dose absorbed by the Epoxy resin insulator. The radiation loads obtained for the inboard mid-plane are compared in Table 4 to the design limits as specified for ITER. It is noted that the design limits can be met with the HCPB reference design. This is also true when replacing the hydride in the LT shield by tungsten carbide [5]. Thus any use of hydrogenous material can be avoided in the HCPB blanket/shield system. With the WCLL reference design, the design limits for the Epoxy radiation dose and the displacement damage to the copper stabilizer cannot be met. This is due to the small dimension of the shield assumed in the WCLL reference design. With the standard material composition, ≅ 20 cm shield have to be added to satisfy the shielding requirements. The total thickness of the WCLL blanket/shield system then sums up to ≅ 100 cm as for the HCPB blanket. This reflects the fact that the shielding efficiencies of the WCLL and the HCPB blanket are comparable as can be seen from the attenuation profiles of the neutron fluxes (Fig. 3).

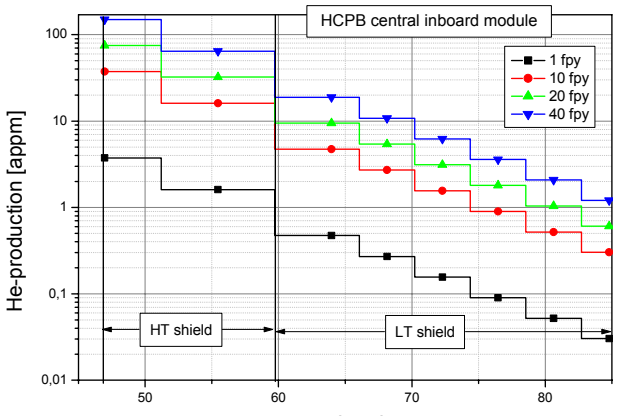

Fig. 3: He-production [appm] in the HT and LT shields of the HCPB blanket at the inboard mid-plane.

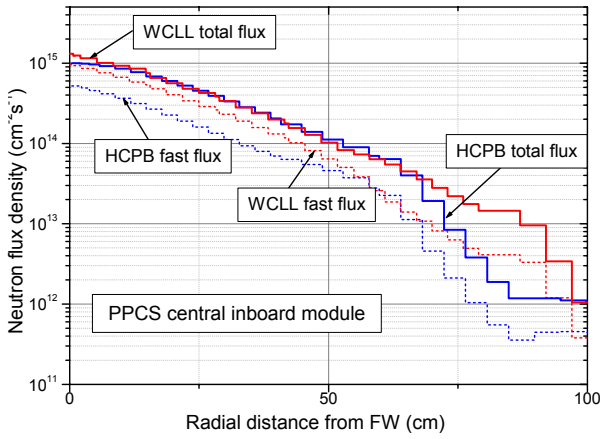

Fig. 4: Radial neutron flux profiles at the inboard mid-plane.

Table 4: Maximum radiation loads to the inboard TF-coil after 40 full power years operation of the near term PPCS reactor models (WCLL and the HCPB reference designs).

	Design limits	HCPB (reference design)	WCLL (reference design)
Integral radiation dose in insulator (Epoxy) [Gy]	$1.0 \cdot 10^{7}$	$1.36 \cdot 10^{7}$	$1.10 \cdot 10^{8}$
Peak fast neutron fluence (E>0.1 MeV) in the NB_3Sn superconductor [cm^{-2}]	$1.0 \cdot 10^{19}$	$1.86 \cdot 10^{18}$	$1.02 \cdot 10^{19}$
Peak displacement damage to copper stabiliser [dpa]	$5.00 \cdot 10^{-4}$	$5.72 \cdot 10^{-4}$	$4.86 \cdot 10^{-3}$
Peak nuclear heating in winding pack [Wcm^{-3}]	$1.0 \cdot 10^{-3}$	$2.99 \cdot 10^{-4}$	$1.38 \cdot 10^{-4}$

Advanced Models C (DCLL) and D (SCLL)

The main reactor parameters of the advanced PPCS reactor models as provided by UKAEA Culham are displayed in Table 6. Detailed three-dimensional MCNP models were developed on the basis of these with the help of available technical drawings.

Table 5: Main reactor parameters of the advanced PPCS reactor models.

	DCLL	SCLL
Major radius [m]	7.5	6.1
Minor radius [m]	2.5	2.03
Plasma elongation	1.9	1.9
Plasma triangularity	0.47	0.47
Source peaking factor	2.5	2.5
Fusion power [MW]	3410	2460

The DCLL blanket concept [6] employs the liquid metal alloy Pb-17Li both as breeder and coolant in the breeding zone and helium gas for the cooling of the first wall made of the low activation ferritic steel Eurofer. Thin SiC_f/SiC flow channel inserts are used as electrical and thermal insulators of the liquid metal channels. Based on a segmentation of the DCLL reactor into 18 toroidal sectors, a MCNP torus sector model of 10° has been constructed including one inboard and 1 ½ outboard segments (Fig. 5).

The SCLL blanket concept [7] employs the liquid metal alloy Pb-17Li again as breeder and coolant and SiC_f/SiC composite as structural material. The use of a SiC_f/SiC structure allows for high coolant temperatures resulting in a high power plant efficiency and, at the same time, a favourable nuclear performance with regard to tritium breeding and activation. Based on a segmentation of the SCLL reactor into 16 toroidal sectors, a MCNP torus sector model of 11.25° has been constructed including, for symmetry reasons, two halves of an inboard segment (with a gap in between), and 1 ½ outboard segments (Fig. 6).

Both advanced blanket concepts provide a good tritium breeding potential due the large-sized liquid metal channels with Pb-17Li as breeder material and a ^6Li enrichment of 90 at%. The DCLL blanket requires a total radial blanket thickness of 50.5 and 85.5 cm, inboard and outboard, respectively (shielding/ manifolds not included), to achieve a global TBR of 1.15. For the SCLL blanket with SiC_f/SiC structure the corresponding total radial blanket thickness amounts to 30.2 and 70.2 cm, inboard and outboard, respectively. The resulting global TBR is 1.1 when using WC as shielding material in the HT shield (see below) and including a breeder zone in the divertor region. The TBR fraction of the latter amounts to 0.125 [5].

Main results of the neutron wall loadings to the first wall of the advanced PPCS reactor models are displayed in Table 6. With both reactor models more than 90 % of the fusion neutron power flows to the first wall of the blanket modules/segments. The blanket coverage of the advanced models is thus higher than assumed for the near term variants..

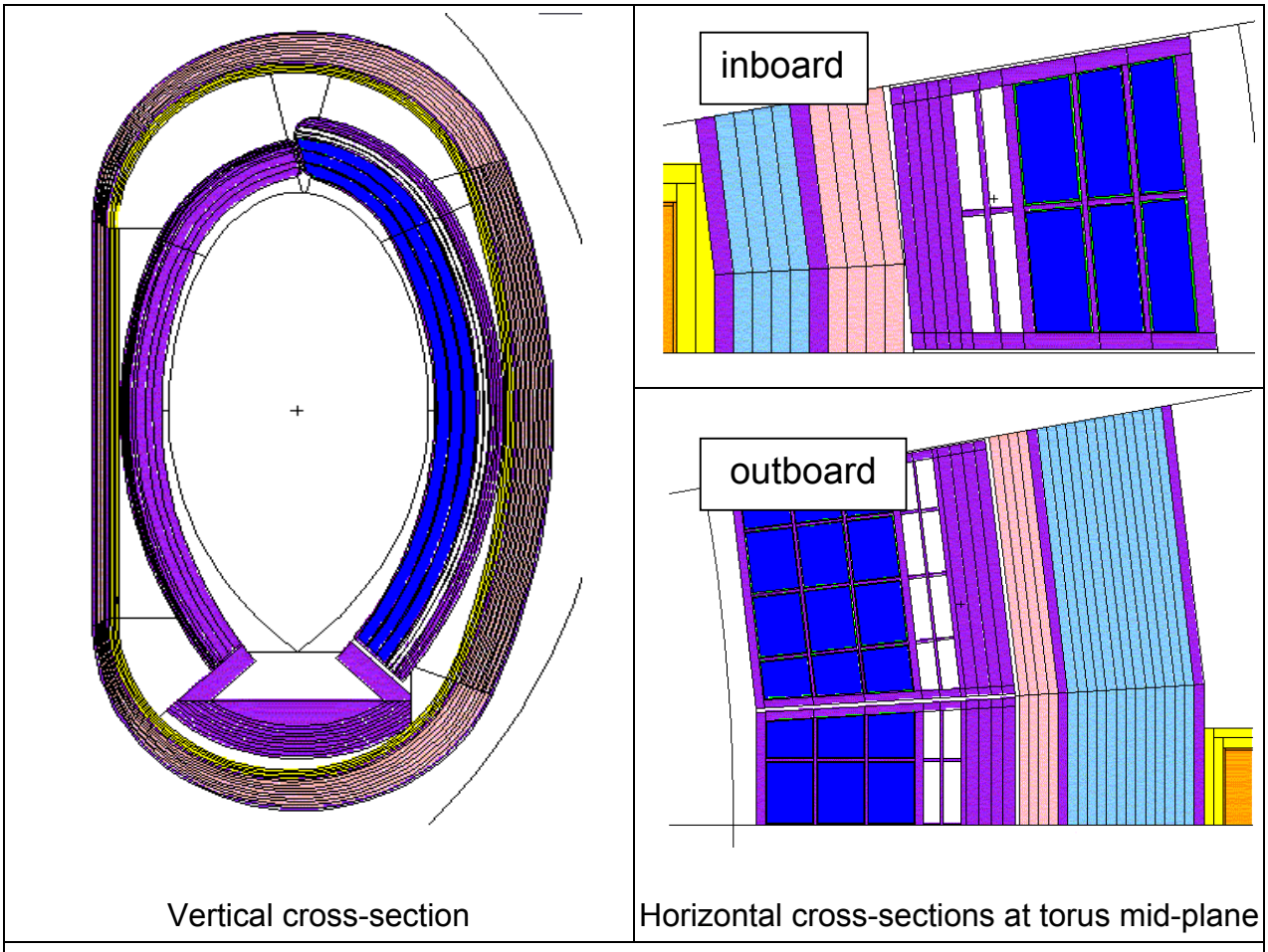

Fig. 5: MCNP torus sector model (10°) of the DCLL reactor

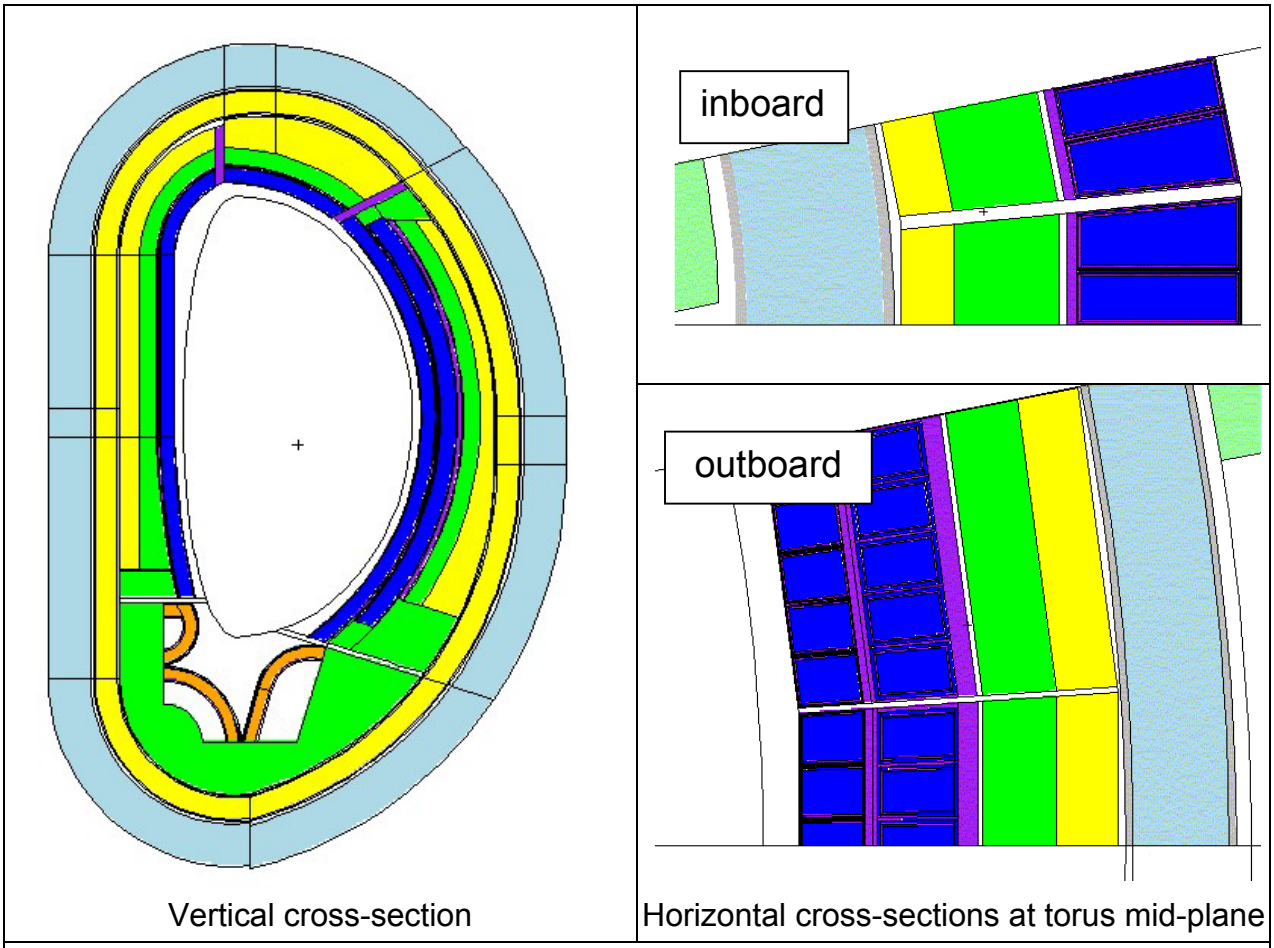

Fig. 6: MCNP torus sector model (11.25°) of the SCLL reactor

Table 6: Neutron wall loading and first wall surface areas of the blanket modules of the advanced PPCS reactor models.

	DCLL	SCLL
First wall surface area [m^2]	1210	746
Fusion neutron power [MW]		
Released in plasma chamber	2728	1968
Loaded to the first wall	2557	1818
Neutron wall loading [MW/m²]		
Inboard peak value	2.69	2.94
Outboard peak value	3.10	3.44
Average value	2.23	2.59

The nuclear power generation is shown in Table 7 as calculated for the DCLL and the SCLL reactors with a unit net electrical power of 1500 MW. In either case, a major fraction of ≅ 80% of the nuclear power is generated in the blanket modules/segments including the first wall. A significant difference is observed for the power generated in the HT and LT shields. This is due to the fact the DCLL concept assumes a Eurofer HT shield while the SCLL concept considers the more efficient WC for both the HT and the LT shield (see below). This results in a considerable higher nuclear power generation in the HT shield of the SCLL reactor (8% of the total nuclear power generation vs. 2% , SCLL and DCLL, respectively). On the contrary, the power generation in the LT shield of the SCLL reactor is significantly lower (less than 0.1% vs. 4% , SCLL and DCLL, respectively). The DCLL concept thus needs to adopt an efficient shielding material in the HT shield to reduce the power generation in the LT shield and thereby improve the energy efficiency. The energy multiplication factor for the SCLL reactor is lower than for the DCLL variant. This is due to the use of SiC as structural material instead of Eurofer (the neutron absorption reactions in steel show a comparatively high energy release).

Table 7: Nuclear power generation [MW] and energy multiplication factors of the advanced PPCS reactor models.

	DCLL	SCLL
First wall	333	243
Blanket	2452	1505
HT shield	65.6	181
LT shield	128.7	1.3
Vacuum vessel	7.6	0.3
Divertor	346	271
Total	3333	2202
Global energy multiplication	1.22	1.13

Shielding of the TF-coil is provided by the HT and LT shields followed by the vacuum vessel. The DCLL reference design [6] assumes a water/steel (Eurofer) LT shield with a thickness of 30 cm following the 13 and 25 cm thick (inboard and outboard, respectively) HT shield made of pure Eurofer. The total thickness of the DCLL blanket/shield system amounts to 110 cm at the inboard side of the reactor. As for the vacuum vessel, the ITER FDR design with a total thickness of 35 cm (inboard) has been adopted. As shown in Table 8 for the inboard mid-plane, the ITER design limits can be met with the assumptions of the DCLL reference design.

The SCLL reactor shows a considerably worse shielding performance than the DCLL reactor. This is, on the one hand, due to the SiC structure which does not significantly absorb neutrons and, on the other hand, due to a rather wide and straight gap assumed in the SCLL concept between the blanket segments (see Fig. 6).The segment gap, however, is subject to design optimization. It could be made smaller and it could be bent (dog-leg type instead of straight gap). For the shielding analyses of the SCLL reactor, the bulk shield option with no segment gap was therefore considered in the first place. A bulk shield represents the best case one could achieve for an optimal shielding efficiency. The worst case would be the straight gap with a width of 4 cm as assumed in the current design of the SCLL reactor.

A number of shield options has been investigated for the SCLL concept [5]. An overview of the material compositions considered for the HT and LT shields and the vacuum vessel is shown in Table 9. The total thickness assumed for the SCLL blanket/shield system amounts to 95 and 138 cm, inboard and outboard, respectively. The thickness of the HT and the LT shield at the inboard side of the reactor amounts to 30 and 35 cm, respectively. The segment gap was shown to enhance the radiation penetrating the vacuum vessel by about four orders of magnitude (Fig. 7). The same is true for the radiation loads to the TF-coil (Table 8). It is noted that sufficient shielding cannot be provided for the case of a 4 cm wide segment gap with the assumed shield thickness. This is even true for the most efficient material combination which is WC with a hydride such as ZrH_2. Nevertheless the WC option (with no water nor hydrides) was adopted for the SCLL reference design as there is enough room to optimize the segment gap design and any use of hydrogenous material can be avoided.

Table 8: Maximum radiation loads to the inboard TF-coil after 40 full power years operation of the advanced PPCS reactor models.

	Design limits	DCLL (reference design)	SCLL (WC + ZrH_2 shield option)	
			4 cm gap	bulk shield
Integral radiation dose in insulator (Epoxy) [Gy]	$1.0 \cdot 10^{7}$	$1.15 \cdot 10^{7}$	$1.32 \cdot 10^{8}$	$1.73 \cdot 10^{4}$
Peak fast neutron fluence (E>0.1 MeV) in the NB_3Sn superconductor [cm^{-2}]	$1.0 \cdot 10^{19}$	$7.54 \cdot 10^{17}$	$8.72 \cdot 10^{18}$	$1.28 \cdot 10^{15}$
Peak displacement damage to copper stabiliser [dpa]	$5.00 \cdot 10^{-4}$	$4.22 \cdot 10^{-4}$	$5.80 \cdot 10^{-3}$	$8.32 \cdot 10^{-7}$
Peak nuclear heating in winding pack [Wcm^{-3}]	$1.0 \cdot 10^{-3}$	$1.64 \cdot 10^{-5}$	$1.67 \cdot 10^{-4}$	$2.64 \cdot 10^{-8}$

Table 9: Material compositions considered for the shield system of the SCLL reactor.

Variant	HT shield	LT shield	Vacuum vessel
WC + ZrH_2	0.1 Pb-17Li, 0.1 SiC, 0.8WC	0.1 He, 0.1 steel, 0.8× (1/3ZrH_2+2/3 WC)	0.1 He, 0.1 steel, 0.8×(1/3ZrH_2+2/3 WC)
WC + H_2O	0.1 Pb-17Li, 0.1 SiC, 0.8WC	0.4 H_2O, 0.6 borated steel	0.4 H_2O, 0.6 borated steel
B_4C + ZrH_2	0.2 He, 0.8 B_4C	0.1 He, 0.9× (0.4 ZrH_2 + 0.6 borated steel)	0.1 He, 0.9× (0.4 ZrH_2 + 0.6 borated steel)
B_4C + WC (no water, no hydrides)	0.1 Pb-17Li, 0.1 SiC, 0.8 B_4C	0.2 He, 0.2 borated steel, 0.6 WC	0.2 He, 0.2 borated steel, 0.6 WC
WC (no water, no hydrides)	0.1 Pb-17Li, 0.1 SiC, 0.8WC	0.2 He, 0.2 borated steel, 0.6 WC	0.2 He, 0.2 borated steel, 0.6 WC

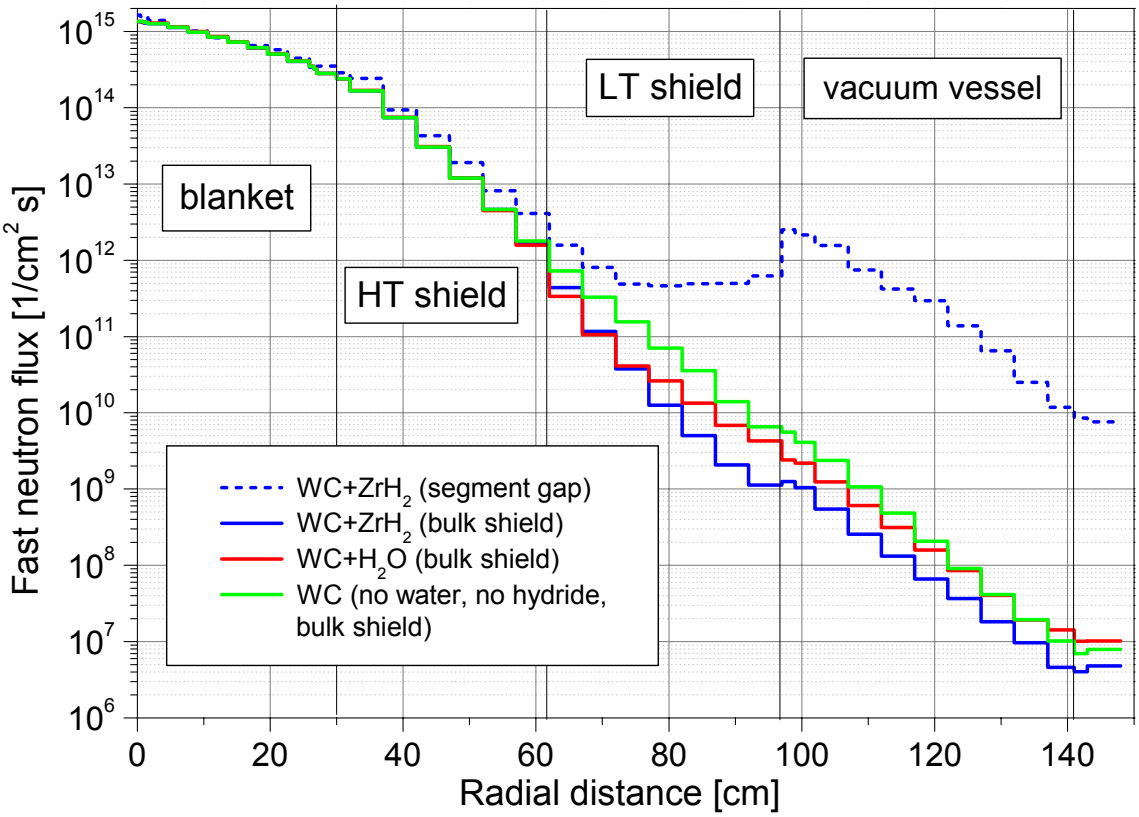

Fig. 7 : Fast (E>0.1 MeV) neutron flux profile at inboard mid-plane of the SCLL reactor.

Staff:

Y.Chen (Institute for Plasma Physics, Hefei, China)
U.Fischer
P. Pereslavtsev (Institute for Nuclear Power Engineering, Obninsk, Russia)
F. Wasastjerna (VTT Processes, Finland)

Literature:

[1] J.F. Briesmeister (ed.), MCNP - A General Monte Carlo N-Particle Transport Code, Version 4C, Los Alamos National Laboratory, Report LA-13709-M, April 2000.

[2] Y. Chen, U. Fischer, P. Pereslavtsev, Neutronic Design Issues of the WCLL and HCPB Power Plant Models, 22nd Symposium Fusion Technology (SOFT-22), Helsinki, September 9-13, 2002

[3] P. Sardain et al, Power Plant Conceptual Study – WCLL Concept, 22nd Symposium Fusion Technology (SOFT-22), Helsinki, September 9-13, 2002

[4] S. Hermsmeyer, S. Malang, Lay-out of the He-cooled solid breeder plant model in the European power plant conceptual study, 22nd Symposium Fusion Technology (SOFT-22), Helsinki, September 9-13, 2002; see also this report.

[5] Y. Chen, U. Fischer, P. Pereslavtsev and F. Wasastjerna, The EU Power Plant Conceptual Study - Neutronic Design Analyses for Near Term and Advanced Reactor Models, Forschungzentrum Karlsruhe, Report FZKA-6763, to be published.

[6] P. Norajitra et al, Conceptual Design of the Dual-Coolant Blanket in the Frame of the EU Power Plant Conceptual Study, 22nd Symposium Fusion Technology (SOFT-22), Helsinki, September 9-13, 2002; see also this report.

[7] L. Giancarli et al, ,In-vessel Component Designs for a Self-Cooled Lithium-Lead Fusion Reactor, 22nd Symposium Fusion Technology (SOFT-22), Helsinki, September 9-13, 2002

TRP-PPCS 2
Reactor Model B (HCPB Blanket)

TRP-PPCS 2-D 10
Mechanical Analysis and Design Integration

The European Power Plant Conceptual Study 2000-2002 was undertaken to investigate the prospect of nuclear fusion power generation, the main goals being to demonstrate (i) the credibility of the power plant designs considered; (ii) the claims for the safety and environmental advantages and for the economic viability of fusion power; and (iii) the robustness of the analyses and conclusions. Within a set of four plant models, the solid breeder concept is one of two concepts positioned as requiring limited technological extrapolation given the development state of the blanket, the materials and the manufacturing technology that have been subject of the longstanding EU HCPB blanket programme.

The conceptual goals of the reactor study implied that the work had to focus on

1. revising the HCPB blanket under the boundary conditions provided within the reactor study and proposing a solution based on large modules

2. providing a complete and consistent plant model based on technologies proposed within HCPB development

3. completing the plant model by a Helium cooled divertor to obey safety demands of excluding the common presence of hot Beryllium and steam in the vacuum vessel

4. optimising the thermal lay-out of the blanket system to demonstrate the potential for economic operation of the plant model.

Blanket

Input by European partners on plant lay-out and modular blanket segmentation was used to determine the geometry and power of the blanket to be designed. A key result of this work is the proposal for a concept of radial blanket segmentation into (a) hot replacement unit containing first wall, breeding zone and high temperature shield and (b) a low temperature shield. Reason for and benefits from this design are

1. a limitation of the weight of modules

2. consumption of the replacement unit, while the low temperature shield can be a lifetime component, leading to a reduction of waste

3. the possibility of using zirconium hydride as moderator in the low temperature shield.

The design shown in Fig. 1 also addresses questions of connecting/separating the coolant supply to the blanket module.

The internal lay-out of the blanket was left identical to the DEMO HCPB reference concept, with only minor changes in pebble bed heights to account for the neutron loading that is specific to the plant lay-out and significantly lower than DEMO. The blanket was thermo-hydraulically laid out and pressure drops determined to use in the cooling system design.

The coolant manifolding of the replacement unit has a steel content of 60% and serves as a hot shield.

The low temperature shield has been proposed to be a Helium cooled box containing 72% steel, 18% ZrH in steel tubes and 10% coolant, at a temperature of less than 300°C. A natural-convection lead loop was proposed as a passive safety system to avoid a large release of hydrogen from the ZrH during an accident. Also, neutronic calculations showed that tungsten carbide would provide sufficient shielding without requiring additional space.

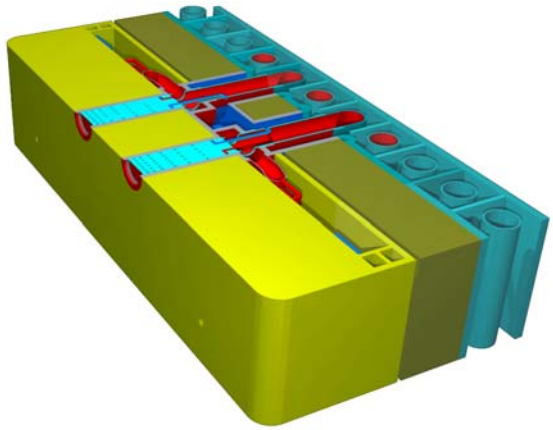

Fig. 1: HCPB blanket large module with shield and manifold.

Divertor

The assumption of ITER-like plasma physics for the limited-extrapolation plant model in conjunction with the concept-driven requirement to use He as divertor coolant started an effort to develop a divertor target plate capable of removing 10 MW/m2 peak heat load. The design measures taken to achieve this goal were

1. a large heat transfer at the back side of the plasma facing wall by means of a narrow pin fin array

2. a concentration of large heat transfer, and corresponding large pressure drop, on a distance of about 5 mm

3. thin structural walls in the regions of the largest heat flux and the use of tungsten to benefit from both thermal conductivity of 100 W/mK and good high-temperature strength.

It could be shown that both maximum temperatures and structural stress in the proposed concept become manageable.

In-vessel manifolding

In the reactor, the in-vessel He manifolding is positioned between the low temperature shield and the vacuum vessel. Radial extension, pressure drop and compatibility of thermal expansion with neighbouring structures are key properties of a lay-out. The minimisation of radial space needs is mainly an economic goal, because plant size and thus capital investment is highly sensitive particularly to the radial extension of the inboard blanket.

The concept proposed in the reactor study is a stiff connection between manifolding and VV: to keep thermal stress between the two entities limited, the manifold features concentric tubes, with the cold leg in the outer, square cross-section, tube and the hot leg in the inner, circular, one. The full potential of reducing manifold space was achieved by further measures ensuring that each module is fed using sufficient coolant channel cross

section: (i) A scheme was proposed of branching the manifold into a divertor branch feeding the lower modules, a top branch feeding modules at the top of the machine and an outboard branch. (ii) The cooling channel cross section required behind each module was established for a couple of alternative groupings of modules within these three branches, and locations with space limitations identified. (iii) It was determined how many manifold channels, of square cross-section in order to fill the manifold space both in radial and in circumferential direction, were needed to feed each module, the figure of merit being pressure drop.

Plant parameters and performance

The task of analysing the economic viability of plant models in the PPCS requires contributions from a number of different disciplines. The fusion reactor system code PROCESS at UKAEA was the main vehicle of integrating plant design and plasma physics for a plant of 1500 MW net electric output, and providing key parameters of the machine. Estimates of blanket energy multiplication, net power conversion efficiency and admissible divertor peak load are the key plant characteristics entering the system code.

Table 1: System code data of the HCPB plant model. * Input.

Parameter	Value
Blanket energy mult.*	1.39
Net conversion efficiency*	40.5%
Divertor peak load*	10 MW/m^2
Fusion power	3.6 GW
Aspect ratio	3.0
Elongation (95% flux)	1.7
Triangularity (95% flux)	0.25
Major radius	8.6 m
Average neutron wall load	2.0 MW/m^2

Plasma parameters from the system code were fed into a neutronic MCNP model of the HCPB plant to provide information on the power distribution in all components, T breeding, shielding, etc. contains a selection of the key parameters. The data confirm that functional requirements are reached. The energy multiplication implies that the power removed exceeds the fusion power by almost 40% due to nuclear processes in blanket, shield and divertor. This value is about twice that of alternative concepts; it implies a significant reduction in installed fusion power, and plant size.

Table 2: Blanket system performance data.

	Blanket	Divertor
Structural material	Eurofer	W/Eurofer
Inlet temperature	300 °C	500 °C
Outlet temperature	500 °C	740 °C
Pressure loss	0.15 MPa	0.2 MPa
Overall power	3966 MW	658 MW

Power density distributions from neutronic analyses are the input for a detailed thermal-hydraulic lay-out of reactor components. Table 2 displays blanket temperatures and pressure losses. The maximum structural temperatures of the cooling plate stay within the limit of 550 °C. The limitation of the pressure drop in manifold and blanket to 0.15 MPa could be achieved by tailoring both manifold and First Wall channel cross section to the module size; this became necessary by the significant increase in module width, from about 2 m in DEMO to more than 4 m for some of the modules. The previous choice of one channel dimension for all modules had to be abandoned because of large differences in module sizes.

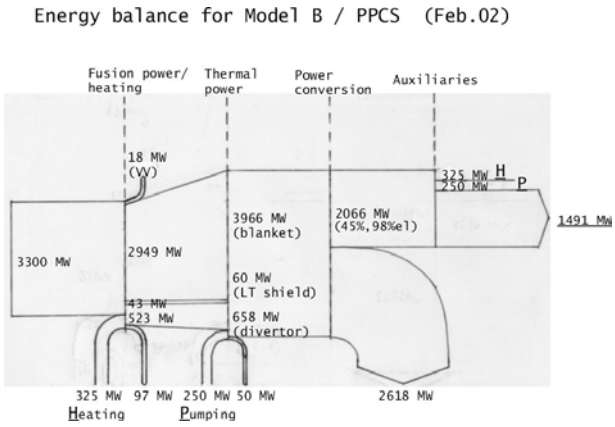

Fig. 2: Energy balance of HCPB plant model

The overall energy balance of the plant is displayed in Figure 2. Here, it has been assumed that all blanket heat and half of the divertor heat produce live steam for a h.p. turbine; the remaining half of the divertor heat is used for a re-heat between h.p. and i.p. turbine. The power conversion efficiency estimate of 40.5% for this scheme is thought to be conservative and needs to be verified.

Conclusions and further work

The PPCS has made an important contribution to sharpening the image of available blanket concepts. For the HCPB solid breeder plant model it has looked at issues of plant safety and plant lay-out and has found a potential for economically attractive power production, under limited extrapolation of required technologies.

For the plant models, the study has required new concepts for a number of systems, mainly due to the adoption of large module segmentation. The detailed lay-out and reactor integration of these systems will determine a large part of future work on the DEMO HCPB blanket.

Staff:

L. Boccaccini
U. Fischer
S. Gordeev
S. Hermsmeyer
S. Malang
H. Schnauder

Literature:

L. Boccaccini, Passive system for cooling the inboard region in case of a severe accident, J. Fus. Eng. Des., vol. 61-64 (2002).

S. Hermsmeyer and S. Malang, Gas-cooled high performance divertor for a power plant, J. Fus. Eng. Des., vol. 61-64 (2002).

S. Hermsmeyer et al., Lay-out of the He-cooled solid breeder model B in the European power reactor study, 22nd SOFT conference, Helsinki, September 2002.

S. Hermsmeyer et al., PPCS model B, FZKA report, to appear.

TRP-PPCS 3
Selection of Advanced Models

TRP-PPCS 3-D 3
Assessment of Dual-Coolant Blanket and Divertor Concepts

Introduction

The advanced dual-coolant (DC) blanket (Fig. 1) is one of the advanced concepts which has been selected for further development within the EU long-term power plant conceptual study (PPCS) program to be launched in 2002.

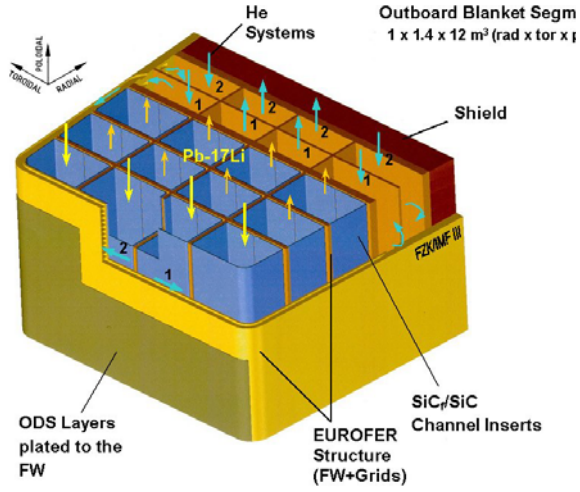

Dual Coolants	T_{Inlet} (°C)	T_{Outlet} (°C)	ΔT (K)
Helium (8 MPa)			
- Overall blanket	**300**	**480**	**180**
- FW	**300**	**440**	**140**
- Grids	**440**	**480**	**40**
Pb-17Li	**460**	**700**	**240**

Fig. 1: Isometric view of an A-DCL outboard segment at torus centre.

Basic assumption and initial input data set for system code simulations

For the first estimation of the input data set for system code simulations some power plant parameters provided for the HCPB model are also assumed for DC model :

Unit size	1.5 GW_e
Recirculating power fraction	0.2
Heating power	203 MW
Average neutron wall load	2.1 MW/m^2
Divertor peak load	4.5 MW/m^2

with an additional assumption

- Entire alpha-power (25 % of the neutron power) is distributed to the first wall of the blankets

Based on these information and assumptions, the following values for DC model have been estimated [1]:

a) Blanket energy multiplication factor

The values of the energy multiplication factor for the blanket system and the overall plant were taken from the PPA 99 [2].

b) Thermohydraulic and net power conversion efficiency

After adapting appropriate thermohydraulic parameters to the power balance in this case, first estimation calculations show that the same value of net power conversion efficiency of 44 % as determined in the PPA study [2] could be further assumed.

c) Inboard and outboard blanket and shield thicknesses:

The estimation of radial thickness yields 1.5 m for the outboard and 1.0 m for the inboard, respectively, taking into account an application of the low temperature and high temperature shields.

d) Limit to first wall heat load

As a consequence of the additional assumption (entire alpha-power distributed to the FW), the FW heat fluxes will increase and may limit the power density. The use of a value of 1 MW/m^2 as a limit for the maximum surface heat flux to the FW, which is lower than the maximum value given in [2] of 1.5 MW/m^2, is considered reasonable for this case.

e) Maximum divertor heat load

During the PPA-study, two helium-cooled divertor concepts had been evaluated. For both of them a heat flux limit of 5 MW/m^2 was estimated. Since the limit on the heat load of the divertor has an decisive impact on the overall performance of the power plant, this issue was re-evaluated in task TRP4 of PPCS, phase II [3]. The main result of this study shows that innovative divertor plates based on porous body heat exchangers made of tungsten alloy can allow - under certain conditions - surface heat fluxes up to 10 MW/m^2. Therefore this value could be suggested as an upper limit.

The initial input data suggested for system code simulations of the DC blanket are summarized below:

Blanket energy multiplication	1.168
net conversion efficiency	44 %
blanket and shield thicknesses (distance between FW and VV): inboard - outboard	 1.0 m 1.5 m
limit to first wall heat load	1 MW/m^2
maximum divertor heat load	10 MW/m^2

Conclusions

The first assessment of an initial set of blanket and divertor parameters (radial build, thermal efficiency, heat load limits, etc.) for the A-DC concept is described. This data set serves as an input for the determination of a set of reactor parameters by UKAEA. This work was drawn extensively on the preparatory study on plant availability (PPA) carried out in 1999.

Staff:

L. Bühler
U. Fischer
S. Malang
P. Norajitra
G. Reimann
H. Schnauder

Literature:

[1] P. Norajitra: Assessment of Dual-coolant Li-Pb/He Blanket and Divertor Concepts (Task TW1-TRP-PPCS3-D3), FZK-Internal Report, December 2001.

[2] P. Norajitra, L. Bühler, U. Fischer, K. Kleefeldt, S. Malang, G. Reimann, H. Schnauder, G. Aiello, L. Giancarli, H. Golfier, Y. Poitevin and J.F. Salavy, The Second Advanced Lead Lithium Blanket Concept Using ODS Steel as Structural Material and SiCf/SiC Flow Channel Inserts as Electrical and Thermal Insulators, FZKA 6385, 1999.

[3] S. Hermsmeyer, K. Kleefeldt, Review and comparative assessment of helium-cooled divertor concepts, FZKA-6597, November 2001.

TRP-PPCS 12
Model C (Dual Coolant Blanket)

TRP-PPCS 12-D 7
MHD related issues

The idea of using liquid metals as breeding material and removing a major fraction of heat by a separate helium cooling has been presented some years ago by Malang et al (1993). In their proposal the authors assumed that an electrically insulating coating covers the duct walls so that magnetohydrodynamic pressure losses are minimized to those in insulating ducts. Now in the improved Dual Coolant Blanket concept it is proposed to use a silicone carbide composite material as insulating insert. Recent data confirmed that the electrical conductivity of SiC is relatively low, $\sigma i = 500(\Omega m)^{-1}$ (Raffray 2001), while older references gave even lower values. Nevertheless, one should keep in mind that the value reported above hold for unirradiated material, " that the electrical resistivity of SiC varies by at least six orders of magnitude depending on the fabrication technique, impurity content, etc." (personal communication with C. Billone, 1999), and that the degree of irradiation degradation of the electric resistivity is unknown at present day.

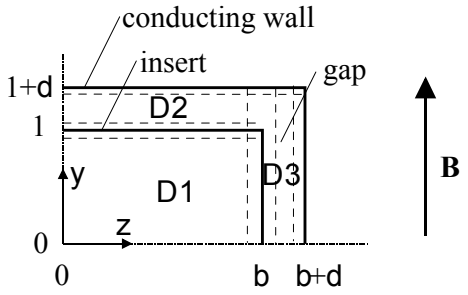

Fig. 1: Geometry of a quarter of a duct in the dual coolant blanket fitted with an insulating insert.

The geometry of the Dual Coolant Blanket consists mainly of rectangular boxes formed by helium-cooled walls. These walls are thermally and electrically insulated from the liquid metal by the SiC/SiC inserts. A quarter of such ducts is shown in Fig. 1. For the case that the insert carries some small amount of current in the tangential direction and assuming a stagnant liquid in the gap of thickness d one could define a tangential wall conductance ratio as

$$c = \sigma_w t_w + \sigma_i t_i + d,$$

where σw and σi stand for the ratio of wall and insulation conductivity respectively, scaled by the fluid conductivity σ, and $tw\ ti,\ d$ stand for the thickness of the wall, the insulating insert and the gap width scaled by L, the half extension of the inner fluid domain measured along magnetic field lines. The conductivity normal to the insulating insert is characterized by

$$\kappa = t_i / \sigma_i .$$

The strength of the magnetic field is measured by the nondimensional Hartmann number

$$Ha = BL\sqrt{\frac{\sigma}{\rho\nu}} = 10^4 - 5\times10^5 .$$

With this assumption the problem reduces to that treated by Bühler and Molokov (1993). The results are briefly outlined below and applied to the present problem. The governing equations can be solved by asymptotic techniques valid for high Hartmann numbers, and one finds finally

$$u = u_c(z)\{1 - \exp(Ha\, y - 1)\},$$

where the core velocity is given by

$$u_c(z) = K\left\{(Ha - \eta)\frac{\cosh(\beta z)}{\cosh(\beta b)} + \eta\right\},$$

with coefficients

$$\beta = \sqrt{\frac{cHa + 1}{c\kappa}} \quad \eta = \frac{c+1}{c + Ha^{-1}} \qquad (1.1)$$

In these equations u stands for the velocity scaled by the average velocity $v0$ in the duct and K for the pressure gradient scaled by $\sigma v0B^2$. The velocity profile is nearly uniform along magnetic field lines and exhibits thin viscous boundary layers of exponential type near the walls which are perpendicular to the field, called Hartmann walls. These viscous layers are known as the Hartmann layers and their thickness scales as $\delta = Ha^{-1}$. The velocity outside the viscous Hartmann layers, in the core, depends on z only. There is the possibility of higher velocities near the sides, where the magnetic field is tangential to the so-called side walls. Along the side walls another type of boundary layer develops. The so-called side layers scale in thickness as $\delta s = Ha^{-1/2}$. It can been shown that for high enough insulation the side layers do not affect the pressure drop or the flow rates in the core of the duct.

The pressure drop is obtained by the condition for volumetric flux

$$\int_{-b}^{b}\int_{-1}^{1} u\,dy\,dz = 4b .$$

Results

For the geometry of the Dual Coolant Blanket and for magnetic fields of 5T the nondimensional parameters are $Ha = 22.7 \times 10^3$, $c = 1.7 \times 10^{-2}$, $\kappa = 43.5$ for liquid metal properties at 580°C and $\sigma i = 500(\Omega m)^{-1}$. The blanket consists of three rows of rectangular ducts where the fluid rises in the duct near the first wall and descends in two rear ducts. For details of the geometry see Fig. 2. For the present design one finds pressure gradients $of\ K = 8.3 \times 10^{-4}\ MPa/m$ and $K = 4.4 \times 10^{-4}\ MPa/m$ for the duct near the first wall and for the rear channels, respectively. In these ducts the average velocity is close to $v0 = 0.07m/s$ and $0.04m/s$. This yields for a blanket of total length of roughly $2m$ a total pressure drop of $\Delta p = 2.5 \times 10^{-3}\ MPa$, a value which is very small. The present calculation applies for the straight channels. The bends at the top or bottom of the blanket turn the flow in a plane perpendicular to the magnetic field lines. Such flows do not cause higher MHD pressure drop than the flow in a straight duct of same average length (Molokov 1995).

Velocity profiles for different values of σi are shown in Fig. 3. If the insert provides high insulation, the velocity is almost uniform in the whole cross section. For higher conductivities one finds an increase of velocity when approaching the side walls, which are parallel to the applied magnetic field. The magnitude of

nondimensional velocity at the side wall may reach relatively high values depending on the insert conductivity. The very low velocity near the duct center may be unfavorable for heat transfer for which a uniform velocity profile would be desirable. Such strongly expressed velocity profiles can not be excluded with the present knowledge about the insulation properties of the SiC material. Currently a value of $\sigma i = 500(\Omega m)^{-1}$ has been proposed but there exist also other references which suggest values which are at least one order of magnitude smaller. The velocity profiles shown in the figure are determined by the nondimensional group β according to (1.1) The thickness of the layers scales as $\delta : \beta^{-1}$ and the maximum velocity as $v : \beta$. The value of β can actively be controlled by choosing proper dimensions of the duct. Decreasing dimensions (along field lines) will have the same effect as improving the insulation of the SiC material so that in practice it is possible to avoid extreme velocities near the sides. On the other hand, flows with high velocity side layers in rectangular ducts promote instabilities which are responsible for intense vortex motion. As a result the peak velocities near the sides could be reduced and the velocity near the center increased. Moreover, intense vortex motions will homogenize the temperature. The answer to this question requires more detailed nonlinear calculations and experiments are required that are beyond the scope of the present laminar study.

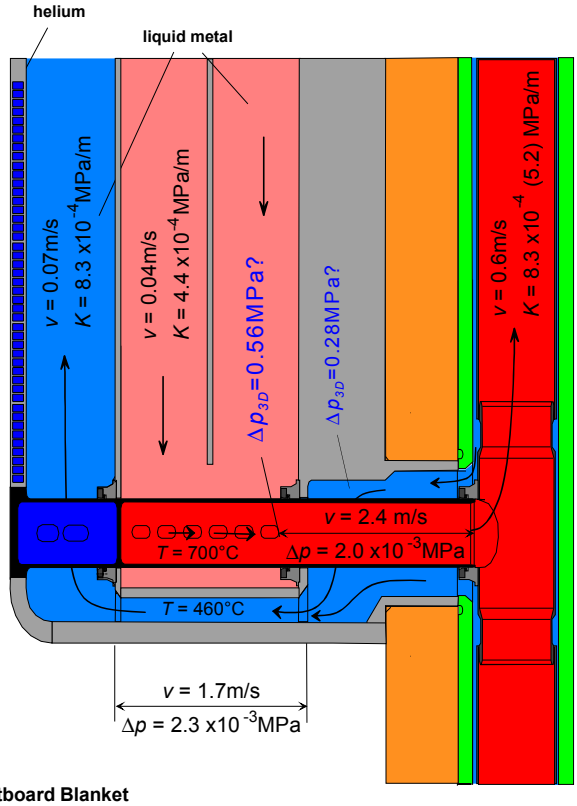

Fig. 2: Sketch of a Dual Coolant Blanket module. Values for pressure gradient K and 3D pressure drop $\Delta p3D$ are added to the figure. Values in brackets indicate results in case of no insulation.

Experimental observations for MHD pressure drop in 3D elements (expansions, contractions) can be correlated by the empirical relation

$$\Delta p_{3D} = \zeta \frac{1}{2} \rho v^2, \quad \text{with} \quad \zeta = f(N, Ha)$$

where ζ is the coefficient of local MHD resistance. Here $N = \frac{\sigma L B^2}{\rho v}$ stands for the interaction parameter. For the geometries investigated in literature, ζ was found in the range of $0.25 < \zeta / N < 2$. Several references report values $of\ \zeta / N < 0.3$ especially for large interaction parameters, i.e. $N\ ?\ 1$. For these reasons we chose for the present estimates $\zeta = 0.5N$ and recommend for precise values more detailed analyses and experiments for the present geometry. Note, The upper limit for ζ / N observed in these experiments depends also on Ha so that at the fusion relevant Hartmann numbers even larger values are possible. These correlations hold for the entrance to the access tube but apply also for the flow in the 'annular' gap with strong expansion to the total toroidal length. The latter geometry is not similar to any geometry for which solution for MHD flows are known. It could be expected that the pressure drop is of the same order of magnitude than that in the central pipe. Nevertheless, since the velocities are smaller the pressure drops (fully established annular flow and Δp_{3D}) could be smaller also.

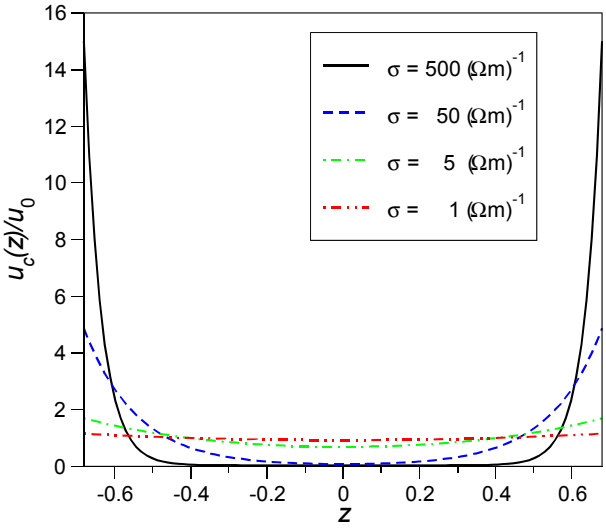

Fig. 3: Core velocity profile for different conductivity of the insulating material in one duct of the outboard blanket.

As a result we find a value of 3D pressure drop at the entrance to the access tube as $\Delta p3D = 0.56\ MPa$ for a flow at $v = 2.6m/s$ and $N = 38$. The formation of thin viscous boundary layers may change the 3D pressure drop values but the order of magnitude should remain. Insulation does not help to eliminate 3D effects because currents shortcut in the liquid metal and not only along the walls. The pressure drop at the expansion from the annular entrance is estimated as $\Delta p3D = 0.28\ MPa$.

The calculations shown above demonstrate that the pressure drop in the whole blanket is negligible in comparison with the pressure drop near 3D elements. This is the case also for the inboard blanket, where the magnetic induction reaches values up to 10T. For these reasons only the 3D pressure drops at the inlet and outlet of the blanket module are shown for inboard conditions. Three-dimensional effects scale as $\Delta p3D : vB^2$ so that $\Delta p3D$ is larger at the inboard blanket although the velocity there is smaller. For $v = 1.4m/s$ we estimate the pressure drop to roughly $\Delta p3D = 1.2\ MPa$ for the contraction and $\Delta p = 0.6\ MPa$ for the expansion.

It has to be noticed that 3D pressure drops have been estimated using correlations which have been obtained for different geometries. The ζ coefficient depends strongly on the geometry. The order of magnitude for pressure drop should be correct but

in order to get more accurate estimates it is recommended to perform experiments using a realistic model geometry and flow parameters close to applications.

Conclusions

Most of the ducts in the Dual Coolant Blanket are straight rectangular ducts for which pressure drop correlations are known. As a result of the analysis the pressure drop in the blanket itself is small if all walls are covered by an electric insulation of 5mm thickness. The pressure drop for the blanket reaches values of about $\Delta p = 2.5 \times 10^{-3}\ MPa$ for a poloidal length of $2m$. This pressure drop is really small and negligible compared with the pressure drop in the elements connecting the blanket with the rear coaxial pipes which feed and drain the blanket. Some estimates demonstrate that electric insulation in these elements is unavoidable for a reasonable performance.

Three-dimensional effects at the strong contractions and expansions will cause the major fraction of pressure drop in the Dual Coolant Blanket. These crucial elements can not be analyzed by standard correlations. Estimates for the current design of the outboard blanket yield $\Delta p = \Delta p3D = 0.84\ MPa$ and $\Delta p = \Delta p3D = 0.1.8\ MPa$ for the inboard blanket. These relatively high values can be reduced if the cross section of the access tubes are enlarged. An increase of the dimensions by 50% would lead to pressured drops of $\Delta p = 0.57\ MPa$ and $\Delta p = 1.29\ MPa$, for the outboard and the inboard blankets, respectively. Any more detailed analysis, however, requires exact three-dimensional modeling which is not the subject of these first estimates. Modeling and computations of inertial flows in expansions will be the subject of the near term research at the *Institut für Kern-und Energietechnik* of the *Forschungszentrum Karlsuhe*.

Finally it should be mentioned that the fraction of the pumping power for the liquid metal coolant is relatively low.

Staff:

L. Bühler

Literature:

[1] Malang, S. et al. : 1993 Dual coolant liquid metal breeder blanket, Fusion Technology 1992, Proceedings of the 17th Symposium on Fusion Technology, Rome, Italy, September 14-18, 1992, *Elsevier Science Publishers,* pp.1424-1428.

[2] Molokov, S.: 1995, Liquid metal flows in insulating elements of self-cooled blankets, *Fusion Engineering and Design* **27**, pp.642-649.

[3] Raffray, A.R. et al.: 2001, Design and Material Issues for High Performance {SiC/SiC}-Based Fusion Power Cores, *Fusion Engineering and Design*, **55**, (1), pp.55-95.

TRP-PPCS 12-D 8
Assessment of Integration of Divertor System to the Power Conversion System

Introduction

The dual-coolant (DC) blanket [1] is one of the EU advanced blanket concepts to be investigated in the frame of the long-term power plant conceptual study (PPCS). It is based on the use of a helium cooled steel structure and a self-cooled Pb-17Li breeding zone. The work on PPCS is drawn extensively on the preparatory study on plant availability carried out in 1999 with an objective to perform the conceptual design of the DC blanket concept where some details are to be selected in accordance with the overall strategy, which allows an extrapolation of the present knowledge between the near-term solutions (helium-cooled pebble bed (HCPB), water-cooled lead-lithium (WCLL) blanket concepts), and the very advanced self-cooled Pb-17Li SiC/SiC (SCLL) blanket concept. In the PPCS the reactor power is adapted to a typical size of commercial reactors of 1,500 MW.

The blanket and divertor designs

A significant change has been made in the PPCS concerning the blanket segmentation which is finally adopted in “large modules” (Fig. 1) in place of the “banana segments” regarded so far with an advantage to reduce the thermal stresses and to cope better with the electro-magnetic forces caused by disruptions. Furthermore, for reduction of waste the blanket is divided into an exchangeable part (i.e. the modules including the hot shield) and a lifetime part (cold shield and coolant manifold). The blanket is divided into large modular segments which build together with the divertor an overall torus coverage and shielding for the magnets behind them. A considerable fraction of the heat energy of up to 15 % is released in the divertor. As already shown in the PPA 99 [2] the integration of the divertor heat power into the power diversion system would help to significantly increase the thermal efficiency leading to a cost saving for the electric power production in a commercial power plant. In principle, divertors cooled by helium, water, or liquid metal are thinkable together with the DC-blanket. However it is meaningful if He-cooled divertors are used because of their relatively high outlet temperature of at least 700 °C which is suitable to combination with a gas turbine system.

A new modular divertor concept [3] based on the use of helium coolant is currently developed (Fig. 2). The divertor target plate is split up into smaller modules, which are favorable to reduce thermal stresses. The concept employs small tiles made of tungsten (1) and brazed to a finger-like (2) (or thimble-like) structure which in this study is assumed to be made of Mo-alloy (TZM). These fingers have a width of 16 mm and a wall thickness of 1 mm and are inserted in a front plate made from TZM. This plate is connected to a back plate by parallel walls (in this study with TZM as material). The cooling surface under each module is enhanced by a pin array. Tungsten is envisaged as a material for the pins. High pressure He with 10 MPa with an inlet temperature of 700 °C flows upwards to the pin array (3) at the outer wall, and then is routed via an inner tube wall (4) downwards to the He manifolds (5) with an outlet temperature of 800 °C. The tiles are of quadratic shape with a mean area of about 16 x 16 mm^2 and 5 mm thick.

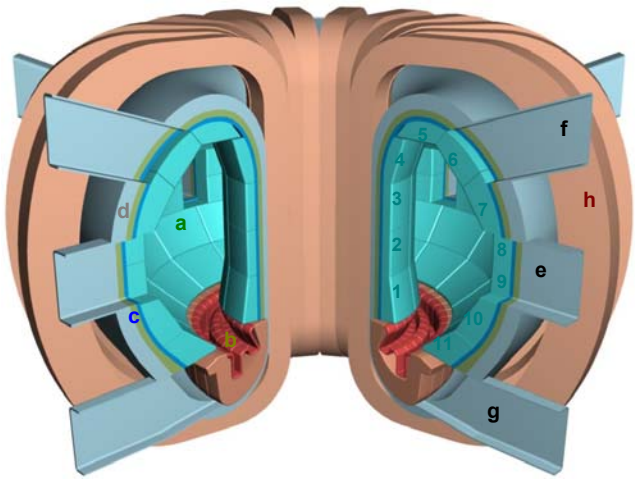

a: 176 blanket mod. (5-6 yrs. lifetime)
b: divertor plates, (2 yrs. lifetime)
c: 30 cm cold shield (permanent)
d: vacuum vessel (IB/OB:35/70 cm)
e: 8 center ports
f: 8 upper ports
g: 4 divertor ports
h: 16 TF coils

Fig. 1: Fusion reactor with large DC blanket modules.

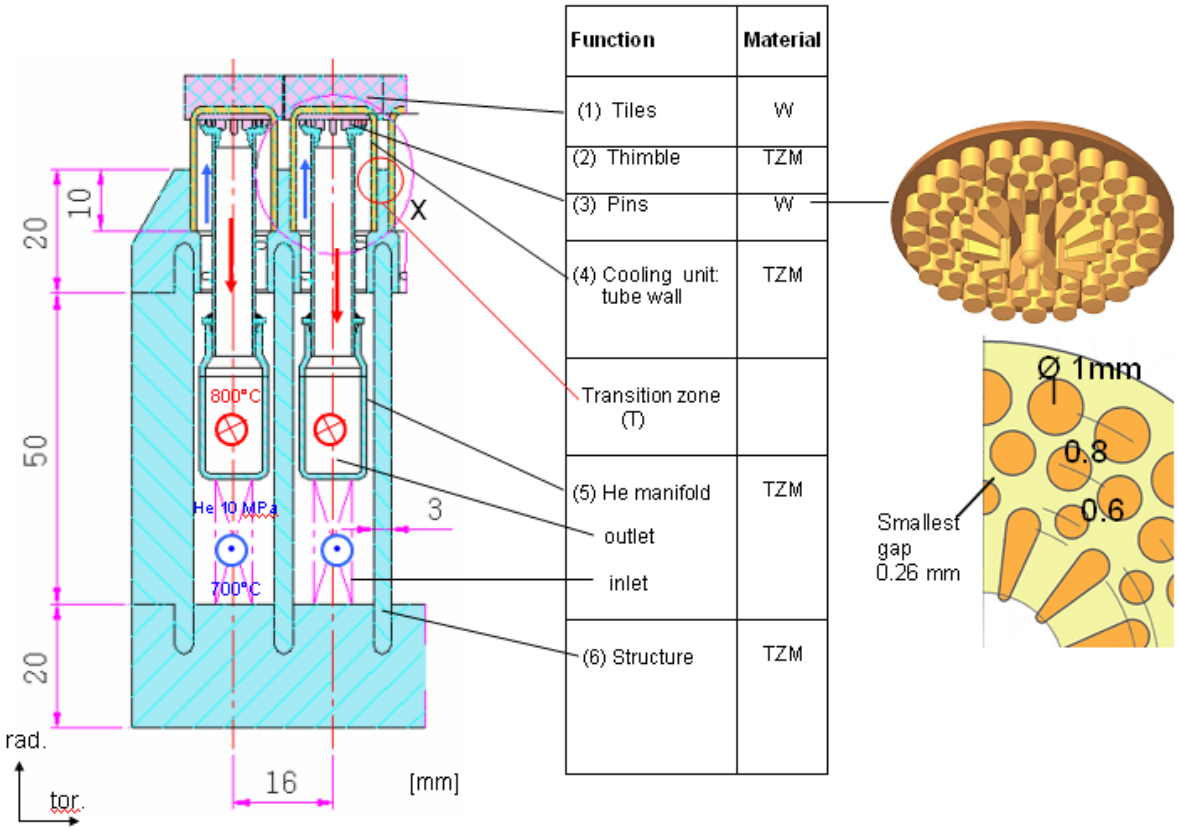

Fig. 2: The FZK He-cooled modular divertor concept with integrated pin array (HEMP).

Energy balance and thermohydraulic layout

The energy balance for the DC blanket concept was performed on the basis of neutronic calculations and system code analyses. On the basis of an electric output of the power plant of 1500 MW the fusion power was determined to 3410 MW assuming a net efficiency for the blanket cycle of 0.43 and an energy multiplication factor of 1.17. The total blanket power of 3408 MW is divided into fractions of 1432 MW for He cooling and 1976 MW for Pb-17Li circuit. The total divertor power amounts to 583 MW which consists of power fractions of 335 MW for the divertor bulk and 248 MW as surface heat power (alpha and heating power) for the divertor target, respectively. A power distribution between Inboard and Outboard targets of 1:4 was assumed leading to a surface heat power of 49.6 MW for the inboard and 198.4 MW for the outboard, respectively, for a 7.5° divertor cassette. With a dimension of an outboard target plate of about 810 mm x 1000 mm (toroidal x poloidal), an average surface heat load of about 3.5 MW/m^2. Taking into account the size of a divertor finger tile of about 16 x 16 mm^2 the number of rows in toroidal direction will be about 51 per cassette and the number of finger units amounts to about 63 per row in poloidal direction.

The helium inlet and outlet temperatures at the target of 700 °C and 800 °C, respectively, (with a temperature rise of 100 K) are assumed. The necessary helium mass flow rate to remove the divertor target heat amounts to about 0.158 kg/s per outboard row. Since the peak surface heat load (in this study: 10 MW/m^2) is expected in a lower region of the target plate of about 1/3 of the poloidal plate height, the cooling of divertor finger units within this region has to be increased with same relationship as the peak-overheating (about factor 2). This leads to a maximum helium mass flow rate of about 0.005 kg/s per finger unit.

The performance of the HEMP design strongly depends on the heat transfer coefficient h.t.c. at the plate of the thimble. The h.t.c. and the pressure loss Δp were calculated for an inlet pressure of 10 MPa. Due to the lack of appropriate models the h.t.c. was assessed using the standard correlations for heat exchanger tube bundles with cross flow as described in detail in [4]. Conservatively, only the pin surfaces were taken into account, not the porting surfaces. The Nusselt (Nu) number is then given by

$$Nu = C(0.3 + \sqrt{Nu_{lam}^2 + Nu_{turb}^2}), \qquad (1)$$

where the indices lam and turb stand for laminar and turbulent and where C represents a parameter for the geometrical arrangement of the pins. Arithmetic mean values for diameter and spacing were used. The laminar and turbulent Nusselt numbers are given as correlations, as well as the pressure loss within the pin array.

The pressure loss Δp is calculated according to [4, 5]. First, the necessary helium mass flow for heat removal was determined and, subsequently, the inlet velocity was calculated. Thereafter, the h.t.c. and the Δp can be determined. The total pressure loss (finger unit and He manifolds) then lead to the necessary pumping power which is set in relation to the target heat power.

A first estimation of the heat transfer coefficient by this means gave a value around 60,000 W/m²K. This is considered to be sufficient to remove the envisaged heat load of at least 10-15 MW/m² on the divertor target with a reasonable effort. The pressure loss of the pin array amounts to about 0.03 MPa, the total pressure loss of one row of fingers and the manifolds to about 0.1 MPa.

The power conversion system

The integration of the divertor into the power conversion system was investigated in detail in [6]. The reference power conversion system for the DC blanket concept is based on the use of a closed 3-compression-stage Brayton gas turbine cycle (Fig. 3). This solution offers a crucial advantage in avoiding the contact of liquid metal with water and to avoid the tritium permeation losses to the environment. For the secondary He loop a high He pressure of 15 MPa was chosen which does not explicitly affect the thermal efficiency of the power conversion system but it is required to simultaneously achieve a high efficiency of the intermediate heat exchangers (IHX) and a low pressure loss ratio. For a suitable adaptation of the thermal powers and the coolant temperatures between the primary and the secondary loops a system of 4 heat exchangers is chosen. The detail data of the four-stage IHX are: 1. Blanket FW, He/He, 1432 MW; 2. Divertor bulk, He/He, 335 MW; 3. Blanket interior, Pb-17Li/He, 1976 MW; 4. Divertor target, He/He, 248 MW (Fig. 4). The total heat power to be transferred amounts to 3991 MW.

In the calculation of the thermal efficiency for the power conversion system, a turbine efficiency of 0.94 and a compressor efficiency of 0.92 were assumed, which are recommended in [7]. The recuperator efficiency was determined by (T10-T3)/(T2-T3) to 0.94. The overall compression ratio amounts to 4.3 (1.63 for each compressor stage). This leads to a thermal efficiency of 0.44. Taking into account the total pumping power of abut 38 MW the net efficiency of the blanket/divertor cycle amounts to approx. 0.43.

Thermal Analysis

Loading conditions and material data

Different from the loading conditions as defined for a power plant, in the thermal and mechanical analyses, DEMO like conditions where assumed: The surface was loaded by a heat flux of 15 MW/m^2. The He coolant temperature was assumed to be 620 °C at the inlet and heated up to 720 °C reaching the top of the finger. Material data were taken from the ITER Materials Property Handbook [8]. The heat transfer coefficient was assumed to increase from 10-40 kW/m^{2}K during the upwards flow to some 50-70 kW/m^{2}K at the hair pin array at the top. Thermal and mechanical analysis were performed with the FE code ABAQUS [9] using 3D models.

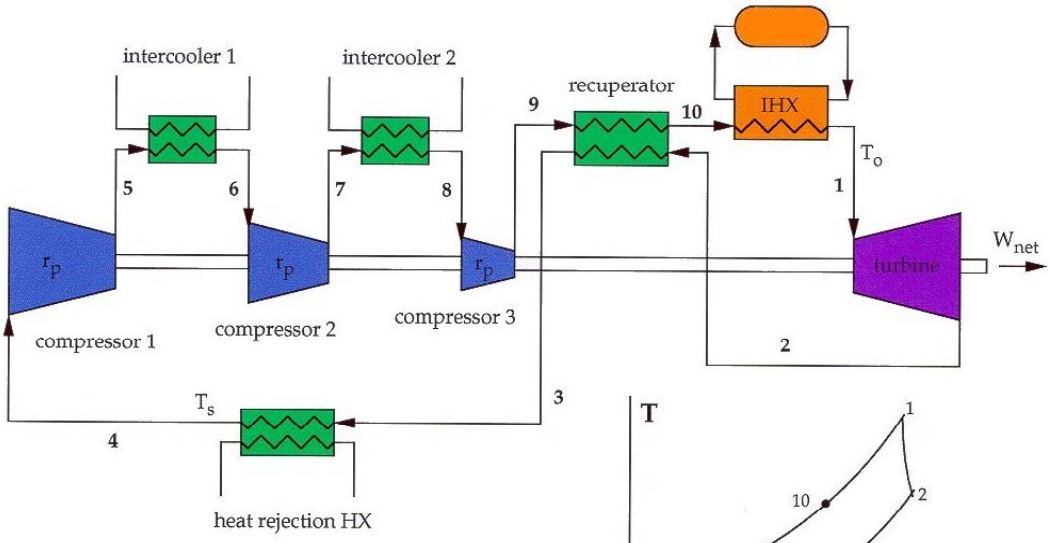

Temperatures (°C)

T1	700	T6	34
T2	295	T7	108
T3	118	T8	34
T4	34	T9	108
T5	108	T10	285

r = 4.3 (r_p = 1.63) , thermal efficiency = 0.44

Fig. 3: A closed Brayton gas turbine cycle with 3-stage compression.

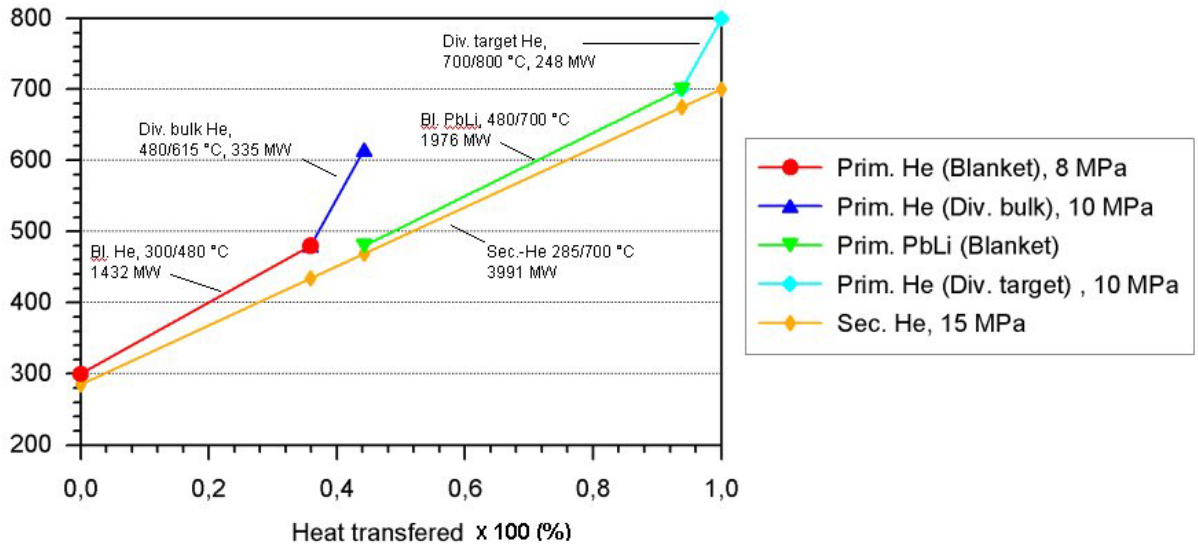

Fig. 4 Heat transfer diagramm for a 3-stage gas turbine cycle with integrated heat power of helium-cooled divertor into power conversion system.

Results

Several variations in the shape of the tile have been considered. The maximum temperature at the top of the 5 mm thick tile is about 2310-2330 °C, the minimum temperature about 1200 °C. The temperature in the TZM finger ranges from cooling temperature up to about 1400 °C at the interface with the tile.

Mechanical Analysis

Loading and sources of stress

There are several sources of loading:

- the cooling pressure 10 MPa which results in primary stress
- 15 MW/m^2 surface heat flux causing secondary stresses
- and, additionally, thermal stresses due to the mismatch of thermal expansion coefficients.

Overview of analyses performed

Besides an elastic analysis several elasto-plastic analyses were performed to quantify the stress levels under monotonic loading and to characterise the cyclic behaviour (allowable elastic or shakedown against unfavourable cyclic plasticity or even ratcheting which has to be avoided). There are several assumptions that have a considerable influence on the amount of plastic strains, like the choice of a 'stress-free temperature'. For this study properties of recrystallised materials were chosen as the most severe assumption, with the exception of the yield strength of TZM, where values in between the recrystallised and stress-released condition were used. Cyclic stress analyses were performed including some series of loading and unloading (heat flux as well as coolant pressure) and temperature changes between operational conditions and RT. Two different assumptions for stress-free conditions were analysed: (a) stress-free at 1500 °C (brazing temperature), which is the most reasonable assumption or (b) stress-free at RT, which, generally, leads to more conservative results.

Results of mechanical analyses

Primary membrane stresses and bending stresses do not exceed 80 MPa, with some local peak stresses up to 130 MPa. In any case the primary loading is less than 1/3 of design allowable ($3S_m$) values. Inelastic analyses exhibit small spots of plastic straining at the corners of the TZM/tungsten (finger/tile) interface. For any of these zones shakedown is observed (deformation stays elastic after one cycle of plastic straining). Cyclic plasticity does not occur anywhere in the component. Hence structural design criteria as required by the ITER structural design code are met. After some preliminary shape optimisation of the tile geometry the maximum plastic strains could be kept below 0.2 %. Stresses in the TZM finger stay below 360-400 MPa during operation as well as residual. The respective maximum values are found at varying locations in the finger.

Conclusions

The design of the DC blanket has been modified using the large modules instead of the “banana” segmentation. A new He-cooled modular divertor concept HEMP which is currently developed by FZK on its own has been adapted to the DC concept. The divertor target plate is split up into small tiles, which are favorable to reduce thermal stresses. The heat transfer surface is enhanced with pin arrays. A first estimation of the heat transfer coefficient gave a value of around 60,000 W/m² which is considered sufficient to remove the envisaged heat load of 10 MW/m² on the divertor target with a reasonable effort. With an integration of the divertor into the power conversion system the net efficiency of the blanket cycle amounts to about 43 %.

Staff:

L. Bühler
E. Diegele
U. Fischer
S. Gordeev
R. Kruessmann
S. Malang
P. Norajitra
G. Reimann
G. Rizzi
H. Schnauder

Literature:

[1] P. Norajitra, L. Bühler, U. Fischer, S. Gordeev, S. Malang, G. Reimann, Conceptual Design of the Dual-Coolant Blanket in the Frame of the EU Power Plant Conceptual Study, 22nd Symposium on Fusion Technology, Helsinki, Finland, September 8-12, 2002.

[2] P. Norajitra, L. Bühler, U. Fischer, K. Kleefeldt, S. Malang, G. Reimann, H. Schnauder, G. Aiello, L. Giancarli, H. Golfier, Y. Poitevin and J.F. Salavy, The Second Advanced Lead Lithium Blanket Concept Using ODS Steel as Structural Material and SiCf/SiC Flow Channel Inserts as Electrical and Thermal Insulators, FZKA 6385, 1999.

[3] E. Diegele, R. Krüssmann, S. Malang, P. Norajitra, G. Rizzi, Modular He-cooled divertor for power plant application, 22nd Symposium on Fusion Technology, Helsinki, Finland, September 8-12, 2002.

[4] VDI – Wärmeatlas, 3th issue 1977, Sheet Ge1 and Ld1.

[5] W. Kalide, Einführung in die Technische Strömungslehre, Hanser, München 1990, pp. 52 – 72.

[6] P. Norajitra, R. Kruessmann, S. Malang, G. Reimann, Assessment of Integration of a He-cooled Divertor System to the Power Conversion System fort the Dual-coolant Blanket Concept (TW2-TRP-PPCS12D8), FZKA-6771, 2002, to appear.

[7] R. Schleicher, A.R. Raffray, C.P. Wong, An assessment of the brayton cycle for high performance power plant, 14th ANS top. meeting, 2000.

[8] ITER Material Property Handbook G74 MA10 00-11-10 W 0.1, ITER Final Design Report, July 2001

[9] ABAQUS User's Manual, Hibbitt, Karlsson & Sorensen, Inc., Pawtucket, RI, USA

TRP-PPCS 12-D 9
Mechanical Analysis, Design Integration and Draft Final Report

Introduction

The dual-coolant (DC) blanket [1] is one of the advanced concepts to be pursued within the EU long-term power plant conceptual study (PPCS). The present work is drawn extensively on the preparatory study on plant availability (PPA) carried out in 1999 with an objective to perform the conceptual design of the DC blanket concept where some details are to be selected in accordance with the overall strategy, which allows an extrapolation of the present knowledge between the near-term blanket concept solutions (the water-cooled lead-lithium - WCLL, and the helium-cooled pebble bed - HCPB), and the very advanced self-cooled Pb-17Li SiC/SiC (SCLL) blanket concept. In the PPCS the reactor power is adapted to a typical size of commercial reactors of 1,500 MWe which requires iterative calculations between the blanket layout and the system code analysis. This task is under the coordination of FZK in co-operation with CEA, UKAEA, VR, EFET and EMPRESARIOS.

The blanket design

A significant change has been made in the PPCS concerning the blanket segmentation which is finally adopted in “large modules” (Fig. 1) in place of the “banana segments” regarded so far with an advantage to reduce the thermal stresses and to cope better with the electro-magnetic forces caused by disruptions. Furthermore, for reduction of waste the blanket is devided into an exchangeable part (i.e. the modules including the hot shield) and a lifetime part (cold shield and coolant manifold). With a segment division of 16 (according to 22,5°), each sector contains 11 modules (No. 1-5 for inboard, IB, and 6-11 for outboard, OB, respectively) arranged over the torus circumference, a total number of the modules amounts to

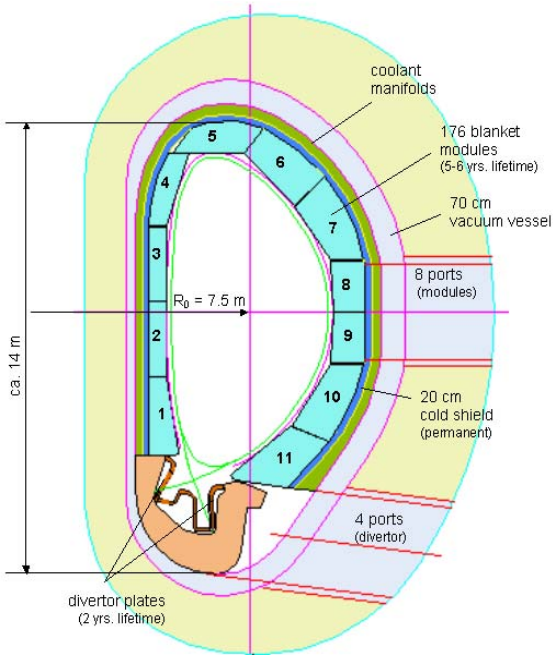

176. The structural blanket design is described in detail in [1].

Fig. 1: Cross section of the fusion reactor torus with dual coolant blanket modules

Fig. 2 shows exemplarily an isometric view of an DC outboard blanket module from the torus equatorial zone. The main DC characteristics are: the use of self-cooled breeding zones with liquid metal Pb-17Li serving as breeder and coolant at the same time, the use of helium-cooled RAFM (reduced activation ferritic/martensitic) steel structure, and the use of SiC_f/SiC flow channel inserts (FCIs) serving as electrical and thermal insulators. The latter minimises the MHD pressure drop (avoids the need for insulating coating on the inner duct walls) and allows a relatively high exit temperature of up to 700 °C for the liquid metal. Thus, as shown in the PPA [2], a thermal efficiency of about 44 % could be reached by using a closed-cycle helium gas turbine in the power conversion system. In addition, the use of oxide dispersion strengthened (ODS) ferritic steel as structural material allows a temperature limit of the first wall (due to creep rupture strength) of up to about 650 °C which is about 100 K higher than that for ferritic material. In the current design the entire blanket structure is made of EUROFER with a 2-3 mm thick ODS layer plated onto the firs wall, within a zone having the maximum temperature beyond 550 °C. This solution offers an advantage of using the high temperature strength of ODS-steel without the fabrication difficulties encountered in welding of ODS structural parts.

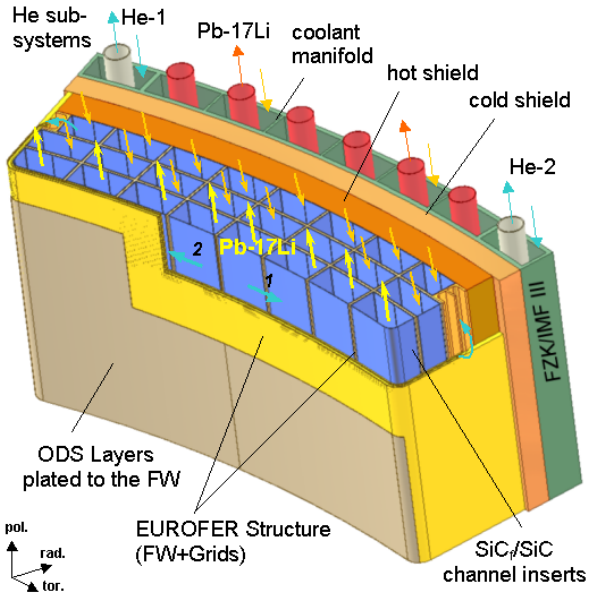

Fig. 2: Isometric view of an equatorial outboard blanket module

Status of the work on PPCS 12

In the PPA [2] the goal was to investigate the potential of this blanket concept. Taking into account the temperature constraints for the FW (creep rupture strength) and the Pb-17Li breeding zone (corrosion), the latter was found to be decisive for the power limitations leading to the maximum values of neutron wall load and surface heat load of 5 MW/m^2 and 0.9 MW/m^2, respectively. The maximal allowable peak surface heat load for the FW could be enhanced to 1.5 MW/m² serving as a margin for e.g. peaking factor uncertainty.

In a continuation of this study the following stage of PPCS is concerned with an assessment of the DC blanket for a case of a standardized commercial power plant. The blanket performance of the reference case is to be adapted to a typical commercial reactor size of e.g. 1500 MW electric power which requires iterative calculations between the blanket layout and the system code analysis concerning neutronic, thermohydraulic, thermomechanic, MHD and velocity calculations.

Table 1: Main data of the DC blanket

Electric Power (MW)	1500
Fusion Power (MW)	3410
Aspect Ratio	3.0
Elongation (X-point, 95% flux)	2.1, 1.9
Triangularity (X-point, 95% flux)	0.7, 0.47
Major Radius (m)	7.5
TF on axis (T)	6.4
Plasma Current (MA)	20.1
Safety factor q(95)	4.5
β_N(thermal, total)	3.4, 4.0
H_H (IPB98y2)	1.3
In-/Outboard blanket and shield thickn. (m): (distance between FW and VV)	1.1 / 1.6
Heating Power (MW)	112
TBR / Energy multiplication factor	1.15 / 1.17
Avg. neutron wall load Bl./Div. (MW/m²)	2.27 / 1.7
Max. surface heat load Bl./Div. (MW/m²)	0.59 / 10
Neutron power Bl./Div. (MW)	2445 / 283
Thermal power Bl./Div. (MW)	3430 / 583

Coolant inlet / outlet temperatures (°C)	
a. Blanket He (8 MPa, 1539 kg/s)	300 / 480
b. Blanket Pb-17Li (46381 kg/s)	480 / 700
c. Divertor target He (10 MPa, 477 kg/s)	700 / 800
d. Secondary loop He (15 MPa)	285 / 700
Pumping power (MW) (a. / b. / c.)	30 / 5 / 3
Net power conversion efficiency[1] (%)	43

[1] *assuming a closed 3-compr.-stage Brayton gas turbine cycle*

Table 2: Size, weight and power of the modules

Module No.	Group	Dimensions (mm)			Weight (kg)		Power (MW)
		radial	toroidal	poloidal	emptied	full	
1	IB	747	1656	2400	3430	15523	10.39
2	IB	545	1660	2300	3287	14876	11.56
3	IB	545	1660	2300	3287	14876	11.28
4	IB	741	1723	2339	3343	15128	11.16
5	IB	959	2423	2300	10254	45721	8.89
6	OB	1301	3110	2276	12619	57667	18.88
7	OB	1341	3548	2004	12499	57749	22.28
8	OB	1035	2965	1573	8361	38043	19.56
9	OB	1035	2965	1573	8361	38043	19.57
10	OB	1340	3639	2200	14037	64987	23.66
11	OB	1408	3049	2320	12639	57657	20.93

Basis for neutronic and the following thermohydraulic calculations is the input provided by UKAEA (Table 1), such as: major radius 7.5 m, minor radius 2.5 m, elongation 1.9, triangularity 0.47, source peaking factor 2.5 and fusion power of 3410 MW which is resulted from the first iteration assuming an energy multiplication factor of 1.17, a thermal efficiency of 0.44, 112 MW heating power (total 252 MW for auxiliarly power leading to a recirculating power fraction of 0.144) and a radial build of the blanket. The 3D MCNP neutronic calculation carried out for 10° torus reactor model yields an average neutron wall load of 2.27 MW/m^2 for the blanket (corresponds to maximum surface heat load of 0.59 MW/m^2), 1.17 MW/m^2 for the divertor and 2.23 MW/m^2 for the whole reactor, respectively. The generated module power amounts in average to about 11 MW for inboard and 21 MW for outboard, respectively (Table 2). The maximum power density was determined to about 19 W/cm^3 in steel, 17.5 W/cm^3 in Pb-17Li and 7 W/cm^3 in SiC_f/SiC, respectively. The multiplication factor

results to 1.22 for the whole reactor including the heat power in the cold shield which is higher than the value in the first iteration. The total tritium breeding ratio was calculated to 1.15 without ports.

The respective data for thermohydraulic layout are: a) First wall: 8 MPa He, inlet/outlet temperatures 300/480 °C, thermal power 1432 MW; b) blanket interior: Pb-17Li, inlet/outlet temperatures 480/700°C, thermal power 1976 MW; c) divertor bulk: 10 MPa He, inlet/outlet temperatures 480/615 °C, thermal power 335 MW, d) divertor target plates: 10 MPa He, inlet/outlet temperatures 700/800 °C, thermal power 248 MW.

An assessment of the maximum FW temperature based on PPA [2] yields about 590°C for a FW thickness of 5 mm with a He velocity of 40 m/s which is far below the engineering layout limit of 650 °C for ODS steel and therefore the induced temperature stresses remain likewise under the permissible limit compared to the PPA results.

For most of the straight rectangular ducts the MHD pressure drop correlations are known. The results of MHD analysis show that the pressure drop in the blanket itself is small if all walls are covered by the electric insulation of 5 mm thickness. In this case a value of 2.5×10^{-3} MPa is determined for a poloidal length of 2 m. This value, however, is negligibly small compared with the pressure drop in the radial access tubes connecting the blanket with the rear coaxial poloidal pipes which feed and drain the blanket modules with the liquid metal. In this zone three-dimensional effects by strong contractions and expansions are prevailing and lead to the dominant fraction of pressure drop. An MHD estimation yields a pressure drop of about 0.57 MPa for the outboard and 1.29 MPa for the inboard modules, respectively. In any case the electric insulation in these elements is required. The pumping power for the whole reactor is estimated to about 5 MW for Pb-17Li and 30 MW for helium taking into account a pump efficiency of 0.8.

For the DC blanket concept a closed 3-compression-stage Brayton gas turbine cycle is considered the reference power conversion system. This solution offers a crucial advantage in avoiding the contact of liquid metal with water and to avoid the tritium permeation losses to the environment. For the secondary He loop a high He pressure (15-18 MPa) was chosen which does not explicitly affect the thermal efficiency of the power conversion system but it is required to simultaneously achieve a high heat exchanger (HX) efficiency and a low pressure loss ratio. An examination of the three-stage heat exchangers (Blanket He/He, Blanket Pb-17Li/He and Divertor He/He) for this case results in a reasonable pressure loss (max.<0.2 MPa).

A new He-cooled modular divertor concept HEMP which is currently developed by FZK on its own [3] has been adapted to the DC concept. The divertor target plate is split up into small tiles, which are favorable to reduce thermal stresses. The heat transfer surface is enhanced with pin arrays. A first estimation of the heat transfer coefficient gave a value of around 60,000 W/m² which is considered sufficient to remove the envisaged heat load of 10 MW/m² on the divertor target with a reasonable effort. The integration of the HEMP divertor into the power conversion system of the DC blanket concept is investigated in detail in [4]. An assessment of the net efficiency of the blanket cycle gave a value of about 43 %.

Conclusions

The dual coolant blanket concept is characterised by its simple construction, simple function, and its high thermal efficiency. The present stage of power plant conceptual study for the dual coolant blanket as a continuation of the PPA 99 study is concerned with an assessment of a case of a standardized commercial power plant with a typical unit size of 1500 MW electric power. The method of blanket segmentation was changed using now a modular segmenting in place of the past " banana" solution. The first iterative calculations comprising the blanket layout regarding neutronic, thermohydraulic, thermomechanic, MHD and velocity field issues and the system code analysis were carried out. A new He-cooled modular divertor concept HEMP which is currently developed by FZK on its own has been adapted to the DC concept. With an integration of the HEMP divertor into the power conversion system the net efficiency of the blanket cycle was assessed to about 43 %. The overall calculation results and the assessment of the net efficiency are in conformity with those from PPA. In the next iteration step only slight changes of the input data are necessary. The final report on this work is planned for the end of 2002.

Staff:

L. Bühler
U. Fischer
S. Gordeev
R. Kruessmann
S. Malang
P. Norajitra
G. Reimann
H. Schnauder

Literature:

[1] P. Norajitra, L. Bühler, U. Fischer, S. Gordeev, S. Malang, G. Reimann, Conceptual Design of the Dual-Coolant Blanket in the Frame of the EU Power Plant Conceptual Study, 22nd Symposium on Fusion Technology, Helsinki, Finland, September 8-12, 2002.

[2] P. Norajitra, L. Bühler, U. Fischer, K. Kleefeldt, S. Malang, G. Reimann, H. Schnauder, G. Aiello, L. Giancarli, H. Golfier, Y. Poitevin and J.F. Salavy, The Second Advanced Lead Lithium Blanket Concept Using ODS Steel as Structural Material and SiCf/SiC Flow Channel Inserts as Electrical and Thermal Insulators, FZKA 6385, 1999.

[3] E. Diegele, R. Krüssmann, S. Malang, P. Norajitra, G. Rizzi, Modular He-cooled divertor for power plant application, 22nd Symposium on Fusion Technology, Helsinki, Finland, September 8-12, 2002.

[4] P. Norajitra, R. Kruessmann, S. Malang, G. Reimann, Assessment of Integration of a He-cooled Divertor System to the Power Conversion System fort the Dual-coolant Blanket Concept (TW2-TRP-PPCS12D8), FZKA-6771, 2002, to appear.

TRP-PPCS 13
Model D (Self-Cooled Lithium Lead Blanket)

TRP-PPCS 13-D 5
MHD Related Issues

The work previously carried out as part of the long term technology R&D programme on the preparatory study on plant availability showed that the use of SiC/SiC composite materials offers a variety of advantages for advanced Self-Cooled Lithium Lead (SCLL) blanket concepts. The use of SiC for the walls of liquid metal filled channels helps to minimize electric currents, the magnetohydrodynamic interaction with the fluid and thus reduces pressure drop. The present subtask focuses on a first estimation of the MHD pressure drop within the blanket.

The geometry has been analyzed after the design of a first blanket model was available. The proposed SCLL design is based on the most attractive features of the previously studied Tauro and ARIES-AT blanket concepts. The front part of the blanket is essentially formed by two concentric boxes where the “cold” Pb-17Li flows at high velocity in the outer gap and returns at low velocity through an inner channel (See Fig. 1). Previous analyses performed for Tauro (Bühler 1999, 2002) showed a possible electrical coupling between the annular flow and the flow in the central pipe with the consequence of partly reversed flow in the gap that could cause closed recirculation loops. This behavior seems to be less severe here because the dividing wall now is thicker than for Tauro providing therefore higher electric resistance for electric currents crossing the wall. Another reason is that in the current SCLL design the annular gap is divided into a number of sub channels, a fact that may prevent the flow from establishing large recirculation loops, which have dimensions of the size of the whole annular region. Finally the gap width in SCLL is much smaller than that used in Tauro. The velocity in the gap is therefore by more than an order of magnitude larger than that in the central channel. If a slight coupling may occur we could rather expect that the gap drives a secondary motion in the inner channel with less severe consequences for heat or mass transfer. For all these reasons we treat the walls as perfect insulators during this fist step of MHD analysis. A confirmation of this assumption by experiments would be desirable.

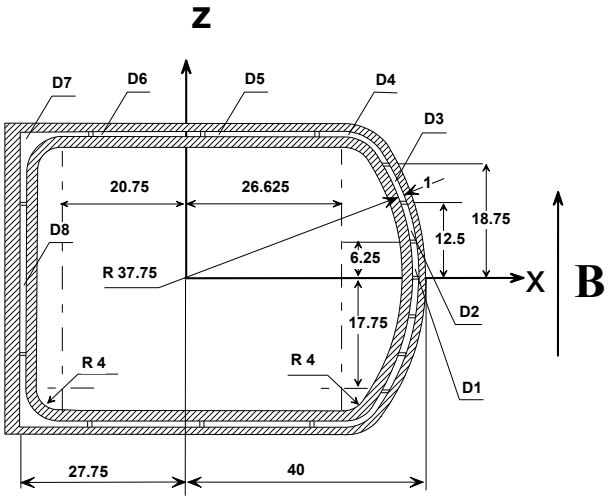

Fig. 1: First design of the front part of the SCLL blanket. All dimensions are scaled with the gap width.

For an efficient analysis the geometry is divided into distinct sub-regions (annular ducts D1-D8 and central duct). It is assumed that in each duct the flow is fully established and satisfies a balance between pressure gradient, viscous forces and Lorentz forces. The flow problem has been solved using a numerical code described by Bühler (1994). In more detail the geometry is shown for duct D2 (Fig. 2). The corners are denoted by ABCD. The corners B and C are the origin of internal parallel layers which spread along magnetic field lines. Velocity profiles are shown in Fig. 3. In the central region between both internal layers the flow is almost uniform. Approaching the outer corners A and D it can be observed that the velocity decreases monotonically to zero. This fact may be unimportant near D. However, near A a reduction of velocity may have a negative influence on heat transfer since A is located at the first wall where the large heat input from the plasma has to be removed. As a consequence higher temperatures have to be expected near A and this fact should be taken into account in future heat transfer analyses. Results for all annular channels near the first wall are summarized in Fig. 4. It can be seen that the velocities are relatively high in duct D1 and decrease continuously with the distance from the x-axis. Results for pressure drop are summarized in Tab. 1. The minimum velocity of 4.2 m/s was required for heat transfer reasons. This velocity determines the pressure gradient in the blanket. Since all annular ducts are connected to the same pressure reservoir this pressure drop determines the velocities in the other channels. As a result the velocity increases when approaching the symmetry plane and reaches values of more than 20 m/s for duct D1. Such high velocities are not really required.

Table 1: Pressure drop and average velocities in the annular ducts for the first design.

Duct	4p(MPa /m)	*v*0 (m /s)
D1	0.1689	20.60
D2	0.1689	13.18
D3	0.1689	8.87
D4	0.1689	5.03
D5	0.1689	4.2

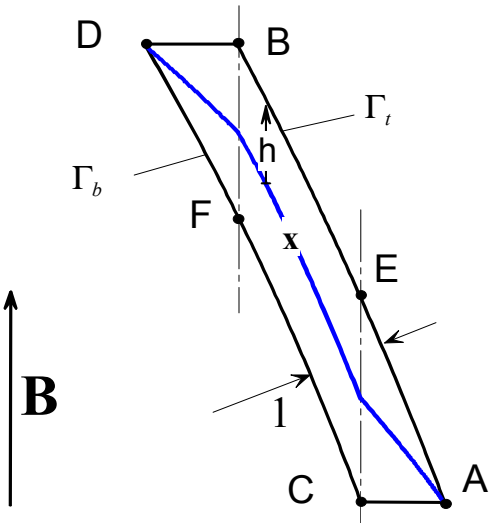

Fig. 2: Example of the computational geometry in the annular region, here for duct D2.

In order to improve the performance, a new design for the front part of the SCLL blanket has been proposed that takes into account specific aspects of MHD flows. The size of the channels has been chosen in such a way that the average velocity in the

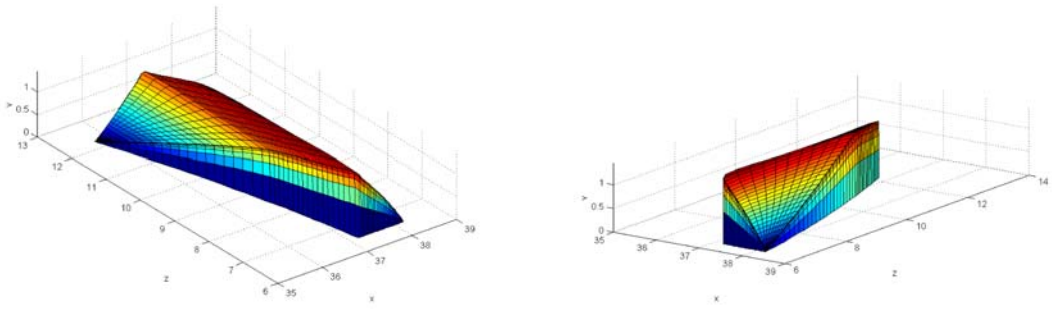

Fig. 3: Nondimensional velocity profile in duct D2 seen from the central duct (left) and from the first wall (right).

ducts is roughly proportional to the surface normal heat flux. A larger radius of curvature near the first wall, as shown in Fig. 5, leads to smaller heat input in ducts 4 and 5 and as a result the velocities required to remove the heat in these channels can be reduced. The heat flux and the required velocities increase along φ. Results for the improved design are shown in Fig. 5.

The results for pressure drop are summarized in Tab. 2. More details can be found in a technical report by Bühler and Giancarli (2002).

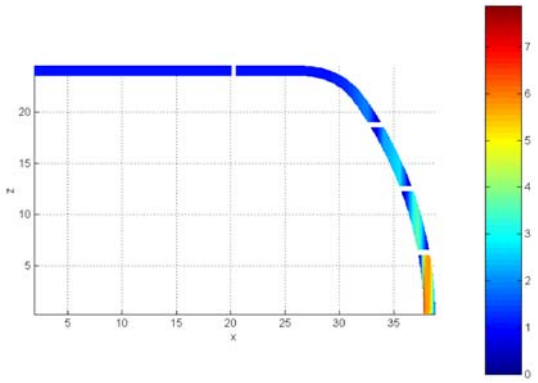

Fig. 4: Nondimensional velocity contours in the annular region.

Table 2: Pressure drop and average velocities in the annular ducts for the improved design.

Duct	4p(MPa /m)	*v*0 (m /s)
D1	0.0567	4.65
D2	0.0567	3.44
D3	0.0567	2.98
D4	0.0567	2.01
D5	0.0567	1.50

Conclusions

The fully developed MHD pressure drop in a typical geometry of the European SCLL blanket has been evaluated, assuming a uniform transverse magnetic field. The calculations show that the circular type of geometry foreseen for the improved design has better MHD performance. The pressure gradient in the annular ducts made by insulating walls is about 4p=0.0567MPa /m at velocities as foreseen in the annular gap v0 =1.5-4.5 m /.s. The pressure drop in the central duct is negligible in comparison with the pressure drop in the annular region. The total pressure drop is mainly created in the annular gap. Its values seem to be on acceptable magnitude. Over the total length L=7.8m of the outboard blanket the pressure drops by Δp=0.44MPa. These results have been obtained assuming a uniform magnetic field of 4 T for the outboard blanket. The top blanket is positioned in a region where the magnetic field is roughly estimated to B=6T while at the inboard blanket we have B=8T . If the geometry for the top and the inboard blanket is the same we can simply estimate the pressure drop there by using the linear dependence of the MHD pressure drop on the magnetic field for a reasonable extrapolation. This yields pressure gradients □p =0.085MPa /m and □p =0.11MPa /m and pressure drops Δp=0.19MPa and Δp=0.85MPa for the top and for the inboard blanket, respectively.

It is found that the core velocity profiles along the first wall exhibit a decrease when approaching the points A at the walls dividing the annular gap into a number of sub channels. This "periodic" velocity distribution may have a negative influence on heat transfer.

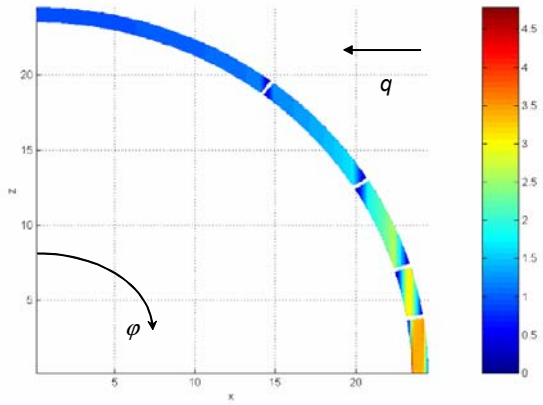

Fig. 5: Nondimensional velocity contours in the annular region for the improved design.

Three-dimensional effects have not been taken into account so far. If we consider the blanket in closer detail we see that the cross sections change slowly along the poloidal height. The magnitude of the toroidal field does also show spatial variations. Both effects should be taken into account in future studies. Additional MHD pressure drop is expected also near the blanket ends, where the flow turns.

From the preliminary drawings of the blanket it is not obvious how the liquid metal is supplied to the blankets. If this is done through relatively thin pipes there exists the possibility that the pressure drop there exceeds the one obtained for the blanket, especially if there is a number of bends in the magnetic field region. It is therefore recommended to make the supplying pipes as short as possible. Finally it should be mentioned that each penetrations through the fringing magnetic field causes an additional irreversible pressure drop.

Staff:

L. Bühler

Literature:

[1] Bühler, L.: 1994, Magnetohydrodynamic flows in arbitrary geometries in strong, non-uniform magnetic fields.-A numerical code for the design of fusion reactor blankets, Fusion Technology 27,pp.3--24.

[2] Bühler, L.: 2001, Fully developed MHD flow in the European TAURO concept for a nuclear fusion blanket, Magnetohydrodynamics 37(1-2), 127–134.

[3] Bühler, L.: 2002 Magnetohydrodynamic flow in the European TAURO blanket, 6th Int. Symp. on Fusion Nuclear Technology (ISFNT-6), San Diego, Calif., April 7-12.

[4] Bühler, L. and Giancarli, L.: 2002, Magnetohydrodynamic flow in the European SCLL blanket, Forschungszentrum Karlsruhe Technical report, FZKA 6778

TRP-PPCS 15
Environmental Assessment

TRP-PPCS 15-D 6
Doses to the Public

Objective

The main objective of this task is to estimate the cost of the "externalities" for models C and D which will be used as input during the economic assessment. In particular, it is necessary to calculate in a consistent way the doses to the public for realistic meteorological and sitting conditions. Results of the assessments will help to evaluate the potential impact to the public with respect to early and late countermeasure actions. These calculations will be a continuation of the assessments performed in the SEAFP and ITER-SEP2 studies and will provide a consistent data set on the doses to the public from a power reactor.

Status of work

As the source terms from the PPCS study were not delivered in time, this task is delayed. No work was carried out in the reporting period.

Staff:

W. Raskob
I. Hasemann
J. Ehrhardt

Underlying Technology

Underlying Technology

Operation and Upgrade of the Fusion Materials Laboratory

The Fusion Materials Laboratory provides the infrastructure for the performance of tasks defined in the EFDA workprogramme related to the characterisation of irradiated and non-irradiated materials. Methods such as optical and electron microscopy, He-pycnometry and Hg porosimetry, crush-, micro-hardness-and charpy tests as well as long time annealing tests are applied.

The PIE of the HFR Phase IB Irradiation Programme was continued. Different OPTIFER and F82H mod materials had been irradiated up to 2.4 dpa at 250 – 450°C. The Charpy impact and tensile testing specimens under investigation represented different heat treatment procedures and welding techniques

Results of the measurements and consecutive analysis are reported in this report in the relevant chapters.

The aim of the investigations was to study the irradiation effects on the mechanical and structural properties of these materials. For this reason the broken samples were also investigated by light optical, scanning electron and transmission electron microscopy.

The investigation of blanket materials was continued with the PIE of EXOTIC-8 material. Both irradiated lithium orthosilicate and beryllium pebbles were tested in terms of tritium and helium release and irradiation-induced changes of porosity and deformation hardness of the structure. Different batches of unirradiated lithium orthosilicate material were characterized with respect to the influence of parameters of the fabrication process on the mechanical and structural properties.

Further samples from JET and TFTR carbon tiles were prepared for the investigation of tritium retention in these materials. In the TLK these samples were analysed.

For the PIE the following equipment was used:

- Charpy and tensile testing devices
- light optical, scanning electron and transmission electron microscopes, electron microprobe analysis
- desorption device with high temperature furnace for tritium and helium release measurements
- He-pycnometer and Hg-porosimeter
- sphere crush and creep testing apparatus

Results of the measurements and consecutive analysis are reported in the respective chapters of this report.

Operation and Upgrade of the Tritium Laboratory Kalrsruhe (TLK)

The Tritium Laboratory Karlsruhe (TLK) is a unique facility within Europe, licensed to handle 40 g of tritium and has an actual inventory of about 25 g. In general the TLK has quite a few similarities with the Tritium Plant of a fusion reactor like ITER, since it comprises a closed tritium cycle including storage, processing of gases for tritium recovery and isotope separation. The operation of the TLK is in itself an essential contribution to the fusion R&D work with tritium. The experience gained has e.g. been utilized for European ITER site studies and licensing considerations.

More than 10 separate glove box systems with a total volume of about 125 m^3 are currently being operated at TLK. The mol sieve beds from the tritium retention systems of each separate glove box arrangement as well as the mol sieve beds from the TLK central tritium retention system need to be periodically regenerated, leading to tritiated water as a product. While this tritiated water - at least for the time being - is waste at TLK, tritium shall be recovered within the ITER Tritium Plant not only for ecological, but also for economical incentives. Therefore also at TLK this water is currently collected and utilized for experiments on water detritiation.

The Tritium Transfer System and Tritium Measurements at TLK

On the whole quite a few components and even complete experimental set-ups at TLK have reached their lifetime, failed or are no longer being used within the ongoing experimental program. Decommissioning, decontamination including recovery of residual tritium and post service examination is therefore an increasing activity at TLK. Any tritiated gases arising from these activities have been transferred to the CAPER facility, since also for ITER waste gases arising from other sources than the vacuum vessel shall eventually be processed by this system.

The extensive experimental program carried out with the CAPER facility in 2002 has involved round the clock operation of the TLK, with frequent transfers of tritium and tritiated hydrogen isotopes between the Caper facility and the TLK infrastructure, i.e. the Tritium Transfer System (TTS), the Tritium Storage System (TLG) and the Isotope Separation System (ISS). Tritium accountancy was carried out by calorimetric measurements. The integral operation of the CAPER facility with the infrastructure of the TLK provides essential information on tritium tracking and control and is a good example for accuracy limitations of accountancy procedures.

Test of the TFMC in the TOSKA facility

After the test phase I with the TFMC alone the TOSKA facility was prepared for the test of the TFMC together with the LCT coil. During TFMC test phase I several problems were found which needed an improvement to run a successful test phase II of the TFMC test. E.g. improvements in the redundancy of the forced flow helium circulation, in the sensitivity of selected sensors on the transient DAS and in the control circuits and interlocks of the 20 kA power supply.

The following hard- and software upgrades have been performed in order to prepare the TOSKA facility for the testing of the TFMC model coil:

PLC programming of interlocks between TFMC, LCT and cryosystem

The PLC programming of the interlocks (configuration, TFMC + LCT) was implemented and tested. Faults in the LCT circuit interlock system have been identified implemented and tested.

UPS system

Fringing fields caused disturbances in the uninterruptible power supply. The magnetic field depending over-current alarm in the uninterruptible power supply (UPS) was checked by a service engineer. The UPS was adjusted. The alarm did not appear after this action. A service of the UPS is planned in 2003 to ensure full functionality.

New centrifugal He pump

The new centrifugal pump was installed. In a test the heat load in the pump have been found to be too high. No improvements were possible in the ´TFMC test phase II. This will be rechecked after end of TFMC test phase II.

20 kA power supply:

A power breaker of the 20 kA switching circuit was disassembled and the contact system was exchanged. After a failure during a routine test the power thyristors have been replaced. Faults in the regulation board software of the 20 kA power supply were localised. The digital controller was replaced by an analogue circuit which was successfully used during test phase II. Effort was spent at the end of the current tests in test phase II to check a changed digital controller for the 20 kA power supply. In test runs with the LCT coil it was found that the results were not satisfying so that the analogue controller was reinstalled. An improvement of the controller will be retried in 2003.

Cryogenic system:
The stability of the cryogenic system during execution of the heating scenario tests (far above the cooling capacity of the refrigerator) was achieved by a careful adjustment of the operation parameters.

Improving sensor sensitivity and calibration

An improvement was achieved by the usage of additional filters and pre-amplifiers and an extremely careful calibration of the inlet temperature measurement after the gas heater in the signal conditioning line of the transient data acquisition system and the SPARTAN scanner. The temperature values are now in good agreement with the measured slow scanner data within ± 0.01 K.

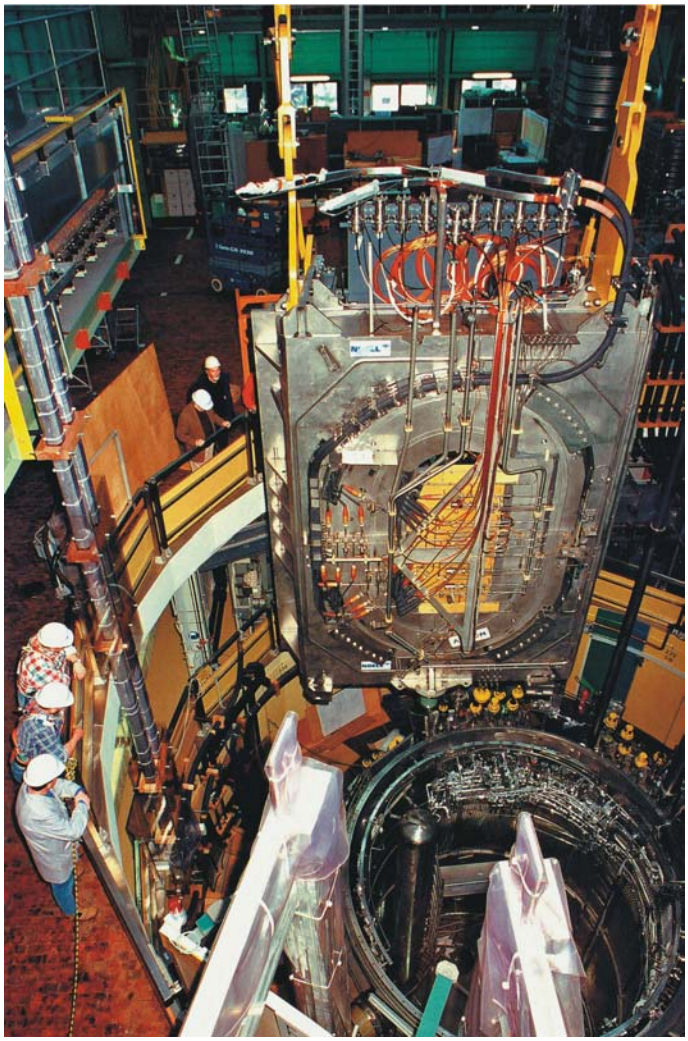

The 63 t TFMC during lifting procedure in the TOSKA facility vacuum vessel

Physics Integration

HGF Strategy Fonds "Advanced ECRH"

Magnetohydrodynamic (MHD) instabilities are one of the main reasons for the limiting confinement of plasmas. The stability is to a large extent determined by the distribution of plasma currents, and to drive localized currents in a plasma is a very important tool to optimize the performance of a tokamak. The suppression of plasma pressure limiting MHD instabilities (so called 'Neoclassical Tearing Modes') has been demonstrated successfully by localized electron cyclotron current drive (ECCD) at ASDEX-Upgrade.

The resonance condition for absorption of the RF-wave is dependent on the magnetic field and by changing the injection angle and/or the RF-frequency, the localization of the externally driven current can be varied.

A multi-frequency tunable 1 MW long pulse gyrotron is highly needed by ASDEX-Upgrade at IPP Garching for advanced ECRH and ECCD experiments. However, multi-frequency gyrotrons have to be equipped with a matched window in order to avoid reflections, this is a Brewster angle window or a tunable double-disk window, both from synthetic diamond.

For an available single-disk window the choice of frequency is reduced due to the thickness of the disk because low reflection is only given for frequencies corresponding to multiples of the half wavelength in the window material. According to the tokamak magnetic field of ASDEX-Upgrade one frequency is 140 GHz. Another should be in the range of 100 to 115 GHz, and using a conventional window disk, the other frequency has to be at about 105 GHz [1].

The $TE_{22,8}$ mode at 140 GHz was chosen as cavity mode [2-4]. The frequency of 105 GHz corresponds to the $TE_{17,6}$ mode. To compare with results from the "Institute for Applied Physics (IAP)" in Nizhny Novgorod, the existing $TE_{22,6}$ gyrotron has been modified to operate in the $TE_{22,8}$ mode. Electron gun, beam tunnel, collector and the superconducting magnet system of the existing $TE_{22,6}$ gyrotron are used in the new experiment. With the $TE_{22,6}$ gyrotron fast frequency step-tunability has been already demonstrated very successfully.

The resonator with uptaper and the quasi-optical mode converter system have been redesigned and are being manufactured. The resonator with uptaper were optimized not only for the two frequencies mentioned but for a series of modes from $TE_{17,6}$ to $TE_{23,8}$ (Fig. 1). Some additional modes from $TE_{24,8}$ to $TE_{25,10}$ can also be excited.

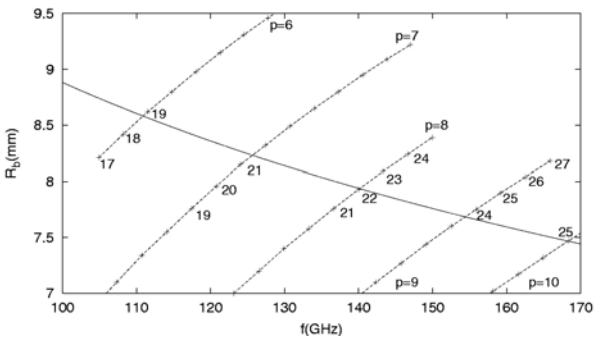

Fig.1: Beam radius as a function of possible output frequencies ($TE_{m,p}$-modes).

A new quasi-optical mode generator for low power tests has been designed and fabricated [5,6]. First measurements of the output field pattern showed a very good performance at most of the gyrotron output frequencies (Fig. 2). A Gaussian-like beam is coupled via two cylindrical lenses and a quasi-parabolic caustic mirror into a perforated gyrotron-like coaxial resonator. The caustic mirror is shaped in a way, so that all waves are tangent to the so-called caustic of the mode. As the eigenvalues of an overmoded resonator are very close to each other, an inner rod is used to improve the mode selection (coaxial resonator). Since all modes of interest for such a gyrotron have a similar structure, with their caustic radius being approximately half the cavity radius, only one set of resonator and lenses is required. Only a minor readjustment of the quasi-optical components is needed for excitation of different modes.

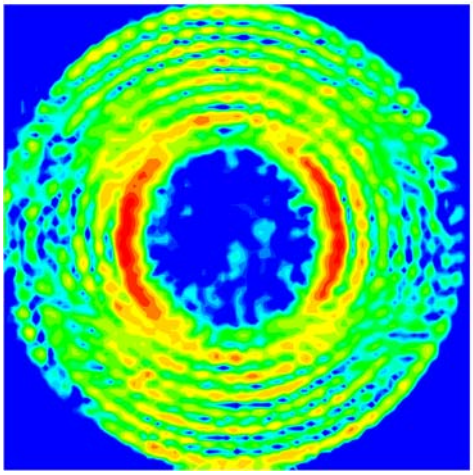

Fig. 2: Horizontal plane of the $TE_{22,8}$-mode excited by the new mode generator.

The quasi-optical mode converter of the gyrotron consists of a dimpled-wall antenna (Denisov-type launcher) and a beamforming mirror system optimized for 9 modes from TE17,6 to TE23,8 [7,8]. For these modes the dimpled-wall antenna shows a well focused beam with low diffraction of the antenna (Fig. 3). The first mirror is a large quasi-elliptical one, the second and third are phase correcting mirrors with a non-quadratical shape of the surface. These two mirrors were also optimized for broadband operation in the 9 design modes.

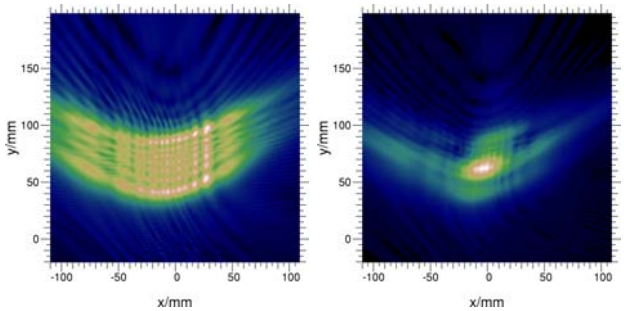

Fig. 3: Output patterns on a plane 50 mm behind a Vlasov antenna (left side) and a Denisov antenna (right side) shown for the $TE_{22,8}$-mode.

First measurements on a 1.923 mm thick, 120 mm diameter chemical vapor deposition (CVD)-diamond disk from DeBeers (Fig. 4) showed a homogeneous distribution of the loss tangent in an elliptic area, which can be used for the elliptic shape of a Brewster angle window [9]. The measured values of the complete disk are between about 2 x 10-5 and 8 x 10-5. The meridian of the loss tangent is 3.6 x 10-5. Due to the ellipitical

shape of the Brewster window only the best area of the disk will be used. A 140 mm diameter disk for a fullsize diamond Brewster angle window has been already ordered.

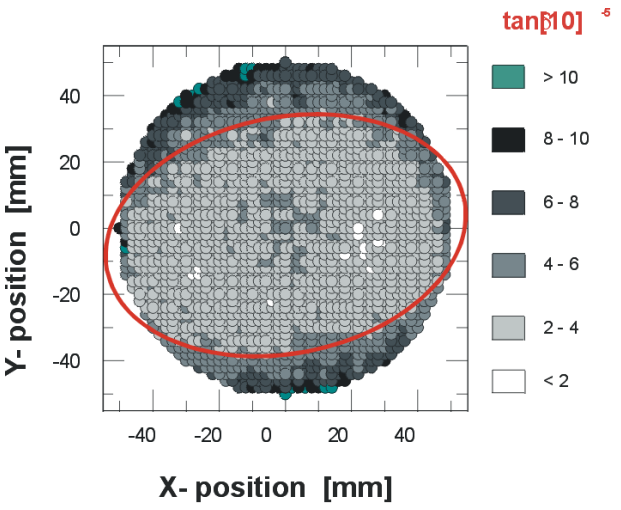

Fig. 4: Measurement of loss tangent of the 120mm diameter CVD-diamond disk for the Brewster angle window.

Staff:

A. Arnold (Uni Karlsruhe)
E. Borie
H. Budig
G. Dammertz
O. Drumm (Uni Karlsruhe)
S. Illy
M.V. Kartikeyan (AvH Fellow)
K. Koppenburg
M. Kuntze
B. Piosczyk
M. Thumm
X. Yang

Literature:

[1] Leuterer, F., K. Kirov, F. Monaco, M. Münich, H. Schütz, F. Ryter, D. Wagner, R. Wilhelm, H. Zohm, T. Franke, K. Voigt, M. Thumm, R. Heidinger, G. Dammertz, K. Koppenburg, W. Kasparek, G. Gantenbein, H. Hailer, G.A. Müller, A. Bogdashov, G. Denisov, V. Kurbatov, A. Kuftin, A. Litvak, S. Malygin, E. Tai, V. Zapevalov: Plans for a new ECRH system at ASDEX Upgrade, 22nd Symp. on Fusion Technology (SOFT), Helsinki, SF, September 9-13, 2002, C17.

[2] Borie, E., A. Arnold, Dammertz, G., O. Drumm, S. Illy, M.V. Kartikeyan, K. Koppenburg, B. Piosczyk, X. Yang, Thumm, M.: A multifrequency step-tunable gyrotron at FZK, 2nd Int. Workshop on Far Infrared Technology, Fukui, Japan, September 12-13, 2002.

[3] Borie, E., G. Dammertz, O. Drumm, S. Illy, M.V. Kartikeyan, K. Koppenburg, B. Piosczyk, M. Thumm, D. Wagner, X. Yang: Possibilities for multifrequency operation of a gyrotron at FZK, IEEE Trans. on Plasma Science, 2002.

[4] Koppenburg, K., A. Arnold, E. Borie, G. Dammertz, O. Drumm, M.V. Kartikeyan, B. Piosczyk, M. Thumm, X. Yang: Design of a multifrequency high power gyrotron at FZK, Proc. 27th Int. Conf. on Infrared and Millimeter Waves, San Diego, USA, 2002, 153-154.

[5] Arnold, A., G. Dammertz, D. Wagner, M. Thumm: Measurements on a mode generator for cold tests of step-tunable gyrotrons, Proc. 27th Int. Conf. on Infrared and Millimeter Waves, San Diego, USA, 2002, pp. 289-290.

[6] Wagner, D., M. Thumm, A. Arnold: Mode generator for the cold test of step-tunable gyrotrons, Proc. 27th Int. Conf. on Infrared and Millimeter Waves, San Diego, USA, 2002, pp. 303-304.

[7] Drumm, O., G. Dammertz, M. Thumm: Design methods for mirrors in a quasi-optical mode converter for a frequency step-tunable gyrotron, Proc. 27th Int. Conf. on Infrared and Millimeter Waves, San Diego, USA, 2002, pp. 191-192.

[8] Drumm, O.: Numerical optimization of quasi-optical mode converter for frequency step-tunable gyrotron, Dissertation, Universität Karlsruhe, FZKA 6754, 2002.

[9] Thumm, M., G. Dammertz, I. Danilov, R. Heidinger, A. Meier: Low and high power experiments on CVD-diamond windows for ECRH, 6th ECH Transmission Line Workshop, General Atomics, San Diego, CA, September 19-20, 2002.

Microwave Heating for Wendelstein 7-X

Introduction

The development of electron cyclotron resonance heating (ECRH) systems is closely linked to the development of stellarators, and one of the key issue for stellarators is the development and demonstration of high power gyrotrons with capability for continuous wave (CW) operation. For the stellarator Wendelstein 7-X now under construction at the Max-Planck-Institute for Plasma Physics (IPP), Germany, a 10 MW ECRH system is foreseen.

The Forschungszentrum Karlsruhe has signed a contract to construct the 10 MW ECRH system at Greifswald, and a European collaboration has been established between the Forschungszentrum Karlsruhe, Centre de Recherche de Physique des Plasmas (CRPP) Lausanne, Institut für Plasmaforschung (IPF) of the University Stuttgart, Commissariat à l´Energie Atomique (CEA) in Cadarache and Thales Electon Devices (TED) in Vélizy, to develop and build the 10 gyrotrons each with an output power of 1 MW for CW operation and to install the complete ECRH system at Greifswald.

Development of the Prototype Gyrotron

The major problems of high power, high frequency gyrotrons are given by the Ohmic heating of the cavity surface, by the dielectric losses in the output window, by the power capability of the collector and by the amount of stray radiation absorbed inside the gyrotron. The technical limit of the power density on the resonator surface is assumed to be 2 kW/cm² for CW operation. For this reason high power gyrotrons are operated in high order volume modes with a large cavity.

A major breakthrough for a CW compatible source is the use of a synthetic diamond window fabricated by chemical vapor deposition (CVD), which allows the design and the operation of a CW tube at the 1 MW power level [1-8]. The single-stage depressed collector brings the overall efficiency of the gyrotron in the 50% range and at the same time significantly reduces the thermal loading on the collector.

The pre-prototype gyrotron tube (Maquette) was tested in short and long pulse operation. The results are given in Figure 3. In short pulse operation an output power of 1.15 MW with an efficiency of 49% (with depressed collector) could be achieved, in long pulse operation the measurements had suffered from arcing inside the RF absorber load and from a pressure rise inside the tube. An output power of about 1 MW could be achieved in 10 s pulse lengths, and the highest energy content of 90 MJ was measured with 640 kW for 140 s [2].

For tokamaks it is essential to counteract plasma pressure driven instabilities by producing a very localized current by modulated electron cyclotron current drive (ECCD). Therefore, modulation of the gyrotron output power is an important tool for tokamaks. In stellarators, the possibility for gyrotron power modulation gives the possibility for heat wave experiments.

Modulation experiments were performed with the pre-prototype tube in two ways: modulation of the cathode voltage and modulation of the depression voltage (voltage between body and collector) [8]. Both methods allowed a modulation between an output power of about 100 kW and 900 kW by changing the accelerating voltage between 69 kV and 82 kV, respectively Fig.1; left and right). The advantages of the depression voltage modulation are simple and cheap high voltage power supplies, however the disadvantage is the increased collector loading at lower output powers. The collector loading measured by the temperature increase between input and output of the cooling water changes by about 30% between about 1.6°C and 2.1°C, whereas for cathode voltage modulation the collector loading is almost constant. For the cathode voltage modulation, a frequency of 50 kHz could be achieved (Fig. 2); for depression voltage modulation the frequency was limited to 1.5 kHz due to the low slew rate of the voltage power supply. Figure 2 gives the modulated output power taken from an RF detector diode. The modulation depth (ratio between maximum and minimum output power) is about 10.

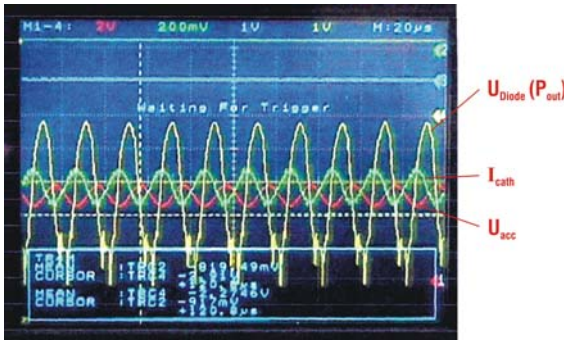

Fig. 2: Scope traces of accelerating voltage, beam current and output power [8].

Fig

era
e of
ge

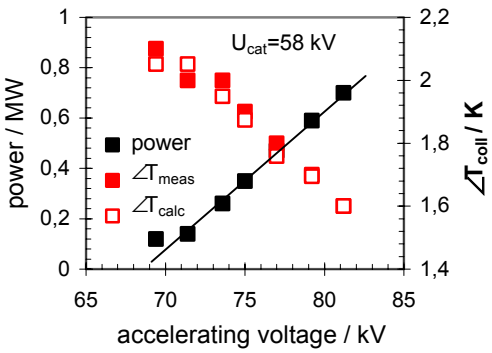

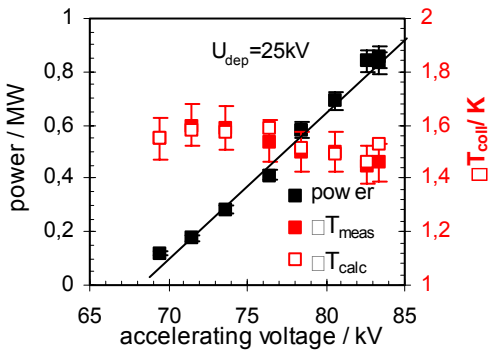

After finishing the experiments with the pre-prototype gyrotron, the tube was delivered to IPP Greifswald and the 1st prototype tube was built by TED and installed at Karlsruhe. In comparison to "Maquette", the prototype tube has been equipped with an improved cooling for the mirror box and an increased stainless steel surface for the absorption of the stray radiation. In addition, the mirror design had been corrected and the window was given a tilt of 1.5 degree with respect to the RF beam axis. This should avoid small reflections even of a matched window going back to the resonator [4]. The window had been fabricated with a new brazing method developed by TED in collaboration with the Forschungszentrum (Ag/Cu-braze). This method allows brazing at higher temperatures (850°C) and avoids corrosion by the cooling water.

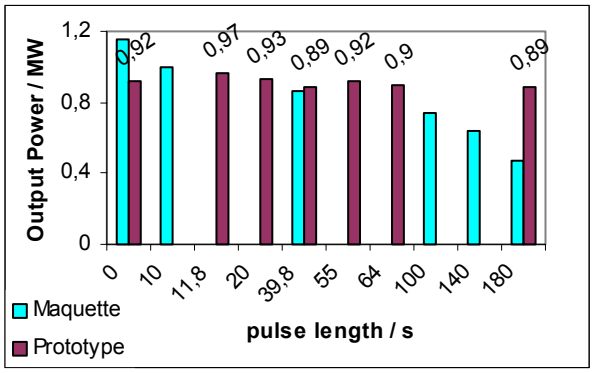

Fig. 3: Output power of the prototype gyrotron for different pulse lengths. Those for the pre-prototype tube "Maquette" are given for comparison.

In order to avoid arcing inside the RF absorber load, the microwave measurement chamber had been equipped with two polarization mirrors, in order to convert the linear polarized output beam into a circularly polarized one. This eliminated the strong absorption in the polarization plane.

The results of the long-pulse experiments of the prototype together with those of the pre-prototype tube "Maquette" are shown in Fig. 3. An output power of 890 kW has been measured at pulse lengths of 180 s. The efficiency has been calculated to 41% with a depression voltage of about 29 kV. For shorter pulse lengths, the output power increased slightly to 970 kW at a pulse length of about 12 s with an efficiency of 44%. It is interesting to consider the power balance for the prototype tube which is possible due to the improved calorimetric measurements. From this it follows that the internal stray radiation does not exceed 1.5% of the total output power. The total stray radiation (internal plus external) has been measured to less than 3.2% of the total output power. This value indicates the quality of both the cavity and the improved quasi-optical mode converter with respect to mode purity. The CVD-diamond window absorbs only approximately 400 W in agreement with the measured loss tangent. It is also interesting to mention that the specified directed beam power of 900 kW has been achieved for 55 s, the total output power was 922 kW (Fig. 3).

The limitation of the pulse length at full power to 180 s is given by the HV power supply. It is possible, however, to operate it continuously at reduced currents of up to 30 A. Table 1 shows the pulse lengths currents and thus power levels. As can be seen, beyond three minutes the pulse length is limited by the pressure increase inside the gyrotron. At an output power of 540 kW the pulse length was limited to about 16 minutes by an interlock signal indicating too high pressure. Despite the low level of internal stray radiation, the reason is mainly seen by the RF absorption on the internal ion getter pumps and the related increase in temperature.

Table 1: Pulse limitations for different output powers [7].

pulse length	power (kW)	current (A)	energy (kJ)	limitation
3m	890	40	160	HV power supply
15m 37s	539	26	505	pressure increase
21m 40s	257	26	350	pressure increase

Series Gyrotrons

The call for tender for series gyrotrons and for the superconducting magnetic system (SCM) was sent to the companies. The answer for the SCM is already available.

Transmission Line

The transmission line consists of single-beam and multi-beam elements (Fig. 4) [9]. For each gyrotron, a matching assembly of five single-beam mirrors is used. Two of these mirrors (M1,M2) match the gyrotron output to a Gaussian beam, two others (P1,P2) are used to set the appropriate polarization. Mirror M4 injects the individual beams into the MBWG system (M5,M6 etc.).

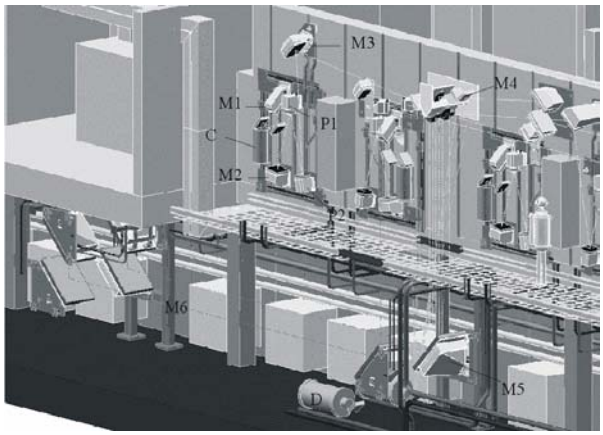

Fig. 4: View into the beam duct with the transmission line.

As the multi-beam wave-guide (MBWG) [10] mainly determines the transmission properties of the complete transmission system, a careful optimisation of the shape of the mirrors as well as their orientation was performed. They feature optimised surfaces with respect to low mode conversion.

Two prototype MBWGs were fabricated, and after minor problems the surface quality now is according to the specifications. Nevertheless, the adhesion of the copper surface electroplated on stainless steel shall be guaranteed by a better quality assurance and small changes during the fabrication procedure.

The measurements on the prototype transmission line at the IPF Stuttgart were continued with an improved input beam. The output beam amplitude pattern of the system is shown in Figure 5 [10]. The efficiency of the transmission line was measured to be about 90% and agrees very well with the theoretical expectation.

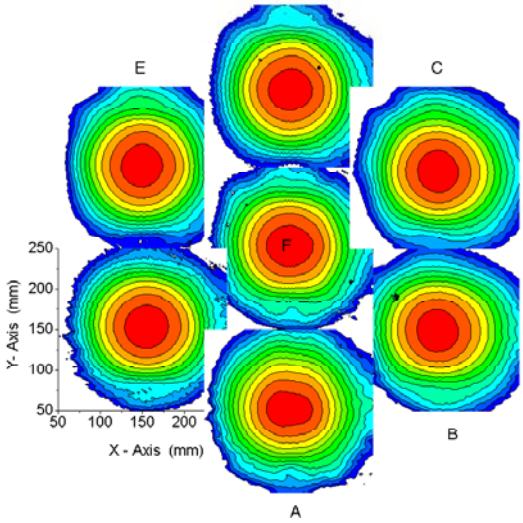

Fi.g. 5: Output power pattern of the prototype transmission line [10].

All the mirrors of the transmission lines inside the beam duct are designed and either fabricated or in fabrication. The first two mirrors (M1,M2) and two polarising mirrors were tested with the prototype gyrotron at the Forschungszentrum. No problems could be found despite poor cooling of these mirrors, especially no arcing on the corrugated surfaces of the polarisers was observed as long as they were clean.

The fabrication of M3 can be completed, the surfaces of M1 and M2 depend on the RF beam parameters of the gyrotrons, so the final machining of the surfaces will only be done after the beam specifications of each gyrotron.

The influence of deformation during operation has been investigated theoretically and experimentally. The mirror deformation turned out to be mainly spherical, resulting in spherical modifications of the phase-fronts of the reflected beams. This only leads to a modification of the beam parameters, but not to a conversion to higher modes. It was shown that even in the worst case, only a change of the beam waist radius of 4% is expected, the beam diameter at the torus window remains practically unchanged.

HV-Systems

At present, the main power supply (65kV, 45 A) from Thales Company does not fulfil completely the specifications concerning the stability. With P-Spice simulations, the design of the HV-modulator was adapted to these restrictions. These adaptations are finished. The proposed action for the PSM-modules of the HV power supplies of Thales showed their effectiveness at the first tests.

Most components for the modulator are now ordered, especially the power supplies for the internal voltages, oil pumps for the tube cooling, heat exchanger etc. The external power supplies for the body voltage are delivered.

The concept of a certificated HV emergency-system at Greifswald has been designed. The concept is now ready to be given to industry for installation. The necessary components are available.

In-vessel Components

In the past, a development had been started to optimise the surface structure for the back reflectors on the inner wall of the plasma vessel**.** Further, the RF stray radiation inside the empty plasma vessel for checking the validity of computer codes had been investigated in collaboration with the Institute of Plasma Physics of the University Milano, Italy. This was performed at the plasma vessel of Wendelstein 7-AS. Due to the similar relative geometry of W7-AS and W7-X it is assumed, that the results can be easily transferred to the conditions of W7-X. Thus the accuracy of predictions can be improved strongly. The parameters for a test-chamber have been fixed. This test-chamber will be used for testing all microwave-sensitive components before installing those into the plasma vessel.

As an alternative option for the Mo-alloys which is planned to be used as wall material in the plasma vessel and which owns high reflectivity for microwaves, the microwave properties of W-coated graphite tiles were investigated. The microwave properties of this material were shown to be very convenient.

The design of the in-vessel RF-antennas has been started.

Auxiliary systems

The water cooling for five gyrotrons (according to the specifications for the cooling system by TED) are installed (Fig. 6) [11]. As one gyrotron (Maquette) is already at place, this gyrotron is already connected to the cooling circuits. This tubing acts as a prototype installation for the other tubes.

Most other cooling circuits are being installed and mostly completed at Greifswald, especially the cooling circuits for the RF absorber load (1 MW at 50 m³/h) and those for the mirror cooling (700 kW at 150 m³/h). The connections to the mirror will be done as soon as those are available.

The automatic liquid nitrogen supply with 600 l/h capacity for the superconducting magnets has been designed. The installation is now under work.

The same applies for the gaseous Helium recovery system with 16 Nm³/h capacity.

Fig. 6: Gyrotron cooling water modul [11].

The vacuum system for evacuation of the superconducting magnetic system has been installed.

For all these installations, the controlling system and the visualization was designed and installed. Further, the low

voltage installations and the installation for the optical and electrical signal transmission are in progress.

The HV emergency concept has been designed, the components are available.

Staff:

IHM / FZK
A. Arnold (Uni KA)
E. Borie
G. Dammertz
B. Eisele
A. Götz
P. Grundel
R. Heidinger (IMF I)
S. Illy
H. Kunkel
K. Koppenburg
M. Kuntze
W. Leonhardt
R. Lukits
D. Mellein
G. Neffe
B. Piosczyk
M. Schmid
W. Spiess
J. Szczesny
M. Thumm

IPF (University Stuttgart)
H. Babilon
P. Brand
G. Gantenbein
H. Hailer
W. Kasparek
M. Krämer
F. Müller
G. Müller
R. Munk
C. Rieper
P. Salzmann
H. Schlüter
P.G. Schüller
R. Schütz
K. Schwörer
R. Wacker
W. Xu

IPP (Greifswald/Garching)
H. Braune
V. Erckmann (PMW)
F. Hollmann
L. Jonitz
H. Laqua
G. Michel
F. Noke
F. Purps
T. Schulz
M. Weißgerber

Literature:

[1] Alberti, S., et al., “European High Power CW Gyrotron Development for ECRH systems”, Fusion Engineering and Design 53, pp. 387-397, 2001.

[2] Dammertz, G., et al., “Development of a 140 GHz, 1 MW, "Continuous Wave Gyrotron for the W7-X Stellarator”, Frequenz 55 (2001),9-10, pp. 270-275.

[3] Dammertz, G., S. Alberti, A. Arnold, E. Borie, V. Erckmann, G. Gantenbein, E. Giguet, R. Heidinger, J.P. Hogge, S. Illy, W. Kasparek, K. Koppenburg, M. Kuntze, H. Laqua, G. LeCloarec, F. Legrand, Y. LeGoff, W. Leonhardt, C. Lievin, R. Magne, G. Michel, G. Müller, G. Neffe, B. Piosczyk, M. Schmid, M. Thumm, M.Q. Tran, "140 GHz, 1 MW, CW gyrotron for fusion plasma heating", Proc. 3rd IEEE Int. Vacuum Electronics Conference (IVEC 2002), Monterey, California, USA, 2002, pp. 330-331.

[4] Dammertz, G., A. Arnold, E. Borie, E. Giguet, R. Heidinger, S. Illy, K. Koppenburg, M. Kuntze, G. LeCloarec, F. Legrand, W. Leonhardt, C. Lievin, G. Müller, G. Neffe, B. Piosczyk, M. Schmid, M. Thumm, M.Q. Tran, "Status of the 1 MW, 140 GHz, CW gyrotron for W7-X", 5th Int. Workshop on Strong Microwaves in Plasmas, Nizhny Novgorod, Russia, August 1-9, 2002, Invited Paper S2.

[5] Thumm, M., "Progress in gyrotron development", 22nd Symp. on Fusion Technology (SOFT), Helsinki, SF, September 9-13, 2002, Invited Paper 12.

[6] Lievin, C., S. Alberti, A. Arnold, E. Borie, G. Dammertz, V. Erckmann, E. Giguet, R. Heidinger, J.P. Hogge, S. Illy, W. Kasparek, K. Koppenburg, M. Kuntze, H. Laqua, G. Le Cloarec, F. Legrand, W. Leonhardt, R. Magne, G. Michel, G. Müller, G. Neffe, B. Piosczyk, M. Schmid, M. Thumm, M.Q. Tran, "Status of the 1 MW, 140 GHz, CW gyrotron for W7-X", 22nd Symp. on Fusion Technology (SOFT), Helsinki, SF, September 9-13, 2002, C20.

[7] Dammertz, G., S. Alberti, A. Arnold, E. Borie, V. Erckmann, G. Gantenbein, E. Giguet, R. Heidinger, J.P. Hogge, S. Illy, W. Kasparek, K. Koppenburg, M. Kuntze, H.P. Laqua, G. LeCloarec, F. Legrand, W. Leonhardt, C. Lievin, R. Magne, G. Michel, G. Müller G. Neffe, B. Piosczyk, M. Schmid, K. Schwoerer, M. Thumm, M.Q. Tran, "Progress of the 1 MW, 140 GHz, CW Gyrotron for W7-X", Proc. 27th Int. Conf. on Infrared and Millimeter Waves, San Diego, USA, 2002, pp. 3-4.

[8] Dammertz, G., S. Alberti, D. Fasel, E. Giguet, K. Koppenburg, M. Kuntze, F. Legrand, W. Leonhardt, C. Lievin, G. Müller, G. Neffe, B. Piosczyk, M. Schmid, A. Sterk, M. Thumm, M.Q. Tran, A.G.A. Verhoeven, "Power modulation capabilities of the 140 GHz/1 MW gyrotron for the stellarator Wendelstein 7-X", 22nd Symp. on Fusion Technology (SOFT), Helsinki, SF, September 9-13, 2002, C5.

[9] Empacher, L. and W. Kasparek, "Analysis of a multiple-beam waveguide for free-space transmission of microwaves, IEEE Trans. Antennas Propagat. AP-49 (2001), pp. 483-493 .

[10] Hailer, H., G. Dammertz, V. Erckmann, G. Gantenbein, F. Hollmann, W. Kasparek, W. Leonhardt, M. Schmid, P.G. Schüller, M. Thumm, M. Weissgerber, "Mirror development for the 140 GHz ECRH system of the stellarator W7-X", 22nd Symp. on Fusion Technology (SOFT), Helsinki, SF, September 9-13, 2002, C44.

[11] Michel, G., P. Brand, G. Dammertz, V. Erckmann, G. Gantenbein, F. Hollmann, L. Jonitz, W. Kasparek, H.P. Laqua, W. Leonhardt, G. Müller, F. Purps, M. Schmid, T. Schulz, M. Thumm, "Progress of the 10 MW ECRH system for W7-X", 12th Joint Workshop on Electron Cyclotron Emission and Electron Cyclotron Resonance Heating (ECE 2002), Aix-en-Provence, France, May 13-16, 2002.

Appendix I: FZK Departments Contributing to the Fusion Programme

FZK Department	FZK Institut/Abteilung	Director	Ext.
Institute for Materials Research	Institut für Materialforschung (IMF)	I. Prof. Dr. K.-H. Zum Gahr	3897
		II. Prof. Dr. O. Kraft	4815
		III. Prof. Dr. H. Haußelt	2518
Institute for Pulsed Power and Microwave Technology	Institut für Hochleistungsimpuls- und Mikrowellentechnik (IHM)	Prof. Dr. M. Thumm	2440
Institute for Nuclear and Energy Technology	Institut für Kern- und Energietechnik (IKET)	Prof. Dr. T. Schulenberg	3450
Institute for Reactor Safety	Institut für Reaktorsicherheit (IRS)	Prof. Dr. D. Cacuci	2550
Institute for Technical Physics	Institut für Technische Physik (ITP)	Prof. Dr. P. Komarek	3500
Institute for Micro Process Engineering	Institut für Mikroverfahrenstechnik (IMVT)	Dr. K. Schubert	3114
- Tritium Laboratory Karlsruhe	- Tritiumlabor Karlsruhe (TLK)	Dr. M. Glugla	3226
Institute for Data Processing and Electronics	Institut für Prozessdatenverarbeitung und Elektronik (IPE)	Prof. Dr. H. Gemmeke	5635

Contributing:

Institute for Nuclear and Particle Physics, Technical University Dresden	Institut für Kern- und Teilchenphysik Technischen Universität Dresden	Prof. Dr. H. Freiesleben	+49 351/4635461
Max-Planck-Institute for Plasma Physics Berlin	Max-Planck-Institut für Plasmaphysik Berlin	Prof. Dr. G. Fussmann	+49 30/20366130
Max-Planck-Institute for Plasma Physics Berlin	Max-Planck-Institut für Plasmaphysik Berlin	Prof. Dr. B. Jüttner	+49 30/20246 760
Institute for Applied Physics University Frankfurt	Institut für Angewandte Physik J.W. Goethe-Universität Frankfurt	Prof. Dr. H. Klein	+49 69/7982 3489

Appendix II: Fusion Programme Management Staff

Head of the Research Unit	Dr. G. Janeschitz	ext. 5460 e-mail: guenter.janeschitz@fusion.fzk.de
Secretariat:	Mrs. I. Sickinger	ext. 5461 e-mail: ingeborg.sickinger@fusion.fzk.de
	Mrs M. Winkelmann	ext. 5466 e-mail: miriam.winkelmann@fusion.fzk.de
Programme Budgets, Administration, Documentation	BW. G. Kast	ext. 5462 e-mail: guenter.kast@fusion.fzk.de
	Mrs. V. Lallemand	ext. 6461 e-mail: vera.lallemand@fusion.fzk.de
	Mrs. I. Pleli	ext. 6461 e-mail: ingrid.pleli@fusion.fzk.de
Blanket Technology, Reactor Studies, Neutron Source, Gyrotron Development, Public Relations	DI. W. Bahm	ext. 5465 e-mail: werner.bahm@fusion.fzk.de
Tritium Technology, Structural Materials, Superconducting Magnets	DI. S. Gross	ext. 5468 e-mail: sigurd.gross@fusion.fzk.de

Address:	**Forschungszentrum Karlsruhe GmbH** **Nuclear Fusion Programme Management** **Post Office Box 3640, D - 76021 Karlsruhe / Germany**
Telephone No:	**07247-82- Extensions .....**
Telefax No:	**07247-82-5467**
world wide web:	**http://www.fzk.de/fusion**

Appendix III: Glossary

ACP	Actived Corrosion Products
ADC	Analog Digital Converter
ADS	Atmosphere Detritiation System
AGHS	Active Gas Handling System
ANFIBE	Ânalysis of Fusion Irradiated Beryllium
ASER	Actively Stabilized External Resonator
BET	Brunauer, Emmet and Teller
BIOMASS	BIOspheric Modelling and ASSessment
BSMI	Bed-structure Mechanical Interaction
CAD	Computer Aided Design
CBM	Carbon Based Materials
CCD	Charge Coupled Device
CCT	Continuous Cooling Transformation
CD	Current Drive
CDA	Conceptual Design Activity
CDE	Conceptual Design Evaluation
CECE	Combined Electrolysis and Catalytic Exchange
CFC	Carbon Fibre Composite
CFD	Computational Fluid Dynamics
CFTM	Creep Fatigue Test Module
CICC	Cable in Conduit Conductor
COINLOSS	Conductor Insulation Loss (software module)
COOLSORP	Measurement of Sorption Isotherms at Cryogenic Temperatures
CP	Cooling Plate
CRPP-EPFL	Centre de Recherches en Physique des Plasmas Ecole Polytechnique Fédérale de Lausanne
CS	Central Solenoïd
CT	Cold Trap
CT	Compact Tension
CVD	Chemical Vapor Deposition
CW	Continuous Wave
D	Deuterium
DBTT	Ductile Brittle Transition Temperature
DCLL	Dual Coolant Lithium-Lead
DNB	Diagnostic Neutral Beam
DP	Dew Point

DT	Deuterium Tritium
DTE1	Deuterium Tritium Experiment 1 at JET
DTL	Drift Tube Linear, accelerator structure
EAF	European Activation File
EASY	European Activation System
EB	Electron Beam
ECE	Electron Cyclotron Emission
EC(R)H	Electron Cyclotron (Resonance) Heating
ECCD	Electron Cyclotron Current Drive
EDM	Electro Discharge Method
EDS	Exhaust Detriation System
EFDA	European Fusion Development Agreement
EFF	European Fusion File
EISSG	European ITER Site Study Group
ELM	Edge Localized Mode
EMPA	Electron Microprobe Analysis
EOL	End-of-Life
ESS	European Spallation Source
EVITA	Experimental Vacuum Ingress Test Apparatus
FBI	F = Force, B = Magnetic Field, I = Current
FCGR	Fatigue Crack Growth Rate
FCI	Flow-channel Inserts
FDR	Final Design Report
FE	Finite Element
FEAT	Fusion Energy Advanced Tokamak
FEM	Finite Element Method
FM	Ferritic-martensitic
FNG	Frascati Neutron Generator
FPCC	Fusion Power Coordination Committee
FW	First Wall
GC	Gas Chromatograph
HCLL	Helium Cooled Lithium-Lead
HCPB	Helium Cooled Pebble Bed
HCS	Helium Cooling Subsystem
HD	Hot Dip
HEBLO	Helium Blanket Test Loop
HECOP	Heat Conduction of Pebble Bed

HEMP	Helium Cooled Modular Divertor Concept with Pin Array
HETP	High Equivalent to a Theoretical Plate
HFI	High Fluence Irradiation
HFR	High Flux Reactor at Petten
HFTM	High Flux Test Module
HIDOBE	High Dose Beryllium Irradiation
HIP	Hot Isostatic Pressing
HNB	Heating Neutral Beam
HP	Heating Plate
HTS	High Temperature Superconducting
HVAC	Heating, Ventilation, Air Conditioning
IAEA	International Atomic Energy Agency
ICS	Intercoil Structure
IEAF	Intermediate Energy Activation File
IFMIF	International Fusion Materials Irradiation Facility
IGA	Inert Gas Atomization
IGUN®	Ion GUN, program code
IP	Impurity Processing
IPF	Institut für Plasmaforschung der Universität Stuttgart
ISRM	Inelastic Strain Rate Modified
ISS	Isotope Separation System
ITER	International Thermonuclear Experimental Reactor
IVP	In Vessel Penetrator
JAERI	Japan Atomic Energy Research Institute
JASS	Joint Assessment of Specific Sites
JETT	J Evaluation on Tensile Test
LARA	Laser-Raman Analysis System
LCF	Low Cycle Fatigue
LCT	Large Coil Task
LEBT	Low Energy Beam Transport
LLW	Low Level Waste
LINAC	Linear Accelerator
LM	Liquid-metal
LOCA	Loss of Coolant Accident
LOFA	Loss of Flow Accident
LPCE	Liquid Phase Catalytic Exchange
LRS	Laser Raman Spectroscopy

LSC	Liquid Scintillation Counting
MAG	Metal Arc Gas (Weld)
MAGS	Magnet Safety (software module)
MBWG	Multi Beam Wave Guide
MCNP	Monte Carlo Neutron Particle
MCE	Multi-channel Effect
MD	Molecular Dynamics
MEBT	Medium Energy Beam Transport
MEKKA	Magneto-hydrodynamic Experiments in Sodium and Potassium Karlsruhe
MFTM	Medium Flux Test Module
MHD	Magneto Hydrodynamics
MPACVD	Microwave Plasma Assisted Chemical Vapor Deposition
MS	Mass Spectrometry
MS	Molecular Sieve
MTS	Material Testing Systems (Trade mark of MTS company)
NB	Neutral Beam
ODS	Oxide Dispersion Strengthened
PCP	Prototype Cryosorption Pump
PD	Point Defect
PERMCAT	Permeator Catalyst
PF	Poloïdal Field
PFC	Plasma Facing Components
PFD	Process Flow Diagram
PFM	Plasma Facing Material
PICOLO	Pb-Li Corrosion Loop
PID	Pipe and Instrumentation Diagram
PIE	Post Irradiation Examination
PKA	Primary Knocked on Atom
PPCS	Power Plant Conceptual Study
QMS	Quadrupole Mass Spectrometer
QTE	Quasi-Thermo-Equilibrium
RA	Reduced Activation
RAFM	Reduced Activation Ferritic Martensitic
REP	Rotating Electrode Process
RF	Radio Frequency
RFQ	Radio Frequency Quadrupol, accelerator structure
R-MHD	Radiation Magnetohydrodynamics

RMS	Root Mean Square
SAD	Secondary Angular Distributions
SAGBO	Stress Accelerated Grain Boundary Oxidation
SANS	Small Angle Neutron Scattering
SCLL	SiC Lithium Lead
SCM	Super Conducting Magnetic System
SDS	Storage and Delivery System
SEM	Scanning Electron Microscope
SiC	Silicon Carbide
SNS	Spallation Neutron Source
SOL	Scrape-off Layer
SULTAN	Superconductor Test Facility, Villigen, Switzerland
TBM	Test Blanket Module
TBR	Tritium Breeding Ratio
TCD	Thermal Conductivity Detector
TCF	Thermal Low Cycle Fatigue
TCWS	Tokamak Cooling Water System
TEM	Transmission Electron Microscope
TEP	Tokamak Exhaust Processing
TES	Tritium Extraction System
TFMC	Toroïdal Field Model Coil
TFTR	Tokamak Fusion Test Reactor
TIG	Tungsten Inert Gas
TIMO	Test Facility for ITER Model Pump
TITAN	Tieftemperaturadsorption
TLK	Tritium Laboratory Karlsruhe
TMS	Tritium Measurement System
TOSKA	Torusspulen Testanordnung Karlsruhe
TPB	Tritium Permeation Barrier
TRM	Tritium Release Module
TTE	Trace Tritium Experiment
TÜV	Technischer Überwachungs Verein
UCT	Uniaxial Compression Test
USE	Upper Shelf Energy
VDE	Vertical Displaced Event
VHP	Vacuum Hot Pressing
VTA	Vertical Test Assemblies

WCLL	Water Cooled Lithium-lead Blanket
WDS	Water Detritation System
XRD	X-ray Diffraction Analysis
ZrCo	Zirconium-Cobalt